How research funders profit from hidden investments *p. 1100*

New books for budding scientists *p. 1104*

Drug leads for malaria *pp. 1112 & 1129*

Science

$15
7 DECEMBER 2018
sciencemag.org

AAAS

A DIGITAL PRODIGY

AlphaZero teaches itself chess, shogi, and Go

pp. 1087, 1118, & 1140

CONTENTS

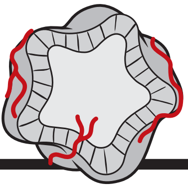

1116 Adapting tissue regeneration

7 DECEMBER 2018 • VOLUME 362 • ISSUE 6419

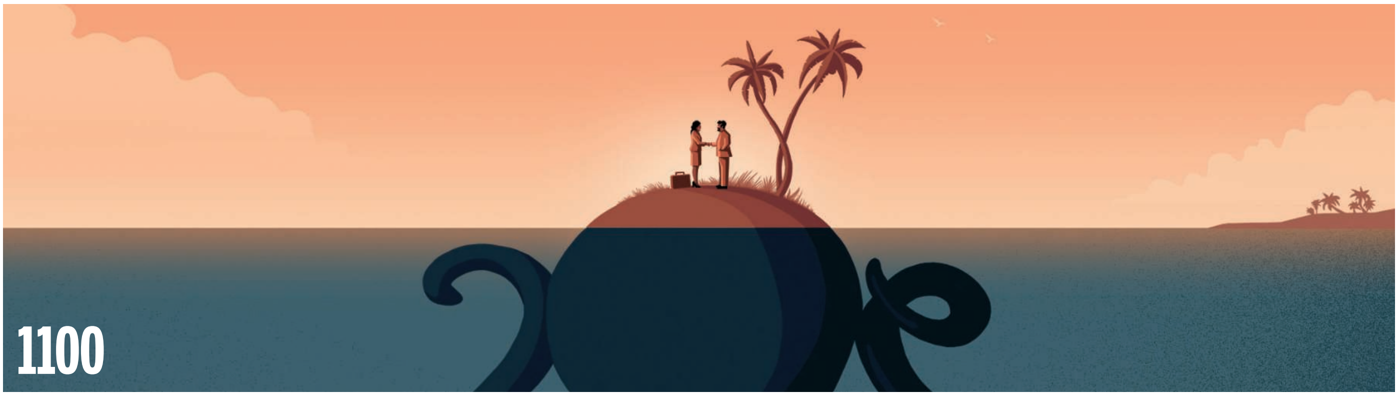

NEWS

IN BRIEF

1088 News at a glance

IN DEPTH

1090 WHAT NOW FOR HUMAN GENOME EDITING?

Claimed creation of CRISPR-edited babies triggers calls for international oversight *By J. Cohen*

1091 For China, a CRISPR first goes too far *By D. Normile*

1092 UNCERTAINTY BOOSTS BREXIT JITTERS FOR U.K. SCIENTISTS

Political turmoil in Parliament threatens a disastrous crash out of the European Union *By E. Stokstad*

1094 UNIVERSAL FLU VACCINE IS 'AN ALCHEMIST'S DREAM'

The rapidly changing virus and a complex immune response stymie vaccine developers *By J. Cohen*

1095 DEMOTION DISMAYS RESEARCHERS AT STORIED DANISH MUSEUM

Merger with biology department could undermine research *By G. Vogel*

FEATURES

1096 TAKING AIM

After her own violent childhood, emergency physician Rebecca Cunningham is jump-starting research to prevent gun deaths in kids *By M. Wadman*

▸ PODCAST

1100 AT ARM'S LENGTH

Major private research funders make secretive offshore investments, raising ethical concerns *By C. Piller*

▸ PODCAST

INSIGHTS

BOOKS *ET AL.*

1104 BOOKS FOR BUDDING SCIENTISTS

PERSPECTIVES

1111 BARRIER(LESS) ISLANDS

No stopping 1D crystals
By B. Kahr and M. D. Ward

▸ REPORT P. 1135

1112 TOWARD A CHEMICAL VACCINE FOR MALARIA

A high-throughput screen puts us on the road to protecting populations against malaria
By M. A. Phillips and D. E. Goldberg

▸ RESEARCH ARTICLE P. 1129

1113 CLIMATE CHANGE AND MARINE MASS EXTINCTION

The end of the Permian Period was catastrophic for life in high-latitude regions *By L. Kump*

▸ RESEARCH ARTICLE P. 1130

1114 BIOENERGETICS THROUGH THICK AND THIN

Membrane fluidity influences the efficiency of oxidative energy metabolism *By E. A. Schon*

▸ REPORT P. 1186

1116 ENDOTHELIAL CELL ADAPTATION IN REGENERATION

Tissue-specific endothelial cells maintain organ homeostasis and instruct regeneration
By J. M. Gomez-Salinero and S. Rafii

1118 MASTERING BOARD GAMES

A single algorithm can learn to play three hard board games *By M. Campbell*

▸ EDITORIAL P. 1087; REPORT P. 1140

POLICY FORUM

1119 FLAWED ANALYSES OF U.S. AUTO FUEL ECONOMY STANDARDS

A 2018 analysis discarded at least $112 billion in benefits *By A. M. Bento* et al.

LETTERS

1122 MODEL VS. EXPERIMENT TO PREDICT CROP LOSSES

By C. Parmesan et al.

1122 Response *By C. A. Deutsch* et al.

1123 NO CONFLICT OF INTEREST IN DATA MONITORING

By J. L. Halperin

CREDITS: (TOP TO BOTTOM) JOSHUA BIRD/*SCIENCE*; STEPHAN SCHMITZ/FOLIO ART; IMAGEBROKER/ALAMY STOCK PHOTO

Downloaded from http://science.sciencemag.org/ on December 10, 2018

Published by AAAS

CONTENTS

7 DECEMBER 2018 • VOLUME 362 • ISSUE 6419

RESEARCH

IN BRIEF

REVIEW

RESEARCH ARTICLES

REPORTS

SIGNAL TRANSDUCTION

DEPARTMENTS

ON THE COVER

Starting from random play and given no domain knowledge except the game rules, the AlphaZero program taught itself to play chess, shogi, and Go, defeating a world champion program in each game. Blue translucent pieces represent AlphaZero's possible moves; percentages indicate the predicted outcome. A single algorithm that can master several complex problems is an important step toward creating a general-purpose machine learning system to tackle real-world problems. See pages 1087, 1118, and 1140.
Image: DeepMind Technologies Limited

CREDITS: (TOP TO BOTTOM) E. HAECKEL; ROBERT NEUBECKER

SCIENCE (ISSN 0036-8075) is published weekly on Friday, except last week in December, by the American Association for the Advancement of Science, 1200 New York Avenue, NW, Washington, DC 20005. Periodicals mail postage (publication No. 484460) paid at Washington, DC, and additional mailing offices. Copyright © 2018 by the American Association for the Advancement of Science. The title SCIENCE is a registered trademark of the AAAS. Domestic individual membership, including subscription (12 months): $165 ($74 allocated to subscription). Domestic institutional subscription (51 issues): $1808; Foreign postage extra: Mexico, Caribbean (surface mail) $55; other countries (air assist delivery): $89. First class, airmail, student, and emeritus rates on request. Canadian rates with GST available upon request, GST #125488122. Publications Mail Agreement Number 1069624. **Printed in the U.S.A.**
Change of address: Allow 4 weeks, giving old and new addresses and 8-digit account number. **Postmaster:** Send change of address to AAAS, P.O. Box 96178, Washington, DC 20090–6178. **Single-copy sales:** $15 each plus shipping and handling; bulk rate on request. **Authorization to reproduce** material for internal or personal use under circumstances not falling within the fair use provisions of the Copyright Act is granted by AAAS to libraries and others who use Copyright Clearance Center (CCC) Pay-Per-Use services provided that $35.00 per article is paid directly to CCC, 222 Rosewood Drive, Danvers, MA 01923. The identification code for *Science* is 0036-8075. *Science* is indexed in the *Reader's Guide to Periodical Literature* and in several specialized indexes.

Published by AAAS

Downloaded from http://science.sciencemag.org/ on December 10, 2018

Science

1200 New York Avenue, NW, Washington, DC 20005
Clarendon House, Clarendon Road, Cambridge, UK CB2 8FH

AAAS

Editor-in-Chief Jeremy Berg

Executive Editor Monica M. Bradford **News Editor** Tim Appenzeller

Editor, Insights Lisa D. Chong **Editors, Research** Valda Vinson, Jake S. Yeston

Research and Insights

DEPUTY EDITORS Julia Fahrenkamp-Uppenbrink(UK), Stella M. Hurtley(UK), Phillip D. Szuromi, Sacha Vignieri **SR. EDITORIAL FELLOW** Andrew M. Sugden(UK) **SR. EDITORS** Gemma Alderton(UK), Caroline Ash(UK), Pamela J. Hines, Paula A. Kiberstis, Marc S. Lavine(Canada), Steve Mao, Ian S. Osborne(UK), Beverly A. Purnell, L. Bryan Ray, H. Jesse Smith, Jelena Stajic, Peter Stern(UK), Brad Wible, Laura M. Zahn **ASSOCIATE EDITORS** Michael A. Funk, Brent Grocholski, Priscilla N. Kelly, Tage S. Rai, Seth Thomas Scanlon(UK), Keith T. Smith(UK) **ASSOCIATE BOOK REVIEW EDITOR** Valerie B. Thompson **LETTERS EDITOR** Jennifer Sills **LEAD CONTENT PRODUCTION EDITORS** Harry Jach, Lauren Kmec **CONTENT PRODUCTION EDITORS** Amelia Beyna, Jeffrey E. Cook, Amber Esplin, Chris Filiatreau, Cynthia Howe, Nida Masiulis **SR. EDITORIAL COORDINATORS** Carolyn Kyle, Beverly Shields **EDITORIAL COORDINATORS** Aneera Dobbins, Joi S. Granger, Jeffrey Hearn, Lisa Johnson, Maryrose Madrid, Shannon McMahon, Jerry Richardson, Alice Whaley(UK), Anita Wynn **PUBLICATIONS ASSISTANTS** Ope Martins, Ronmel Navas, Hilary Stewart(UK), Alana Warnke, Brian White **EXECUTIVE ASSISTANT** Jessica Slater **ASI DIRECTOR, OPERATIONS** Janet Clements(UK) **ASI SR. OFFICE ADMINISTRATOR** Jessica Waldock(UK)

News

NEWS MANAGING EDITOR John Travis **INTERNATIONAL EDITOR** Martin Enserink **DEPUTY NEWS EDITORS** Elizabeth Culotta, Lila Guterman, David Grimm, Eric Hand, David Malakoff **SR. CORRESPONDENTS** Daniel Clery(UK), Jon Cohen, Jeffrey Mervis, Elizabeth Pennisi **ASSOCIATE EDITORS** Jeffrey Brainard, Catherine Matacic **NEWS WRITERS** Adrian Cho, Jennifer Couzin-Frankel, Jocelyn Kaiser, Kelly Servick, Robert F. Service, Erik Stokstad(Cambridge, UK), Paul Voosen, Meredith Wadman **INTERN** Frankie Schembri **CONTRIBUTING CORRESPONDENTS** Warren Cornwall, Ann Gibbons, Mara Hvistendahl, Sam Kean, Eli Kintisch, Kai Kupferschmidt(Berlin), Andrew Lawler, Mitch Leslie, Eliot Marshall, Virginia Morell, Dennis Normile(Shanghai), Charles Piller, Tania Rabesandratana(London), Emily Underwood, Gretchen Vogel(Berlin), Lizzie Wade(Mexico City) **CAREERS** Donisha Adams, Rachel Bernstein(Editor), Katie Langin **COPY EDITORS** Julia Cole (Senior Copy Editor), Cyra Master (Copy Chief) **ADMINISTRATIVE SUPPORT** Meagan Weiland

Executive Publisher Rush D. Holt

Publisher Bill Moran

DIRECTOR, BUSINESS STRATEGY AND PORTFOLIO MANAGEMENT Sarah Whalen **DIRECTOR, PRODUCT AND CUSTOM PUBLISHING** Will Schweitzer **MANAGER, PRODUCT DEVELOPMENT** Hannah Heckner **BUSINESS SYSTEMS AND FINANCIAL ANALYSIS DIRECTOR** Randy Yi **DIRECTOR, BUSINESS OPERATIONS & ANALYST** Eric Knott **ASSOCIATE DIRECTOR, PRODUCT MANAGMENT** Kris Bishop **SENIOR SYSTEMS ANALYST** Nicole Mehmedovich **SENIOR BUSINESS ANALYST** Cory Lipman **MANAGER, BUSINESS OPERATIONS** Jessica Tierney **BUSINESS ANALYSTS** Meron Kebede, Sandy Kim, Jourdan Stewart **FINANCIAL ANALYST** Julian Iriarte **ADVERTISING SYSTEM ADMINISTRATOR** Tina Burks **SALES COORDINATOR** Shirley Young **DIRECTOR, COPYRIGHT, LICENSING, SPECIAL PROJECTS** Emilie David **DIGITAL PRODUCT ASSOCIATE** Michael Hardesty **RIGHTS AND PERMISSIONS ASSOCIATE** Elizabeth Sandler **RIGHTS, CONTRACTS, AND LICENSING ASSOCIATE** Lili Catlett **RIGHTS & PERMISSIONS ASSISTANT** Alexander Lee

DIRECTOR, INSTITUTIONAL LICENSING Iquo Edim **ASSOCIATE DIRECTOR, RESEARCH & DEVELOPMENT** Elisabeth Leonard **SENIOR INSTITUTIONAL LICENSING MANAGER** Ryan Rexroth **INSTITUTIONAL LICENSING MANAGERS** Marco Castellan, Chris Murawski **SENIOR OPERATIONS ANALYST** Lana Guz **MANAGER, AGENT RELATIONS & CUSTOMER SUCCESS** Judy Lillibridge

WEB DEVELOPMENT DIRECTOR David Levy **PROJECT MANAGER** Virginia Bramante

DIGITAL MEDIA DIRECTOR OF ANALYTICS Enrique Gonzales **DIGITAL REPORTING ANALYST** Timothy Frailey **MULTIMEDIA MANAGER** Sarah Crespi **MANAGING WEB PRODUCER** Kara Estelle-Powers **DIGITAL PRODUCER** Jessica Hubbard **VIDEO PRODUCERS** Chris Burns, Meagan Cantwell

DIGITAL/PRINT STRATEGY MANAGER Jason Hillman **QUALITY TECHNICAL MANAGER** Marcus Spiegler **DIGITAL PRODUCTION MANAGER** Lisa Stanford **ASSISTANT MANAGER DIGITAL/PRINT** Rebecca Doshi **SENIOR CONTENT SPECIALISTS** Steve Forrester, Antoinette Hodal, Lori Murphy **CONTENT SPECIALISTS** Jacob Hedrick, Kimberley Oster

DESIGN DIRECTOR Beth Rakouskas **DESIGN MANAGING EDITOR** Marcy Atarod **SENIOR DESIGNER** Chrystal Smith **DESIGNER** Christina Aycock **GRAPHICS MANAGING EDITOR** Alberto Cuadra **GRAPHICS EDITOR** Nirja Desai **SENIOR SCIENTIFIC ILLUSTRATORS** Valerie Altounian, Chris Bickel **SCIENTIFIC ILLUSTRATOR** Alice Kitterman **INTERACTIVE GRAPHICS EDITOR** Jia You **SENIOR GRAPHICS SPECIALISTS** Holly Bishop, Nathalie Cary **PHOTOGRAPHY MANAGING EDITOR** William Douthitt **PHOTO EDITOR** Emily Petersen **IMAGE RIGHTS AND FINANCIAL MANAGER** Jessica Adams

SENIOR EDITOR, CUSTOM PUBLISHING Sean Sanders: 202-326-6430 **ASSISTANT EDITOR, CUSTOM PUBLISHING** Jackie Oberst: 202-326-6463 **ADVERTISING PRODUCTION OPERATIONS MANAGER** Deborah Tompkins **SR. PRODUCTION SPECIALIST/GRAPHIC DESIGNER** Amy Hardcastle **SR. TRAFFIC ASSOCIATE** Christine Hall **DIRECTOR OF BUSINESS DEVELOPMENT AND ACADEMIC PUBLISHING RELATIONS, ASIA** Xiaoying Chu: +86-131 6136 3212, xchu@aaas.org **COLLABORATION/CUSTOM PUBLICATIONS/JAPAN** Adarsh Sandhu + 81532-81-5142 asandhu@aaas.org **EAST COAST/E. CANADA** Laurie Faraday: 508-747-9395, FAX 617-507-8189 **WEST COAST/W. CANADA** Lynne Stickrod: 415-931-9782, FAX 415-520-6940 **MIDWEST** Jeffrey Dembksi: 847-498-4520 x3005, Steven Loerch: 847-498-4520 x3006 **UK EUROPE/ASIA** Roger Goncalves: TEL/FAX +41 43 243 1358 **JAPAN** Kaoru Sasaki (Tokyo): + 81 (3) 6459 4174 ksasaki@aaas.org

ASSOCIATE DIRECTOR, BUSINESS DEVELOPMENT Justin Sawyers **GLOBAL MARKETING MANAGER** Allison Pritchard **DIGITAL MARKETING ASSOCIATE** Aimee Aponte **MARKETING MANAGER, JOURNALS** Shawana Arnold **MARKETING ASSOCIATES** Mike Romano, Tori Velasquez **SENIOR DESIGNER** Kim Huynh **TRADE SHOW COORDINATOR** Andrew Clamp

GLOBAL SALES DIRECTOR ADVERTISING AND CUSTOM PUBLISHING Tracy Holmes: +44 (0) 1223 326525 **CLASSIFIED** advertise@sciencecareers.org **SALES MANAGER, US, CANADA AND LATIN AMERICA SCIENCE CAREERS** Claudia Paulsen-Young: 202-326-6577, **EUROPE/ROW SALES** Sarah Lelarge **SALES ADMIN ASSISTANT** Kelly Grace +44 (0)1223 326528 **JAPAN** Miyuki Tani(Osaka): +81 (6) 6202 6272 mtani@aaas.org **CHINA/TAIWAN** Xiaoying Chu: +86-131 6136 3212, xchu@aaas.org

AAAS BOARD OF DIRECTORS, CHAIR Susan Hockfield **PRESIDENT** Margaret A. Hamburg **PRESIDENT-ELECT** Steven Chu **TREASURER** Carolyn N. Ainslie **CHIEF EXECUTIVE OFFICER** Rush D. Holt **BOARD** Cynthia M. Beall, May R. Berenbaum, Rosina M. Bierbaum, Kaye Husbands Fealing, Stephen P.A. Fodor, S. James Gates, Jr., Michael S. Gazzaniga, Laura H. Greene, Robert B. Millard, Mercedes Pascual, William D. Provine

SUBSCRIPTION SERVICES For change of address, missing issues, new orders and renewals, and payment questions: 866-434-AAAS (2227) or 202-326-6417, FAX 202-842-1065. Mailing addresses: AAAS, P.O. Box 96178, Washington, DC 20090-6178 or AAAS Member Services, 1200 New York Avenue, NW, Washington, DC 20005

INSTITUTIONAL SITE LICENSES 202-326-6730 **REPRINTS:** Author Inquiries 800-635-7181 **COMMERCIAL INQUIRIES** 803-359-4578 **PERMISSIONS** 202-326-6765, permissions@aaas.org **AAAS Member Central Support** 866-434-2227 www.aaas.org/membercentral.

Science serves as a forum for discussion of important issues related to the advancement of science by publishing material on which a consensus has been reached as well as including the presentation of minority or conflicting points of view. Accordingly, all articles published in *Science*—including editorials, news and comment, and book reviews—are signed and reflect the individual views of the authors and not official points of view adopted by AAAS or the institutions with which the authors are affiliated.

INFORMATION FOR AUTHORS See www.sciencemag.org/authors/science-information-authors

BOARD OF REVIEWING EDITORS (Statistics board members indicated with **S**)

Adriano Aguzzi, *U. Hospital Zürich*
Takuzo Aida, *U. of Tokyo*
Leslie Aiello, *Wenner-Gren Foundation*
Judith Allen, *U. of Manchester*
Sebastian Amigorena, *Institut Curie*
Meinrat O. Andreae, *Max Planck Inst. Mainz*
Paola Arlotta, *Harvard U.*
Johan Auwerx, *EPFL*
David Awschalom, *U. of Chicago*
Clare Baker, *U. of Cambridge*
Nenad Ban, *ETH Zürich*
Franz Bauer, *Pontificia Universidad Católica de Chile*
Ray H. Baughman, *U. of Texas at Dallas*
Carlo Beenakker, *Leiden U.*
Kamran Behnia, *ESPCI*
Yasmine Belkaid, *NIAID, NIH*
Philip Benfey, *Duke U.*
Gabriele Bergers, *VIB*
Bradley Bernstein, *Mass. General Hospital*
Peer Bork, *EMBL*
Chris Bowler, *École Normale Supérieure*
Ian Boyd, *U. of St. Andrews*
Emily Brodsky, *U. of California, Santa Cruz*
Ron Brookmeyer, *U. of California, Los Angeles* (**S**)
Christian Büchel, *UKE Hamburg*
Dennis Burton, *Scripps Research*
Carter Tribley Butts, *U. of California, Irvine*
Gyorgy Buzsaki, *New York U. School of Med.*
Blanche Capel, *Duke U.*
Annmarie Carlton, *U. of California, Irvine*
Nick Chater, *U. of Warwick*
Ib Chorkendorff, *Denmark TU*
James J. Collins, *MIT*
Robert Cook-Deegan, *Arizona State U.*
Lisa Coussens, *Oregon Health & Science U.*
Alan Cowman, *Walter & Eliza Hall Inst.*
Carolyn Coyne, *U. of Pittsburgh*
Roberta Croce, *VU Amsterdam*
Jeff L. Dangl, *U. of North Carolina*
Tom Daniel, *U. of Washington*
Chiara Daraio, *Caltech*
Nicolas Dauphas, *U. of Chicago*
Frans de Waal, *Emory U.*
Stanislas Dehaene, *Collège de France*
Robert Desimone, *MIT*
Claude Desplan, *New York U.*
Sandra Díaz, *Universidad Nacional de Córdoba*
Dennis Discher, *U. of Penn.*
Gerald W. Dorn II, *Washington U. in St. Louis*
Jennifer A. Doudna, *U. of California, Berkeley*
Bruce Dunn, *U. of California, Los Angeles*
William Dunphy, *Caltech*
Christopher Dye, *U. of Oxford*
Todd Ehlers, *U. of Tübingen*
Jennifer Elisseeff, *Johns Hopkins U.*
Tim Elston, *U. of North Carolina*
Nader Engheta, *U. of Penn.*
Barry Everitt, *U. of Cambridge*
Vanessa Ezenwa, *U. of Georgia*
Ernst Fehr, *U. of Zürich*
Michael Feuer, *The George Washington U.*
Toren Finkel, *U. of Pittsburgh Med. Ctr.*
Kate Fitzgerald, *U. of Mass.*
Gwenn Flowers, *Simon Fraser U.*
Peter Fratzl, *Max Planck Inst. Potsdam*
Elaine Fuchs, *Rockefeller U.*
Eileen Furlong, *EMBL*
Jay Gallagher, *U. of Wisconsin*
Susan Gelman, *U. of Michigan*
Daniel Geschwind, *U. of California, Los Angeles*
Karl-Heinz Glassmeier, *TU Braunschweig*
Marta Gonzalez, *U. of California, Berkeley*
Ramon Gonzalez, *Rice U.*
Elizabeth Grove, *U. of Chicago*
Nicolas Gruber, *ETH Zürich*
Kip Guy, *U. of Kentucky College of Pharmacy*
Taekjip Ha, *Johns Hopkins U.*
Christian Haass, *Ludwig Maximilians U.*
Sharon Hammes-Schiffer, *Yale U.*
Wolf-Dietrich Hardt, *ETH Zürich*
Louise Harra, *U. College London*
Michael Hasselmo, *Boston U.*
Jian He, *Clemson U.*
Martin Heimann, *Max Planck Inst. Jena*
Carl-Philipp Heisenberg, *IST Austria*
Ykä Helariutta, *U. of Cambridge*
Janet G. Hering, *Eawag*
Kai-Uwe Hinrichs, *U. of Bremen*
David Hodell, *U. of Cambridge*
Lora Hooper, *UT Southwestern Med. Ctr.*
Fred Hughson, *Princeton U.*
Randall Hulet, *Rice U.*
Auke Ijspeert, *EPFL*
Akiko Iwasaki, *Yale U.*
Stephen Jackson, *USGS and U. of Arizona*
Kai Johnsson, *EPFL*
Peter Jonas, *IST Austria*
Matt Kaeberlein, *U. of Washington*
William Kaelin Jr., *Dana-Farber Cancer Inst.*
Daniel Kammen, *U. of California, Berkeley*
Abby Kavner, *U. of California, Los Angeles*
Masashi Kawasaki, *U. of Tokyo*
V. Narry Kim, *Seoul Nat. U.*
Robert Kingston, *Harvard Med. School*
Nancy Knowlton, *Smithsonian Institution*
Etienne Koechlin, *École Normale Supérieure*
Alexander Kolodkin, *Johns Hopkins U.*
Thomas Langer, *U. of Cologne*
Mitchell A. Lazar, *U. of Penn.*
David Lazer, *Harvard U.*
Stanley Lemon, *U. of North Carolina*
Ottoline Leyser, *U. of Cambridge*
Wendell Lim, *U. of California, San Francisco*
Marcia C. Linn, *U. of California, Berkeley*
Jianguo Liu, *Michigan State U.*
Luis Liz-Marzán, *CIC biomaGUNE*
Jonathan Losos, *Harvard U.*
Ke Lu, *Chinese Acad. of Sciences*
Christian Lüscher, *U. of Geneva*
Fabienne Mackay, *U. of Melbourne*
Anne Magurran, *U. of St. Andrews*
Oscar Marín, *King's College London*
Charles Marshall, *U. of California, Berkeley*
Christopher Marx, *U. of Idaho*
Geraldine Masson, *CNRS*
C. Robertson McClung, *Dartmouth College*
Rodrigo Medellín, *U. of Mexico*
Graham Medley, *London School of Hygiene & Tropical Med.*
Jane Memmott, *U. of Bristol*
Edward Miguel, *U. of California, Berkeley*
Tom Misteli, *NCI, NIH*
Yasushi Miyashita, *U. of Tokyo*
Richard Morris, *U. of Edinburgh*
Alison Motsinger-Reif, *NC State U.* (**S**)
Daniel Nettle, *Newcastle U.*
Daniel Neumark, *U. of California, Berkeley*
Kitty Nijmeijer, *TU Eindhoven*
Helga Nowotny, *Austrian Council*
Rachel O'Reilly, *U. of Warwick*
Harry Orr, *U. of Minnesota*
Pilar Ossorio, *U. of Wisconsin*
Andrew Oswald, *U. of Warwick*
Isabella Pagano, *Istituto Nazionale di Astrofisica*
Margaret Palmer, *U. of Maryland*
Elizabeth Levy Paluck, *Princeton U.*
Jane Parker, *Max Planck Inst. Cologne*
Giovanni Parmigiani, *Dana-Farber Cancer Inst.* (**S**)
Samuel Pfaff, *Salk Inst. for Biological Studies*
Julie Pfeiffer, *UT Southwestern Med. Ctr.*
Matthieu Piel, *Institut Curie*
Kathrin Plath, *U. of California, Los Angeles*
Martin Plenio, *Ulm U.*
Albert Polman, *FOM Inst. for AMOLF*
Elvira Poloczanska, *Alfred-Wegener-Inst.*
Julia Pongratz, *Ludwig Maximilians U.*
Philippe Poulin, *CNRS*
Jonathan Pritchard, *Stanford U.*
David Randall, *Colorado State U.*
Félix A. Rey, *Institut Pasteur*
Trevor Robbins, *U. of Cambridge*
Amy Rosenzweig, *Northwestern U.*
Mike Ryan, *U. of Texas at Austin*
Mitinori Saitou, *Kyoto U.*
Shimon Sakaguchi, *Osaka U.*
Miquel Salmeron, *Lawrence Berkeley Nat. Lab*
Nitin Samarth, *Penn. State U.*
Jürgen Sandkühler, *Med. U. of Vienna*
Alexander Schier, *Harvard U.*
Wolfram Schlenker, *Columbia U.*
Susannah Scott, *U. of California, Santa Barbara*
Vladimir Shalaev, *Purdue U.*
Beth Shapiro, *U. of California, Santa Cruz*
Jay Shendure, *U. of Washington*
Brian Shoichet, *U. of California, San Francisco*
Robert Siliciano, *Johns Hopkins U. School of Med.*
Uri Simonsohn, *U. of Penn.*
Lucia Sivilotti, *U. College London*
Alison Smith, *John Innes Centre*
Richard Smith, *U. of North Carolina* (**S**)
Mark Smyth, *QIMR Berghofer*
Pam Soltis, *U. of Florida*
John Speakman, *U. of Aberdeen*
Tara Spires-Jones, *U. of Edinburgh*
Allan C. Spradling, *Carnegie Institution for Science*
Paula Stephan, *Georgia State U.*
V. S. Subrahmanian, *U. of Maryland*
Ira Tabas, *Columbia U.*
Sarah Teichmann, *U. of Cambridge*
Shubha Tole, *Tata Inst. of Fundamental Research*
Wim van der Putten, *Netherlands Inst. of Ecology*
Bert Vogelstein, *Johns Hopkins U.*
Kathleen Vohs, *U. of Minnesota*
David Wallach, *Weizmann Inst. of Science*
Jane-Ling Wang, *U. of California, Davis* (**S**)
David Waxman, *Fudan U.*
Jonathan Weissman, *U. of California, San Francisco*
Chris Wikle, *U. of Missouri* (**S**)
Terrie Williams, *U. of California, Santa Cruz*
Ian A. Wilson, *Scripps Research* (**S**)
Yu Xie, *Princeton U.*
Jan Zaanen, *Leiden U.*
Kenneth Zaret, *U. of Penn. School of Med.*
Jonathan Zehr, *U. of California, Santa Cruz*
Maria Zuber, *MIT*

Published by AAAS

EDITORIAL

Chess, a Drosophila of reasoning

The recent world chess championship saw Magnus Carlsen defend his title against Fabiano Caruana. But it was not a contest between the two strongest chess players on the planet, only the strongest humans. Soon after I lost my rematch against IBM's Deep Blue in 1997, the short window of human-machine chess competition slammed shut forever. Unlike humans, machines keep getting faster, and today a smartphone chess app can be stronger than Deep Blue. But as we see with the AlphaZero system (see pages 1118 and 1140), machine dominance has not ended the historical role of chess as a laboratory of cognition.

"...machine dominance has not ended the historical role of chess as a laboratory of cognition."

Much as the *Drosophila melanogaster* fruit fly became a model organism for geneticists, chess became a *Drosophila* of reasoning. In the late 19th century, Alfred Binet hoped that understanding why certain people excelled at chess would unlock secrets of human thought. Sixty years later, Alan Turing wondered if a chess-playing machine might illuminate, in the words of Norbert Wiener, "whether this sort of ability represents an essential difference between the potentialities of the machine and the mind."

Much as airplanes don't flap their wings like birds, machines don't generate chess moves like humans do. Early programs that attempted it were weak. Success came with the "minimax" algorithm and Moore's law, not with the ineffable human combination of pattern recognition and visualization. This prosaic formula dismayed the artificial intelligence (AI) crowd, who realized that profound computational insights were not required to produce a machine capable of defeating the world champion.

But now the chess fruit fly is back under the microscope. Based on a generic game-playing algorithm, AlphaZero incorporates deep learning and other AI techniques like Monte Carlo tree search to play against itself to generate its own chess knowledge. Unlike top traditional programs like Stockfish and Fritz, which employ many preset evaluation functions as well as massive libraries of opening and endgame moves, AlphaZero starts out knowing only the rules of chess, with no embedded human strategies. In just a few hours, it plays more games against itself than have been recorded in human chess history. It teaches itself the best way to play, reevaluating such fundamental concepts as the relative values of the pieces. It quickly becomes strong enough to defeat the best chess-playing entities in the world, winning 28, drawing 72, and losing none in a victory over Stockfish.

I admit that I was pleased to see that AlphaZero had a dynamic, open style like my own. The conventional wisdom was that machines would approach perfection with endless dry maneuvering, usually leading to drawn games. But in my observation, AlphaZero prioritizes piece activity over material, preferring positions that to my eye looked risky and aggressive. Programs usually reflect priorities and prejudices of programmers, but because AlphaZero programs itself, I would say that its style reflects the truth. This superior understanding allowed it to outclass the world's top traditional program despite calculating far fewer positions per second. It's the embodiment of the cliché, "work smarter, not harder."

AlphaZero shows us that machines can be the experts, not merely expert tools. Explainability is still an issue—it's not going to put chess coaches out of business just yet. But the knowledge it generates is information we can all learn from. AlphaZero is surpassing us in a profound and useful way, a model that may be duplicated on any other task or field where virtual knowledge can be generated.

Machine learning systems aren't perfect, even at a closed system like chess. There will be cases where an AI will fail to detect exceptions to their rules. Therefore, we must work together, to combine our strengths. I know better than most people what it's like to compete against a machine. Instead of raging against them, it's better if we're all on the same side.

–Garry Kasparov

Garry Kasparov *is the former world chess champion and the author of* Deep Thinking: Where Machine Intelligence Ends and Human Creativity Begins. *He is chairman of the Human Rights Foundation, New York, NY, USA. kasparov@hrf.org*

10.1126/science.aaw2221

CREDITS: (INSET) DEEPMIND TECHNOLOGIES LIMITED; (RIGHT) IGOR KHODZINSKIY

Downloaded from http://science.sciencemag.org/ on December 10, 2018

Published by AAAS

NEWS

31% Increase in reported measles cases worldwide in 2017, according to the World Health Organization. It blamed the 1-year rise partly on antivaccine messages in Europe and the collapse of Venezuela's health system. Measles killed an estimated 110,000 people in 2017, most of them children.

IN BRIEF

Edited by **Jeffrey Brainard**

SPACE SCIENCE

Sample return probe arrives at asteroid

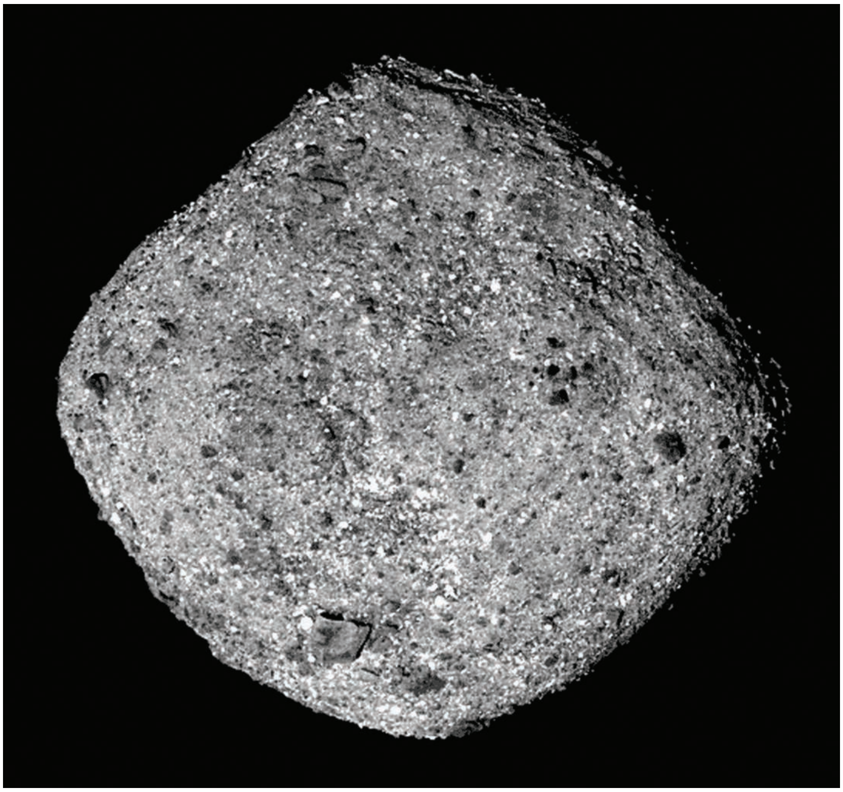

After a 2-year journey, OSIRIS-REx, NASA's $800 million asteroid sample return mission, arrived at its target, an ancient, half-kilometer-wide space rock called Bennu, in search of clues to the formation of the solar system. On 3 December, the spacecraft pulled to within 20 kilometers of the diamond-shaped asteroid. In January 2019, Bennu will become the smallest object circled by a spacecraft when OSIRIS-REx enters an orbit 1.25 kilometers from the surface, enabling it to study the asteroid in detail. The probe will spend more than a year scouting for sampling sites and in mid-2020 will swoop close enough to gather up to 2 kilograms of dust and gravel using a 3-meter robotic arm. A capsule containing that haul will return to Earth in 2023—the first materials NASA will have returned from space since the Apollo moon rocks.

Brazil drops climate summit

SCIENCE POLICY | Brazil last week withdrew its offer to host the 2019 United Nations Climate Change Conference, signaling a shift in the country's stance on global warming. President Michel Temer's administration cited budgetary constraints to explain the withdrawal, but President-elect Jair Bolsonaro, a far-right politician who will take office on 1 January 2019, later said he took part in the decision. Bolsonaro argues that the U.N. climate treaty, known as the Paris agreement, threatens the country's sovereignty over the Amazon; his pick as minister of foreign affairs, Ernesto Araújo, recently wrote that climate change is a "dogma" used in a globalist plot to hurt capitalism for the benefit of China. Scientists and environmentalists denounced the conference decision as ceding Brazil's leadership role in combatting global climate change.

Gene drive moratorium blocked

BIOTECHNOLOGY | For the second time in 2 years, a United Nations body last week voted down a controversial proposal to ban "gene drives," technology that can rapidly spread one or more genes through animals in the wild and might be used to control disease-causing mosquitoes and other harmful organisms. Instead, the Convention on Biological Diversity, meeting in Sharm El Sheikh, Egypt, called on governments to conduct risk assessments before releasing gene drive organisms in the wild and to get informed consent of local communities or indigenous peoples. Scientists had argued against a moratorium, citing the research's potential in the fight against malaria, for example, whereas advocacy groups warned that gene drive organisms could have unintended consequences beyond the target populations. In a separate decision, the convention rejected a hotly debated proposal requiring researchers to get permission from a country before studying publicly available genetic data on organisms originating there. Scientists had warned that the plan would stifle research (*Science*, 6 July, p. 14). Conference delegates agreed only to commission further study of the issue.

PHOTO: NASA'S GODDARD SPACE FLIGHT CENTER/UNIVERSITY OF ARIZONA

Downloaded from http://science.sciencemag.org/ on December 6, 2018

Published by AAAS

ENERGY

Offshore mapping blasts off

In a reversal, the U.S. National Oceanic and Atmospheric Administration has agreed to allow five oil and gas firms to conduct seismic surveys—which use blasts of sound to map seafloor geology—off the Atlantic coast from New Jersey to Florida. The decision is certain to draw legal challenges from environmental groups, who say the agency has underestimated the number of whales, turtles, and other sea creatures likely to be harmed or bothered by the intense noise from submerged air guns. The move is part of a larger effort by President Donald Trump's administration to relax restrictions on offshore drilling imposed by former President Barack Obama. Most Atlantic coastal states oppose such development, worrying it could harm tourism and fishing industries.

Underwater air gun bursts used for oil exploration off the U.S. Atlantic coast will create noise shown elsewhere to injure and disrupt migrations of whales and dolphins.

PHOTO: CHRISTIAN ASLUND

Feynman's unwelcomed prize sold

PHYSICS | Richard Feynman, the iconoclastic physicist who helped lay the theoretical foundation for modern particle physics, detested prizes and honors—so much so that he considered refusing his share of the 1965 Nobel Prize in Physics. Last week, Feynman's heirs parted with the irksome award, as Sotheby's in New York City auctioned it for $975,000. Fifty-three years ago, Feynman's third of the prize money totaled $18,333—$129,000 in today's dollars. He said he was going to use the cash to pay his taxes. In a separate auction this week, Christie's fetched nearly $2.9 million for another relic of science history, a 1954 letter in which Albert Einstein writes, "The word God is for me nothing but the expression of and product of human weaknesses."

Italy dismisses health experts

PUBLIC HEALTH | Italian Minister of Health Giulia Grillo on 3 December fired 30 experts serving on the 56-member National Health Council, sparking fears that she could replace them with vaccine skeptics. Grillo, who belongs to the vaccine-skeptic populist party Five Star Movement, wrote on Facebook that she had "chosen to open the door to other deserving personalities." The Five Star Movement came to power in April, promising to scrap a law from the previous government that had made 10 childhood vaccinations mandatory. In 2017, Italy reported 5098 cases of measles, a third of all reported cases in the European Union.

Celebrity astrophysicist accused

#METOO | Astrophysicist and science communicator Neil deGrasse Tyson came under investigation last week because of sexual misconduct allegations from three women. Ashley Watson, former assistant on the documentary series *Cosmos*, which Tyson has periodically hosted, told Patheos, an interfaith dialogue website, that she quit because of his inappropriate sexual advances and comments. Physicist Katelyn Allers of Bucknell University in Lewisburg, Pennsylvania, says Tyson groped her at an afterparty of an American Astronomical Society event in 2009. Patheos also reported a year ago that musician Tchiya Amet said Tyson drugged and raped her when they were graduate school classmates in 1984. In a Facebook post, Tyson claimed the first two incidents were misinterpreted gestures for which he apologized, and he denied the third. Fox Broadcasting and National Geographic, which have aired *Cosmos*, say they are investigating the allegations, as did the American Museum of Natural History in New York City, where Tyson directs the Hayden Planetarium.

DeepMind aces protein folding

COMPUTER SCIENCE | Mastering chess and Go was just for starters. Fresh off its board-game triumphs, the Google-owned artificial intelligence firm DeepMind took top honors on 2 December in the 13th Critical Assessment of Structure Prediction, a biannual competition aimed at predicting the 3D structure of proteins. Competing teams were given the linear sequence of amino acids for 90 proteins, for which the 3D shape was known but not yet published. Teams then computed how those sequences would fold up. Though DeepMind had not previously joined this competition, the predictions of its AlphaFold software were more accurate than those of its 97 competitors. DeepMind built on previous algorithm strategies; one of them predicts the distance in 3D space between every pair of amino acids in a sequence, based on analyses of thousands of known amino acid sequences and their observed, folded protein structures.

Downloaded from http://science.sciencemag.org/ on December 6, 2018

Published by AAAS

IN DEPTH

BIOLOGY

What now for human genome editing?

Claimed creation of CRISPR-edited babies triggers calls for international oversight

By **Jon Cohen**

Few seemed more surprised by the tide of outrage unleashed by the claim that the first gene-edited babies had been created with the revolutionary lab tool called CRISPR than He Jiankui, the scientist responsible. On the eve of the International Summit on Human Genome Editing in Hong Kong, China, last week, He, a researcher at nearby Southern University of Science and Technology in Shenzhen, China, had dinner at the city's Le Méridien Cyberport with a few of the meeting's organizers. The news of He's claim had just broken, and shock waves were starting to reverberate. But the reports were still so fresh that the diners sat in the restaurant without being disturbed.

"He arrived almost defiant," says Jennifer Doudna, who did landmark CRISPR work at the University of California (UC), Berkeley. She and the other conference organizers politely asked He questions about the scientific details and rationale of his work, the permissions he had secured to conduct it, and how he recruited hopeful parents to participate and informed them about risks. He asked them whether his planned talk 2 days later should include data about the twin girls, who had a gene altered to make them resistant to HIV infection. "We were all like, 'Uh, yes,'" Doudna says.

After more than an hour of questioning, He had had enough. "He just seemed surprised that people were reacting negatively about this," Doudna says. "By the end of the dinner he was pretty upset and left quite abruptly."

Bioethicist Alta Charo of the University of Wisconsin Law School in Madison says He seemed "quite sincere" in his aim to engineer babies who would not suffer the illness and stigma that had plagued their HIV-infected father. He appeared to believe he had complied with ethical guidelines for what's known as germline editing—creating heritable alterations in early embryos, sperm, or eggs. "That kind of rocked me back," Charo says. "He talked about Robert Edwards, the 'father' of IVF [in vitro fertilization]. I got the strong impression that he saw Robert Edwards as a kind of hero, a paradigm breaker, a disrupter, and that he wanted to model himself after that."

It seems unlikely history will view He in the same light as Edwards, who won a Nobel Prize, but the Chinese researcher certainly is a disrupter. His claim has triggered widespread calls for mechanisms to prevent others from germline editing humans until there's an international consensus that the CRISPR technology has matured and there's a convincing medical need. And it has sparked concern that his actions could set back less problematic applications of gene editing: treating diseases by editing nongerm cells, which do not pass their DNA to future generations. "I do hope that this very visible misadventure does not cause a cloud over the entire area of gene editing for therapeutic benefit," says Francis Collins, director of the U.S. National Institutes of Health (NIH) in Bethesda, Maryland, who issued an unusually blunt condemnation of He's work. "I think that would be utterly irrational."

First, though, scientists, ethicists, and government officials are trying to understand how and why He staged this experiment, whether it accomplished the limited success he claims, and whether the babies are healthy. In a hastily arranged, hourlong session at the summit, He reported that in one of the twins, his team had successfully mutated both copies of the gene for CCR5, a protein on immune cells that HIV exploits to establish an infection. Several of his slides were too dense with information for the audience

At the summit, Nobel laureate David Baltimore condemned He Jiankui's work.

PHOTOS: (TOP TO BOTTOM) ANTHONY KWAN/BLOOMBERG/GETTY IMAGES; ISAAC LAWRENCE/AFP/GETTY IMAGES

Downloaded from http://science.sciencemag.org/ on December 6, 2018

Published by AAAS

For his talk at last week's summit, He Jiankui was accompanied by security guards because of threats.

to immediately digest. But closer analysis led many researchers to assert later that both girls had evidence of at least one normal *CCR5* gene, which would mean they were completely susceptible to the AIDS virus. What's more, He has not yet tested whether HIV can infect cells taken from the girls.

At the summit's end, organizers called for an independent assessment of He's work. Some take comfort in the doubts. "I would actually hope … there's not genome-edited humans brought into this world yet," says pediatrician Matthew Porteus of Stanford University in Palo Alto, California, one of the organizers. "It just puts a pit in my stomach."

He said his team has a plan for long-term follow-up of the twins' health, although he did not explain who would fund it. To the relief of many at the meeting, He did present extensive, if preliminary, data indicating that CRISPR had not made unwanted "off-target" cuts in the genomes of the babies, a key safety concern in genome editing. During the questions, He revealed that a second woman is pregnant with a gene-edited baby. A paper on the twins is being considered by a peer-reviewed journal, He said, adding he had been dissuaded from posting it as a preprint. (He did not return requests for comment.)

Taking the podium after He's talk, David Baltimore, a Nobel laureate from the California Institute of Technology in Pasadena who also helped organize the meeting, decried the "failure of self-regulation" by He and the scientific community. The central problem, Baltimore tells *Science*, is that "we had no authority to stop him," which he says "is the dilemma in trying to police the international scientific world."

At the summit's end, the organizing panel, which had representatives from eight countries, concluded that He's experiment was irresponsible, violated international norms, failed to meet ethical standards, did not have a sufficient medical justification, and lacked transparency. Their statement mirrored reactions in China (see sidebar).

The organizer's statement noted the promise of heritable germline editing but said it still remained too risky. The statement disappointed some by not demanding a strict moratorium, instead calling for "a rigorous, responsible translational pathway toward such trials." The meeting organizers pointedly noted that germline editing would require "strict independent oversight" but offered no specific recommendations for how that might be done.

Several commenters recalled the biology community's response to the advent of genetic engineering in the 1970s, which at that

For China, a CRISPR first goes too far

By **Dennis Normile**, *in Shanghai, China*

Does a Chinese scientist's claim that he used CRISPR to create two baby girls resistant to HIV show that research ethics here are more permissive than elsewhere? Many Chinese researchers dispute the notion, as do experts elsewhere. "I still believe there is no ethical divide between China and the West," says Reidar Lie, a bioethicist at the University of Bergen in Norway who has written extensively about China's bioethical issues. "This is clear," he says, from the reactions of ministries, institutions, and scientists who have forcefully condemned the study, by He Jiankui of the Southern University of Science and Technology (SUST) in Shenzhen, China. Lie adds that He "shares the same characteristic as many other scientists at the frontiers of knowledge: overestimating the benefits of their own research, and underestimating the risks."

Yet in the wake of the scandal, some are calling for tighter regulations and better oversight. "There is an urgent need for a national ethics review committee," former Vice Minister of Health Huang Jiefu told *Global Times*, a daily tabloid and website controlled by the Chinese Communist Party. Currently, every hospital and institute has its own ethics committee, but many lack the medical, ethical, and legal expertise to review cutting-edge procedures, Huang said. Lie agrees that there are gaps in China's regulatory efforts, but says the existing framework just needs strengthened enforcement powers and upgraded expertise.

Many questions remain about He's work, including where he did it, how it was financed, and whether his scientific claims are valid (see main story, p. 1090). An official investigation by a joint team from Guangdong province and the city of Shenzhen is ongoing, and SUST has announced its own inquiry. He himself has not publicly spoken since he presented his work at a gene-editing meeting on 28 November and did not respond to requests for comment. But some details about his work have emerged.

In an online report that was later removed, for instance, *Sanlian Life Week* magazine described how He turned to the HIV/AIDS support network Baihualin China League to help recruit couples in which the man was infected with HIV. One told the magazine he and his wife dropped out of the study because he was "unwilling to be a guinea pig," according to a copy of the article shared on Twitter. The network's head said he regretted his collaboration with He: "I am very worried about these families and children," he wrote in a statement.

Until now, China's share in the CRISPR revolution was a source of national pride. Chinese scientists were the first to create gene-edited monkeys, in 2014, and produced the first ever gene-edited human embryos a year later. In 2016, they became the first to start clinical trials using CRISPR to alter genes in somatic cells, which are not passed on to the next generation; today, 10 CRISPR-related trials to treat diseases such as cancer and HIV/AIDS are recruiting patients in China, more than in the rest of the world combined. But the scientific community "was nearly unanimous" that He's work crossed a red line, says Wei Wensheng, a molecular biologist at Peking University in Beijing. In a statement typical of many issued over the past week, the Chinese Academy of Medical Sciences in Beijing said gene editing is "still at a basic stage," and that changing the germ line should be off limits.

He appears to have violated the Ethical Guiding Principles on Human Embryonic Stem Cell Research, a brief document promulgated jointly by the health and science ministries in December 2003 that prohibits implanting human embryos created for research purposes into the womb. But the guidelines do not specify any penalties for noncompliance. "In some countries, such activity would lead to imprisonment, but China still lacks a relevant legal and policy framework," bioethicist Zhai Xiaomei of the Chinese Academy of Medical Sciences and Peking Union Medical College told *China Science Daily*. She called for politicians to strengthen legislation as soon as possible.

Meanwhile, the news fascinated the Chinese public, according to the website What's on Weibo, which tracks China's most popular social media platform. "In 100 years time, this might be considered pioneering work," said one comment. "This is unfortunate for the children, it is unfortunate for China, and it is unfortunate for mankind," another Weibo user countered, reflecting the majority view.

"What He did will almost inevitably have a backlash from the public and possibly from regulators," says Wei, who worries that the actions of a single research group gone rogue will trigger new rules that could have punishing implications for legitimate research.

Downloaded from http://science.sciencemag.org/ on December 6, 2018

Published by AAAS

time raised the specter of DNA-engineered microbes escaping from labs and wreaking havoc. Baltimore, who played a prominent role in the famed 1975 Asilomar conference on that topic, says the field figured out a way to control the use of recombinant DNA technology. “We never had any international authority, but we got international agreement, and, as far as I know everybody lived up to it.”

In the United States, NIH established a Recombinant DNA Advisory Committee (RAC) to oversee related work that received federal government support. It no longer reviews many proposals, but, Collins says, “It’s likely that a reinvented version” could serve as a public forum for “intense, scientific debate about an area of some scientific potential but where there are many unknowns—and this would certainly be one of them.”

James Wilson, who heads the gene therapy program at the University of Pennsylvania, suggests the U.S. Food and Drug Administration (FDA) could serve as an excellent oversight venue of the controversial research. But, he notes, the agency would have to forgo its many confidentiality restrictions and allow more public discussion of proposals.

For now, FDA is not even allowed to review germline editing experiments in humans. “It’s effectively prohibited in the United States,” says Harvard Medical School Dean George Daley, a stem cell researcher in Boston who was a summit organizer.

> ***“I do hope this very visible misadventure does not cause a cloud over the entire area of gene editing for therapeutic benefits.”***
>
> **Francis Collins**, National Institutes of Health

The summit triggered a discussion about whether the United Nations could serve as the home for an international oversight group, and its World Health Organization announced this week it would establish a team of experts to set guidelines and standards for human genome editing.

An immediate response is needed, Doudna stresses. “I’d love to see the national science academies from several countries within a month come up with a set of draft guidelines that would be somehow affiliated with a RAC-like body,” she says. Daley agrees. “We have to aspire to some kind of a universal agreement amongst scientists and clinicians about what’s permissible,” he says. “Those who violate those international norms are held out in stark relief.”

Whether He would have consulted with any oversight body is unclear. Several researchers say He discussed with them the idea of implanting edited human embryos. Porteus says when He informed him he was about to launch a trial to do that, “I spent the next 45 minutes telling him this was a terrible thing to do and he needed to stop immediately and talk to more people, particularly people in China. My regret is I didn’t go public.”

To others, He was more coy about his actions. “If I had any sense that he was actually trying to do this I would have organized a meeting with him and others,” says William Hurlbut, a physician and ethicist at Stanford who met with He a handful of times and corresponded regularly with him. “I was intentionally trying to slow him down and influence his thinking.”

Collins, Doudna, and many others say they have difficulty coming up with any genetic disorders that should even be considered for germline editing now. Couples who have concerns about passing on a disease mutation can use preimplantation genetic diagnosis (PGD), notes Collins, a procedure in which researchers can screen IVF embryos and implant only those without the mutation. Although there are instances where parents both have two copies of a disease gene and are certain to pass it on to all embryos, those are exceedingly rare, he adds.

Daley, part of a growing camp that strongly disagrees, counters that PGD doesn’t work 100% of the time. And, he says, “Rarity alone doesn’t detract from the imperative of trying to give medical support.”

Researchers discussing He’s feat frequently refer to the case of Martin Cline, a hematologist at UC Los Angeles who in 1980 conducted pioneering gene therapy research in other countries rather than wait for his own institution to approve his proposed studies. In the aftermath of intense media scrutiny, Cline resigned as chief of his school’s hematology-oncology division and lost several NIH grants. “I regret to say this, but I think the consequences of my experiment set the field back several years because of all the regulations and oversights,” says Cline, who is retired and living in Stinson Beach, California. Cline says he paid a high price for what he now sees as having moved too fast. “I lost a significant part of a career I loved,” says Cline, who switched to oncology.

Another human genome editing summit is planned for 2021. It will be hard to surpass Hong Kong’s drama. “One of our concerns was this was going to be a really boring summit,” Charo says. “Everything you look at here, the closer you get, the stranger this whole story becomes.” ■

POLICY

Uncertainty boosts Brexit jitters for U.K. scientists

Political turmoil in Parliament threatens a disastrous crash out of the European Union

By **Erik Stokstad**

U.K. scientists dreading the country’s impending departure from the European Union, known as Brexit, now face possible outcomes ranging from undesirable to potentially disastrous—with an outside chance of a last-minute reprieve. Two and a half years after a divisive popular vote to leave the European Union, against the wishes of most scientists, politicians must soon decide whether the divorce will be orderly or chaotic. “Everyone’s just holding their breath,” says economist Philip McCann of the University of Sheffield in the United Kingdom, part of a team studying the implications of Brexit. “If it’s a disorderly exit, the consequences could be very, very severe.”

On 11 December, Parliament will vote on a withdrawal agreement that Prime Minister Theresa May reached with the European Union in November. It lays out the terms of a costly but smooth departure from the European Union, starting in March 2019. If the agreement is rejected, the United Kingdom could crash out instead, triggering chaos at the border, food shortages, and economic hardship. But a growing number of politicians, including former science minister Sam Gyimah, who resigned last week to protest the withdrawal agreement, are now agitating for a second referendum that might reverse the first one.

Ever since that referendum in June 2016, many U.K. scientists have lamented the loss of EU membership perks that Brexit will mean. It will end the free movement of researchers across the English Channel and Irish Sea. It could prevent U.K. researchers from applying to EU grant programs. And the country will leave the Euratom treaty, which governs the operations of the Joint European Torus, a fusion facility near Oxford, U.K., and give

Downloaded from http://science.sciencemag.org/ on December 6, 2018

Published by AAAS

Prime Minister Theresa May hopes to persuade Parliament to accept a plan for an orderly Brexit.

PHOTO: THIERRY ROGE/AVALON.RED/NEWSCOM

up a role in ITER, a much larger fusion research reactor being built near Cadarache in France.

Only a few U.K. scientists see more upside than down. Simon Willcock, a tropical ecologist at Bangor University in the United Kingdom who supports Brexit, believes liberation from EU regulations will allow the United Kingdom to set its own science-based public policies, including reforms to agricultural subsidies. "I can see the U.K. being more of a risk taker, more of an innovator," he says.

If both the United Kingdom and the European Union accept the 585-page draft agreement, the landing could be soft. The deal doesn't specifically address research, but it would minimize disruption through a 2-year extension of the status quo while future participation in EU programs is negotiated. U.K. researchers could apply for EU grants during that period, for example.

The European Union is expected to greenlight the withdrawal agreement, which includes a $50 billion divorce bill and would require the United Kingdom to follow EU laws during the transition without any say in them. Those conditions mean the agreement faces tough prospects in the U.K. Parliament. Hardline Brexit proponents within May's Conservative Party say it doesn't offer enough independence. Other opponents include "Remainers" in the Labour and Conservative parties, who argue that even a soft Brexit would be too damaging.

A deadlocked Parliament could default to a no-deal Brexit, which would send the value of the pound plummeting 25% and shrink the U.K. economy by 8% in the following months, according to a report released last week by the Bank of England. Airlines flying between the United Kingdom and Europe could be grounded, because the United Kingdom would leave the European Union's aviation regulations. New customs checks could strangle trade with Europe. An oversight committee in Parliament last week called a lack of preparation at ports for consequences such as massive backlogs of trucks "extremely worrying."

All that would hurt research. Many reagents and other supplies, such as antibodies and cell-growth media, are imported. U.K.-based pharmaceutical companies are stockpiling drugs used in some clinical trials as well as routine medicines. Some researchers are considering whether they also need to stock up. "You don't want to feel alarmist, but you have to think about the sustainability of your experiments," says Jennifer Rohn, a cell biologist at University College London who needs expensive and perishable cell-growth media made in Europe. But Oscar Marín, a developmental neurobiologist at King's College London, says a supply shortage is the least of his worries. "To be honest, the disruption will be of such an order that not having the right antibody will be meaningless."

A no-deal exit would also immediately void many research agreements. The U.K. government has said that if the European Union terminates grants to U.K. teams, the treasury will take over the payments. But U.K. researchers couldn't apply for new EU grants. It's also not clear whether they could continue to lead existing collaborations with European partners. The legal status of joint clinical trials—about 40% of U.K. trials include sites in the European Union—is murky, and how data might be transferred is uncertain.

"We are very concerned about a no-deal outcome," says Beth Thompson, head of U.K. and EU policy at the Wellcome Trust, a biomedical philanthropy in London.

Regardless of how the United Kingdom departs, it will have to negotiate new science agreements with the European Union. The European Union's Horizon Europe program will fund $113 billion in research from 2021 to 2027, and the U.K. government wants to participate as an associated member, a status Norway and a few other non-EU countries already have. But associate membership will likely cost more than it brings home in grants, and some fear the government might trim the domestic research budget to compensate. As an associate, the United Kingdom might also lose influence over the program's goals. "There's no deal we could get that would be as good as the one we have at the moment," says Anne Glover, head of The Royal Society of Edinburgh.

Nevertheless, both the United Kingdom and the European Union would benefit from maintaining close scientific ties, so the chances are good for agreements on funding programs, research regulations on clinical trials, and Euratom, says Venki Ramakrishnan, who heads The Royal Society in London. Speed will be crucial, he says. "The longer the uncertainty, the less of a player we'll be in European science."

To many, the largest risk that Brexit poses for science is the same one that threatens the whole United Kingdom: a recession, which would jeopardize recent large increases in domestic research funding and could cause a brain drain. The end of free movement with the European Union also has "huge implications for science," says Naomi Weir, deputy director of the Campaign for Science and Engineering in London, which advocates for a smooth and affordable research immigration system. A long-awaited government white paper on immigration is expected to be published this month. Ministers have said they will welcome foreign talent, but Weir worries about an increased burden on employers and an advisory committee proposal for a £30,000 minimum salary for all immigrants, which could complicate hiring of technical staff.

Some scientists want a do-over. "Brexit is simply bad for science," says Paul Nurse, head of The Francis Crick Institute in London. "The best thing would be to go back and say we made a mistake." But the politics of a second referendum are tortuous, and time is short. As the maelstrom intensifies, many researchers are focusing on their work. Nurse, however, urges more to speak out. "The scientific community really has to indicate why it's so worried," he says. "I don't think we've done enough." ■

Downloaded from http://science.sciencemag.org/ on December 6, 2018

BIOMEDICINE

Universal flu vaccine is 'an alchemist's dream'

The rapidly changing virus and a complex immune response stymie vaccine developers

By **Jon Cohen**, *in Nashville*

What if instead of lining up for a flu shot of unknown effectiveness each fall, people could receive one vaccine that protects against all strains and lasts for many years, if not for life? It could spare incalculable amounts of suffering, and even eliminate terrifying pandemics. Scientists have spent decades trying to concoct such a "universal" flu vaccine and, at times, they seem to have made solid headway. But it remains an "alchemist's dream," as one virologist declared last month at a gathering on the topic organized by the Human Vaccines Project, a nonprofit based in New York City.

New funding has boosted the research: $160 million next year from the National Institute of Allergy and Infectious Diseases (NIAID) in Bethesda, Maryland, up from $60 million 2 years ago. But the quest is an exercise in humility, leading flu researchers said at the meeting. "Every year we learn that we know less and less about this virus," says Martin Friede, a biochemist who coordinates the Initiative for Vaccine Research at the World Health Organization in Geneva, Switzerland.

Each year, vaccinemakers concoct a new preparation that contains harmless versions of flu strains in circulation the previous year. These seasonal vaccines have a mediocre efficacy of 20% to 60%, in part because the vaccine is often a poor match for the virus people actually contract (*Science*, 22 September 2017, p. 1222). Other, less obvious factors highlighted at the meeting also influence the response to the seasonal vaccine, including the immune system's memory of past exposure to viral variants.

In theory, a universal flu vaccine would work if it contained parts of the virus that remained the same from year to year and do not vary between strains—so-called conserved epitopes. But no one has yet found the viral pieces capable of stimulating an immune response that stops most flu viruses afflicting humans.

Seasonal vaccines aim to trigger the immune system's B cells to produce antibodies against the top part of hemagglutinin, one of two main proteins on the surface of influenza viruses. Several candidate universal vaccines focus instead on the "stem" of the mushroom-shaped protein because it has many epitopes that differ little between viral subtypes. So far, vaccines that feature this portion have underwhelmed researchers. "Stem antibodies as a class are not very potent," says James Crowe, an immunologist at Vanderbilt University here who helped organize the meeting.

A handful of other universal flu vaccines are now in early human trials. Each one exploits conserved regions of the virus to maximize breadth, and some attempt to increase potency with immune stimulants called adjuvants or other strategies.

David Morens, a pediatrician at NIAID, noted that many studies have found that antibody levels to the virus's second surface protein, neuraminidase, better correlate with protection from disease. Improving seasonal vaccines by selecting those that best trigger neuraminidase antibody production is "potentially low-hanging fruit," Morens says. The same strategy could also improve the effectiveness of potential universal vaccines.

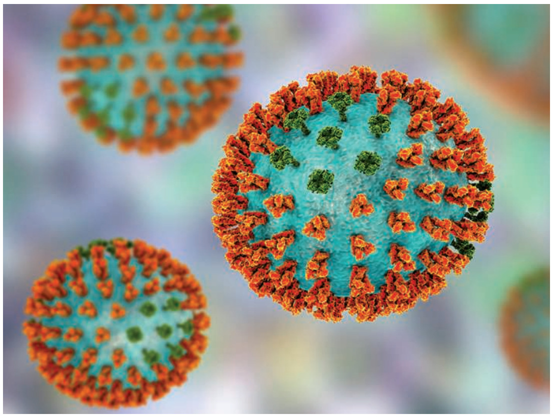

Universal flu vaccines must outwit ever-changing influenza surface proteins, hemagglutinin (orange) and neuraminidase (green).

IMAGE: KATERYNA KON/SCIENCE SOURCE

Designers of a universal flu vaccine face another quandary, speakers at the meeting noted: an immune phenomenon called imprinting. The first influenza virus or flu vaccine children experience has a profound impact on the breadth and potency of their immune responses to later infections with different flu strains. For example, the infamous 1918 influenza pandemic, which likely killed more than 100 million people, was caused by a virus subtype known as H1N1. ("H" is for hemagglutinin and "N" is for neuraminidase.) Oddly, the death rate was much higher than normal among young adults, who are ordinarily the least likely to die from influenza. Studies found this was because exposure to H1N1 triggered strong antibody responses to a virus of a different subtype—likely H3N8—which they had seen as children a few decades before. "Tickle [the memory B cells] a little bit and they explode," says Scott Hensley, a molecular biologist at the University of Pennsylvania's Perelman School of Medicine. "And they dominate subsequent immune responses," causing the response to a new virus to miss its mark.

To learn more about "original antigenic sin," NIAID is evaluating proposals for a study that would follow infants for up to 7 years to track how their initial influenza exposure impacts later immune responses. In the meantime, Hensley suggests the first flu vaccine children receive be packed with many versions of common human subtypes, a possible step toward a universal vaccine because it should offer broader protection than seasonal ones.

Meeting presenters also described how computer programs can help guide vaccine design. Ted Ross of the University of Georgia in Athens explained that his group scans the DNA encoding hemagglutinin's head for conserved sequences that they can then combine into a universal vaccine. Crowe's lab starts with antibodies instead. They use a supercomputing technique to analyze the shape of billions of antibodies and select ones calculated to have the broadest reach; ultimately, they hope to reverse engineer proteins that, used in a vaccine, would trigger these antibodies.

Lisa Wagar, an immunologist at Stanford University in Palo Alto, California, has created a new testbed for vaccine researchers. Instead of monitoring the immune response in blood, she simulates the first immune defenses an invading virus meets in the respiratory tract. She has used tonsils, which are rich in mucosal tissue, taken from children to grow tonsil-like "organoids" that can help evaluate experimental influenza vaccines.

At the gathering's closing, Wayne Koff, who heads the Human Vaccines Project, said it was "sobering" that if a universal flu vaccine meeting had been held in the 1960s it would have discussed the same obstacles. "We are really at the beginning of the dance," Koff said. ■

Downloaded from http://science.sciencemag.org/ on December 6, 2018

Published by AAAS

PHOTO: ISTOCK.COM/CARSTENBRANDT

A meteorite in a museum's courtyard helped inspire the discovery of a giant impact crater in Greenland.

NATURAL HISTORY

Demotion dismays researchers at storied Danish museum

Merger with biology department could undermine research

By **Gretchen Vogel**

Over the past decade, the 40 researchers at the Natural History Museum of Denmark in Copenhagen have published more than 100 papers in *Nature* and *Science*, putting it among the world's top research museums. But budget pressures are forcing a reorganization that will split museum research from curation and outreach. The museum's scientists are dismayed, and several prominent group leaders say they may leave.

Previously, the museum was its own department within the University of Copenhagen. But last month, the university announced that, as of 1 January 2019, the museum will be demoted to a unit within the biology department. Roughly half of the 40 researchers will remain part of that unit; they will give up some of their research to focus on curation and outreach. The other half will become full faculty within the biology department—including the geologists and astrophysicists. These scientists will lose their museum affiliation, and exchange their curatorial roles for increased teaching duties.

Divorcing the scientists' dual roles will curtail the fruitful cross-pollination of curation and research, says Carsten Rahbek, who heads the museum's Center for Macroecology, Evolution and Climate and who is slated to become a biology professor. (The center will move with him.) "The curation is driven by the research," he says. "It's not like a library where you go borrow a book and then go do cutting-edge research. If you don't have a say in how [the collection] develops, in 2 or 3 years you won't be able to use it anymore."

The museum grew out of a 2001 merger of the university's Botanical Garden, Botanical Museum and Library, Geological Museum, and Zoological Museum. The vision, says Eske Willerslev, who studies ancient DNA and heads the museum's Centre for GeoGenetics, was to "create a prominent place where citizens could [find] the best researchers and look over their shoulders." Research collaborations have since led to major discoveries about human migrations and the effects of climate change on biodiversity. Just last month, a team led by a museum glaciologist announced in *Science Advances* the discovery of a giant impact crater under Greenland's ice sheet (*Science*, 16 November, p. 738).

But the museum is under financial pressure. Although it will begin construction next year on a 950 million Danish kroner ($144 million) building to house state-of-the-art exhibits, the museum has run budget deficits in recent years. Last week, it laid off 17 people, including some research staff. Moving some of the researchers out of the museum and into the biology department—and boosting their teaching loads—will help shore up finances, says Museum Director Peter Kjærgaard.

Kjærgaard says focusing the museum's resources on curation and outreach will make its collections more widely available for researchers, the public, companies and nonprofits. John Renner Hansen, dean of the university's Faculty of Science, says researchers who want to maintain their museum affiliation will have to do significant curation and outreach work. But he argues that current collaborations can continue. Labs and offices won't move at all. "There are no physical changes, just a change of organization," he says.

But the formal separation of the researchers from the museum is damaging, even if it is not physical, says Minik Rosing, a museum geochemist who is also slated to join the biology department faculty. "It's a redefinition of what a museum is, and what it means," he says. Rosing, Rahbek, and Willerslev all say they may leave the university if the plans go forward. "We would prefer to stay and support the museum, but if its mission changes so completely, we will have to go elsewhere," Rosing says.

The separation is not only bad for the researchers; public outreach will also suffer, predicts Évelyne Heyer, who heads the department of eco-anthropology at the National Museum of Natural History in Paris. "It's not enough to present the collections," she says. "You have to teach the people what the collection can do." ■

Downloaded from http://science.sciencemag.org/ on December 7, 2018

Published by AAAS

FEATURES

Downloaded from http://science.sciencemag.org/ on December 6, 2018

TAKING AIM

After her own violent childhood, emergency physician Rebecca Cunningham is jump-starting research to prevent gun deaths in kids

By **Meredith Wadman**, *in Ann Arbor, Michigan*

PHOTO: MELANIE MAXWELL

Published by AAAS

Rebecca Cunningham has only one kind of memory from her early childhood: violence. Her father shattered mirrors, tore up the house, and beat and threatened to kill her mother. Cunningham, then less than 5 years old, remembers her older sister trying to protect her.

"When my father would start in with my mother, my sister would cover my eyes and try to hide with me behind the couch," recalls Cunningham, now a 48-year-old emergency physician and researcher at the University of Michigan (UM) here. "The police were in and out of the house a lot. If there had been a gun in my home in those years, my mother certainly would have been killed."

One day Cunningham's father, a lawyer, called her mother threatening to kill her. Her mother changed the locks on their New Jersey house. She sent Cunningham's two older siblings to live with a safely distant foster family. And she bought a handgun.

Did that pistol make Cunningham and her mother safer? Public health experts can't answer that question: A 2003 study that examined whether abused women living apart from their abusers are safer with a gun was inconclusive. No study since has delved into the issue.

It's one of myriad questions about firearms and violence that remain unanswered, largely because of a dearth of funding to explore them. Guns are the second-leading cause of death of children and teens in the United States, after motor vehicle crashes (see graphic, right). In 2016, the most recent year for which data are available, they killed nearly 3150 people aged 1 to 19, according to data from the Centers for Disease Control and Prevention (CDC) in Atlanta. Cancer killed about 1850. But this year, the National Institutes of Health (NIH) in Bethesda, Maryland, spent $486 million researching pediatric cancer and $4.4 million studying children and guns, according to its RePORTER database.

That's because gun violence research has been operating under a chill for more than 2 decades. In 1996, Congress crafted an amendment, named for its author, then–Arkansas Representative Jay Dickey (R), preventing CDC—the government's lead injury prevention agency—from spending money "to advocate or promote gun control."

That law was widely interpreted as banning any CDC studies that probe firearm violence or how to prevent it. The agency's gun injury research funding was quickly zeroed out, and other health agencies grew wary. The few dozen firearm researchers who persisted were forced to rely on modest amounts from other agencies or private funders (see table, p. 1098) to tackle a massive problem.

Now, there may be early signs of a thaw. In March, in the wake of the mass shooting at a Parkland, Florida, high school, Congress wrote that CDC is free to probe the causes of gun violence, despite the Dickey amendment. (The agency has not done so, citing a lack of money.) And annual firearm-related funding from NIH, according to a search of its RePORTER database, roughly tripled after a 2013 presidential directive that was issued in the wake of the mass shooting at Sandy Hook Elementary School in Newtown, Connecticut. Just as importantly, the agency began to flag firearm violence in some of its calls for research.

A heavy toll

Firearms are the second-leading cause of death in children in the United States, after motor vehicle crashes. In the decade ending in 2016, more children died from gun injuries than from cancer.

Fatalities of 1–18-year-olds (2006–2016)

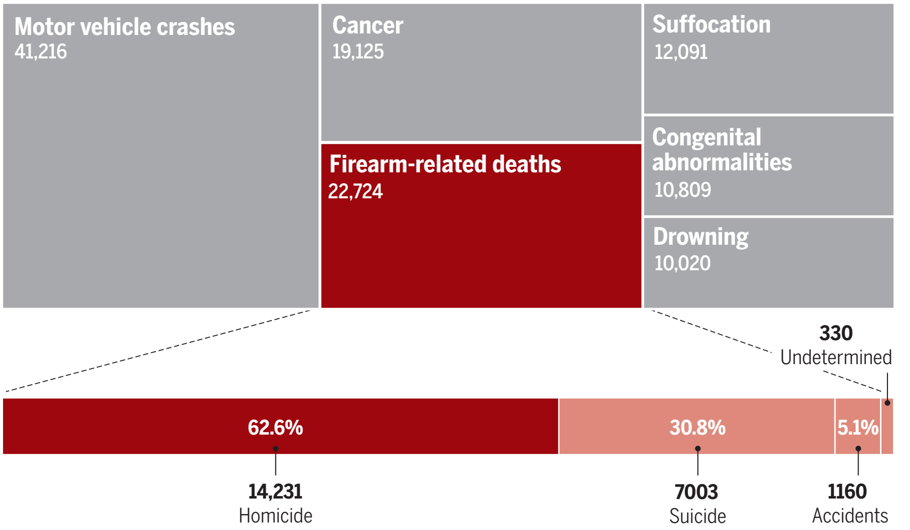

That's why Cunningham is now in charge of the largest firearm research grant that NIH has awarded in at least 30 years. With $4.9 million from NIH's Eunice Kennedy Shriver National Institute of Child Health and Human Development (NICHD), she is co-directing a 5-year project to build capacity for researching firearm injuries in children. Cunningham and UM public health expert Marc Zimmerman are leading 27 scientists at a dozen institutions in work they hope will carry the field forward for years after this funding ends in 2022.

The grant is not designed to answer one particular question. Rather, the goal is to lay out what questions need answering first. The researchers are building a user-friendly archive of existing data and launching pilot studies. And they are training the young scientists who they hope will come after them.

Cunningham's grant "is unique" in U.S.-funded gun violence research, and not just for its size, says Garen Wintemute, a gun violence researcher at the University of California, Davis, who co-authored one paper with Cunningham but is not part of this grant. "In the last 20 years this is the first time that an award has been made not just to do a project, but to set up an infrastructure that would allow a lot of projects to be done."

Although gun rights groups continue to insist that public health scientists steer clear of gun violence, some researchers are feeling empowered to push back. Last week, surgeons writing in *JAMA Surgery* called on CDC to restart its own gun violence research. And last month, the National Rifle Association (NRA) in Fairax, Virginia, provoked a firestorm when it tweeted that "self-important anti-gun doctors" should "stay in their lane." Hundreds of emergency department doctors tweeted back, many including photographs of their scrubs, hands, and shoes bloodied from treating gunshot victims. More than 40,000 health care professionals, including Cunningham, signed an open letter to NRA complaining that the group has hobbled gun violence research, declaring, "This is our lane!"

All the same, there's still little public money for gun research. And given the polarizing politics, Cunningham's team must walk a fine line: probing gun violence without being seen as advocating gun control. But she's betting that this is the begin-

CREDITS: (GRAPHIC) A. CUADRA/SCIENCE; (DATA) CDC

Downloaded from http://science.sciencemag.org/ on December 6, 2018

Published by AAAS

ning of the end of the funding chill. Her forward-looking NIH award "is more than another grant," she says. "[It's] the end of the silencing of a generation of scientists."

WEARING A WHITE COAT and with the requisite stethoscope draped around her neck, Cunningham recently showed visitors around a trauma bay stuffed with monitors, tubing, and tanks at UM's University Hospital, which serves Ann Arbor and its rural surroundings. She works in the emergency department here several times a month. (She is also associate vice president for health sciences research at UM, and the fourth-leading NIH grantee among U.S. emergency room doctors.)

The young trauma patients Cunningham sees here underscore the need for research on guns and children. "The teen suicide survivors that I remember most clearly are kids or young adults who have blown off the front of their face," Cunningham says. "Those are some of the worst trauma patients I have seen because they are awake and utterly miserable. And they are going to have just devastating injuries."

After working her way through college and medical school, Cunningham did her medical residency at UM in the late 1990s. She spent months staffing an emergency department 80 kilometers north in Flint, Michigan, an impoverished city where she saw a different kind of gun violence. After street shootings, she saw victims "shot in the leg, shot in the arm, shot in the belly, shot in the chest … often multiple gunshot wound victims in one night. More than once, the teen was the second in the family to be killed. I cared for young children caught in crossfire walking to school."

She was often pregnant with one of her three daughters when she had to sit down with a mother to tell her that her child had been shot and killed. It was, she says, "completely senseless."

After her residency, Cunningham began 2 decades of research studying the impacts of violence on youth, but for many years she saw no way to study gun violence in particular. "No mentor of mine would touch it."

In 2010, Cunningham finally published a paper with guns in the title—a survey of handgun access in teens visiting the emergency department in Flint. Four years later, she came across a bigger opportunity.

In August 2014, NIH's child health institute sent out a broad call for team proposals to build research capacity for preventing any prominent cause of childhood injury. As Cunningham read the announcement, one sentence leapt off the page: "Increasingly, attention is being paid to firearm-related injury as a serious public health concern."

She contacted NICHD to make sure she had not misread its intent. She was told she had not. She and Zimmerman's first proposal was sent back for revisions. But on a second try, it received a perfect score from an NIH review panel.

One week later, Donald Trump was elected president. Given that NRA had funneled $30 million to Trump's campaign, NIH officials privately fretted about gun research. "The election makes everything more complicated," one administrator emailed to another (*Science*, 20 October 2017, p. 286). But in September 2017, the grant money arrived, and Cunningham's team went to work, calling itself the Firearm Safety Among Children and Teens (FACTS) Consortium.

A generation of scarcity

During the past 22 years, public funding for gun violence research has been modest. Private funders have tried to compensate.

FUNDING SOURCE	TOTAL FUNDING (1996–2018)
U.S. National Institutes of Health	$58 million
U.S. Department of Justice	$39 million
State of California	$6 million
Joyce Foundation	$24 million
California Wellness Foundation	$10 million
Laura and John Arnold Foundation	$20 million pledged (2018)

DATA: FOIA/NIH: NIH REPORTER DATABASE

Four months later, a 19-year-old former student gunned down 17 students and staff at Marjorie Stoneman Douglas High School in Parkland. "My inbox was flooded with researchers wanting to join FACTS—even to volunteer," Cunningham says. "The idea that the topic is too political to study is passing with the urgency created after Parkland."

CUNNINGHAM'S OWN sense of urgency predates any news event. "My interest in gun violence prevention has … roots [in] lived experience," she says. After his wife kicked him out in the mid-1970s, Cunningham's father continued to stalk her and 5-year-old Cunningham, banging on the front door and breaking windows. To escape him, her mother began a series of moves to low-rent apartments in other towns. They relied on food stamps while Cunningham attended four schools in 3 years.

"We were terrified," Cunningham says. "I was scared my mother would be killed. She was scared she would be killed. My father told her not infrequently that he had a gun and would find her." The fear only lifted years later, after her father died.

Cunningham says her early experience helps her "understand that people sometimes buy guns when they think the law cannot protect them."

In late October, Cunningham convened the first in-person meeting of the FACTS team in a daylong event in a UM conference room. The roughly two dozen researchers and handful of trainees present included many of the public health scientists actively doing firearm research today: grizzled epidemiologists who are still standing after the 22-year funding drought; surgeons-in-training; data mavens; and clinical psychologists such as Rinad Beidas, an associate professor at the University of Pennsylvania who has been studying whether and how counseling parents on gun safety could be incorporated into routine pediatric visits.

"The overarching purpose here is how to rebuild the field," Cunningham told the meeting as it opened. "We want more firearm researchers at the end of this who know what they are doing."

Their animating principle is that gun violence, like any other public health bane, can be tackled scientifically, divorced from any political agenda. "There is a science to injury prevention," Cunningham says. She and others note that decades of studies on motor vehicle safety led to evidence-based policies such as car seat and seat belt laws, which have dramatically reduced childhood motor vehicle fatalities even though many more cars are on the road.

In the case of firearms, Cunningham says, "the person, the gun, the home environment—all are modifiable in some way or another. We have not even started to try to address the ways that make the combination safer."

The scientists discussed 10 candidate pilot projects over 5 hours; Cunningham and Zimmerman will soon decide which will move forward.

One project proposes to enlist focus groups of gun owners to craft effective safe storage messages, aiming to curb teen suicide in Michigan's Upper Peninsula. In such rural areas, the rate of suicide by gun is almost twice that in urban areas of the United States. Another proposed study, a survey, would separately ask teens and their gun-owning parents how accessible the household's guns are, to reality check parents' views.

A third proposal makes the chilling assumption that it won't be long until the next mass school shooting. In its aftermath, Megan Ranney, an emergency physician at Brown University, would study young people's use of social media to characterize post-traumatic stress and anxiety, as well

Downloaded from http://science.sciencemag.org/ on December 6, 2018

Published by AAAS

Family and friends commemorate DrayQuan Jones, 16, who was shot and killed this spring in Flint, Michigan. Guns disproportionately kill African-American children.

PHOTO: JAKE MAY/THE FLINT JOURNAL-MLIVE.COM/AP PHOTOS

as resilience. Fewer than 1% of gun deaths in children and teens occur in schools. But Ranney believes school shootings may have much broader mental health impacts.

Cunningham, who radiates both affability and the decisiveness of a seasoned emergency physician, ran the meeting as part pep talk, part crash assignment. She shut down digressions and poured on doses of budget reality when suggestions got too ambitious. "This is not a democracy, as I tell my children," she reminded the group.

Given the constraints imposed by the congressional amendment, Cunningham and her team are at pains to emphasize that they are not coming after anybody's guns. The official NIH project description promises to respect "gun ownership as an important part of the cultural fabric of U.S. society."

Cunningham is blunt: "Our goals are not political. We are not aiming to decrease total gun numbers. We respect Second Amendment rights."

The team has signed up gun-owning stakeholders to advise them. These include groups like Gun Owners for Responsible Ownership, based in Lake Grove, Oregon, and individuals like James Berlin, police chief and former SWAT team leader in the Detroit suburb of Roseville, Michigan.

Berlin, in a phone interview, said he has turned down other research groups over the years because "it seemed like they were trying to find facts that fit their foregone conclusions." Cunningham's team struck him differently. "They are actually trying to get the answers" on pediatric gun deaths, he says, "so it doesn't happen in the future." He adds of Cunningham: "She made me feel like my opinion mattered."

But hard-line gun rights groups have refused to work with the team. Only "the most tame" groups have signed on, David Hemenway, a veteran injury prevention researcher at Harvard University's T.H. Chan School of Public Health in Boston, said at the meeting.

"It's year one," Cunningham replied. "There's more time for more voices." But she acknowledged that local and national NRA chapters had failed to return her team's repeated phone messages and emails. (NRA also did not respond to *Science*'s repeated requests for comment for this article.) The National Shooting Sports Foundation in Newtown, the gun industry's trade association, declined to sign on because of "concern about the 'public health' focus," Bill Brassard, the group's senior communications director, wrote in refusing Cunningham's request.

In a statement provided to *Science* last month, Brassard added, "Though we do not oppose research per se, too often 'research' from some in the public health field is biased and designed to advance a predetermined antigun policy outcome. … Gun-related violence is largely a criminal justice matter and not a public health issue."

FOR A WOMAN WHO began life at more risk than most for gun violence, Cunningham has landed well. She divorced—because "marriages are miracles"—then remarried and now co-commands a blended family of five teenagers. She lives on the outskirts of Ann Arbor, on a forested lot with a chicken coop overseen by her daughters. Her 77-year-old mother, who is also happily remarried, lives nearby. She still has the gun, stored away, unloaded.

Like many U.S. parents, Cunningham finds her own children affected by gun violence. "My kids come home after those shootings and they are terrified in school."

But despite powerful public reaction to school shootings, some experts are not as sanguine about the future of gun research as Cunningham. "I don't see this as a turning point," says David Studdert, a health policy expert at Stanford Law School in Palo Alto, California, who's not part of the FACTS project. And pediatrician Fred Rivara, a FACTS team member and veteran firearm researcher at the University of Washington in Seattle, worries about future funding for his young trainees.

However, Wintemute, who has studied gun violence for 30 years, thinks this may be a watershed moment. He notes Cunningham's grant and other new money—his group recently received a $5 million award from the state of California—plus the groundswell of physician activity on Twitter. "It's entirely possible that this is the beginning of a new mobilization," he says.

Cunningham is confident that the problem of gun violence can be solved with science—and with participation from all sides. So, she keeps searching for common ground. "We are not having any conversations here that are an 'us and them' narrative," she told scientists at the meeting. "We are about reducing kids dying." ■

Downloaded from http://science.sciencemag.org/ on December 6, 2018

Published by AAAS

AT ARM'S LENGTH

Major private research funders make secretive offshore investments, raising ethical concerns

By **Charles Piller**

A few years ago, scientists funded by the Wellcome Trust, one of the world's wealthiest private philanthropies, published sobering findings about the deadly effects of air pollution. In a long-term study of elderly residents of Hong Kong, China, those exposed to higher levels of smog—especially tiny particles of soot produced by burning fossil fuels—were more likely to die of cancer than people who breathed cleaner air.

The study, published in *Cancer Epidemiology, Biomarkers & Prevention* in 2016 by researchers from the University of Hong Kong and the University of Birmingham in the United Kingdom, is one of many to highlight the health threats posed by soot. And it is just one product of the extensive investments that Wellcome, with $29.3 billion in assets, has made in environmental science. "We aim to stimulate research excellence and develop global collaborations to drive change," the London-based philanthropy explains on a web page that highlights its commitment to making "cities healthy and environmentally sustainable."

The trust does not highlight, however, that some of the more than $1.2 billion it has handed out annually in recent years comes from investments in companies that contribute to the same problems the philanthropy wants to solve. Not long before the Hong Kong study was published, for example, the trust became an investor in Varo Energy, a company based in Cham, Switzerland, that sells fuel to shipping firms. One of Varo's main products is bunker fuel for marine engines: a cheap, sulfurous residue of oil refining that is a major source of soot pollution. Particulates billowing from ship stacks contribute to the premature deaths of 250,000 people annually, researchers estimate.

Wellcome didn't invest directly in Varo. But according to a trove of confidential documents known as the Paradise Papers, many of them leaked from a law firm that helped manage such deals, Wellcome committed $50 million to an offshore investment fund, Carlyle International Energy Partners, based in the Cayman Islands. That fund, in turn, owns a stake in the energy firm. (Wellcome declined to give details on its offshore holdings.)

Large investors commonly use offshore funds to maximize returns, in part by reducing the taxes investors would otherwise pay to their home nations. Though offshore investments can be legal, they are controversial—partly because the funds' activities are nearly always tightly held secrets. And Wellcome's investment in bunker fuel illustrates a common contradiction facing some major scientific grantmakers

ILLUSTRATION: STEPHAN SCHMITZ/FOLIO ART

Downloaded from http://science.sciencemag.org/ on December 10, 2018

Published by AAAS

involved in offshore investing. Specifically, offshore investments can have impacts that diminish or negate the high-minded social experiments, education, and research backed by science funders, according to a *Science* investigation. And their routine use of offshore funds raises questions about transparency, accountability, and social responsibility.

Critics of offshore investing also say that foundations, by lending their sterling reputations to offshore strategies, are helping legitimize tactics that others widely use to bend or break the law—including investors eager to conceal lawful but extreme tax avoidance as well as criminals seeking to hide illicit profits and launder money. Such practices deprive governments around the world of revenue, the critics note, worsening economic inequality and undermining efforts to repair crumbling infrastructure.

The secrecy surrounding offshore funds complicates efforts to document exactly how much money major research charities have moved into such vehicles—or where the cash ends up. *Science* gained some insight by reviewing publicly available tax returns and financial statements and by searching the roughly 13.4 million leaked documents in the Paradise Papers, more than half of which came from Appleby, a global law firm founded in Hamilton, Bermuda, and one of the world's leading offshore dealmakers. (The papers were shared with *Science* by the International Consortium of Investigative Journalists in Washington, D.C., which acquired them from the *Süddeutsche Zeitung* newspaper in Munich, Germany.)

Science examined seven of the largest private research funders and found that, according to conservative estimates, they have in recent years placed and committed more than $5 billion to funds in offshore tax and secrecy havens. Missing data and a lack of precision in many documents, however, suggest the philanthropies' investments are larger (see table, p. 1102). Among the investigation's findings:

- Wellcome committed more than $926 million of its holdings to at least 57 tax haven funds, documents from the Paradise Papers indicate. Other offshore investments were shown in the foundation's tax returns. (Totals could not be determined but in 2007, Wellcome's offshore holdings were so extensive that Appleby ranked the foundation as its 14th largest client.) In a statement to *Science*, Wellcome officials declined to discuss the size or placement of its assets in offshore accounts, saying they "do not collect or keep" data relating to tax domicile.
- The Howard Hughes Medical Institute in Chevy Chase, Maryland, which has $20.4 billion in assets, holds at least $891 million in offshore funds, from which it earned $123 million in the year ending 31 August 2017, according to public documents. It declined to discuss its investments.
- The Robert Wood Johnson Foundation in Princeton, New Jersey, which has $10.8 billion in assets, has placed at least $3 billion in offshore havens. Foundation officials discussed their investing practices with *Science*.
- The Bill & Melinda Gates Foundation in Seattle, Washington, has no apparent involvement in offshore funds, according to the Paradise Papers and public documents.
- Three other private research funders—the David and Lucile Packard Foundation, the Gordon and Betty Moore Foundation, and the William and Flora Hewlett Foundation, all based in Silicon Valley in California—have made offshore investments of up to $168 million each, according to the Paradise Papers and public documents. In written statements, the foundations said they comply with tax laws but declined to comment otherwise.

> ***"Shouldn't we be more than a private investment company that uses its excess cash flow for good?"***
>
> **Dana Bezerra**, Heron Foundation

Foundation officials and philanthropy experts say offshore investment can play an important role in enabling those charities to meet their fiduciary responsibility to nurture their endowments. But the practice also opens the foundations to intense criticism. "Foundations that invest in tax havens need to know that … they are alongside criminals, tax evaders, and kleptocrats," says Gabriel Zucman, a University of California, Berkeley, economist who has studied offshore investing. Such foundations are helping "normalize these practices and blow up the volume, so the infrastructure exists also for the illegal uses," says Annette Alstadsæter, an economist at the Norwegian University of Life Sciences in Oslo. "They are robbing the taxpayers," says economist and Nobel laureate Joseph Stiglitz of Columbia University, and "are giving life to an institutional arrangement which is basically nefarious and bad for our global society."

FOR AT LEAST A CENTURY, wealthy individuals and institutions have moved money outside their home nations—for example, by parking it in the anonymous numbered accounts made famous by Swiss banks. In recent decades, however, the popularity and complexity of offshore investing has grown dramatically. Some small nations and territories—including the Cayman Islands, Bermuda, and Malta—have aggressively moved to become offshore havens by promising secrecy, light regulation, and low or no taxes on profits.

As of 2014, at least 8% of the world's financial wealth—some $7.6 trillion—was invested in funds based in offshore havens, estimates Zucman, who wrote a seminal 2015 book on the topic. Offshore funds enabled companies to legally avoid paying $130 billion in U.S. taxes each year, he estimates. And illegal tax evasion involving offshore funds subtracted an additional $35 billion annually.

In the past, many philanthropies—which national governments ordinarily exempt from most taxes because they are seen as providing a public service—would have viewed tax avoidance as shameful, says Brooke Harrington, an economist at Copenhagen Business School. But no more. In the United States, for example, many foundation officers regard minimizing taxes "almost as a necessity," she says. "If you don't do that, you're not fulfilling your responsibility to donors. Kind of the way corporate directors will say: 'It's our duty to maximize shareholder value, and that includes reducing our tax payments to as close to zero as possible.'"

But some foundation officials tell *Science* that, because their tax burdens are already low, other factors are more important to their decisions to invest offshore. For example, fund managers increase profits for themselves and their clients by avoiding costly regulatory red tape, says Edmond Ghisu, chief investment counsel at Robert Wood Johnson. Offshore havens often have minimal requirements on "how many records [funds] need to have" and "how open their books and records need to be to investors," he says. The Cayman Islands, for example, "has risen to the top" in popularity among money managers because it has scant reporting requirements, Ghisu says.

Offshore funds can also open doors to a wider array of investment options and top advisers, who often run the funds from offices in financial centers such as New York City or London. Ghisu, for instance, says his foundation looks first for "the best managers, to maximize our returns so that we have resources that we can deploy in support of our mission." Wellcome takes a similar position. "Many of the best-performing funds have offshore domiciles," it wrote in a state-

Downloaded from http://science.sciencemag.org/ on December 10, 2018

Published by AAAS

ment. “Our successful long-term investment strategy,” it added, “is based on exposure to a globally diversified range of asset classes.”

Normally, fund managers, not the foundations, choose investments. But some foundations bar certain investments that they believe would pose conflicts of interest. Robert Wood Johnson, for instance, says it has no involvement in firearms, alcohol, or tobacco. “For us to invest in, say, a tobacco company, would be so antithetical to what we want to do that it would be a travesty,” says Brian O’Neil, the foundation’s chief investment officer.

Yet Robert Wood Johnson’s offshore investments and managers have still generated controversy. Tax returns show that since at least 2014, the foundation has invested heavily in Cayman Islands funds managed by GSO Capital Partners, a unit of the investment titan Blackstone Group, headquartered in New York City. The foundation’s most recent filing showed about $50 million in those funds. GSO has drawn harsh criticism for how it handles credit default swaps—a once-exotic type of risk-hedging security that became notorious for contributing to the Great Recession. U.S. lawmakers and regulators have reined in the swaps, which are legal, but they remain less regulated elsewhere. “The hedge fund industry can’t do what it wants to do under the onshore regulations of the U.S. because it’s too risky,” Harrington says. “But the Caymans will let them do it.”

When money flows offshore

The Paradise Papers and publicly available financial statements reveal some, but not all, offshore investments and commitments by seven private foundations that are major funders of scientific research.

FOUNDATION	ENDOWMENT ASSETS*	KNOWN OFFSHORE INVESTMENTS
Bill & Melinda Gates Foundation	$51.8 billion	None
Wellcome Trust	$29.3 billion	$926 million
Howard Hughes Medical Institute	$20.4 billion	$891 million
Robert Wood Johnson Foundation	$10.8 billion	$3+ billion
William and Flora Hewlett Foundation	$9.9 billion	$168 million
David and Lucille Packard Foundation	$7.9 billion	$140 million
Gordon and Betty Moore Foundation	$6.9 billion	$40 million

*Restricted and unrestricted net assets, as of most recent audited financial statements

DATA: PARADISE PAPERS; FOUNDATIONS’S MOST RECENT TAX RETURNS AND AUDITED FINANCIAL STATEMENTS

In particular, GSO has drawn scrutiny for swaps that involve distressed companies and a strategy in which GSO offers a troubled firm an incentive to intentionally default on a loan, triggering a process that enables GSO to realize hefty profits. For years, such deals have attracted substantial media attention and lawsuits. A recent investigative story in the *Financial Times* said such practices made GSO the industry’s “biggest predator.” GSO told the paper it has acted legally and in a manner “consistent with the expectations of its sophisticated market participants.”

In April, the U.S. Commodity Futures Trading Commission took notice, decrying the kinds of actions taken by GSO as “manipulation” that “may severely damage the integrity” of the market. GSO then stepped away from a pending deal. At about the same time, Robert Wood Johnson officials raised their own concerns with GSO. O’Neil says the firm has “really backed off” from the controversial swaps.

Critics contend that offshore machinations increase income inequality by reducing tax funds for public services while shifting the tax burden from companies and wealthy individuals to the middle class. And, as studies funded by Robert Wood Johnson itself have suggested, inequality can damage public health. For example, the foundation underwrote a landmark 2015 study showing extreme income inequality—rather than poverty alone—is a key contributor to ill health and shorter life expectancy. The foundation has also funded grassroots campaigns to address such problems, including a public-private partnership in Richmond, where residents suffer from some of the nation’s worst income inequality. But O’Neil rejects the suggestion that the foundation’s own investment practices contribute to inequality. “I don’t think you can take the harm that is caused by that and impute it to us.”

At Wellcome, where researching the effects of climate change has become one focus of giving, officials consider environmental issues when making investment choices, the trust said in a statement to *Science*. But Wellcome declined to discuss how those concerns have shaped its offshore investments. And public records indicate environmental issues have not prevented the foundation from taking hefty, ongoing, direct equity stakes in fossil fuel companies—including Royal Dutch Shell of The Hague, Netherlands, and Schlumberger of Houston, Texas—whose operations have drawn criticism from climate change, environmental, and human rights advocates.

Wellcome has resisted calls to divest from the firms, saying the investments serve as leverage to influence corporate practices. “Engaging with these companies will strengthen their commitments toward reducing carbon emissions more effectively than divestment,” it argued. The foundation declined to describe how it engages with the companies or to what effect. But even if direct shareholders can wield influence through moral suasion or proxy votes, critics of offshore investing note that such engagement is rarely possible for investors in offshore energy funds, which are often structured to insulate owners from company actions.

Wellcome also notes that its investment profits—directly from Shell or indirectly through Cayman Islands funds that invest in energy firms—fuel the trust’s good works, including projects that fight the impacts of global warming. But Dana Bezerra, a prominent advocate for ethical investing by charities and head of the Heron Foundation in New York City, questions that reasoning. “It’s a justice question,” she says. “I have yet to meet a community willing to trade off our ability to generate returns with their clean water and healthy soil, on the promise that we’ll be back to fix it with charitable dollars in the future.” (Heron, she says, screens its entire $307 million investment portfolio to ensure that it supports—or at least does not counter—the foundation’s philanthropic goal to fight poverty.)

TO SOME CRITICS of offshore investing, its biggest downside is secrecy. The lack of transparency can make it difficult for donors, grant recipients, and the public to reach their own conclusions about whether an offshore investment poses a potential conflict.

Most offshore funds, for example, carry vague names that offer few hints about their purpose. For example, Howard Hughes holds $187 million in “Coastland Relative Value Fund Ltd.” and “Cerberus HH Partners LP” (managed by a company named after the mythological three-headed hound that prevents the damned from escaping through the gates of hell). Robert Wood Johnson has $143 million in another canine-inspired fund, “Hound Partners OS.” All three are based in the Caymans.

The funds rarely reveal to the public where they place investments—and normally also bar their investors from sharing that information. Both Wellcome and Robert Wood Johnson, for example, say confidentiality agreements with fund managers prohibit them from making such disclosures. Fund managers often want to avoid leaks of sensitive information that could move markets or aid competitors.

Sometimes, even investors don’t know how offshore funds use their money. O’Neil says in his experience, there are “only a few funds that really don’t tell us anything.” But contracts revealed in the Paradise Papers

Downloaded from http://science.sciencemag.org/ on December 10, 2018

Published by AAAS

A cargo ship steams through the Bosphorus past Istanbul, Turkey. The Wellcome Trust invests through an offshore fund in a firm selling ship fuel, which is a major source of particulate air pollution. It also funds studies that highlight the dangers that particulate pollution poses to human health.

PHOTO: BULENT KILIC/AFP/GETTY IMAGES

specify that investors often have no "liability, obligation, or responsibility whatsoever" for how a fund operates or any obligation to verify that the fund has actually used its money for planned investments.

Such opacity is not appropriate for charitable institutions, established for social benefit, Bezerra says. "Not only should you [provide investment details], but you are compelled to because you are managing money in the public trust," she says. "Shouldn't we be more than a private investment company that uses its excess cash flow for good?"

TO REDUCE ETHICAL CONFLICTS, Stiglitz says policymakers should change charity governance rules to make it "a violation of fiduciary responsibility to engage in something that might have reputation risk," such as investing in an offshore tax haven with a "sleazy" repute.

Persuading policymakers to make such changes, however, is likely to be difficult, in part because foundations typically operate under a patchwork of national and local laws. Instead, some observers believe action will have to come from foundation board members and officials. One needed reform, Bezerra says, is to end—or at least curb—the "perverse incentive" that foundations create for their investment officers, who make many of the day-to-day decisions about how to grow or protect a charity's endowment. Their compensation is often tightly tied to how well their investment portfolio performs. And good performance is handsomely rewarded. In 2016, Wellcome's Danny Truell (who retired last year) made $5.8 million and O'Neil made $1.8 million; last year, Landis Zimmerman of Howard Hughes made $3 million. Each was by far the highest paid employee of his foundation.

At Wellcome, the incentives are based on performance of the portfolio as a whole. Robert Wood Johnson ties compensation for O'Neil and others to both investment performance and "alignment of investment objectives with foundation's mission and strategic objectives," such as maximizing returns and ensuring that no funds are invested in tobacco, alcohol, or firearms.

Requiring managers to place social, environmental, and philanthropic goals—not just investment returns—at the heart of their investment choices need not mean they will miss financial targets, Bezerra says. Last year, Heron's holdings gained nearly 16%, according to the foundation. In comparison, at Robert Wood Johnson—the major science philanthropy most heavily concentrated in offshore funds—the portfolio rose by about 13%.

Such policy changes would probably require approval from a foundation's board of directors. In general, however, board members often prefer to focus on grantmaking and rarely become deeply involved in investment decisions, philanthropy experts say. At Wellcome, for instance, former board member Peter Smith says investment issues arose just a few times during his 10-year tenure, from 2005 to 2014. In one case from 2013, he recalls, board members learned from media reports that Wellcome had invested in a payday lender accused of preying on the poor. The 13-member board ultimately directed trust staff to divest from the company, says Smith, an epidemiologist at the London School of Hygiene & Tropical Medicine.

"There is a tension," Smith says, "between the philanthropic mission that the trust has as a charity and the way in which it invests to maximize the income … which [charity officials] say they have a duty to do." But the tensions surrounding offshore investments never came up at any board meeting he attended, he says. Smith didn't pass judgment when asked whether the trust's holdings in a bunker fuel merchant contradict the charity's goals. But, "If there were things that were ethically dubious, then I would have expected it to be discussed at the board level," he says.

James Gavin, a physician and diabetes expert at Healing Our Village, a health care company in Atlanta, who served as a trustee of Robert Wood Johnson a decade ago, says that if offshore investing undermines the foundation's philanthropic goals, "that would be of extreme concern." But he, too, doesn't recall board discussions of the practice.

The increased scrutiny surrounding offshore investing, driven partly by the release of the Paradise Papers, is making it more likely that charities—including research funders—will have to grapple with the issue, observers say. That's a good thing, says Dana Lanza, who heads the Oakland, California, nonprofit Confluence Philanthropy, which encourages foundations to align investment choices with their philanthropic mission. Foundations that invest heavily in offshore havens, she says, need to ask themselves a basic question: "Do you owe it to the world to be an ethical investor?" ■

The methodology for this story is online at https://scim.ag/OffshoreMethodology. Jia You contributed reporting. The story was supported by the Science *Fund for Investigative Reporting.*

Downloaded from http://science.sciencemag.org/ on December 10, 2018

Published by AAAS

INSIGHTS

BOOKS *et al.*

ILLUSTRATION: KAILEY WHITMAN

AAAS/SUBARU SB&F PRIZES FOR EXCELLENCE IN SCIENCE BOOKS

Books for budding scientists

From audacious space missions and quantum physics to clean cookstoves and coral nurseries, this year's finalists for the AAAS/Subaru SB&F Prizes for Excellence in Science Books dare to go where few children's titles have gone before. Sponsored by Subaru of America and facilitated by the American Association for the Advancement of Science (AAAS, the publisher of *Science*), the competition celebrates high-quality children's science books. Read on for reviews written by the staff of the *Science* family of journals and a few friends. —**Valerie Thompson**

MIDDLE GRADES SCIENCE BOOK

Champion

Reviewed by **Caroline Ash**[1]

The American chestnut once grew straight, tall, and true in the forests of the United States. Then at the start of the 20th century, a fatal fungus blight disease nearly made this prized tree extinct. But thanks to the persistence of American chestnut lovers and scientists in China, Europe, and America, this iconic tree is on the way to restoration. In *Champion*, Sally Walker tells the story of how disaster was averted, revealing the technical details of the three-pronged rescue program.

The first step was to cross-breed American trees with resistant varieties. The second approach was to inoculate vulnerable trees with weakened blight fungus to stimulate their immunity. Last, genetically modified saplings bearing a gene for an enzyme that reduces levels of toxic oxalic acid produced by the blight were developed.

Descriptions of the technical details entailed at each step are very clearly explained throughout the text, without shying away from complexity. The story of how the research unfolded is told through the voices of the dedicated scientists involved. Clearly, the establishment of the breeding programs were long labors of love, spanning decades; a little more of this passion could have been transmitted in the text. Still, there is a lot of inspiring biology to be learned from this case study. All in all, this is a great story for more sophisticated junior biologists.

Champion: The Comeback Tale of the American Chestnut Tree, *Sally M. Walker, Henry Holt and Co., 2018, 144 pp.*

My First Book of Quantum Physics

Reviewed by **Jelena Stajic**[2]

Quantum physics has an image problem. Spooky, wacky, strange—the adjectives often used to describe its inner workings—paint a picture of an esoteric discipline. Yet, it is the rules of quantum physics that dictate the structure of matter, that help interpret the signals from distant stars, and that make your smartphone run. This message is nicely conveyed in *My First Book of Quantum Physics*, an illustrated guide for children 8 and older (and their parents).

The book follows the development of quantum physics largely chronologically, explaining why classical physics was not sufficient to describe the subatomic world. It then moves on to concepts such as particle-wave duality, the uncertainty principle, and radioactivity. A number of physicists make appearances, from Isaac Newton to Marie Curie,

Downloaded from http://science.sciencemag.org/ on December 10, 2018

Published by AAAS

but it is the familiar cartoon form of Albert Einstein that serves as a guide throughout the book (Einstein's ambivalent attitude toward quantum mechanics notwithstanding). The illustrations are clear, eye-catching, and consistent; the authors occasionally anthropomorphize inanimate objects to make concepts more accessible (for example, an electron "feels comfortable" in its orbit) but largely avoid sounding condescending.

Most commendably, the narrative does not stop in the 1930s. Particle accelerators, the Standard Model of particle physics, and the Higgs boson all get well-deserved mentions, but so do everyday "quantum gadgets," such as laser pointers and light-emitting diode (LED) lights. The book leaves young readers with a sense of quantum physics as a vibrant, active pursuit that has and will continue to influence their lives in very real ways.

My First Book of Quantum Physics, *Kaid-Sala Ferrón Sheddad, Illustrated by Eduard Altarriba, Button Books, 2018, 48 pp.*

Impact!

Reviewed by **Marc S. Lavine**[3]

Although movies have magnified the potential damage that Earth might suffer from the arrival of an asteroid or comet, there are legitimate reasons to be concerned and there is an ongoing need to track celestial objects that could cause major damage. In starting *Impact!* with the story of a meteor that exploded over the Russian city of Chelyabinsk in 2013, Elizabeth Rusch captures the terror and damage larger space debris can cause. Even though the impact site was more than 80 km outside the city, the shock wave it created shattered glass, rattled buildings, and caused roofs to collapse.

Spotting and tracking asteroids is almost as hard as finding needles in haystacks, while identifying and deciphering previous impacts requires careful detective work. This is especially true when trying to analyze a large impact crater that might be kilometers in diameter, where the impact both compressed the ground and turned the layers of earth and rock upside down. Rusch introduces us to individuals who either track celestial objects or investigate past impacts and to the tools of the trade required to study them. She even reveals how amateur scientists can get involved. And if your interests veer from science to science fiction, she closes with a range of ways one might alter the trajectory of an asteroid, should the need ever arise.

Impact!, Asteroids and the Science of Saving the World, *Elizabeth Rusch, Photography by Karin Anderson, HMH Books for Young Readers, 2017, 80 pp.*

Itch!

Reviewed by **Seth Scanlon**[4]

In this delightful—if slightly disquieting—work, Anita Sanchez artfully describes the ways in which a variety of organisms make us itch. Much attention is directed toward familiar insects and arachnids that cause humans discomfort. In addition, Sanchez elucidates the various ways that fungi (such as those that cause athlete's foot) and plants (such as nettle, poison ivy, cacti, and prickly pears) can induce the urge to scratch.

These pruritogenic pests also allow the author to pivot onto various historical topics in a fun and appealing manner. Lice, for example, serve as a jumping-off point to describe the unhygienic conditions experienced by soldiers during World War I, whereas fleas are introduced in the context of the hugely popular flea circuses of the 19th century.

Along the way, Sanchez offers a whole host of useful tips for preventing or relieving itchiness. After reading this book, you should be able to remove embedded caterpillar bristles, soothe a nettle's sting, avoid mosquito bites, and deodorize a pet that has encountered a skunk. This wealth of information is reinforced with approachable, humorous, and eye-catching illustrations by Gilbert Ford.

Downloaded from http://science.sciencemag.org/ on December 10, 2018

Published by AAAS

The book concludes with a thought-provoking discussion of the neurological and immunological origins of itch. In addition, Sanchez discusses how scratching can (at least temporarily) allay irritation as well as other benefits it can provide. This author/illustrator team is to be commended for conveying a cornucopia of data in an enjoyable and engaging way.

Itch!: Everything You Didn't Want to Know About What Makes You Scratch, *Anita Sanchez, Illustrated by Gilbert Ford, HMH Books for Young Readers, 2018, 80 pp.*

Trash Revolution

Reviewed by **Hadassah Nusinovich Ucko**, **Solomon Nusinovich Ucko**, *and* **Yevgeniya Nusinovich**[5]

Trash Revolution explains how common materials are produced and recycled and suggests solutions to various real-world problems related to resource consumption, waste management, and climate change. In addition to widely known recommendations such as "reduce, reuse, recycle," the authors present many solutions made possible by cutting-edge research, such as making biodegradable plastics from stale food and using bacteria to grow compostable fabrics.

The technical information is interspersed with humor and kid-friendly touches—"#gratitude," for example, is associated with the invention of toilet paper. In addition to general information, the authors provide handy reference charts comparing the benefits and drawbacks of different materials, as well as specific recommendations for handling them. However, some of these suggestions seemed unattainable to us. For example, the authors recommend making your home "a junk-mail-free zone," but offer no suggestions for how that could be achieved.

We noted a few minor problems, such as a mistaken characterization of deuterium as an extra molecule inside water molecules, a gratuitous negative comment about genetically modified organisms, and a surprisingly positive discussion of waste incinerators that neglected to mention any concerns about their fumes and effects on human health. Overall, however, it is very informative, with thoughtful explanations of what we can all do to make environmentally friendly choices.

Trash Revolution: Breaking the Waste Cycle, *Erica Fyvie, Illustrated by Bill Slavin, Kids Can Press, 2018, 64 pp.*

Pedestrians walk along the rewilded High Line park in New York City.

PHOTO: YUEN MAN CHEUNG/ALAMY STOCK PHOTO

Rewilding

Reviewed by **Sacha N. Vignieri**[6]

As the human population grows, we are relentlessly encroaching on the natural habitats that surround us. This book defines and describes the science and process of an increasingly important mechanism for conservation known as "rewilding."

Rewilders, we learn, want to restore habitats to their prehuman states, creating environments that can support native species and give them room to thrive. The authors first describe the basics of this process, including why it is important, and then discuss several examples of where, why, and how rewilding is happening. These include everything from the Pleistocene rewilding plan, which advocates reintroducing modern stand-ins for megafauna that went extinct at the end of the last ice age, to the rewilding of New York City's "High Line," an abandoned, elevated train track where lacewing insects have been released to prevent infestations of harmful bugs.

The book is well targeted toward middle-grade readers because it accurately describes rewilding while remaining accessible and interesting. The authors' positive tone is both refreshing and important. They present rewilding stories in a way that clearly lays out why the process is ecologically important and why it is important for human society as well.

Rewilding: Giving Nature a Second Chance, *Jane Drake and Ann Love, Annick Press, 2017, 88 pp.*

CHILDREN'S SCIENCE PICTURE BOOK

Living Things and Nonliving Things

Reviewed by **Tage Rai**[7]

If we wanted to define "games," we might say they involve competing, keeping score, following rules, and having fun. However, in some games, players cooperate and don't keep score. And while all games have rules, so do many other activities that may or may not be fun. In this book, Kevin Kurtz extends this line of argument to the nature of life.

Are living things the only ones that move, or grow, or reproduce? Kurtz elegantly reveals that some nonliving things can do these things, whereas some living things can't.

Astute readers may find themselves wishing for a deeper discussion of viruses. Viruses lack cells of their own, but they confiscate their host's cellular machinery to replicate themselves, thus complicating any cellular definition of life. The conceptual ambiguity of viruses underscores a deeper, albeit understandable, omission from the book: the existential quandary of death.

Ultimately, Kurtz ends with the unsettling realization that there is no categorical distinction between living and nonliving. Instead, he proposes a family resemblance model in which something that has many of the characteristics shared by living things probably belongs to the category.

The book is beautifully illustrated with high-quality photographs of nature, animals,

Downloaded from http://science.sciencemag.org/ on December 10, 2018

Published by AAAS

and inventions. Despite its simple text, *Living Things and Nonliving Things* is deceptively deep and provides a valuable lesson in scientific uncertainty.

Living Things and Nonliving Things: A Compare and Contrast Book, *Kevin Kurtz, Arbordale Publishing, 2017, 32 pp.*

Many

Reviewed by **Jennifer Sills**[8]

In *Many*, a rosy-cheeked, red-haired explorer tries to answer the question so many scientists have pondered: "How many different kinds of living things are there on the planet?" She discovers elephants and oak trees, mushrooms and beetles, and mites and microbes. All of these species, she realizes, are interdependent, forming complex ecosystems.

Here, the story takes a dark turn: Humans have been poisoning and destroying these ecosystems, and many living things have disappeared forever. We have a responsibility, our forlorn narrator warns: We don't want to reach a point at which we have to "count down instead of up."

The story's whimsical tone, which belies its sobering message, will engage readers, but the highlights of the book are the detailed watercolor illustrations that infuse each landscape and statistic with warmth and appeal. Vibrant colors throughout the pages of discovery contrast with the abrupt shift to muted browns on the pages of destruction. The emotional punch the images deliver will be more effective in motivating readers to act than trivia about mushrooms ever could be.

Many: The Diversity of Life on Earth, *Nicola Davies, Illustrated by Emily Sutton, Candlewick, 2017, 40 pp.*

What Do They Do with All That Poo?

Reviewed by **Steve Mao**[9]

On any given day, an individual zoo can produce more than 5000 pounds of animal waste. So, "what do they do with all that poo?"

The first part of this book makes it clear that poop comes in different sizes, shapes, and colors and that these properties are related to the distinct diets, anatomies, and physiologies of different animals. How animals use their waste can also affect the characteristics of their poop, as well as how and when they poop. Wombats, for example, excrete upward of 100 cube-shaped droppings every evening to mark their territory, whereas sloths descend from their treetop habitat to poop on the ground just once a week.

How do zoos deal with animal waste? Some is just sent off to landfills, but some is also used to monitor the health of the animals. Some is processed into compost for local gardens, and some is recycled to make useful products such as paper and fuel.

Although there's no main character, every animal is easily related to. The drawings are vivid and, by and large, accurate. (Wombats, however, do not build a scat-fence, as one illustration seems to suggest.)

Most of the animals highlighted in this book are mammals, but it would have been fun to read about the excretions of other species. Perhaps this will be the topic of a follow-up title (book "number 2," if you will).

What Do They Do with All That Poo?, *Jane Kurtz, Illustrated by Allison Black, Beach Lane Books, 2018, 40 pp.*

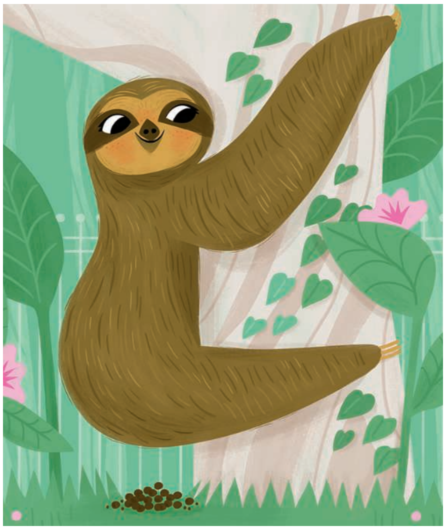

ILLUSTRATION: ALLISON BLACK AND SIMON & SCHUSTER

A House in the Sky

Reviewed by **Sacha N. Vignieri**[6]

The sight of a common squirrel can inspire squeals of delight from young children. They might ask, "Is it going home?" as the squirrel disappears up a tree. *A House in the Sky*, Steve Jenkins's lovely story on animal homes, provides answers that will satisfy such questions while providing more detail for a similarly curious adult or older child. "Some houses are made of bubbles," reads one passage, for example. Below, the author elaborates: "A Siamese fighting fish takes a gulp of air and then blows it back out. It does this over and over again, creating a floating nest made of bubbles to protect its babies."

Illustrator Robbin Gourley's playful yet beautiful renderings reinforce the book's message. "Look up—a house in the sky!" reads another page. The common swift, rendered in muted browns against a pale blue sky, spends months on the wing, we learn, eating, drinking, and sleeping in the air.

Young children are naturally curious about animals. Jenkins's sweet exploration of how and where they live provides an opportunity to connect with older readers and to dig a little deeper together.

A House in the Sky: And Other Uncommon Animal Houses, *Steve Jenkins, Illustrated by Robbin Gourley, Charlesbridge, 2018, 32 pp.*

The Brilliant Deep

Reviewed by **Julia Fahrenkamp-Uppenbrink**[10]

With sparing words and mesmerizing, soft-colored paintings, *The Brilliant Deep* tells the story of Ken Nedimyer, an American fish collector and "live rock farmer" who found a way to restore the world's coral reefs by growing coral colonies in underwater nurseries and then planting them onto dying reefs.

Nedimyer has long loved the ocean. One of the book's most memorable images shows him as a boy, looking out over the sea, all its secrets hidden beneath the surface. On the next page, he is snorkeling through an underwater world teeming with life. We follow along as he learns to scuba dive and begins to collect fish to study in aquariums at home.

As an adult, Nedimyer uses his expertise with growing "living rocks"—rocks covered with sponges and other invertebrates that are used in aquariums—to cultivate coral. The book ends on a note of hope as Nedimyer and his organization, the Coral Restoration Foundation, begin to help other countries save their reefs as well.

The simple scientific explanations given throughout the book are easy to understand and are woven into the story in a way that does not distract. However, the main text does not mention climate change or other human threats. A two-page spread at the end merely cites complicated reasons, including changing ocean temperatures and overfishing, for the decline of coral reefs. This is a missed opportunity. Nevertheless, I can only recommend this beautiful and inspiring book, which shows what love for nature combined with human ingenuity can achieve.

The Brilliant Deep: Rebuilding the World's Coral Reefs, *Kate Messner, Illustrated by Matthew Forsythe, Chronicle Books, 2018, 48 pp.*

Downloaded from http://science.sciencemag.org/ on December 10, 2018

Published by AAAS

Awakened by his mother's coughing—the result of cooking indoors over an open flame—Iqbal contemplates how to win his school's sustainability-themed science fair.

ILLUSTRATION: REBECCA GREEN/KIDS CAN PRESS LTD.

Iqbal and His Ingenious Idea

Reviewed by **Jennifer Sills**[8]

Amid monsoons and the daily prayers of Ramadan, Iqbal dreams of winning his school's sustainability-themed science contest. His mother and baby sister Rupa have developed a cough from sitting inside cooking food over an open fire. With the help of his other sister, Sadia, Iqbal finds a way to help them by turning an umbrella into a solar cooker.

Iqbal's story is steeped in the customs and language of Bangladesh while celebrating universal human qualities such as curiosity and ingenuity. Sadia's role is realistic; she joins her brother in school and helps him build his stove, but unlike Iqbal, she is expected to help with childcare and cooking.

Author Elizabeth Suneby seamlessly weaves Bengali words into the text, describing, for example, how Iqbal offers the first serving of "semai"—a dessert made with vermicelli noodles served at "Eid al-Fitr" (the holiday that marks the end of Ramadan)—to Sadia to thank her for her help. Illustrator Rebecca Green's colored pencil illustrations depict Iqbal's family and their village in vivid detail. The book's appendices provide an explanation of the benefits of clean cookstoves and a glossary of Bengali words.

Readers can also follow instructions to create their own solar cooker. The project will require a pizza box, aluminum foil, plastic wrap, and a lot of patience—the stove will take 30 or 40 minutes to heat up in the sun.

Iqbal and His Ingenious Idea: How a Science Project Helps One Family and the Planet, *Elizabeth Suneby, Illustrated by Rebecca Green, Kids Can Press, 2018, 32 pp.*

HANDS-ON SCIENCE BOOK

Alexander Graham Bell for Kids

Reviewed by **Marc S. Lavine**[3]

Alexander Graham Bell is best known for his invention of the telephone, but this wasn't the work that he found most rewarding. Teaching deaf students to finger spell and to speak, using the visible alphabet developed by his father, was his lifelong passion. Bell's grandfather voice trained students with speech problems such as stuttering, and his mother had severe loss of hearing. His interest in speech and sound was critical to many of his future inventions.

In *Alexander Graham Bell for Kids*, Mary Kay Carson weaves together key events and influences that shaped Bell's life, and in turn how he shaped the world around him. Although he was a poor student in school, Bell spent his life learning from the written works of others, from ongoing tinkering and innovation, and from the many colleagues and connections he made throughout his life.

Bell's invention of the telephone has largely overshadowed his many other contributions, such as his work on early versions of the phonograph and metal detectors and his work on airplanes and hydrofoil boats. These inventions often brought him into conflict with other inventors of the day, including Thomas Edison and Elisha Gray.

The book includes many sidebars to explain the scientific principles behind each invention, as well as 21 hands-on activities, that enhance the narrative. But perhaps the true value of the books comes from all the little stories, previously unknown to me, that show the richness of his life, such as Bell's role in connecting Helen Keller with her teacher, Anne Sullivan, and Bell's role in supporting *Science* magazine during its early years.

Alexander Graham Bell for Kids: His Life & Inventions with 21 Activities, *Mary Kay Carson, Chicago Review Press, 2018, 144 pp.*

Light Waves

Reviewed by **Marc S. Lavine**[3]

From the dim flicker of a candle flame to the daily illumination provided by the Sun, visible light enables us to see our world. Despite its presence all around us, the properties of light can be confusing and counterintuitive. Why, for example, does light, which travels in a straight line, appear to bend, when looking at a straw in a glass of water? Or why does our reflection invert when we look at the front of a metal spoon? Using a mix of illustrations and simple experiments aimed at a younger reader, David Adler explains the basic composition, behavior, and properties of light.

Through the casting of shadows by using a flashlight and a tower of wooden blocks, Adler teaches readers about objects that are transparent, translucent, or opaque. We are shown how to divide white light into a spectrum of colors when it passes through a prism, and from this, we are taught why objects have different colors depending on which part of the visible spectrum they reflect rather than absorb.

At times, the writing seems aimed at older readers; however, a glossary at the end helpfully pulls together all the optics terminology.

Light Waves, *David A. Adler, Illustrated by Anna Raff, Holiday House, 2018, 32 pp.*

Downloaded from http://science.sciencemag.org/ on December 10, 2018

Published by AAAS

Dog Science Unleashed

Reviewed by **Brent Grocholski**[11]

Dogs make for the perfect assistants for the activities in *Dog Science Unleashed*. This vivid volume lays out two dozen or so exercises that double as experiments, the goal of which is to better understand canine senses and physiology.

The experiments are well described, with step-by-step instructions and photos. Most are easy to set up and only require household items. Exceptional photography accompanies the instructions and helps readers to understand the activities. The wild card, as you might guess, is your pooch's willingness to help unleash the dog science. But that shouldn't be a problem for most dogs; many of the activities involve treats and toys.

In an activity called "A Puzzle for Your Pooch," the authors provide instructions for setting up an experiment to see whether your dog can learn to extract treats from a muffin tin. In another, readers learn how to craft a homemade stethoscope out of a funnel and an empty paper towel tube and to use it to listen to their dog's heartbeat.

Some of the activities are more targeted to helping understand the particular dog you are working with. In "Half Bath," for example, readers are encouraged to determine whether shampoo is right for their pup by washing only one side and monitoring odor, dirt, and oil levels over a month. However, the book sticks to a scientific approach, even for these activities.

What the book does not provide are broad insights into dog behavior or socialization. But focusing on more universal and less variable traits is probably for the best in a home experiment–driven book.

Dog Science Unleashed: Fun Activities to Do with Your Canine Companion, *Jodi Wheeler-Toppen, Photography by Matthew Rakola, National Geographic Kids, 2018, 80 pp.*

A human-pooch foot race teaches young readers how to create a repeatable experiment.

PHOTO: MATTHEW RAKOLA FOR NATIONAL GEOGRAPHIC KIDS

Dig In!

Reviewed by **Michael Funk**[12]

Modern agriculture has given us seedless watermelons, tomatoes in February, and apple varieties with trademarked names and intensive marketing. However, there remains something magical about planting a seed, watching it sprout, and after a long season, tasting the fruit (or vegetables) of one's work and dedication. *Dig In!* encourages kids to get in the kitchen and rescue neglected stems and seeds for experimentation in the garden.

The book features 12 simple projects, some of which may be better controlled versions of events already happening in your crisper drawer. In particular, growing lettuce, onions, and potatoes from sprouts is nearly foolproof. Others, such as garlic and ginger, might require some preparation. Growing plants from seeds requires the most patience, but the wonder of seeing sprouts emerge from soil is sure to delight kids of all ages.

The projects in *Dig In!* are simple and can be started in an old cup or newspaper pots. Alongside the garden projects are recipes that can be the source of the seeds or sprouting material. The pairing might encourage picky eaters to give celery or herbs a chance, although I would not expect to harvest much from your sprouts and seedlings unless you have a working garden already.

Nevertheless, intrepid young gardeners should find these projects inspiring and will hopefully want to learn more about how their food is grown as a result.

Dig In!: 12 Easy Gardening Projects Using Kitchen Scraps, *Kari Cornell, Photography by Jennifer S. Larson, Millbrook Press, 2018, 64 pp.*

Bug Lab for Kids

Reviewed by **Lauren Kmec**[13]

How do you measure a beetle's strength or the speed of a centipede? *Bug Lab for Kids*, by entomologist John Guyton, reveals the answers to these questions, among others.

The book is divided into nine well-organized units, each containing several lab exercises. An introductory section provides helpful advice regarding appropriate attire for fieldwork, first aid treatment for bites and stings, and the importance of keeping a field notebook. Another unit offers a straightforward primer on the scientific method.

Would-be entomologists start by learning how to make and use a collection net, as well as how to care for live critters. More sophisticated collection techniques, such as the use of an aspirator to capture very tiny insects, are also covered. Readers can then embark on a variety of activities to observe insects in their natural habitat.

Other labs include a spiderweb search, a papier-mâché wasp's nest construction project, a multiweek butterfly-rearing operation, and a taste test of edible insect "treats" (not for the faint of heart!). Although special equipment such as a blacklight is required for some experiments, many of the necessary tools can be constructed from household materials or purchased inexpensively.

Interspersed throughout the book are fun and surprising snippets of bug trivia: Moths navigate by the moon, bees "dance" to communicate with other bees, and horned dung beetles can pull 1000 times their own weight. These tidbits bolster Guyton's message that although bugs may not be cute or cuddly, they are indeed fascinating.

Bug Lab for Kids: Family-Friendly Activities for Exploring the Amazing World of Beetles, Butterflies, Spiders, and Other Arthropods, *John W. Guyton, Quarry Books, 2018, 144 pp.*

Downloaded from http://science.sciencemag.org/ on December 10, 2018

Published by AAAS

YOUNG ADULT SCIENCE BOOK

Rocket Men

Reviewed by **Laura M. Zahn**[14]

The year was 1968. Protests against the Vietnam war filled the streets of America, and the United States and the Soviet Union were racing to the moon. In 1969, men would walk on its surface. However, before we could accomplish this feat, we needed to be sure that they could get there and return safely.

Focusing on the Apollo 8 mission—the first manned mission to orbit the moon—in *Rocket Men*, Robert Kurson vividly transports the reader into the minds of the people involved, especially the astronauts and their wives, as they prepared for and underwent this perilous mission. The possibility of death is a recurring theme. Kurson repeatedly reminds the reader of the fatal fire that claimed the lives of the Apollo 1 astronauts and the experimental nature of space travel. Yet, fear was not at the forefront for Frank Borman, Bill Anders, and Jim Lovell. Instead, the book emphasizes how these brave men were willing to sacrifice everything for their country.

This story, about a little-recalled but major move forward into space, will captivate readers of all ages, but as a full-length chapter book with few illustrations or pictures, older readers will have an easier time with this book. Kurson's evocative writing places the Apollo 8 mission into historical perspective and allows us to vicariously experience the launch of the Saturn V rocket and the awe felt by the first men to leave low Earth orbit.

Rocket Men: The Daring Odyssey of Apollo 8 and the Astronauts Who Made Man's First Journey to the Moon, *Robert Kurson, Random House, 2018, 384 pp.*

Chasing New Horizons

Reviewed by **Keith T. Smith**[15]

On 14 July 2015, the New Horizons spacecraft flew past Pluto, capturing headlines around the world. *Chasing New Horizons* tells the story of that mission: how it was designed, funded, built, launched, and operated. The narrative is as recalled by Alan Stern, the mission's principal investigator, written up by the astrobiologist and science communicator David Grinspoon. This provides great insider access, although it's clearly a subjective view.

A brief introduction explains how Pluto was discovered in 1930 and why, in the 1980s, planetary scientists began to lobby for a mission to visit it. Teenagers may struggle with the subsequent chapters, however, which describe how the mission was designed and funded. These sections are a labyrinth of NASA committees, working groups, design proposals, and advisory reports. The second half of the book is far more engaging, covering the spacecraft's launch in 2006, its flyby of Jupiter in 2007, and the Pluto encounter itself. Those chapters come alive with the authors' passion for exploration and the excitement of finally reaching the destination.

Throughout *Chasing New Horizons*, there is a strong sense of the team's drive to make the most of the brief Pluto flyby and the meticulous planning that required. The authors emphasize the important roles played by engineers, project managers, and mission controllers, reminding readers that it takes more than a good idea and talented scientists to fly a successful mission.

Chasing New Horizons: Inside the Epic First Mission to Pluto, *Alan Stern and David Grinspoon, Picador, 2018, 320 pp.*

Built

Reviewed by **Donna Riley**[16]

Roma Agrawal's *Built* is a full-throated celebration of structural engineering. The book nicely balances innovative new builds such as The Shard in London with tried-and-true designs such as the Middle Eastern water transport system known as the *qanat*. Classic narratives of the Brooklyn Bridge and the Hancock Tower are interspersed with more obscure examples, including a lovely description of spider silk as bridge material.

Agrawal makes passing reference to workplace gender discrimination. Stark in their normalcy and minimized as anomalies, her vignettes nonetheless may elicit a #metoo from many readers as they serve to remind us how far we have yet to go in building inclusive work environments in engineering.

Agrawal, like many engineers, is almost absolute in her optimism: "The possibilities are limited only by our imaginations—for whatever we can dream up, engineers can make real." But whiz-bang technical feats alone cannot solve problems such as our water crises, for example. This points to perhaps the biggest shortcoming of the book: a missing discussion of how public policy interfaces with large engineering projects and the processes by which such projects are planned, funded, administered, and maintained.

In all, *Built* is a welcome addition to the library of accessible reads on engineering.

Editor's Note: For a full-length review of Built, *see "Behind the scenes of the built environment," Science* ***359****, 1108 (2018).*

Built: The Hidden Stories Behind Our Structures, *Roma Agrawal, Bloomsbury USA, 2018, 320 pp.*

Spying on Whales

Reviewed by **Sacha N. Vignieri**[6]

Whales are massive, their habitat is enormous, their life spans can be much longer than our own, and their intellect is both compelling and mysterious. We are captivated by whales, yet they remain difficult to know.

Nick Pyenson enters into this long affair from a paleontological perspective, being most interested in how these remarkable creatures evolved from four-legged terrestrial ancestors to marine leviathans and in the many forms they took in between. As he describes his pursuit of this knowledge, we see how challenging it really is to study these animals, both those that existed in the past and those with whom we share the world now.

Throughout the book, Pyenson brings his readers where he goes, whether it be on an adventure in the Atacama desert to solve a mystery involving dozens of intact fossil whale skeletons, or to an internal destination—his heart—as he contemplates the fact that in a single right whale's lifetime, the world has gone from being rich with whales to being nearly without them. In the end, the reader takes away an improved knowledge of whales, especially their history, but perhaps even more importantly, a deeper understanding of the intertwining of our fates.

Spying on Whales: The Past, Present, and Future of Earth's Most Awesome Creatures, *Nick Pyenson, Viking, 2018, 336 pp.*

10.1126/science.aav9720

Downloaded from http://science.sciencemag.org/ on December 10, 2018

---

[1] *The reviewer is a senior editor at* Science. *Email: cash@science-int.co.uk* [2] *The reviewer is a senior editor at* Science. *Email: jstajic@aaas.org* [3] *The reviewer is a senior editor at* Science. *Email: mlavine@aaas.org* [4] *The reviewer is an associate editor at* Science. *Email: sscanlon@science-int.co.uk* [5] *The reviewer is a senior editor at* Science Translational Medicine. *Email: ynusinov@aaas.org* [6] *The reviewer is a deputy editor at* Science. *Email: svignier@aaas.org* [7] *The reviewer is an associate editor at* Science. *Email: trai@aaas.org* [8] *The reviewer is the letters editor at* Science. *Email: jsills@aaas.org* [9] *The reviewer is a senior editor at* Science. *Email: smao@aaas.org* [10] *The reviewer is a deputy editor at* Science. *Email: jfahrenkamp@science-int.co.uk* [11] *The reviewer is an associate editor at* Science. *Email: bgrochol@aaas.org* [12] *The reviewer is an associate editor at* Science. *Email: mfunk@aaas.org* [13] *The reviewer is a lead content production editor at* Science. *Email: lkmec@aaas.org* [14] *The reviewer is a senior editor at* Science. *Email: lzahn@aaas.org* [15] *The reviewer is an associate editor at* Science. *Email: ksmith@science-int.co.uk* [16] *The reviewer is the Kamyar Haghighi head of the School of Engineering Education, Purdue University, West Lafayette, IN 47907, USA. Email: riley@purdue.edu*

Published by AAAS

PERSPECTIVES

NANOMATERIALS

Barrier(less) islands

No stopping 1D crystals

By **Bart Kahr** *and* **Michael D. Ward**

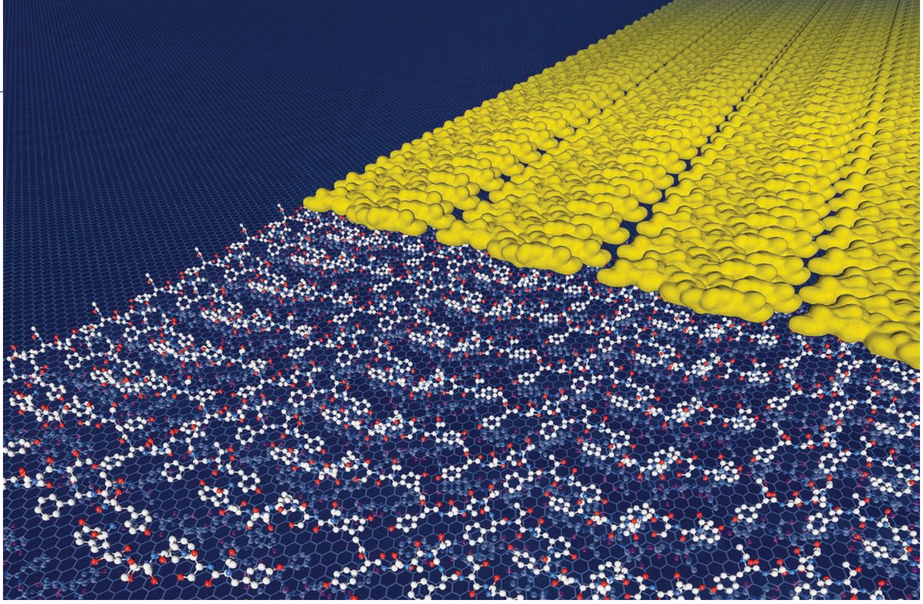

Peptides assemble from solution onto a surface of MoS_2 as highly ordered 2D arrays through the assembly of 1D rows (yellow). Nucleation of the 1D rows has no energetic barrier, which is characteristic of 2D crystalline films and 3D crystals.

Crystal nuclei—the minute collections of molecules needed to spark crystal growth—are small, short-lived, and generally unobserved. Classical nucleation theory, a model for the earliest stages of crystallization, is an accounting of the free-energy debits for creating an interface between crystals and the medium from which they grow, and the free energy credits for enlarging the interior of the crystal (*1, 2*). On page 1135 of this issue, Chen *et al.* (*3*) report the growth of one-dimensional (1D) peptide crystals in rows on crystalline substrates, which subsequently assemble laterally row by row into films (and ultimately 2D arrays) (see the figure). Growth rates along and perpendicular to the rows, measured by scanning probe microscopy, support the absence of an activation barrier that typically must be surmounted to overcome the surface energy. This unexpected challenge to the classical nucleation theory arises from high-resolution imaging that captures kinetic measurements for very small molecular aggregates (*4*). No matter the sophistication of our models, looking ever more closely at growing crystals often reveals unanticipated mechanisms (*5*).

A crystallization process without an activation barrier for nucleation suggests indifference. But epitaxy (*6, 7*)—the oriented overgrowth of a crystal on a crystalline substrate—strongly guides peptide assembly. Chen *et al.* used the latter process and observed that peptides (each consisting of seven amino acids) associated pairwise at their carboxyl termini through hydrogen bonds, resulting in palindromic dimers. Aggregates of just eight dimers long assembled at 30° from one of the three principal lattice vectors, which were defined by the closest distance between sulfur atoms in the molybdenum disulfide (MoS_2) crystalline substrate. Because MoS_2 is trigonal and the peptides have diad symmetry at best, the rows of dimers adopt three equivalent orientations on the surface. Dimers measuring 1.1 nm by 4.7 nm are canted by 60° with respect to the longitudinal row direction, tantamount to 1D crystals with a pseudo-rectangular unit cell 0.55 nm (longitudinal) by 4.1 nm (lateral). Only the former dimension is commensurate with the MoS_2 lattice, however.

A 2D circular crystal, according to classical nucleation theory, grows through a competition between the unfavorable line tension of the perimeter and the favorable area free energy. The former grows as the first power of the radius, and the latter grows with the square of the radius. Competition between oppositely signed terms of different dimensional dependencies also gives rise to a critical radius and nucleation activation barrier. Likewise, in 3D crystals, there exists a competition between quadratic (surface) and cubic (volume) dependencies. But what happens when the nucleus is quasi–one dimensional, as in the self-assembling rows of peptides on MoS_2? As Chen *et al.* note, for a 1D nucleus just one dimer wide, both the line tension and the free energy of the row scale with the first power of the length. Thus, longitudinal growth rates decreased linearly with decreasing peptide concentration, reaching a value of zero near the equilibrium peptide concentration. This signals the absence of an activation barrier for nucleation and a critical size of zero, a concept that is counterintuitive to everyday crystal growers.

Two-dimensional "island" growth of crystals was observed to occur row by row, and the lateral growth rate appears to depart from the exponential dependence on peptide concentration expected from classical nucleation theory (*8*). This behavior is reminiscent of small-molecule, lyotropic nematic mesophases made of 1D chains by isodesmic noncovalent association—that is, when molecular chains line up in an entropically driven process of liberating solvating water molecules (*9*). In the system of Chen *et al.*, row-by-row growth likewise may be entropically driven as more surface water can be expelled from MoS_2 if the rows associate in parallel to form a dense film. Coupled with strong interactions between the rows, this effect may compensate for incommensurism with the substrate in the lateral direction.

Chen *et al.* have shown that the earliest stages of crystal growth point to the limitations of classical nucleation theory, a theory that has never anticipated a crystal for which size and perimeter both scale in the same way with a geometric measure. These observations may guide further the design and fabrication of crystalline molecular films using epitaxial growth (*10*). They could inform on the fabrication of thin films with unique and highly ordered structures otherwise not attainable, with potential impact on electronic devices, from solar cells to light-emitting diodes to field effect transistors. ■

Department of Chemistry, Molecular Design Institute, New York University, New York, NY 10003, USA. Email: bart.kahr@nyu.edu; mdw3@nyu.edu

ILLUSTRATION: MICHAEL PERKINS/PACIFIC NORTHWEST NATIONAL LABORATORY

REFERENCES

1. P. J. M. Smeets *et al.*, *Proc. Natl. Acad. Sci. U.S.A.* **114**, E7882 (2017).
2. P. G. Vekilov, in *Kinetics and Thermodynamics of Multistep Nucleation and Self-Assembly in Nanoscale Materials*, S. A. Rice *et al.*, Eds. (Wiley, 2012), pp. 79–109.
3. J. Chen *et al.*, *Science* **362**, 1135 (2018).
4. Y. Ono, J. Kumaki, *Macromolecules* **51**, 7629 (2018).
5. A. G. Shtukenberg *et al.*, *Proc. Natl. Acad. Sci. U.S.A.* **110**, 17195 (2013).
6. M. Meissner *et al.*, *ACS Nano* **10**, 6474 (2016).
7. M. D. Ward, *ACS Nano* **10**, 6424 (2016).
8. D. Gebauer *et al.*, *Chem. Soc. Rev.* **43**, 2348 (2014).
9. P. J. Collings *et al.*, *Liq. Cryst. Rev.* **3**, 1 (2015).
10. M. Gobbi *et al.*, *Adv. Mater.* **30**, 1706103 (2018).

10.1126/science.aav7009

Downloaded from http://science.sciencemag.org/ on December 6, 2018

Published by AAAS

INFECTIOUS DISEASE

Toward a chemical vaccine for malaria

A high-throughput screen puts us on the road to protecting populations against malaria

By **Margaret A. Phillips**[1] *and*
Daniel E. Goldberg[2]

Despite considerable progress in combating malaria, it remains one of the world's most important infectious diseases, with 50% of the world population at risk of developing the disease and a mortality rate of ~0.5 million annually (*1*). The lack of an effective vaccine and the relentless ability of the *Plasmodium* parasite responsible for malaria to develop drug resistance has contributed to the continuing disease burden (*2*–*4*). Artemisinin-combination therapies (ACTs) are the mainstay of current treatment regimens, but decreased effectiveness, particularly in Southeast Asia, threatens our ability to control this disease. A global effort to develop new drugs for the treatment and prevention of malaria is under way but not guaranteed to succeed (*3*, *5*, *6*). These efforts include a systematic attempt to target all life-cycle stages of the parasite to allow combination therapies to be developed, which are also likely to reduce the development of resistance. High-throughput screens (HTSs) designed to identify small drug-like molecules that prevent growth of blood-stage parasites (*7*, *8*) and target-based approaches have identified new compounds that are currently in preclinical development and/or various stages of human clinical trials for treatment of malaria (*3*). Missing from these efforts has been a high-throughput technology to find liver stage–specific chemotypes. On page 1129 of this issue, Antonova-Koch *et al.* (*9*) report an HTS effort that has filled this gap. They identify a substantial number of new chemical starting points with potent liver-stage antimalarial activity, promising a new capacity to feed compounds through the drug development pipeline for chemoprotection.

Life cycle of the *P. falciparum* malaria parasite

An infected mosquito injects sporozoites, which replicate in the liver using enormous metabolic activity. From each hepatocyte, ~10^5 merozoites enter the bloodstream, invade red blood cells (RBCs), and set up an amplifying cycle. A chemical vaccine that targets the early liver stage could minimize resistance.

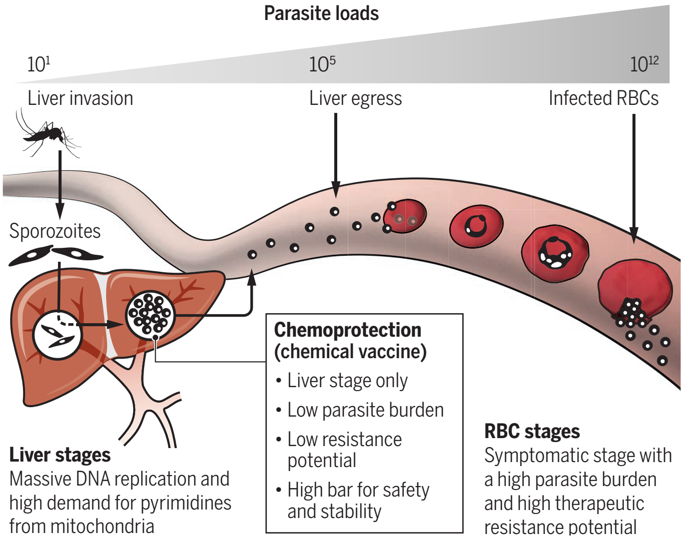

GRAPHIC: A. KITTERMAN/*SCIENCE*

As efforts to eliminate malaria increase, the need for chemoprotective agents to protect vulnerable populations will also increase (*3*). The idea is to find a long-lasting agent to treat infections before they become symptomatic and to develop these into a chemical vaccine (that is, a drug that protects against disease). The best malaria stage of infection to target for this approach is the one in the liver. The malaria life cycle begins when an infected mosquito injects sporozoites into a person, some of which find their way to the liver to establish infection (*10*) (see the figure). After replication in hepatocytes, malaria parasites burst out and infect erythrocytes, setting up an amplifying intraerythrocytic cycle. From 10^1 sporozoites that reach the liver, up to 10^5 merozoites will emerge into the blood, and up to 10^{12} will then build up in the bloodstream during a severe infection. A drug that blocks parasite replication in the liver works on a much lower parasite burden and thus has a lower chance of encountering and selecting for a rare parasite with a resistance mutation than do blood stage–active compounds. This is particularly so if a compound does not have activity on both stages and therefore does not put selective pressure on a large blood-stage parasite load.

Plasmodium falciparum is responsible for most malaria cases, and it is the most deadly, whereas *Plasmodium vivax* has the greatest global distribution. Antonova-Koch *et al.* made a strategic choice to use the rodent malaria parasite *Plasmodium berghei* for their screen. This conferred many advantages over using a human parasite: ease of production, minimal biohazard risk, more rapid life cycle, and ability to infect hepatoma cell lines that are more facile to use and do not detoxify the compounds being screened. From an initial hit rate of ~4%, a subset (~10^4) were prioritized for evaluation in confirmation assays, leading to the validation of ~10^3 compounds with good drug-like properties that have potent liver-stage activity and minimal cytotoxicity on host liver cells. Of these, 631 were profiled on additional *Plasmodium* species and life-cycle stages. Interestingly, two-thirds of these hits are specific for liver-stage parasites, highlighting the previously unknown biology of this stage and promising new cellular insights if compound targets can be determined. This is a goal that will require innovative approaches. The subset of compounds that were also active against blood-stage *P. falciparum* parasites contained a high proportion of mitochondrial inhibitors (43%) across diverse scaffolds. The mitochondrion in malaria parasites is critical for pyrimidine biosynthesis, a pathway that is essential for cell replication to generate the mature schizont in both blood and liver infections (see the figure). Demand for pyrimidine nucleotide bases is even greater in the liver stage, in which one sporozoite is replicated to generate 20,000 merozoites (*10*). Drugs that target enzymes required for pyrimidine nucleotide biosynthesis are effective for both malaria treatment and chemoprevention, including the cytochrome bc1 inhibitor atovaquone, which is an approved antimalarial agent used mainly for

---

[1] Department of Biochemistry, University of Texas Southwestern Medical Center, Dallas, TX 75390, USA.
[2] Division of Infectious Diseases, Department of Medicine and Department of Molecular Microbiology, Washington University School of Medicine, Saint Louis, MO 63110, USA. Email: margaret.phillips@utsouthwestern.edu; dgoldberg@wustl.edu

Downloaded from http://science.sciencemag.org/ on December 10, 2018

Published by AAAS

chemoprevention, and DSM265, an inhibitor of dihydroorotate dehydrogenase, currently in clinical development (*3*, *5*, *6*). The surprisingly high percentage of dual-acting compounds that hit these targets suggests that this pathway is one of the most vulnerable pathways shared between the blood and liver stages.

Not all hits from the *P. berghei* HTS worked on liver-stage *P. vivax* infections; the crossover was only ~25%. This may be partially explained by assay differences and by compound metabolism in the primary human hepatocytes used for the *P. vivax* assay. This latter issue could be engineered out of any compound series during lead optimization. It remains to be seen how many of the identified chemotypes will ultimately have liver-stage activity against both *P. vivax* and the deadly *P. falciparum*. Extrapolating from experience with compounds on blood stages of the rodent and human parasites, a large majority are likely to be effective against all *Plasmodium* species.

Now comes the hard work of prioritizing these hit compounds and optimizing them to have the properties of a chemical vaccine for clinical development. Recent work to develop chemical vaccines for HIV (*11*) and to formulate atovaquone as an injectable for chemoprevention in malaria (*12*) provide the beginnings of proof of concept for this strategy. The potential advantages of liver stage–specific chemoprotection in terms of simpler field implementation and low resistance propensity must be balanced with a need for high safety when used to protect a whole asymptomatic community (more so than a short-term treatment given to a discrete population of patients). Additionally, compounds must be stable, have a long half-life, and be amenable to slow delivery formulation, such as a long-acting injectable that will also have the benefit of improving compliance. Because of these complexities, there is a need to have a substantial list of candidate compounds. Thanks to the work of Antonova-Koch *et al.*, we have such a list. ■

REFERENCES

1. World Health Organization (WHO), *World Malaria Report* (WHO, 2017); www.who.int/malaria/publications/world-malaria-report-2017/en.
2. B. Blasco *et al.*, *Nat. Med.* **23**, 917 (2017).
3. M. A. Phillips *et al.*, *Nat. Rev. Dis. Primers* **3**, 17050 (2017).
4. N. J. White *et al.*, *Lancet* **383**, 723 (2014).
5. J. N. Burrows *et al.*, *Malar. J.* **16**, 26 (2017).
6. R. Hooft van Huijsduijnen, T. N. Wells, *Curr. Opin. Pharmacol.* **42**, 1 (2018).
7. F. J. Gamo *et al.*, *Nature* **465**, 305 (2010).
8. W. A. Guiguemde *et al.*, *Nature* **465**, 311 (2010).
9. Y. Antonova-Koch *et al.*, *Science* **362**, eaat9446 (2018).
10. A. M. Vaughan, S. H. I. Kappe, *Cold Spring Harb. Perspect. Med.* **7**, a025486 (2017).
11. R. J. Landovitz *et al.*, *Curr. Opin. HIV AIDS* **11**, 122 (2016).
12. R. P. Bakshi *et al.*, *Nat. Commun.* **9**, 315 (2018).

10.1126/science.aav7479

PALEONTOLOGY

Climate change and marine mass extinction

The end of the Permian Period was catastrophic for life in high-latitude regions

By **Lee Kump**

Voluminous emissions of carbon dioxide to the atmosphere, rapid global warming, and a decline in biodiversity—the storyline is modern, but the setting is ancient: The end of the Permian Period, some 252 million years ago. For the end-Permian, the result was catastrophic: the greatest loss of plant and animal life in Earth history (*1*). Understanding the details of how this mass extinction played out is thus crucial to its use as an analog for our future. On page 1130 of this issue, Penn *et al.* (*2*) add an intriguing clue: The extinction was most severe at high latitudes. Using a state-of-the-art climate model that was interpreted in terms of physiological stress, the authors further identify the killer as hypoxia, which was brought on by warm temperatures and ocean deoxygenation.

> ***"If warming and oxygen loss... happened quickly, massive die-off was destined to occur."***

A number of kill mechanisms for end-Permian extinction have been proposed, most triggered by the tremendous volcanic activity associated with the emplacement of the vast lava flows of the Siberian Traps, the eruption of which was coincident with the mass extinction (*3*). The Siberian Traps are estimated to have released tens of thousands of petagrams of carbon as carbon dioxide and methane (*4*), explaining the 10° to 15°C tropical warming revealed by oxygen isotope compositions of marine fossils (*5*). On land, unbearably hot temperatures and hypoxia likely were the main cause of mass extinction of plants and animals (*6*), although ultraviolet radiation exposure from a collapsed ozone shield contributed as well (*7*). Rapid warming also likely led to the loss of oxygen from the ocean's interior, extending up onto the continental shelves—a conclusion supported both by the widespread distribution of indicators for marine anoxia in sedimentary rocks (*8*) and by numerical modeling of the Permian ocean-atmosphere system (*9*).

Once considered nonselective, mass extinctions are increasingly revealing patterns of differential impact across species, lifestyles, and geographic locations through their fossil records (*10*). A geographic pattern to Permian extinction, however, has remained elusive. Benefiting from the paleontological community's creation of the expansive Paleobiology Database (*11*), Penn *et al.* discovered a meridional gradient to extinction intensity: Groups of organisms that were restricted to higher latitudes prior to the extinction suffered higher proportions of extinction than those established at low latitudes. What was it about living at high latitudes that predisposed marine organisms to extinction?

Penn *et al.* took an innovative approach to answering this question by coupling state-of-the-art computer simulations of end-Permian environmental change to a quantitative estimate of habitat loss for presumed Permian ecotypes. To establish the environmental (temperature and oxygen) tolerance of Permian ecotypes, Penn *et al.* used studies of modern organisms, grouped into ecotypes that they argue should be representative of the oxygen demands of Permian organisms. From these studies, a metabolic index was assigned to each ecotype, reflecting the critical balance between oxygen supply and demand. Model temperature and oxygen distributions before and during the end-Permian event were then used to map regions of the ocean where the metabolic index fell below the critical value (hypoxic threshold) at which oxygen supply (fundamentally related to the oxygen concentration of the water in which the organism lived, itself a function of ocean circulation, temperature, and rates of aerobic decomposition) could not support the physiological demands of daily life (feeding, reproduction, and defense). The authors found that ecotypes that favored high latitudes before the event preferentially suffered extinction because of their relatively high hypoxic thresh-

---

Department of Geosciences, College of Earth and Mineral Sciences, The Pennsylvania State University, University Park, PA 16802, USA. Email: lrk4@psu.edu

Downloaded from http://science.sciencemag.org/ on December 10, 2018

Published by AAAS

old. In other words, as the waters in which they had lived warmed and lost oxygen, they had nowhere to go to avoid hypoxic stress. Tropical ecotypes were preadapted to low oxygen and higher temperatures, and thus were better able to survive global warming (see the figure).

Paleoenvironmental reconstruction is challenging enough, but paleophysiological studies like that of Penn *et al.* are particularly vexing because the organisms whose traits one would like to understand and incorporate into a model are gone. Instead, studies of living organisms must be used. Penn *et al.* are aware of this limitation of their study and they go to great lengths to show that taxonomic biases, including a bias in the data on living organisms toward more active lifestyles relative to that which predominated in the Permian, have no substantial impact on their general conclusions. Other limitations of their study include both potential biases in the fossil record and required assumptions concerning the nutrient inventory of the Permian ocean and the oxygen concentration of the atmosphere at that time. Nutrients and atmospheric oxygen are important determinants of the oceanic pattern and severity of anoxia at a given climate state of the past, yet there are limited data on these factors. Another factor not considered in this study is the rate of climate change during the end-Permian event. If warming and oxygen loss were imposed slowly, perhaps high-latitude organisms could have adapted to warming and oxygen loss, whereas if these changes happened quickly, massive die-off was destined to occur. Existing geochronological constraints on the fossil record (*3*) suggest that the rates of these changes were rapid.

Marine mass extinction

Modeled patterns of ocean warming (top) and oxygen depletion (middle) suggest that hypoxia may explain why extinction of marine organisms (bottom) was more intense at high latitudes than in the tropics during the latest Permian Period.

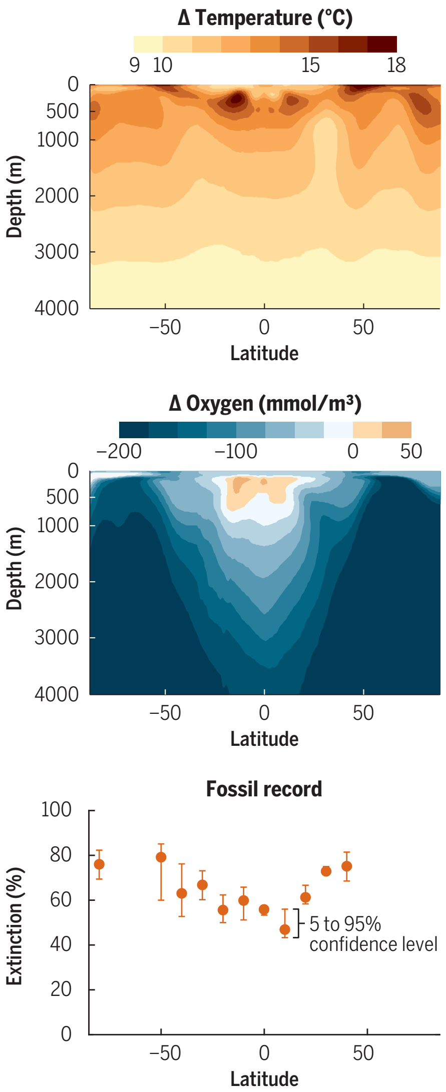

As our understanding of the drivers and consequences of end-Permian climate change and mass extinction improves, the lessons for the future become clear. Our modern-day "Siberian Trap" is fossil fuel burning, which is driving up atmospheric carbon dioxide to concentrations that Earth has not witnessed for millions of years. The planet is warming and the oceanic response of deoxygenation is already being detected in coastal zones and the open ocean (*12*). The Permian world may have been more susceptible to rapid climate change and its attendant environmental and biotic effects; carbon cycle–stabilizing calcareous plankton hadn't yet evolved (*13*), and the supercontinent of Pangaea's arid interiors and sluggish tectonics lowered the threshold for abrupt climate change (*14*). But even if it represents an extreme case, the lesson is clear: Continued or accelerated fossil fuel burning presents a risk that must be reversed or mitigated so that we can avoid a fate anything like that of the end-Permian. ■

REFERENCES

1. D. Erwin, *Extinction: How Life on Earth Nearly Ended 250 Million Years Ago* (Princeton Univ. Press, 2015).
2. J. Penn *et al.*, *Science* **362**, eaat1327 (2018).
3. S. D. Burgess, S. A. Bowring, S.-Z. Shen, *Proc. Natl. Acad. Sci. U.S.A.* **111**, 3316 (2014).
4. H. Svensen *et al.*, *Nature* **429**, 542 (2004).
5. Y. Sun *et al.*, *Science* **338**, 366 (2012).
6. R. B. Huey, P. D. Ward, *Science* **308**, 398 (2005).
7. H. Visscher *et al.*, *Proc. Natl. Acad. Sci. U.S.A.* **101**, 12952 (2004).
8. P. B. Wignall, R. J. Twitchett, *Science* **272**, 1155 (1996).
9. Y. Cui, L. R. Kump, *Earth Sci. Rev.* **149**, 5 (2015).
10. J. L. Payne, A. M. Bush, N. A. Heim, M. L. Knope, D. J. McCauley, *Science* **353**, 1284 (2016).
11. https://paleobiodb.org/
12. A. Oschlies, P. Brandt, L. Stramma, S. Schmidtko, *Nat. Geosci.* **11**, 467 (2018).
13. A. J. Ridgwell, M. J. Kennedy, K. Caldeira, *Science* **302**, 859 (2003).
14. L. R. Kump, *Philos. Trans. R. Soc. A* **376**, 20170078 (2018).

10.1126/science.aav736

METABOLISM

Bioenergetics through thick and thin

Membrane fluidity influences the efficiency of oxidative energy metabolism

By **Eric A. Schon**

The cells in all biological systems are composed of a limited number of molecular constituents, mainly proteins, nucleic acids, carbohydrates, and lipids. Of these, lipids tend to receive the shortest shrift, as they are typically considered to be merely the building blocks of membranes that provide a scaffold in which the "important" molecules, such as enzymes or signaling proteins, reside. In recent years, and with the advent of advanced lipidomics techniques, we have learned that "a lipid is a lipid is a lipid" is simply not true, and that the lipid composition of membranes can have profound effects on the behavior and activity of its resident macromolecules. For example, some lipids, such as members of the phosphatidylinositol family, are important signaling molecules. However, what is less appreciated is that the physical composition of lipid membranes can have profound effects on cellular behavior as well. On page 1186 of this issue, Budin *et al.* (*1*) use the Gram-negative bacterium *Escherichia coli* and the budding yeast *Saccharomyces cerevisiae* as model systems to show that the fluidity of a membrane, as determined by its lipid composition, can have huge effects on the efficiency of aerobic energy production (respiration) by the highly hydrophobic, membrane-embedded, oxidative phosphorylation (OxPhos) system.

The OxPhos system in aerobic organisms, located in the plasma membrane of prokaryotes and in the mitochondria of eukaryotes, comprises two elements: a multicomponent respiratory chain that pumps H^+ ions (protons) derived from the reduced forms of nicotinamide adenine dinucleotide (NADH) and flavin adenine dinucleotide ($FADH_2$) across a topologically closed membrane, generating a proton gradient, and an adenosine triphos-

Department of Neurology and Department of Genetics and Development, Columbia University Medical Center, New York, NY 10032, USA. Email: eas3@columbia.edu

GRAPHIC: J. YOU/*SCIENCE*

Downloaded from http://science.sciencemag.org/ on December 6, 2018

Published by AAAS

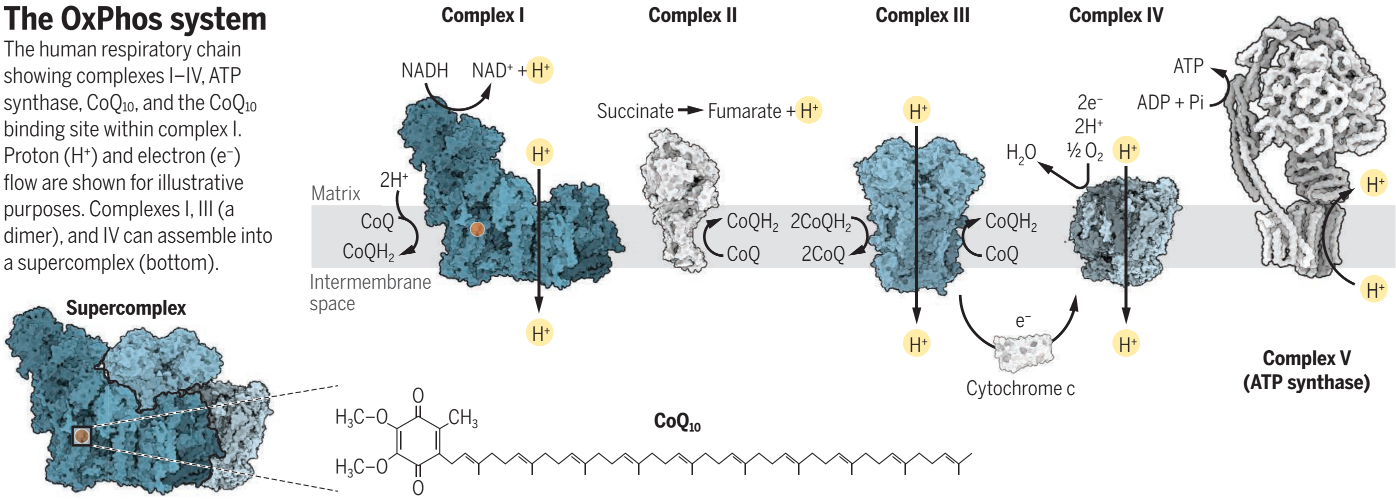

The OxPhos system

The human respiratory chain showing complexes I–IV, ATP synthase, CoQ_{10}, and the CoQ_{10} binding site within complex I. Proton (H^+) and electron (e^-) flow are shown for illustrative purposes. Complexes I, III (a dimer), and IV can assemble into a supercomplex (bottom).

GRAPHIC: V. ALTOUNIAN/*SCIENCE* BASED ON LETTS *ET AL.* (*15*)

phate (ATP) synthase that uses this gradient to drive ATP synthesis. The requisite electroneutrality is maintained by transferring an equivalent number of electrons through the respiratory electron transport chain to molecular oxygen. The primary source of the electrons is complex I (an NADH dehydrogenase) and complex II (a succinate dehydrogenase). The electrons are transferred first to a highly hydrophobic and mobile membrane-localized electron carrier called coenzyme Q (CoQ; also called ubiquinone), then to complex III (a CoQ reductase), then to a cytochrome, and finally to complex IV (a cytochrome oxidase), where oxygen is reduced to produce water (see the figure).

Do collisional interactions among the various respiratory components affect ATP production? Budin *et al.* hypothesized that by altering membrane fluidity they might be able to answer this question and perhaps determine which component of the OxPhos system is diffusion-limited. By titrating the viscosity of the OxPhos-containing plasma membrane in *E. coli*, they showed that the growth rate and aerobic respiration of the cells was increased at low viscosity—which allows for greater lateral movement of membrane-embedded molecules—and was decreased at high viscosity. This implies that increased membrane fluidity accelerated interactions among the OxPhos components. The result was also replicated in a eukaryote (*S. cerevisiae*) in which mitochondrial membrane fluidity was manipulated.

These data support a role for diffusion of the OxPhos components within the membrane, but did not single out any component that could diffuse more rapidly and thereby be controlling. There is an obvious candidate for this role: CoQ, a dwarf among the giant respiratory complexes. Using a combination of energy-transfer experiments and mathematical modeling based on assumptions of random molecular motion and collision-mediated reactions, Budin *et al.* concluded that CoQ diffusivity indeed influences respiratory flux—a result that had been predicted on kinetic grounds decades earlier by a number of groups (*2*–*5*).

The experimental elegance of this work was made possible, in part, by the use of bacteria and yeast, which have relatively simple OxPhos systems and well-defined genetics. The downside of this approach, however, is its unclear relevance to mammalian bioenergetics. Specifically, complex I in *E. coli* comprises only 14 subunits (versus 45 in humans) and binds not only CoQ but also menaquinone, or vitamin K_2, a CoQ lacking methoxy groups that is not synthesized in humans. Also, although some fungi contain a complex I enzyme that is similar to that in mammals (*6*), *S. cerevisiae* does not; instead, it contains two unrelated NADH dehydrogenases (*7*). It might be useful to explore mitochondrial membrane fluidity in one of these other fungi.

Another aspect of the CoQ-diffusivity connection that is still unclear is its role in electron transfer as a component of "supercomplexes" (also called "respirasomes"). In higher organisms, including humans, complexes I, III, and IV can co-assemble into supercomplexes (*8*), but neither *E. coli* nor *S. cerevisiae* contain supercomplexes that incorporate a relevant complex I analogous to that in humans (*7*, *9*). This is important because complex I contains a channel that allows for the entry of CoQ and the exit of reduced $CoQH_2$ for transfer of electrons to complex III. In the supercomplex, there is essentially no lipid barrier to this transfer, and the proximity of complexes I and III in the supercomplex could mean that if CoQ redox turnover is increased, it occurs via a non–lipid-mediated mechanism, although currently there is no evidence to support this (*10*). However, even in this situation there still may be an appreciable degree of viscosity-mediated control of electron transfer to complex III, as there is "free" complex I in the mitochondrial inner membrane, as well as "free" complex II, which is not a component of the supercomplex.

The identification of CoQ as a rate-limiting molecule in electron flow along the respiratory chain not only has relevance for our understanding of the basic biology and biophysics of aerobic energy metabolism, but has medical implications as well. There are a number of human diseases associated with CoQ_{10} deficiency (human CoQ has a hydrophobic side chain composed of 10 isoprenoid subunits), both primary (for example, mutations in CoQ biosynthesis genes) and secondary (for example, CoQ_{10} deficiency as a downstream consequence of other causes) (*11*), with attempts to ameliorate them by treating with CoQ_{10} or with CoQ analogs, such as MitoQ and EPI-743 (*12*). Thus, the role of membrane fluidity in controlling the efficiency of OxPhos in mammals, both in normal (*13*) and diseased (*14*) states, is an important but relatively unexplored aspect of aerobic energy metabolism that deserves further investigation. ■

REFERENCES AND NOTES

1. I. Budin *et al.*, *Science* **362**, 1186 (2018).
2. B. Chazotte, C. R. Hackenbrock, *J. Biol. Chem.* **264**, 4978 (1989).
3. G. Lenaz, M. L. Genova, *Biochim. Biophys. Acta* **1787**, 563 (2009).
4. C. I. Ragan, I. R. Cottingham, *Biochim. Biophys. Acta* **811**, 13 (1985).
5. P. R. Rich, *FEBS Lett.* **130**, 173 (1981).
6. K. Parey *et al.*, *eLife* **7**, e39213 (2018).
7. R. A. Stuart, *J. Bioenerg. Biomembr.* **40**, 411 (2008).
8. J. A. Letts *et al.*, *Nature* **537**, 644 (2016).
9. A. M. Melo, M. Teixeira, *Biochim. Biophys. Acta* **1857**, 190 (2016).
10. J. G. Fedor, J. Hirst, *Cell Metab.* **28**, 525 (2018).
11. C. M. Quinzii, M. Hirano, *Biofactors* **37**, 361 (2011).
12. P. K. Rai *et al.*, *Br. Med. Bull.* **116**, 5 (2015).
13. M. J. Torres *et al.*, *Cell Metab.* **27**, 167 (2018).
14. K. Kuter *et al.*, *Biochim. Biophys. Acta* **1862**, 741 (2016).
15. J. A. Letts, L. A. Sazanov, *Nat. Struct. Mol. Biol.* **24**, 800 (2017).

ACKNOWLEDGMENTS

Supported by NIH, the U.S. Department of Defense, and the J. Willard and Alice S. Marriott Foundation.

10.1126/science.aav7629

Downloaded from http://science.sciencemag.org/ on December 6, 2018

Published by AAAS

REGENERATION

Endothelial cell adaptation in regeneration

Tissue-specific endothelial cells maintain organ homeostasis and instruct regeneration

By **Jesus M. Gomez-Salinero** *and* **Shahin Rafii**

Endothelial cells (ECs) cover the inner wall of blood and lymph vasculature in normal and malignant tissues. It is widely appreciated that ECs are endowed with unique phenotypic, structural, functional, and angiocrine secretory attributes, generating specialized vascular subpopulations with organotypic and diseased-tissue signatures (*1, 2*). To achieve this high level of organ and tumor heterogeneity, ECs have acquired malleable cellular features that allow them to adapt to normal physiological stressors and to promote tissue homeostasis and regeneration. This is exemplified during liver regeneration in which defined angiocrine (meaning EC-derived) signals from liver sinusoidal ECs initiate and resolve liver regeneration through paracrine signaling to hepatocytes. By contrast, stressed and irritated ECs maladapt to a pathological microenvironment, such as inflamed or chronically injured tissues, favoring fibrosis and tumorigenesis. Thus, EC adaptive functions have beneficial or detrimental effects in organ physiology. Understanding the molecular determinants of EC adaptability could reveal therapeutic targets to facilitate wound healing without fibrosis, combat tumorigenesis, or develop efficacious strategies for organ regeneration, long-term engraftment of bioartificial organs, and tissue transplantation.

Endothelial cells manifest at least two modes of plasticity: cellular and functional. Cellular plasticity encompasses their capacity to generate different EC types (in arteries, veins, or capillaries) and even nonvascular cell types, including hematopoietic cells and parenchymal cells (*3*). During development and in adulthood, this plasticity is regulated in part by the induction of organotypic transcription factors (TFs) that instruct ECs to transition into defined cellular states. Discovery of the molecular pathways that mastermind the cellular plasticity of ECs has paved the way for designing strategies to generate adult hematopoietic stem cells in vitro. For example, identification of four TFs, collectively termed FGRS TFs, has enabled in vitro reprogramming of adult human and mouse ECs by transducing them with FGRS TFs into engraftable hematopoietic stem cells for the treatment of blood disorders (*4*). Identifying other pioneer TFs that direct conversion of ECs to nonvascular cell types will advance the field of direct reprogramming for therapeutic organ regeneration.

Functional plasticity refers to the capacity of ECs to tailor and adapt cellular processes to completely different tissue-specific chores, such as sustaining the blood-brain barrier or adjusting the dynamic filtration function of liver sinusoids and kidney glomeruli. The tissue-specific specialization of ECs orchestrates organogenesis during development, stem cell homeostasis, and regeneration throughout adulthood. The precise mechanism by which ECs acquire this level of heterogeneity is unknown and could be mediated by as yet unrecognized intrinsic genetic and epigenetic regulators governed by signals relayed from the extrinsic microenvironment. These signals emanate from the immediate surrounding microenvironment, including nonvascular cells, extracellular matrix, metabolic signals, and biomechanical forces. Chronic stressors, such as inflammatory and injury signals, elicit an aberrant vascular response, setting the stage for fibrosis, organ dysfunction, and tumorigenesis (*3*).

On the contrary, during regeneration, angiocrine cues supplied from activated ECs in response to injury of surrounding tissue orchestrate scar-free regeneration. For example, release of angiogenic factors by neighboring parenchymal cells induces liver ECs to deploy angiocrine factors, such as angiopoietin-2 (ANG2), R-spondin-3 (RSPO3), and WNT9B, that sustain hepatic homeostasis; or angiocrine secretion of hepatocyte growth factor (HGF) and WNT2 from liver ECs that mediate mouse liver regeneration after partial hepatectomy (*1, 5*). In response to injury, lung epithelial cells produce vascular endothelial growth factor A (VEGF-A) and fibroblast growth factors (FGFs) that activate lung ECs to supply matrix metalloprotease–14 (MMP14) and bone morphogenetic protein 4 (BMP4) and increase the bioavailability of epidermal growth factor (EGF) ligands and thrombospondins, thereby igniting lung epithelial regeneration (*1, 6*) (see the figure). Similarly, tissue-specific ECs supply defined angiocrine factors that contribute to organogenesis and metabolic homeostasis of other organs, including pancreas, myocardium, central nervous system, and even reproductive organs, including testes and ovaries (*1*). Notably, at steady state and during organ regeneration, microenvironmental cues program ECs to establish a nurturing vascular niche to choreograph self-renewal and differentiation of tissue-specific stem cells, including hematopoietic, spermatogonial, and neural repopulating cells (*1, 7*). Similarly, excessive release of tumor vascular niche–derived angiocrine factors supports the emergence of tumor-initiating cells (which have stem cell–like properties) that promote chemoresistance (*8*).

During organ repair, aberrant signals might corrupt the regenerative functions of ECs, leading to fibrosis and tumorigenesis. Persistent stress-induced stimulation of ECs could alter the organ-specific function of ECs, favoring scarring through a maladaptation process, including endothelial-to-mesenchymal transition (*3*), whereby ECs acquire fibroblastic features. An association between several chronic diseases and deregulated endothelium has recently been established, for instance, in dementia or cardiovascular diseases (*9, 10*). Mechanistically, differential signaling pathway activation in ECs can favor fibrosis over regeneration. For example, in the liver, differential activation of the C-X-C chemokine ligand 12 (CXCL12) cognate receptors, with CXCR7 predominantly expressed over CXCR4, on ECs induces expression of angiocrine factors that promote healing without fibrosis (*7*). By contrast, chronic inflammation caused by the ligation of biliary ducts results in dominant CXCR4 activation over CXCR7, which promotes healing with profibrotic changes. These dichotomous responses of liver ECs indicate that differential expression and activation of specific inflammatory receptors on ECs could relay external cues in favor of regeneration instead of fibrosis and vice versa.

Stress-induced responses of ECs also play important roles in promoting cancer at the expense of regeneration. The malleability of ECs forces them to participate in two-way cross-talk with their disrupted microenvironment, inducing the release of abnormal angiocrine factors and thereby setting the stage for tumorigenesis and tumor growth. For example, the excessive and dysregulated release of FGF4 by tumor cells triggers the expression of the E26 transformation-specific TF ETS2

Division of Regenerative Medicine, Ansary Stem Cell Institute, Department of Medicine, Weill Cornell Medicine, New York, NY, USA. Email: srafii@med.cornell.edu

Downloaded from http://science.sciencemag.org/ on December 10, 2018

Published by AAAS

and the cell surface receptor Jagged-1 in the tumor endothelium. This maladaptive EC response activates the angiocrine release from ECs of protumorigenic insulin-like growth factor 1 (IGF1) and decreases expression of antitumorigenic IGF binding protein IGFBP7, reinforcing aggressive and chemoresistant tumor growth (*8*). Moreover, ECs in distant, noncancerous organs can respond to the signals supplied by tumor cells, thereby facilitating metastasis through the activation of Notch and the expression of vascular cell adhesion molecule 1 (VCAM1) on the distal endothelium (*11*). These tumor-associated changes in the endothelium favor the persistence of invasiveness and treatment-refractory cancer stem cells. Therefore, tumor EC–derived angiocrine factors or their triggers are potential druggable anticancer targets.

Endothelial cells in organ regeneration

Endothelial cells (ECs) are key mediators in the regulation of organ physiology and malignant cell pathophysiology. They form vascular conduits and also supply angiocrine factors (such as WNTs, HGF, and MMPs) that regulate organ homeostasis. Under stress conditions, ECs can maladapt, supplying factors that promote the development of fibrosis, cancer, and other maladies. The use of tissue-specific ECs will be essential to choreograph functional organ regeneration and repair.

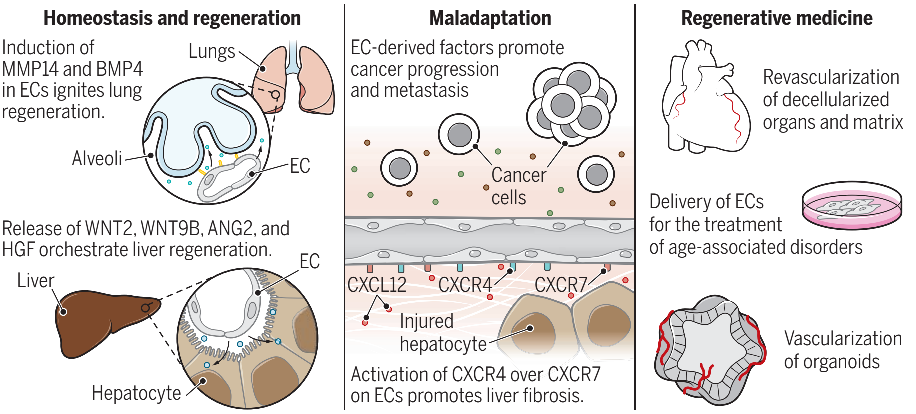

GRAPHIC: JOSHUA BIRD/*SCIENCE*

The intrinsic malleability of ECs makes them ideal for regenerative medicine, as does their localization in vessel walls, allowing easy access to infused drugs, and their expression of organ-specific markers allows the development of strategies to modulate the function of specific EC types. Furthermore, EC regeneration has potential for the treatment of aged organs. For example, oxidative stress leads to attrition of ECs, which increasingly occurs with age, altering hematopoietic stem cell activity and perturbing lineage differentiation. Notably, intravenous transplantation of ECs from young mice can revert this phenotype in aged mice (*12, 13*). Moreover, epigenetic manipulation of human blood-circulating EC progenitors transiently augments vasculogenesis after ischemia (*14*). Rejuvenation of the senescent EC state, by the infusion of specific as yet unrecognized cytokines or the infusion of young ECs, could set the stage for the treatment of aging-associated maladies.

Uncovering the molecular determinants of EC adaptability could enable deconvolution of the intricate pathways that drive adult organ repair that has defied developmental biologists for decades. For example, although development of in vitro techniques, such as tissue-specific organoids and organ-on-a-chip models, have enhanced our understanding of tissue morphogenesis, these models do not fully explain the mechanism for the resistance of certain tissues such as lung, heart, intestines, and kidneys to self-repair. The development of vascularized organoids will not only allow deciphering of the pathways that choreograph tissue repair, but also enable manufacturing of mini-organs for regenerative medicine and facilitate their long-term in vivo engraftment. Additionally, vascularized tumoroids (tumor organoids) could be developed to evaluate the influence of different drugs in the emergence of cancer during organ regeneration processes, as ECs have a primary role in tumor development and expansion (*8*). Clearly, innovating techniques to generate adaptable autologous ECs that can arborize organoids may lead to transformative therapeutic paths in the near future. However, engineering of long-lived, responsive, and malleable organotypic ECs from, preferably, patient ECs is necessary and a main challenge to overcome.

Decellularized human organ scaffolds are another area of active regenerative medicine investigation to enable organ replacements. This approach has been hampered by the lack of proper seeding of adaptable ECs within the narrow confines of decellularized capillaries. This is a major problem because placement of current decellularized scaffolds in patients often results in poor functional recovery due to poor vascularization. Populating the decellularized matrix with durable and adaptable ECs will enhance the life span and improve the survival of these potentially lifesaving implants (*15*).

Translation of these concepts to the clinical setting poses a herculean task and is compounded by two major obstacles: social and scientific. From a social standpoint, one of the main obstacles to overcome is the rampant proliferation of pseudoscientific clinics and stem cell tourism that promise false hope to desperate patients (*16*). Their unsupervised approach without regulatory oversight could adversely affect the health of patients because nonvalidated treatments may delay the approval of evidence-based treatments. From a scientific perspective, capitalizing on the regenerative and rejuvenating functions of ECs by employing tissue-specific TFs, the conversion of autologous adult ECs into organotypic ECs, and vascularizing organ models in vitro so that they reach human size will lead to innovative therapeutic strategies. For example, these approaches could open the door to the development of artificial organs for transplantation, as well as the manufacture of human organs in donor animals. Importantly, one of the main limitations yet to be circumvented is the development of nonimmunogenic organs.

Notwithstanding these caveats, translation to the regeneration field could be augmented by formulating standard procedures to incorporate vascular networks within implants that can sustain their long-term engraftment and provide the proper tissue-specific angiocrine signals to drive organ repair without scarring and tumorigenesis. Achievement of these goals will bring us closer to fulfilling the promise of regenerative medicine to treat millions of disabled patients worldwide who need organ replacement. ■

REFERENCES AND NOTES

1. S. Rafii *et al.*, *Nature* **529**, 316 (2016).
2. D. J. Nolan *et al.*, *Dev. Cell* **26**, 204 (2013).
3. E. Dejana *et al.*, *Nat. Commun.* **8**, 14361 (2017).
4. R. Lis *et al.*, *Nature* **545**, 439 (2017).
5. H. G. Augustin *et al.*, *Science* **357**, eaal2379 (2017).
6. J.-H. Lee *et al.*, *Cell* **156**, 440 (2014).
7. B.-S. Ding *et al.*, *Nature* **505**, 97 (2014).
8. Z. Cao *et al.*, *Cancer Cell* **31**, 110 (2017).
9. C. Iadecola, *Neuron* **80**, 844 (2013).
10. M. J. Gimbrone Jr. *et al.*, *Circ. Res.* **118**, 620 (2016).
11. E. Wieland *et al.*, *Cancer Cell* **31**, 355 (2017).
12. A. P. Kusumbe *et al.*, *Nature* **532**, 380 (2016).
13. M. G. Poulos *et al.*, *J. Clin. Invest.* **127**, 4163 (2017).
14. S. Fraineau *et al.*, *Stem Cell Rep.* **9**, 1573 (2017).
15. A. F. Pellegata *et al.*, *Front. Bioeng. Biotechnol.* **6**, 56 (2018).
16. D. Sipp *et al.*, *Nature* **561**, 455 (2018).

ACKNOWLEDGMENTS

S.R. is the founder of, and an unpaid consultant to, Angiocrine Bioscience, San Diego, California.

10.1126/science.aar4800

Downloaded from http://science.sciencemag.org/ on December 10, 2018

Published by AAAS

COMPUTER SCIENCE

Mastering board games

A single algorithm can learn to play three hard board games

By **Murray Campbell**

From the earliest days of the computer era, games have been considered important vehicles for research in artificial intelligence (AI) (*1*). Game environments simplify many aspects of real-world problems yet retain sufficient complexity to challenge humans and machines alike. Most programs for playing classic board games have been largely human-engineered (*2*, *3*). Sophisticated search methods, complex evaluation functions, and a variety of game-specific tricks have allowed programs to surpass the best human players. More recently, a learning approach achieved superhuman performance in the hardest of the classic games, Go (*4*), but was specific for this game and took advantage of human-derived game-specific knowledge. Subsequent work (*5*) removed the need for human knowledge, and additional algorithmic enhancements delivered further performance improvements. On page 1140 of this issue, Silver *et al.* (*6*) show that a generalization of this approach is effective across a variety of games. Their AlphaZero system learned to play three challenging games (chess, shogi, and Go) at the highest levels of play seen.

AlphaZero is based on reinforcement learning (*7*), a very general paradigm for learning to act in an environment that rewards useful actions. In the case of board games, the learning agent plays moves in the game and is typically trained by playing large numbers of games against itself. The first major success for reinforcement learning and games was the TD-Gammon program (*8*), which learned to play world-class backgammon in the early 1990s by using neural networks. More recently, deep (many-layer) neural networks were combined with reinforcement learning in an approach dubbed "deep reinforcement learning," which received widespread interest after it was successfully applied to learn Atari video games directly from screen input (*9*).

The approach described by Silver *et al.* augments deep reinforcement learning with a general-purpose searching method, Monte Carlo tree search (MCTS) (*10*). Although MCTS has been the standard searching method used in Go programs for some time, until now, there had been little evidence of its value in chess or shogi programs. The strongest programs in both games have relied on variations of the alpha-beta algorithm, used in game-playing programs since the 1950s.

Silver *et al.* demonstrated the power of combining deep reinforcement learning with an MCTS algorithm to learn a variety of games from scratch. The training methodology used in AlphaZero is a slightly modified version of that used in the predecessor system AlphaGo Zero (*5*). Starting from randomly initialized parameters, the neural network continually updates the parameters on the basis of the outcome of self-play games. AlphaZero learned to play each of the three board games very quickly by applying a large amount of processing power, 5000 tensor processing units (TPUs), equivalent to a very large supercomputer.

Contemplating the next move

In the game between AlphaZero (white) and Stockfish (black), there were several moves that were reasonable for AlphaZero to consider. After 1000 move-sequence simulations, the red moves were rejected, and after 100,000 simulations, AlphaZero chose the blue move over orange.

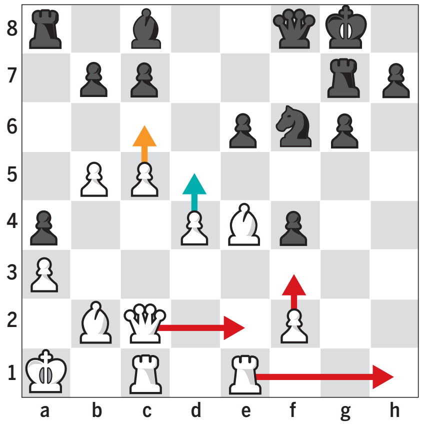

Once trained, evaluating the systems is not entirely trivial, and there are many pitfalls that can affect the measurements. Silver *et al.* used a large variety of testing conditions which, taken together, provide convincing evidence of the superiority of the trained systems over the previous state-of-the-art programs. Some of the early test games played between AlphaZero and the chess program Stockfish were released to the public and created something of a sensation in the chess community, with much analysis and commentary on the amazing style of play that AlphaZero exhibited (see the figure). Note that neither the chess or shogi programs could take advantage of the TPU hardware that AlphaZero has been designed to use, making head-to-head comparisons more difficult.

Chess, shogi, and Go are highly complex but have a number of characteristics that make them easier for AI systems. The game state is fully observable; all the information needed to make a move decision is visible to the players. Games with partial observability, such as poker, can be much more challenging, although there have been notable successes in games like heads-up no-limit poker (*11*, *12*). Board games are also easy in other important dimensions. For example, they are two-player, zero-sum, deterministic, static, and discrete, all of which makes it easier to perfectly simulate the evolution of the game state through arbitrary sequences of moves. This ability to easily simulate future states makes MCTS, as used in AlphaZero, practical. Multiplayer video games such as StarCraft II (*13*) and Dota 2 (*14*) have been proposed as the next game-playing challenges as they are partially observable and have very large state spaces and action sets, creating problems for AlphaZero-like reinforcement learning approaches.

Games have been popular research domains in AI in part because it is easy to identify games in which humans are better than computers. Chess, shogi, and Go are immensely complex, and numerous human players have devoted much of their lives to understanding and playing these games at the professional level. The AlphaZero approach still has limitations that could be addressed (for example, large computational requirements, brittleness, and lack of interpretability), but this work has, in effect, closed a multidecade chapter in AI research. AI researchers need to look to a new generation of games to provide the next set of challenges. ■

IBM Research, T.J. Watson Research Center, Yorktown Heights, NY 10598, USA. Email: mcam@us.ibm.com

REFERENCES AND NOTES

1. C. Shannon, *Philos. Mag.* **41**, 256 (1950).
2. J. Schaeffer *et al.*, *AI Mag.* **17**, 21 (1996).
3. M. Campbell *et al.*, *Artif. Intell.* **134**, 57 (2002).
4. D. Silver *et al.*, *Nature* **529**, 484 (2016).
5. D. Silver *et al.*, *Nature* **550**, 354 (2017).
6. D. Silver *et al.*, *Science* **362**, 1140 (2018).
7. R. Sutton, A. Barto, *Reinforcement Learning: An Introduction* (MIT Press, 1998).
8. G. Tesauro, *Commun. ACM* **38**, 58 (1995).
9. V. Mnih *et al.*, *Nature* **518**, 529 (2015).
10. R. Coulom, *Int. Conf. Comput. Games* **2006**, 72 (2006).
11. M. Moravčík *et al.*, *Science* **356**, 508 (2017).
12. N. Brown, T. Sandholm, *Science* **359**, 418 (2018).
13. O. Vinyals *et al.*, arXiv:1708.04782 [cs.LG] (16 August 2017).
14. OpenAI, OpenAI Five, 25 June 2018; https://blog.openai.com/openai-five/.

ACKNOWLEDGMENTS
Thanks to T. Klinger and G. Tesauro for their comments.

10.1126/science.aav1175

GRAPHIC: N. CARY/*SCIENCE*

Downloaded from http://science.sciencemag.org/ on December 10, 2018

Published by AAAS

POLICY FORUM

ENVIRONMENTAL ECONOMICS

Flawed analyses of U.S. auto fuel economy standards

A 2018 analysis discarded at least $112 billion in benefits

By **Antonio M. Bento[1,2], Kenneth Gillingham[3,2], Mark R. Jacobsen[4,2], Christopher R. Knittel[5,2], Benjamin Leard[6], Joshua Linn[7], Virginia McConnell[6], David Rapson[8], James M. Sallee[9,2], Arthur A. van Benthem[10,2], Kate S. Whitefoot[11]**

In addition to greenhouse gas emissions and fuel economy, analyses must also consider effects on pollution, safety, and traffic congestion.

Corporate Average Fuel Economy (CAFE) and greenhouse gas (GHG) emissions standards for passenger vehicles and light trucks have long been a centerpiece of the U.S. strategy to reduce energy use and GHG emissions and increase energy security. Under the authority of the Energy Independence and Security Act, the Environmental Protection Agency (EPA), and the National Highway Traffic Safety Administration (NHTSA) jointly set GHG and CAFE standards to reach 55 miles per gallon by 2025. A 2016 draft technical assessment report (TAR) affirmed by the EPA in January 2017 concluded that the 2022–2025 standards were technologically feasible and that benefits far exceeded costs. But under the current administration, those agencies are now challenging that conclusion in a 2018 Notice of Proposed Rulemaking (NPRM), which proposes freezing standards at model year (MY) 2020 levels through 2025. Its analysis finds that the costs of the previous standards now exceed benefits. With the agencies currently in the process of determining whether the rule should be finalized, we describe how the 2018 analysis has fundamental flaws and inconsistences, is at odds with basic economic theory and empirical studies, is misleading, and does not improve estimates of costs and benefits of fuel economy standards beyond those in the 2016 analysis.

A COMPREHENSIVE PROTOCOL

A benefit-cost analysis (see table S1) for fuel economy standards grounded on basic economic principles must consider the behavior of consumers and automakers as well as keep account of several externalities (*1*). It must consider a range of parameter values and assumptions to account for inherent uncertainty as well as the impact of related policies that determine the relevant baseline against which the standards are compared.

Modeling consumer behavior should include the purchase of general goods and new or used vehicles. Consumers trade off vehicle prices for various vehicle attributes (for example, performance, safety features, seating capacity, and so on). They also decide how much to drive and whether to keep or scrap their older vehicles.

A comprehensive analysis would allow automakers to comply with standards by adjusting vehicle prices, improving fuel economy, and altering performance and other vehicle attributes (*2*–*5*). It would also recognize that technology is determined by automaker investments, while accounting for learning-by-doing and knowledge spillovers that, over time, may lower the compliance costs.

Modeling of the interaction between new and used vehicle markets is critical to determine the resulting size of the total fleet and its composition, as well as the prices of vehicles (relative to the price of other goods). Prices, fuel economy, and other attributes determine the total cost of ownership, which affects total vehicle miles traveled (VMT), as well as willingness to pay for vehicles (*1*, *6*).

A comprehensive protocol should also consider costs and benefits that arise from "external effects," including GHG emissions, energy security, local air pollution, safety, and traffic congestion (*7*), which are affected by fleet size and its composition and the total number of miles driven.

In the case of safety, four additional outcomes are relevant: changes in vehicle weights and sizes, distribution of weights and sizes in the entire fleet, distribution of vehicle vintage, and sorting of individuals into vehicles on the basis of their risk preferences, risk profiles, and preferences for other vehicle attributes (*8*–*10*).

Valuation parameters are critical for converting impacts into costs and benefits. The value of a statistical life is used to value fatalities, whereas the social cost of carbon is used for valuing the benefits of reduced gasoline use (*11*, *12*). Other valuation parameters reflect the value of energy security and the health costs of tailpipe emissions. A comprehensive protocol should also account for other factors, including changes in gasoline prices over time.

TWO FLAWED ANALYSES

Both the 2016 and 2018 analyses deviate from the comprehensive protocol outlined above because they do not explicitly model consumer choices and tend to miss important trade-offs between general consumption, vehicle choice, and VMT. On the supply side, the modeling of the new and used car markets does not fully consider important interactions between these markets. As a consequence, multimarket adjustments, and resulting outcomes such as the size of the fleet, fleet composition, and prices of vehicles, are captured imperfectly. Incomplete accounting for such adjustments also affects the magnitudes of the external costs and benefits.

The 2018 analysis did attempt to incorporate several channels of adjustment that were missing from the 2016 TAR (see table S1, fourth column). However, the most impactful channels were added in an ad hoc way that runs afoul of the proposed protocol outlined above, existing research, and basic economic principles. As a result, the changes in the 2018 NPRM are misleading. Although we do not endorse the 2016 TAR, the 2018 analysis failed to advance our understanding of the true costs and benefits of fuel economy standards.

Downloaded from http://science.sciencemag.org/ on December 10, 2018

PHOTO: ISTOCK.COM/PLHERRERA

---

[1]University of Southern California, Los Angeles, CA, USA. [2]National Bureau of Economic Research, Cambridge, MA, USA. [3]Yale University, New Haven, CT, USA. [4]University of California, San Diego, CA, USA. [5]Massachusetts Institute of Technology, Cambridge, MA, USA. [6]Resources for the Future, Washington, DC, USA. [7]University of Maryland, College Park, MD, USA. [8]University of California, Davis, CA, USA. [9]University of California, Berkeley, CA, USA. [10]University of Pennsylvania, Philadelphia, PA, USA. [11]Carnegie Mellon University, Pittsburgh, PA, USA. Email: abento@usc.edu

Published by AAAS

There are stark differences between the costs and benefits assigned to the 2022–2025 standards in the 2016 and 2018 analyses, reflecting differences in assumptions. The figure shows the costs and benefits from the affirmed 2022–2025 CAFE standards, relative to the proposed rollback levels as calculated by the agencies [see supplementary materials (SM) section G for the GHG emissions standards]. To interpret impacts of a rollback of the standard in the context of the figure, one should change the signs of all costs and benefits. For the CAFE standard, the 2016 review finds a net benefit of $87.6 billion, whereas the 2018 analysis finds a net loss of $176.6 billion. Or, in other words, the proposed rollback of the standard (relative to existing levels) would generate a net benefit based on the assumptions made in the 2018 analysis and a net loss based on the 2016 analysis; for the GHG emissions standard, the 2016 review finds a net benefit of $97.2 billion, whereas the 2018 analysis finds a net loss of $200.6 billion (see the SM for details).

The 2018 analysis reports benefits that are roughly twice as high as those in the 2016 analysis, primarily from benefits owing to lower driving costs that increase miles traveled that consumers value (that is, the rebound effect). The 2018 analysis doubles the magnitude of the rebound effect despite recent literature estimating smaller rebound effects (see the SM for details). Whereas in the NPRM analysis, the higher rebound effect hardly affects net benefits—as additional benefits from avoided car crashes under the rollback are offset by lost benefits from reduced VMT—it doubles the number of avoided fatalities generated by this effect, contributing to a total of 12,700 lives. The assumption regarding the higher rebound effect may lead to unfounded concerns about unintended safety consequences of the current standards.

Accounting only for domestic benefits from reducing carbon emissions (ignoring international benefits) scaled down the social cost of carbon from $48 per metric ton to $7 per metric ton, reducing GHG benefits from $27.8 billion in 2016 to $4.3 billion in 2018. A more minor difference is that the analyses make slightly different assumptions about the extent to which consumers value future fuel savings from driving a more fuel-efficient car (see SM section C for further discussion of the impact on net benefits).

2016 and 2018 benefit-cost analyses of CAFE standards

Stark differences between the 2016 and 2018 estimates reflect fundamental flaws and inconsistencies in the 2018 analysis. See supplementary materials.

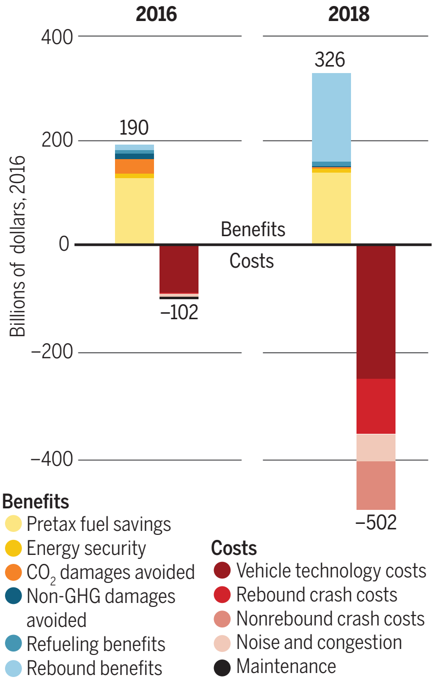

SIX MILLION MISSING USED CARS

A central difference between the 2016 and 2018 reports is the projection of the total fleet size of cars and light-duty trucks. Economic theory predicts that tighter standards make new vehicles more expensive, on average. This also translates into more expensive used vehicles, on average, because they are substitutes for new vehicles (*6*). As a consequence, as standards increase vehicle prices, total fleet size should decrease over time. Conversely, a rollback should lead to increased demand for vehicles, resulting in a larger fleet that will be newer, on average.

By contrast, the 2018 proposal argues that the rollback in standards will shrink the overall fleet by 6 million vehicles in the year 2029, compared with the current standards. This is inconsistent with basic economic principles. If prices of vehicles decrease (relative to other general-purpose goods), we expect more individuals to purchase vehicles and drive them rather than use other modes of travel. The 2018 NPRM analysis reaches the opposite conclusion based on ad hoc integration of a newly developed vehicle scrappage model with the NHTSA's Volpe model (the CAFE Compliance and Effects Modeling System).

We have identified two major shortcomings of this approach. First, this newly developed model departs substantially from state-of-the-art vehicle scrappage models (*6*, *13*) (see the SM for further details). Second, in relation to the comprehensive framework, the 2018 NPRM does not account for changes in used vehicle prices that result from interactions between new and used car markets as a result of the standard (see the SM for additional discussion). As a result, this new model violates simple economic principles; leads to misleading conclusions related to the overall size of the fleet, fleet composition, and the amount of scrappage; and undermines EPA and NHTSA modeling efforts to improve the understanding of the costs and benefits of fuel economy standards.

These 6 million "missing" vehicles have important implications. A larger fleet leads to higher miles driven, gasoline use, and external costs. Total driving, excluding the rebound effect, should increase (as opposed to decrease) with the rollback relative to keeping the previous standards. Driving scales with fleet size, and newer cars are driven more. As VMT increases, gasoline consumption and the external effects of GHG emissions, local air pollution, traffic fatalities, congestion, and energy security of the rollback will be larger than reported in the 2018 analysis, potentially by considerable amounts.

Crash fatalities and injuries can increase (as opposed to decrease) with the rollback. The 2018 analysis concludes that the rollback will result in a $90.7 billion gain from reduced fatalities and property damages, a result driven almost exclusively by a 2.4% reduction in fleet-wide VMT (changes in fleet composition play a minor role in the 2018 analysis). If we hold fleet size fixed (adding back the missing 6 million used cars), this $90.7 billion gain is likely to fall to near zero. This is a conservative calculation and should be interpreted as a lower bound, because we anticipate that rollback would cause the fleet to grow, possibly driving this term below zero (see the SM for further details).

COMPLIANCE COST INCONSISTENCIES

The EPA and NHTSA estimate costs of hundreds of different fuel-saving technologies and model how manufacturers will add these technologies and combinations of technologies using least-cost algorithms. For the 2016 TAR analysis, the estimates of costs by the EPA for GHG standards are less than half of the costs for the same rule estimated by the NHTSA for CAFE standards. This is in part because the EPA assumes that California and other states' Zero Emission Vehicle (ZEV) mandate will be in place in future years. With many electric vehicles already in the fleet, the incremental cost of meeting the higher fuel economy standards of the federal rule is considerably lower. The NHTSA implicitly assumes that there is no ZEV mandate, which leads to higher calculated costs. The 2018 NPRM does the same.

For a clearer comparison of technology costs, we focus on differences in the NHTSA's estimates of costs in the 2016 and 2018 analyses (see the figure). According to the NHTSA,

GRAPHIC: N. CARY/SCIENCE

Downloaded from http://science.sciencemag.org/ on December 10, 2018

Published by AAAS

the 2018 costs are more than two times higher than the earlier TAR costs. Some of the cost differences are a result of plausible changes in economic conditions, such as an increase in future new vehicle sales owing to higher income growth and lower gasoline prices. Another important difference, however, is due to the fact that the agencies changed the model years affected by the standards in the 2018 analysis. In the 2016 analysis, the costs of the MY 2022–2025 standards are assessed relative to a baseline fixed at MY 2021 levels. By contrast, the 2018 NPRM argues that the standards should be frozen a year earlier and compares the costs of meeting the existing standards for MY 2021–2025 relative to standards fixed at the MY 2020 level. The agencies claim that the previous standards are no longer feasible and appropriate, but they do not even examine the technology costs for this change in the standards in the 2018 assessment of alternatives. We can show, however, that this change accounts for roughly 12% of the difference in costs for the 2016 and 2018 standards (see the figure; for more discussion of this point, see the SM].

Notwithstanding these differences, we still find that reported per-vehicle costs with the GHG emissions standards are about 80 to 150% higher for MY 2022–2025 vehicles in the 2018 proposal than in the 2016 NHTSA analysis (see fig. S3 for details). In addition to the difference in model years being regulated, four other main factors account for these cost differences.

First, automakers can comply with the regulations by transferring fuel economy "credits" between their passenger car fleet and their light-truck fleet, so that if one fleet overcomplies with the regulations, the other can undercomply within some limit. Credit transferring is also possible across years, so that if an automaker exceeds fuel economy performance in one year, it can meet a less stringent standard in another year. But these flexibilities were not included in the 2018 analysis for MY 2021–2025 (although credit transferring was possible from years before 2021), raising the estimated costs. The NHTSA is prohibited by statute from considering all of these flexibilities in the setting of standards, whereas the EPA is not subject to this restriction. In the 2016 TAR, compliance flexibilities were included in the NHTSA analysis but did not influence the setting of the standards.

Second, the 2018 analysis removed some projected future technology options that were considered in the 2016 analysis (for example, Atkinson engines with cylinder deactivation and exhaust recirculation). Omitting these projected lower-cost options, the 2018 analysis predicts that a substantially higher deployment of more-expensive technologies is necessary to meet the standards: 24% of vehicles in the 2018 analysis are projected to be strong hybrids by MY 2025, whereas only 2.6% are in the 2016 analysis.

Third, the analysis assumes that longer time periods are required to redesign many vehicles to meet the standards in a given year, requiring manufacturers to add fuel-saving technologies earlier, thereby incurring higher costs for more years.

Fourth, the specified costs for electrified vehicles are considerably higher (20 to 50%) than in the 2016 analysis owing to different battery assumptions (for example, electrode thickness limited to 100 microns) and including additional vehicle electrification components (for example, liquid cooling systems) recommended by the National Academies (*14*). In summary, although some of the changes in technology assumptions in the 2018 analysis are plausible, overall it uses pessimistic assumptions of future technology availability and performance compared with the 2016 analysis.

SAFETY VALVE INSTEAD OF ROLLBACK

We conclude that the 2018 analysis has several fundamental flaws and inconsistencies. In addition to the points we have raised, others have articulated why a global, rather than a domestic, social cost of carbon is the appropriate parameter to value GHG emissions reductions (*11*, *12*), and we agree. Using a global estimate of the social cost of carbon and the correct impact of changes to total fleet size reduces the net benefits of the rollback for the CAFE standard (from $176 billion to $64 billion). Or, in other words, at least $112 billion was discarded in the 2018 analysis. Furthermore, of this, at least $88.3 billion comes from accounting for the missing 6 million cars. For the rollback to have negative net benefits, one only needs to reduce the 2018 technology costs by 26%, which still doubles the costs from the 2016 analysis; using the technology costs from the 2016 analysis implies that the standard will have large positive net benefits. In general, these conclusions also apply to the GHG emissions standard (see the SM for further details).

Under any scenario, the case for a rollback could be made if compliance costs are sufficiently high, but both the 2016 TAR and 2018 NPRM have likely overestimated compliance costs. Neither analysis considers the full extent of options that manufacturers have available to respond to these policies, including changes in vehicle prices, performance, and other attributes. Relative to the 2016 TAR, the 2018 NPRM seems to compound this mistake, leading to greater overestimates of compliance cost by not accounting for the full extent of banking and borrowing credits and by using pessimistic assumptions regarding technology costs.

Given the substantial departure from a comprehensive protocol for benefit-cost analysis, we cannot conclude that the rollback will produce welfare gains, and we instead predict that it will result in unintended consequences. For example, in anticipation of higher standards, automakers accumulated CAFE credits, which they intended to use in the future as a strategy for lowering compliance costs. A rollback of the standard would lead to a de facto devaluation of these credits, penalizing automakers who have been leaders in technological innovation.

Furthermore, economic theory predicts that, for the same level of standard, costs of compliance decline as a result of learning-by-doing and spillover benefits from technology development across automakers. Therefore, we see no economic justification to keep the standard flat from 2020 to 2025, even ignoring the external societal benefits of the standard. Instead, standards should increase over time in stable and predictable ways.

We certainly recognize the inherent uncertainty in estimating costs of compliance through technologies, but we recommend the introduction of a safety valve to address this concern, rather than a rollback. Safety valves, common in cap-and-trade programs, allow firms to purchase compliance credits at a predetermined price, effectively capping compliance costs and allowing for less technology improvement if it turns out to be highly expensive (*15*). A rollback is an unnecessarily blunt way to achieve the same goal and introduces regulatory uncertainty into an industry that needs to make long-run technological investments for the future. ■

REFERENCES

1. A. M. Bento *et al.*, *Am. Econ. Rev.* **99**, 667 (2009).
2. M. Jacobsen, *Am. Econ. J. Econ. Policy* **5**, 148 (2013).
3. K. Whitefoot *et al.*, *Environ. Sci. Technol.* **51**, 10307 (2017).
4. T. Klier, J. Linn, *Rand J. Econ.* 1756 (2012).
5. C. Knittel, *Am. Econ. Rev.* **101**, 3368 (2011).
6. M. Jacobsen, A. van Benthem, *Am. Econ. Rev.* **105**, 1312 (2015).
7. I. Parry *et al.*, *J. Econ. Lit.* **45**, 373 (2007).
8. M.R. Jacobsen, *Am. Econ. J. Appl. Econ.* **5**, 1 (2013).
9. M.L. Anderson, M. Auffhammer, *Rev. Econ. Stud.* **81**, 535 (2013).
10. A. M. Bento *et al.*, "The effect of fuel economy standards on vehicle weight dispersion and accident fatalities" (Working paper w23340, *National Bureau of Economic Research*, 2017).
11. W. Pizer *et al.*, *Science* **346**, 1189 (2014).
12. National Academies of Sciences, Engineering, and Medicine, *Valuing Climate Damages: Updating Estimation of the Social Cost of Carbon Dioxide* (The National Academies Press, Washington, DC, 2017).
13. A. M. Bento *et al.*, *Energy J.* **39**, 1 (2018).
14. National Research Council, *Cost, Effectiveness, and Deployment of Fuel Economy Technologies for Light-Duty Vehicles* (National Academies Press, Washington, DC, 2015).
15. B. Leard, V. McConnell, *Rev. Environ. Econ. Policy* **11**, 207 (2017).

SUPPLEMENTARY MATERIALS

www.sciencemag.org/content/362/6419/1119/suppl/DC1

10.1126/science.aav1458

Downloaded from http://science.sciencemag.org/ on December 10, 2018

Published by AAAS

Insects affected by warming temperatures have reduced commercial maize yield in Peru.

LETTERS

Edited by **Jennifer Sills**

Model vs. experiment to predict crop losses

In their Report "Increase in crop losses to insect pests in a warming climate" (31 August, p. 916), C. A. Deutsch *et al.* use expected effects of higher temperatures on insect metabolic rates to predict increasing rates of consumption by pests and increasing pest population densities. These predictions fail to recognize the complexity and idiosyncratic nature of plant-insect relationships. They do not take into account changes in plant defense, which can respond to both warming temperatures and enhanced CO$_2$ (eCO$_2$) in ways that harm some insects and help others (*1*, *2*). Furthermore, Deutsch *et al.* assume that insects will develop predictably faster in response to winter warming. However, warmer winters actually retard development in species whose springtime awakening requires accumulated winter chilling (vernalization) (*3*). Finally, Deutsch *et al.* assume that pest population dynamics are simple functions of developmental rates. We doubt this is realistic in the presence of temperature-sensitive predators and diseases and in the context of pest control (*4*).

Deutsch *et al.* may have oversimplified the problem, but their concern is justified. In an experiment estimating effects of moderate warming on maize in Peru, commercial yield was reduced by more than 90% (far more than Deutsch *et al.*'s prediction), a reduction that was, indeed, ascribed mainly to increased herbivory (*5*). The question tackled by Deutsch *et al.* is extremely important, but the answers will vary among regions and be specific to each crop-pest interaction. We need experiments that compare yields of target crops in replicated experimental treatments that simulate future conditions of both climate and eCO$_2$ in the presence and absence of pests. These experiments seem not yet to exist (*6*). When they do, we should be able to generate better-informed predictions, both of changes in crop yield and of the roles that insect pests will play in those changes.

Camille Parmesan[1,2,3]*, Michael E. Hanley[2], Michael C. Singer[1,2]
[1]Theoretical and Experimental Ecology, CNRS/Université Paul Sabatier, 09200 Moulis, France.
[2]Biological and Marine Sciences, Plymouth University, Drake Circus, Plymouth PL48AA, UK.
[3]Geological Sciences, University of Texas, Austin, Austin, TX 78712, USA.
*Corresponding author.
Email: camille.parmesan@plymouth.ac.uk

REFERENCES

1. P. Stiling, T. Cornelissen, *Glob. Change Biol.* **13**, 1 (2007).
2. C. Robinet, A. Roques, *Integrat. Zool.* **5**, 132 (2010).
3. S. Stålhandske, K. Gotthard, O. Leimar, *J. Anim. Ecol.* **86**, 718 (2017).
4. V. Seufert, N. Ramankutty, J. A. Foley, *Nature* **485**, 229 (2012).
5. R. Tito, H. L. Vasconcelos, K. J. Feeley, *Glob. Change Biol.* **24**, E592 (2018).
6. C. Lesk, E. Coffel, A. W. D'Amato, K. Dodds, R. Horton, *Nat. Clim. Change* **7**, 713 (2017).

10.1126/science.aav4827

Response

Our Report draws attention to a complex but understudied issue: How will climate warming alter losses of major food crops to insect pests? Because empirical evidence on plant-insect-climate interactions is scarce and geographically localized, we developed a physiologically based model that incorporates strong and well-established effects of temperature on metabolic rates and on population growth rates. We acknowledged that other factors are involved, but the ones we analyzed are general, robust, and global (*1*–*3*).

Parmesan and colleagues argue that our model is overly simplistic and that any general model is premature. They are concerned that our model does not incorporate admittedly idiosyncratic and geographically localized aspects of plant-insect interactions. Some local effects, such as evidence that warmer winters will harm some insects but not others, were in fact evaluated in our sensitivity analyses and shown to be minor (see the Report's Supplementary Materials). Other phenomena, such as plant defenses that benefit some insects and threaten others, are relevant but are neither global nor directional. Furthermore, because Parmesan *et al.* present no evidence that such idiosyncratic and localized interactions will outweigh the cardinal and universally strong impacts of temperature on populations and on metabolic rates (*1*–*3*), their conclusion is subjective.

We agree with Parmesan and colleagues that the question of future crop losses is important and needs further study, that targeted experimental data are needed (as we wrote in our Report), and that our estimates are likely to be conservative (as we concluded, but for reasons different from theirs). However, we strongly disagree with their recommendation to give research priority to gathering localized experimental data. That strategy will only induce a substantial time lag before future crop losses can be addressed.

We draw a lesson from models projecting future climates. Those models lack the "complexity and idiosyncratic nature" of many climate processes, but by building from a few robust principles, they successfully capture the essence of climate patterns and trends (*4*). Similarly, we hold that the most expeditious and effective

Downloaded from http://science.sciencemag.org/ on December 6, 2018

PHOTO: IMAGEBROKER/ALAMY STOCK PHOTO

Published by AAAS

way to anticipate crop losses is to develop well-evidenced ecological models and use them to help guide targeted experimental approaches, which can subsequently guide revised ecological models. Experiments and models should be complementary, not sequential.

Curtis A. Deutsch[1,2*], **Joshua J. Tewksbury**[3,4,5], **Scott C. Merrill**[6], **Raymond B. Huey**[2], **David S. Battisti**[7], **Rosamond L. Naylor**[8]
[1]School of Oceanography, University of Washington, Seattle, WA 98195, USA. [2]Department of Biology, University of Washington, Seattle, WA 98195, USA. [3]Future Earth, University of Colorado, Boulder, CO 80303, USA. [4]Department of Environmental Studies, University of Colorado, Boulder, CO 80303, USA. [5]School of Global Environmental Studies, Colorado State University, Fort Collins, CO 80523, USA. [6]Department of Plant and Soil Science, University of Vermont, Burlington, VT 05405, USA. [7]Department of Atmospheric Sciences, University of Washington, Seattle, WA 98195, USA. [8]Department of Earth System Science and the Center on Food Security and the Environment, Stanford University, Stanford, CA 94305, USA.
*Corresponding author. Email: cdeutsch@uw.edu

REFERENCES

1. R. B. Huey, D. Berrigan, *Am. Nat.* **158**, 204 (2001).
2. V. M. Savage *et al.*, *Am. Nat.* **163**, 429 (2004).
3. U. M. Irlich, J. S. Terblanche, T. M. Blackburn, S. L. Chown, *Am. Nat.* **174**, 819 (2009).
4. T. F. Stocker *et al.*, in *Climate Change 2013: The Physical Science Basis. Contribution of Working Group I to the Fifth Assessment Report of the Intergovernmental Panel on Climate Change*, T. F. Stocker *et al.*, Eds. (Cambridge Univ. Press, 2013), pp. 33–115.

10.1126/science.aav7405

No conflict of interest in data monitoring

The News Feature "Hidden conflicts?" (C. Piller, 6 July, p. 16) alleges that after serving as a member of a Food and Drug Administration (FDA) advisory panel for a nominal per diem payment, I later received inappropriate payments from the manufacturer (AstraZeneca) for serving on and chairing data monitoring committees (DMCs) overseeing AstraZeneca-sponsored research. Those assertions are inaccurate. The universities conducting clinical trials, not AstraZeneca, compensated DMC members for their time. More important, the OpenPayments database still reports inaccurate payments far in excess of the amount I received from the university. AstraZeneca has acknowledged that it mistakenly reported my name and attributed inaccurate amounts to me in its filing to the database and has agreed to correct these errors.

Serving on a DMC does not involve conducting research, and I did not conduct research on any drug for AstraZeneca after serving on the FDA panel. The DMCs on which I served oversaw the safety of participants enrolled in two postapproval trials funded through research contracts with academic institutions, not contracts with AstraZeneca. Members of DMCs are required to act independently of trial sponsors; they are not investigators. Their responsibility is to ensure the safety of trial participants and scientific integrity of studies to advance research. In this case, the outcomes of both trials were unfavorable to AstraZeneca. Regardless of the outcome, however, I had no financial relationship with the company; the fees, which were nominal, came to me through the university. Serving on a DMC is not a conflict of interest but a public service. My role was to protect the interests of patients, science, and the public.

Jonathan L. Halperin
Icahn School of Medicine at Mount Sinai, New York, NY 10029-6574, USA.
Email: jonathan.halperin@mountsinai.org

10.1126/science.aau9738

Downloaded from http://science.sciencemag.org/ on December 6, 2018

Published by AAAS

RESEARCH

Progress toward practical valleytronic devices

Li et al., *p. 1149*

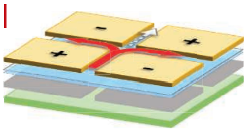

IN *SCIENCE* JOURNALS

Edited by **Stella Hurtley**

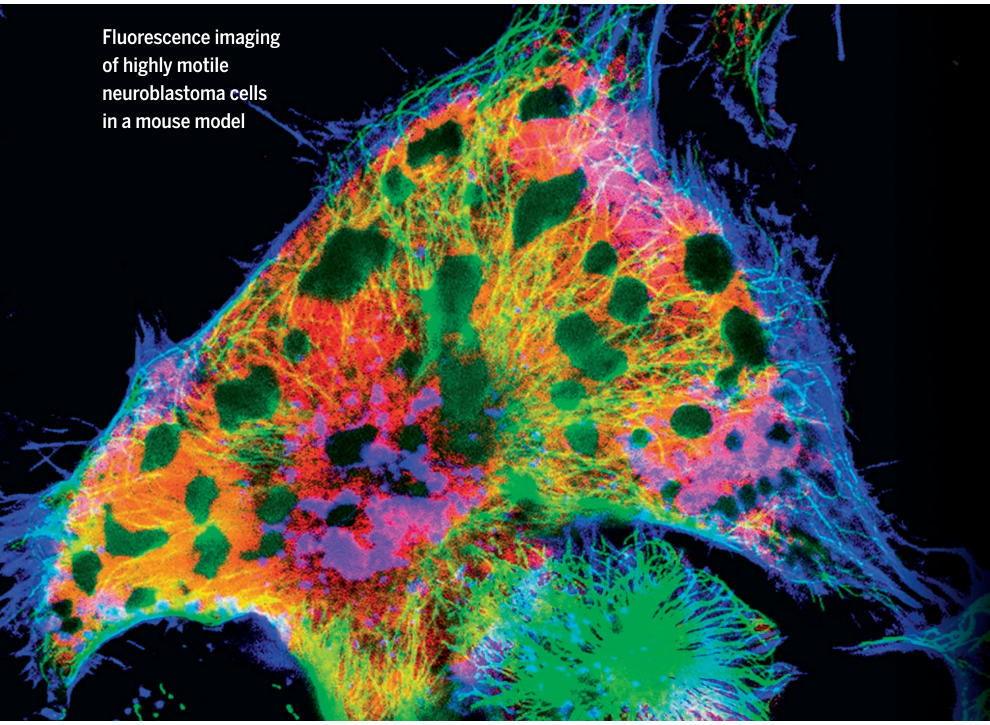

Fluorescence imaging of highly motile neuroblastoma cells in a mouse model

CANCER

A systematic look at a childhood tumor

Neuroblastomas—the most common tumor type in infants—develop from fetal nerve cells, and their clinical course is highly variable. Some neuroblastomas are fatal despite treatment, whereas others respond well to treatment and some undergo spontaneous regression without treatment. Ackermann *et al.* sequenced more than 400 pretreatment neuroblastomas and identified molecular features that characterize the three distinct clinical outcomes. Low-risk tumors lack telomere maintenance mechanisms, intermediate-risk tumors harbor telomere maintenance mechanisms, and high-risk tumors harbor telomere maintenance mechanisms in combination with RAS and/or p53 pathway mutations. —PAK

Science, this issue p. 1165

MICROBIOLOGY

Actively persistent *Salmonella*

A proportion of *Salmonella* cells can enter a reversible state of growth arrest, which allows them to tolerate environmental stress such as antibiotics. Stapels *et al*. found that these cells are not dormant but are actively modulating their environment. *Salmonella* within their host macrophage niche deployed a specialized type 3 secretory system called SPI-2 to deliver virulence factors, including SteE, into host cells. SteE changed the cytokine profile of the infected macrophages to reprogram them into a noninflammatory and infection-permissive state. Thus, when antibiotics were removed, the *Salmonella* could reemerge and cause disease. —CA

Science, this issue p. 1156

HUMAN GENETICS

Genetic architecture of developmental disorders

The genetics of developmental disorders (DDs) is complex. Martin *et al*. wanted to determine the degree of recessive inheritance of DDs in protein-coding genes. They examined the exomes of more than 6000 families in populations with high and low proportions of consanguineous marriages. They found that 3.6% of DDs in individuals of European ancestry involved recessive coding disorders, less than a tenth of the levels previously estimated. Furthermore, among South Asians with high parental relatedness, rather than most of the disorders arising from inherited variants, fewer than half had a recessive coding diagnosis. —LMZ

Science, this issue p. 1161

MOLECULAR BIOLOGY

DNA methylation promotes transcription

DNA methylation generally represses transcription, but in some instances, it has also been implicated in transcription activation. Harris *et al*. identified a protein complex in *Arabidopsis* that is recruited to chromatin by DNA methylation. This complex specifically activated the transcription of genes that are already mildly transcribed but had no effect on transcriptionally silent genes such as transposable elements. The complex thereby counteracts the repression effect caused by transposon insertion in neighboring genes while leaving transposons silent. Thus, by balancing both repressive and activating transcriptional effects, DNA methylation can act to fine-tune gene expression. —SYM

Science, this issue p. 1182

MATERIALS SCIENCE

Tunable materials respond to magnetic field

Although certain four-dimensional (4D) printed materials can respond to external stimuli, these are hard to control or

IMAGES (TOP TO BOTTOM): LI *ET AL.*; VSHYUKOVA/SCIENCE SOURCE

Published by AAAS

feature long response times. Jackson *et al.* created tunable materials that can respond to an applied magnetic field by incorporating liquids that contain ferromagnetic microparticles into 3D-printed polymer tubes. In tests, these structures responded to a magnetic field in under a second. The approach could see broad applications in fields that include soft robotics, transportation systems, and smart wearable technology. —PJB

Sci. Adv. 10.1126/sciadv.aau6419 (2018).

IMMUNOLOGY

Optimal affinity

Germinal center (GC) B cells are essential to generating protective antibody responses and are selected through a process of affinity maturation. Kwak *et al*. now define intrinsic properties of human GC B cells that are critical to antigen affinity discrimination. They identified B cell antigen receptor–containing actin-rich pod-like structures that facilitated formation of highly stable immunological synapses and antigen internalization when GC B cells engaged high-affinity antigens. These structures were important in setting thresholds for affinity selection and driving GC B cell responses. —CNF

Sci. Immunol. **3**, eaau6598 (2018).

COMPUTER SCIENCE

One program to rule them all

Computers can beat humans at increasingly complex games, including chess and Go. However, these programs are typically constructed for a particular game, exploiting its properties, such as the symmetries of the board on which it is played. Silver *et al*. developed a program called AlphaZero, which taught itself to play Go, chess, and shogi (a Japanese version of chess) (see the Editorial, and the Perspective by Campbell). AlphaZero managed to beat state-of-the-art programs specializing in these three games. The ability of AlphaZero to adapt to various game rules is a notable step toward achieving a general game-playing system. —JS

Science, this issue p. 1140; see also pp. 1087 and 1118

BATTERIES

Working toward fluoride batteries

Owing to the low atomic weight of fluorine, rechargeable fluoride-based batteries could offer very high energy density. However, current batteries need to operate at high temperatures that are required for the molten salt electrolytes. Davis *et al*. push toward batteries that can operate at room temperature, through two advances. One is the development of a room-temperature liquid electrolyte based on a stable tetraalkylammonium salt–fluorinated ether combination. The second is a copper–lanthanum trifluoride core-shell cathode material that demonstrates reversible partial fluorination and defluorination reactions. —MSL

Science, this issue p. 1144

QUANTUM MATERIALS

Twisting a route for surface plasmons

Graphene is an atomically thin material that supports highly confined plasmon polaritons, or nano-light, with very low loss. The properties of graphene can be made richer by introducing and then rotating a second layer so that there is a slight angle between the atomic registry. Sunku *et al*. show that the moiré patterns that result from such twisted bilayer graphene also provide confined conducting channels that can be used for the directed propagation of surface plasmons. Controlling the structure thereby provides a pathway to control and route surface plasmons for a nanophotonic platform. —ISO

Science, this issue p. 1153

IN OTHER JOURNALS

Edited by **Caroline Ash** *and* **Jesse Smith**

Fire feedback explains the Miocene expansion of the grassland biome.

PHOTO: RICHARD DU TOIT/MINDEN PICTURES/GETTY IMAGES

PALEOECOLOGY

Fire and grassland evolution

Global grassland underwent a massive expansion in the late Miocene epoch, 5 million to 8 million years ago. Karp *et al.* examined the role of fire in this expansion, through measurements of fire-derived hydrocarbons and grass-diagnostic carbon isotopes in sediments in Pakistan. They found evidence of a simultaneous increase in seasonality of precipitation and the occurrence of regular fire along with the opening of the landscape and the expansion of grasslands. Their results indicate that a grassland-fire feedback system was a key driver in the expansion of grasslands, a relationship that has remained an integral feature of this ecosystem ever since. —AMS

Proc. Natl. Acad. Sci. U.S.A. **115**, 12130 (2018).

NEUROSCIENCE

Inhibition in the fear-learning circuitry

Many mental health disorders can be traced to abnormal associative learning. The basolateral amygdala of the brain plays a central role in associative learning and the formation of emotional memories and motivated behaviors. The relevance of the amygdala's anatomical substructure for the acquisition of memories is less clear. Tipps *et al*. used neuron-specific chemogenetics to systematically probe the circuitry and signaling mechanisms involved in auditory fear learning in mice. Stimulating inhibitory interneurons or inhibiting pyramidal cells was enough to induce an association between a behavior and an auditory cue. This understanding is key to developing

Published by AAAS

WATER RESOURCES

Managing an unwelcome effect

One of the biggest challenges presented by climate change is water resource management. In the western United States, the storage and release of water by the mountain snowpack is a critical component controlling the summertime flow of headwaters of California's major reservoirs. Rhoades *et al.* describe how mountain snowpacks will be affected by climate change in that region and how that can be expected to influence peak water volume, peak timing, accumulation rate, and melt rate of water discharge. Among other effects, they project that by the end of the century, peak snowpack timing will occur 4 weeks earlier and peak water volume will be 80% lower under a high–greenhouse gas–emissions scenario. —HJS

Geophys. Res. Lett. 10.1029/2018GL080308 (2018).

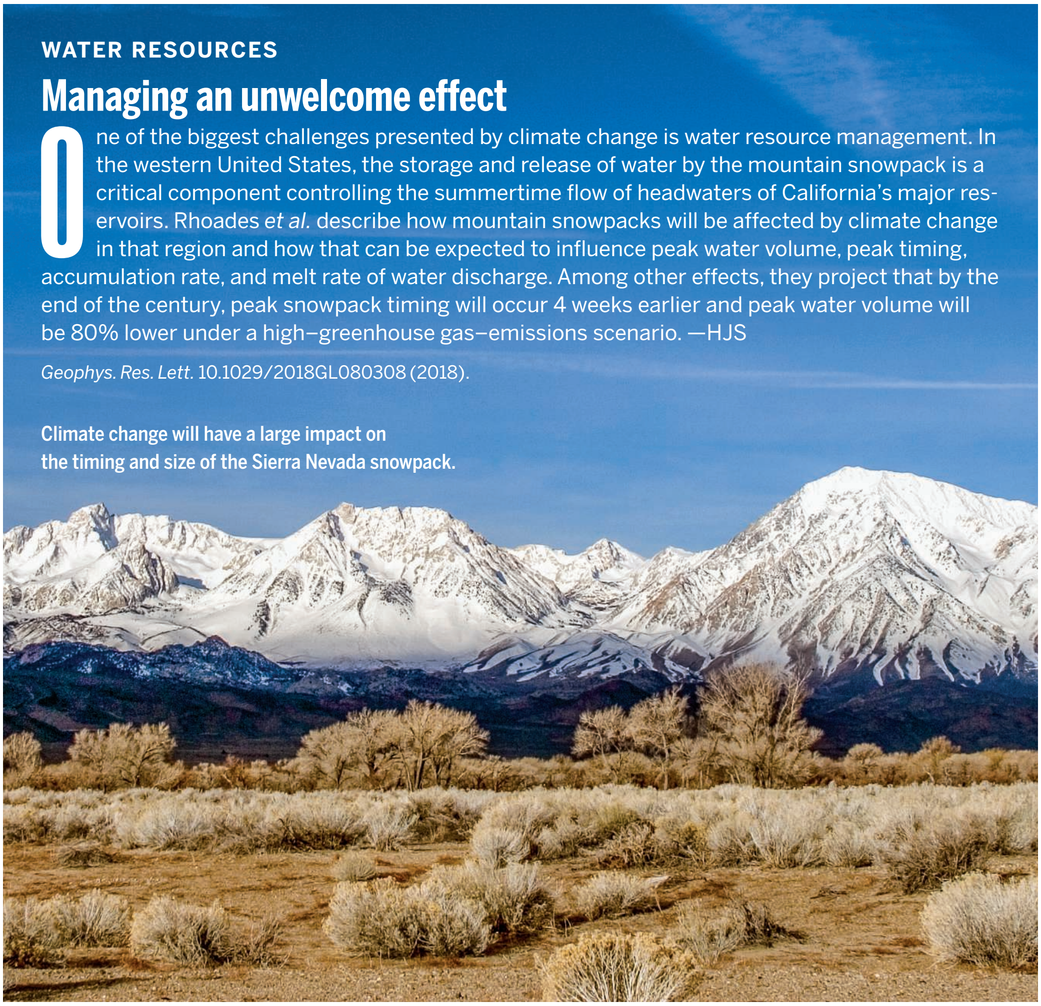

Climate change will have a large impact on the timing and size of the Sierra Nevada snowpack.

therapies for diseases in which associative learning has been disrupted. —PRS

eNeuro **5**, ENEURO.0272-18.2018 (2018).

CELL BIOLOGY

Keeping a toehold on the matrix

Within our bodies, most tissues are organized in association with an extracellular matrix. The matrix keeps cells where they are supposed to be, and cells adhere to the matrix via integrin-containing cell adhesions. During mitosis, cells round up and release their tight association with the matrix. Lock *et al.* show that despite this, mitotic cells ensure that they retain their correct location by using a so-called reticular form of cell adhesion. A range of adherent cultured human cells was found to show this property. Reticular adhesions lack several components of classical adhesion complexes, including talin and actin. A key constituent of reticular adhesions is integrin β5, and a lack of it interfered with the retention of spatial localization through normal mitotic cell divisions. —SMH

Nat. Cell Biol. **20**, 1290 (2018).

OPTOELECTRONICS

Steering electrons in graphene

Guiding and controlling the movement of electrons in solid-state systems is crucial for applications such as ultrafast electronics and the generation of high-harmonic light. Although such electronic control is readily achieved in semiconductors, metals and small-bandgap materials can pose more of a challenge. Heide *et al*. show that they can control the trajectory of electrons within the two-dimensional plane of graphene using a double pulse from a laser. Tuning the relative polarization between the two pulses by carefully varying the time delay between them allows the direction electron flow to be manipulated on femtosecond time scales. Such an optical technique offers a relatively simple route to study the electronic and topological properties of other two-dimensional materials on ultrafast time scales. —ISO

Phys. Rev. Lett. **121**, 207401 (2018).

PHYSICS

Identifying localization in two dimensions

Disordered interacting quantum many-body systems can become hopelessly localized. This so-called many-body localization has been studied in one-dimensional systems. In two dimensions, experiments indicate that the localization persists, but because it is difficult to tell the difference between no thermalization and slow thermalization, more theoretical work is needed. Relying on an approximate numerical method, Wahl *et al*. undertook large-scale simulations of a two-dimensional lattice of bosonic atoms in the presence of interactions and disorder. At intermediate disorder strengths, the on-site entanglement entropies exhibited a bimodal distribution, indicating a coexistence of localized and thermalized states; as disorder was increased, localized states took over. The authors were able to extract a critical disorder strength and set a benchmark for future experiments. —JS

Nat. Phys. 10.1038/s41567-018-0339-x (2018).

MICROBIOME

Global aeroplankton dispersal

Airborne particulates include large numbers of living organisms, as well as dust, pollutants, and other chemicals. Cáliz *et al*. collected aeroplankton fortnightly for 7 years in the Spanish Pyrenees. High-throughput sequencing of 16*S* and 18*S* amplicons identified microbes, including potential pathogens, that had made landfall in rain and snow. Distinct seasonal and climate signals in the data associated with the origin of the air masses. For example, winter microbial fallout originated from as far away as the North American taiga, and summer-occurring organisms contained desert-adapted bacteria from North Africa. Over the collection period, air-mass origins shifted, possibly as a result of climate change. Most atmospheric microbes are cosmopolitan, and it seems the upper atmosphere acts as a global highway for many taxa. —CA

Proc. Natl. Acad. Sci. U.S.A. **115**, 12229 (2018).

PHOTO: ISTOCK.COM/SIERRARAT

Published by AAAS

ALSO IN *SCIENCE* JOURNALS

Edited by **Stella Hurtley**

CARBON CYCLE

Animals count

Flux across the carbon cycle is generally characterized by contributions from plants, microbes, and abiotic systems. Animals, however, move vast amounts of carbon, both through ecosystem webs and across the landscape. Schmitz *et al*. review the different contributions that animal populations make to carbon cycling and discuss approaches that allow for better monitoring of these contributions. —SNV

Science, this issue p. 1127

HUMAN GENOMICS

Complex processes in the settling of the Americas

The expansion into the Americas by the ancestors of present day Native Americans has been difficult to tease apart from analyses of present day populations. To understand how humans diverged and spread across North and South America, Moreno-Mayar *et al*. sequenced 15 ancient human genomes from Alaska to Patagonia. Analysis of the oldest genomes suggests that there was an early split within Beringian populations, giving rise to the Northern and Southern lineages. Because population history cannot be explained by simple models or patterns of dispersal, it seems that people moved out of Beringia and across the continents in a complex manner. —LMZ

Science, this issue p. 1128

ANTIMALARIALS

A path to tackle liver-stage parasites

Malaria parasites are evolutionarily prepared to resist drug attack. Resistance is emerging to even the latest frontline combination therapies, which target the blood stages of the *Plasmodium* parasite. As an alternative strategy, Antonova-Koch *et al*. investigated the possibilities of drugs against liver-stage parasites (see the Perspective by Phillips and Goldberg). To do so, they devised a luciferase-reporter drug screen for the rodent parasite *Plasmodium berghei*. Three rounds of increasingly stringent screening were used. From this regime, several chemotypes that inhibit *Plasmodium* mitochondrial electron transport were identified. Excitingly, several new scaffolds, with as-yet-unknown modes of action but solely targeting the parasites' liver stages, emerged as promising drug leads for further development. —CA

Science, this issue p. 1129;
see also p. 1112

NANOMATERIALS

No barriers to growing a row

Classical nucleation theory predicts that two-dimensional islands on a surface must reach a critical size before they continue to grow; below that size, they dissolve. Chen *et al*. used phage display to select for short peptides that would bind to molybdenum disulfide (MoS_2) (see the Perspective by Kahr and Ward). Hexagonal arrays of these peptides grew epitaxially as dimers but without a size barrier—the critical nuclei size was zero. Although two-dimensional arrays formed, growth occurred one row at time. Classical nucleation theory indeed predicts the absence of a barrier for such one-dimensional growth. —PDS

Science, this issue p. 1135;
see also p. 1111

CLIMATE IMPACTS

Drivers of the "Great Dying"

Though our current extinction crisis is substantial, it pales in comparison to the largest extinction in Earth's history, which occurred at the end of the Permian Period. Referred to as the "Great Dying," this event saw the loss of up to 96% of all marine species and 70% of terrestrial species. Penn *et al*. explored the extinction dynamics of the time using Earth system models in conjunction with physiological data across animal taxa (see the Perspective by Kump). They conclude that increased marine temperatures and reduced oxygen availability were responsible for a majority of the recorded extinctions. Because similar environmental alterations are predicted outcomes of current climate change, we would be wise to take note. —SNV

Science, this issue p. 1130;
see also p. 1113

POLYMERS

Beating the heat by blending

Charge carriers move through semiconductor polymers by hopping transport. In principle, these polymers should be more conductive at higher temperatures. In practice, conductivity drops at high temperatures because interchain contacts are disrupted, which limits potential applications. Gumyusenge *et al*. now show that appropriate blending of a semicrystalline conjugated polymer with an insulating polymer that has a high glass-transition temperature creates a morphology that stabilizes a network of semiconductor channels. High charge conductivity was maintained in these materials up to 220°C. —PDS

Science, this issue p. 1131

VALLEYTRONICS

Making a practical valleytronics device

Two-dimensional materials with a hexagonal lattice, such as graphene, have two distinct "valleys" in their band structure. Researchers in the emerging field of valleytronics hope that these valley degrees of freedom can be exploited as information carriers, but making valleytronic devices is tricky. Li *et al*. created chiral valley Hall states on the boundary between oppositely gated regions of bilayer graphene. They then guided these so-called kink states through their sample using spatially modulated gating, demonstrating right and left turns, as well as a valley valve function. —JS

Science, this issue p. 1149

BIOPHYSICS

How membrane viscosity affects respiration

In bacteria, energy production by the electron transport chain occurs at cell membranes and can be influenced by the lipid composition of the membrane. Budin *et al*. used genetic engineering to influence the concentration of unsaturated branched-chain fatty acids and thus control membrane viscosity (see the Perspective by Schon). Experimental measurements and mathematical modeling indicated that rates of respiratory metabolism and rates of cell growth were dependent on membrane viscosity and its effects on diffusion. Experiments on yeast mitochondria also showed similar effects. Maintaining efficient respiration may thus place evolutionary constraints on cellular lipid composition. —LBR

Science, this issue p. 1186;
see also p. 1114

REGENERATION

Do endothelial cells hold the key to success?

Endothelial cells line the inner vascular wall, and their phenotype and behavior can vary according to the organ in which they are situated and

Published by AAAS

the environment. Not only do endothelial cells form the barrier of vessel walls, they also can participate in signaling with the surrounding tissue to promote regeneration and growth. In a Perspective, Gomez-Salinero and Rafii discuss how endothelial cells contribute to wound healing, regeneration, and disease states, such as cancer, and how our growing understanding of endothelial cell plasticity might advance regenerative medicine and the development of artificial organs for transplant. —GKA

Science, this issue p. 1116

SIGNAL TRANSDUCTION

Regulation of RAS by ubiquitination

The protein LZTR1 is mutated in human cancers and developmental diseases. Work from two groups now converge to implicate the protein in regulating signaling by the small guanosine triphosphatase RAS. Steklov *et al*. showed that mice haploinsufficient for LZTR1 recapitulated aspects of the human disease Noonan syndrome. Their biochemical studies showed that LZTR1 associated with RAS. LZTR1 appears to function as an adaptor that promotes ubiquitination of RAS, thus inhibiting its signaling functions. Bigenzahn *et al*. found LZTR1 in a screen for proteins whose absence led to resistance to the tyrosine kinase inhibitors used to treat cancers caused by the BCR-ABL oncogene product. Their biochemical studies and genetic studies in fruitflies also showed that loss of LZTR1 led to increased activity of RAS and signaling through the mitogen-activated protein kinase pathway. —LBR

Science, this issue p. 1177, p. 1171

CANCER

Expanding the landscape of immunotherapy targets

Most searches for druggable tumor-specific antigens (TSAs) start with an examination of peptides derived from protein-coding exons. Laumont *et al*. took a different approach and found numerous TSAs that derived from aberrant expression of noncoding sequences in murine cell lines and in B-lineage acute lymphoblastic leukemia and lung cancer patient samples. They validated the immunogenicity and efficacy of TSA vaccination for select antigens in mouse models of cancer. Noncoding regions are a potentially rich source of TSAs that could greatly expand the number of targetable antigens across different cancers, including those with low mutational burdens. —CAC

Sci. Transl. Med. **10**, eaau5516 (2018).

CELL BIOLOGY

Cleaving a different function for p62

The scaffold protein p62 has a critical role in autophagy, the regulated intracellular degradation of proteins and organelles. Sanchez-Garrido *et al*. identified a proteolytic fragment of human p62, called p62^{TRM} that had a distinct function from full-length p62 (see the Focus by Martens). Instead of promoting autophagy, p62^{TRM} regulated responses to nutrient availability. This function was lost in p62 variants with disease-associated mutations in the cleavage site, suggesting that defective nutrient sensing may account for some of the symptoms of patients with p62 mutations. —WW

Sci. Signal. **11**, eaat6903, eaav3530 (2018).

Published by AAAS

REVIEW SUMMARY

CARBON CYCLE

Animals and the zoogeochemistry of the carbon cycle

Oswald J. Schmitz*, **Christopher C. Wilmers**, **Shawn J. Leroux**, **Christopher E. Doughty**, **Trisha B. Atwood**, **Mauro Galetti**, **Andrew B. Davies**, **Scott J. Goetz**

BACKGROUND: Modern advances in remote-sensing technology are providing unprecedented opportunities to accurately measure the global distribution of carbon held in biomass within ecosystems. Such highly spatially resolved measures of biomass carbon are intended to provide an accurate inventory of global carbon storage within ecosystems. They are also needed to test the accuracy of carbon cycle models that predict how global changes that alter biogeochemical functions—such as carbon assimilation via photosynthesis, carbon losses via plant and microbial respiration, and organic matter deposition in soils and sediments—will affect net ecosystem carbon uptake and storage. Emerging ecological theory predicts that wild animals stand to play an important role in mediating these biogeochemical processes. Furthermore, many animal species roam widely across landscapes, creating a spatial dynamism that could regulate spatial patterning of vegetation biomass and carbon uptake and soil carbon retention. But such zoogeochemical effects are not measured by current remote-sensing approaches nor are they factored into carbon cycle models. Studies are now providing new quantitative insights into how the abundance, diversity, and movement of animal species across landscapes influence the nature and magnitude of zoogeochemical affects. These insights inform how to account for animals in remote-sensing applications and in carbon cycle models to more accurately predict carbon exchange between ecosystems and the atmosphere in the face of global environmental change.

ADVANCES: Zoogeochemical effects have been measured using manipulative experiments that exclude or add focal wild animal species or along landscape gradients where animal abundances or diversity vary naturally. Our review of these studies, which cover a wide diversity of taxa (vertebrates and invertebrates and large- and small-bodied organisms) and ecosystems, reveals that animals can increase or decrease rates of biogeochemical processes, with a median change of 40% but ranging from 15 to 250% or more. Moreover, models that embody zoogeochemical effects reveal the potential for considerable under- or overestimates in ecosystem carbon budgets if animal effects are not considered. The key challenge, in light of these findings, is comprehensively accounting for spatially dynamic animal effects across landscapes. We review new developments in spatial ecosystem ecology that offer the kind of analytical guidance needed to link animal movement ecology to geospatial patterning in ecosystem carbon uptake and storage. Considerations of animal movement will require highly resolved spatially explicit understanding of landscape features, including topography, climate, and the spatial arrangement of habitat patches and habitat connectivity within and among ecosystems across landscapes. We elaborate on advances in remote-sensing capabilities that can deliver these critical data. We further review new geospatial statistical methods that, when combined with remote-sensing data and spatial ecosystem modeling, offer the means to comprehensively understand and predict how zoogeochemical-driven landscape processes regulate spatial patterns in carbon distribution.

ON OUR WEBSITE

Read the full article at http://dx.doi.org/10.1126/science.aar3213

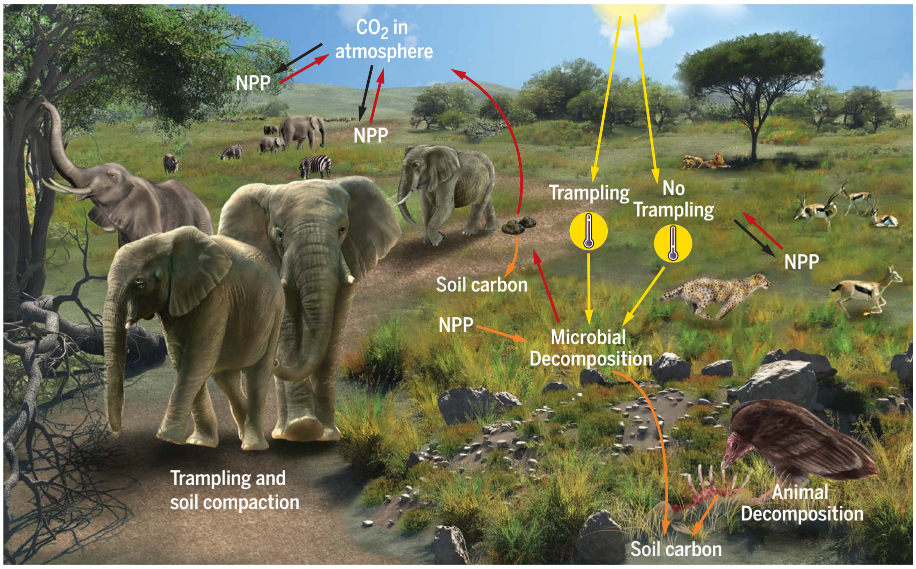

The myriad animal zoogeochemical effects on carbon cycling. Animals can mediate net carbon sequestration by plants (net primary productivity, NPP) by altering CO$_2$ uptake into (black arrows) and from (red arrows) ecosystems. Herbivore grazing and tree browsing can alter the spatial distribution of plant biomass. Predators can modify herbivore impacts via predation and predator-avoidance behavior. Animal trampling compacts soils and alters soil temperatures by changing the amount of solar radiation reaching soil surfaces (yellow arrows). Animals also change the chemical quality of organic matter that enters the soil pool (orange arrows).

CREDIT: NICOLE FULLER/SAYO-ART

OUTLOOK: There is growing interest to slow climate change by enlisting ecological processes to recapture atmospheric carbon and store it within ecosystems. Wild animal species are rarely considered as part of the solution. Instead, it is often held that managing habitat space to conserve wild animals will conflict with carbon storage. Our integrative review offers a pathway forward for deciding when and how conserving or managing a diversity of animal species could in fact enhance ecosystem carbon uptake and storage. Such understanding informs international climate and biodiversity initiatives such as those described by the United Nations Convention on Biological Diversity and national biodiversity strategies and climate action plans. All of these initiatives require better resolution of how biodiversity effects on ecosystem structure and biogeochemical functioning will become altered by global change. ■

The list of author affiliations is available in the full article online.
*Corresponding author. Email: oswald.schmitz@yale.edu
Cite this article as O. J. Schmitz *et al.*, *Science* 362, eaar3213 (2018). DOI: 10.1126/science.aar3213

Downloaded from http://science.sciencemag.org/ on December 6, 2018

REVIEW

CARBON CYCLE

Animals and the zoogeochemistry of the carbon cycle

Oswald J. Schmitz[1]*, Christopher C. Wilmers[2], Shawn J. Leroux[3], Christopher E. Doughty[4], Trisha B. Atwood[5], Mauro Galetti[6], Andrew B. Davies[7], Scott J. Goetz[4]

Predicting and managing the global carbon cycle requires scientific understanding of ecosystem processes that control carbon uptake and storage. It is generally assumed that carbon cycling is sufficiently characterized in terms of uptake and exchange between ecosystem plant and soil pools and the atmosphere. We show that animals also play an important role by mediating carbon exchange between ecosystems and the atmosphere, at times turning ecosystem carbon sources into sinks, or vice versa. Animals also move across landscapes, creating a dynamism that shapes landscape-scale variation in carbon exchange and storage. Predicting and measuring carbon cycling under such dynamism is an important scientific challenge. We explain how to link analyses of spatial ecosystem functioning, animal movement, and remote sensing of animal habitats with carbon dynamics across landscapes.

Understanding the biogeochemical processes and feedbacks regulating carbon uptake and storage within ecosystems is key to predicting and managing atmospheric CO_2 concentrations and the rate and extent of climatic change (1–3). Concerted efforts, abetted by modern advances in remote-sensing technology, are providing unprecedented opportunities to accurately measure the global distribution of carbon held in biomass within ecosystems (3–5). Such highly resolved measures of spatial variation in biomass carbon are needed to provide an accurate inventory of global carbon storage within ecosystems (5, 6) and reliably test and refine carbon cycle models used to make predictions about the relationships between ecosystem structure, biogeochemical functioning, and carbon storage (2).

Contemporary carbon cycle models have largely evolved [e.g., (3, 7, 8)] under the assumption that carbon uptake and allocation to biomass is controlled by nutrient and water limitation, microbial mineralization of organic matter and weathering of geological parent material, and climate and hydrological regimes. The models account for carbon that is distributed in live plant biomass, plant detritus, and organic matter entering soils by characterizing fundamental biogeochemical processes driving ecosystem carbon exchange and storage. These processes include carbon assimilation via photosynthesis, losses via autotrophic (plant) and heterotrophic (microbial) respiration, and organic matter deposition in soils and sediments.

Carbon cycle models typically do not, however, account for the biomass or effects of animals (herbivores and carnivores) in higher trophic levels of ecosystems. Granted, herbivores and carnivores in many ecosystems tend to be progressively less abundant (by orders of magnitude) than plants, owing to low transfer efficiencies of nutrients and carbon from plants to these higher trophic levels (5, 9, 10). The existence of such a pyramidal trophic structure has led to the reasoning that animals are entirely dependent upon the availability of plant biomass. Furthermore, their comparative rarity makes it unlikely that they will exert strong feedback control on ecosystem processes (9, 10). Hence, it may seem reasonable to assume that animals are unlikely to have substantial effects on biogeochemical processes and carbon storage, and consequentially construct the carbon budget without considering their contributions (6). But animals can cause important positive and negative feedback effects that alter the trophic structure of ecosystems (11) and, furthermore, may influence carbon cycling (9, 12) despite their comparatively low biomass representation within ecosystems. Failure to account for these feedbacks could result in under- or overestimates in the capacity of ecosystems to take up and store carbon (Fig. 1).

Until very recently, most studies measuring animal feedback effects have focused on herbivores. Numerous studies have experimentally measured the amount of plant biomass that is removed by herbivores and attendant changes in plant species composition, inferring how such changes influence the fate of carbon in ecosystems (13). However, herbivorous and nonherbivorous animals are hypothesized to influence carbon cycling via many other mechanisms that affect ecosystem biogeochemical processes and properties directly (9, 12). These influences, which we call zoogeochemical effects, include mediation of carbon uptake via photosynthesis, autotrophic and heterotrophic respiration, and soil organic matter deposition and alteration of the physical and chemical properties of organic matter and soils and sediments.

We review here studies that have explicitly measured the zoogeochemical effects by a diversity of animal taxa (vertebrates and invertebrates and large- and small-bodied organisms) in several ecosystems globally. Additionally, animals can control the magnitude of carbon exchange with soil reservoirs, influencing both short- and long-term carbon turnover rates (Fig. 1). Such zoogeochemical effects are not measured by current remote sensing, nor are they included in carbon cycle models (2), and therefore contribute to critical uncertainties about the fate of carbon in key global reservoirs. This currently limits our ability to accurately calculate carbon budgets and predict future climate change. We show how to overcome this limitation by reviewing recent efforts to estimate the implications of changes in animal species abundance on regional carbon budgets.

A further consideration is that many animal species roam widely across landscapes (14). Animal movements create a spatial dynamism that connects geographic locations across landscapes via active transport of nutrients and seeds and temporal variation in the location and abundance of herbivores and carnivores. Disrupting animal movements can alter the spatial patterning of plant and animal biomass across landscapes and trophic controls over ecosystem functioning (14–17). These spatial effects are not embodied in conventional carbon cycle models (3, 7, 8) or carbon inventories (5). If lessons from historical losses of large migratory animals are any indication, these spatial effects need to be included because they can be large (18). It is estimated that population reductions and extinctions of large migratory mammals during ancient and more modern times in Earth's history have resulted in alterations of global methane emissions to the atmosphere by 0.8 to 34.8% (18). Attendant changes in land surface cover affecting both global atmospheric CO_2 concentrations and biophysical properties such as albedo or evapotranspiration have been noted as well (19, 20). Modern global environmental changes such as habitat fragmentation and land-use conversion continue to alter the composition and abundance of animal species in many ecosystems (21) and change the extent and geospatial locations of their movements across landscapes (22). Evidence shows that such loss and disruption of movement introduces the risk that ecosystems could even flip from being carbon sinks to sources (Fig. 1). To address this uncertainty, we review recent modeling efforts that can be used

---

[1]School of Forestry and Environmental Studies, Yale University, New Haven, CT, USA. [2]Department of Environmental Studies, University of California, Santa Cruz, Santa Cruz, CA, USA. [3]Department of Biology, Memorial University of Newfoundland, St. John's, NF, Canada. [4]School of Informatics, Computing and Cyber Systems, Northern Arizona University, Flagstaff, AZ, USA. [5]Department of Watershed Sciences and the Ecology Center, Utah State University, Logan, UT, USA. [6]Instituto de Biociências, Departamento de Ecologia, Universidade Estadual Paulista, Rio Claro, Brazil. [7]Department of Global Ecology, Carnegie Institution for Science, Stanford, CA, USA.
*Corresponding author. Email: oswald.schmitz@yale.edu

Downloaded from http://science.sciencemag.org/ on December 6, 2018

to integrate zoogeochemical effects with carbon models and budget estimates. We further discuss model developments that include animal movement ecology, using case examples to show how such integration can deepen understanding of carbon cycling in the face of global environmental changes. Ultimately, we offer insights about how to link animal spatial ecology, ecosystem modeling, and remote sensing—the kind of integration that is needed to improve the ability to accurately predict and manage the carbon cycle across landscapes.

Mechanisms and magnitudes of animal effects on ecosystem carbon balance

Fundamentally, zoogeochemical effects become manifested as a consequence of direct and indirect interactions among carnivores, herbivores, and plants within food chains in ecosystems (*9*, *12*, *13*). Herbivorous animals directly remove plant biomass, assimilate some of the embodied nutrients and carbon to build animal biomass through growth and development, and release additional carbon to the soil via egestion and to the atmosphere via respiration (*9*, *12*). Herbivory

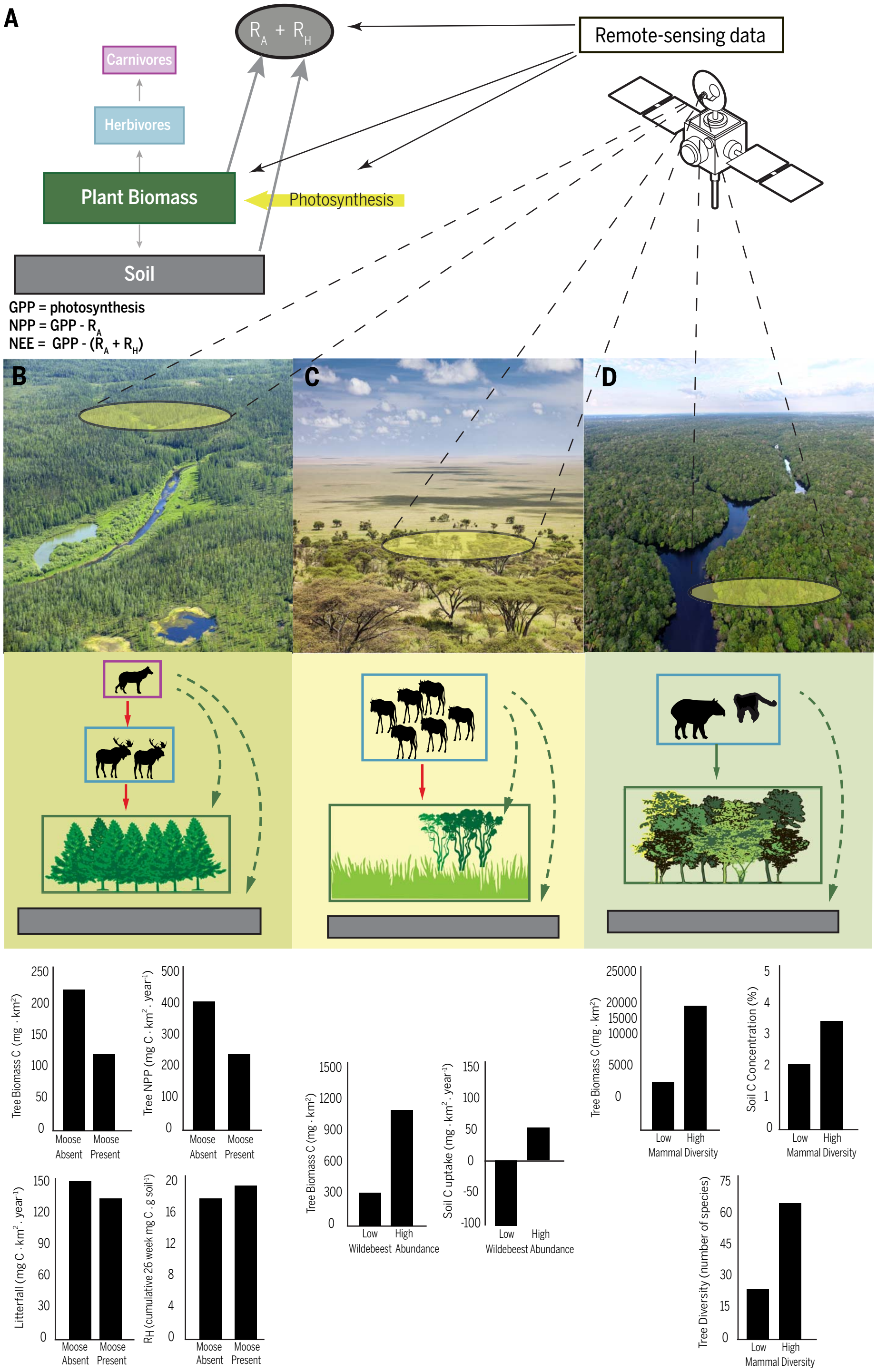

Fig. 1. Remote sensing does not measure important animal controls on landscape carbon. (**A**) Modern remote-sensing methods measure biogeochemical processes, including plant carbon uptake via photosynthesis and autotrophic (R_A) and heterotrophic (R_H) respiration, and inventory standing biomass carbon across landscapes. These measures can be used to estimate landscape-scale carbon cycle processes, including GPP, NPP, and NEE, which is information used to test carbon cycle models and construct carbon budgets. These methods focus on the plant trophic level (green) and do not include the biogeochemical contributions of herbivore and carnivore trophic levels (blue and purple, respectively) that tend to be less abundant in ecosystems. Remote sensing also cannot measure carbon storage in the soil reservoir (gray). (**B** to **D**) Animals directly (solid arrows) and indirectly (dashed arrows) control carbon dynamics in ecosystems though trophic interactions that reduce plant and animal biomass (red arrows), which ramify to have positive indirect effects on carbon uptake and storage in plants and in soil reservoirs. Failing to account for animal effects can lead to biases in carbon accounting. Consideration of animal effects will become increasingly important as global environmental changes such as land conversion, habitat loss, and exploitation stand to alter animal abundances and impacts across landscapes. Loss of predators such as wolves from boreal forest ecosystems (B) can lead to a rise in moose herbivore abundances, leading to declines in forest tree biomass and soil carbon storage (gray box). Loss of migrating grazing wildebeest herbivores in savanna ecosystems (C) can lower grazing pressure and lower soil carbon (gray box), owing to a concomitant rise in the frequency and extents of wildfires that consume combustible standing grass and woodland biomass. Loss of large mammal frugivores and attendant reduction in dispersal of large seeds in tropical forests (D) can lead to changes in tree community composition via reduction in abundance and biomass production of carbon dense trees (trees with black shading). Data from experimental and observational analyses (as shown in the graphs) reveal that variation in animal abundances can lead to large variation in carbon exchange and storage, sometimes even causing ecosystems (e.g., savanna) to switch from being carbon sources when animals are not abundant to becoming carbon sinks when they are highly abundant. C, carbon. Data were obtained from the following references: (B) boreal forest (*28*), (C) savanna (*15*), and (D) tropical forest (*36*). [Photos (from left to right): Serg Zastavkin/Shutterstock; mdd/Shutterstock; Costa Rodrigues/Shutterstock. Images: Vertyr/Depositphotos (African tree); Sonechko/Depositphotos (trees and grasses); airin.dizain/Depositphotos (wildebeest); YurikswO/Depositphotos (moose); Cundrawan703/Depositphotos (wolf)]

Downloaded from http://science.sciencemag.org/ on December 6, 2018

leaves less plant biomass available for photosynthesis, and plant stress from herbivore damage may further decrease plant photosynthetic rates and increase rates of autotrophic respiration (R_A) and heterotrophic respiration (R_H), all of which could decrease net primary productivity (NPP) and alter net ecosystem carbon exchange (NEE). Herbivores may also selectively feed on different plant species, thereby potentially altering the plant diversity and carbon density of standing biomass, given that plant species vary in their capacity to fix carbon and allocate it toward structural tissue and antiherbivore defense (*9*, *12*). Predators, through direct interactions with herbivore prey, could reverse the effects of herbivores. By reducing herbivore abundances and by causing changes in herbivore behavior and physiology, predators can have indirect effects on plant biomass, photosynthesis, and respiration, ultimately affecting NPP and NEE and fluxes of CO_2 and CH_4 between ecosystems and the atmosphere (*12*, *13*). Frugivorous animals disperse consumed seeds during the course of their movement, thereby determining the spatial distribution and diversity and abundance of plant species that take up and store carbon within ecosystems. Large animals can further influence ecosystem processes by trampling and compacting or perturbing soil surfaces and sediments, which can alter surface temperatures and chemical reactions that enhance soil or sediment carbon retention or exacerbate carbon release. Finally, animals can influence soil or sediment microbial activity by altering the amount and chemical content of organic matter that becomes available to microbes for decomposition (*12*, *13*).

Resolving the magnitude of zoogeochemical effects requires the use of manipulative experiments that systematically exclude or add focal animal species or of observational studies that take advantage of variation in natural animal abundance across landscape locations. We searched (*23*) the published literature for studies that fit the dual criteria of (i) having measured wild-animal effects explicitly on biogeochemical processes using (ii) experimental animal removals or additions, or systematic analyses across gradients of animal abundances or diversity. Studies that met these criteria reveal that animal effects are consistent with the various hypothesized mechanisms (Fig. 2).

Herbivore exclusion experiments show that animals can affect carbon dynamics by changing the species composition of the plant community —including tundra herbs and shrubs, saltmarsh grasses, and boreal and tropical forest trees—by selectively foraging. Individual cases show herbivore effects ramify by triggering changes in any or all of the following: above- and belowground plant biomass allocation, photosynthesis (gross primary production, or GPP) and NPP, and ecosystem respiration rates ($R_A + R_H$). In some cases, such as muskox in arctic mire and geese and hares in tidal saltmarshes (Fig. 2), herbivore presence enhances CO_2 uptake and carbon storage by 20 to 25% (*24*, *25*). Large grazers furthermore can protect carbon in sediments by changing physical and chemical processes (e.g., redox potential as a measure of organic matter decomposition and microbial carbon mineralization) via compaction from trampling (*24*). But in other cases—such as caribou, muskox, and geese in the arctic; marmots, mice, and invertebrates in alpine meadows; and moose in boreal forests—grazing and browsing herbivores cause a 15 to 70% decrease in CO_2 uptake (Fig. 2) by altering plant community composition, photosynthetic rates, and ecosystem respiration (*26*–*29*). Some cases, such as muskox in arctic mire and barnacle geese in arctic wet meadows (Fig. 2), reveal that animals can have conflicting positive and negative effects on different biogeochemical processes and properties. For example, muskox-caused CH_4 release could offset any gains in carbon storage owing to their enhancement of CO_2 uptake, and barnacle geese enhance soil carbon retention despite reducing CO_2 uptake by plants (*25*, *30*).

Manipulating the trophic structure of ecosystems shows that predators can reverse the effects of herbivores (Fig. 2). In grasslands, grasshoppers cause a 17% reduction in CO_2 uptake, relative to experimental controls that contain only plants. As with vertebrate herbivores, the grasshoppers modify the plant community composition, which cascades to alter NEE through changes in rates of photosynthesis and whole-ecosystem respiration (*31*). The addition of spider predators, which control grasshopper foraging, more than reverses the grasshopper effect by increasing CO_2 uptake by 46% (Fig. 2). The net effect of predators is that the fully intact food chain causes 22% more CO_2 uptake than experimental plant-only control conditions in which there are no animals. In humic lakes, zooplankton feed on methanotrophic bacteria—bacteria that consume and metabolize methane as their carbon source for energy—with the consequence that lakes emit CH_4 to the atmosphere (*32*). The reduction of zooplankton abundance after experimental introduction of zooplanktivorous perch caused a 50% reduction in CH_4 emission (Fig. 2) by releasing the bacteria from heavy consumption by zooplankton. In other experimental systems (freshwater ponds and streams), predatory stickleback fish and stonefly insects enhance carbon capture and retention by 88 to 90% (Fig. 2). Here, predation on zooplankton and macroinvertebrates increases algal CO_2 uptake for production, thereby reducing the concentrations of dissolved inorganic carbon in the water column that could otherwise be released to the atmosphere (*33*). Food chain interactions in lakes can also modulate CO_2 exchange in ways that depend on the number of predatory trophic levels present (Fig. 2). In three-trophic-level lakes containing minnow predators, zooplankton prey, and algae, minnows controlled the abundance of zooplankton, releasing algae from zooplankton grazing (*34*). The addition of bass predators to create a four-trophic-level system in which bass prey on minnows reversed this effect, resulting in more zooplankton and less algal biomass (*34*). Although lakes tend to be a net source of CO_2 to the atmosphere, the three-level system emitted 27% less CO_2 than the four-level system. The strength of this effect varied, however, with the level of nutrient supply. Nutrient enrichment, which enhanced algal production, magnified the difference in CO_2 exchange between the two kinds of systems. The effect of nutrient enrichment of algal production along with predator control of algal-feeding zooplankton meant that the three-level system became a net CO_2 sink. The four-level system became net carbon neutral. Consequently, there was 90% less CO_2 retained in the lake in the presence of bass than in their absence (Fig. 2).

Manipulative experiments have been completed within small spatial extents—most on the order of tens to hundreds of square meters but sometimes reaching up to several hectares—because of logistical constraints imposed by the need to physically control for animal presence or absence and extraneous environmental variables, and to make precise measures of carbon storage and exchange. This inevitably begs the question of whether the insights are scalable to the large spatial extents needed for management to make a difference in the carbon budget but also scalable to the extent that variation in the magnitude of biophysical environmental factors could swamp out any animal effect. Observational studies that have measured animal effects across larger spatial extents of entire ecosystems reveal that the insights about mechanisms and magnitude of effects are indeed scalable.

Grazing halos, patches largely devoid of seagrasses and macroalgae, surround many coral reef patches globally. They are large and ubiquitous enough to be detected by high-resolution remote sensing (*35*). Analyses in a ~10-km^2 area near Heron Island in Australia's Great Barrier Reef revealed that predators can cause the appearance of these halos by altering foraging behavior of herbivorous fishes (*35*). Sharks persistently cruise hunt near the reef patches. The perceived threat of predation causes herbivorous fish to feed heavily near the coral patches, staying in close proximity to the escape cover afforded by the coral. As a consequence, the highly grazed halos have lower vegetation canopy height and cover and, hence, 24% less carbon stored in their sediments than do areas beyond the halos that have little or no grazing impact (*35*).

Wildebeest in the 25,000-km^2 Serengeti savanna-woodland were decimated by disease and poaching before the 1960s, reducing their numbers from about 1.2 million to 300,000 animals (*15*). In turn, the accumulated, ungrazed aboveground vegetation fueled wildfires that consumed 80% of the ecosystem annually, leading to a net release of CO_2 to the atmosphere. Disease management and antipoaching enforcement over the ensuing decades has led to wildebeest population recovery, reducing the extent and intensity of wildfires (*15*). Wildebeest grazing is now causing a large fraction of carbon from combustible aboveground plant biomass to be released as dung that becomes incorporated by insects into soil reservoirs that are not prone to burning. The recovered grazing regime restored the Serengeti as a net CO_2 sink—estimated to be large enough today to offset all of east Africa's annual fossil fuel CO_2 emissions (*9*)—by

Downloaded from http://science.sciencemag.org/ on December 6, 2018

facilitating carbon capture and build-up in soil reservoirs and in savanna-woodland regrowth (*15*).

Conserving mammal species diversity in tropical forests maintains a diversity of functional roles—including frugivory and seed dispersal that supports tree reproduction, herbivory that modulates plant production, and provisioning of organic matter for soil storage—that are all functionally related to carbon capture (*36*). Consequently, carbon retention in woody biomass and in soil increases by 230 to 400% across a 3.5-fold increase in mammalian species diversity (Fig. 2). This effect of animal diversity is detectable across a 48,000-km^2 area despite considerable background spatial variation in biophysical properties across the landscape (*36*).

Sea otters can enhance carbon uptake within a 12,000-km^2 stretch of western North American coastal marine kelp forests by 1100% via the same mechanisms observed in small-scale trophic manipulation experiments (Fig. 2). Sea otters enhance kelp biomass carbon retention by preying on sea urchins that decimate coastal marine kelp forests (*37*).

The gathered evidence shows that animals can have both positive and negative impacts on biogeochemical processes driving ecosystem carbon uptake and storage, with a median change of 40%, relative to conditions without the focal animal present. Hence, animal effects on ecosystems should not be assumed to be negligible. Moreover, human impacts are increasingly causing multiple animal species to be lost from ecosystems—called defaunation (*21*)—as a result of poaching and overfishing, culling to reduce human-wildlife conflicts, illegal trade, logging, and habitat loss due to conversion to other land uses. Humans also have restored animal species to ecosystems, with a push to restore more—called rewilding (*38*). Estimates of the potential effects of species losses or rewilding on regional ecosystem carbon budgets reveal that they may not be trivial and may even have unintended consequences.

Changes in animal species and regional carbon budgets

In neotropical forests, large carbon-dense hardwood trees make a sizeable contribution to carbon uptake and storage. Their successful regeneration across the landscape is predicated on the presence of large frugivorous vertebrates that disperse the large seeds from such trees across long distances. But large frugivores are preferred by hunters and are thus most threatened by overhunting. Simulation analyses evaluated the effects of systematically losing large-bodied seed-dispersers, relative to random extinctions of any seed-dispersing vertebrates and found that such losses could alter the community composition of trees with different carbon storage traits (wood density, tree diameter, and tree height) with implications for aboveground carbon stored in tree biomass within the Atlantic forest region (*39*). The loss of trees dispersed by large-bodied frugivores (*39*) revealed a potential reduction in carbon storage capacity of 4 to 37% (*40*). Similar magnitudes of effect have been estimated for other forested regions of the Amazon (*41*). The erosion of carbon storage capacity via shifts in tree species composition can persist up to 100 years after defaunation (*42*), and smaller frugivores that are less preferred by hunters are unlikely to substitute

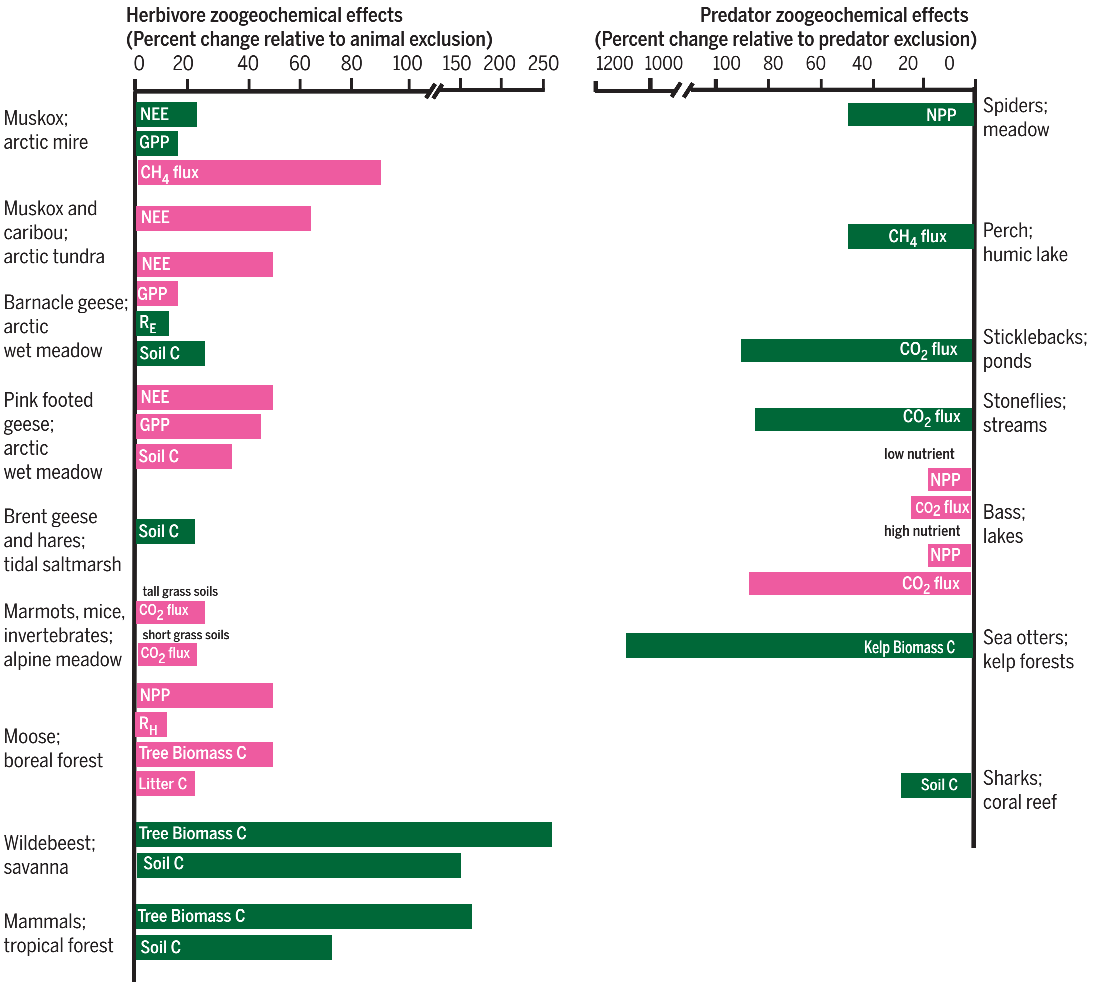

Fig. 2. Animal zoogeochemical effects in ecosystems. Experiments that exclude focal animals and observational studies across a range of focal animal species abundances reveal that animals can change the amount of carbon that is stored within ecosystems or exchanged between ecosystems and the atmosphere. Animal interventions in biogeochemical processes can both enhance (green bars) and reduce (pink bars) the amount of carbon stored in ecosystems. Animal effects can be appreciable, ranging from 10 to 1100%, with a median change of 40%. Data were obtained from (*24*–*37*). C, carbon; R_E, whole-ecosystem respiration.

Downloaded from http://science.sciencemag.org/ on December 6, 2018

the seed-dispersal services of their larger counterparts (39).

Analyses comparing effects of simulated declines of large-seeded animal-dispersed trees on carbon storage in woody biomass among African, American, Asian, and Australian tropical forests reveal that animals may not always affect ecosystem carbon balance owing to geographic differences in the dependence of tropical trees on animal seed dispersal. African, American, and South Asian forests, which have high proportions of animal-dispersed tree species, stand to lose their carbon with defaunation (43). Southeast Asian and Australian forests, alternatively, harbor trees that are less reliant on animals to disperse their seeds, and accordingly, defaunation has lesser consequences for forest carbon (43).

Wolves have been highlighted as important predators in North American terrestrial ecosystems, and their restoration has been hailed as a means to restore ecosystem functioning (38). Wolves can have an indirect effect on plant biomass, NPP, and NEE by reducing the abundances and changing the foraging behavior of large herbivores such as moose in boreal forests and elk in grasslands (44). Carbon budget analyses reveal, however, that this single species can propagate different net effects in different ecosystems. In boreal forest ecosystems, wolves control moose populations and thereby reverse the negative effects of moose on NPP and NEE (Fig. 1). Here wolf predation reduces the damage moose inflict on boreal plants—especially deciduous trees that tend to have high NPP and litter production for soil storage (Fig. 1)—thereby changing the plant community composition of the forest ecosystem in ways that enhance carbon storage in soil. Hence, culling wolves to enhance game populations could have a negative impact on carbon storage. Alternatively, in shortgrass prairie, elk stimulate NPP by enhancing nutrient cycling within the ecosystem. Wolves (along with other predators such as bears and cougars) reduce elk density and foraging, which in turn is estimated to reduce both NPP stimulation and NEE. Hence, restoration of wolves with the intention to restore grassland ecosystem functioning (38) can have negative impacts on ecosystem carbon balance. Estimates show that the strength of this effect should vary, however, with background soil-nutrient level. In nutrient-poor environments, wolf predation should reduce NEE by 78%, whereas in nutrient-richer environments, it should be reduced by 52% (44).

The ability to construct carbon budgets that account for animal effects for a wider range of species is currently limited by a fragmentary understanding of the biogeochemical effects of any given animal species (Fig. 2). This is because empirical studies have tended to measure only one to a few of the full complement of zoogeochemical processes operating in any one system. Moreover, a given animal species can have both positive and negative impacts on different process within a system (Fig. 2). Hence, the total net effects of any particular animal species on carbon balance remain largely unknown. An important research need is to develop more comprehensive understanding of the net effects of different, and potentially interacting, zoogeochemical mechanisms on ecosystem carbon balance. This will require confronting complexity due to interplay between myriad animal interactions and feedbacks. Resolving such complexity must be guided by new kinds of ecosystem models that account for animal impacts on plant and animal biomass carbon, NPP, R_A, R_H, and soil organic matter deposition (biomass carbon content of excreta, egesta, and plant litterfall). Models embodying these zoogeochemical processes hold promise to offer a more complete picture of animal effects on carbon cycling.

Ecosystem models embodying zoogeochemical processes

At their core, newer ecosystem models are founded on the conventional compartment structure used in classic ecosystem modeling, including soil elemental pools and plants (Fig. 3A) with the addition of herbivores and predators (45–49). The models capture the essential biogeochemical processes, including elemental uptake by plants from the abiotic environment (i.e., carbon uptake from the atmosphere and nitrogen uptake from soils) and elemental transfer and loss to and from all compartments through trophic interactions, respiration, excretion, egestion, and leaching out of the ecosystem as a result of physical processes. The models embody principles of ecological stoichiometry, namely how organisms and their interactions in ecosystems affect the balance of nutrients and energy. Typically, there is a focus on fluxes and pool sizes of nitrogen and carbon, but the focus could easily be extended to considerations of other important elements such as phosphorus. The models are formulated to obey fundamental mass-balance requirements such that, at equilibrium, elemental inputs to the ecosystem equal elemental losses from the ecosystem plus storage.

One such model has motivated systematic experimental and observational analyses exploring and comparing how two key ways that the top-down effects of predators may affect cycling and thereby modulate the amount of carbon exchanged between ecosystem reservoirs (e.g., soils and plants) and the atmosphere (49). Predators may cause cascading effects by killing and consuming their prey, thereby reducing herbivore biomass and herbivory and causing increased amounts of plant-based carbon to enter soil organic matter storage pools. The mere presence of predators within ecosystems may also cause nonconsumptive fear effects that increase respiratory costs at the expense of production owing to chronic stress (31, 50). Herbivores compensate by switching preferences from plants high in nitrogen to plants higher in soluble carbohydrate carbon (50). This alters herbivore elemental balance via altered uptake from plants and elemental release via respiration, excretion, and egestion. The herbivore diet shift alters the species composition of the plant community and the amount of carbon in senescent plant matter entering the soil storage pool (50). Active-hunting predators generally cause consumptive effects; sit-and-wait predators cause nonconsumptive effects (50). The feedbacks from predator nonconsumptive effects may be most important to whole-ecosystem elemental stocks, production and efficiency rates, and recycling fluxes by changing the stoichiometric balance of all trophic levels (50).

When parameterized with data from long-term experimentation in meadow ecosystems (49), the model predicts that there should be a 2.5× increase in soil carbon storage across a gradient from sit-and-wait predator dominance to active-hunting predator dominance. This trend has been empirically validated using manipulative experiments and a landscape-scale survey of soil carbon retention among 15 different meadows comprised of spider predators, grasshopper prey, and three functional groups of plants represented by the carbon-dense herb goldenrod (*Solidago rugosa*), nitrogen-rich grasses, and a variety of other herbs (51). Along a gradient of shifting dominance of sit-and-wait predators to a dominance of active-hunting predators, there is a 1.7× increase in aboveground NPP driven by shifts in *Solidago* biomass and, in reasonable agreement with model predictions, a 2× increase in soil carbon retention (51). Biophysical factors such as total live-plant biomass, degree of land-use development around the fields, field age, and soil texture were not significant predictors of the trend in soil carbon retention (51).

Incorporating spatial dynamics

Most ecosystem models used to predict carbon dynamics are spatially implicit, simply modeling exchanges between ecosystem reservoirs and the atmosphere within a fixed geographic space. But animal movement creates a spatial dynamism that connects geographic locations across landscapes (52-54). For example, beyond their impacts on Serengeti savanna-woodland carbon, migrating wildebeest also affect carbon cycling in the river ecosystems that flow through the Serengeti. Specifically, their mass drowning while trying to ford the Mara River is alone estimated to contribute ~100,000 kg of carcass-derived carbon, which represents an 18 to 191% subsidy of dissolved organic carbon to the Mara River during peak carcass-deposition time (55). Evidence suggests that the impacts of large terrestrial ungulates on carbon cycling across ecosystems into freshwater environments may be ubiquitous (56). Migratory animals have the potential for large impacts on carbon dynamics across landscapes (14, 57) because they are typically gregarious and directly redistribute large quantities of carbon across landscapes via transport and release during migration. For example, streams with migratory Pacific salmon carcasses have different riparian plant overstory and understory communities than streams without Pacific salmon driving potential differences in riparian forest carbon sequestration (58).

Theory of spatial ecosystem ecology (59-61) has been advanced precisely to begin predicting how animal movement between source and

Downloaded from http://science.sciencemag.org/ on December 6, 2018

recipient locations influence the nature and strength of controls over ecosystem functioning within the source and recipient locations (Fig. 3). Different spatial locations could range from different habitat patches arrayed across a landscape within a single ecosystem [e.g., forest patches separated by a developed-land matrix (*62*)] to different ecosystems arrayed across a broader regional landscape [e.g., grassland and woodland ecosystems (*62*)]. Animal movement across landscapes can subsidize recipient locations via an influx of new prey or predators, as well as animal transported nutrients and materials such as nitrogen and phosphorus in dung and urine, or as organic matter in carcasses that are deposited in the recipient locations (*59*).

This theory predicts that animal subsidies via movement of live animals and transport of nutrients and material into recipient locations can cause a switch in ecosystem functioning, from being controlled predominantly by nutrient supply to largely being controlled by animal effects (*59*). Empirical synthesis of field experiments and observational studies support the prediction that animal subsidies can cause switches in trophic control in recipient locations. The strongest, persistent effects came from an influx of nutrients and herbivores (versus influx of predators) into recipient locations (*16*). These kinds of animal movements and nutrient translocations can be represented in spatial ecosystem theory in a variety of ways, ranging from consideration of landscapes organized as mosaics of multiple patches to lattices parameterized for realistic landscapes (Fig. 3, B and C). In its simplest form, animal effects across landscapes can be

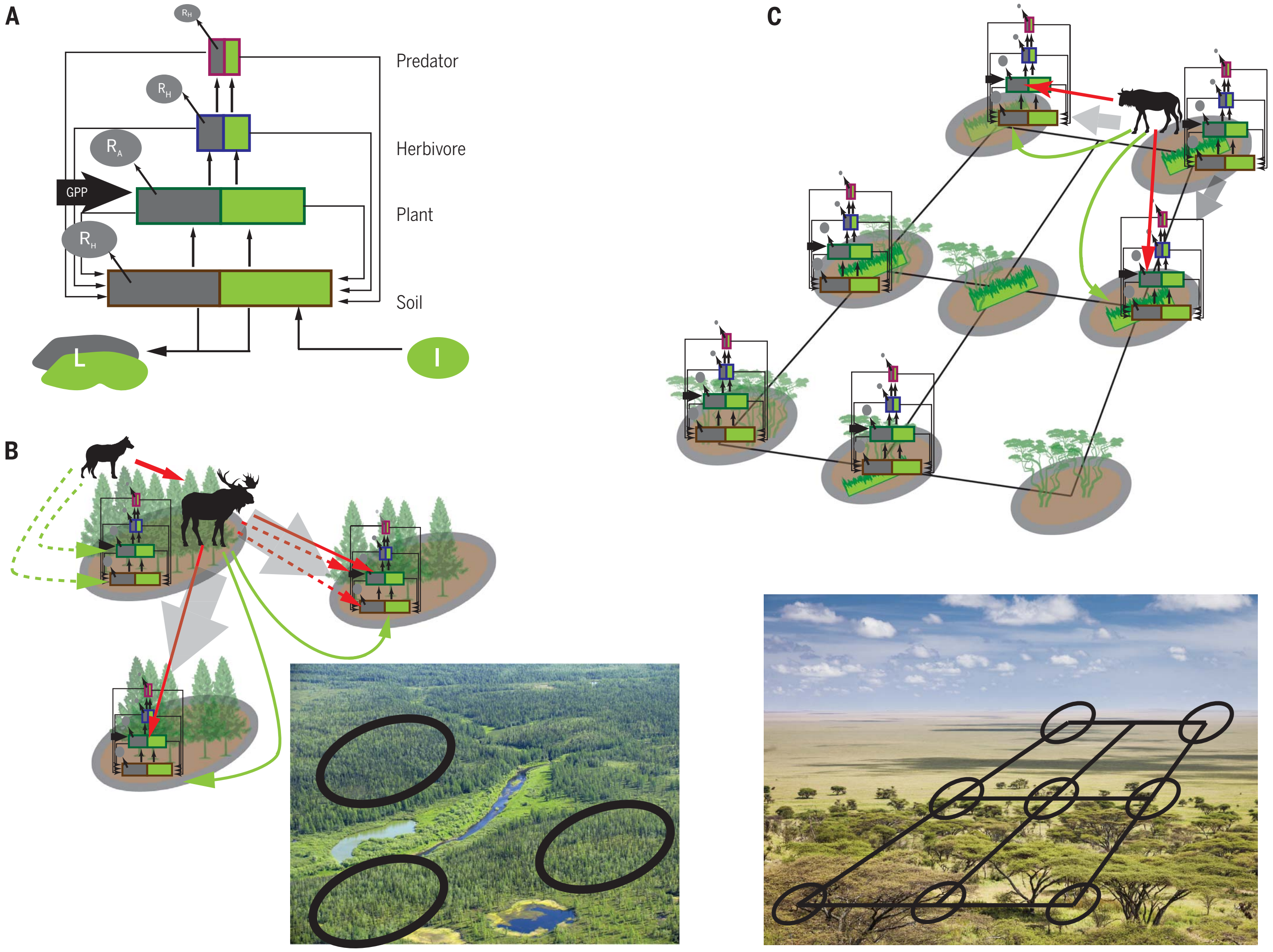

Fig. 3. Ecosystem modeling to accommodate animal feedbacks and spatial dynamics. (**A** to **C**) General nonspatial ecosystem models (A) consider soil, plant, herbivore, and predator trophic compartments arranged as biomass pyramids. The models account for fluxes of nitrogen (green) and carbon (gray) due to trophic exchange between trophic compartments. The models further include CO$_2$ uptake by plants (GPP), autotrophic respiration (R$_A$), heterotrophic respiration (R$_H$) recycling fluxes from each trophic compartment to soil, weathering inputs (I) to soil, and leaching (L) from soil. As such, they respect mass-balance requirements of ecosystem functioning. The models can be made spatially explicit by considering landscapes either in terms of patch (B) or lattice (C) configurations, with ecosystem trophic structure and functioning prevalent at each location. Within spatial locations, animals drive ecosystem functioning via direct effects (solid arrows) such as trophic interactions (red arrows) and indirect effects (dashed arrows) mediated by trophic interactions that can enhance carbon storage in biomass within plant and abiotic compartments. Animals also connect different spatial locations through movement (gray arrows) from source to recipient locations. During such movements, they translocate nutrients to recipient locations (green arrows) or consume nutrients (nitrogen and carbon) contained within biomass in recipient locations (solid red arrows). They thereby can control the amount of biomass carbon that eventually enters and is retained in the soil compartment within a spatial location by changing organic matter inputs and heterotrophic respiration. Net ecosystem carbon exchange and storage is quantified by summing carbon pool sizes and fluxes across the spatial locations. [Photos (left to right): Serg Zastavkin/Shutterstock; mdd/Shutterstock. Images: Vertyr/Depositphotos (African tree); Sonechko/Depositphotos (trees and grasses); airin.dizain/Depositphotos (wildebeest); YurikswO/Depositphotos (moose); Cundrawan703/Depositphotos (wolf)]

Downloaded from http://science.sciencemag.org/ on December 6, 2018

represented with distance decay functions [e.g., (63)] or dispersal kernels [e.g., (64)]. More mechanistic representations of animal movement can be built into spatially explicit theory in continuous time with reaction-diffusion equations (65) and in discrete-time with integrodifference equations [e.g., (66)] to characterize the changing influence of animals away from source areas.

An example of the promise of incorporating animal movement effects comes from a parameterized lattice model, representative of the entire Serengeti savanna-woodland landscape (67). The modeled landscape was divided into 10 km–by–10 km cells, to account for grass and woodland distribution based on spatial empirical data on these vegetation groups. The modeling evaluated how movement between cells and feeding by grazing versus browsing herbivores within them could affect the landscape distribution of grass and woodland relative to biophysical drivers of plant distribution such as wildfire and rainfall (67). Simulations revealed that browsers and fire together cause a decline in woodland cover and tree biomass, a negative effect that would intensify if grazers were absent, because large amounts of combustible grass biomass would remain standing across the landscape. Migratory movement in response to rainfall patterns determines grazer presence across the landscape. Hence, grazers play an important role in mediating the strength of impact of fire and browsers across the entire landscape by reducing fuel as they respond to rainfall-driven grass production across the landscape. This creates a feedback that exerts strong effects on spatial patterns of woodland patches (67), thereby explaining the observed measures of landscape-scale variation in carbon capture and storage (15).

Opportunity to link remote sensing with animal movement and zoogeochemical effects

The impacts of animal movement on the global carbon cycle still need to be predicted and quantified. Movement underlies behavioral decisions about where to forage and seek shelter that impact NPP and NEE (68) at multiple scales, ranging from the habitat patch to the home range to migratory destinations. Fundamentally, considerations of animal movement will require a highly resolved spatially explicit understanding of landscape features, including topography, climate, habitat structure, and the spatial arrangement of habitat patches and habitat connectivity within and among ecosystems across landscapes.

Modern remote-sensing technology can deliver highly spatially resolved data on functional and structural properties of vegetation within ecosystems. Light detection and ranging (LIDAR) (69–71), in particular, can provide full three-dimensional characterization of habitat structure, including vertical profiles of cover, biomass, and carbon density, as well as underlying surface topography and integrative metrics of vertical biomass profiles like foliage height diversity (4, 72). When combined with image data, such as those from the Landsat series of satellites, LIDAR data can provide detailed insight into the topography and spatial arrangement of habitat patches across landscapes (73, 74), which can be related to the spatial distribution and movement of animal species across a landscape (75, 76). Nevertheless, airborne or satellite remote-sensing methods with broad geographic scope (2, 77) are limited in their ability to detect and quantify animal biomass and animal effects, especially nutrient inputs and carbon storage in soil. This underscores the need to develop greater synergy in the use of on-the-ground sampling and remote-sensing methods (2, 78).

As a complement to remote sensing, on-the-ground surveys of animal abundance using spatial capture-recapture approaches (79) and plot sampling of soil biogeochemistry [e.g., (36)] can advance understanding of the dynamism driving the spatially explicit effects of animals. New geospatial statistical methods reveal the promise of quantitatively characterizing biogeochemical landscapes using spatial nutrient and carbon distribution modeling. Outputs from such models could provide the kinds of key data layers (80, 81) needed for spatial ecosystem models to connect animal movements, spatial animal biomass, trophic interactions, and carbon cycling to fundamental landscape attributes (nutrition) that motivate why and where animals move across landscapes [e.g., (67)].

The spatial mapping of biogeochemical landscapes, in combination with data from modern biologging devices (82), offers the means to test predictions of spatial ecosystem models about the net effects of animal movement on nutrient and carbon dynamics in terms of landscape attributes that motivate their movement behavior and interactions with other species. Biologging involves the use of remote sensors that can continuously measure most aspects of an animal's state (e.g., location, behavior, caloric expenditure, and interactions with other animals) and external environment (e.g., temperature, salinity, and depth). Modern technology, such as accelerometers sampling at 16 Hz or faster, can be used to determine the behavior of individual animals (e.g., feeding), whereas Fastloc GPS allows for subminute spatial sampling over long time scales (82). This technology facilitates linking measures of animal physiology (and hence nutrient demand) to foraging and movement behavior that is motivated by spatially heterogeneous resource supplies. In addition to landscape context, the spatial distribution of many herbivore prey species is influenced by their fear from perceived predation (34, 49). Ambush predators will often use cover (e.g., areas of higher carbon) to stalk prey, leading prey to disproportionately avoid those areas [e.g., (35, 83)]. Thus, monitoring predator interactions with their prey can offer an understanding of the indirect effects of predators on carbon cycling mediated by herbivore spatial responses to predator presence.

The promise of using remote sensing and on-the-ground sampling to provide the kind of synergy we call for is illustrated by a series of studies combining on-the-ground data on African elephant densities with LIDAR-derived measurements of woody vegetation. Elephants are a dominant driver of vegetation change and treefall in African ecosystems (84–87). Moreover, sex-specific elephant density data revealed that bull elephants, but not breeding herds, surpassed abiotic controls as the dominant driver of change in aboveground carbon stocks, which decreased only where bull densities exceeded 0.5 bulls km^{-2} (87). Effects of bull elephants are, however, landscape dependent, leading to decreases in carbon along rivers, at mid-elevations, and on steeper slopes. By contrast, carbon density mostly increases across the rest of the landscape regardless of elephant densities. Data collected from a companion-exclusion experiment further confirmed the dominant role of elephants in driving carbon change, with significantly slower carbon gains occurring only where elephants had access to woody vegetation.

This elephant study, along with examinations of wildebeest impacts in savanna (15, 67), provides a blueprint for the new kinds of multipronged research that is needed to understand and predict landscape-scale effects of animals. Such research begins with animal exclosure experiments to measure rates of the full complement of zoogeochemical processes [GPP, R_A, R_H, and organic matter (litter, excreta and egesta) deposition rates and leaching losses]. These measures can be used to parameterize ecosystem models and predict how much carbon should be distributed among different biomass pools, especially in soil and plants. Model predictions can then be tested via systematic sampling of carbon density within plots in the vicinity of the exclosure experiments. It is noteworthy that the strength of animal effects can covary or interact with the effects of biophysical properties across landscapes—including soil type, soil moisture, and soil nutrients—to influence plant biomass (88–90). This calls for landscape-scale experiments that replicate exclosures along landscape biophysical gradients to disentangle variation arising from animal effects from variation due to local biophysical conditions (88–90). The location of experimental sites can be informed by remotely sensed characterization of biophysical conditions, including landforms and vegetation structure [e.g., (87, 88)] and statistical distribution models of soil nutrient concentrations (80, 81). Studies involving multiple animal species should consider using nested experimental designs—modeled after the African KLEE, UHURU, and GLADE experiments—that use fencing to selectively exclude animal species across landscape nutrient and rainfall gradients (90). Movement analyses in combination with remotely sensed biophysical conditions can facilitate understanding of pathways by which animal subsidies flow across landscapes. These data, along with animal population surveys along those pathways, enable an accounting of the per capita rates of animal-mediated spatial exchange of nutrient and carbon among areas across landscapes. This information can be input as model parameters to refine predictions and tests of spatial variation in biomass carbon (Fig. 3).

Downloaded from http://science.sciencemag.org/ on December 6, 2018

Conservation and management implications

There is growing interest to actively enlist natural ecological processes to recapture atmospheric carbon and store it within ecosystems (91, 92). Proposed solutions focus on managing plants and microbes, owing to the huge role they play in forming carbon sinks within ecosystems (91–93). Conserving or managing wild animal species to control carbon exchange between ecosystems and the atmosphere is rarely considered as part of the portfolio of natural carbon-recapture solutions. The thinking, in fact, often holds that managing habitat space to conserve wild animals within ecosystems will conflict with allocating space to capture and store carbon, or, if both can happen in the same locations, they are, nonetheless, functionally unrelated (94–96). The evidence presented here shows that failing to quantitatively account for the positive and negative zoogeochemical effects of animals can mean missed opportunities to enhance carbon uptake by ecosystems or failure to achieve carbon management targets.

Attention has also turned to the prospect of compensating for the functional losses of wild animals using domestic livestock (90, 97). Indeed, methane emissions from modern cattle production are estimated to now fully compensate for estimated methane emission loss due to historical large mammal extinctions (18). But grazing cattle do not always compensate directly for functional losses of similarly sized modern wild herbivore grazers (90, 98). The magnitude of cattle effects varies with biophysical conditions of landscapes, including soil texture, moisture and nutrient status, and wet versus dry climates (98, 99). Cattle exclusion experiments reveal that heavy cattle grazing uniformly reduces ecosystem carbon uptake and soil storage as well as increases carbon fluxes from ecosystems to the atmosphere (99, 100). This effect is opposite to that of similarly sized wild grazers such as Serengeti wildebeest and North American elk. Although grazing intensity could be managed to align with biophysical conditions in ways that encourage grassland carbon sequestration (97, 98), the effects would still be highly localized given livestock herding practices. Hence, such management could not replicate the kind of grazing impact exerted by wild animals that migrate in large herds across the vast spatial scales of landscapes. Moreover, cattle cannot at all compensate for loss of browsing herbivores that affect savanna woody vegetation (89) or for browsing herbivores and frugivores residing in forest ecosystems, where much of the defaunation is happening. Hence, mounting evidence that large wild animals can control ecosystem carbon dynamics argues for considering the effects of their losses via defaunation as much as deforestation (21, 97) when accounting for human impacts on the global carbon cycle.

Carbon storage is only one among a larger portfolio of land uses. Hence, there will inevitably be conflicts over priorities for land allocation (94). In such cases, it would be helpful to quantify the marginal gains or losses of animal effects to assist in adjudicating trade-off decisions about how much land to allocate for carbon storage. Such analyses [e.g., (15, 36)] can help quantify the marginal returns for conserving targeted abundances of animals. For instance, in the Serengeti savannah-woodland ecosystem, carbon storage increases by 15% for every 100,000 additional wildebeest that live within the ecosystem, with diminishing returns as the population size reaches its carrying capacity. Across the existing range of mammal diversity, the tropical forest of Guyana stores, on average, 10 to 15% more carbon for each of the 60-plus mammal species that are conserved. There is a need to expand the scope of this kind of research, measuring zoogeochemical effects across landscape gradients in focal animal abundances. Data from such studies can generate important quantitative insight about the relationships between rates of change in animal abundance and rates of change in ecosystem carbon storage.

Conclusions

We have shown the many ways in which zoogeochemical effects can control ecosystem carbon storage and exchange across broad landscapes. Consequently, animals should be considered as an integral part of the portfolio of natural carbon-recapture solutions. Without such consideration, there may be serious inaccuracies in both carbon cycle models and anticipated global changes, which may lead to ineffective policy formulation for natural carbon storage. We challenge researchers to better represent how movement and abundances of animals may affect changes to the carbon cycle and how this will affect our future climate. Motivating tests and refinement of new spatial ecosystem models that consider animal feedbacks within trophic biomass pyramids through the integration of landscape-scale experiments, cutting-edge remote-sensing technology, and statistical models and data layers representing spatial biophysical conditions of landscapes offers a clear path to meet such an exciting challenge.

REFERENCES AND NOTES

1. R. A. Houghton, Balancing the global carbon budget. *Annu. Rev. Earth Planet. Sci.* **35**, 313–347 (2007). doi: 10.1146/annurev.earth.35.031306.140057
2. D. Schimel *et al.*, Observing terrestrial ecosystems and the carbon cycle from space. *Glob. Chang. Biol.* **21**, 1762–1776 (2015). doi: 10.1111/gcb.12822; pmid: 25472464
3. G. B. Bonan, S. C. Doney, Climate, ecosystems, and planetary futures: The challenge to predict life in Earth system models. *Science* **359**, eaam8328 (2018). doi: 10.1126/science.aam8328; pmid: 29420265
4. S. J. Goetz, R. O. Dubayah, Advances in remote sensing technology and implications for measuring and monitoring forest carbon stocks and change. *Carbon Manag.* **2**, 231–244 (2011). doi: 10.4155/cmt.11.18
5. Y. M. Bar-On, R. Phillips, R. Milo, The biomass distribution on Earth. *Proc. Natl. Acad. Sci. U.S.A.* **115**, 6506–6511 (2018). doi: 10.1073/pnas.1711842115; pmid: 29784790
6. C. Le Quéré *et al.*, Global carbon budget 2017. *Earth Syst. Sci. Data* **10**, 405–448 (2018). doi: 10.5194/essd-10-405-2018
7. M. Heimann *et al.*, Evaluation of terrestrial carbon cycle models through simulations of the seasonal cycle of atmospheric CO_2: First results of a model intercomparison study. *Global Biogeochem. Cycles* **12**, 1–24 (1998). doi: 10.1029/97GB01936
8. S. Zaehle *et al.*, Evaluation of 11 terrestrial carbon-nitrogen cycle models against observations from two temperate Free-Air CO_2 Enrichment studies. *New Phytol.* **202**, 803–822 (2014). doi: 10.1111/nph.12697; pmid: 24467623
9. O. J. Schmitz *et al.*, Animating the carbon cycle. *Ecosystems (N. Y.)* **17**, 344–359 (2014). doi: 10.1007/s10021-013-9715-7
10. S. Leroux, M. Loreau, in *Trophic Ecology: Bottom-Up and Top-Down Interactions Across Aquatic and Terrestrial Systems*, T. C. Hanley, K. J. La Pierre, Eds. (Cambridge Univ. Press, 2015) pp. 3–27.
11. J. A. Estes *et al.*, Trophic downgrading of planet Earth. *Science* **333**, 301–306 (2011). doi: 10.1126/science.1205106; pmid: 21764740
12. T. B. Atwood *et al.*, Predators help protect carbon stocks in blue carbon ecosystems. *Nat. Clim. Chang.* **5**, 1038–1045 (2015). doi: 10.1038/nclimate2763
13. A. J. Tanentzap, D. A. Coomes, Carbon storage in terrestrial ecosystems: Do browsing and grazing herbivores matter? *Biol. Rev. Camb. Philos. Soc.* **87**, 72–94 (2012). doi: 10.1111/j.1469-185X.2011.00185.x; pmid: 21635684
14. S. Bauer, B. J. Hoye, Migratory animals couple biodiversity and ecosystem functioning worldwide. *Science* **344**, 1242552 (2014). doi: 10.1126/science.1242552; pmid: 24700862
15. R. M. Holdo *et al.*, A disease-mediated trophic cascade in the Serengeti and its implications for ecosystem C. *PLOS Biol.* **7**, e1000210 (2009). doi: 10.1371/journal.pbio.1000210; pmid: 19787022
16. D. C. Allen, J. S. Wesner, Synthesis: Comparing effects of resource and consumer fluxes into recipient food webs using meta-analysis. *Ecology* **97**, 594–604 (2016). doi: 10.1890/15-1109.1; pmid: 27197387
17. C. L. Atkinson, K. A. Capps, A. T. Rugenski, M. J. Vanni, Consumer-driven nutrient dynamics in freshwater ecosystems: From individuals to ecosystems. *Biol. Rev. Camb. Philos. Soc.* **92**, 2003–2023 (2017). doi: 10.1111/brv.12318; pmid: 28008706
18. F. A. Smith *et al.*, Exploring the influence of ancient and historic megaherbivore extirpations on the global methane budget. *Proc. Natl. Acad. Sci. U.S.A.* **113**, 874–879 (2016). doi: 10.1073/pnas.1502547112; pmid: 26504225
19. C. E. Doughty, A. Wolf, C. B. Field, Biophysical feedbacks between the Pleistocene megafauna extinction and climate: The first human-induced global warming? *Geophys. Res. Lett.* **37**, L15703 (2010). doi: 10.1029/2010GL043985
20. S. A. Zimov *et al.*, Steppe-tundra transition: A herbivore-driven biome shift at the end of the Pleistocene. *Am. Nat.* **146**, 765–794 (1995). doi: 10.1086/285824
21. R. Dirzo *et al.*, Defaunation in the Anthropocene. *Science* **345**, 401–406 (2014). doi: 10.1126/science.1251817; pmid: 25061202
22. M. A. Tucker *et al.*, Moving in the Anthropocene: Global reductions in terrestrial mammalian movements. *Science* **359**, 466–469 (2018). doi: 10.1126/science.aam9712; pmid: 29371471
23. We searched the published literature using two search engines: Google Scholar and ISI Web of Science. We searched with the following key words: animals and carbon cycling, animals and biogeochemistry, animals and ecosystem carbon balance, wild herbivores, and carbon cycling. We filtered out studies that did not examine effects of wild animals. We filtered out studies that simulated animal effects (e.g., vegetation clipping). We then filtered out studies that were not experimental or systematic (i.e., studies needed to exclude animals or animal abundance had to vary across landscapes). Finally, we filtered out studies that did not report on direct measures of biogeochemical processes or properties (e.g., biomass carbon, NPP, NEE, respiration, and biophysical impacts).
24. K. Elschot, J. P. Bakker, S. Temmerman, J. van de Koppel, T. J. Bouma, Ecosystem engineering by large grazers enhances carbon stocks in a tidal salt marsh. *Mar. Ecol. Prog. Ser.* **537**, 9–21 (2015). doi: 10.3354/meps11447
25. J. M. Falk, N. M. Schmidt, T. R. Christensen, L. Ström, Large herbivore grazing affects the vegetation structure and greenhouse gas balance in a high arctic mire. *Environ. Res. Lett.* **10**, 045001 (2015). doi: 10.1088/1748-9326/10/4/045001
26. S. M. P. Cahoon, P. F. Sullivan, E. Post, J. M. Welker, Large herbivores limit CO_2 uptake and suppress carbon cycle responses to warming in West Greenland. *Glob. Change Biol.* **18**, 469–479 (2012). doi: 10.1111/j.1365-2486.2011.02528.x

Downloaded from http://science.sciencemag.org/ on December 6, 2018

27. R. van Der Wal *et al.*, Spring feeding by pink-footed geese reduces carbon stocks and sink strength in tundra ecosystems. *Glob. Chang. Biol.* **13**, 539–545 (2007). doi: 10.1111/j.1365-2486.2006.01310.x
28. P. F. McInnes, R. J. Naiman, J. Pastor, Y. Cohen, Effects of moose browsing on vegetation and litter of the boreal forest, Isle Royale, Michigan, USA. *Ecology* **73**, 2059–2075 (1992). doi: 10.2307/1941455
29. A. C. Risch, A. G. Haynes, M. D. Busse, F. Filli, M. Schütz, The responses of soil CO_2 fluxes to progressively excluding vertebrate and invertebrate herbivores depends on ecosystem type. *Ecosystems (N. Y.)* **16**, 1192–1202 (2013). doi: 10.1007/s10021-013-9676-x
30. S. Sjögersten, R. van der Wal, S. J. Woodin, Habitat type determines herbivory controls over CO_2 fluxes in a warmer Arctic. *Ecology* **89**, 2103–2116 (2008). doi: 10.1890/07-1601.1; pmid: 18724721
31. M. S. Strickland, D. Hawlena, A. Reese, M. A. Bradford, O. J. Schmitz, Trophic cascade alters ecosystem carbon exchange. *Proc. Natl. Acad. Sci. U.S.A.* **110**, 11035–11038 (2013). doi: 10.1073/pnas.1305191110; pmid: 23776213
32. S. P. Devlin, J. Saarenheimo, J. Syväranta, R. I. Jones, Top consumer abundance influences lake methane efflux. *Nat. Commun.* **6**, 8787 (2015). doi: 10.1038/ncomms9787; pmid: 26531291
33. T. B. Atwood *et al.*, Predator-induced reduction of freshwater carbon dioxide emissions. *Nat. Geosci.* **6**, 191–194 (2013). doi: 10.1038/ngeo1734
34. D. E. Schindler, S. R. Carpenter, J. J. Cole, J. F. Kitchell, M. L. Pace, Influence of food web structure on carbon exchange between lakes and the atmosphere. *Science* **277**, 248–251 (1997). doi: 10.1126/science.277.5323.248
35. T. B. Atwood *et al.*, Predators shape sedimentary organic carbon storage in a coral reef ecosystem. *Front. Ecol. Evol.* **6**, 110 (2018). doi: 10.3389/fevo.2018.00110
36. M. Sobral *et al.*, Mammal diversity influences the carbon cycle through trophic interactions in the Amazon. *Nat. Ecol. Evol.* **1**, 1670–1676 (2017). doi: 10.1038/s41559-017-0334-0; pmid: 28993614
37. C. C. Wilmers, J. A. Estes, M. Edwards, K. L. Laidre, B. Konar, Do trophic cascades affect the storage and flux of atmospheric carbon? An analysis of sea otters and kelp forests. *Front. Ecol. Environ.* **10**, 409–415 (2012). doi: 10.1890/110176
38. J.-C. Svenning *et al.*, Science for a wilder Anthropocene: Synthesis and future directions for trophic rewilding research. *Proc. Natl. Acad. Sci. U.S.A.* **113**, 898–906 (2016). doi: 10.1073/pnas.1502556112; pmid: 26504218
39. C. Bello *et al.*, Defaunation affects carbon storage in tropical forests. *Sci. Adv.* **1**, e1501105 (2015). doi: 10.1126/sciadv.1501105; pmid: 26824067
40. L. Culot, C. Bello, J. L. F. Batista, H. T. Z. do Couto, M. Galetti, Synergistic effects of seed disperser and predator loss on recruitment success and long-term consequences for carbon stocks in tropical rainforests. *Sci. Rep.* **7**, 7662 (2017). doi: 10.1038/s41598-017-08222-4; pmid: 28794422
41. C. A. Peres, T. Emilio, J. Schietti, S. J. M. Desmoulière, T. Levi, Dispersal limitation induces long-term biomass collapse in overhunted Amazonian forests. *Proc. Natl. Acad. Sci. U.S.A.* **113**, 892–897 (2016). doi: 10.1073/pnas.1516525113; pmid: 26811455
42. M. D. de Paula *et al.*, Defaunation impacts on seed survival and its effect on the biomass of future tropical forests. *Oikos* **127**, 1526–1538 (2018). doi: 10.1111/oik.05084
43. A. M. Osuri *et al.*, Contrasting effects of defaunation on aboveground carbon storage across the global tropics. *Nat. Commun.* **7**, 11351 (2016). doi: 10.1038/ncomms11351; pmid: 27108957
44. C. C. Wilmers, O. J. Schmitz, Effects of gray wolf-induced trophic cascades on ecosystem carbon cycling. *Ecosphere* **7**, e01501 (2016). doi: 10.1002/ecs2.1501
45. S. R. Hall, J. B. Shurin, S. Diehl, R. M. Nisbet, Food quality, nutrient limitation of secondary production, and the strength of trophic cascades. *Oikos* **116**, 1128–1143 (2007). doi: 10.1111/j.0030-1299.2007.15875.x
46. S. J. Leroux, M. Loreau, Consumer-mediated recycling and cascading trophic interactions. *Ecology* **91**, 2162–2171 (2010). doi: 10.1890/09-0133.1; pmid: 20715638
47. M. Loreau, *From Populations to Ecosystems: Theoretical Foundations for a New Ecological Synthesis* (Princeton Univ. Press, 2010).
48. R. D. Bassar *et al.*, Direct and indirect ecosystem effects of evolutionary adaptation in the Trinidadian guppy (*Poecilia reticulata*). *Am. Nat.* **180**, 167–185 (2012). doi: 10.1086/666611; pmid: 22766929
49. S. J. Leroux, O. J. Schmitz, Predator-driven elemental cycling: The impact of predation and risk effects on ecosystem stoichiometry. *Ecol. Evol.* **5**, 4976–4988 (2015). doi: 10.1002/ece3.1760; pmid: 26640675
50. D. Hawlena, O. J. Schmitz, Physiological stress as a fundamental mechanism linking predation to ecosystem functioning. *Am. Nat.* **176**, 537–556 (2010). doi: 10.1086/656495; pmid: 20846014
51. O. J. Schmitz, R. W. Buchkowski, J. R. Smith, M. Telthorst, A. E. Rosenblatt, Predator community composition is linked to soil carbon retention across a human land use gradient. *Ecology* **98**, 1256–1265 (2017). doi: 10.1002/ecy.1794; pmid: 28273334
52. D. G. Jenkins *et al.*, Does size matter for dispersal distance? *Glob. Ecol. Biogeogr.* **16**, 415–425 (2007). doi: 10.1111/j.1466-8238.2007.00312.x
53. M. A. Tucker, T. J. Ord, T. L. Rogers, Evolutionary predictors of mammalian home range size: Body mass, diet and the environment. *Glob. Ecol. Biogeogr.* **23**, 1105–1114 (2014). doi: 10.1111/geb.12194
54. E. G. Ofstad, I. Herfindal, E. J. Solberg, B.-E. Sæther, Home ranges, habitat and body mass: Simple correlates of home range size in ungulates. *Proc. Biol. Sci.* **283**, 20161234 (2016). doi: 10.1098/rspb.2016.1234; pmid: 28003441
55. A. L. Subalusky, C. L. Dutton, E. J. Rosi, D. M. Post, Annual mass drownings of the Serengeti wildebeest migration influence nutrient cycling and storage in the Mara River. *Proc. Natl. Acad. Sci. U.S.A.* **114**, 7647–7652 (2017). doi: 10.1073/pnas.1614778114; pmid: 28630330
56. E. S. Bakker, J. F. Pagès, R. Arthur, T. Alcoverro, Assessing the role of large herbivores in the structuring and functioning of freshwater and marine angiosperm ecosystems. *Ecography* **39**, 162–179 (2016). doi: 10.1111/ecog.01651
57. C. E. Doughty *et al.*, Global nutrient transport in a world of giants. *Proc. Natl. Acad. Sci. U.S.A.* **113**, 868–873 (2016). doi: 10.1073/pnas.1502549112; pmid: 26504209
58. M. D. Hocking, J. D. Reynolds, Impacts of salmon on riparian plant diversity. *Science* **331**, 1609–1612 (2011). doi: 10.1126/science.1201079; pmid: 21442794
59. S. J. Leroux, M. Loreau, Subsidy hypothesis and strength of trophic cascades across ecosystems. *Ecol. Lett.* **11**, 1147–1156 (2008). doi: 10.1111/j.1461-0248.2008.01235.x; pmid: 18713270
60. M. Loreau, N. Mouquet, R. D. Holt, Meta-ecosystems: A theoretical framework for a spatial ecosystem ecology. *Ecol. Lett.* **6**, 673–679 (2003). doi: 10.1046/j.1461-0248.2003.00483.x
61. F. Massol *et al.*, Linking community and ecosystem dynamics through spatial ecology. *Ecol. Lett.* **14**, 313–323 (2011). doi: 10.1111/j.1461-0248.2011.01588.x; pmid: 21272182
62. I. Gounand, E. Harvey, C. J. Little, F. Altermatt, Meta-Ecosystems 2.0: Rooting the theory into the field. *Trends Ecol. Evol.* **33**, 36–46 (2018). doi: 10.1016/j.tree.2017.10.006; pmid: 29102408
63. M. W. McCoy, M. Barfield, R. D. Holt, Predator shadows: Complex life histories as generators of spatially patterned indirect interactions across ecosystems. *Oikos* **118**, 87–100 (2009). doi: 10.1111/j.1600-0706.2008.16878.x
64. J. M. Morales, T. A. Carlo, The effects of plant distribution and frugivore density on the scale and shape of dispersal kernels. *Ecology* **87**, 1489–1496 (2006). doi: 10.1890/0012-9658(2006)87[1489:TEOPDA]2.0.CO;2; pmid: 16869425
65. R. S. Cantrell, C. Cosner, *Spatial Ecology Via Reaction-Diffusion Equations* (Wiley Series in Mathematical and Computational Biology, Wiley, 2003).
66. S. Dewhirst, F. Lutscher, Dispersal in heterogeneous habitats: Thresholds, spatial scales, and approximate rates of spread. *Ecology* **90**, 1338–1345 (2009). doi: 10.1890/08-0115.1; pmid: 19537553
67. R. M. Holdo, R. D. Holt, J. M. Fryxell, Grazers, browsers, and fire influence the extent and spatial pattern of tree cover in the Serengeti. *Ecol. Appl.* **19**, 95–109 (2009). doi: 10.1890/07-1954.1; pmid: 19323175
68. W. M. Getz, D. Saltz, A framework for generating and analyzing movement paths on ecological landscapes. *Proc. Natl. Acad. Sci. U.S.A.* **105**, 19066–19071 (2008). doi: 10.1073/pnas.0801732105; pmid: 19060192
69. M. A. Lefsky, W. B. Cohen, G. G. Parker, D. J. Harding, Lidar remote sensing for ecosystem studies. *Bioscience* **52**, 19–30 (2002). doi: 10.1641/0006-3568(2002)052[0019:LRSFES]2.0.CO;2
70. K. T. Vierling, L. A. Vierling, W. A. Gould, S. Martinuzzi, R. M. Clawges, Lidar: Shedding new light on habitat characterization and modeling. *Front. Ecol. Environ.* **6**, 90–98 (2008). doi: 10.1890/070001
71. K. M. Bergen *et al.*, Remote sensing of vegetation 3-D structure for biodiversity and habitat: Review and implications for lidar and radar spaceborne missions. *J. Geophys. Res. Biogeosci.* **114**, 1–13 (2009). doi: 10.1029/2008JG000883
72. H. Tang, R. Dubayah, Light-driven growth in Amazon evergreen forests explained by seasonal variations of vertical canopy structure. *Proc. Natl. Acad. Sci. U.S.A.* **114**, 2640–2644 (2017). doi: 10.1073/pnas.1616943114; pmid: 28223505
73. M. C. Hansen *et al.*, High-resolution global maps of 21st-century forest cover change. *Science* **342**, 850–853 (2013). doi: 10.1126/science.1244693; pmid: 24233722
74. A. B. Davies, G. P. Asner, Advances in animal ecology from 3D-LiDAR ecosystem mapping. *Trends Ecol. Evol.* **29**, 681–691 (2014). doi: 10.1016/j.tree.2014.10.005; pmid: 25457158
75. S. J. Goetz *et al.*, Lidar remote sensing variables predict breeding habitat of a Neotropical migrant bird. *Ecology* **91**, 1569–1576 (2010). doi: 10.1890/09-1670.1; pmid: 20583698
76. R. Kays, M. C. Crofoot, W. Jetz, M. Wikelski, Terrestrial animal tracking as an eye on life and planet. *Science* **348**, aaa2478 (2015). doi: 10.1126/science.aaa2478; pmid: 26068858
77. M. M. Bustamante *et al.*, Toward an integrated monitoring framework to assess the effects of tropical forest degradation and recovery on carbon stocks and biodiversity. *Glob. Chang. Biol.* **22**, 92–109 (2016). doi: 10.1111/gcb.13087; pmid: 26390852
78. W. Turner *et al.*, Remote sensing for biodiversity science and conservation. *Trends Ecol. Evol.* **18**, 306–314 (2003). doi: 10.1016/S0169-5347(03)00070-3
79. J. Royle, R. B. Chandler, R. Sollmann, B. Gardner, *Spatial Capture-Recapture* (Academic Press, 2014).
80. K. Sitters, C. L. Atkinson, N. Guelzow, P. Kelly, L. L. Sullivan, Spatial stoichiometry: Cross-ecosystem material flows and their impact on recipient ecosystems and organisms. *Oikos* **124**, 920–930 (2015). doi: 10.1111/oik.02392
81. S. J. Leroux *et al.*, Stoichiometric distribution models: Ecological stoichiometry at the landscape extent. *Ecol. Lett.* **20**, 1495–1506 (2017). doi: 10.1111/ele.12859; pmid: 29027338
82. C. C. Wilmers *et al.*, The golden age of bio-logging: How animal-borne sensors are advancing the frontiers of ecology. *Ecology* **96**, 1741–1753 (2015). doi: 10.1890/14-1401.1; pmid: 26378296
83. A. T. Ford *et al.*, Large carnivores make savanna tree communities less thorny. *Science* **346**, 346–349 (2014). doi: 10.1126/science.1252753; pmid: 25324387
84. G. P. Asner, S. R. Levick, Landscape-scale effects of herbivores on treefall in African savannas. *Ecol. Lett.* **15**, 1211–1217 (2012). doi: 10.1111/j.1461-0248.2012.01842.x; pmid: 22863324
85. G. P. Asner, N. Vaughn, I. P. J. Smit, S. Levick, Ecosystem-scale effects of megafauna in African savannas. *Ecography* **39**, 240–252 (2015). doi: 10.1111/ecog.01640
86. P. J. Mograbi *et al.*, Humans and elephants as treefall drivers in African savannas. *Ecography* **40**, 1274–1284 (2017). doi: 10.1111/ecog.02549
87. A. B. Davies, A. Gaylard, G. P. Asner, Megafaunal effects on vegetation structure throughout a densely wooded African landscape. *Ecol. Appl.* **28**, 398–408 (2018). doi: 10.1002/eap.1655; pmid: 29178395
88. E. S. Bakker *et al.*, Combining paleo-data and modern exclosure experiments to assess the impact of megafauna extinctions on woody vegetation. *Proc. Natl. Acad. Sci. U.S.A.* **113**, 847–855 (2016). doi: 10.1073/pnas.1502545112; pmid: 26504223
89. R. M. Pringle, K. M. Prior, T. M. Palmer, T. P. Young, J. R. Goheen, Large herbivores promote habitat specialization and beta diversity of African savanna trees. *Ecology* **97**, 2640–2657 (2016). doi: 10.1002/ecy.1522; pmid: 27859102
90. J. R. Goheen *et al.*, Conservation lessons from large-mammal manipulations in East African savannas: The KLEE, UHURU, and GLADE experiments. *Ann. N. Y. Acad. Sci.* **1429**, 31–49 (2018). doi: 10.1111/nyas.13848; pmid: 29752729

Downloaded from http://science.sciencemag.org/ on December 6, 2018

91. B. W. Griscom *et al*., Natural climate solutions. *Proc. Natl. Acad. Sci. U.S.A.* **114**, 11645–11650 (2017). doi: 10.1073/pnas.1710465114; pmid: 29078344
92. R. A. Houghton, A. A. Nassikas, Negative emissions from stopping deforestation and forest degradation, globally. *Glob. Chang. Biol.* **24**, 350–359 (2018). doi: 10.1111/gcb.13876; pmid: 28833909
93. U. Stockmann *et al*., The knowns, known unknowns and unknowns of sequestration of soil organic carbon. *Agric. Ecosyst. Environ.* **164**, 80–99 (2013). doi: 10.1016/j.agee.2012.10.001
94. E. Nelson *et al*., Efficiency of incentives to jointly increase carbon sequestration and species conservation on a landscape. *Proc. Natl. Acad. Sci. U.S.A.* **105**, 9471–9476 (2008). doi: 10.1073/pnas.0706178105; pmid: 18621703
95. B. B. N. Strassburg *et al*., Global congruence of carbon storage and biodiversity in terrestrial ecosystems. *Conserv. Lett.* **3**, 98–105 (2010). doi: 10.1111/j.1755-263X.2009.00092.x
96. C. D. Thomas *et al*., Reconciling biodiversity and carbon conservation. *Ecol. Lett.* **16** (suppl. 1), 39–47 (2013). doi: 10.1111/ele.12054; pmid: 23279784
97. G. P. Hempson, S. Archibald, W. J. Bond, The consequences of replacing wildlife with livestock in Africa. *Sci. Rep.* **7**, 17196 (2017). doi: 10.1038/s41598-017-17348-4; pmid: 29222494
98. M. E. McSherry, M. E. Ritchie, Effects of grazing on grassland soil carbon: A global review. *Glob. Chang. Biol.* **19**, 1347–1357 (2013). doi: 10.1111/gcb.12144; pmid: 23504715
99. D. Xiong, P. Shi, X. Zhang, C. B. Zou, Effects of grazing exclusion on carbon sequestration and plant diversity in grasslands of China—A meta-analysis. *Ecol. Eng.* **94**, 647–655 (2016). doi: 10.1016/j.ecoleng.2016.06.124
100. G. Zhou *et al*., Grazing intensity significantly affects belowground carbon and nitrogen cycling in grassland ecosystems: A meta-analysis. *Glob. Chang. Biol.* **23**, 1167–1179 (2017). doi: 10.1111/gcb.13431; pmid: 27416555

ACKNOWLEDGMENTS

Funding: Work on this study was supported by funding from the Yale School of Forestry and Environmental Studies (O.J.S.), NSERC Discovery Grant RGPIN 435372-2013 (S.J.L.), and NASA grants NNL15AA03C and NNX17AG51G (S.J.G.). **Competing interests:** The authors declare no competing interests.

10.1126/science.aar3213

Downloaded from http://science.sciencemag.org/ on December 6, 2018

RESEARCH ARTICLE SUMMARY

HUMAN GENOMICS

Early human dispersals within the Americas

J. Víctor Moreno-Mayar*, Lasse Vinner*, Peter de Barros Damgaard*, Constanza de la Fuente*, Jeffrey Chan*, Jeffrey P. Spence* *et al.*

INTRODUCTION: Genetic studies of the Pleistocene peopling of the Americas have focused on the timing and number of migrations from Siberia into North America. They show that ancestral Native Americans (NAs) diverged from Siberians and East Asians ~23,000 years (~23 ka) ago and that a split within that ancestral lineage between later NAs and Ancient Beringians (ABs) occurred ~21 ka ago. Subsequently, NAs diverged into northern NA (NNA) and southern NA (SNA) branches ~15.5 ka ago, a split inferred to have taken place south of eastern Beringia (present-day Alaska and western Yukon Territory).

RATIONALE: Claims of migrations into the Americas by people related to Australasians or by bearers of a distinctive cranial morphology ("Paleoamericans") before the divergence of NAs from Siberians and East Asians have created controversy. Likewise, the speed by which the Americas were populated; the number of basal divergences; and the degrees of isolation, admixture, and continuity in different regions are poorly understood. To address these matters, we sequenced 15 ancient human genomes recovered from sites spanning from Alaska to Patagonia; six are ≥10 ka old (up to ~18× coverage).

RESULTS: All genomes are most closely related to NAs, including those of two morphologically distinct Paleoamericans and an AB individual. However, we also found that the previous model is just a rough outline of the peopling process: NA dispersal gave rise to more complex serial splitting and early population structure—including that of a population that diverged before the NNA-SNA split—as well as admixture with an earlier unsampled population, which is neither AB nor NNA or SNA. Once in the Americas, SNAs spread widely and rapidly, as evidenced by genetic similarity, despite differences in material cultural, between >10-ka-old genomes from North and South America. Soon after arrival in South America, groups diverged along multiple geographic paths, and before 10.4 ka ago, these groups admixed with a population that harbored Australasian ancestry, which may have been widespread among early South Americans. Later, Mesoamerican-related population(s) expanded north and south, possibly marking the movement of relatively small groups that did not necessarily swamp local populations genetically or culturally.

ON OUR WEBSITE

Read the full article at http://dx.doi.org/10.1126/science.aav2621

CONCLUSION: NAs radiated rapidly and gave rise to multiple groups, some visible in the genetic record only as unsampled populations. At different times these groups expanded to different portions of the continent, though not as extensively as in the initial peopling. That the early population spread widely and rapidly suggests that their access to large portions of the hemisphere was essentially unrestricted, yet there are genomic and archaeological hints of an earlier human presence. How these early groups are related or structured, particularly those with Australasian ancestry, remains unknown. Rapid expansion, compounded by the attenuating effect of distance and, in places, by geographic and social barriers, gave rise to complex population histories. These include strong population structure in the Pacific Northwest; isolation in the North American Great Basin, followed by long-term genetic continuity and ultimately an episode of admixture predating ~0.7 ka ago; and multiple independent, geographically uneven migrations into South America. One such migration provides clues of Late Pleistocene Australasian ancestry in South America, whereas another represents a Mesoamerican-related expansion; both contributed to present-day South American ancestry. ■

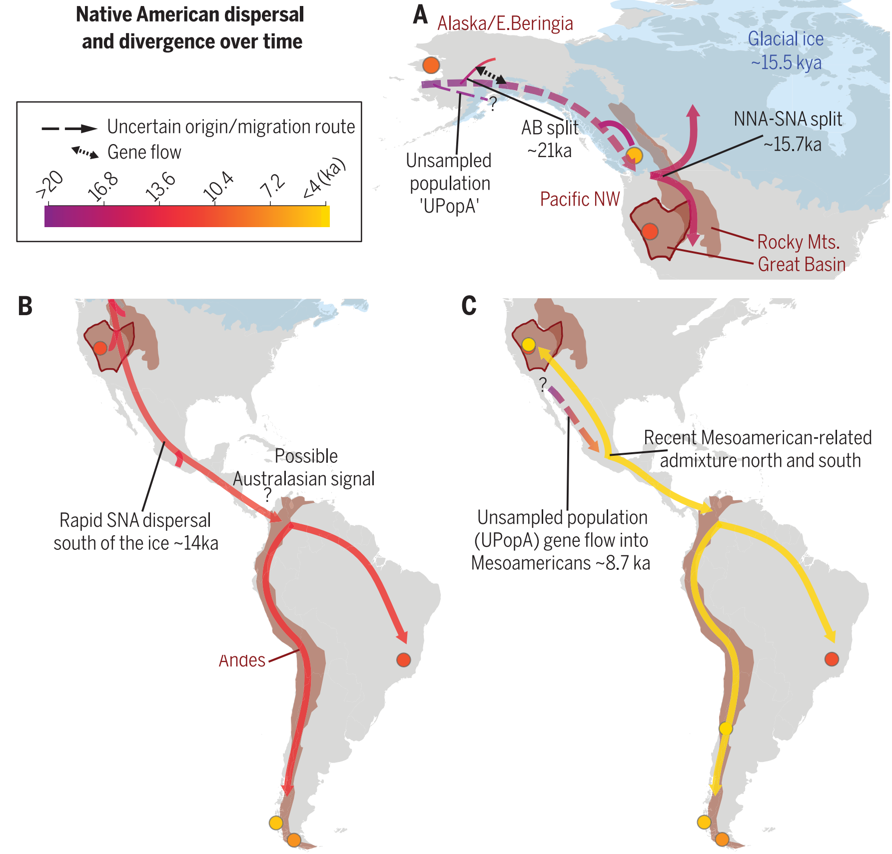

NA dispersal and divergence over time. Schematic representation of the sampling points included in this study (circles) and our main conclusions (presented geographically and temporally). (**A**) Population history of the basal AB, NNA, and SNA branches in North America. kya, thousand years ago. (**B**) Early, rapid dispersal of SNAs across the continent (~14 ka ago). (**C**) Recent Mesoamerican-related expansion north and south. Arrows do not correspond to specific migration routes.

The list of author affiliations is available in the full article online.
*These authors contributed equally to this work.
Corresponding authors: Eske Willerslev (ewillerslev@snm.ku.dk); David J. Meltzer (dmeltzer@smu.edu); Yun S. Song (yss@berkeley.edu)

Cite this article as J. V. Moreno-Mayar *et al.*, *Science* **362**, eaav2621 (2018). DOI: 10.1126/science.aav2621

Downloaded from http://science.sciencemag.org/ on December 10, 2018

RESEARCH ARTICLE

HUMAN GENOMICS

Early human dispersals within the Americas

J. Víctor Moreno-Mayar[1]*, Lasse Vinner[1]*, Peter de Barros Damgaard[1]*, Constanza de la Fuente[1]*, Jeffrey Chan[2]*, Jeffrey P. Spence[3]*, Morten E. Allentoft[1], Tharsika Vimala[1], Fernando Racimo[1], Thomaz Pinotti[4], Simon Rasmussen[5], Ashot Margaryan[1,6], Miren Iraeta Orbegozo[1], Dorothea Mylopotamitaki[1], Matthew Wooller[7], Clement Bataille[8], Lorena Becerra-Valdivia[9], David Chivall[9], Daniel Comeskey[9], Thibaut Devièse[9], Donald K. Grayson[10], Len George[11], Harold Harry[12], Verner Alexandersen[13], Charlotte Primeau[13], Jon Erlandson[14], Claudia Rodrigues-Carvalho[15], Silvia Reis[15], Murilo Q. R. Bastos[15], Jerome Cybulski[16,17,18], Carlos Vullo[19], Flavia Morello[20], Miguel Vilar[21], Spencer Wells[22], Kristian Gregersen[1], Kasper Lykke Hansen[1], Niels Lynnerup[13], Marta Mirazón Lahr[23], Kurt Kjær[1], André Strauss[24,25], Marta Alfonso-Durruty[26], Antonio Salas[27,28], Hannes Schroeder[1], Thomas Higham[9], Ripan S. Malhi[29], Jeffrey T. Rasic[30], Luiz Souza[31], Fabricio R. Santos[4], Anna-Sapfo Malaspinas[32], Martin Sikora[1], Rasmus Nielsen[1,33,34], Yun S. Song[2,33,35]†, David J. Meltzer[1,36]†, Eske Willerslev[1,37,38]†

Studies of the peopling of the Americas have focused on the timing and number of initial migrations. Less attention has been paid to the subsequent spread of people within the Americas. We sequenced 15 ancient human genomes spanning from Alaska to Patagonia; six are ≥10,000 years old (up to ~18× coverage). All are most closely related to Native Americans, including those from an Ancient Beringian individual and two morphologically distinct "Paleoamericans." We found evidence of rapid dispersal and early diversification that included previously unknown groups as people moved south. This resulted in multiple independent, geographically uneven migrations, including one that provides clues of a Late Pleistocene Australasian genetic signal, as well as a later Mesoamerican-related expansion. These led to complex and dynamic population histories from North to South America.

Previous genomic studies have estimated that ancestral Native Americans (NAs) diverged from Siberian and East Asian populations ~25,000 ± 1100 years ago (25 ± 1.1 ka ago) (1, 2), with a subsequent split 22 to 18.1 ka ago within that ancestral lineage between later NAs and Ancient Beringians (ABs). NAs then diverged into two branches, northern NAs (NNAs) and southern NAs (SNAs), ~17.5 to 14.6 ka ago (2–4), a process inferred to have taken place south of eastern Beringia (present-day Alaska and western Yukon Territory). All contemporary and ancient NA individuals for whom genome-wide data have been generated before this study derive from either the NNA or SNA branch.

However, disagreement exists over claims of earlier migrations into the Americas by people possibly related to Australasians or by bearers of a distinctive cranial form ("Paleoamericans") (5, 6). Whether additional splits occurred within the Americas, how many migratory movements north and south took place, and the speed of human dispersal at different times and regions are also contentious. In contrast to models based on contemporary and Pleistocene-age genetic data (3, 4), genomic studies of later Holocene human remains indicate postdivergence admixture between basal NA groups (7). Overall, the degree of population isolation, admixture, or continuity in different geographic regions of the Americas after initial settlement is poorly understood (7–9).

Genome sequences from the Late Pleistocene and Early Holocene are rare. If we are to resolve how the peopling process occurred, more sequences are needed beyond the three currently available: Anzick1 from Montana (~12.8 ka old) (3), Kennewick Man/Ancient One from Washington (~9 ka old) (10), and USR1 from Alaska (~11.5 ka old) (1).

Dataset and method summary

We engaged and sought feedback from Indigenous groups linked to the ancestral individuals analyzed in this study by using the recommendations for genomics research with Indigenous communities (11–13). We obtained genome sequences from 15 ancient human remains (Fig. 1A). These include remains from Trail Creek Cave 2, Alaska (radiocarbon dated to ~9 ka ago; ~0.4× genomic depth of coverage); Big Bar Lake, British Columbia (~5.6 ka old; ~1.2× coverage); and Spirit Cave, Nevada (~10.7 ka old; ~18× coverage); four individuals from Lovelock Cave, Nevada (ranging in age from ~1.95 to 0.6 ka old; ~0.5× to ~18.7× coverage); five individuals from Lagoa Santa, Brazil (~10.4 to ~9.8 ka old; ~0.18× to ~15.5× coverage); one individual each from the Punta Santa Ana and Ayayema sites in Patagonian Chile (~7.2 and ~5.1 ka old, with ~1.5× and ~10.6× coverage, respectively); and an Incan mummy from Mendoza, Argentina (estimated to be ~0.5 ka old; ~2.5× coverage) (14) [all ^{14}C ages are in calibrated years (13, 15)] (Fig. 1, A and B). We also sequenced a ~15.9× genome from a ~19th-century Andaman islander, used as a proxy for Australasian ancestry in models involving admixture into NAs (2, 6, 13, 16). All DNA extracts were confirmed to contain fragments with characteristic ancient DNA misincorporation patterns and low contamination levels (<3%) (13). The Spirit Cave, Lovelock 2, and Lovelock 3 genomes were generated solely from uracil-specific excision reagent–treated (USER) extracts, confirmed to contain characteristic ancient DNA misincorporation patterns before treatment (13, 17).

To assess the genetic relationships among these and other ancient and contemporary human genomes, we compiled a whole-genome comparative dataset of 378 individuals (13). Additionally, we merged these data with a single-nucleotide polymorphism (SNP) panel of 167 worldwide populations genotyped for 199,285 SNPs, enriched in NA populations whose European and African ancestry components have been identified and masked (2, 4, 13, 18) (Fig. 1A). Of particular interest are the Mixe, a Mesoamerican reference group representing an early internal branch within SNAs, before the divergence of South Americans (4), which lacks the Australasian ancestry signal documented among some Amazonian groups (2, 6, 16).

We explored the ancient individuals' broad genetic affinities initially by using model-based clustering (19) and multidimensional scaling (MDS) (Fig. 1, C to F) (13). MDS was applied to both the identity-by-state distance matrix for all individuals (20) and the f_3 distance matrix over populations included in the SNP array dataset (13, 21, 22). We then tested specific hypotheses by computing error-corrected and genotype-based D statistics (13, 21, 23) and fitting admixture graphs (4, 13, 21, 24) (Figs. 2, 3, and 4). Furthermore, we inferred demographic and temporal parameters by using the joint site frequency spectrum (SFS) (25, 26) and linkage disequilibrium (27, 28) information (Fig. 5). These efforts enabled us to explore finer-scale complex models by using whole-genome data (13). The average depth of coverage of the genomes presented in this study ranges widely, which meant that not all genomes could be used in all analyses, as specified (13).

Our aim is to understand broad patterns in the dispersal, divergence, and admixture of people throughout the Americas. Given the highly uneven distribution of genome samples in time and space, our results are expressed—as much as possible—chronologically from oldest to youngest and geographically from north to south to mirror how the peopling of the Americas proceeded.

Insights into early eastern Beringian populations from an Alaskan genome

Although the earliest archaeological evidence for a human presence in eastern Beringia remains

Downloaded from http://science.sciencemag.org/ on December 10, 2018

disputed, people were present in Alaska by at least 14.4 ka ago (29). Genomic insights from the USR1 genome indicate that ABs (1) remained isolated in interior Alaska until at least the terminal Pleistocene and were an outgroup to NNAs and SNAs. It was inferred that the NNA-SNA population split occurred outside of eastern Beringia (1, 2). By contrast, recent findings suggest that the ancestral population of NNAs existed north of the continental ice sheets (9).

The Trail Creek Cave genome is from a tooth of a young child recovered from Alaska's Seward Peninsula (13). This individual clusters adjacent to USR1 in MDS analyses (Fig. 1C) (13) and carries a similar distribution of ancestry components (Fig. 1F) (13). The Trail Creek individual and USR2 (found with and a close relative to USR1) harbor the same mitochondrial DNA (mtDNA) haplogroup, B2, but not the derived B2 variant found elsewhere in the Americas (1, 13). Genotype-based *D* statistics of the form *D*(Aymara, NA; TrailCreek, Yoruba) and *D*(USR1, TrailCreek; NA, Yoruba) suggest that Trail Creek forms a clade with USR1 that represents an outgroup to other NAs (13). This placement was supported by fitting *f* statistic–based admixture graphs (13, 21).

The procedure described here, which was also used for other samples, relies on a "seed graph" that incorporates the formation of the ancestral NA group and its three basal branches (ABs, NNAs, and SNAs) (1, 30, 31). The seed graph includes the following leaves: Yoruba (representing Africans), Mal'ta (ancient north Eurasians), Andaman (Australasians), Han (East Asians), USR1 (ABs), Athabascan (NNAs), and Spirit Cave (SNAs) (see below) (13). We enumerated all possible extensions of the seed graph where an individual genome, Trail Creek in this case, was added as either a nonadmixed or an admixed population (32). We optimized the parameters for each topology by using qpGraph (21) and favored the graph producing the best likelihood and the lowest residuals between observed and predicted *f* statistics. Given that admixed models yield better likelihood scores (because of the additional parameters being optimized), we considered an admixed model to be an improvement compared with its nonadmixed counterpart only if the absolute difference between fit scores (log likelihoods) was greater than ~4.6, corresponding to a *P* value of ~0.01 in a standard likelihood ratio test (30). In agreement with the exploratory analyses, we found the model in which the Trail Creek and USR1 individuals form a clade to be the most likely (Fig. 2A) (13).

These results suggest that the USR1 and Trail Creek individuals were members of an AB metapopulation that occupied eastern Beringia and remained isolated from other NA populations during the Late Pleistocene and Early Holocene. Finding two members of the AB population, from sites ~750 km apart, with similar artifact technologies (13) supports the inference that the SNA-NNA split occurred south of eastern Beringia (1, 9). The alternative, that NNAs and SNAs split in Alaska, seems less likely; it would have required several thousand years of strong population structure prior to ~16 ka ago to differentiate those groups from each other and from ABs, as well as a separate SNA presence, which has yet to be found (1). These data indicate that the Athabascans and Inuit, who inhabit Alaska today and are NNAs but with additional Siberian-related ancestry (1, 4, 18, 33), presumably moved north into the region sometime after ~9 ka ago, the age of the Trail Creek individual (1, 13).

Rapid dispersal of the SNA population across the Rockies and into South America

The NNA-SNA split is estimated to have taken place ~17.5 to 14.6 ka ago (1, 2). Members of the SNA branch ultimately reached southern South America, and on the basis of mtDNA, Y chromosome, and genome-wide evidence, this likely occurred quickly (2, 7, 8, 34, 35). This movement gave rise to serial splitting and early population structure, with Mesoamericans being the most deeply divergent group, followed by South Americans east and west of the Andes (4, 36). However, genomic data from Spirit Cave (10.7 ka old) and Lagoa Santa (10.4 ka old), the oldest sites in this study, show that the SNA dispersal pattern south of the continental ice sheets involved complex admixture events between earlier-established populations.

MDS and ADMIXTURE, as well as a TreeMix tree focused on SNA genomes, reveal that the Spirit Cave and Lagoa Santa individuals were members of the SNA branch (Fig. 1, C and F) (13). Within that branch, Spirit Cave is closest to Anzick1, whereas Lagoa Santa is closest to southern SNA groups. Two of the Lagoa Santa individuals carry the same mtDNA haplogroup (D4h3a) as Anzick1, yet three of the Lagoa Santa individuals harbor the same Y chromosome haplogroup as the Spirit Cave genome (Q-M848) (13). Nonetheless, MDS transformations restricted to SNAs (Fig. 1, D and E) (13), together with TreeMix graphs including admixture (13), suggest that these ancient North and South American individuals are closely related, regardless of Lagoa Santa's affinity to present-day South American groups.

We formally tested this scenario by fitting *f* statistics–based admixture graphs and found that even though the Anzick1, Spirit Cave, and Lagoa Santa individuals are separated by ~2 ka and thousands of kilometers, genomes from these three individuals can be modeled as a clade to the exclusion of the Mesoamerican Mixe (13). Although we did not find evidence rejecting this clade by using TreeMix and *D* statistics (13), further SFS-based modeling indicates that the Mixe most likely carry gene flow from an unsampled outgroup and form a clade with Lagoa Santa. Including nonzero outgroup admixture into the Mixe when fitting an *f* statistics–based admixture graph resulted in a significantly better fit (likelihood ratio test; $P < 0.05$) (Fig. 3, A and B) (13). Hereafter, we refer to that outgroup as unsampled population A (UPopA), which is neither AB, NNA, or SNA and which we infer split off from NAs ~24.7 ka ago, with an age range between 30 and 22 ka ago [95% confidence interval (CI); this large range is

Downloaded from http://science.sciencemag.org/ on December 10, 2018

---

[1]Centre for GeoGenetics, Natural History Museum of Denmark, University of Copenhagen, 1350 Copenhagen, Denmark. [2]Computer Science Division, University of California, Berkeley, CA 94720, USA. [3]Computational Biology Graduate Group, University of California, Berkeley, CA 94720, USA. [4]Departamento de Genética, Ecologia e Evolução, Instituto de Ciências Biológicas, Universidade Federal de Minas Gerais, Belo Horizonte, MG, Brazil. [5]Department of Bio and Health Informatics, Technical University of Denmark, Lyngby, Denmark. [6]Institute of Molecular Biology, National Academy of Sciences, 7 Hasratian Street, 0014 Yerevan, Armenia. [7]Alaska Stable Isotope Facility, Water and Environmental Research Center, University of Alaska Fairbanks, Fairbanks, AK 99775, USA. [8]Department of Earth and Environmental Sciences, University of Ottawa, Ottawa, Canada. [9]Oxford Radiocarbon Accelerator Unit, Research Lab for Archaeology and the History of Art, School of Archaeology, University of Oxford, 1-2 South Parks Road, Oxford, OX1 3TG, UK. [10]Department of Anthropology and Quaternary Research Center, University of Washington, Seattle, WA 98185, USA. [11]Fallon Paiute-Shoshone Tribe, 565 Rio Vista Drive, Fallon, NV 89406, USA. [12]Stswecem'c/Xgat'tem Band, Dog Creek, BC V0L 1J0, Canada. [13]Laboratory of Biological Anthropology, Department of Forensic Medicine, University of Copenhagen, Copenhagen, Denmark. [14]University of Oregon Museum of Natural and Cultural History, Eugene, OR 97403, USA. [15]Departamento de Antropologia, Museu Nacional, Universidade Federal do Rio de Janeiro, Rio de Janeiro, Brazil. [16]Canadian Museum of History, Gatineau, Québec K1A 0M8, Canada. [17]Department of Anthropology, University of Western Ontario, London, Ontario, Canada. [18]Department of Archaeology, Simon Fraser University, Burnaby, BC, Canada. [19]Equipo Argentino de Antropología Forense, Independencia 644-3A, Edif. EME1, Córdoba, Argentina. [20]Universidad de Magallanes, Instituto de la Patagonia, Av. Manuel Bulnes, 01890, Punta Arenas, Región de Magallanes y Antártica, Chile. [21]National Geographic Society, 1145 17th Street NW, Washington, DC 20036, USA. [22]Department of Integrative Biology, University of Texas at Austin, Austin, TX 78712, USA. [23]Leverhulme Centre for Human Evolutionary Studies, Department of Archaeology, University of Cambridge, Cambridge, UK. [24]Museu de Arqueologia e Etnologia, Universidade de São Paulo, Av. Prof. Almeida Prado, 1466 Butantã, 05508-070 São Paulo, Brazil. [25]Institute for Archaeological Sciences, Palaeoanthropology and Senckenberg Centre for Human Evolution and Palaeoenvironment, University of Tübingen, 72070 Tübingen, Germany. [26]Department of Sociology, Anthropology, and Social Work, Kansas State University, 1603 Old Claflin Place, Manhattan, KS 66506, USA. [27]Unidade de Xenética, Departamento de Anatomía Patolóxica e Ciencias Forenses, Instituto de Ciencias Forenses, Facultade de Medicina, Universidade de Santiago de Compostela (USC), Spain. [28]GenPoB Research Group, Instituto de Investigaciones Sanitarias (IDIS), Hospital Clínico Universitario de Santiago (SERGAS), Galicia, Spain. [29]Department of Anthropology, School of Integrative Biology, Carl R. Woese Institute for Genomic Biology, University of Illinois at Urbana-Champaign, Urbana, IL 61801, USA. [30]U.S. National Park Service, 4175 Geist Road, Fairbanks, AK 99709, USA. [31]LACICOR – Conservation Science Laboratory, CECOR – Center for Conservation and Restoration of Cultural Properties, Federal University of Minas Gerais, Belo Horizonte, MG, Brazil. [32]Department of Computational Biology, University of Lausanne, Swiss Institute of Bioinformatics, Lausanne, Switzerland. [33]Department of Statistics, University of California, Berkeley, CA 94720, USA. [34]Department of Integrative Biology, University of California, Berkeley, CA 94720, USA. [35]Chan Zuckerberg Biohub, San Francisco, CA 94158, USA. [36]Department of Anthropology, Southern Methodist University, Dallas, TX 75275, USA. [37]Department of Zoology, University of Cambridge, Downing Street, Cambridge CB2 3EJ, UK. [38]Wellcome Trust Sanger Institute, Wellcome Genome Campus, Hinxton, Cambridge CB10 1SA, UK.

*These authors contributed equally to this work.

†Corresponding author. Email: ewillerslev@snm.ku.dk (E.W.); dmeltzer@smu.edu (D.J.M.); yss@berkeley.edu (Y.S.S.)

a result of the analytical challenge of estimating divergence and admixture times in the absence of UPopA genome data]. This age range overlaps with the inferred split of NAs from Siberians and East Asians 26.1 to 23.9 ka ago (*1*) and the divergence of USR1 from other NAs (23.3 to 21.2 ka ago). This temporal overlap, which cannot be fully resolved into a relative sequence with current data, suggests that multiple splits took place in Beringia within a short span of time. Depending on how close these splits ultimately prove to be, they could imply that moderate structure existed within Beringia (*1*, *37*), possibly along with indirect gene flow from Siberians, perhaps via other NA populations. Under a model with a

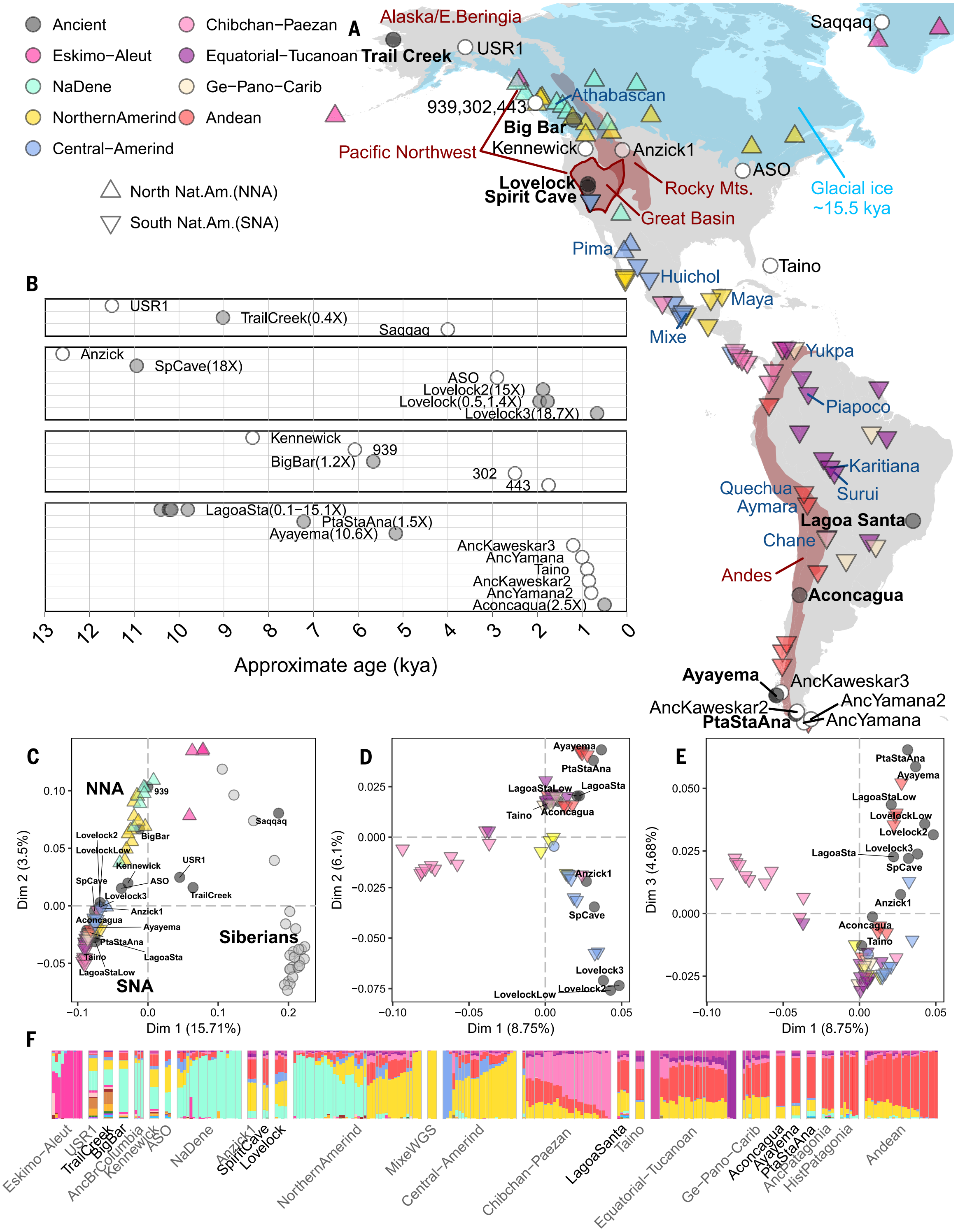

Fig. 1. Ancient genome overview and broad genetic affinities. (**A**) Sampling locations for ancient genomes (circles) (newly reported genomes are labeled in bold) and present-day NAs [triangles colored by the grouping used in (*2*, *4*)]. NNAs and SNAs were classified by following (*1*). Present-day whole-genome data are labeled in dark blue. Broad geographic features mentioned in the text are shown in dark red; the extent of glacial ice sheets ~15.5 ka ago (kya) (*73*) is shown in light blue. Anc, ancient; Pta Sta Ana, Punta Santa Ana. (**B**) Calibrated radiocarbon ages for ancient genomes. Open circles, previously published genomes; filled circles with depth of coverage, genomes from this study. SpCave, Spirit Cave; LagoaSta, Lagoa Santa. (**C**) MDS plot from the f_3 distance matrix computed from a subset of the SNP array dataset (~200,000 sites), including Siberian and NA populations. Dim, dimension. (**D** and **E**) MDS plots similar to the plot in (C), showing the first three dimensions for SNA groups only. (**F**) ADMIXTURE proportions with the assumption of $K = 16$ ancestral populations. Bars represent individuals; colors represent ancestral components. For clarity, we show only NAs. Three individuals are represented for populations with $n > 3$ genomes, and single genomes are represented as wider bars. Siberians and NAs are organized according to (*4*). WGS, whole-genome sequence; Hist, historic.

Downloaded from http://science.sciencemag.org/ on December 10, 2018

pulselike gene flow, we inferred a probability of ~11% gene flow from UPopA into the Mixe ~8.7 ka ago (95% CI, 0.4 to 13.9 ka ago; the wide interval potentially reflects unmodeled continuous migration) (Fig. 5) (*13*). Thus, we favor a model where the common ancestor of the Anzick1 and Spirit Cave individuals diverged from the common ancestor of the Lagoa Santa and Mixe individuals ~14.1 ka ago (95% CI, 13.2 to 14.9 ka ago), perhaps as the Lagoa Santa–Mixe ancestral population was moving southward. We infer that the Lagoa Santa population diverged from the Mixe shortly thereafter, ~13.9 ka ago (95% CI, 12.8 to 14.8 ka ago) (Fig. 5) (*13*). The proximity of these estimated divergence times suggests that the dispersal process was very rapid on an archaeological time scale, as populations expanded across North America perhaps in a matter of centuries and then into eastern South America within a millennium or two.

Australasian ancestry in Early Holocene South America and claims of Paleoamericans

Both the Spirit Cave and Lagoa Santa individuals have been identified as Paleoamericans (*38*, *39*), connoting a cranial morphology distinct from that of modern NAs. Interpretations of this pattern range from its being the result of a separate earlier migration into the Americas to its arising from population continuity with in situ differentiation owing to factors such as isolation and drift (*13*, *40*–*42*). We examined whether this morphology might be associated with ancient Australasian genetic ancestry found in present-day Amazonian groups (*2*, *6*). However, no morphometric data are available for present-day peoples with this genetic signal (*6*), nor has this signal been detected in any ancient skeleton with this morphology (*2*, *10*).

To test for the Australasian genetic signal in NAs, we computed *D* statistics of the form *D*(NA, NA; Eurasian, Yoruba), where NA represents all newly sequenced and reference high-depth NA genomes (*13*). In agreement with previous results (*6*), we found that the Amazonian Suruí share a larger proportion of alleles with Australasian groups (represented by Papuans, Australians, and Andaman Islanders) than do the Mixe (*13*). Lagoa Santa yielded results similar to those obtained for the Suruí: The analyzed Lagoa Santa genome also shares a larger proportion of alleles with Australasian groups, but not with other Eurasians, than do Mesoamerican groups (the Mixe and Huichol) (Fig. 4) (*13*). However, the Australasian signal is not present in the Spirit Cave individual, and we include this distinction in the admixture graph modeling (Figs. 3A and 4A) (*13*). We inferred less than 3% European contamination in the Lagoa Santa genome (<3%) (*13*) and show that this finding is robust to potential European contamination by computing "contamination-corrected" f_4 statistics (Fig. 4B) (*13*). The presence of the Australasian genomic signature in Brazil 10.4 ka ago and its absence in all genomes tested to date that are as old or older and located farther north present a challenge in accounting for its presence in Lagoa Santa.

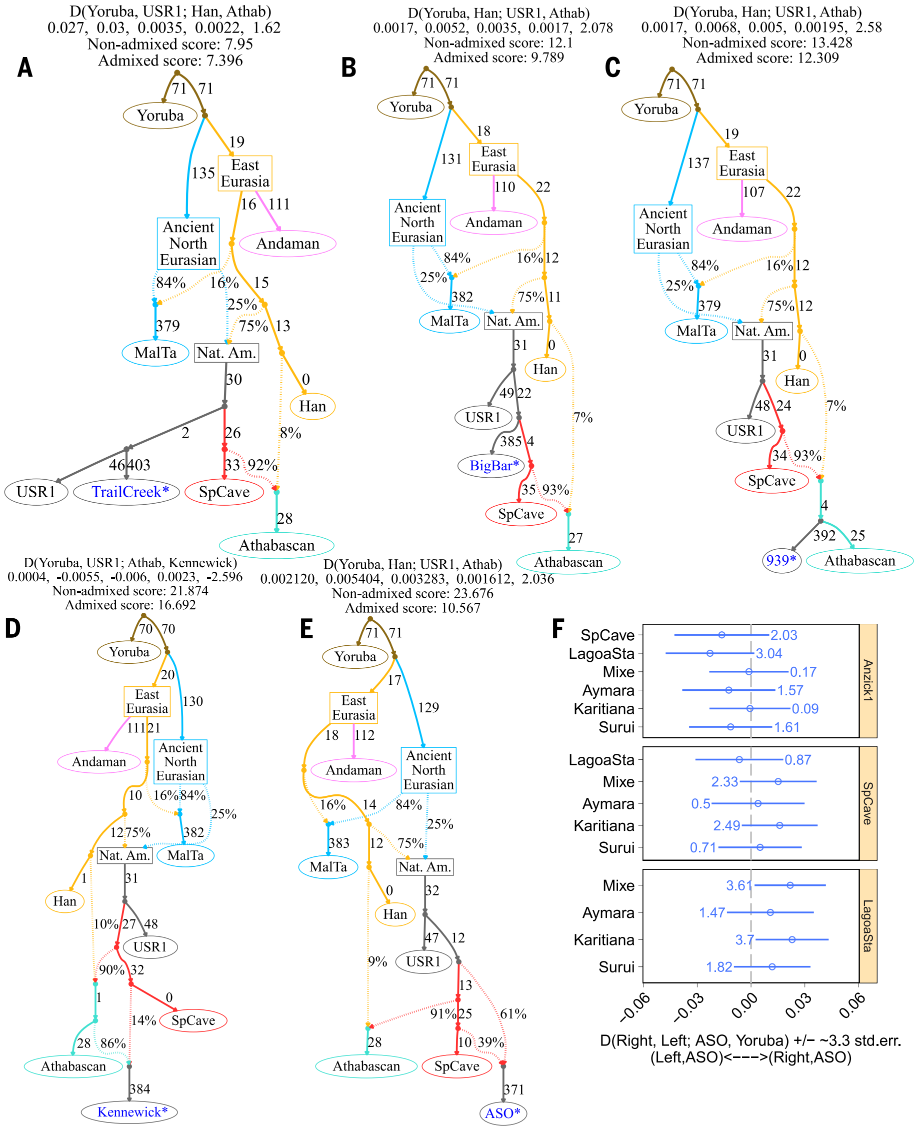

Fig. 2. Admixture graphs modeling the ancestry of ancient North American genomes. We enumerated all possible extensions of the seed graph (*13*) where we added Trail Creek (**A**), Big Bar (**B**), 939 (**C**), Kennewick Man/Ancient One (**D**), and ASO (**E**) genomes each as a nonadmixed or an admixed population and optimized the parameters for each topology by using qpGraph. In each graph, the test population is shown in blue. We show the best-fitting model for each genome as inferred from the final fit score. Above each graph, we show the four populations leading to the worst *D* statistic residual; the observed value for this statistic, the expected value under the fitted model, the residual, the SE of the residual, and the *z*-score for the residual; and the model fit scores. Numbers to the right of solid lines are proportional to the optimized drift; percentages to the right of dashed lines represent admixture proportions. Athab, Athabascan; Nat. Am., Native American. (**F**) Error-corrected *D* statistics restricted to transversion polymorphisms testing the genetic affinity between ASO individuals and different SNA pairs. Points represent *D* statistics, and error bars represent ~3.3 SEs (std. err.) (*P* ~ 0.001). For each test, we show the absolute *z*-score beside its corresponding *D* value. A pool of the five sequenced individuals represents the Lagoa Santa population.

Notably, all sequenced Paleoamericans (including Kennewick Man/Ancient One) (*2*, *10*) are genetically closer to contemporary NAs than to any other ancient or contemporary group sequenced to date.

Multiple dispersals into South America

Genome-wide data from contemporary populations suggested a single expansion wave into South America with little gene flow between groups (*4*) [but see (*36*)]. By contrast, analysis of later Holocene genomes suggests that South Americans derived from one or more admixture events between two ancestral NA groups, possibly via multiple movements into South America (*7*).

To test these competing scenarios, we performed an exhaustive admixture graph search, as described above. We fitted a seed graph involving Yoruba, Mal'ta, Andaman, Han, Anzick1, Spirit Cave, Lagoa Santa, and Mixe (present-day Mesoamerican)

Downloaded from http://science.sciencemag.org/ on December 10, 2018

genomes and tested all possible "nonadmixed" and "admixed" models for SNAs: the Mesoamerican Maya and Yukpa of Venezuela, groups east (the Suruí, Karitiana, Piapoco, and Chané) and west (the Aymara and Quechua) of the spine of the Andes, six ancient Patagonians [one from Ayayema, one from Punta Santa Ana, and four individuals from (43)], the ancient Taino (44), and the Aconcagua Incan mummy (14) (Fig. 1B) (13). This analysis indicates that most present-day South American populations do not form a clade with Lagoa Santa but instead derive from a mixture of Lagoa Santa– and Mesoamerican-related ancestries (Fig. 3A) (13). We confirmed these results by computing standard and error-corrected *D* statistics of the form *D*(LagoaSanta, SNA; Mixe, Yoruba) and *D*(Mixe, SNA; LagoaSanta, Yoruba) (Fig. 3B) (13). For most groups, these statistics are inconsistent with a simple tree and indicate multiple dispersals into South America.

The ~5.1-ka-old Patagonian Ayayema genome is an exception; it forms a clade with the Lagoa Santa population. This suggests that the arrival of the Mesoamerican-related ancestry occurred post–5.1 ka ago and/or that it did not reach the remote region inhabited by the Ayayema individual's ancestors (Fig. 3C) (13). This result is qualitatively mirrored by the 7.2-ka-old Punta Santa Ana individual (both cluster with present-day Patagonians and form a clade with Lagoa Santa). However, the low coverage of Punta Santa Ana may reduce our power to detect possible Mesoamerican-related admixture (Fig. 3C) (13).

We further explored the fit of the model (Fig. 3A) for each South American group by fixing the Australasian contribution into Lagoa Santa and the Mesoamerican contribution (Fig. 3, D and E) into the test SNA population across a range of values (13). Whereas an Australasian contribution of less than 1% and greater than ~6% results in a significant decrease in likelihood (likelihood ratio test; $P < 0.05$), the Mesoamerican contribution has a wider range of plausible values (Fig. 3E) (13). Yet modeling each SNA group with little to no Mesoamerican-related admixture consistently yields significantly lower fit scores ($P < 0.05$) (13), except for the Ayayema individual (Fig. 3D) (13).

The Australasian contribution into Lagoa Santa was consistently nonzero when we modeled South Americans, although we did not observe in

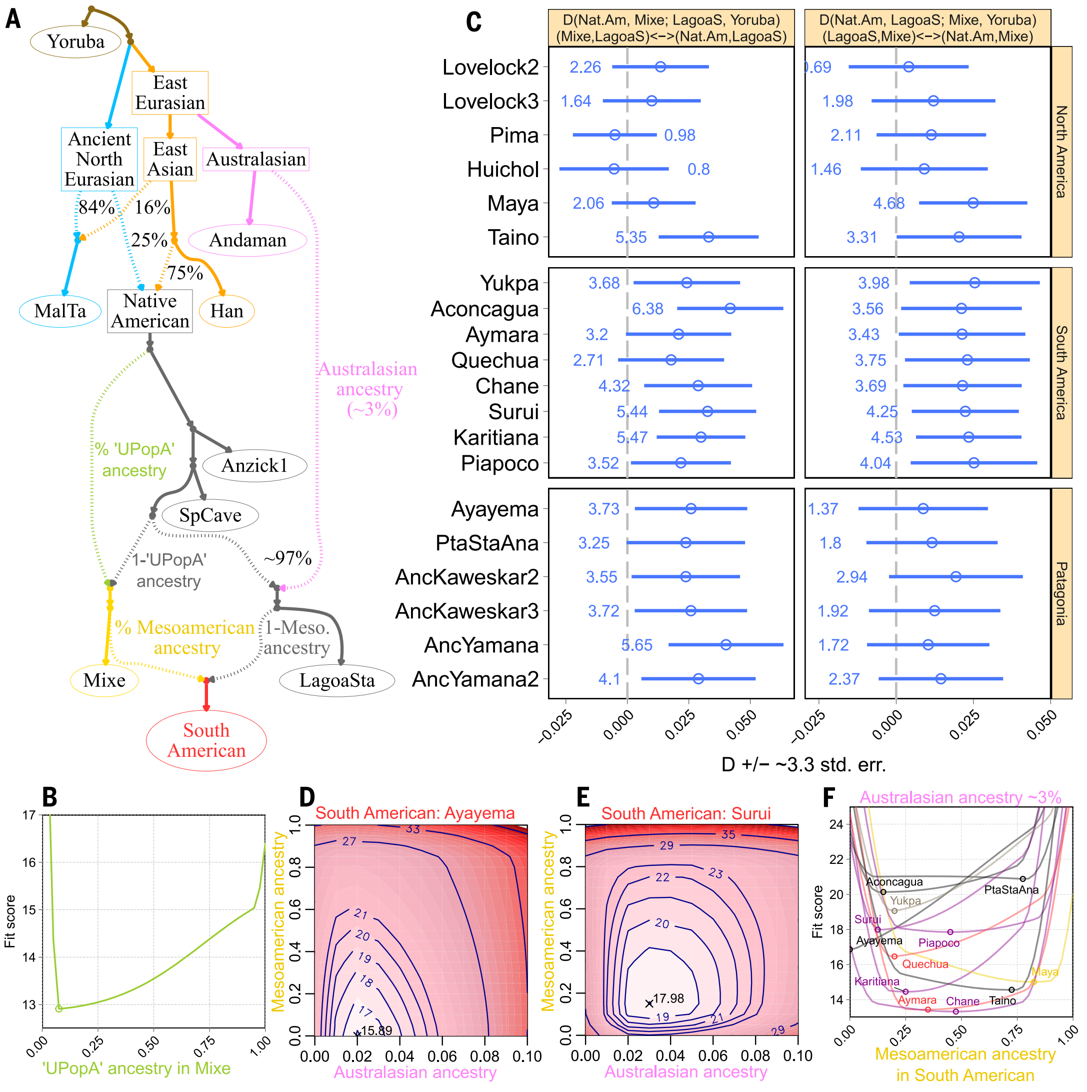

Fig. 3. *f* statistics–based tests show a rapid dispersal into South America, followed by Mesoamerican-related admixture. (**A**) Schematic representation of a model for SNA formation. This model represents a reasonable fit to most present-day populations (13). UPopA-, Mixe-, and Australasian-related admixture lines are color-coded as in subsequent panels. Meso., Mesoamerican. (**B**) Fit score of the graph shown in (A) (excluding South Americans) as a function of "unsampled admixture" in the Mixe. The point indicates the unsampled admixture proportion that yields the best fit score. (**C**) Error-corrected *D* statistics showing that Lagoa Santa (LagoaS), Mixe, and most SNA genomes cannot be modeled by using a simple tree. (Top) The tested null hypothesis, together with an indication of the pair of populations with excess allele sharing, depending on the sign of D. SNA populations are organized according to their sampling location (labels on the right). Points represent *D* statistics, and error bars represent ~3.3 SEs (which corresponds to a *P* value of ~0.001 in a *Z* test). For each test, we show the absolute *z*-score beside its corresponding *D* value. (**D** and **E**) Fit score surfaces for the "admixed" SNA model with fixed Mixe and Australasian admixture proportions. For the Ayayema and Suruí, we explored the fit of the model shown in (A) across a grid of values for the Mixe proportion in SNAs {0,0.05,...,1} and the Australasian contribution to Lagoa Santa {0,0.01,...0.1}. "X" indicates the parameter combination yielding the best score. Contour lines were drawn such that all parameter combinations contained within a given line yield a fit score lower than that indicated by the contour label. (**F**) A one-dimensional representation of (D) and (E) for all SNA populations. In this case, we fixed the Australasian contribution to Lagoa Santa at 3%. Each line is labeled at the value that yields the best fit score. We compared different models on the basis of their fit scores, where a difference of ~3 corresponds to a *P* value of ~0.05 and a difference of ~4.6 corresponds to a *P* value of ~0.01. For (B), a pool of the five sequenced individuals represents the Lagoa Santa population. For (C) to (F), we considered the called-genotype dataset excluding transitions (13) and used the high-depth Sumidouro5 individual as a representative of the Lagoa Santa population.

Downloaded from http://science.sciencemag.org/ on December 10, 2018

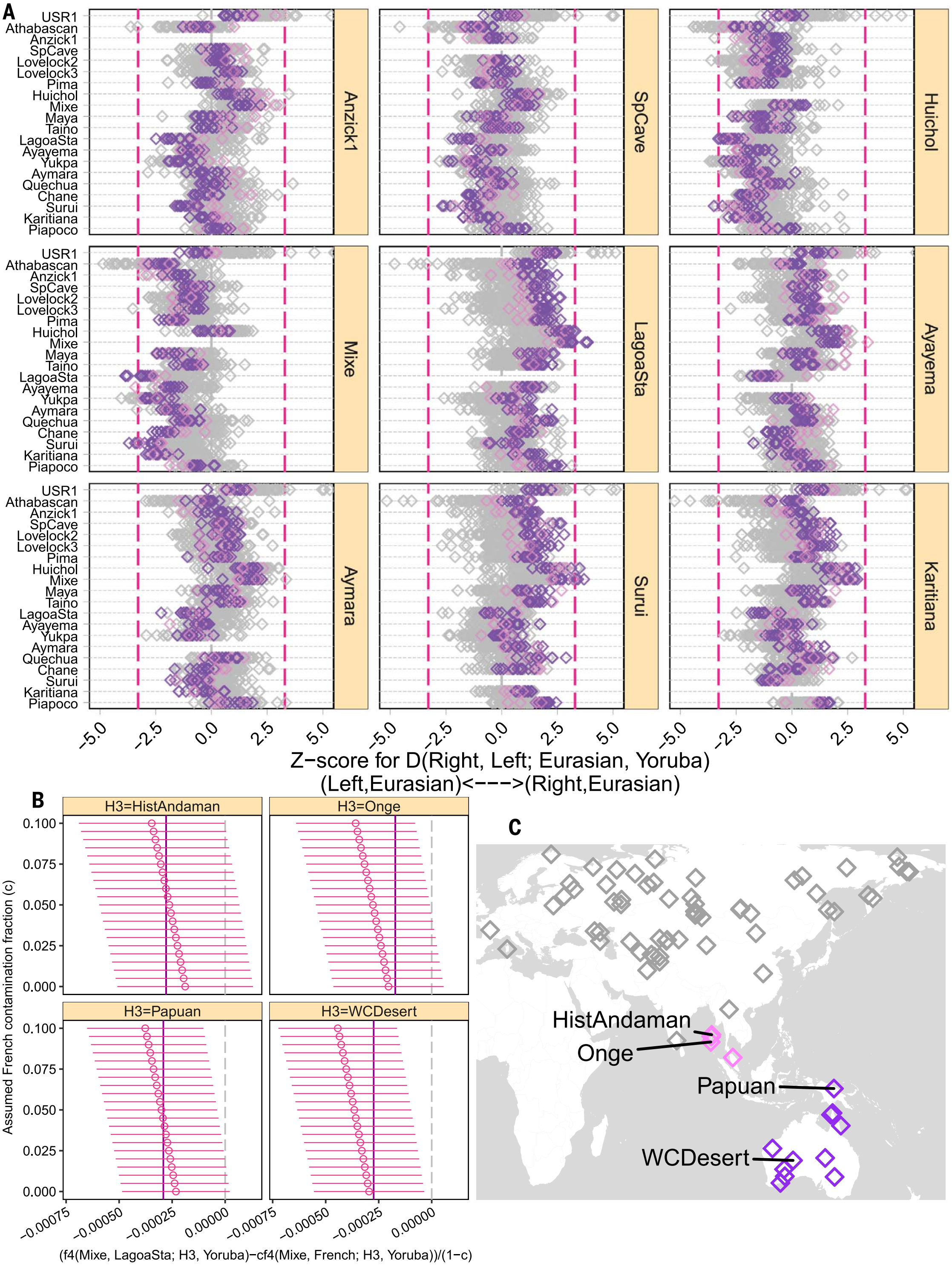

Fig. 4. Allele sharing symmetry tests for pairs of NAs, relative to present-day Eurasian groups. (**A**) We computed D statistics of the form D(NA, NA; Eurasian, Yoruba) to test whether a given NA group carries excess "non-NA" ancestry compared with other NAs. For each statistic, we obtained a z-score (diamonds) on the basis of a weighted block jackknife procedure over 5-Mb blocks. Vertical lines represent ~3.3 and ~-3.3 (which correspond to a P value of ~0.001). In this case, we show only results for present-day Eurasian populations (*13*). Purple, Oceanians; pink, Southeast Asians; gray, non-Australasians. (**B**) Contamination-corrected f_4 statistics of the form f_4(Mixe, Lagoa Santa; Australasian, Yoruba). For each statistic, we subtracted the value of f_4(Mixe, French; Australasian, Yoruba), weighted by an assumed contamination fraction c ranging between 0 and 10% (y axis). Points represent f_4 statistics, and error bars represent ~3.3 SEs. We observe that the apparent allele sharing between Lagoa Santa and Australasians increases as a function of the correction. As a reference, we show the values of f_4(Mixe, Suruí; Australasian, Yoruba) as solid vertical lines. All tests are from the whole-genome dataset described in (*13*) and excluding transition polymorphisms. H3, D-statistic term (see the supplementary materials); WCDesert, Ngaanyatjarra from western central desert. (**C**) Approximate sampling locations for Australasian groups highlighted in (A).

Downloaded from http://science.sciencemag.org/ on December 10, 2018

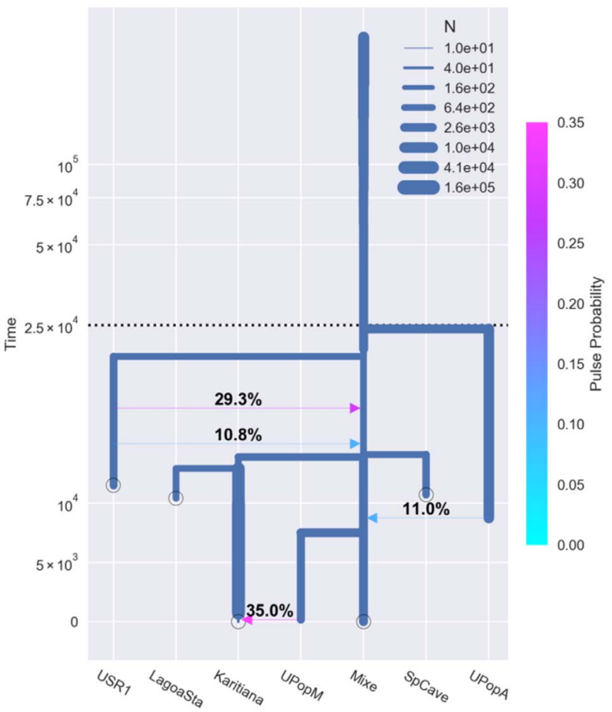

Fig. 5. Demographic history of SNAs. A schematic representation of the most likely model relating the ancient USR1, Anzick1, Spirit Cave, and Lagoa Santa genomes and the present-day Mixe (n = 3 genomes) and Karitiana (n = 5 genomes). Demographic parameters were inferred by using momi2 (13). This model features a quick north-to-south splitting pattern for SNAs over a period shorter than 2 ka, with later admixture from an outgroup (UPopA) into the Mesoamerican Mixe. In addition, we found evidence of gene flow from the latter into present-day South Americans, represented in this case by the Karitiana. Admixture pulses from USR1 into the ancestors of other NAs follow the inference in (1).

every case a significant improvement when modeling Australasian admixture into SNA groups through Lagoa Santa (13). This result suggests that this ancestry was widespread among early South Americans. Although we are unable to estimate the Lagoa Santa–related admixture proportion for these groups with confidence, we observe a general trend for populations east of the Andes (e.g., the Suruí) to bear more of this ancestry than Andean groups (e.g., the Aymara) (Fig. 3F) (13). A possible explanation for this difference is that greater Mesoamerican-related admixture occurred on the western side of the Andes.

Lastly, we explored the demographic history of present-day South Americans by using both joint SFS (momi2) (25, 26) and linkage disequilibrium information [SMC++ (27) and diCal2 (28)]. We seek to understand these groups' relationships to Lagoa Santa—which also provides an indirect means of assessing the effects of admixture on the Australasian signature. For the SFS analysis, we selected the Karitiana, the only SNA population for which a sufficient number of unadmixed genomes are publicly available (n = 5); for the diCal analysis, we used the Karitiana, Aymara (n = 1 genome), and Suruí (n = 2 genomes) (13). From SFS analysis, we infer that the ancestors of Lagoa Santa and Karitiana diverged from each other ~12.9 ka ago (95% CI, 10.4 to 14.0 ka ago). Subsequently, the latter received gene flow from a Mesoamerican-related population, which already carried admixture from the outgroup UPopA (Fig. 5) (13). With the assumption of pulselike migration, this points to recent gene flow (~35%) from the Mesoamerican-related group into Karitiana (Fig. 5), possibly suggesting ongoing admixture over an extended period. When we allowed for two pulses, we inferred substantial gene flow in both the recent and distant past (13). The diCal2 results are consistent for the Karitiana, Aymara, and Suruí populations, showing that their demographic histories involved a mixture between a Lagoa Santa–related source and a Mixe-related source (13).

Overall, our findings suggest that soon after arrival, South Americans diverged along multiple geographic paths (36). That process was further complicated by the arrival of a second independent migration and gene flow in Middle to Late Holocene times. Later admixture potentially reduced the Australasian signature that might have been carried by earlier inhabitants.

Long-term population continuity in the North American Great Basin and the Numic Expansion

Mesoamerican-related expansion possibly had a bearing on a later, unresolved pattern seen in North America. In the western Great Basin of North America, paleoenvironmental evidence indicates decreased effective precipitation and increased aridity during the Middle Holocene, which led to a human population decline (45, 46). By ~5 ka ago, regional populations were rebounding, but whether these were descendants of the previous inhabitants is unknown. Unclear also is the relationship between those later Holocene groups and the people present in the region at the time of European contact and today. Linguistic evidence suggests that ancestors of Numic speakers presently inhabiting the region today arrived recently, perhaps ~1 ka ago. There is also archaeological evidence of changes in material culture around that time, though how those relate to the linguistic turnover is uncertain. Nor is it known whether these changes are related to population admixture or replacement. Patterns and changes in language, material culture, and genetics need not be congruent or causally linked (47). Thus, the so-called Numic Expansion hypothesis has been highly debated (46, 48); we address the population aspect by comparing genomes from Spirit Cave and Lovelock Cave (Fig. 1A) (13).

MDS and ADMIXTURE analyses, as well as D statistics of the form D(SpiritCave, Lovelock2/3; NA, Yoruba), suggest that despite the ~9 ka separating the Spirit Cave and Lovelock individuals, they form a clade with respect to other NAs (Fig. 1, C to F) (13). We tested that topology through the same admixture graph search implemented for SNAs (13). We were not able to reject the model without Mesoamerican-related admixture for Lovelock 2 (~1.9 ka old). However, the ~0.7-ka-old Lovelock 3 individual received Mesoamerican admixture from a group that was likely not present in the region just ~1.2 ka earlier, at the time of Lovelock 2. Because we do not know the language(s) that may have been involved, we cannot securely attribute this admixture to arriving Numic speakers [the Mixe, whom we use as a proxy for Mesoamerican ancestry, fall in a separate language family from Numic (49)]. Notably, we also observe genetic continuity, suggesting that there was not a complete population replacement.

Present-day Pima from northern Mexico can also best be modeled as a Mesoamerican-related mixture. However, the Pima require admixture from a branch splitting above the Mixe–Spirit Cave divergence, likely an NNA population (13). We cannot specify a particular source population. These patterns indicate that complex population movements and mixture occurred after the initial settlements of the Great Basin and Southwest from both the north and south.

Long-term complex population history in the Pacific Northwest

Pacific Northwest groups had a Late Pleistocene demographic history argued to be distinct from that of early SNA groups (1, 2, 9, 18, 33). To explore the population history and the relationship of regional populations to NNAs and SNAs, we assessed the genetic affinities between the 5.6-ka-old Big Bar Lake individual from the Fraser Plateau of central British Columbia and other NAs. Given their relative geographic proximity, we included the 939, 302, and 443 individuals from coastal British Columbia (9) and the Kennewick Man/Ancient One (10). As these genomes have been deemed representatives of NNAs, we also included genomic data from ancient southwestern Ontario (ASO) individuals, who are closely related to Algonquin (NNA) populations (7).

These ancient North American individuals clustered separately from SNA populations in both MDS transformations, and their ancestry component distribution closely resembles that of NNA populations (Fig. 1, C and F) (13). However, we observed genetic differentiation between these individuals and other North American populations. Whereas the ancient coastal British Columbian individuals clustered together with present-day

Downloaded from http://science.sciencemag.org/ on December 10, 2018

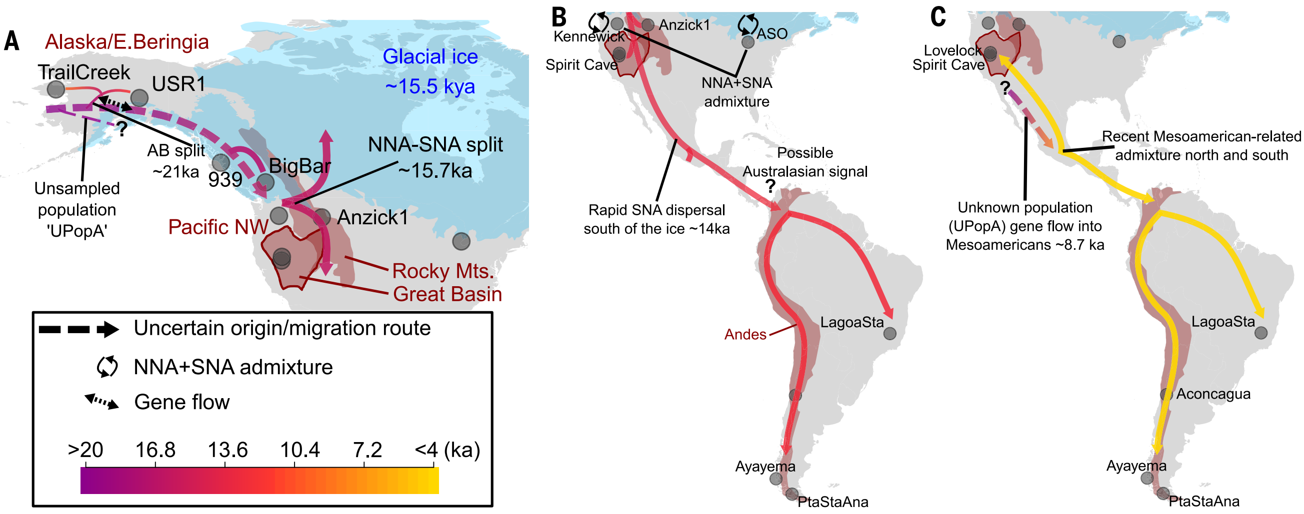

Fig. 6. Schematic depiction of the processes of human dispersal and divergence in the Americas, arranged chronologically. (**A**) Initial entry into eastern Beringia and then into unglaciated North America, ~25 to ~13 ka ago, during which multiple splits occurred: first those in Beringia (UPopA and ABs from the NNA-SNA line), followed by the Big Bar ancestral population split from the NNA-SNA line, and then lastly the NNA-SNA split south of eastern Beringia. NNA groups remained in northern North America, whereas SNA groups began to disperse across the North American continent. (**B**) Period of dispersal hemisphere-wide, ~14 to ~6 ka ago, during which time SNAs moved rapidly from North into South America, resulting in the close affinities of the nearly contemporaneous Spirit Cave and Lagoa Santa individuals. Early South American populations possibly carried an Australasian-related admixture, as seen in the Lagoa Santa individual, and diverged west and east of the Andes. There was also admixture in North America between the NNA and SNA groups before 9 ka ago that formed the population of which Kennewick Man/Ancient One was a member. It is inferred that during this period but after 9 ka ago (the age of the Trail Creek AB individual), NNA groups moved north into Alaska. (**C**) Population expansion out of Mesoamerica sometime after ~8.7 ka ago. These groups moved north into the Great Basin, resulting in a population turnover after 2 ka ago, evidenced by the difference between the Lovelock 2 and Lovelock 3 individuals. In South America, that expansion contributed to the ancestry of most South American groups but did not reach Patagonia by 5.1 ka ago, the time of the Ayayema individual.

Athabascan and Tsimshian speakers from the region, the ASO group and Kennewick Man/Ancient One were placed in an intermediate position between NNAs and SNAs. Although the Big Bar individual was placed close to NNA populations not carrying recent Siberian admixture (Fig. 1, C and F) (13), *D* statistics of the form *D*(Aymara, NA; BigBar, Yoruba) and *D*(USR1, NA; BigBar, Yoruba) suggest that Big Bar represents a previously undetected outgroup to non-AB NAs, one that diverged before the NNA-SNA split (13).

To describe the genetic ancestry of these individuals, we used the admixture graph search strategy (13). In agreement with previous results, the ancient coastal British Columbian individuals are best modeled as a clade with Athabascans, who bear Siberian-related admixture (Fig. 2C). However, the best-fitting model suggests that the Big Bar individual represents a population that split before the NNA-SNA divergence but after AB divergence and without Siberian admixture (Fig. 2B) (13). Lastly, in accordance with their placement in both MDS transformations, we observed that Kennewick Man/Ancient One and ASO individuals are best modeled as deriving a fraction of their ancestry from an SNA-related source, represented by Spirit Cave in this case (Fig. 2, D and E) (13). We confirm this through error-corrected *D* statistics (Fig. 2F) (13) suggesting gene flow between ASO individuals and an SNA group that diverged after the split of Anzick1 and that did not bear recent Mesoamerican-related ancestry.

Thus, the broader population history in this region was evidently marked by admixture between the NNA and SNA branches that most likely gave rise to the ancestors of Kennewick Man/Ancient One and ASO individuals and by isolation between groups in coastal British Columbia (represented by the 939 individual) and interior British Columbia (represented by Big Bar).

Discussion

The genomes described here do not undermine the previously established tree in which AB splitting from ancestral NAs is followed by the basal NNA-SNA split south of eastern Beringia. However, they show that the tree is at best a rough outline of the peopling process. We now find that once south of eastern Beringia, NAs radiated rapidly and gave rise to multiple populations, some of which are visible in the genetic record only as unsampled populations and which at different times expanded to different portions of the continent, though not as extensively as in the initial peopling (Fig. 6).

Rapid movement from North to South America is evident genetically (Fig. 6, A and B) and had been anticipated from the "archaeologically-instantaneous" appearance of sites throughout the hemisphere dating to just after 13 ka ago (50, 51). The evidence suggests that the mechanism of movement was not simply gradual population growth and incremental geographic expansion but rather was more akin to leap-frogging across large portions of the diverse intervening landscape (52). If this result holds, it predicts that additional terminal Pleistocene samples will fit on a starlike pattern, as observed in this study.

That the early population evidently spread widely and rapidly but somewhat unevenly across the Americas in turn suggests that their access to large portions of the hemisphere was essentially unrestricted (52). Yet the genetic record contains hints of early unsampled populations (6) (Fig. 5), and the material culture associated with that rapid spread (Clovis and later) is distinct from and postdates the earliest secure archaeological presence in the Americas at 14.6 ka ago (53). How these early groups are related, particularly those with excess Australasian ancestry, and their degree of structure remain largely unknown.

The Australasian signal is not present in USR1 or Spirit Cave and appears only in Lagoa Santa. None of these individuals have UPopA- or Mesoamerican-related admixture, which apparently dampened the Australasian signature in South American groups, such as the Karitiana (Figs. 4 and 5). These findings suggest that the Australasian signal, possibly present in a structured ancestral NA population (16), was absent in NA before the Spirit Cave–Lagoa Santa split. Either groups carrying this signal were already present in South America when the ancestors of Lagoa Santa reached the region, or Australasian-related groups arrived later but before 10.4 ka ago (the Lagoa Santa ^{14}C age). That this signal has not been previously documented in North America implies that an earlier group possessing it had disappeared or that a later-arriving group passed through North America without leaving any genetic trace (Fig. 6, A and C). If such a signal

Downloaded from http://science.sciencemag.org/ on December 10, 2018

is ultimately detected in North America, it could help determine when groups bearing Australasian ancestry arrived, relative to the divergence of SNA groups.

Although we detected the Australasian signal in one of the Lagoa Santa individuals identified as a Paleoamerican, it is absent in other Paleoamericans (2, 10), including the Spirit Cave genome with its strong genetic affinities to Lagoa Santa. This indicates that the Paleoamerican cranial form is not associated with the Australasian genetic signal, as previously suggested (6), or any other specific NA clade (2). The Paleoamerican cranial form, if it is representative of broader population patterns, evidently did not result from separate ancestry but likely from multiple factors, including isolation, drift, and nonstochastic mechanisms (2, 10, 13, 54).

The attenuating effects of distance, compounded (in places) by geographic barriers, led to cultural drift and regional adaptations, even early in the peopling process (52, 55). It was previously surmised that Clovis (Anzick1) and Western Stemmed (Spirit Cave) technologies (46, 56) represented "genetically divergent, founding groups" (57). It appears instead that the divergence is principally cultural, between genetically close populations living on opposite sides of the Rocky Mountains. This result affirms the point that archaeological, anatomical, and genetic records are not necessarily congruent (47).

That one of the principal isolating mechanisms was likely geographic helps explain the long-term population continuity in the Great Basin. Continuity existed despite fluctuating human population densities and the cultural and linguistic changes that occurred over a 9-ka span (46). In the Pacific Northwest, geographic barriers were less formidable, but we surmise that the region's natural richness and diversity may have led groups to inhabit different environmental niches, which resulted in the emergence of social boundaries that maintained population separation. In this region's long history, we find evidence that groups on the coast (e.g., 939) and their contemporaries in the interior (Big Bar) were as genetically distinct as are present-day groups (18) (Fig. 6A). How or whether such differences map to the region's rich linguistic complexity and material culture differences is not known (13, 58). Previous research on mtDNA and Y sequences hypothesized a shared origin for Pacific Northwest populations, followed by divergence due to isolation and drift (18). That Big Bar represents a previously unseen, isolated population supports its ancestral isolation and drift but implies that the initial peopling of the region was complex and structured.

We also found evidence of a later Mesoamerican admixture, which though geographically extensive was not associated with a "wave" throughout the Americas, nor did it inevitably lead to replacement. Rather, it appears to mark the movement north and south (Fig. 6C) of what may have been relatively small groups that did not necessarily swamp local populations genetically or culturally, as illustrated by admixture in the Lovelock 3 individual. Regardless of whether this marks the Numic Expansion, it was associated with evidence of cultural continuity as well as change; it was not an instance of population replacement. How or whether this Mesoamerican-related expansion is expressed culturally in South America is not known.

The genomes reported here fill gaps in our temporal and spatial coverage and are valuable anchor points that reveal that the human population history of the Americas. As has long been expected (52) and is characteristic of human population histories around the world (59), the peopling process was marked by complex local and long-range demographic processes over time. The peopling of the Americas will likely prove more complicated still. As we have found, there was a previously unknown population in the Americas (UPopA), as well as one that harbored an Australasian signal in the Late Pleistocene and reached South America, yet left no apparent traces in North America. In addition, all of our evidence of the peopling process is from archaeologically known groups: Clovis (Anzick) and later populations. Yet there is archaeological evidence of an earlier, pre-Clovis presence in the Americas, one for which we have yet to recover any ancient DNA. How these various population threads may ultimately come together and how these populations are related to NAs past and present remain to be resolved.

Materials and methods

Laboratory procedures

Ancient DNA work was performed in dedicated clean laboratory facilities at the Centre for GeoGenetics, Natural History Museum, University of Copenhagen. Extraction, treatment, and library build protocols followed for each sample are detailed in (13). Sequencing was carried out in Illumina HiSeq instruments.

Data processing

Sequencing reads were trimmed for Illumina adaptors by using AdapterRemoval (60) and mapped to the human reference genome build 37 by using BWA v.0.6.2-r126 (61) with disabled seeding (–l parameter) (62). Reads with mapping quality lower than 30 were discarded, polymerase chain reaction duplicates were identified by using MarkDuplicates (63), and local realignment was carried out by using GATK (64). Genotype calls for high-coverage samples were generated by using SAMtools mpileup (65) and filtered according to the method of (2). Called genotypes were phased with impute2 (66, 67) by using the 1000 Genomes phased-variant panel (phase 3) as a reference and the HapMap recombination rates. The final call set was masked by using a 35-mer "snpability" mask with a stringency of 0.5 (68) and the strict accessible regions from the 1000 Genomes Project (69).

Ancient DNA data authentication

We examined the fragment length distributions and the base substitution patterns by using bamdamage (20). We estimated mtDNA, X chromosome, and nuclear contamination by using contamMix (70), ANGSD (71), and DICE (72), respectively.

Population structure analyses

We investigated the broad relationships between ancient and present-day genomes by using model-based clustering as implemented in ADMIXTURE (19) and MDS applied to the identity-by-state (20) and f_3 distance (21, 22) matrices.

D statistics

We computed *D* statistics to formally test hypotheses of treeness and gene flow. Genotype-based *D* statistics were computed as detailed in (21), and error-corrected *D* statistics were computed according to the method of (23). For both approaches, standard errors were estimated through a weighted block jackknife approach over 5-Mb blocks.

Admixture graph fitting

We used qpGraph to fit *f* statistics–based admixture graphs (4, 21). We implemented an exhaustive admixture graph search where we considered a seed graph onto which a test population was added as either a nonadmixed or an admixed group in every possible position. Extensions of the seed graph were enumerated by using the admixturegraph R package (32). We evaluated each topology on the basis of its fit score, the *z*-score of the worst residual between the observed and predicted *D* statistics, and the presence of zero-length internal edges and carried out likelihood ratio tests by following (30). For all tests, we considered only transversion polymorphisms.

Demographic inference

We estimated marginal population sizes over time for different NA groups by using SMC++ (27). We then used momi2 (25, 26) to infer demographic parameters for a number of models with the joint SFS. CIs were obtained through a nonparametric bootstrap procedure. We confirmed the SFS-based inference by using diCal2 (28), which relies on linkage disequilibrium information, to infer key demographic parameters relating pairs of NA populations. A detailed description of laboratory and analytical methods is provided in (13).

REFERENCES AND NOTES

1. J. V. Moreno-Mayar *et al*., Terminal Pleistocene Alaskan genome reveals first founding population of Native Americans. *Nature* **553**, 203–207 (2018). doi: 10.1038/nature25173; pmid: 29323294
2. M. Raghavan *et al*., Genomic evidence for the Pleistocene and recent population history of Native Americans. *Science* **349**, aab3884–aab3884 (2015). doi: 10.1126/science.aab3884; pmid: 26198033
3. M. Rasmussen *et al*., The genome of a Late Pleistocene human from a Clovis burial site in western Montana. *Nature* **506**, 225–229 (2014). doi: 10.1038/nature13025; pmid: 24522598
4. D. Reich *et al*., Reconstructing Native American population history. *Nature* **488**, 370–374 (2012). doi: 10.1038/nature11258; pmid: 22801491
5. W. A. Neves, M. Hubbe, Cranial morphology of early Americans from Lagoa Santa, Brazil: Implications for the settlement of the New World. *Proc. Natl. Acad. Sci. U.S.A.* **102**, 18309–18314 (2005). doi: 10.1073/pnas.0507185102; pmid: 16344464

Downloaded from http://science.sciencemag.org/ on December 10, 2018

6. P. Skoglund *et al*., Genetic evidence for two founding populations of the Americas. *Nature* **525**, 104–108 (2015). pmid: 26196601
7. C. L. Scheib *et al*., Ancient human parallel lineages within North America contributed to a coastal expansion. *Science* **360**, 1024–1027 (2018). doi: 10.1126/science.aar6851; pmid: 29853687
8. B. Llamas *et al*., Ancient mitochondrial DNA provides high-resolution time scale of the peopling of the Americas. *Sci. Adv.* **2**, e1501385–e1501385 (2016). doi: 10.1126/sciadv.1501385; pmid: 27051878
9. J. Lindo *et al*., Ancient individuals from the North American Northwest Coast reveal 10,000 years of regional genetic continuity. *Proc. Natl. Acad. Sci. U.S.A.* **114**, 4093–4098 (2017). doi: 10.1073/pnas.1620410114; pmid: 28377518
10. M. Rasmussen *et al*., The ancestry and affiliations of Kennewick Man. *Nature* **523**, 455–458 (2015). pmid: 26087396
11. J. Bardill *et al*., Advancing the ethics of paleogenomics. *Science* **360**, 384–385 (2018). doi: 10.1126/science.aaq1131; pmid: 29700256
12. K. G. Claw *et al*., A framework for enhancing ethical genomic research with Indigenous communities. *Nat. Commun.* **9**, 2957 (2018). doi: 10.1038/s41467-018-05188-3; pmid: 30054469
13. See supplementary materials.
14. A. Gómez-Carballa *et al*., The complete mitogenome of a 500-year-old Inca child mummy. *Sci. Rep.* **5**, 16462 (2015). doi: 10.1038/srep16462; pmid: 26561991
15. P. J. Reimer *et al*., IntCal13 and Marine13 Radiocarbon Age Calibration Curves 0–50,000 Years cal BP. *Radiocarbon* **55**, 1869–1887 (2013). doi: 10.2458/azu_js_rc.55.16947
16. P. Skoglund, D. Reich, A genomic view of the peopling of the Americas. *Curr. Opin. Genet. Dev.* **41**, 27–35 (2016). doi: 10.1016/j.gde.2016.06.016; pmid: 27507099
17. A. W. Briggs *et al*., Removal of deaminated cytosines and detection of in vivo methylation in ancient DNA. *Nucleic Acids Res.* **38**, e87–e87 (2010). doi: 10.1093/nar/gkp1163; pmid: 20028723
18. P. Verdu *et al*., Patterns of admixture and population structure in native populations of Northwest North America. *PLOS Genet.* **10**, e1004530 (2014). doi: 10.1371/journal.pgen.1004530; pmid: 25122539
19. D. H. Alexander, J. Novembre, K. Lange, Fast model-based estimation of ancestry in unrelated individuals. *Genome Res.* **19**, 1655–1664 (2009). doi: 10.1101/gr.094052.109; pmid: 19648217
20. A.-S. Malaspinas *et al*., bammds: A tool for assessing the ancestry of low-depth whole-genome data using multidimensional scaling (MDS). *Bioinformatics* **30**, 2962–2964 (2014). doi: 10.1093/bioinformatics/btu410; pmid: 24974206
21. N. Patterson *et al*., Ancient admixture in human history. *Genetics* **192**, 1065–1093 (2012). doi: 10.1534/genetics.112.145037; pmid: 22960212
22. Q. Fu *et al*., The genetic history of Ice Age Europe. *Nature* **534**, 200–205 (2016). doi: 10.1038/nature17993; pmid: 27135931
23. S. Soraggi, C. Wiuf, A. Albrechtsen, Powerful inference with the D-Statistic on low-coverage whole-genome data. *G3 (Bethesda)* **8**, 551–566 (2018). doi: 10.1534/g3.117.300192; pmid: 29196497
24. J. K. Pickrell, J. K. Pritchard, Inference of population splits and mixtures from genome-wide allele frequency data. *PLOS Genet.* **8**, e1002967 (2012). doi: 10.1371/journal.pgen.1002967; pmid: 23166502
25. J. A. Kamm, J. Terhorst, Y. S. Song, Efficient computation of the joint sample frequency spectra for multiple populations. *J. Comput. Graph. Stat.* **26**, 182–194 (2017). doi: 10.1080/10618600.2016.1159212; pmid: 28239248
26. J. A. Kamm, J. Terhorst, R. Durbin, Y. S. Song, Efficiently inferring the demographic history of many populations with allele count data. bioRxiv 287268 [Preprint]. 23 March 2018. doi: 10.1101/287268
27. J. Terhorst, J. A. Kamm, Y. S. Song, Robust and scalable inference of population history from hundreds of unphased whole genomes. *Nat. Genet.* **49**, 303–309 (2017). doi: 10.1038/ng.3748; pmid: 28024154
28. M. Steinrücken, J. A. Kamm, Y. S. Song, Inference of complex population histories using whole-genome sequences from multiple populations. bioRxiv 026591 [Preprint]. 16 September 2015. doi: 10.1101/026591
29. C. E. Holmes, in *From the Yenisei to the Yukon: Interpreting Lithic Assemblage Variability in Late Pleistocene/Early Holocene Beringia*, T. Goebel, I. Buvit, Eds. (Peopling of the Americas, Texas A&M Univ., ed. 1, 2011).
30. M. Lipson, D. Reich, A working model of the deep relationships of diverse modern human genetic lineages outside of Africa. *Mol. Biol. Evol.* **34**, 889–902 (2017). pmid: 28074030
31. M. Raghavan *et al*., Upper Palaeolithic Siberian genome reveals dual ancestry of Native Americans. *Nature* **505**, 87–91 (2014). doi: 10.1038/nature12736; pmid: 24256729
32. K. Leppälä, S. V. Nielsen, T. Mailund, admixturegraph: An R package for admixture graph manipulation and fitting. *Bioinformatics* **33**, 1738–1740 (2017). doi: 10.1093/bioinformatics/btx048; pmid: 28158333
33. P. Flegontov *et al*., Na-Dene populations descend from the Paleo-Eskimo migration into America. bioRxiv 074476 [Preprint]. 13 September 2016. .doi: 10.1101/074476
34. E. Tamm *et al*., Beringian standstill and spread of Native American founders. *PLOS ONE* **2**, e829 (2007). doi: 10.1371/journal.pone.0000829; pmid: 17786201
35. M. C. Bortolini, R. González-José, S. L. Bonatto, F. R. Santos, Reconciling pre-Columbian settlement hypotheses requires integrative, multidisciplinary, and model-bound approaches. *Proc. Natl. Acad. Sci. U.S.A.* **111**, E213–E214 (2014). doi: 10.1073/pnas.1321197111; pmid: 24398530
36. D. N. Harris *et al*., Evolutionary genomic dynamics of Peruvians before, during, and after the Inca Empire. *Proc. Natl. Acad. Sci. U.S.A.* **115**, E6526–E6535 (2018). doi: 10.1073/pnas.1720798115; pmid: 29946025
37. D. A. Bolnick, J. A. Raff, L. C. Springs, A. W. Reynolds, A. T. Miró-Herrans, Native American Genomics and Population Histories. *Annu. Rev. Anthropol.* **45**, 319–340 (2016). doi: 10.1146/annurev-anthro-102215-100036
38. W. A. Neves, M. Hubbe, L. B. Piló, Early Holocene human skeletal remains from Sumidouro Cave, Lagoa Santa, Brazil: History of discoveries, geological and chronological context, and comparative cranial morphology. *J. Hum. Evol.* **52**, 16–30 (2007). doi: 10.1016/j.jhevol.2006.07.012; pmid: 16996575
39. R. L. Jantz, D. W. Owsley, Variation among early North American crania. *Am. J. Phys. Anthropol.* **114**, 146–155 (2001). doi: 10.1002/1096-8644(200102)114:2<146::AID-AJPA1014>3.0.CO;2-E; pmid: 11169904
40. N. von Cramon-Taubadel, A. Strauss, M. Hubbe, Evolutionary population history of early Paleoamerican cranial morphology. *Sci. Adv.* **3**, e1602289 (2017). doi: 10.1126/sciadv.1602289; pmid: 28261661
41. W. A. Neves, J. F. Powell, A. Prous, E. G. Ozolins, M. Blum, Lapa Vermelha IV Hominid 1: Morphological affinities of the earliest known American. *Genet. Mol. Biol.* **22**, 461–469 (1999). doi: 10.1590/S1415-47571999000400001
42. R. González-José, M. C. Bortolini, F. R. Santos, S. L. Bonatto, The peopling of America: Craniofacial shape variation on a continental scale and its interpretation from an interdisciplinary view. *Am. J. Phys. Anthropol.* **137**, 175–187 (2008). doi: 10.1002/ajpa.20854; pmid: 18481303
43. C. de la Fuente *et al*., Genomic insights into the origin and diversification of late maritime hunter-gatherers from the Chilean Patagonia. *Proc. Natl. Acad. Sci. U.S.A.* **115**, E4006–E4012 (2018). doi: 10.1073/pnas.1715688115; pmid: 29632188
44. H. Schroeder *et al*., Origins and genetic legacies of the Caribbean Taino. *Proc. Natl. Acad. Sci. U.S.A.* **115**, 2341–2346 (2018). doi: 10.1073/pnas.1716839115; pmid: 29463742
45. L. A. Louderback, D. K. Grayson, M. Llobera, Middle-Holocene climates and human population densities in the Great Basin, western USA. *Holocene* **21**, 366–373 (2011). doi: 10.1177/0959683610374888
46. D. K. Grayson, *The Great Basin: A Natural Prehistory* (Univ. of California, revised and expanded ed., 2011).
47. N. N. Johannsen, G. Larson, D. J. Meltzer, M. Vander Linden, A composite window into human history. *Science* **356**, 1118–1120 (2017). doi: 10.1126/science.aan0737; pmid: 28619897
48. D. B. Madsen, D. Rhode, Eds., *Across the West: Human Population Movement and the Expansion of the Numa* (Univ. of Utah, 1994).
49. L. Campbell, *American Indian Languages: The Historical Linguistics of Native America* (Oxford Univ., 1997).
50. L. Bueno, G. Politis, L. Prates, J. Steele, Eds., A Late Pleistocene/Early Holocene Archaeological 14C Database for Central and South America: Palaeoenvironmental Contexts and Demographic Interpretations. *Quat. Int.* **301**, 1–158 (2013).
51. M. R. Waters, T. W. Stafford Jr., Redefining the age of Clovis: Implications for the peopling of the Americas. *Science* **315**, 1122–1126 (2007). doi: 10.1126/science.1137166; pmid: 17322060
52. D. J. Meltzer, *First Peoples in a New World: Colonizing Ice Age America* (Univ. of California, 2009).
53. T. D. Dillehay *et al*., Monte Verde: Seaweed, food, medicine, and the peopling of South America. *Science* **320**, 784–786 (2008). doi: 10.1126/science.1156533; pmid: 18467586
54. G. R. Scott *et al*., Sinodonty, Sundadonty, and the Beringian Standstill model: Issues of timing and migrations into the New World. *Quat. Int.* **466**, 233–246 (2018). doi: 10.1016/j.quaint.2016.04.027
55. M. I. Eren, B. Buchanan, M. J. O'Brien, Social learning and technological evolution during the Clovis colonization of the New World. *J. Hum. Evol.* **80**, 159–170 (2015). doi: 10.1016/j.jhevol.2015.01.002; pmid: 25666759
56. L. Becerra-Valdivia *et al*., Reassessing the chronology of the archaeological site of Anzick. *Proc. Natl. Acad. Sci. U.S.A.* **115**, 7000–7003 (2018). doi: 10.1073/pnas.1803624115; pmid: 29915063
57. D. L. Jenkins *et al*., Clovis age Western Stemmed projectile points and human coprolites at the Paisley Caves. *Science* **337**, 223–228 (2012). doi: 10.1126/science.1218443; pmid: 22798611
58. C. E. Hughes *et al*., Genetic Structure of First Nation Communities in the Pacific Northwest. *Hum. Biol.* **88**, 251–263 (2016). doi: 10.13110/humanbiology.88.4.0251; pmid: 28826319
59. R. Nielsen *et al*., Tracing the peopling of the world through genomics. *Nature* **541**, 302–310 (2017). doi: 10.1038/nature21347; pmid: 28102248
60. S. Lindgreen, AdapterRemoval: Easy cleaning of next-generation sequencing reads. *BMC Res. Notes* **5**, 337 (2012). doi: 10.1186/1756-0500-5-337; pmid: 22748135
61. H. Li, R. Durbin, Fast and accurate short read alignment with Burrows-Wheeler transform. *Bioinformatics* **25**, 1754–1760 (2009). doi: 10.1093/bioinformatics/btp324; pmid: 19451168
62. M. Schubert *et al*., Improving ancient DNA read mapping against modern reference genomes. *BMC Genomics* **13**, 178 (2012). doi: 10.1186/1471-2164-13-178; pmid: 22574660
63. Picard, http://picard.sourceforge.net.
64. M. A. DePristo *et al*., A framework for variation discovery and genotyping using next-generation DNA sequencing data. *Nat. Genet.* **43**, 491–498 (2011). doi: 10.1038/ng.806; pmid: 21478889
65. H. Li *et al*., The Sequence Alignment/Map format and SAMtools. *Bioinformatics* **25**, 2078–2079 (2009). doi: 10.1093/bioinformatics/btp352; pmid: 19505943
66. B. N. Howie, P. Donnelly, J. Marchini, A flexible and accurate genotype imputation method for the next generation of genome-wide association studies. *PLOS Genet.* **5**, e1000529 (2009). doi: 10.1371/journal.pgen.1000529; pmid: 19543373
67. B. Howie, J. Marchini, M. Stephens, Genotype imputation with thousands of genomes. *G3 (Bethesda)* **1**, 457–470 (2011). doi: 10.1534/g3.111.001198; pmid: 22384356
68. SNPable Regions, http://lh3lh3.users.sourceforge.net/snpable.shtml.
69. The 1000 Genomes Project Consortium, A global reference for human genetic variation. *Nature* **526**, 68–74 (2015). doi: 10.1038/nature15393; pmid: 26432245
70. Q. Fu *et al*., A revised timescale for human evolution based on ancient mitochondrial genomes. *Curr. Biol.* **23**, 553–559 (2013). doi: 10.1016/j.cub.2013.02.044; pmid: 23523248
71. T. S. Korneliussen, A. Albrechtsen, R. Nielsen, ANGSD: Analysis of Next Generation Sequencing Data. *BMC Bioinformatics* **15**, 356 (2014). doi: 10.1186/s12859-014-0356-4; pmid: 25420514
72. F. Racimo, G. Renaud, M. Slatkin, Joint Estimation of Contamination, Error and Demography for Nuclear DNA from Ancient Humans. *PLOS Genet.* **12**, e1005972 (2016). doi: 10.1371/journal.pgen.1005972; pmid: 27049965
73. A. S. Dyke, A. Moore, L. Robertson, "Deglaciation of North America" (Geological Survey of Canada Open File 1547, 2003).
74. J. Lindo *et al*., The genetic prehistory of the Andean highlands: 7000 years BP though European contact. *Sci. Adv.* **4**, eaau4921 (2018). doi: 10.1126/sciadv.aau4921
75. C. Posth *et al*., Reconstructing the Deep Population History of Central and South America. *Cell* **175**, 1185–1197 (2018). doi: 10.1016/j.cell.2018.10.027

ACKNOWLEDGMENTS

For permission and cooperation in providing human remains for this study, we thank the Native Village of Deering, Alaska; the Fallon Paiute-Shoshone Tribe; the Consejo de Monumentos Nacionales, Chile; and the Canadian Museum of History and the Stswecem'c Xgat'tem, Metlakatla, and Lax Kw'alaams First Nations. See (*74*, *75*) for related analyses of ancient DNA samples from the Americas. We thank J. Ramos-Madrigal, L. Orlando,

Downloaded from http://science.sciencemag.org/ on December 10, 2018

G. Renaud, F. Vieira, L. Benson, A. Bergström, T. Ferraz, and J. E. Santos-Júnior for discussions; M. Drummond, F. Zimmermann, and T. Tisler for image processing; B. Chestnut, B. Baldwin, and D. Cossette for help and support; and the Danish National High-throughput Sequencing Centre for assistance with data generation. St. John's College, Cambridge University, provided E.W. and D.J.M. a congenial venue for scientific discussions. **Funding:** GeoGenetics members were supported by the Lundbeck Foundation, the Danish National Research Foundation (DNRF94), and KU2016. Study of the Lagoa Santa human remains was partly funded by the Augustinus Foundation. J.Ch. is supported in part by an NSF graduate research fellowship. J.Ch., J.P.S., and Y.S.S. are supported in part by the National Institutes of Health grant R01-GM094402, a Microsoft Azure research award, and a Packard Fellowship for Science and Engineering. A.St. was funded by FAPESP (2017/16451-2). Study of Patagonian samples by M.A.-D. was sponsored by the National Geographic Society, Genographic Program, grant 14-01. H.S. was supported by HERA and the European Union's Horizon2020 Research and Innovation Programme (grant 649307). J.T.R. was supported by funding from the National Park Service Shared Beringian Heritage Program. A.-S.M. thanks the Swiss National Science Foundation and the European Research Council (ERC starting grant) for funding. Y.S.S. is a Chan Zuckerberg Biohub Investigator. D.J.M. is supported by the Quest Archaeological Research Fund and the Potts and Sibley Foundation. **Author contributions:** The project was conceived by E.W., J.V.M.-M., and D.J.M. and headed by E.W. L.V., P.D.B.D., C.D.L.F., M.E.A., A.M., M.I.O., D.M., and H.S. processed ancient DNA. J.V.M.-M., S.Ra., and T.P. assembled datasets. J.V.M.-M., J.Ch., J.P.S., T.V., F.R., T.P., and Y.S.S. analyzed genetic data with input from P.D.B.D. and C.D.L.F. R.N., Y.S.S., M.S., and A.-S.M. supervised bioinformatic and statistical analyses. Radiocarbon analyses were done by L.B.-V., D.Ch., D.Co., T.D., and T.H. C.V., F.M., M.V., S.W., K.G., N.L., M.M.L., K.K., and L.S. excavated, curated, sampled, or described human remains. D.J.M., D.K.G., V.A., C.P., J.E., C.R.-C., S.Re., M.Q.R.B., J.Cy., M.W., C.B., K.L.H., M.M.L., A.St., A.Sa., F.M., M.A.-D., and J.T.R conducted archaeological and bioanthropological analyses and provided contextualization. L.G. and H.H. partnered with R.S.M. and E.W. to engage with indigenous communities. All authors contributed to data interpretation. J.V.M.-M., D.J.M., Y.S.S., and E.W. wrote the manuscript, with input from J.Ch., J.P.S., M.A.-D., R.S.M., J.T.R., T.P., F.R.S., A.-S.M., and the other authors. **Competing interests**: The authors declare no competing interests. **Data and materials availability:** Sequence data are available at the ENA under accession PRJEB29074.

SUPPLEMENTARY MATERIALS

www.sciencemag.org/content/362/6419/eaav2621/suppl/DC1
Materials and Methods
Supplementary Text
Figs. S1 to S80
Tables S1 to S18
References (*76*–*223*)

3 September 2018; accepted 30 October 2018
Published online 8 November 2018
10.1126/science.aav2621

Downloaded from http://science.sciencemag.org/ on December 10, 2018

RESEARCH ARTICLE SUMMARY

ANTIMALARIALS

Open-source discovery of chemical leads for next-generation chemoprotective antimalarials

Yevgeniya Antonova-Koch, Stephan Meister, Matthew Abraham, Madeline R. Luth, Sabine Ottilie, Amanda K. Lukens, Tomoyo Sakata-Kato, Manu Vanaerschot, Edward Owen, Juan Carlos Jado Rodriguez, Steven P. Maher, Jaeson Calla, David Plouffe, Yang Zhong, Kaisheng Chen, Victor Chaumeau, Amy J. Conway, Case W. McNamara, Maureen Ibanez, Kerstin Gagaring, Fernando Neria Serrano, Korina Eribez, Cullin McLean Taggard, Andrea L. Cheung, Christie Lincoln, Biniam Ambachew, Melanie Rouillier, Dionicio Siegel, François Nosten, Dennis E. Kyle, Francisco-Javier Gamo, Yingyao Zhou, Manuel Llinás, David A. Fidock, Dyann F. Wirth, Jeremy Burrows, Brice Campo, Elizabeth A. Winzeler*

INTRODUCTION: Malaria remains a devastating disease, affecting 216 million people annually, with 445,000 deaths occurring primarily in children under 5 years old. Malaria treatment relies primarily on drugs that target the disease-causing asexual blood stages (ABS) of *Plasmodium* parasites, the organisms responsible for human malaria. Whereas travelers may rely on short-term daily chemoprotective drugs, those living in endemic regions require long-term malaria protection such as insecticide-treated nets (ITNs) and vector control. However, ITNs do not fully shield individuals from malaria, may lose potency with time, and can be bulky and difficult to use. Another concern is that mosquitos may become resistant to the active insecticides that are used in ITNs and vector control.

RATIONALE: As the possibility of malaria elimination becomes more tangible, the ideal antimalarial medicine profile should include chemoprotection. Chemoprotective medicines typically work against the exoerythrocytic parasite forms that invade and develop in the liver and are responsible for the earliest asymptomatic stage of the infection. Such medicines could be formulated to provide long-acting prophylaxis, safeguarding individuals that are living near or traveling to areas that have been cleared of parasites. Long-acting chemoprotection in endemic regions could also greatly reduce circulating parasite numbers and potentially replace a vaccine in an elimination campaign. Although millions of compounds have been screened for activity against parasite ABS, and some have been subsequently tested for potential prophylactic activity, large-scale searches that begin with prophylactic activity have not been performed because of the complexity of the assay: This assay requires the production of infected laboratory-reared mosquitoes and hand-dissection of the sporozoite-infected salivary glands from mosquito thoraxes.

RESULTS: To discover leads for next-generation chemoprotective antimalarial drugs, we used luciferase-expressing *Plasmodium* spp. parasites, dissected from more than a million mosquitoes over a 2-year period, to test more than 500,000 compounds for their ability to inhibit liver-stage development of malaria (681 compounds showed a half-maximal inhibitory concentration of <1 μM). Cluster analysis identified potent and previously unreported scaffold families, as well as other series previously associated with chemoprophylaxis. These leads were further tested through multiple phenotypic assays that predict stage-specific and multispecies antimalarial activity. This work revealed compound classes that are likely to provide symptomatic relief from blood-stage parasitemia in addition to providing protection. Target identification by use of functional assays, in vitro evolution, or metabolic profiling revealed 58 mitochondrial inhibitors but also many chemotypes possibly with previously unknown mechanisms of action, some which may disrupt the host pathogen signaling.

CONCLUSION: Our data substantially expands the set of compounds with demonstrated activity against two known targets of chemoprotective drugs, cytochrome bc1 and dihydroorotate dehydrogenase. These present a rich collection of chemical diversity that may be exploited by members of the community seeking to accelerate malaria elimination with chemoprotection and chemoprophylaxis through open-source drug discovery. ■

ON OUR WEBSITE

Read the full article at http://dx.doi.org/10.1126/science.aat9446

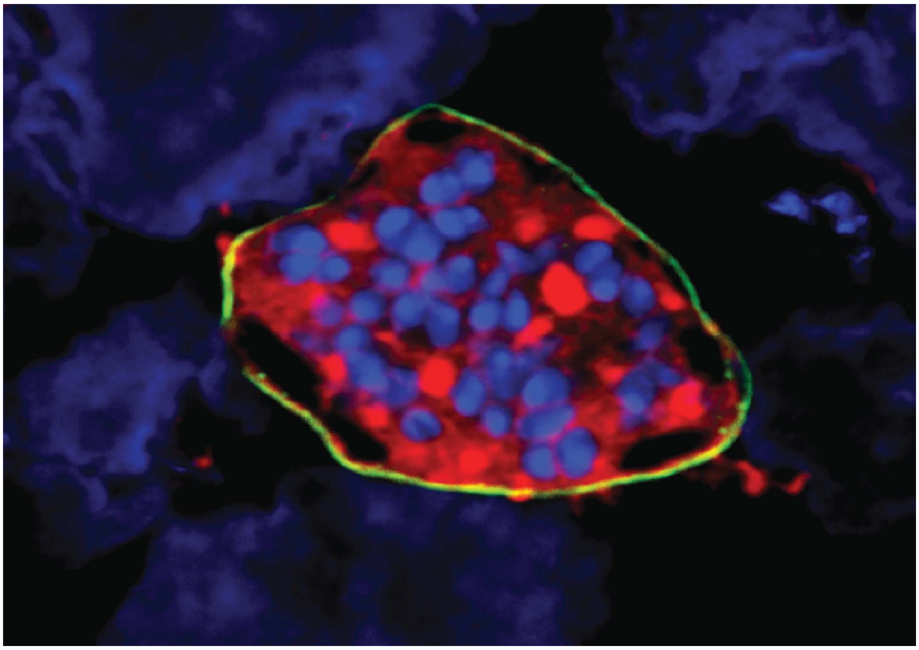

A *Plasmodium vivax* liver-stage schizont on a lawn of hepatocytes. The parasite schizont has been stained with antibodies to parasite HSP70 (red) and UIS4 (yellow). Cell (parasite and hepatoma) nuclei are shown in blue. This study identifies compounds that can prevent the development of these liver-stage parasites and may function as chemoprotective drugs for malaria.

The list of author affiliations is available in the full article online.

*Corresponding author. Email: ewinzeler@ucsd.edu

Cite this article as Y. Antonova-Koch *et al.*, *Science* **362**, eaat9446 (2018). DOI: 10.1126/science.aat9446

Downloaded from http://science.sciencemag.org/ on December 10, 2018

RESEARCH ARTICLE

ANTIMALARIALS

Open-source discovery of chemical leads for next-generation chemoprotective antimalarials

Yevgeniya Antonova-Koch[1], Stephan Meister[1]*, Matthew Abraham[1], Madeline R. Luth[1], Sabine Ottilie[1], Amanda K. Lukens[2,3], Tomoyo Sakata-Kato[3], Manu Vanaerschot[4], Edward Owen[5], Juan Carlos Jado Rodriguez[1], Steven P. Maher[6,7], Jaeson Calla[1], David Plouffe[8], Yang Zhong[8], Kaisheng Chen[8], Victor Chaumeau[9,10], Amy J. Conway[6,7], Case W. McNamara[8]†, Maureen Ibanez[8], Kerstin Gagaring[8]†, Fernando Neria Serrano[11], Korina Eribez[1], Cullin McLean Taggard[1], Andrea L. Cheung[1], Christie Lincoln[1], Biniam Ambachew[1], Melanie Rouillier[12], Dionicio Siegel[13], François Nosten[9,10], Dennis E. Kyle[6,7], Francisco-Javier Gamo[12], Yingyao Zhou[8], Manuel Llinás[5,14], David A. Fidock[4], Dyann F. Wirth[2,3], Jeremy Burrows[12], Brice Campo[12], Elizabeth A. Winzeler[1,13]‡

To discover leads for next-generation chemoprotective antimalarial drugs, we tested more than 500,000 compounds for their ability to inhibit liver-stage development of luciferase-expressing *Plasmodium* spp. parasites (681 compounds showed a half-maximal inhibitory concentration of less than 1 micromolar). Cluster analysis identified potent and previously unreported scaffold families as well as other series previously associated with chemoprophylaxis. Further testing through multiple phenotypic assays that predict stage-specific and multispecies antimalarial activity distinguished compound classes that are likely to provide symptomatic relief by reducing asexual blood-stage parasitemia from those which are likely to only prevent malaria. Target identification by using functional assays, in vitro evolution, or metabolic profiling revealed 58 mitochondrial inhibitors but also many chemotypes possibly with previously unidentified mechanisms of action.

Malaria remains a devastating disease, with 216 million annual cases and 445,000 deaths, primarily in children under 5 years old. Malaria treatment relies primarily on drugs that target the disease-causing asexual blood stages (ABS) of the parasite *Plasmodium falciparum*. These drugs include the 4-aminoquinolines piperaquine and amodiaquine, the antifolates pymimethamine and sulfadoxine, and the endoperoxides artemisinin and its derivatives artesunate, artemether, and dihydroartemisinin (*1*). Artemisinin-based combination therapies (ACTs, such as artemether-lumefantrine) are being used worldwide as first-line treatments (*1*).

Although estimated malaria mortality rates have decreased by 47% worldwide since 2000 (*1*), in Southeast Asia resistance has emerged to the artemisinins, and ACT treatment failures are rising (*2*). In anticipation of eventual widespread ACT failure, there has been a focused and coordinated effort to place new antimalarial candidates into the drug development pipeline (www.mmv.org/research-development/rd-portfolio) (*3*). However, in vitro resistance can be generated for most of these new classes in ABS parasites (*4*), suggesting that the antimalarial pipeline will require continuous replenishment.

An alternative approach is to create drugs that prevent malaria by inhibiting parasites during their initial stage of development in the liver before their initiation of symptomatic blood-stage infection. Using chemotherapy for prophylaxis is a well-established tool to prevent malaria caused by different *Plasmodium* spp. To prevent malaria, travelers may take oral atovaquone plus proguanil, doxycycline, or mefloquine. In endemic regions of seasonal malaria in West Africa, children are given SPAQ [sulphadoxine-pyrimethamine (SP) plus amodiaquine] as seasonal malaria chemoprevention, and pregnant women, who are the most vulnerable group, may also take SP for intermittent preventative therapy (*5*).

Drugs that selectively affect the developing liver stages of *P. falciparum* and the relapsing species, *Plasmodium vivax*, have the potential to engage new protein targets not present nor required in parasite blood stages. Such drugs could overcome both the problem of resistance and compliance. The number of parasites in the early liver stage are low (hundreds, versus billions in the blood stage), reducing the probability that drug resistance–conferring mutations might emerge. This feature could make these liver-active compounds suitable for chemoprotection and, with sufficient demonstrated safety, for mass drug-administration or malaria-elimination campaigns.

To identify chemoprotective candidates, we applied a liver-stage phenotypic screen to a library of >500,000 small molecules. Our data identify new scaffold families that exclusively target liver stages that may provide prophylactic protection, as well as new scaffolds that act against known targets such as dihydroorotate dehydrogenase (DHODH). These data comprise new leads for antimalarial open-source drug discovery.

Primary screening results

Previous high-throughput screens for antimalarial compounds have generally focused on the ABS, which can be readily cultured en masse (*6*–*8*). To discover hits with possible protective activity, blood stage–active compounds have been further retested against malaria hepatic stages, often using sporozoites from the rodent malaria species *Plasmodium yoelii* or *Plasmodium berghei* (*9*, *10*). Because there are no suitable methods for axenically culturing sporozoites (which are responsible for liver-stage infection), this retesting has required the production of infected laboratory-reared mosquitoes and hand dissection of the sporozoite-infected salivary glands from mosquito thoraxes. Despite this complex challenge, thousands of compounds have been examined by using this general workflow progression, leading to previously unidentified chemoprotective candidates, including KAF156 (*11*), KDU691 (*12*), DDD107498 (*13*), and BRD3444 (*14*). However, this approach would not reveal compounds that might protect from infection without affecting

Downloaded from http://science.sciencemag.org/ on December 10, 2018

---

[1]School of Medicine, University of California, San Diego, 9500 Gilman Drive 0760, La Jolla, CA 92093, USA. [2]Harvard T. H. Chan School of Public Health, 665 Huntington Avenue, Boston, MA 02115, USA. [3]The Broad Institute, 415 Main Street, Cambridge, MA 02142, USA. [4]Division of Infectious Diseases, Department of Microbiology and Immunology, Columbia University Medical Center, New York, NY 10032, USA. [5]Department of Biochemistry and Molecular Biology and Center for Malaria Research, Pennsylvania State University, University Park, PA 16802, USA. [6]Center for Tropical and Emerging Global Diseases, University of Georgia, 500 D. W. Brooks Drive, Athens, GA 30602, USA. [7]Department of Global Health, University of South Florida, 3720 Spectrum Boulevard, Tampa, FL 33612, USA. [8]The Genomics Institute of the Novartis Research Foundation, 10675 John J Hopkins Drive, San Diego, CA 92121, USA. [9]Shoklo Malaria Research Unit, Mahidol Oxford Research Unit, Faculty of Tropical Medicine, Mahidol University, Mae Sot, Thailand. [10]Centre for Tropical Medicine and Global Health, Nuffield Department of Medicine, University of Oxford, Oxford, UK. [11]Tres Cantos Medicines Development Campus, Malaria DPU, GlaxoSmithKline, Severo Ochoa 2, Tres Cantos 28760, Madrid, Spain. [12]Medicines for Malaria Venture, Post Office Box 1826, 20 Route de Pre-Bois, 1215 Geneva 15, Switzerland. [13]Skaggs School of Pharmacy and Pharmaceutical Sciences, University of California, San Diego, 9500 Gilman Drive 0741, La Jolla, CA 92093, USA. [14]Department of Chemistry and Center for Infectious Diseases Dynamics, Pennsylvania State University, University Park, PA 16802, USA.
*Present address: BioSero, San Diego, CA 92122, USA. †Present address: California Institute for Biomedical Research, La Jolla, CA, USA.
‡Corresponding author. Email: ewinzeler@ucsd.edu

blood stages nor identify compounds that modulate human hepatocyte targets and prevent parasite liver-stage development.

Recently, a screening method was developed that was suitable for testing many compounds against liver-stage parasites (*10*). This assay (*Pbluc*) relies on an antifolate-resistant *P. berghei* rodent parasite that constitutively expresses luciferase during the sporozoite stage (*15*). Sporozoites are dissected from mosquitoes, washed, and layered on confluent HepG2 cells that have been preincubated with compounds. If the parasites are able to establish a successful exoerythrocytic stage infection, even if only 1 to 2% of the hepatocytes are infected, the cultures will emit enough light in the presence of luciferin to be detected with sensitive instruments. Light intensity is proportional to parasite infection rate, and this simple assay can be run by using 1536-well plates. The *P. berghei* system has a distinct advantage over the human pathogen, *P. falciparum*, in that this parasite can infect a variety of hepatoma cell lines, which results in ease of use and reproducibility. Furthermore, the development period is only 48 hours, which means that hepatocyte cultures do not overgrow, and special coculture systems are not needed. Sporozoite yields are generally higher, and there are fewer biosafety precautions. In addition, because cellular detoxification systems have been generally lost from hepatoma cell lines, compounds remain potent, easing their discovery. The assay has shown to be very predictive of causal prophylactic activity. We thus sought to apply this screening method to a large library, with the goal of finding a larger selection of starting points for chemoprophylactic drugs.

Screening was conducted by using a library of 538,273 compounds from Charles River consisting of small molecules with an average weight of 369 Da (60.06 to 1298 Da). The library was mostly drug-like (versus probe-like), with an average logP of 3, an average number of hydrogen bond donors of 1.1, and 5.9 hydrogen bond acceptors. On average, each compound had 6.2 rotatable bonds; 5270 compounds were represented in duplicate or triplicate (table S1). Substantial structural redundancy was included in the library to establish structure-activity relationships in scaffold families. In contrast to many previously published studies (*6*–*8*), all the compounds in the library, including hits and negatives, have structures and are commercially available, facilitating use by the community.

The screen was run over an 18-month period, with ~20,000 compounds screened weekly (Fig. 1) to accommodate the time-consuming production of infected *Anopheles* mosquitoes. Each week, a team dissected ~1000 mosquitoes, from which the sporozoites were isolated and cleaned. Approximately 1000 sporozoites were added in a 5 μl volume per well plate by using a bottlevalve instrument to a lawn of HepG2-CD81 cells that had been prespotted into the 1536-well plates with 50 nl of compounds at 0.5 to 7.84 mM (Fig. 1). After a 48-hour incubation, luciferin was added, and luminescence was measured. Because a compound that kills hepatocytes could result in reduced luciferase signal (because parasites presumably need a live hepatocyte for intracellular survival), we also tested a randomly selected subset of the compounds (~179,600) for hepatocyte toxicity using a Cell-Titer Glo assay (materials and methods) that measures the number of viable cells based on the amount of adenosine 5′-triphosphate (ATP) that is present (*HepG2tox*).

Cheminformatic analysis of the primary screen

After collating the data and ranking the percentage inhibition for 538,273 compounds from the 1536-well screen, 64,172 compounds showed inhibition of >50%, and 21,336 showed inhibition levels of >75% (Fig. 1). Although a higher-than-normal number of false positives and negatives is expected for a single-point screen (data may be affected by edge effects, transfer errors, or variation in dispense volumes), the initial screen was informative. For example, the library included 197 ABS-active compounds that had been previously tested in a high-content imaging screen of *P. yoelii* liver stages (*9*), including 18 compounds with activity of less than 10 μM (data file S1). Of those, 15 showed >50% inhibition in the primary screen. Likewise, the majority of compounds that were considered inactive in the high-content imaging screen showed <75% inhibition here (129 out of 163) (data file S1).

To further evaluate the quality of the primary *Pbluc* data, we performed compound clustering (Fig. 2 and data file S2). We hierarchically clustered all 538,273 compounds in the primary screen and separated clusters using a minimum Tanimoto coefficient of 0.85 similarity (materials and methods). From this, we identified 281,090 compound clusters, with an average hit fraction of 0.016 ± 0.112. We calculated the probability of hit enrichment (>83% inhibition in *Pbluc*) by chance for each cluster (data file S2). Not unexpectedly, certain scaffold families with known activity against *Plasmodium* liver stages, such as the phosphatidylinositol-4-OH kinase (PI4K)–inhibiting imidazopyrazine family (*12*), included a high proportion of highly active compounds. For example, with an imidazopyrazine group (family 227215), 11 of the 14 members were highly active [average 81.1%, $\log_{10}$ probability of distribution by chance ($\log_{10}$ p) = –15.16] (Fig. 2A), and these were similar to the known imidazopyrazine KDU691 (*12*). Likewise, scaffold family 37533 consisted of four members where all four members in the library were more than 80% active (average 88.4%). All were very similar to MMV390048, another PI4K inhibitor (Fig. 2B). Atovaquone-like scaffolds (cluster 68966) were also present in the library and active at rates higher than expected by chance (eight of nine members active, $\log_{10}$ p = –10.88) (Fig. 2C). The hit fractions of cluster 69866, 37533, and 227215 (0.89, 0.75, and 0.79, respectively) are all in the top 1.1 percentile when considering the entire library.

Several additional scaffold families with known activity against malaria parasites were also found in the library and showed activity, although these families would not have been discovered with cluster analysis at the similarity thresholds used. For example, cycloguanil (83.4% inhibition) was found to be active in the 538,273-compound library but had only one close relative (> 85% Tanimoto similarity), which was not active ($\log_{10}$ p = –1.31). Relaxing the stringency, however, revealed three other relatives, one of which was also primary hit ($\log_{10}$ p = –2.42) (Fig. 2E). Likewise, compounds similar to DSM265 (*16*) and DDD107498 (Fig. 2, F and G) (*13*), two other potent compounds with nanomolar activity against exoerythrocytic stages, were also identified through relaxed similarity searching but were in clusters that might have arisen through chance (MMV011256, one of three active, $\log_{10}$ p = –1.35; MMV1478835, two of nine active, $\log_{10}$ p –1.40; MMV1370261, one of two active, $\log_{10}$ p = –1.50) or were singletons (MMV1386820).

Reconfirmation

To obtain a reasonable working set for reconfirmation (9989 compounds), we selected compounds that showed >83% *Pbluc* inhibition and *HepG2tox* of less than 50%, when available (data file S3). Cut off and filtering criteria did not bias physicochemical properties of primary hits, whose subset compounds had similar properties to the larger library, with weights of 388 Da (985.1 to 136.2), 1.1 hydrogen bond donors, 5.5 hydrogen bond acceptors, and 5.9 rotatable bonds on average (fig. S1 and table S2). To confirm primary hits, the location of wells with possible active compounds were identified, and then a hit-picking instrument was used to reassemble a collection for reconfirmation (data file S3). We arrayed these hit compounds in eight-point dose-response format (5 nM to 10 μM) and reassessed their potency and efficacy in duplicate in three different assays—including the *Pbluc* assay, the *HepG2tox* assay, and a counterscreen—to test whether a given compound would inhibit firefly luciferase in a biochemical assay (*Ffluc*). Altogether, complete *Pbluc* dose-response curves could be fitted for 5942 compounds [half-maximal inhibitory concentration (IC_{50}) < 15.4 μM, average 4.71 μM], and 681 showed complete *Pbluc* inhibition at all tested concentrations (18 compounds) or an IC_{50} of <1 μM (663 compounds) (data file S3). However, of the 5942 reconfirmed hits, 790 demonstrated moderate inhibition of hepatocyte viability [*HepG2tox* CC_{50} (50% cytotoxicity concentration) < 2X *Pbluc* IC_{50} and *HepG2tox* CC_{50} < maximum tested concentration], and 465 of these also interfered with firefly luciferase production (*Ffluc* IC_{50} < 2X *Pbluc* IC_{50} and *Ffluc* IC_{50} < maximum tested concentration) (data file S3).

Adding these data to our cluster analysis (Fig. 2) showed enrichment of false positives arising from the use of luciferase as a surrogate for parasite development. For example, 526 scaffolds of the imidazopyridine-carboxamide group (128188) were found in the library of 538,273 compounds, of which 145 were in the hit list ($\log_{10}$ p < –100) (data file S2). Of these, 116

Downloaded from http://science.sciencemag.org/ on December 10, 2018

showed biochemical luciferase inhibition <10 μM (29 less than 1 μM) (data files S2 and S3). Visualization showed that other less abundant scaffolds, such as those in cluster 30984 or 4198, also showed enrichment of luciferase activity at higher rates than expected by chance (Fig. 2 and data file S2). Likewise, some enriched scaffold families ($\log_{10}$ p = −14.45) were clearly toxic to human cells (cluster 95979) (Fig. 2 and data file S2).

To further establish the integrity of the hits, we next assembled a collection of compounds for third-round, independent testing. The nontoxic second round hits were filtered through the general medicinal chemistry compound filters by using Biovia ScienceCloud. This filtering removed 619 compounds that either failed Lipinski's rule of 5 (based on calculated properties) as a surrogate for "drug-like"; had structural features consistent with high chemical reactivity or instability; had a high likelihood of nonspecific covalent interaction, such as thiourea; or was an enone, which would react with nucleophiles such as thiols or disrupt disulphide bonds (17). The remaining set was then prioritized on the basis of potency (IC_{50}) and calculated lipophilicity (cLogP), yielding 953 compounds prioritized as follows: 445 actives with IC_{50} < 1 μM (most potent—no additional cLogP filter), 268 actives >1 μM but clogP < 2.5 (low lipophilicity compounds with lower potency), and 240 actives >1 μM but 2.5 < clogP < 3 (as above, with moderate lipophilicity).

With this set of 953 compounds, we interrogated the databases of commercially available compounds for acquisition, confirmation, and further profiling; 631 (repurchased validation set) were available and thus further characterized (data file S4). These compounds were

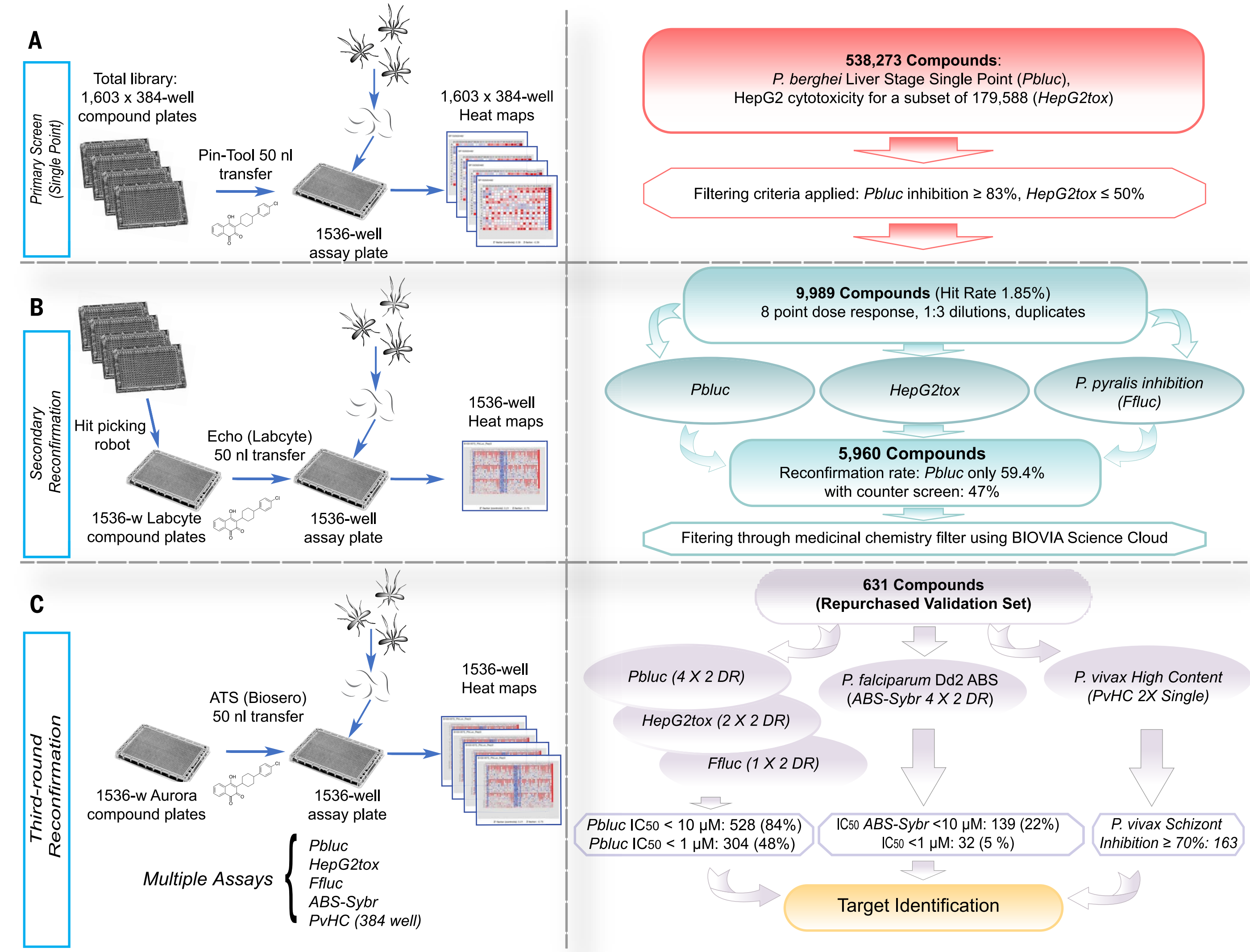

Fig. 1. Screen workflow. (**A**) The Charles River library (538,273 compounds) was plated into 1603 384-well plates. For the primary *Pbluc* single-point screen, compounds from four of the 384-well plates were transferred with a pin-tool instrument (50 nl per well) into 1536-well assay plates containing seeded HepG2 cells (3×10^3 cells per well). The next day, *P. berghei* luciferase–expressing sporozoites were freshly prepared from infected *Anopheles stephensi* mosquitoes, and ~1000 sporozoites in a 5 μl volume were added to each well. After 48 hours, *P. berghei*–Luc growth within hepatocytes was measured with bioluminescence. (**B**) To prepare source plates for the first round of reconfirmation (second round of screening), the 9989 hit compounds were transferred from the original 384-well library with an automated hit-picking system and serially diluted into eight points (1:3 dilutions) for dose-response screening in duplicate. The hit compounds (50 nl per well) in serial dilutions were acoustically transferred into assay wells containing HepG2 cells for *Pbluc* and *HepG2tox* assays. In addition, biochemical recombinant luciferase inhibition assay (*Ffluc*) were also performed. (**C**) For final reconfirmation (third round), 631 compounds prepared from re-sourced powders and were serially diluted (10 points, 1:3 dilution) and plated into Aurora 1536-well compound plates. Compounds (50 nl per well) were acoustically transferred into 1536-well assay plates. Multiple dose-respose assays such as *Pbluc*, *HepG2tox*, *Ffluc*, and *ABS-Sybr* were performed to determine IC_{50} in the third round of screening. A *P. vivax* liver schizont formation high-content assay in single-point (2X) was also performed.

Downloaded from http://science.sciencemag.org/ on December 10, 2018

arrayed within the 1536-well plate format into 10-point dose response, tested in duplicate (technical replicates), and counterscreened in multiple different assays, repeated up to four times with different sporozoite batches. Two separate *HepG2tox* assays and one *Ffluc* also were performed. Retesting showed a high reconfirmation rate (82% with an average *Pbluc* IC$_{50}$ < 10 μM) and 376 compounds with *Ffluc* IC$_{50}$ and *HepG2tox* CC$_{50}$ < 2× *Pbluc* IC$_{50}$ (fig. S2). All compounds were also tested in dose-response format against ABS of the multidrug-resistant *P. falciparum* Dd2 strain, using a standard SYBR green incorporation blood-stage assay that identifies compounds that prevent growth and development (*ABS-Sybr*; four biological replicates) (*6*).

Activity against *P. vivax*

To better understand species specificity, the aforementioned repurchased validation set (631), reconfirmed in eight-point dose assays with *Pbluc*, was also tested against the human pathogen *P. vivax*. For this, we used a single-point high-content imaging screen (*PvHCI*), with primary human hepatocytes maintained in 384 well plates. Hepatocytes were inoculated with *P. vivax* sporozoites dissected from mosquitoes fed with blood obtained from malaria patients. The following day, compounds were added to a final concentration of 10 μM and then reapplied at days 2 and 3 and 4. After compound treatment, cultures were fixed on day 6 after infection, stained with immunoreagents against PvUIS4 (materials and methods), and we performed high-content imaging and analysis to score each well for growth of liver schizonts. Of the 631 compounds screened in this single-point assay, 163 were confirmed to inhibit *P. vivax* schizont growth by at least 70% (normalized to positive control KDU691) (data file S4) in at least one of two biological replicates, and 91 were confirmed in both replicates (fig. S2). This confirmation rate was achieved despite several critical differences between the rodent and human assays, including hepatic metabolism of unoptimized compounds and addition of compound on day 1 after infection (*PvHCI*) instead of preinfection (*Pbluc*). Furthermore, 12 compounds (fig. S2) were considered not reconfirmed in a third round of *P. berghei* testing but were nevertheless still active in *P. vivax* (for example, MMV1288041 inhibited *P. vivax* by 100% in both replicates and had an IC$_{50}$ of *P. berghei* 3.27 μM in second-round testing), highlighting how experimental design and analysis constraints (for example, curve-fitting compounds that did not fully inhibit growth in *Pbluc* at 10 μM, the highest concentration tested, would be considered "not confirmed") could lead to possible false negatives. On the other hand, compounds could lose potency over repeated use

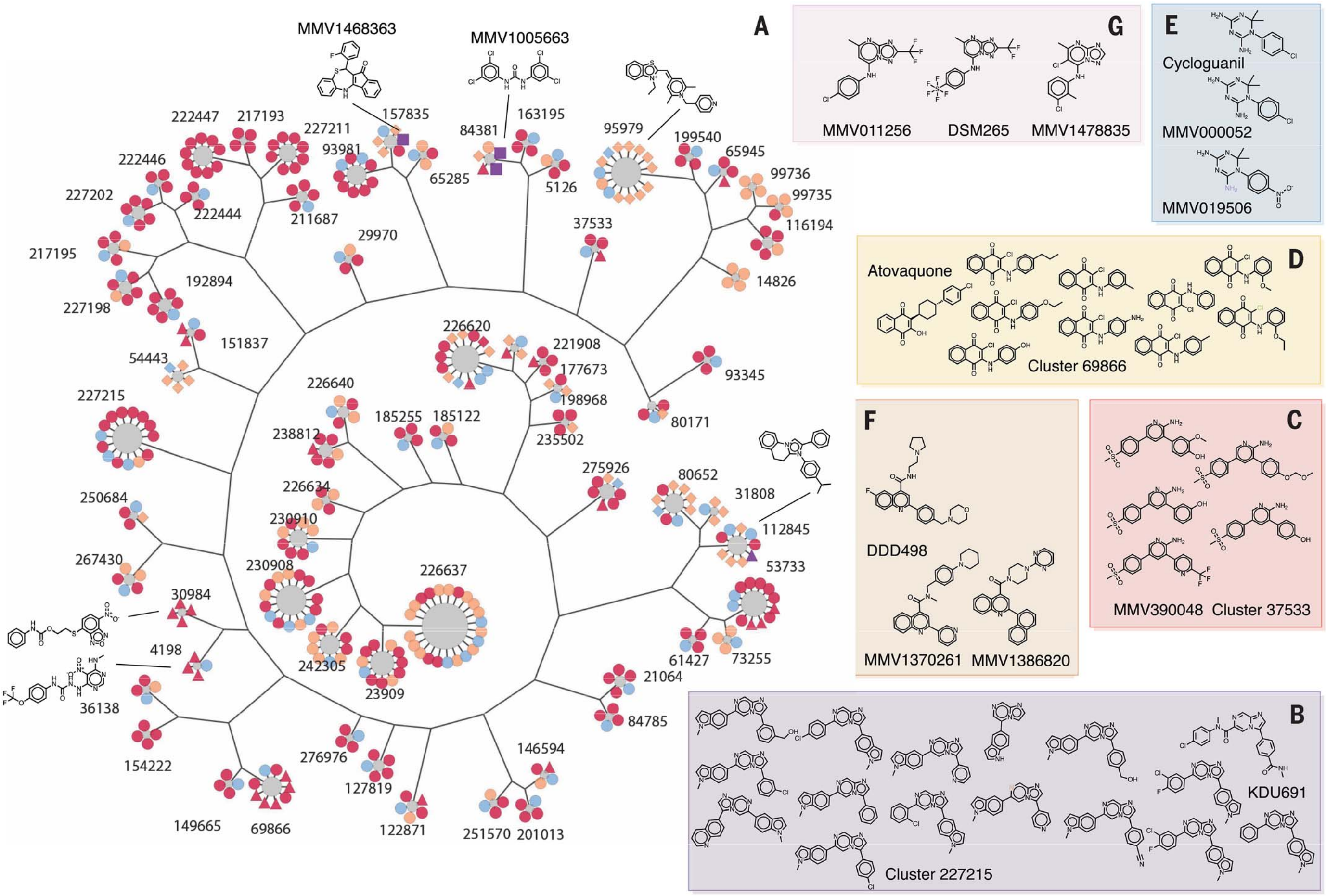

Fig. 2. Cluster analysis. (**A**) For display, 405 compounds from 68 clusters that show a *P* value ≤ 0.05, cluster size ≥ 4, and hit fraction ≥ 0.75 are presented (data file S2). Most common substructure (MCS) per cluster is identified by using the top three active compounds, and a hierarchical tree was constructed from the MCSs to illustrate the intergroup connection. Compound members were then added to surround MCS nodes. All compound nodes are colored by hit status and shaped by other annotations. Primary hits are orange, reconfirmation hits (*Pbluc* IC$_{50}$ < 10 μM) are red, third-round reconfirmation set (631 compounds) is purple, and others are light blue. *P. falciparum* asexual blood state–active compounds (*ABS-Sybr* IC$_{50}$ < 10μM) are indicated by squares, luciferase inhibitors (*Ffluc* IC$_{50}$ < *Pbluc* IC$_{50}$ / 2) are indicated by triangles, hepatocyte toxic (primary *HepG2tox* > 50% or *HepG2tox* CC$_{50}$ < *Pbluc* IC$_{50}$ / 2) are indicated by diamonds, and the rest are shown as circles. (**B** to **G**) Active compounds in selected clusters [(B), (C), and (D)] with hit fractions of less than 0.75, as well as examples of singleton hits that are similar to the known antimalarial compounds, (E) cycloguanil, (F) DDD107498 (*13*), and (G) DSM265 (data file S3) (*16*).

Downloaded from http://science.sciencemag.org/ on December 10, 2018

owing to freeze-thaw and hydration, there could be differences in liver-stage schizogony between *P. vivax* and *P. berghei* (liver schizonts produce far greater quantities of liver merozoites over six additional days of development in comparison to the 72-hour liver cycle of *P. berghei*), and the wild-type *P. vivax* may be more drug-sensitive than *P. berghei*–ANKA-GFP-Luc-SM_{CON} or *P. falciparum* Dd2, both of which are resistant to some antifolates.

Activity against *P. falciparum* blood stages

To further study the function of the third-round compounds, we next tested whether the repurchased validation set of 631 would be active against *P. falciparum* ABS parasites. The active set showed several known chemotypes. One example, MMV1468363, showed a high degree of similarity to tetracyclic benzothiazepines, which are known cytochrome bc1 inhibitors (*18*). There were seven closely related members of the tetracyclic benzothiazepines scaffold family in the larger library, and six of the seven showed inhibition rates of greater than 85% in the primary screen ($\log_{10}$ p = –7.969, cluster 157835) (Fig. 2). Another recognizable scaffold was that of MMV1005663, similar to the possible FabI inhibitor trichlocarban, as well as the liver stage–active malaria box member, MMV665852 (*19*). This latter compound is associated with amplifications of the gene encoding phospholipid flippase, *pfatp2* (*19*). This compound series (cluster 84381) was represented multiple times in the library, with all five tested members showing strong inhibition (average 93%, $\log_{10}$ p = –7.34) in the primary screen (Fig. 2).

Three hundred ninety-eight liver-active compounds were inactive in *P. falciparum ABS-Sybr* (average IC_{50} of > 10 μM) (fig. S2), highlighting the rich new untapped chemical space that was sampled by using this screening cascade when compared with the ABS-first cascade. Although some could be due to species-specific activities, 130 compounds were active against both *P. vivax* (in at least one replicate) and *P. berghei* schizonts (fig. S2) but were inactive against ABS. Although our use of antifolate-resistant *P. berghei* and a multidrug-resistant *P. falciparum* strain may influence this result, most of these scaffolds likely affect parasite or human processes that exist only in the hepatic stages. These scaffolds generally did not show any similarities to known antimalarials, but several of these were supported by strong statistical overrepresentation in the primary screen (Fig. 2 and data file S2). For example, seven of the nine members of the imidazoquinoline cluster (112845) were active in the primary screen ($\log_{10}$ p = –8.89) (Fig. 2).

Mechanism of action studies reveal an abundance of mitochondrial transport chain inhibitors

To further investigate the mechanism of action of 13 of the most potent ABS hits (Fig. 3A), we acquired additional compound from commercial vendors. Because most, if not all, target identification methods require activity in *P. falciparum* blood stages, all compounds selected for initial target discovery were active against ABS parasites, with an average IC_{50} of 465 nM (range of 13 nM to 1.2 μM).

As an initial pass, we first subjected the compounds to metabolic profiling (*20*). This liquid chromatography–mass spectrometry (LC-MS)–based method measures several hundred metabolites and identifies those that show statistically significant increases or decreases upon parasite compound exposure (data file S5). Whereas three gave ambiguous results, 10 of the 13 analyzed scaffolds gave a metabolic profile signature analogous to that of atovaquone (fig. S3), indicating that these 10 most likely interfere with one or more targets in the mitochondrial electron transport chain (mETC), a known druggable pathway for *P. falciparum* blood and liver stages (Fig. 3A). The set of 13 compounds represents 11 distinct scaffolds (Fig. 3B), so this degree of functional overlap would not have been predicted by structure alone. To our knowledge, none of the molecules have been previously identified as acting against the mitochondrial electron transport pathway.

To further confirm that these 10 compounds (representing eight chemotypes) inhibited the mETC, we took advantage of a transgenic parasite line that overexpresses the *Saccharomyces cerevisisae* dihydroorotate dehydrogenase (Dd2-ScDHODH) (*21*). Unlike the type-2 *P. falciparum* enzyme that is dependent on cytochrome bc_1 for ubiquinone, the cytosolic type-1 yeast enzyme can use fumarate as an electron acceptor. This allows the transgenic parasites to bypass the need for ETC activity to provide ubiquinone to PfDHODH (*21*). Compounds that target PfDHODH or other enzymes along the mETC lose potency in the Dd2-ScDHODH transgenic cell line. As expected, the Dd2-ScDHODH parasites show marked (24.8 to >1000-fold) resistance to the 10 compounds with the mETC metabolic profile (Fig. 3C and table S3). Furthermore, a variation of this functional assay can distinguish between inhibitors of PfDHODH and cytochrome bc1. Specifically, the addition of proguanil to Dd2-ScDHODH parasites restores the inhibitory capabilities of cytochrome bc1 inhibitors; however, growth is not affected in the case of PfDHODH inhibitors. Three out of six mitochondrial inhibitors tested in these conditions were not inactivated by proguanil, suggesting a profile consistent with PfDHODH inhibition (Fig. 3C and table S4). To further investigate mitochondrial inhibition, and because there are multiple potential targets, we used an in vitro evolution and whole-genome analysis (IViEWGA) approach (*22*) to further elucidate the molecular target of several of the compounds, including MMV1454442, MMV1432711, and MMV142795. First, three independent lines resistant to MMV1454442 were isolated after growing in sublethal concentrations of compound. The resistant clones showed an average 4.2-fold shift in the IC_{50} (range of 1.9 to 9.4) (table S5). Whole-genome sequencing of the nine clones (three each from three independent selections), as well as the drug-sensitive parent clone to 78-fold coverage (table S6), revealed that the resistant lines carried either a single-nucleotide variant $Phe^{188}Ile$ (Fig. 3D and data file S6) or a copy number variant (table S8) in *P. falciparum* dihydroorotate dehydrogenase (PF3D7_0603300), which is a well-validated drug target in *P. falciparum* (*16*). This result is consistent with proguanil not affecting growth inhibition in Dd2-ScDHODH parasites (Fig. 3C). MMV1454442, an amino-triazol, although somewhat similar to a pyrrole-based DHODH inhibitor (*23*), is a previously unidentified chemotype, which would not have been predicted with structural information alone. The Phe^{188} residue is located in the species-selective inhibitor-binding pocket of PfDHODH (*24*) and has been shown to be in contact with the known DHODH inhibitor leflunomide (*25*) and the triazolopyrimidine DSM338 (Fig. 3D) (*26*). Furthermore, mutation of this residue has been shown to confer resistance to the alkylthiophene inhibitor Genz-669178 (*27*), suggesting that MMV1454442 likely shares the same space (Fig. 3D).

IViEWGA of MMV1432711-resistant parasites revealed they had acquired one of two nonsynonymous single-nucleotide variants (SNVs) in the gene encoding cytochrome b (data file S7). The amino acid mutations found, $Tyr^{126}Cys$ and $Val^{259}Leu$, are located within helix C in the ubiquitinol-binding pocket of cytochrome b, a catalytically important subunit of the cytochrome bc_1 complex that contains two reaction sites, Q_o (ubiquitinone reduction site) and Q_i (ubiquitinol oxidation site). MMV1432711 has a chemical scaffold similar to that of the Q_i inhibitors, so we used a homology model of PfCYTb (Fig. 3E) to resolve the mode of binding. Docking into the model showed that MMV1432711 is likely a class II inhibitor. The allele Y126C was previously reported to confer resistance to decoquinate (*28*) and MMV008149 (*29*). To our knowledge, allele $Val^{259}Leu$ has not been reported in the literature.

For compound MMV1427995 {2-[(5,6-diphenyl-1,2,4-triazin-3-yl)thio]-1-(pyrrolidin-1-yl)propan-1-one}, in vitro evolution studies yielded two resistant lines that were cloned for further phenotyping and whole-genome sequencing (tables S5 and S6). Clones showed an average 2.6-fold IC_{50} shift (range of 1.8- to 3.4-fold) in susceptibility to MMV1427995 (table S5). Sequencing revealed that both clones carried the amino acid mutation, $Arg^{95}Lys$, in cytochrome b, located in the matrix-oriented region of the protein after the second transmembrane domain (Fig. 3E and data file S6). One clone also carried an additional $Pro^{102}Thr$ mutation in cytochrome c oxidase subunit 1. This mutation is located between the second and third transmembrane domain, is not located in any of the iron or copper redox centers, and is, to our knowledge, the first described mutation in cytochrome c oxidase selected for during compound exposure. However, this mutation did not induce a higher resistance level than did the $Arg^{95}Lys$ mutation alone and may thus represent a compensatory mutation. MMV1427995 is a different scaffold family (also overrepresented in the initial set of screening hits) from known

Downloaded from http://science.sciencemag.org/ on December 10, 2018

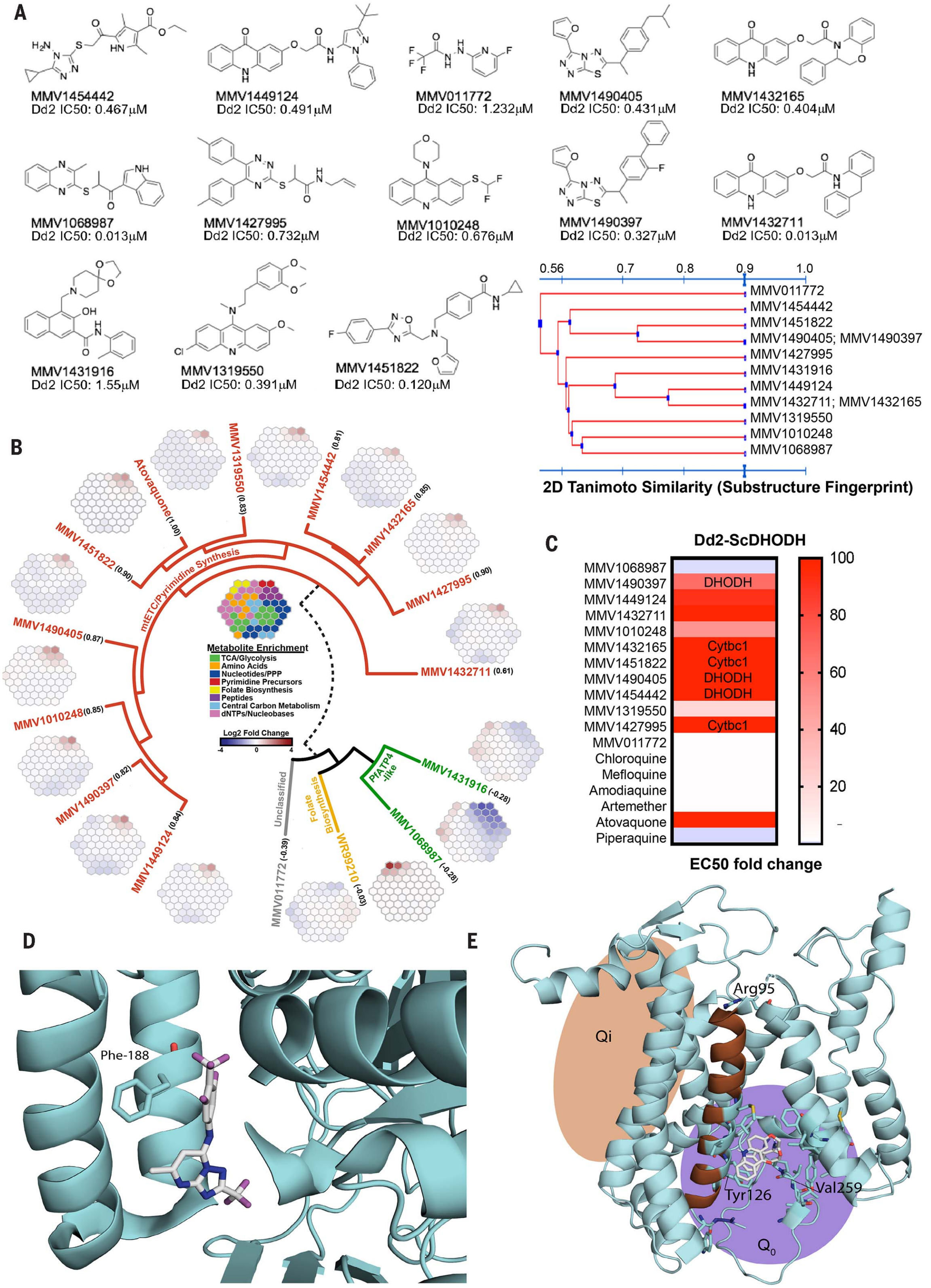

Fig. 3. Target identification studies. (**A**) Chemical structures and IC_{50} of select antimalarial compounds identified as hits. Tanimoto clustering demonstrates that most molecules are structurally distinct, although some share similar scaffolds. (**B**) Metabolomic analysis reveals that 10 of the 13 compounds likely target the mETC and pyrimidine biosynthesis pathways. Robust increases in pyrimidine biosynthesis precursors *N*-carbamoyl-L-aspartate (CA) and dihydroorotate (DHO) are signatures of metabolic disruption of de novo pyrimidine biosynthesis. The metaprints for MMV1068987 and MMV1431916 are similar to the metaprint of the PfATP4 inhibitor KAE609, whereas the metaprint for MMV011772 is inconclusive. The numbers below each compound name indicate the Pearson correlation with an atovaquone profile (fig. S3). (**C**) IC_{50} of each compound in Dd2 cells expressing *S. cerevisiae* DHODH normalized to parent. The transgenic Dd2-ScDHODH strain expresses the cytosolic type 1 DHODH from *S. cerevisiae* (ScDHODH) and is resistant to *P. falciparum* mETC inhibitors. Ablation of compound activity in this cell line relative to its parent indicates inhibition of DHODH or downstream effectors in the mETC such as Cytbc1. Atovaquone, a known Cytb inhibitor, was included as a positive control, whereas other licensed antimalarials with mETC-independent mechanisms of action serve as negative controls. (**D**) Location of $Phe^{188}Ile$ mutation found in whole-genome sequences of MMV1454442-resistant parasites by using a crystal structure of PfDHODH (4ORM) (27). Amino acid residue 188 is highlighted in magenta. The structure shows a known PfDHODH inhibitor, DSM338 (27), cocrystalized with the protein. (**E**) Homology model of PfCytb (from PDB 1BE3) (35) with $Tyr^{126}Cys$ and $Val^{259}Leu$ mutations (highlighted in magenta) from MMV1432711-resistant parasites. The Arg^{95} has previously been implicated in atovaquone binding and resistance (36).

Downloaded from http://science.sciencemag.org/ on December 10, 2018

P. falciparum cytochrome bc1 inhibitors, and its target would not have been predicted through similarity searching.

Given the high number of mitochondrial inhibitors in the dataset, we further examined the set of 631 compounds (repurchased validation set). All 631 compounds were tested in duplicate in eight-point ABS dose response in two *P. falciparum* D10–derived lines (*21*), one of which expresses ScDHODH (fig. S4 and data file S7) in the presence and absence of 1 μM proguanil in duplicate (~80,000 data points). Of the 136 compounds with ABS activity, visual inspection showed that 78 were likely not mitochondrial inhibitors, and 58 showed profiles consistent with mitochondrial inhibition (figs. S4 and S5 and data file S7). Of these, 10 were clear DHODH inhibitors (including the three shown in Fig. 3), one was a potential DHODH inhibitor, and 47 were likely or possible cytochrome bc1 inhibitors (including all nine from Fig. 3 that were tested). Strong nonrandom structure-activity relationships are evident (fig. S5), validating the assay. For example, six of the seven compounds that were more than 55% similar to MMV1042937 (fig. S5, fourth row) in the set of 631 were predicted to be cytochrome bc1 inhibitors ($\log_{10}$ p = –6.09). The seventh, MMV1457596, was missed because the IC_{50} were all >10 μM, but visual inspection of the curves showed an ~75% reduction in signal at 10 μM for the ScDHODH line relative to the PfDHODH line (data file S7).

Discussion

Previous open-access high-throughput screens have had a great impact on malaria research, and we anticipate that our data provide a rich resource in the search for new antimalarials. Despite the reliance on a nonhuman malaria species for screening, the repeated rediscovery of chemotypes with known, potent activity against *P. falciparum* blood stages and *P. vivax* liver schizonts, or clinical efficacy in humans, shows that the data from this rodent malaria model are predictive. Furthermore, liver schizonticidal activity is a required component of next-generation antimalarials proposed by Medicines for Malaria Venture, critical components of which include prophylactic and chemoprotective liver-stage efficacy after single exposure (TCP4) (*30*). Another advantage of the *Pbluc* assay is the reduced metabolic capacity of the host cells used; this should result in a higher hit rate with metabolically liable compounds in a high-throughput phenotypic screen. Last, although it is possible that some compounds were missed through the use of a rodent parasite, rodent malaria remains an efficient and important in vivo model for drug efficacy testing; compounds that do not act in this model would be costlier to progress into animal causal prophylaxis testing. In addition, some of the compounds that have activity here may eventually show activity against *P. vivax* hypnozoites, and if a radical cure chemotype is to be found, its discovery would be made much more likely through elimination of liver schizont-inactive compounds. The use of the low-cost rodent model allowed a much higher number of compounds to be evaluated than would be possible with human parasites, which can be difficult and expensive to acquire. The large size of the library used here facilitated compound clustering and allowed a probabilistic identification of active families.

The high number of parasite mitochondrial inhibitors (57) that were discovered with combined target identification methods is perhaps not surprising given that compounds were selected for target identification on the basis of potency, and substantial work has shown that mitochondrial inhibitors are very potent antimalarials. Nevertheless, the dataset contains a rich set of other ABS scaffolds that could still be good starting points for medicinal chemistry efforts designed to improve potency, selectivity, and reduced toxicity. The picomolar inhibitor and clinical candidate KAE609 was derived from an ~90 nM IC_{50} starting point that was discovered in a high-throughput ABS screen (*31*).

Although our target identification efforts showed that several compounds with activity across species were mostly in known target classes, a much larger number of compounds were active in the liver stages and had no activity in the blood stages. These presumably act against host pathways that the parasite requires for development, or alternatively, the infected cell may be weakened by the presence of a parasite and be more susceptible to killing by compounds that target essential host cellular processes. It is worthwhile to mention that because there are no reported antimalarial compounds with exclusive prophylactic activity, and methods for target identification are not readily available for compounds that do not act in the blood stage, we are unable to conclude much about their mechanism of action. Nevertheless, the scaffolds should still represent important starting points for prophylaxis stage drugs and exploring new mechanism of actions.

In theory, liver-stage antimalarial compounds could function as more cost-effective "chemical vaccines" that could replace conventional vaccines in malaria-elimination campaigns, provided sufficient safety. A fully protective conventional vaccine has never been developed for malaria (*32*); vaccines are very species-specific (and potentially strain-specific), whereas chemotherapy is generally not, and vaccines, which typically consist of recombinant protein or a heat-killed organism, require maintenance of a cold chain. In the case of the irradiated or attenuated cryopreserved sporozoite vaccine (*33*), the cost of goods (sporozoites that are hand-dissected from infected mosquitoes) will be much higher than a small-molecule therapy. We estimate that it costs 10 cents per well to create the 1000 sporozoites needed for one well of a 1536-well plate. Creating enough sporozoites to immunize a human would cost many times this amount.

In an analogous situation, long-acting, injectable HIV drugs have now been developed, and their deployment may help to prevent the spread of the HIV virus (*34*). Such intramuscular or subcutaneous chemoprotection injections or "chemical vaccines" can be deployed in resource-poor settings, and patient compliance is not as much of an issue as with standard, orally available tablet drugs. Because the injectable typically consists of a small molecule, refrigeration and maintenance of a cold chain may not be needed. The cost of goods for an injectable that needs to be supplied once every 1 to 3 months will most likely be lower than the cumulative cost of a tablet that needs to be taken every day, even considering the cost of a syringe and a health care worker to provide delivery. There are also other low-cost delivery methods, such as patches. Thus, it seems entirely feasible that a contribution to the eradication of malaria could come through the use of a long-acting chemical vaccine.

Materials and methods

A detailed description is provided in the supplementary materials.

REFERENCES AND NOTES

1. World Health Organization (WHO), *World Malaria Report 2017* (WHO, 2017).
2. B. Blasco, D. Leroy, D. A. Fidock, Antimalarial drug resistance: Linking *Plasmodium falciparum* parasite biology to the clinic. *Nat. Med.* **23**, 917–928 (2017). doi: 10.1038/nm.4381; pmid: 28777791
3. M. A. Phillips *et al*., Malaria. *Nat. Rev. Dis. Primers* **3**, 17050 (2017). doi: 10.1038/nrdp.2017.50; pmid: 28770814
4. E. L. Flannery, D. A. Fidock, E. A. Winzeler, Using genetic methods to define the targets of compounds with antimalarial activity. *J. Med. Chem.* **56**, 7761–7771 (2013). doi: 10.1021/jm400325j; pmid: 23927658
5. J. R. Matangila, P. Mitashi, R. A. Inocêncio da Luz, P. T. Lutumba, J. P. Van Geertruyden, Efficacy and safety of intermittent preventive treatment for malaria in schoolchildren: A systematic review. *Malar. J.* **14**, 450 (2015). doi: 10.1186/s12936-015-0988-5; pmid: 26574017
6. D. Plouffe *et al*., In silico activity profiling reveals the mechanism of action of antimalarials discovered in a high-throughput screen. *Proc. Natl. Acad. Sci. U.S.A.* **105**, 9059–9064 (2008). doi: 10.1073/pnas.0802982105; pmid: 18579783
7. W. A. Guiguemde *et al*., Chemical genetics of *Plasmodium falciparum*. *Nature* **465**, 311–315 (2010). doi: 10.1038/nature09099; pmid: 20485428
8. F. J. Gamo *et al*., Thousands of chemical starting points for antimalarial lead identification. *Nature* **465**, 305–310 (2010). doi: 10.1038/nature09107; pmid: 20485427
9. S. Meister *et al*., Imaging of *Plasmodium* liver stages to drive next-generation antimalarial drug discovery. *Science* **334**, 1372–1377 (2011). doi: 10.1126/science.1211936; pmid: 22096101
10. J. Swann *et al*., High-throughput luciferase-based assay for the discovery of therapeutics that prevent malaria. *ACS Infect. Dis.* **2**, 281–293 (2016). doi: 10.1021/acsinfecdis.5b00143; pmid: 27275010
11. K. L. Kuhen *et al*., KAF156 is an antimalarial clinical candidate with potential for use in prophylaxis, treatment, and prevention of disease transmission. *Antimicrob. Agents Chemother.* **58**, 5060–5067 (2014). doi: 10.1128/AAC.02727-13; pmid: 24913172
12. C. W. McNamara *et al*., Targeting *Plasmodium* PI(4)K to eliminate malaria. *Nature* **504**, 248–253 (2013). doi: 10.1038/nature12782; pmid: 24284631
13. B. Baragaña *et al*., A novel multiple-stage antimalarial agent that inhibits protein synthesis. *Nature* **522**, 315–320 (2015). doi: 10.1038/nature14451; pmid: 26085270
14. N. Kato *et al*., Diversity-oriented synthesis yields novel multistage antimalarial inhibitors. *Nature* **538**, 344–349 (2016). doi: 10.1038/nature19804; pmid: 27602946
15. B. Franke-Fayard *et al*., Murine malaria parasite sequestration: CD36 is the major receptor, but cerebral pathology is unlinked to sequestration. *Proc. Natl. Acad. Sci. U.S.A.* **102**, 11468–11473 (2005). doi: 10.1073/pnas.0503386102; pmid: 16051702

Downloaded from http://science.sciencemag.org/ on December 10, 2018

16. M. A. Phillips *et al*., A long-duration dihydroorotate dehydrogenase inhibitor (DSM265) for prevention and treatment of malaria. *Sci. Transl. Med.* **7**, 296ra111 (2015). doi: 10.1126/scitranslmed.aaa6645; pmid: 26180101
17. J. B. Baell, J. W. M. Nissink, Seven Year Itch: Pan-Assay Interference Compounds (PAINS) in 2017-Utility and Limitations. *ACS Chem. Biol.* **13**, 36–44 (2018). doi: 10.1021/acschembio.7b00903; pmid: 29202222
18. C. K. Dong *et al*., Identification and validation of tetracyclic benzothiazepines as *Plasmodium falciparum* cytochrome bc_1 inhibitors. *Chem. Biol.* **18**, 1602–1610 (2011). doi: 10.1016/j.chembiol.2011.09.016; pmid: 22195562
19. A. N. Cowell *et al*., Mapping the malaria parasite druggable genome by using in vitro evolution and chemogenomics. *Science* **359**, 191–199 (2018). doi: 10.1126/science.aan4472; pmid: 29326268
20. E. L. Allman, H. J. Painter, J. Samra, M. Carrasquilla, M. Llinás, Metabolomic profiling of the malaria box reveals antimalarial target pathways. *Antimicrob. Agents Chemother.* **60**, 6635–6649 (2016). doi: 10.1128/AAC.01224-16; pmid: 27572391
21. H. J. Painter, J. M. Morrisey, M. W. Mather, A. B. Vaidya, Specific role of mitochondrial electron transport in blood-stage *Plasmodium falciparum*. *Nature* **446**, 88–91 (2007). doi: 10.1038/nature05572; pmid: 17330044
22. M. R. Luth, P. Gupta, S. Ottilie, E. A. Winzeler, Using in vitro evolution and whole genome analysis to discover next generation targets for antimalarial drug discovery. *ACS Infect. Dis.* **4**, 301–314 (2018). doi: 10.1021/acsinfecdis.7b00276; pmid: 29451780
23. V. Patel *et al*., Identification and characterization of small molecule inhibitors of *Plasmodium falciparum* dihydroorotate dehydrogenase. *J. Biol. Chem.* **283**, 35078–35085 (2008). doi: 10.1074/jbc.M804990200; pmid: 18842591
24. N. A. Malmquist, R. Gujjar, P. K. Rathod, M. A. Phillips, Analysis of flavin oxidation and electron-transfer inhibition in *Plasmodium falciparum* dihydroorotate dehydrogenase. *Biochemistry* **47**, 2466–2475 (2008). doi: 10.1021/bi702218c; pmid: 18225919
25. D. E. Hurt, J. Widom, J. Clardy, Structure of *Plasmodium falciparum* dihydroorotate dehydrogenase with a bound inhibitor. *Acta Crystallogr. D Biol. Crystallogr.* **62**, 312–323 (2006). doi: 10.1107/S0907444905042642; pmid: 16510978
26. X. Deng *et al*., Fluorine modulates species selectivity in the triazolopyrimidine class of *Plasmodium falciparum* dihydroorotate dehydrogenase inhibitors. *J. Med. Chem.* **57**, 5381–5394 (2014). doi: 10.1021/jm500481t; pmid: 24801997
27. L. S. Ross *et al*., In vitro resistance selections for *Plasmodium falciparum* dihydroorotate dehydrogenase inhibitors give mutants with multiple point mutations in the drug-binding site and altered growth. *J. Biol. Chem.* **289**, 17980–17995 (2014). doi: 10.1074/jbc.M114.558353; pmid: 24782313
28. T. G. Nam *et al*., A chemical genomic analysis of decoquinate, a *Plasmodium falciparum* cytochrome b inhibitor. *ACS Chem. Biol.* **6**, 1214–1222 (2011). doi: 10.1021/cb200105d; pmid: 21866942
29. V. C. Corey *et al*., A broad analysis of resistance development in the malaria parasite. *Nat. Commun.* **7**, 11901 (2016). doi: 10.1038/ncomms11901; pmid: 27301419
30. J. N. Burrows, R. H. van Huijsduijnen, J. J. Möhrle, C. Oeuvray, T. N. C. Wells, Designing the next generation of medicines for malaria control and eradication. *Malar. J.* **12**, 187 (2013). doi: 10.1186/1475-2875-12-187; pmid: 23742293
31. B. K. Yeung *et al*., Spirotetrahydro beta-carbolines (spiroindolones): A new class of potent and orally efficacious compounds for the treatment of malaria. *J. Med. Chem.* **53**, 5155–5164 (2010). doi: 10.1021/jm100410f; pmid: 20568778
32. A. Ouattara *et al*., Designing malaria vaccines to circumvent antigen variability. *Vaccine* **33**, 7506–7512 (2015). doi: 10.1016/j.vaccine.2015.09.110; pmid: 26475447
33. B. Mordmüller *et al*., Sterile protection against human malaria by chemoattenuated PfSPZ vaccine. *Nature* **542**, 445–449 (2017). doi: 10.1038/nature21060; pmid: 28199305
34. R. J. Landovitz, R. Kofron, M. McCauley, The promise and pitfalls of long-acting injectable agents for HIV prevention. *Curr. Opin. HIV AIDS* **11**, 122–128 (2016). doi: 10.1097/COH.0000000000000219; pmid: 26633643
35. S. Iwata *et al*., Complete structure of the 11-subunit bovine mitochondrial cytochrome bc1 complex. *Science* **281**, 64–71 (1998). doi: 10.1126/science.281.5373.64; pmid: 9651245
36. D. Birth, W. C. Kao, C. Hunte, Structural analysis of atovaquone-inhibited cytochrome bc1 complex reveals the molecular basis of antimalarial drug action. *Nat. Commun.* **5**, 4029 (2014). doi: 10.1038/ncomms5029; pmid: 24893593

ACKNOWLEDGMENTS

We thank A. Rodriguez and the New York University for providing *P. berghei*–infected mosquitoes, the Pennsylvania State University Metabolomics Core Facility (University Park, Pennsylvania) for critical analytical expertise, and H. Painter for valuable input on the metabolomics experimental setup. We also thank G. LaMonte for assistance with parasite culture and P. Hinkson (Harvard Chan School) for technical support, and we thank S. Mikolajczak (Center for Infectious Disease Research) for the PvUIS4 antibodies. DNA sequencing was performed at the University of California, San Diego (UCSD), with support from the Institute of Genomic Medicine Core. The red blood cells used in this work were sourced ethically, and their research use was in accord with the terms of the informed consents. The compound library was acquired from Charles River. We thank the Shoklo Malaria Research Unit staff involved in this study, especially P. Kittiphanakun, S. N. Hsel, N. Keereepitoon, and S. Saithanmettajit for their help in mosquito rearing and *P. vivax* infection. **Funding:** E.A.W. is supported by grants from the NIH (5R01AI090141, R01AI103058, and P50GM085764) and by grants from the Bill & Melinda Gates Foundation (OPP1086217 and OPP1141300) as well as from Medicines for Malaria Venture (MMV). M.L.L. received support from Bill & Melinda Gates Foundation Phase II Grand Challenges (OPP1119049). This work was also funded in part by National Institutes of Health grant R01AI093716 supporting D.F.W., A.K.L., and T.S.K.; D.E.K. and S.P.M. are supported by grants from the Bill & Melinda Gates Foundation (OPP1023601), the Georgia Research Alliance, and the Medicines for Malaria Venture (RD/15/0022). The Human Subjects protocol for the *P. vivax* study was approved by the Oxford Tropical Medicine Ethical Committee, Oxford University, England (TMEC 14-016 and OxTREC 40-14). The Shoklo Malaria Research Unit is part of the Mahidol Oxford Research Unit, supported by the Wellcome Trust of Great Britain. The Human Subjects protocol for the UCSD *P. falciparum* study was approved by The Scripps Research Institute Institutional Review Board as part of the Normal Blood Donor Service. **Author contributions:** E.A.W. designed experiments, wrote the manuscript, and analyzed data. Y.A.K. performed exoerythrocytic, luciferase, ABS and toxicity dose-response assays; analyzed data; and wrote portions of the manuscript; M.A. and C.M.T. performed ABS assays and analyzed data; S.M., M.A., M.E., C.G., K.G., D.P., M.I., and C.W.M. performed primary and secondary *Pbluc* activity screens; Y.A.K., K.E., J.C., and B.A. performed secondary exo-erythrocytic form activity screens. C.L. analyzed data. Y.Z., K.C., and Y.Z. performed cheminformatics analysis. M.L.L. and E.O. performed the metabolomics assay and analyzed the data. S.P.M., A.J.C., V.C., F.N., and D.E.K. performed *P. vivax* studies. M.R., B.C., and J.B. sourced compounds and designed experiments. D.F.W., A.K.L., F.J.G., and F.N.S. performed mitochondrial inhibitor studies. D.F.W., A.K.L., J.C.J.R., T.S.K., M.V., and D.A.F. performed in vitro evolution experiments and analyzed the data; M.L. analyzed sequence data and performed ScDHODH experiments; and S.O. sourced compounds, analyzed data, and wrote the manuscript. **Competing interests:** E.A.W. is on the scientific advisory board of the Tres Cantos Open Lab Foundation. **Data and materials availability:** DNA sequences have been deposited in the shortread sequence archive (www.ncbi.nlm.nih.gov/sra) under accession no. SRP134381. Metabolomics data has been deposited in the NIH Metabolomics Workbench under accession no. PR000719. All other data are available in the manuscript or the supplementary materials. This work is licensed under a Creative Commons Attribution 4.0 International (CC BY 4.0) license, which permits unrestricted use, distribution, and reproduction in any medium, provided the original work is properly cited. To view a copy of this license, visit http://creativecommons.org/licenses/by/4.0/. This license does not apply to figures/photos/artwork or other content included in the article that is credited to a third party; obtain authorization from the rights holder before using such material.

SUPPLEMENTARY MATERIALS

www.sciencemag.org/content/362/6419/eaat9446/suppl/DC1
Materials and Methods
Figs. S1 to S4
Tables S1 to S8
References (*37*–*46*)
Data Files S1 to S7

26 April 2018; accepted 18 October 2018
10.1126/science.aat9446

Downloaded from http://science.sciencemag.org/ on December 10, 2018

RESEARCH ARTICLE SUMMARY

CLIMATE IMPACTS

Temperature-dependent hypoxia explains biogeography and severity of end-Permian marine mass extinction

Justin L. Penn*, Curtis Deutsch*, Jonathan L. Payne, Erik A. Sperling

INTRODUCTION: Climate change triggered by volcanic greenhouse gases is hypothesized to have caused the largest mass extinction in Earth's history at the end of the Permian Period (~252 million years ago). Geochemical evidence provides strong support for rapid global warming and accompanying ocean oxygen (O_2) loss, but a quantitative link among climate, species' traits, and extinction is lacking. To test whether warming and O_2 loss can mechanistically account for the marine mass extinction, we combined climate model simulations with an established ecophysiological framework to predict the biogeographic patterns and severity of extinction. Those predictions were confirmed by a spatially explicit analysis of the marine fossil record.

RATIONALE: The impact of climate change on marine biodiversity depends on both its magnitude and on species' diverse biological sensitivities. Tolerances of marine animals to warming and O_2 loss are physiologically related and can be represented in a single metric: the ratio of temperature-dependent O_2 supply and demand rates. This ratio, termed the Metabolic Index (Φ), measures the environmental scope for aerobic activity and is governed by ocean conditions as well as thermal and hypoxia sensitivity traits that vary across species. If climate warming and O_2 loss reduce Φ below the species-specific minimum requirement for sustained ecological activity (Φ^{crit}), the ocean would no longer support active aerobic metabolism and, by extension, long-term population persistence.

RESULTS: We simulated the greenhouse gas–driven global warming at the end of the Permian using a model of Earth's climate and coupled biogeochemical cycles that matches geochemical proxy data. The imposed increase in atmospheric greenhouse gas levels raises near-surface ocean temperatures by more than ~10°C and depletes global marine O_2 levels by almost 80%.

To predict the impact of these changes on animal habitat and survival, we measured the frequencies of Metabolic Index traits in diverse living species and used them to define a set of model ecophysiotypes. We populated the model Permian ocean with each ecophysiotype wherever conditions provide viable habitat ($\Phi \geq \Phi^{crit}$), yielding an ocean with diverse, locally adapted ecophysiotypes throughout all regions. Across the climate transition, however, ocean warming increases the metabolic O_2 demand amid declining supply; this removes large fractions of global aerobic habitat for the vast majority of ecophysiotypes and implies a high likelihood of extinction. We simulated the resulting mass extinction of ecophysiotypes and found a robust geographic pattern: Extinction intensity should have been lower in the tropics than at high latitudes. The cause of lower tropical extinction is that organisms initially inhabiting these warm, low-O_2 environments can better exploit those conditions when they arise globally, whereas the habitats of more polar species disappear completely.

ON OUR WEBSITE

Read the full article at http://dx.doi.org/10.1126/science.aat1327

To test the geographic selectivity of the model extinction, we compared model predictions to spatially explicit reconstructions of genus extinction from the marine fossil record. We found that across diverse taxonomic groups, the observed extinction intensity indeed increases with latitude, consistent with the predicted signature of aerobic habitat loss. Comparison of the model to the fossil record implies that temperature-dependent hypoxia can account for more than half of the observed magnitude of regional extinction (i.e., extirpation).

CONCLUSION: Ocean warming and O_2 loss simulated in an Earth System Model of end-Permian climate change imply widespread loss of aerobic habitat among animal types with diverse thermal and hypoxia tolerances. The resulting extinctions are predicted to select most strongly against higher-latitude species, whose biogeographic niche disappears globally. The combined physiological stresses of ocean warming and O_2 loss largely account for the spatial pattern and magnitude of extinction observed in the fossil record of the "Great Dying." These results highlight the future extinction risk arising from a depletion of the ocean's aerobic capacity that is already under way. ■

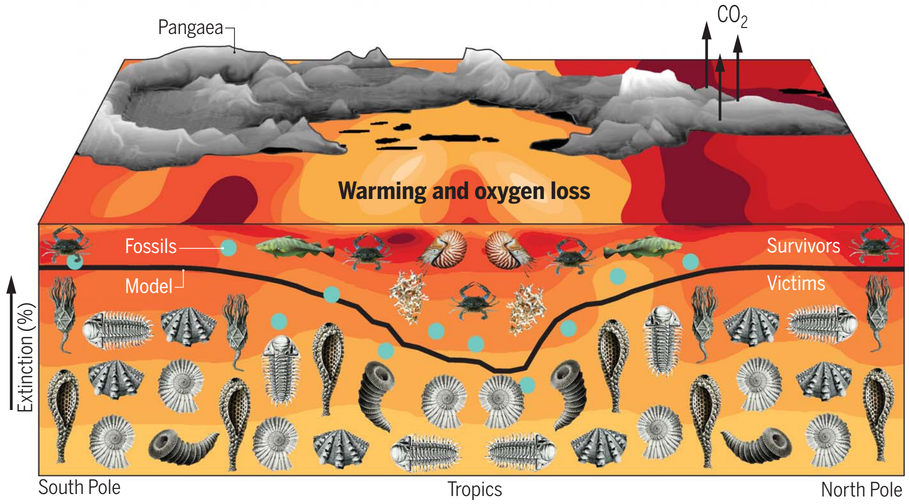

Schematic illustration of temperature-dependent hypoxia as a driver of the end-Permian marine mass extinction. Greenhouse gas forcing in a model of Earth's climate at the end of the Permian drives ocean warming (contours) and oxygen loss that match geochemical proxy data. Ocean warming raises the organismal O_2 demand amid declining supply. The resulting loss of aerobic habitat for diverse physiologies induces a mass extinction in model animal types (line) whose geographic signature—increased severity outside of the tropics—is consistent with reconstructions from the marine fossil record (circles).

ILLUSTRATION BY J. PENN AND C. DEUTSCH; FOSSIL DRAWINGS BY E. HAECKEL; PHOTOS BY W. KAVENEY (BLUE CRAB), H. FJELD (ATLANTIC COD), J. WHITE (CHAMBERED NAUTILUS)

The list of author affiliations is available in the full article online.
*Corresponding author. Email: jpenn@uw.edu (J.L.P.); cdeutsch@uw.edu (C.D.)

Cite this article as J. L. Penn *et al.*, *Science* **362**, eaat1327 (2018). DOI: 10.1126/science.aat1327

Downloaded from http://science.sciencemag.org/ on December 6, 2018

Penn *et al.*, *Science* **362**, 1130 (2018) 30 November 2018 **1 of 1**

RESEARCH ARTICLE

CLIMATE IMPACTS

Temperature-dependent hypoxia explains biogeography and severity of end-Permian marine mass extinction

Justin L. Penn[1]*, Curtis Deutsch[1,2]*, Jonathan L. Payne[3], Erik A. Sperling[3]

Rapid climate change at the end of the Permian Period (~252 million years ago) is the hypothesized trigger for the largest mass extinction in Earth's history. We present model simulations of the Permian/Triassic climate transition that reproduce the ocean warming and oxygen (O_2) loss indicated by the geologic record. The effect of these changes on animal survival is evaluated using the Metabolic Index (Φ), a measure of scope for aerobic activity governed by organismal traits sampled in diverse modern species. Modeled loss of aerobic habitat predicts lower extinction intensity in the tropics, a pattern confirmed with a spatially explicit analysis of the marine fossil record. The combined physiological stresses of ocean warming and O_2 loss can account for more than half the magnitude of the "Great Dying."

Volcanic greenhouse gas release is widely hypothesized to have been the geological trigger for the largest mass extinction event in Earth's history at the end of the Permian Period [~252 million years (Ma) ago] (*1*, *2*). At least two-thirds of marine animal genera and a comparable proportion of their terrestrial counterparts were eliminated, but the mechanisms connecting environmental change to biodiversity collapse remain strongly debated. Geological and geochemical evidence points to high temperatures in the shallow tropical ocean (*3*, *4*), an expansion of anoxic waters (*5*–*8*), ocean acidification (*9*–*12*), changes in primary productivity (*13*, *14*), and metal (*15*) or sulfide (*16*, *17*) poisoning as potential culprits. However, a quantitative, mechanistic framework connecting climate stressors to biological tolerance is needed to assess and differentiate among proposed proximal causes.

In this study, we tested whether rapid greenhouse warming and the accompanying loss of ocean O_2—the two best-supported aspects of end-Permian environmental change—can together account for the magnitude and biogeographic selectivity of end-Permian mass extinction in the oceans. Specifically, we simulated global warming across the Permian/Triassic (P/Tr) transition using a model of Earth's climate and coupled biogeochemical cycles, validated with geochemical data. We then used key physiological and ecological traits measured in a diverse group of extant species to predict the magnitude and distribution of habitat loss due to the temperature-driven increase of metabolic O_2 demand amid declining supply (*18*). To assess the explanatory power of this model, we compared the predicted patterns of extinction to the global marine fossil record.

Climate warming and ocean O_2 loss

We simulated the P/Tr climate transition using the Community Earth System Model, which computes the exchanges of mass, energy, and momentum among interacting atmosphere, ocean, land surface, and sea ice components (*19*). Embedded in the ocean circulation are biogeochemical cycles of O_2, carbon, and nutrients driven by multiple plankton types. An initial climate state was equilibrated under low greenhouse gas concentrations and reconstructed paleogeography (*19*, *20*). The model was then subjected to an instantaneous increase in greenhouse gas concentration that was sustained for 3000 years in order to reach a warm, near-equilibrium climate (fig. S1). The initial climate and subsequent radiative forcing were achieved by manipulating atmospheric pCO_2 (partial pressure of CO_2) across levels chosen to reproduce tropical ocean temperatures implied by isotopic proxy records (*3*, *4*, *19*, *21*). Because the rate and timing of climate change, as well as the resulting biotic disturbance, are not precisely known, the analysis of model output was based on pre-disturbance and post-disturbance equilibrium states, which we refer to simply as Permian and Triassic, respectively.

The modeled Permian and Triassic climates are consistent with geological proxy data for ocean temperature. The imposed increase in atmospheric pCO_2 raises model near-surface temperatures by ~11°C in the Paleo-Tethys sea (Fig. 1A), consistent with reconstructions from the $\delta^{18}O$ of biogenic (conodont microfossil) apatite ($\delta^{18}O_{apatite}$; Fig. 1B). Modeled warming is amplified in the near-surface ocean outside of the tropics (Fig. 1A) and throughout the upper ocean relative to the deep (Fig. 1C). Warming and fresh water input to the high-latitude surface ocean (fig. S2) together strengthen density stratification and weaken deep-water formation. From its near-modern state in the Permian, the meridional overturning circulation slows in the Triassic by more than 80% in both hemispheres (fig. S3). Deep ocean stagnation reaches its full extent after just ~300 years and persists unabated for the duration of the simulation (~3000 years).

The modeled Permian and Triassic climates are also consistent with geological proxies for marine anoxia. Abrupt warming and its attendant effects deplete the global marine O_2 inventory by ~76% (~140 mmol/m^3), leading to extensive Triassic seafloor anoxia (Fig. 1D) that spans the entire northern portion of the Panthalassa Ocean and the eastern tropics, similar to the observed distribution of deeper-ocean sediments deposited under anoxic conditions [e.g., (*6*, *22*)]. The global fraction of anoxic bottom water (f_{anox}) in the Permian (~0.1%) is close to modern values (~0.2%) but rises to ~40% in the Triassic (Fig. 1E), consistent with the expansion inferred from uranium isotopes in marine carbonates (*7*, *8*).

O_2 loss is nearly complete in the abyss, but varies strongly with latitude throughout the upper ocean (Fig. 1F). At high latitudes, anoxia develops in waters as shallow as 150 m. In contrast, O_2 declines weakly or increases in portions of the tropical thermocline. This pattern of O_2 change cannot be explained by decreases in gas saturation alone. It requires additional changes in the cumulative loss of O_2 from microbial respiration below the surface ocean. Warming increases the rate of phytoplankton growth, whereas stratification increases their exposure to adequate sunlight, especially in high latitudes where deep convection and sea ice cover decline markedly. As a result, surface nutrients are drawn down in mid- and high latitudes and are exported in sinking particles to the deep sea (*14*), thereby reducing the nutrient supply to the tropical surface ocean (*23*) (fig. S4). This shift in nutrient distribution in turn lessens the microbial O_2 demand in the tropical thermocline, partially counteracting the lowered gas saturation and limiting O_2 loss, even while anoxia develops elsewhere.

Aerobic habitat loss

The effect of warming and O_2 loss on biodiversity in the end-Permian ocean depends not only on the magnitude and pattern of environmental change, but also on the sensitivities of marine animals. Tolerances to hypoxia and warming are physiologically related (*24*) and can be represented in a single metric, the Metabolic Index (Φ), derived from the ratio of temperature-dependent rates of O_2 supply and demand (*18*, *19*):

$$\Phi = A_o \frac{pO_2}{\exp\left[\frac{-E_o}{k_B}\left(\frac{1}{T} - \frac{1}{T_{ref}}\right)\right]} \qquad (1)$$

---

[1]School of Oceanography, University of Washington, Seattle, WA 98195, USA. [2]Department of Biology, University of Washington, Seattle, WA 98195, USA. [3]Department of Geological Sciences, Stanford University, Stanford, CA 94305, USA.
*Corresponding author. Email: jpenn@uw.edu (J.L.P.); cdeutsch@uw.edu (C.D.)

Downloaded from http://science.sciencemag.org/ on December 6, 2018

where pO_2 and T are the O_2 partial pressure and temperature of ambient water, respectively; k_B is Boltzmann's constant; and the parameters A_o (kPa^{-1}) and E_o (eV) represent fundamental physiological traits of a species. The inverse of A_o (i.e., $1/A_o$, in kPa) is the minimum pO_2 that can sustain the resting metabolic rate (i.e., the "hypoxic threshold") at a reference temperature (T_{ref}), and E_o is the temperature sensitivity of that threshold (Fig. 2A). The Metabolic Index measures the capacity of an environment to support aerobic activity by a factor of Φ above an organism's minimum requirement in a complete resting state ($\Phi = 1$). For both marine and terrestrial animals, the energy required for sustained activity (e.g., feeding, reproduction, defense) is elevated by a factor of ~1.5 to 7 above resting metabolic demand (*18*, *25*) and represents an ecological trait, termed Φ^{crit}. If climate warming and O_2 loss reduce the Metabolic Index for an organism below its species-specific Φ^{crit}, the environment would no longer have the capacity to support active aerobic metabolism and, by extension, long-term population persistence.

We evaluated the range and frequency of traits governing the Metabolic Index across diverse modern species (*19*). Physiological traits ($1/A_o$ and E_o) were estimated in 61 species that span benthic and pelagic habitats in all ocean basins across four phyla (Arthropoda, Chordata, Mollusca, and Cnidaria). The species include 28 malacostracans, 21 fishes, three bivalves and cephalopods, two copepods, and one each for gastropods, ascidians, scleractinian corals, and sharks (table S1); their range of body mass spans eight orders of magnitude. The ecological trait (Φ^{crit}) was estimated for 26 species with adequate biogeographical data. All parameters exhibited well-defined distributions reflecting the diversity and frequency of key metabolic traits among modern taxa at multiple levels of taxonomic hierarchy (fig. S5) (*19*).

We used the observed trait distributions to define a set of model ecophysiotypes and populate the model Permian ocean with each ecophysiotype wherever its traits and ocean conditions provide viable habitat ($\Phi \geq \Phi^{crit}$). Although modern species and the environments they encounter differ from those present during the Permian, the use of modern hypoxia traits to define Permian ecophysiotypes is grounded in two considerations. First, among well-sampled modern taxonomic groups, including arthropods, chordates, and mollusks, the distributions of hypoxia traits are not significantly different (fig. S5, B to D) (*19*). This overlap of distributions implies a strong selective pressure for diverse physiological strategies for hypoxia tolerance and would apply to any cosmopolitan taxonomic group, including Permian phyla not well represented in our database. Second, the broad similarity in the temperature and O_2 conditions encountered today and in the simulated Permian climate (fig. S6) suggests that, whatever their other anatomical and physiological differences, the Permian aerobic environment should have selected for a range and frequency of hypoxia traits comparable to those of modern species. To test the adaptive suitability of modern trait diversity to the Permian ocean, we examined whether all ecophysiotypes find suitable habitat, and whether every region of the Permian ocean would be habitable by some subset of modern ecophysiotypes.

Variations in Permian environmental conditions and the three Metabolic Index traits give rise to a diverse set of biogeographic ranges (Fig. 2, B to D). For average physiological traits of the studied species ($1/A_o$ ~ 4.5 kPa and E_o ~ 0.4 eV), Φ decreases with depth in the upper 1000 m but increases with latitude, restricting ecophysiotypes with higher ratios of active to resting metabolic rates to the extratropics (Fig. 2B). Because

Downloaded from http://science.sciencemag.org/ on December 6, 2018

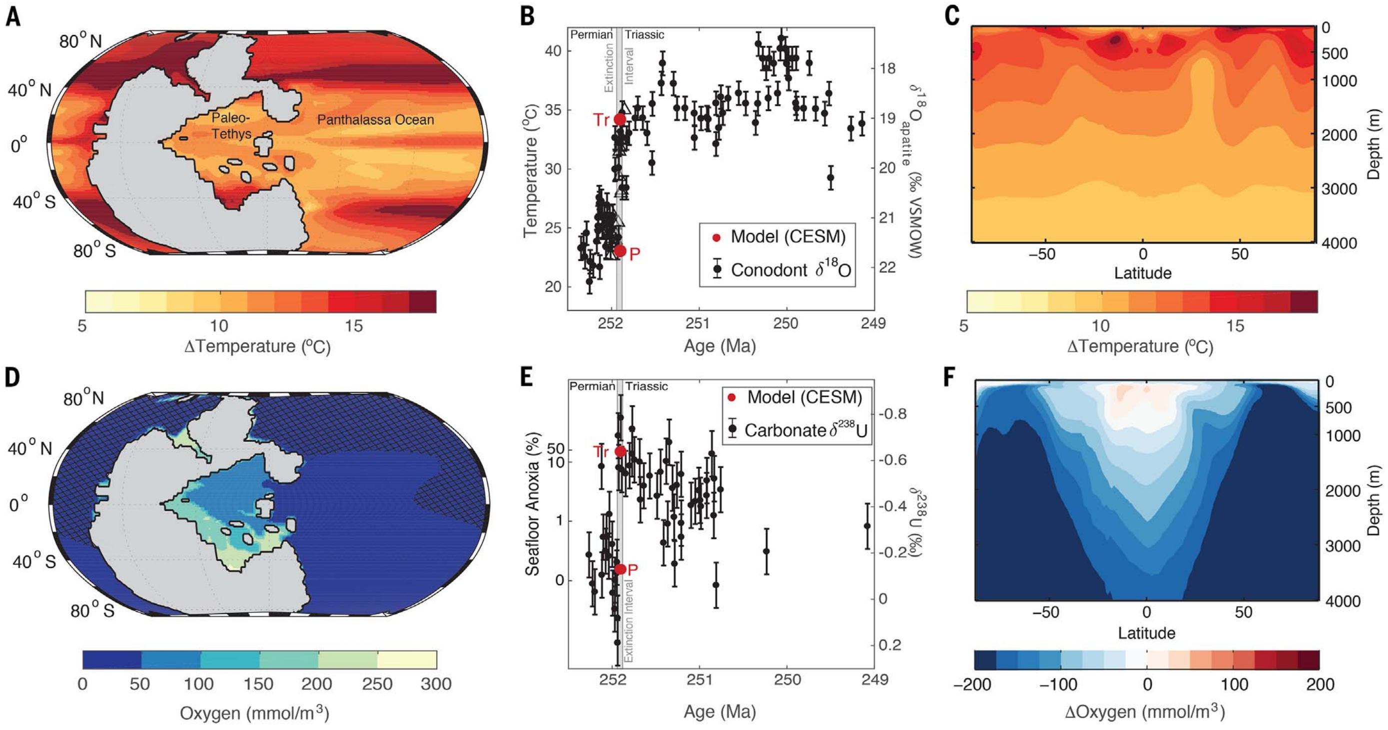

Fig. 1. Permian/Triassic ocean temperature and O_2. (**A**) Map of near-surface (0 to 70 m) ocean warming across the Permian/Triassic (P/Tr) transition simulated in the Community Earth System Model. The region in gray represents the supercontinent Pangaea. (**B**) Simulated near-surface ocean temperatures (red circles) in the eastern Paleo-Tethys (5°S to 20°N) and reconstructed from conodont $\delta^{18}O_{apatite}$ measurements (black circles) (*4*). The time scale of the $\delta^{18}O_{apatite}$ data (circles) has been shifted by 700,000 years to align it with $\delta^{18}O_{apatite}$ calibrated by U-Pb zircon dates (open triangles) (*1*), which also define the extinction interval (gray band). Error bars are 1°C. (**C**) Simulated zonal mean ocean warming (°C) across the P/Tr transition. (**D**) Map of seafloor oxygen levels in the Triassic simulation. Hatching indicates anoxic regions ($O_2 < 5$ mmol/m^3). (**E**) Simulated seafloor anoxic fraction f_{anox} (red circles). Simulated values are used to drive a published one-box ocean model of the ocean's uranium cycle (*8*) and are compared to $\delta^{238}U$ isotope measurements of marine carbonates formed in the Paleo-Tethys (black circles). Error bars are 0.1‰. (**F**) Same as in (C) but for simulated changes in O_2 concentrations (mmol/m^3).

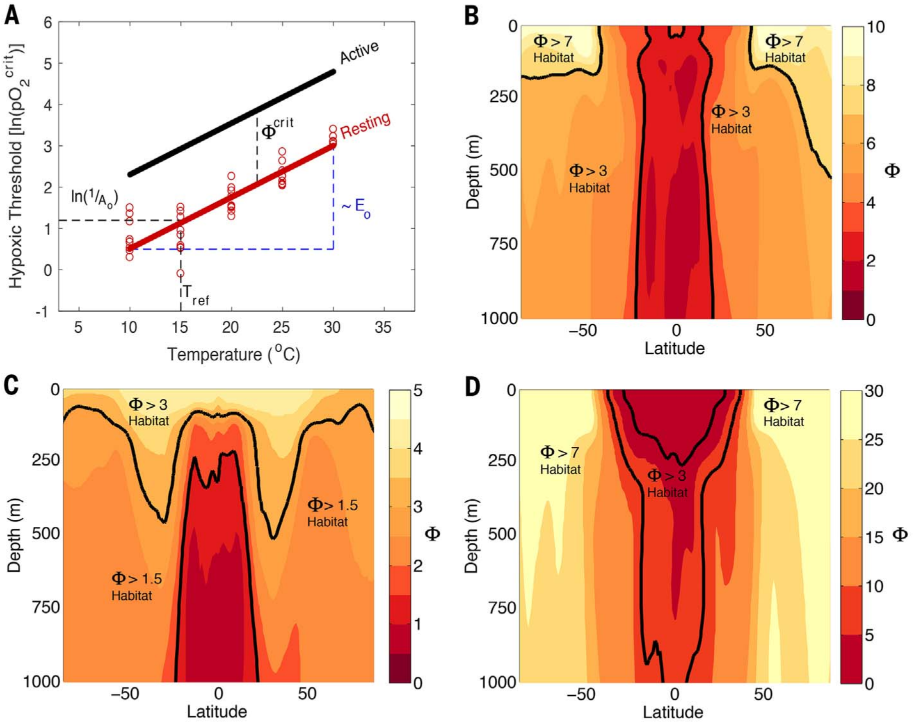

Fig. 2. Physiological and ecological traits of the Metabolic Index (Φ) and its end-Permian distribution. (**A**) The critical O$_2$ pressure (pO_2^{crit}) needed to sustain resting metabolic rates in laboratory experiments (red circles, *Cancer irroratus*) vary with temperature with a slope proportional to E_o from a value of $1/A_o$ at a reference temperature (T_{ref}), as estimated by linear regression when $\Phi = 1$ (*19*). Energetic demands for ecological activity increase hypoxic thresholds by a factor Φ^{crit} above the resting state, a value estimated from the Metabolic Index at a species' observed habitat range limit. (**B**) Zonal mean distribution of Φ in the Permian simulation for ecophysiotypes with average $1/A_o$ and E_o (~4.5 kPa and 0.4 eV, respectively). (**C** and **D**) Variations in Φ for an ecophysiotype with weak (C) and strong (D) temperature sensitivities (E_o = 0 eV and 1.0 eV, respectively), both with $1/A_o$ ~ 4.5 kPa. Example values of Φ^{crit} (black lines) outline different distributions of available aerobic habitat for a given combination of $1/A_o$ and E_o.

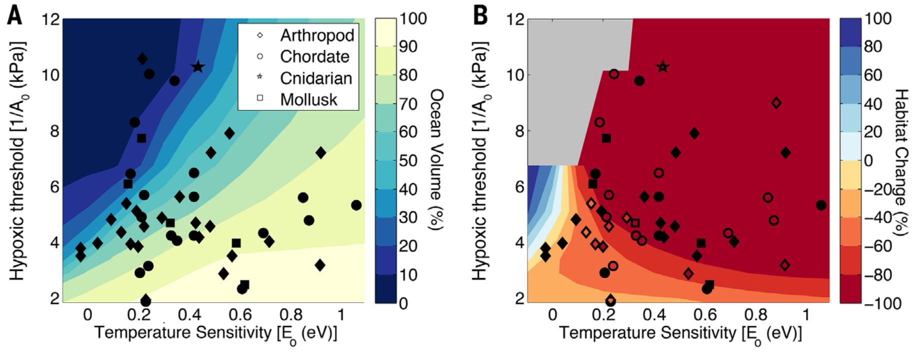

Fig. 3. Aerobic habitat during the end-Permian and its change under warming and O$_2$ loss. (**A**) Percentage of ocean volume in the upper 1000 m that is viable aerobic habitat ($\Phi \geq \Phi^{crit}$) in the Permian for ecophysiotypes with different hypoxic threshold parameters $1/A_o$ and temperature sensitivities E_o. (**B**) Relative (percent) change in Permian aerobic habitat volume (ΔV_i, where i is an index of ecophysiotype) under Triassic warming and O$_2$ loss. Colored contours are for ecophysiotypes with $\Phi^{crit} = 3$. Measured values of $1/A_o$ and E_o in modern species are shown as black symbols, but in (B) these are colored according to habitat changes at a species' specific Φ^{crit} where an estimate of this parameter is available. The gray region at upper left indicates trait combinations for which no habitat is available in the Permian simulation.

the hypoxic threshold scales the magnitude of Φ linearly (Eq. 1), variations in this parameter have an effect on the distribution of habitat similar to that of Φ^{crit}. In contrast, the temperature sensitivity parameter determines where Φ reaches its extreme values for a given distribution of temperature and O$_2$ (Fig. 2, C and D). For ecophysiotypes whose hypoxic thresholds are only weakly temperature-dependent (E_o < 0.1 eV), Φ is maximized in the shallow low-latitude ocean (Fig. 2C). For the most temperature-sensitive ecophysiotypes (E_o ~ 1.0 eV), Φ is greatest in the relatively cold waters of the high-latitude upper ocean and aerobic habitat expands with depth (Fig. 2D). The predicted niche partitioning leaves virtually no part of the Permian ocean uninhabited, partially confirming the relevance of modern trait diversity for the Permian.

Metabolic Index traits also have a strong impact on the predicted volume of available aerobic habitat (Fig. 3A). Ecophysiotypes with higher temperature sensitivities are able to inhabit the largest ocean volumes because most deep waters in the simulated Permian ocean are cold. In turn, ecophysiotypes with low hypoxic thresholds and/or low values of Φ^{crit} can occupy the largest ocean regions for a given temperature sensitivity. Simulated Permian habitat is available for ~95% of modern Metabolic Index trait combinations, both as global ocean volume (points in Fig. 3A) and as area on the seafloor (fig. S7A), further confirming that extant trait diversity is well adapted to the end-Permian ocean and is thus a sensible baseline for examining habitat loss and extinction.

Across the simulated climate transition, warming and O$_2$ loss remove a major fraction of aerobic habitat in the upper 1000 m for most ecophysiotypes (Fig. 3B) by lowering their metabolic indices below Φ^{crit}. The loss of habitat exceeds 90% for an ecophysiotype with the average traits; the vast majority (~95%) of ecophysiotypes experience declines, with magnitudes ranging from ~20% to 100% (fig. S8). Habitat loss preferentially selects against organisms with high hypoxic thresholds, high ratios of active to resting metabolic rates, and/or high temperature sensitivities. The former two traits impart low initial habitat volumes (Fig. 3A), whereas high temperature sensitivities amplify the decline in Φ per degree of warming. These patterns of differential habitat loss across ecophysiotypes are also found for coastal seafloor habitats (fig. S7B) and are qualitatively similar across ocean depth, but the average magnitude of habitat loss increases in the abyss because of the more complete O$_2$ loss (fig. S9).

Geography of global extinction

The severity of aerobic habitat loss predicted across the warming interval implies a high likelihood of extinction for many ecophysiotypes. We simulated the extinction of ecophysiotypes, defined by a fractional loss of global aerobic habitat volume (ΔV_i, where i indexes ecophysiotype) exceeding a specified critical threshold (V^{crit}; Fig. 4A) (*19*), in waters above a maximum depth. Because maximum habitat depth and V^{crit} are poorly known ecological traits that are likely

Downloaded from http://science.sciencemag.org/ on December 6, 2018

to vary across species, we computed the extinction across a wide range of values for these parameters. However, the geographical signature of the predicted mass extinction remains essentially the same irrespective of habitat depth and V^{crit}; extinction intensity should have been lower for tropical communities than for those at higher latitudes.

The latitudinal gradient of extinction predicted from the Metabolic Index arises from the fundamental niche partitioning of Permian ecophysiotypes across latitude prior to the warming (Fig. 4B and fig. S10A). Ecophysiotypes with higher hypoxic thresholds and/or ratios of active to resting metabolisms are preferentially exterminated when the high latitudes warm and lose O_2 because they have no escape from inhospitable conditions. In contrast, ecophysiotypes whose Permian habitat includes the tropics must have traits pre-adapted to warm, low-O_2 environments and can better exploit these conditions when they arise globally. The extinction gradient is thus predicted to occur as long as the temperature-dependent hypoxia tolerance varies among ecophysiotypes, and as long as those with lower tolerance are confined to higher-latitude waters with a greater capacity to support aerobic activity. Under these conditions, the extinction pattern is only weakly dependent on the spatial gradients of climate warming and O_2 loss (fig. S10B), and holds regardless of the precise frequency distribution of Permian traits (figs. S10B, S11, and S12); the pattern also holds if habitat is defined by area on the seafloor or volume in the water column (fig. S13).

To test the predicted geographic selectivity of aerobic habitat loss, we compared the model extinction patterns to the reconstructed distribution of genus extinction across latitude (Fig. 4A and table S2) derived from fossil occurrences in the Paleobiology Database (*19*). The global mean magnitude of extinction estimated from the fossil compilation (~65% of genera) agrees with globally aggregated estimates (*26*) but displays a previously undescribed gradient across latitude, consistent with the model predictions. The observed extinction intensity increases by ~20% from the tropics to high latitudes, reaching at least 75% of genera outside of the tropics in both hemispheres. This trend is found in multiple taxonomic groupings, including those phyla with traits multiply sampled among modern taxa (arthropods, chordates, and mollusks) and in those that are not (fig. S14A). It is also robust to latitudinal differences in sampling intensity (fig. S14, B to D) and changes in the preservation of major depositional environments (fig. S15) (*19*). The correspondence between the simulated and observed geographic patterns of selectivity strongly implicates aerobic habitat loss, driven by rapid warming, as a main proximate cause of the end-Permian extinction.

Magnitude of regional extinction

Unlike the global extinction of ecophysiotypes, regional extinction (i.e., extirpation) in the model does not depend on V^{crit} or habitat depth. The simulated extirpation is defined at a given location by the percentage of ecophysiotypes whose Metabolic Index is pushed below Φ^{crit} by Triassic climate change (*19*). Similar to global extinction, the extirpation of ecophysiotypes is elevated at higher latitudes but increases less systematically from the tropics (Fig. 4C). This pattern of ecophysiotype loss arises from the counteracting influences of global warming and O_2 loss on local aerobic habitat. Declining seawater O_2 concentrations drive extirpation in up to ~70% of ecophysiotypes in the high latitudes, but its impact diminishes to less than ~20% of ecophysiotypes in the tropics, where O_2 loss is weak (Fig. 1F). The effect of warming predicts the opposite pattern, with peak extirpation of ~65% at the equator dropping to ~20% at the poles. Local aerobic habitat is more sensitive per degree of warming in the tropics than in the high latitudes because Φ is already close to Φ^{crit} for the majority of Permian ecophysiotypes (Fig. 2, B to D). The realized impact of temperature on local habitat is therefore largest in the tropics because the pattern of upper-ocean warming is relatively constant across latitude (Fig. 1C), in contrast to the pattern of O_2 loss (Fig. 1F).

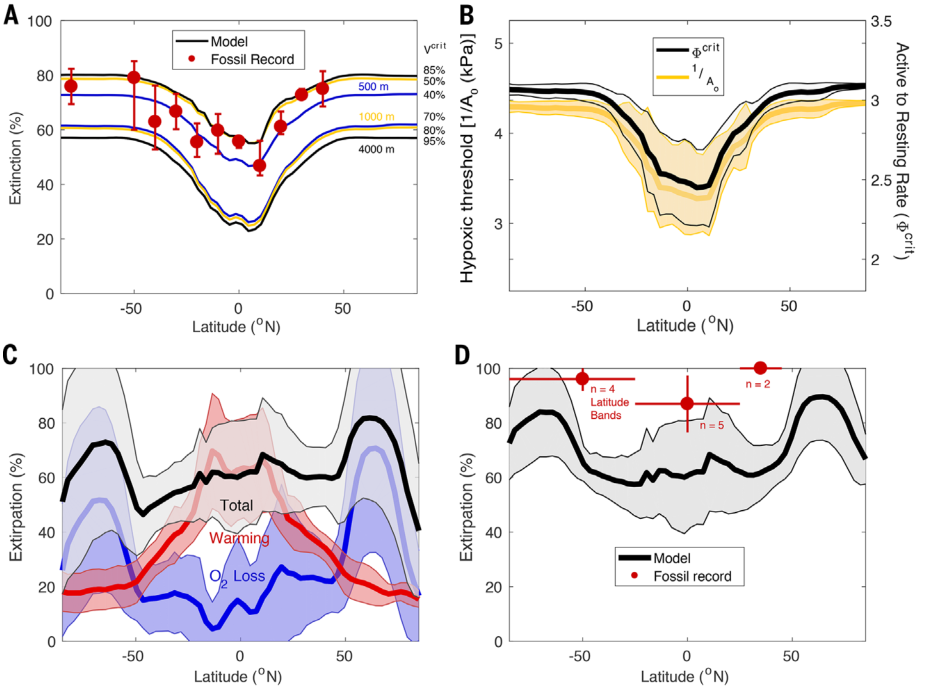

Fig. 4. Global and regional extinction at the end of the Permian. (**A**) Global extinction versus latitude, as predicted for model ecophysiotypes and observed in marine genera from end-Permian fossil occurrences in the Paleobiology Database (PBDB). Model extinction is calculated from the simulated changes in Permian global aerobic habitat volume (ΔV_i) under Triassic warming and O_2 loss (*19*). The maximum depth of initial habitat and fractional loss of habitat resulting in extinction (V^{crit}) are varied from 500 to 4000 m (colors) and from 40 to 95% (right-axis labels), respectively. The observed extinction of genera combines occurrences from all phyla in the PBDB (points). Error bars are the range of genera extinction across two taxonomic groupings: phyla multiply sampled in the modern physiology data (arthropods, chordates, and mollusks) and all other phyla. Latitude bands with fewer than five Permian fossil collections are excluded. The average range is used for latitude bands missing extinction estimates from both taxonomic groupings (i.e., 80°S, 30°S, and 40°N). The main latitudinal trend—increased extinction away from the tropics—is found when including all data together and when restricting to the best-sampled latitude bands (fig. S14). In all panels, model values are averaged across longitude and above 500 m. (**B**) Average hypoxic threshold and Φ^{crit} across ecophysiotypes versus latitude in the Permian. In (B) to (D), shading represents the 1σ standard deviation at each latitude. (**C**) Regional extinction (i.e., extirpation) versus latitude for model ecophysiotypes, with individual contributions from warming and the loss of seawater O_2 concentration. Extirpation occurs in locations where the Metabolic Index meets the active demand of an ecophysiotype in the Permian ($\Phi \geq \Phi^{crit}$) but falls below this threshold in the Triassic ($\Phi < \Phi^{crit}$). (**D**) Same as (C) but including globally extinct ecophysiotypes (using a maximum habitat depth of 1000 m and V^{crit} = 80%), and as observed in marine genera from end-Permian and early Triassic fossil occurrences of all phyla in the PBDB. Observed extirpation magnitudes are averaged across tropical and extratropical latitude bands (red points and horizontal lines). Regional 1σ standard deviations are shown as vertical lines.

Downloaded from http://science.sciencemag.org/ on December 6, 2018

To test the predicted intensity of regional extinction, we used fossil occurrence data to estimate the extirpation of marine genera across the end-Permian extinction (*19*). The fossil extirpation intensities are more severe than fossil extinction intensities across all latitude bands (global mean ~93% ± 8% spatial SD) but show a similar gradient, increasing outside of the tropics (Fig. 4D). Extirpation exceeds extinction because not all locally lost genera disappeared globally, whereas all extinct genera were, by definition, extirpated everywhere. We can account for the effect of globally extinct ecophysiotypes in the model extirpation by using a combination of V^{crit} and habitat depth that predicts an equal contribution of aerobic habitat loss to both the observed regional and global extinction (*19*). Doing so increases the extirpation outside of the tropics, yielding a latitudinal gradient similar to the fossil data.

If we assume that the fossil occurrences primarily reflect habitat conditions above 500 m water depth (*27*), the global mean magnitude of ecophysiotype extirpation (67% ± 18% spatial SD) accounts for ~72% of the mean observed magnitude of genera extirpation (i.e., 93%; Fig. 4D). Including in this comparison the spatial variations in model extirpation yields a range explaining ~53 to 92% of the observed extirpation magnitude. Additional extinctions due to temperature-dependent hypoxia would have likely arisen from ecological interactions (*28*), including food web effects, because hypoxia-tolerant species could still be eliminated if they were dependent on hypoxia-vulnerable ones. Temperature-dependent hypoxia can thus account for the majority of biodiversity losses during the end-Permian mass extinction.

Discussion

Global warming and ocean O_2 loss were accompanied by other Earth system changes during the end-Permian crisis that likely added to the effects of temperature-dependent hypoxia. In our simulations, net primary productivity is reduced by ~40% globally, with strongest declines in the low latitudes, where essential nutrient supply to phytoplankton is most curtailed (fig. S4). Thus, acting alone, productivity losses would amplify extinction risk outside of the high latitudes, opposite to the pattern observed in the fossils.

Outgassing of CO_2 from the Siberian Traps would also have acidified the ocean (*12*), causing additional impacts via hypercapnia and/or reduced calcification (*9*, *29*). These CO_2 effects are hypothesized to drive taxonomically selective extinctions, which may account for the ~10% lower mean genus extinction intensity for arthropods, chordates, and mollusks than for other less physiologically buffered phyla (fig. S14A). For the most heavily calcified animals in our modern trait dataset, the cold-water coral *Lophelia pertusa* and the scallop *Pecten maximus*, predicted losses of aerobic habitat are ~94% and ~100%, respectively, suggesting a high extinction risk for calcifiers even without a direct CO_2 effect. Attributing taxonomically selective extinction (*9*, *29*) to physiological mechanisms will require more metabolic trait data, including from CO_2 effects on both calcification and aerobic habitat (hypercapnia), and from Permian phyla underrepresented in our database. However, the latitudinal gradient of extinction arising from the carbon cycle perturbation is unlikely to explain higher rates of tropical species persistence, for the same reason that hypoxia increases extinction at higher latitudes. Because the most corrosive waters are found poleward, species least tolerant of low pH or carbonate saturation would have been confined to the tropics and thus without refuge in an acidifying ocean.

The end-Permian mass extinction resulted in the largest loss of animal diversity in Earth's history, and its proposed geologic trigger—volcanic greenhouse gas release—is analogous to anthropogenic climate forcing. Predicted patterns of future ocean O_2 loss under climate change (*30*, *31*) are broadly similar to those simulated here for the P/Tr boundary. Moreover, greenhouse gas emission scenarios projected for the coming centuries (*32*) predict a magnitude of upper ocean warming by 2300 CE that is ~35 to 50% of that required to account for most of the end-Permian extinction intensity. Given the fundamental nature of metabolic constraints from temperature-dependent hypoxia in marine biota, these projections highlight the potential for a future mass extinction arising from depletion of the ocean's aerobic capacity that is already under way.

REFERENCES AND NOTES

1. S. D. Burgess, S. Bowring, S. Z. Shen, High-precision timeline for Earth's most severe extinction. *Proc. Natl. Acad. Sci. U.S.A.* **111**, 3316–3321 (2014). doi: 10.1073/pnas.1317692111; pmid: 24516148
2. J. L. Payne, M. E. Clapham, End-Permian mass extinction in the oceans: An ancient analog for the twenty-first century? *Annu. Rev. Earth Planet. Sci.* **40**, 89–111 (2012). doi: 10.1146/annurev-earth-042711-105329
3. M. M. Joachimski *et al.*, Climate warming in the latest Permian and the Permian-Triassic mass extinction. *Geology* **40**, 195–198 (2012). doi: 10.1130/G32707.1
4. Y. Sun *et al.*, Lethally hot temperatures during the Early Triassic greenhouse. *Science* **338**, 366–370 (2012). doi: 10.1126/science.1224126; pmid: 23087244
5. P. B. Wignall, R. J. Twitchett, Oceanic anoxia and the end Permian mass extinction. *Science* **272**, 1155–1158 (1996). doi: 10.1126/science.272.5265.1155; pmid: 8662450
6. Y. Isozaki, Permo-Triassic boundary superanoxia and stratified superocean: Records from Lost Deep Sea. *Science* **276**, 235–238 (1997). doi: 10.1126/science.276.5310.235; pmid: 9092467
7. G. A. Brennecka, A. D. Herrmann, T. J. Algeo, A. D. Anbar, Rapid expansion of oceanic anoxia immediately before the end-Permian mass extinction. *Proc. Natl. Acad. Sci. U.S.A.* **108**, 17631–17634 (2011). doi: 10.1073/pnas.1106039108; pmid: 21987794
8. K. V. Lau *et al.*, Marine anoxia and delayed Earth system recovery after the end-Permian extinction. *Proc. Natl. Acad. Sci. U.S.A.* **113**, 2360–2365 (2016). doi: 10.1073/pnas.1515080113; pmid: 26884155
9. A. H. Knoll, R. K. Bambach, J. L. Payne, S. Pruss, W. W. Fischer, Paleophysiology and end-Permian mass extinction. *Earth Planet. Sci. Lett.* **256**, 295–313 (2007). doi: 10.1016/j.epsl.2007.02.018
10. J. L. Payne *et al.*, Erosional truncation of uppermost Permian shallow-marine carbonates and implications for Permian-Triassic boundary events. *Bull. Geol. Soc. Am.* **119**, 771–784 (2007). doi: 10.1130/B26091.1
11. J. L. Payne *et al.*, Calcium isotope constraints on the end-Permian mass extinction. *Proc. Natl. Acad. Sci. U.S.A.* **107**, 8543–8548 (2010). doi: 10.1073/pnas.0914065107; pmid: 20421502
12. M. O. Clarkson *et al.*, Ocean acidification and the Permo-Triassic mass extinction. *Science* **348**, 229–232 (2015). doi: 10.1126/science.aaa0193; pmid: 25859043
13. M. R. Rampino, K. Caldeira, Major perturbation of ocean chemistry and a "Strangelove Ocean" after the end-Permian mass extinction. *Terra Nova* **17**, 554–559 (2005). doi: 10.1111/j.1365-3121.2005.00648.x
14. S. E. Grasby, B. Beauchamp, J. Knies, Early Triassic productivity crises delayed recovery from world's worst mass extinction. *Geology* **44**, 779–782 (2016). doi: 10.1130/G38141.1
15. S. E. Grasby, H. Sanei, B. Beauchamp, Catastrophic dispersion of coal fly ash into oceans during the latest Permian extinction. *Nat. Geosci.* **4**, 104–107 (2011). doi: 10.1038/ngeo1069
16. L. R. Kump, A. Pavlov, M. A. Arthur, Massive release of hydrogen sulfide to the surface ocean and atmosphere during intervals of oceanic anoxia. *Geology* **33**, 397–400 (2005). doi: 10.1130/G21295.1
17. K. Grice *et al.*, Photic zone euxinia during the Permian-triassic superanoxic event. *Science* **307**, 706–709 (2005). doi: 10.1126/science.1104323; pmid: 15661975
18. C. Deutsch, A. Ferrel, B. Seibel, H. O. Pörtner, R. B. Huey, Climate change tightens a metabolic constraint on marine habitats. *Science* **348**, 1132–1135 (2015). doi: 10.1126/science.aaa1605; pmid: 26045435
19. See supplementary materials.
20. J. T. Kiehl, C. A. Shields, Climate simulation of the latest Permian: Implications for mass extinction. *Geology* **33**, 757–760 (2005). doi: 10.1130/G21654.1
21. C. Romano *et al.*, Climatic and biotic upheavals following the end-Permian mass extinction. *Nat. Geosci.* **6**, 57–60 (2013). doi: 10.1038/ngeo1667
22. E. A. Sperling, J. C. Ingle, A Permian-Triassic boundary section at Quinn River Crossing, northwestern Nevada, and implications for the cause of the Early Triassic chert gap on the western Pangean margin. *Bull. Geol. Soc. Am.* **118**, 733–746 (2006). doi: 10.1130/B25803.1
23. J. L. Sarmiento, N. Gruber, M. A. Brzezinski, J. P. Dunne, High-latitude controls of thermocline nutrients and low latitude biological productivity. *Nature* **427**, 56–60 (2004). doi: 10.1038/nature02127; pmid: 14702082
24. H. O. Pörtner, R. Knust, Climate change affects marine fishes through the oxygen limitation of thermal tolerance. *Science* **315**, 95–97 (2007). doi: 10.1126/science.1135471; pmid: 17204649
25. C. C. Peterson, K. A. Nagy, J. Diamond, Sustained metabolic scope. *Proc. Natl. Acad. Sci. U.S.A.* **87**, 2324–2328 (1990). doi: 10.1073/pnas.87.6.2324; pmid: 2315323
26. S. M. Stanley, Estimates of the magnitudes of major marine mass extinctions in earth history. *Proc. Natl. Acad. Sci. U.S.A.* **113**, E6325–E6334 (2016). doi: 10.1073/pnas.1613094113; pmid: 27698119
27. H. Song *et al.*, Anoxia/high temperature double whammy during the Permian-Triassic marine crisis and its aftermath. *Sci. Rep.* **4**, 4132 (2014). doi: 10.1038/srep04132; pmid: 24549265
28. P. D. Roopnarine, K. D. Angielczyk, S. C. Wang, R. Hertog, Trophic network models explain instability of Early Triassic terrestrial communities. *Proc. Biol. Sci.* **274**, 2077–2086 (2007). doi: 10.1098/rspb.2007.0515; pmid: 17609191
29. A. H. Knoll, R. K. Bambach, D. E. Canfield, J. P. Grotzinger, Comparative Earth history and Late Permian mass extinction. *Science* **273**, 452–457 (1996). doi: 10.1126/science.273.5274.452
30. R. J. Matear, A. C. Hirst, Long-term changes in dissolved oxygen concentrations in the ocean caused by protracted global warming. *Global Biogeochem. Cycles* **17**, 1125 (2003). doi: 10.1029/2002GB001997
31. L. Bopp *et al.*, Multiple stressors of ocean ecosystems in the 21st century: Projections with CMIP5 models. *Biogeosciences* **10**, 6225–6245 (2013). doi: 10.5194/bg-10-6225-2013
32. M. Collins *et al.*, *Climate Change 2013: The Physical Science Basis. Contribution of Working Group I to the Fifth Assessment Report of the Intergovernmental Panel on Climate Change* (Cambridge Univ. Press, 2013).

ACKNOWLEDGMENTS

We gratefully acknowledge the technical support of H. Frenzel, C. Bitz, and A. Winguth, data contributions from B. Seibel, and all those who contributed to the PaleoBiology Database, inspiration from R. Huey, the suggestions of three anonymous reviewers, and high-performance computing support from Yellowstone (ark:/85065/d7wd3xhc) provided by NCAR's Computational and Information Systems Laboratory. **Funding:** Supported by grants from the

Downloaded from http://science.sciencemag.org/ on December 6, 2018

Gordon and Betty Moore Foundation (GBMF#3775) and NSF (OCE-1419323 and OCE-1458967). E.A.S. was supported by a Sloan Research Fellowship. **Author contributions:** C.D. initiated the study; J.L.Pe. designed and conducted model simulations; J.L.Pe. and C.D. analyzed model output; J.L.Pa. and E.A.S. analyzed fossil data; and J.L.Pe. and C.D. wrote the paper with input from all authors. **Competing interests:** The authors declare no competing interests. **Data and materials availability:** The locations of all data used in this study are provided in the supplementary materials. Climate model output is available at Figshare; doi: 10.6084/m9.figshare.7357193.

SUPPLEMENTARY MATERIALS

www.sciencemag.org/content/362/6419/eaat1327/suppl/DC1
Materials and Methods
Supplementary Text
Figs. S1 to S15
Tables S1 to S3
References (*33*–*71*)

30 January 2018; accepted 19 October 2018
10.1126/science.aat1327

Downloaded from http://science.sciencemag.org/ on December 6, 2018

REPORT

POLYMERS

Semiconducting polymer blends that exhibit stable charge transport at high temperatures

Aristide Gumyusenge[1], Dung T. Tran[1], Xuyi Luo[1], Gregory M. Pitch[2], Yan Zhao[1], Kaelon A. Jenkins[1], Tim J. Dunn[3], Alexander L. Ayzner[2], Brett M. Savoie[4]*, Jianguo Mei[1]*

Although high-temperature operation (i.e., beyond 150°C) is of great interest for many electronics applications, achieving stable carrier mobilities for organic semiconductors at elevated temperatures is fundamentally challenging. We report a general strategy to make thermally stable high-temperature semiconducting polymer blends, composed of interpenetrating semicrystalline conjugated polymers and high glass-transition temperature insulating matrices. When properly engineered, such polymer blends display a temperature-insensitive charge transport behavior with hole mobility exceeding 2.0 $cm^2/V{\cdot}s$ across a wide temperature range from room temperature up to 220°C in thin-film transistors.

The performance of inorganic semiconductors optimized for operation at ambient temperatures degrades at elevated temperatures. Charge carriers are thermally promoted across the band gap, which leads to increased carrier densities, junction leakages, and reduced charge carrier mobility (*1*–*3*). To improve the device performance and lifetime in these harsh thermal conditions, wide-bandgap materials have been utilized (*4*, *5*). Alternatively, active or passive cooling, thermally engineered packaging, as well as electrical isolation between multiple transistors are used to maintain the optimal electronic performance (*6*). By contrast, organic semiconductors commonly display thermally activated charge transport features (*7*, *8*). Charge transport is facilitated in organics with moderate temperature increases, leading to improved performance (*9*). However, this thermally activated charge transport becomes counteracted by unstable morphologies and disrupted molecular packing at higher temperatures, especially in polymer thin films (*10*, *11*). Although devices such as organic field-effect transistors are now common (*12*), their operation is normally at ambient conditions. High-temperature annealing effects have been explored in organic semiconductors (*13*–*15*), but in all reports, charge-carrier mobilities have been temperature dependent and start to decline at >150°C.

Blending semiconducting polymers with insulating hosts has been used as a general strategy to improve electronic performance, processability, and mechanical and environmental stability in electronic devices (*16*–*18*). Preserving close intermolecular interactions and packing motifs at elevated temperatures is the key challenge, especially for semiconducting polymers (*10*, *19*). We hypothesized that interpenetrating networks between semicrystalline conjugated polymers and high glass-transition (T_g) insulating polymers can confine conformational changes of semiconducting polymer chains at elevated temperatures. To test this concept, we first select diketopyrrolopyrrole-thiophene (DPP-T; P1), a high-performance conjugated polymer, and poly(N-vinyl carbazole) (PVK, T_g ~220°C) as the high-Tg host (Fig. 1A) and studied blends from 40 to 90 weight % (wt %) of PVK in spin-cast films. The blends with between 55 and 65 wt % PVK formed interpenetrating channels between the conjugated polymer P1 and the rigid host PVK, as observed from atomic force microscopy (AFM) images (Fig. 1B and fig. S1).

Testing the blend films in field-effect transistors (FETs) under ambient and inert conditions, we observed thermally stable operations at high temperatures up to 220°C with hole mobilities as high as 2.5 $cm^2/V{\cdot}s$ at the blend ratios of 55 to 65 wt % PVK that created a bicontinuous morphology with interconnected P1 domains (Fig. 1C and fig. S2). With loadings outside this range, undesired vertical or large lateral phase segregation occurs, which leads to the loss of thermal stability. The mobility of the pristine semiconductor P1 decreases to 8% at 220°C. Ultraviolet-visible (UV-Vis) absorption spectra (Fig. 1D) revealed an increase in the *0-0* vibronic peak intensities upon approaching the optimal blending ratios, indicative of increasing ordering and π-π interactions between P1 chains in the confined domains (*20*–*22*). The bottom surface morphology analysis confirms that the interpenetrating structure is preserved at the gate interface in the thermally stable high-performance blends (fig. S3).

To elucidate the observed thermal stability of the 60 wt % PVK blend versus pure P1, we use in situ temperature-dependent UV-Vis spectroscopy, AFM, and grazing incidence x-ray diffraction (GIXD), as well as molecular dynamics simulations to study the effect of temperature on the intermolecular interactions of the semiconducting chains. Upon heating, the UV-Vis absorption spectra of pristine P1 films revealed a blue shift of 35 nm in the maximum absorption peak, accompanied by a decrease in both the *0-0* and the *0-1* peaks (Fig. 2A). These phenomena are consistent with the polymer chains' deaggregating and reorganizing caused by the thermal energy disrupting the crystallites. For the blend films, the chain ordering and interchain interactions were less affected upon heating, in comparison with pristine P1 films, as evidenced by the less pronounced decrease of the *0-0* vibronic peak intensity. More distinctively, the *0-0* vibronic peak that vanished in the P1 films was retained in the blended films even at temperatures up to 220°C (Fig. 2B). The temperature-dependent AFM analysis also revealed that the microscale morphology of the pristine P1 films changes upon heating, whereas the P1/PVK blend film morphology is not affected by heating (fig. S4). Together, these observations indicated that the matrix polymer effectively confined the semiconducting polymer and limited dihedral twisting and larger structural reorganizations that were responsible for the loss of the carrier mobility at high temperatures.

In situ temperature-dependent GIXD studies showed that in the 60% PVK blend film, the π-π stacking distance of P1 was reduced from 3.70 to 3.64 Å, relative to the pristine P1 (Fig. 3, C and D, and fig. S5). In both cases, the π-π stacking distance increased when the thin films were heated and reached 3.79 and 3.73 Å at 200°C for the pure P1 and the PVK blend films, respectively.

---

[1]Department of Chemistry, Purdue University, 560 Oval Drive, West Lafayette, IN 47907, USA. [2]Department of Physical & Biological Sciences-Chemistry and Biochemistry, University of California Santa Cruz, 1156 High Street, Santa Cruz, CA 95064, USA. [3]SLAC National Accelerator Laboratory, Stanford University, 2575 Sand Hill Road, Menlo Park, CA 94025, USA. [4]Charles D. Davidson School of Chemical Engineering, 480 Stadium Mall Drive, Purdue University, West Lafayette, IN 47906, USA.
***Corresponding author. Email: bsavoie@purdue.edu (B.M.S.); jgmei@purdue.edu (J.M.)**

Downloaded from http://science.sciencemag.org/ on December 6, 2018

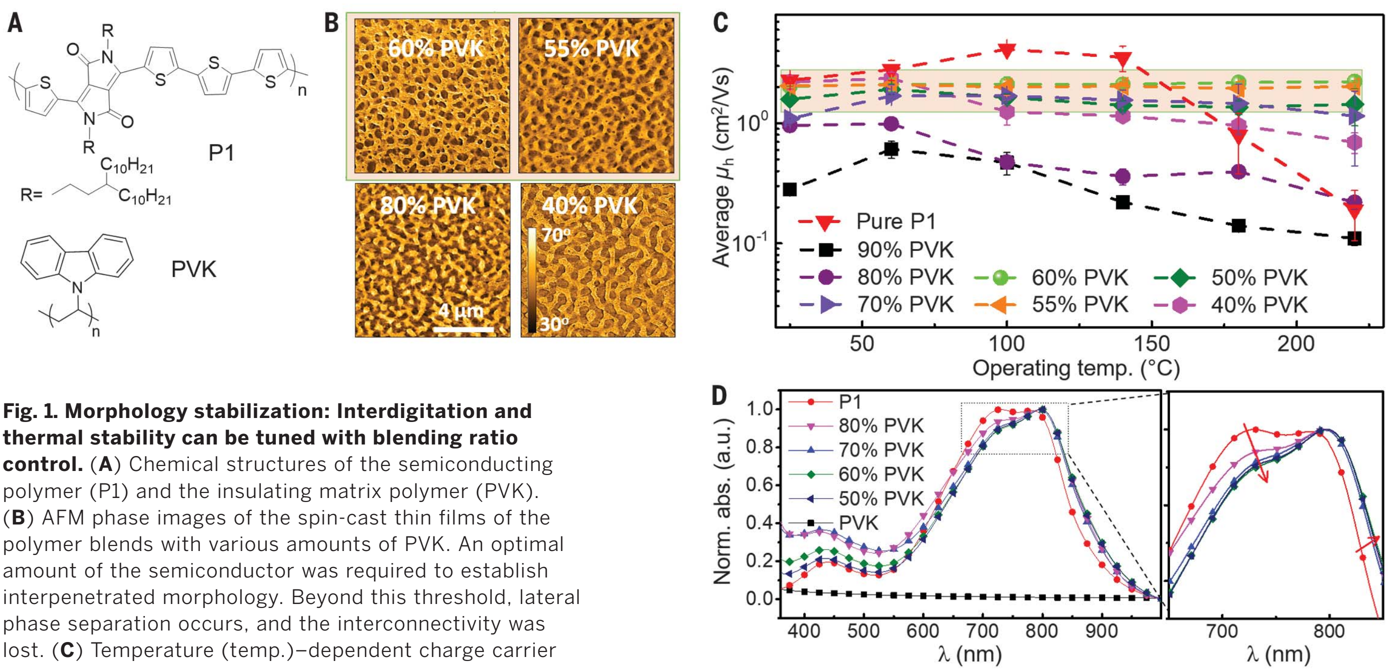

Fig. 1. Morphology stabilization: Interdigitation and thermal stability can be tuned with blending ratio control. (**A**) Chemical structures of the semiconducting polymer (P1) and the insulating matrix polymer (PVK). (**B**) AFM phase images of the spin-cast thin films of the polymer blends with various amounts of PVK. An optimal amount of the semiconductor was required to establish interpenetrated morphology. Beyond this threshold, lateral phase separation occurs, and the interconnectivity was lost. (**C**) Temperature (temp.)–dependent charge carrier mobility in FET devices based on P1 blends containing various ratios of PVK. The data points represent the average hole mobility measured from 10 different devices for each blending ratio, and the error bars represent the standard deviation from the average. The pure P1 data are also plotted. (**D**) Normalized UV-Vis absorption spectra (Norm. abs.) of P1-PVK blends with varying amounts of the matrix polymer. The confinement of the semiconductor within rigid domains of the host led to increased ordering of the conjugated polymer chains. a.u., arbitrary units.

To evaluate the effect of this π-π stacking confinement on the polymer dihedral distribution, molecular dynamics modeling was performed. In these simulations, the π-π separation of the semiconducting polymer chains was restrained to model varying levels of confinement, and the resulting dihedral distributions were compared to characterize the polymer reorganization dynamics (Fig. 3E). At π-π confinements of 3.0 Å, we observed complete conservation of the dihedral distributions at all temperatures. Notably, the CCCN dihedral, corresponding to the DPP-T conformations, exhibited interconversion between gauche conformers, but there was no evidence of gauche-to-trans interconversion (i.e., the onset of chain twisting) at any temperature. Likewise, the SCCC dihedral angle, corresponding to the thiophene-thiophene conformations, broadened with temperature but remained sharply peaked. By contrast, at π-π confinements of 5.0 Å, the SCCC dihedral distribution is broadened at all temperatures, and the CCCN dihedral exhibits gauche-to-trans interconversion at all temperatures (Fig. 3, F and G). Systematic studies of the dihedral distributions under confinements from 3 to 6 Å allowed us to conclude that large-scale DPP-T reorganizations began relatively abruptly once fluctuations in the interchain π-π separation reach ~5 Å (figs. S7 to S9). On the basis of these results, we interpret the π-π confinement exhibited by the bicontinuous P1/PVK blends to play a critical role in restricting intrachain reorganization and enabling temperature-insensitive mobility. This mechanism suggests that this confinement strategy should be general to other semiconducting polymers embedded in similarly rigid matrix polymers or potentially to other confinement strategies like channel templating. The relatively broad range of blending concentrations that exhibit temperature insensitivity (40 to 70%) implies that this effect is relatively insensitive to the width of the confined semiconducting domains.

To evaluate the stability of the blend films under prolonged thermal stress, the fabricated FET devices were subjected to constant heating at 150°C for 6 hours in air. For inorganic semiconductors, prolonged heating leads to increased charge-carrier density and uncontrolled thermal doping (*23*). For organics, prolonged heating, especially above the T_g or the melting point of the semiconductors, leads to morphology changes and device performance degradation (*10*, *11*, *15*). In contrast with the pristine P1 devices under the same conditions, the devices based on the 60% PVK blends retained excellent electronic properties (as high as 95% of the original mobility) under thermal stress (Fig. 3A). The FET devices made from pristine P1 showed a declining on-off current ratio (I_{ON}/I_{OFF}) and increased threshold voltages under constant heating, consistent with earlier observation of unstable morphologies at high temperatures. The thermally stabilized blend-based FET devices retain an on-off current ratio higher than 10^3 and threshold voltages below 3 V after thermal stressing (Fig. 3, B to D).

To demonstrate the generality of our blending strategy, we explore the FET thermal stability of P1 blended with four other high-T_g matrices i.e., polycarbonate (PC), polyacenaphthylene (PAC), polyetherimide (PEI), and Matrimid 5218 (MI) (Fig. 4A). We first optimized the blending ratios to attain interpenetrating morphologies (fig. S10A). FET devices based on these optimized blends exhibited thermally stable charge transport and the P1/PAC blend pair could reach hole mobilities as high as 2.0 cm^2/V·s that were stable up to 220°C in open air (Fig. 4B). The optimized P1/PC blend only provided thermally stable operation up to 180°C, which is near the T_g of the host. We also tested other donor-acceptor semiconductors based on high-performance DPP (P2) (*20*) and isoindigo (P3) (*24*) (Fig. 4C) and studied the thermal stability of their blend films with the champion high-Tg matrices, i.e., PVK and PAC. After optimizing the blend ratios to obtain an interpenetrating morphology (fig. S10B), FET devices with excellent thermal stability up to 220°C were also achieved

Downloaded from http://science.sciencemag.org/ on December 6, 2018

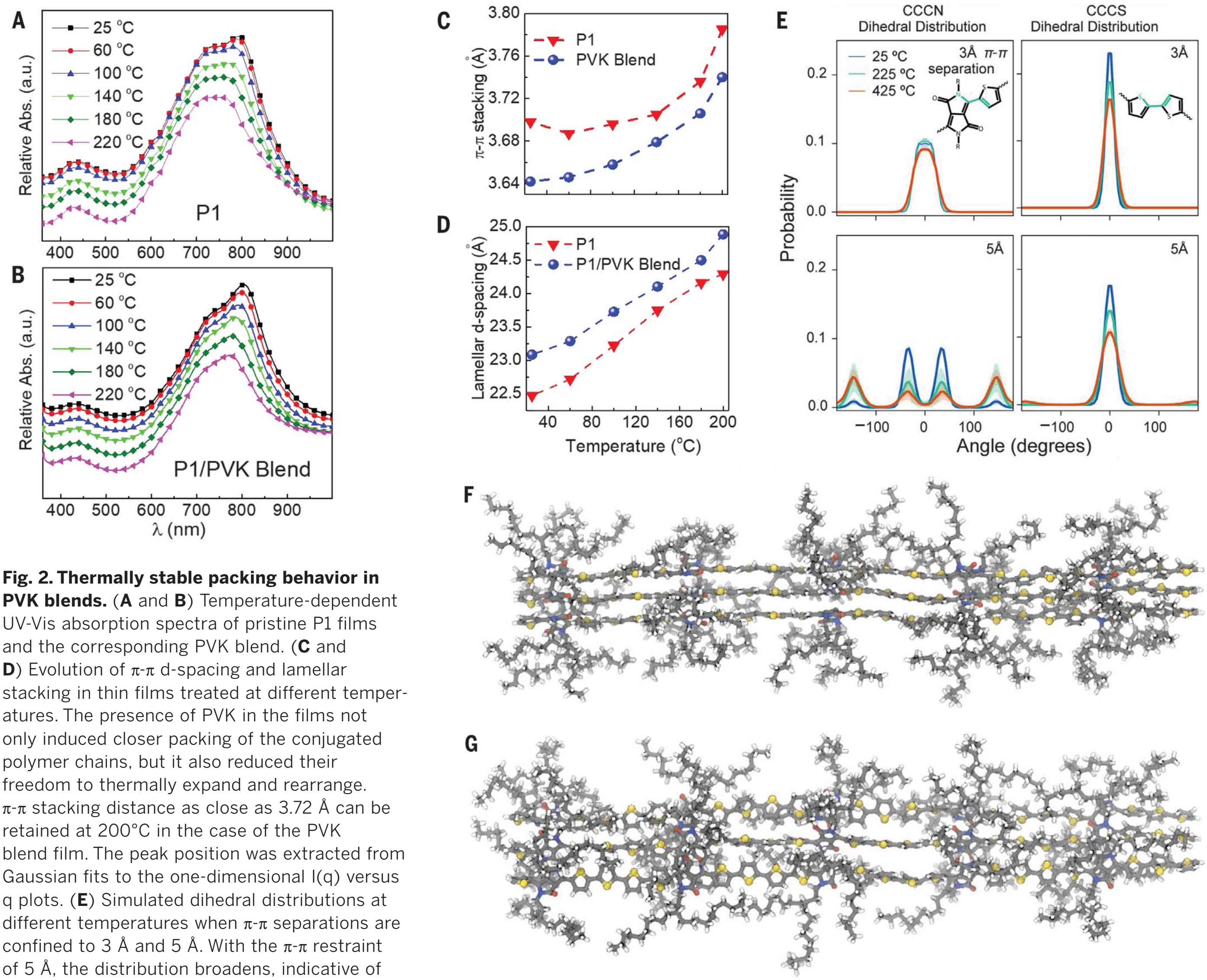

Fig. 2. Thermally stable packing behavior in PVK blends. (**A** and **B**) Temperature-dependent UV-Vis absorption spectra of pristine P1 films and the corresponding PVK blend. (**C** and **D**) Evolution of π-π d-spacing and lamellar stacking in thin films treated at different temperatures. The presence of PVK in the films not only induced closer packing of the conjugated polymer chains, but it also reduced their freedom to thermally expand and rearrange. π-π stacking distance as close as 3.72 Å can be retained at 200°C in the case of the PVK blend film. The peak position was extracted from Gaussian fits to the one-dimensional I(q) versus q plots. (**E**) Simulated dihedral distributions at different temperatures when π-π separations are confined to 3 Å and 5 Å. With the π-π restraint of 5 Å, the distribution broadens, indicative of chains twisting at all temperatures. (**F** and **G**) Packing behavior of DPP-T chains when confined to 3 Å and 5 Å, respectively.

Downloaded from http://science.sciencemag.org/ on December 6, 2018

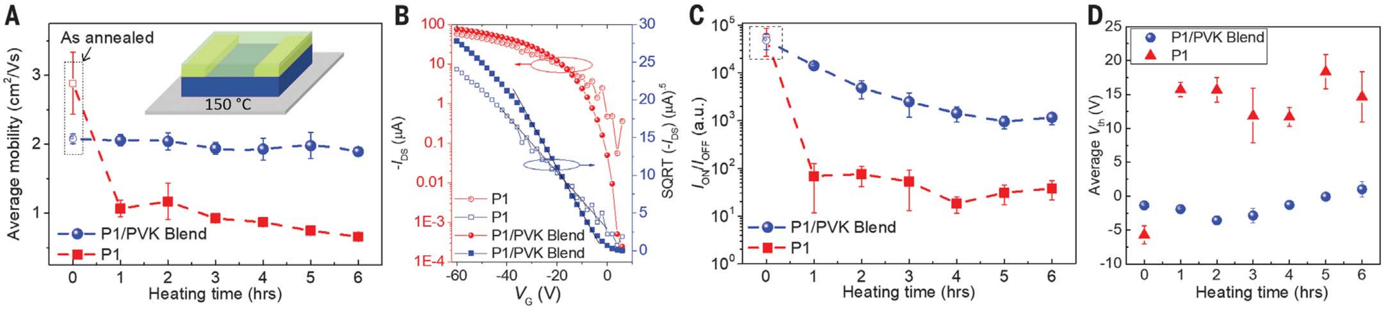

Fig. 3. Effect of thermal stress on FET devices and thermal stability of PVK blends. (**A**) Measured hole mobilities under constant thermal stress for 6 hours. A sudden decline in mobility was observed for pure P1 when the FET device is heated. The blend can retain its original mobility after 6 hours. (**B**) Characteristic transfer curves of FET devices based on P1 with and without PVK after 1 hour of heating. SQRT, square root. (**C**) Impact of heating on the I_{ON}/I_{OFF}. After 1 hour of heating, the ratio fell to nearly 10 for the devices based on P1 while remaining > 10^4 for the blend devices. (**D**) Threshold voltages (V_{th}) for FET devices based on the 60% PVK blends (below 3 V) and pure P1 (exceeding 20 V) upon prolonged heating. The data points represent the average values measured from 10 different devices, and the error bars represent the standard deviation from the average.

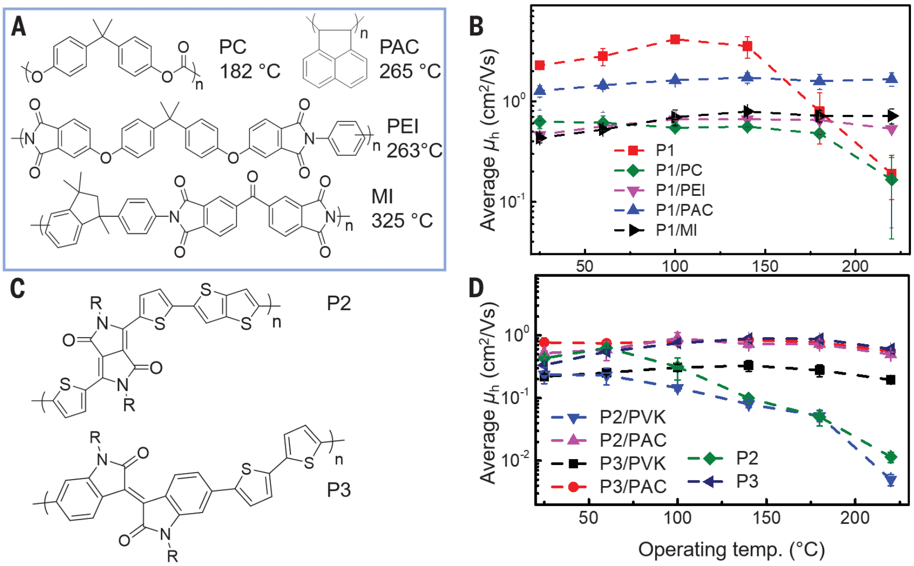

Fig. 4. Attaining universal thermal stability in semiconducting polymer blends. (**A**) Molecular structures and glass-transition temperatures of the representative matrix polymers tested for high-temperature charge transport. Matrimid 5218; PEI, polyetherimide. (**B**) Hole mobilities of FET devices based on the optimized blends of P1 in four different matrices measured in open air. (**C**) Molecular structures of additional semiconducting polymers studied for thermally stable blends. (**D**) Measured FET mobilities from the blend films of P2 and P3 with PVK and PAC used as the host matrices. The blend combinations that had stable close packing exhibited hole mobilities stable up to 220°C. The data points represent the average mobility values measured from 10 different devices, and the error bars represent the standard deviation from the average.

(Fig. 4D). Temperature-dependent UV-Vis absorption analyses on the blend films of P2 and P3 confirmed that those blend pairs with thermally insensitive charge transport properties exhibited a similar behavior as the P1/PVK blend at high temperatures (figs. S11 to S14). One exception was the P2/PVK pair, which did not present a thermally stable charge transport behavior (Fig. 4D). Likewise, this pair did not preserve the characteristic intermolecular interaction vibronic peak upon heating, indicating that this was a necessary feature in stable blends (fig. S12). We also noticed that the pristine P3 film exhibited a nearly thermally stable operation across the tested temperature range. Consistent with the thermally stable blends previously discussed, the P3 film itself also exhibited strong intermolecular interactions even at high temperatures (fig. S13), which suggested the organization of P3 is unusually robust among the studied semiconductors. Lastly, the blending strategy was tested for n-type semiconducting systems, and the blend films that form interpenetrating morphologies exhibited thermally stable operation in comparison with the pristine thin films (fig. S20).

To design high-temperature semiconducting polymer blends, a few requirements appear to be essential: (i) a host matrix with a T_g higher than the desired operating temperature; (ii) a semicrystalline semiconducting polymer; (iii) the interpenetration of the semiconducting component into the host matrix; and (iv) improved intermolecular π-π stacking within semiconducting channels that can be retained at high temperature. The use of high-T_g matrices is demonstrated to be a general strategy to attain these properties by minimizing spatial rearrangements within the polymer films at elevated temperatures. We hypothesized that the superior ordering in the confined channels enhanced charge transport by reduced activation energy and trap density.

REFERENCES AND NOTES

1. P. G. Neudeck, R. S. Okojie, L.-Y. Chen, *Proc. IEEE* **90**, 1065–1076 (2002).
2. S. M. Sze, in *Physics of Semiconductor Devices*, K. K. Ng, Ed. (Wiley-Interscience, ed. 3, 2007).
3. J. Watson, G. Castro, *J. Mater. Sci. Mater. Electron.* **26**, 9226–9235 (2015).
4. T. P. Chow, R. Tyagi, *IEEE Trans. Electron Dev.* **41**, 1481–1483 (1994).
5. P. G. Neudeck *et al.*, *IEEE Electron Device Lett.* **29**, 456–459 (2008).
6. B. Hunt, A. Tooke, in *Proceedings of the 18th European Microelectronics Packaging Conference* (IEEE, 2011), pp. 1–5.
7. G. Horowitz, *Adv. Mater.* **10**, 365–377 (1998).
8. H. Sirringhaus *et al.*, *Nature* **401**, 685–688 (1999).
9. V. Coropceanu *et al.*, *Chem. Rev.* **107**, 926–952 (2007).
10. Y. Zhao *et al.*, *Adv. Mater.* **29**, 1605056 (2017).
11. J. Chen *et al.*, *J. Polym. Sci., B, Polym. Phys.* **44**, 3631–3641 (2006).
12. H. Sirringhaus, *Adv. Mater.* **26**, 1319–1335 (2014).
13. T. Sekitani, S. Iba, Y. Kato, T. Someya, *Appl. Phys. Lett.* **85**, 3902–3904 (2004).
14. J. T. Kintigh *et al.*, *J. Phys. Chem. C* **118**, 26955–26963 (2014).
15. M. Seifrid, M. J. Ford*Adv. Mater.* **29**, 1605511 (2017).
16. S. Goffri *et al.*, *Nat. Mater.* **5**, 950–956 (2006).
17. A. Kumar, M. A. *Adv. Mater.* **21**, 4447–4451 (2009).
18. S.-Y. Min *et al.*, *Nat. Commun.* **4**, 1773 (2013).
19. E. K. Lee, M. Y. Lee, C. H. Park, H. R. Lee, J. H. Oh, *Adv. Mater.* **29**, 1703638 (2017).
20. Y. Lei *et al.*, *Adv. Mater.* **28**, 6687–6694 (2016).
21. Y. Lei *et al.*, *Sci. Rep.* **6**, 24476 (2016).
22. F. C. Spano, C. Silva, *Annu. Rev. Phys. Chem.* **65**, 477–500 (2014).
23. W. Wondrak, *Microelectron. Reliab.* **39**, 1113–1120 (1999).
24. R. Stalder, J. Mei, K. R. Graham, L. A. Estrada, J. R. Reynolds, *Chem. Mater.* **26**, 664–678 (2014).

ACKNOWLEDGMENTS

We thank the Stanford Synchrotron Radiation Laboratory (a national user facility operated by Stanford University on behalf of the U.S. Department of Energy, Office of Basic Energy Sciences, under contract no. DE-AC02-76SF00515) for providing the equipment for the GIXD measurements. **Funding:** This work was supported by the Office of Naval Research Young Investigator Program (ONR YIP Award, no. N00014-16-1-2551) and the National Science Foundation (NSF CAREER Award, no. 1653909). **Author contributions:** A.G. and J.M. designed the experiments; A.G. processed the thin films, did the morphology characterizations, and fabricated and characterized the transistor devices; D.T.T. and Y.Z. helped with the measurements under nitrogen. X.L. synthesized the conjugated polymers; D.T.T. performed the DSC measurements; K.A.J. helped with the UV-Vis measurements. G.M.P., T.J.D, and A.L.A. designed and performed the GIXD measurements. B.M.S. designed and performed all the computational work. A.G., B.M.S., and J.M. organized the data and wrote the manuscript, and all authors contributed to the editing of the manuscript. J.M. conceived and directed the project. **Competing interests:** A.G. and J.M. are inventors on a patent application no. 62677648 submitted by the Office of Technology Commercialization Purdue Research Foundation. **Data and materials availability:** All data needed to evaluate the conclusions in the manuscript are provided in the manuscript or the supplementary materials.

SUPPLEMENTARY MATERIALS

www.sciencemag.org/content/362/6419/1131/suppl/DC1
Materials and Methods
Tables S1 to S3
Figs. S1 to S20
References (*25*–*33*)

1 August 2018; accepted 29 October 2018
10.1126/science.aau0759

Downloaded from http://science.sciencemag.org/ on December 6, 2018

NANOMATERIALS

Building two-dimensional materials one row at a time: Avoiding the nucleation barrier

Jiajun Chen[1,2], Enbo Zhu[3,4], Juan Liu[5], Shuai Zhang[2], Zhaoyang Lin[6], Xiangfeng Duan[6,7], Hendrik Heinz[5], Yu Huang[3,7]*, James J. De Yoreo[1,2]*

Assembly of two-dimensional (2D) molecular arrays on surfaces produces a wide range of architectural motifs exhibiting unique properties, but little attention has been given to the mechanism by which they nucleate. Using peptides selected for their binding affinity to molybdenum disulfide, we investigated nucleation of 2D arrays by molecularly resolved in situ atomic force microscopy and compared our results to molecular dynamics simulations. The arrays assembled one row at a time, and the nuclei were ordered from the earliest stages and formed without a free energy barrier or a critical size. The results verify long-standing but unproven predictions of classical nucleation theory in one dimension while revealing key interactions underlying 2D assembly.

Assembly of two-dimensional (2D) molecular arrays on surfaces has been extensively investigated to understand the structural relation between substrate and film (*1*–*6*), revealing a rich world of frameworks (*1*, *2*, *6*), tilings (*1*, *7*), and chiral architectures (*1*, *8*). Recognition of the electronic (*9*), optical (*9*), chemical (*2*–*4*), and mechanical (*10*) properties of 2D materials has intensified interest in their formation, yet little attention has been given to the underlying mechanism. Whether assembly is described by concepts of classical nucleation theory (CNT) (*11*) or falls within the broader context of "nonclassical" pathways involving formation, aggregation, and transformation of transient precursors (*12*) remains unknown. Using peptides chosen by genetic selection (*13*, *14*) for their binding affinity to MoS_2 (0001), we investigated nucleation of 2D arrays by molecularly resolved in situ atomic force microscopy (AFM) and molecular dynamics (MD) simulations.

The peptides consisted of seven amino acids [Tyr-Ser-Ala-Thr-Phe-Thr-Tyr (YSATFTY), named MoSBP1] with acylated and amidated N and C termini, respectively, to reduce electrostatic interactions (*15*) (fig. S1). When incubated with freshly cleaved MoS_2 substrates, MoSBP1 assembled into elongated islands aligned along three equivalent directions on MoS_2 (0001) and exhibited aspect ratios that decreased with increasing peptide concentration (Fig. 1, A to C). The islands were ~0.7 nm in height (fig. S2), indicating that they were one monolayer thick, and consisted of parallel rows with a periodicity of 4.1 nm (Fig. 1, D to F, and fig. S3). Comparison of the row directions to the underlying MoS_2 (0001) lattice demonstrated that they formed at an angle of 30° to the densest sulfur packing directions (fig. S4).

Molecular-resolution imaging showed that each row consists of ~1.1 nm × 4.7 nm units running at ~60° to the rows (Fig. 1, E and F), demonstrating the highly ordered structure of each row (Fig. 1F and fig. S5). The dimensions and symmetry of the units were consistent with dimer formation with the same termini of the two monomers facing one another (C-to-C or N-to-N), as indicated by the following observations: (i) The length of each unit was ~1.7 times the maximum possible length of a fully extended MoSBP1 molecule. (ii) The units exhibited two-fold symmetry down to a submolecular level. (iii) The central portion of each unit was higher than the ends, suggesting overlap of the peptides in that region. (iv) The absence of chains extending along the direction parallel to the dimers, which would result in variable row widths, excluded an N-to-C or C-to-N association within the dimers. (v) Ring-like structures ~0.5 nm in diameter, similar to the size reported in other AFM studies of a flat-lying phenyl ring (*16*), lay symmetrically on both sides of the rows (fig. S5C).

To understand the detailed structure and key interactions that stabilized the film, we performed MD simulations using the CHARMM-Interface force field (*17*) starting with single

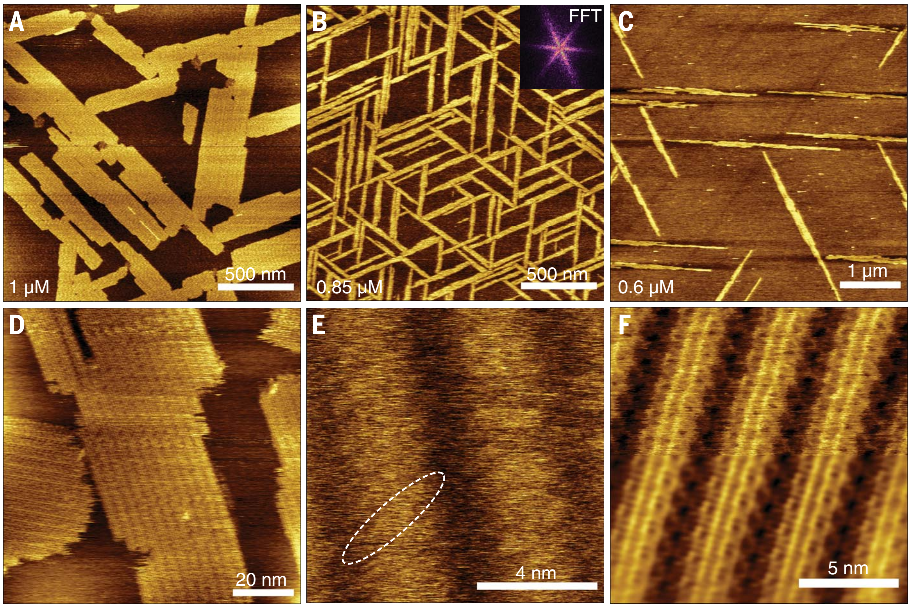

Fig. 1. In situ AFM images of MoSBP1 on MoS_2 (0001). (**A** to **C**) Self-assembled structure at different concentrations. (**D**) Islands consist of co-aligned rows with uniform spacing. (**E**) Non–contact mode image shows that each row consists of small building blocks lying at ~60° to the row orientation. (**F**) High-resolution contact mode image shows detailed structure with connections between rows. The bottom half of (F) was fast Fourier transform–filtered.

---

[1] Department of Materials Science and Engineering, University of Washington, Seattle, WA 98195, USA. [2] Physical Sciences Division, Pacific Northwest National Laboratory, Richland, WA 99352, USA. [3] Department of Materials Science and Engineering, University of California, Los Angeles, CA 90095, USA. [4] School of Materials Science and Engineering, Beijing Institute of Technology, Beijing 100081, P. R. China. [5] Department of Chemical and Biological Engineering, University of Colorado, Boulder, CO 80309, USA. [6] Department of Chemistry and Biochemistry, University of California, Los Angeles, CA 90095, USA. [7] California NanoSystems Institute, University of California, Los Angeles, CA 90095, USA.
*Corresponding author. Email: james.deyoreo@pnnl.gov (J.J.D.Y.); yhuang@seas.ucla.edu (Y.H.)

Downloaded from http://science.sciencemag.org/ on December 6, 2018

peptides in different orientations on MoS_2 (Fig. 2, A to D). The MoSBP1 binding energy E_{ads} was −96 ± 9 kcal/mol in the preferred orientation (Fig. 2A) and originated from the replacement of ~25 water molecules in direct contact with MoS_2 surface; these were weakly bound and gained more hydrogen bonds upon release into the solution (fig. S6, A to C). The entropy gain of water was partially compensated by entropy loss of the peptide upon binding, as shown on similar surfaces (*18*), and the free energy of adsorption was approximately −103 ± 10 kcal/mol (see supplementary text). We tested all possible peptide orientations, without constraints in any direction, and found that the backbone preferred to align in the densest sulfur packing direction (Fig. 2, A to D). Defining the direction of a single peptide as the orientation perpendicular to the main body of the peptide, we found a strong preference for single peptides to align at 30°, 90°, and 150° relative to the $[2\bar{1}\bar{1}0]$ direction of the MoS_2 lattice (Fig. 2, B to E), matching the observed row directions.

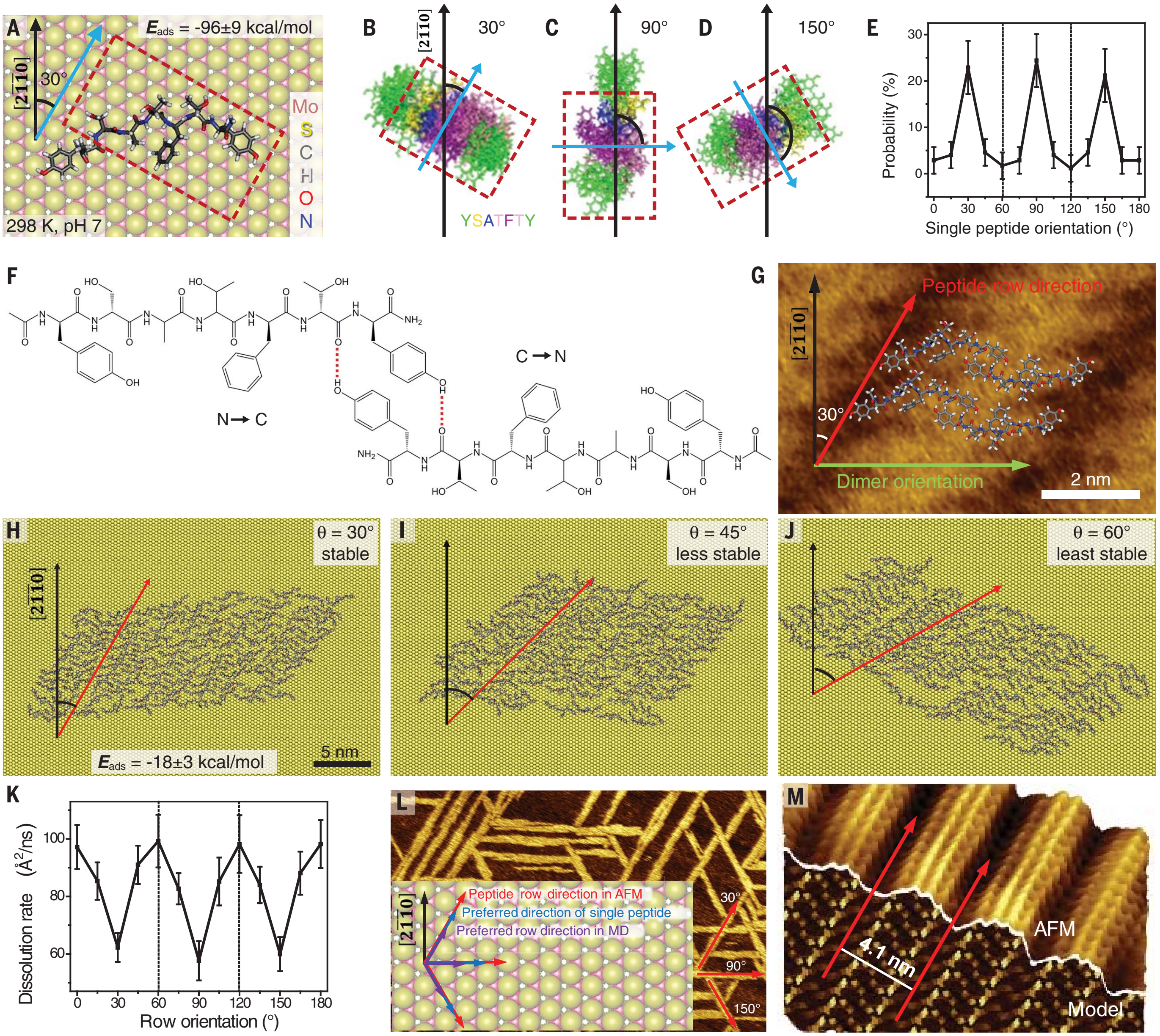

Fig. 2. Predicted alignments of MoSBP1, dimers, and assemblies on MoS_2 (0001) from MD simulations. (**A**) Favorable binding conformation of a single peptide. (**B** to **D**) Preferred orientations of single peptides on the surface, colored by residue (A, Ala; F, Phe; S, Ser; T, Thr; Y, Tyr). Red boxes and blue arrows in (A) to (D) show main body and direction of a single peptide. (**E**) The probability of a single peptide at different angles relative to the $[2\bar{1}\bar{1}0]$ direction. (**F**) Proposed dimer arrangement stabilized by hydrogen bonds. (**G**) The most stable dimer conformation, overlaid on an AFM image. The dimer direction points from a phenyl ring at one end of the dimer to another phenyl ring at the other end, which shows a 60° difference from the row direction. (**H** to **J**) Snapshots of ~20-nm peptide assemblies with the dimer arrangement in (G) at different orientations on the surface. (**K**) The stability is highest, and the dissolution rate is lowest, at angles of 30°, 90°, and 150°. (**L**) Preferred orientations from MD agree with experimental results. (**M**) Simulated AFM image of peptide rows along the preferred orientation is consistent with AFM data. Error bars in (E) and (K) denote SD in the simulation.

Downloaded from http://science.sciencemag.org/ on December 6, 2018

To understand the stabilization of peptide rows, we simulated numerous dimer configurations, the most stable of which is shown schematically in Fig. 2F and overlaid on an AFM image in Fig. 2G. We tested the stability of large assemblies of these dimers ~20 nm in size with different row orientations relative to the lattice in MD simulations (Fig. 2, H to J). Peptide row stability was again substantially higher when aligned at 30°, 90°, and 150° relative to $[2\bar{1}\bar{1}0]$ (Fig. 2, K and L). In all cases, some disorder was introduced during the simulation, presumably because of the smaller domain size relative to experiments and some limitations in both conformation sampling and force fields.

The most stable structures (Fig. 2, H and K) were consistent with the topography seen by AFM (Fig. 2, L and M); a simulated AFM image based on the MD results (Fig. 2M) confirmed the importance of the phenyl rings of Tyr and Phe in surface recognition and attachment (fig. S6, A to C). The dimer itself was stabilized by hydrogen bonds between the –OH of Tyr^7 and the –C=O of Thr^6, and possibly by π-π stacking between phenyl rings (Fig. 2F). Interestingly, the adsorption of multiple peptides in large assemblies reduced the attraction per peptide from –96 to –18 kcal/mol (Fig. 2, A and H). Although this energy still corresponded to strong binding (fig. S6, E and F), this result indicated that the required removal of 25 water molecules to bind a single peptide was kinetically prohibited and that the ordered domains of dimer rows represented a metastable state, which was more rapidly achieved

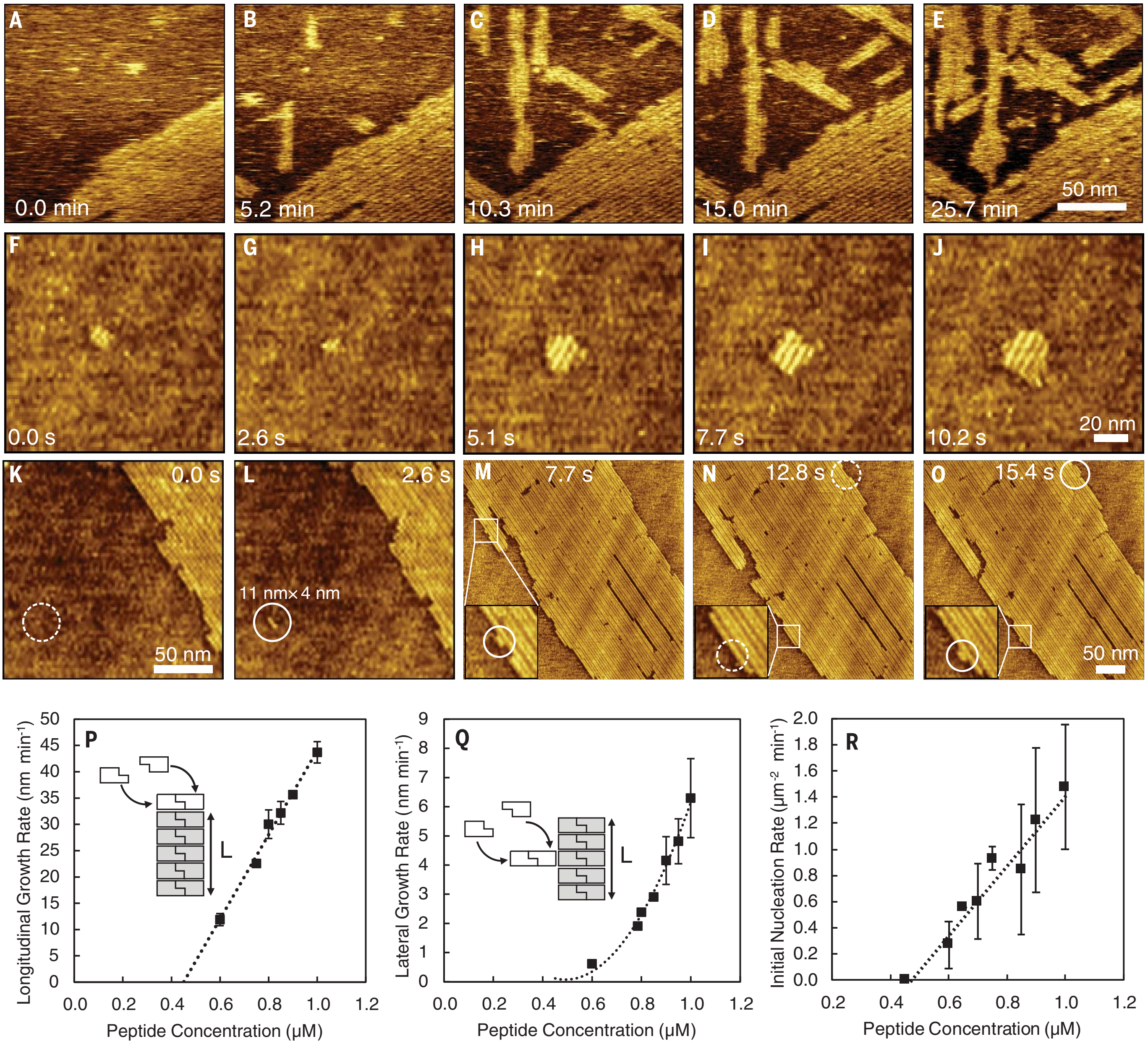

Fig. 3. Nucleation and growth dynamics of MoSBP1 on MoS$_2$ (0001). (**A** to **E**) In situ AFM images show that the peptides attached to the surface and directly grew into ordered structures. (**F** to **O**) In situ high-speed AFM images show formation and development of a small island [(F) to (J)]; nucleation of a single row [(K) and (L)]; and creation of new rows adjacent to existing ones [(M) to (O)]. Circles highlight regions where new rows appear (dashed, before; solid, after). (**P** to **R**) Longitudinal (P) and lateral (Q) island growth rates and initial nucleation rate (R) versus peptide concentration.

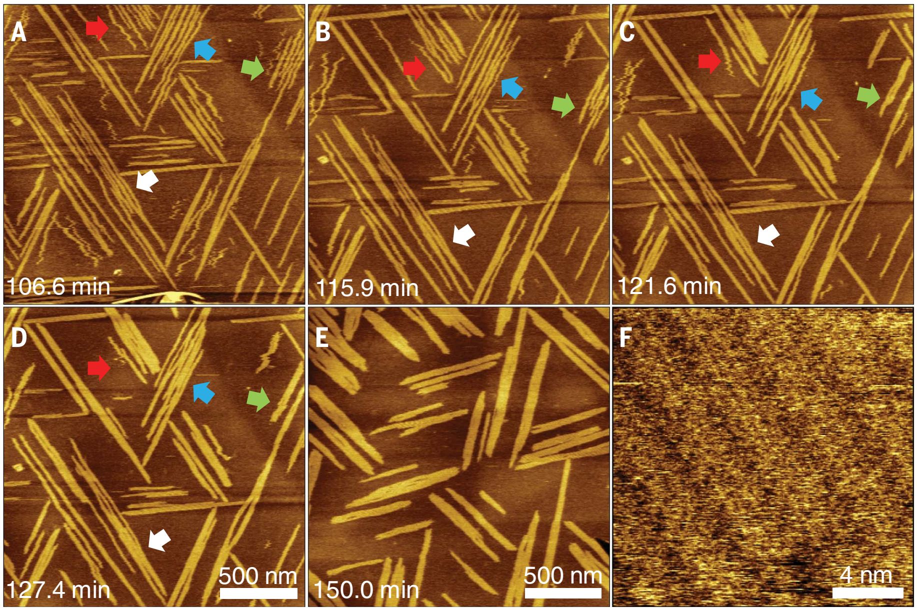

Fig. 4. In situ AFM images of MoSBP1 on HOPG. (**A** to **D**) Sequence of images showing that rows of MoSBP1 on HOPG can diffuse across the surface (arrows), aggregating with other rows to form immobile islands. (**E**) Aggregated islands at another location show the final state of these single rows as constituents of compact 2D islands. (**F**) High-resolution image shows the highly ordered structure of these islands.

via hydrogen bonding and van der Waals interactions.

We further investigated the pathway and kinetics of array formation by continuously monitoring assembly by AFM, with scan rates as high as 2.56 s per frame (Fig. 3, A to O, fig. S7, and movie S1). The results showed that MoSBP1 nuclei exhibited the elongated structure of mature islands and grew along the preferred lattice directions from their first appearance, with no evidence of a transient precursor phase or attachment of large clusters over the course of ~900 sequential frames, according to our current time resolution (Fig. 3, F to O, fig. S7, and movie S1). Moreover, the characteristic 4.1-nm rows aligned along one of the three preferred directions were observed even in the smallest islands with lengths as short as ~8 dimers (~9 nm) (Fig. 3, G and L), further indicating a direct nucleation pathway. Simulation of single peptides and circular dichroism spectra showed that MoSBP1 tended to remain in a monomeric state in bulk solution, which suggests that monomers were the likely growth unit (see supplementary text).

In the early stages of assembly, a few islands grew along directions lying at 30° to the preferred directions, but disappeared over time (~25 min) (fig. S8). Islands that grew along the preferred directions sometimes dissolved as nearby islands grew (~10 min) (fig. S9). These observations demonstrated both the higher stability of islands exhibiting dominant orientations and the reversibility of peptide binding (movie S1).

To understand the energetic controls on assembly, we used time-resolved in situ data to measure nucleation and growth rates, which revealed the crucial role of row-by-row assembly in controlling film formation. The longitudinal growth rate v_{lg} was proportional to peptide concentration c (Fig. 3P), whereas the lateral growth rate v_{la} was proportional to c^2 (Fig. 3Q). The initial nucleation rate J_n was also proportional to c (Fig. 3R), as was the number density of nuclei n_∞ approached asymptotically as time $t \rightarrow \infty$ (fig. S10). Moreover, the concentration below which $J_n = 0$ (0.48 μM), within error, was identical to that at which v_{lg} and v_{la} reached zero (0.45 μM)—that is, the island solubility limit c_e—and there was no lower limit to the size of nuclei that grew spontaneously (fig. S11). Thus, nucleation began as soon as c exceeded c_e, $J_n \propto c$, and the critical island size $N_c = 0$.

These observations are seemingly in violation of predictions of CNT, which hold that 2D islands exhibit a critical size below and above which islands will, on average, dissolve and grow, respectively, and that N_c should scale inversely with supersaturation σ. Moreover, in two dimensions, CNT predicts an exponential dependence of J_n on σ, leading to a strongly nonlinear dependence on c (*11*, *19*). We can reconcile the apparent contradictions and understand all of the observed phenomena by recognizing that, although the final islands are 2D, they form one row at a time. The free energy barrier of CNT arises from the difference in the dimensional dependence between the free energy change ΔG associated with the drop in chemical potential upon crystallization and that associated with surface (3D) or line (2D) tension of the new phase. In two dimensions, the (negative) first term scales with island area A, whereas the (positive) second term is proportional to the perimeter. The second term dominates at small size, but the first term eventually wins out, giving rise to a barrier at finite A and a critical size N_c (*11*, *19*) (fig. S12). In contrast, in one dimension, both contributions to ΔG are proportional to the length L of the nucleus; consequently, there is no barrier, and $N_c = 0$ (fig. S12). Thus, when the assembly process is viewed as continual nucleation of 1D rows, rather than conflicting with CNT, the results verify its long-standing prediction that nucleation of 1D structures occurs without a free energy barrier.

The distinction between the nucleation kinetics of MoSBP1 rows and that of amyloid fibrils, which constitute a quasi-1D material, further highlights the 1D nature of MoSBP1 nucleation. In the amyloid fibril system, which exhibits similar 1D growth behavior, a two-step condensation-ordering process with a nucleation barrier is widely observed (*20*). However, in that system, the initial formation of the disordered oligomeric precursor phase constitutes the nucleation step and leads to the typical shape of the nucleation barrier in three dimensions as described by CNT (*20*).

The fact that there is no free energy barrier to nucleation does not mean that nucleation occurs in the absence of density fluctuations, which all systems at finite temperature must possess. However, when building 1D structures, even density fluctuations that create dimers create supercritical nuclei, because the monomer defines the critical cluster size. The lack of a free energy barrier also does not mean that nucleation—or, for that matter, growth—is unopposed by kinetic barriers associated with molecular-level processes, such as desolvation, conformational changes, or breaking and making of hydrogen bonds. However, these activation barriers are fundamentally different from free energy barriers that are associated with the ability of the system to explore all the available configurational states and are governed by the probability of forming an island larger than the critical size. The activation barriers do not depend on supersaturation and thus have no impact on the dependence of J_n on σ. However, because J_n depends exponentially on both the free energy barrier and the activation barrier, both are important in determining the frequency of nucleation. Thus, even though the lack of a free energy barrier leads to a linear dependence of rate on concentration, the finite activation barrier ensures that nucleation occurs nonetheless through discrete events.

The difference in the concentration dependence of longitudinal and lateral growth rates can also be understood as a consequence of row-by-row growth. Monomers that attach at the row ends are strongly bound, and every attachment is an independent event. Thus, v_{lg} should be linear in c, as observed (Fig. 3P). However, when a new row ($n = 2$) forms adjacent to the first ($n = 1$), the weakness of end-to-end binding causes the attached monomers to have low stability, such that the creation of a stable dimer requires a second attachment event before the first monomer detaches (Fig. 3Q). Hence, v_{1a} should be quadratic in c. This difference explains why increasing c leads to smaller island aspect ratios (Fig. 1, A to C): The rate at which rows $n \geq 2$ are created relative to the rate at which existing rows lengthen is proportional to $(c - c_e)$. In addition, the fact that the lateral growth rate also reaches zero at $c = c_e$ further demonstrates the barrier-free nature of nucleation in this system. The lateral growth rate is directly proportional to the rate at which new rows nucleate heterogeneously along existing rows. Although this rate can be expected to exceed that of new, isolated rows (i.e., homogeneous nucleation), in CNT the kinetics of heterogeneous nucleation are governed by the same expressions with a modified value of the surface or line tension. Thus, a critical size and barrier would be expected for 2D nuclei.

The question then arises as to why the nucleation rate of the first row is linear in c, whereas that of rows $n \geq 2$ is quadratic. We constructed a set of rate equations to describe the creation and destruction of all adsorbed species, including monomers, dimers, and rows (see supplementary text), and derived the initial nucleation rate dn/dt (near $t = 0$):

$$\frac{dn}{dt} \approx \frac{k_m^+ k_n^+ c^2}{c(k_m^+ + k_n^+) + k_m^-} - \frac{k_m^+ k_n^+ c_e^2}{c_e(k_m^+ + k_n^+) + k_m^-} \tag{1}$$

where k_m^+, k_n^+, and k_m^- are the rate coefficients for monomer adsorption, attachment to an adsorbed monomer to form a nucleus, and desorption, respectively. In the limit of high k_m^- (i.e., low coverage), $J_n \propto c^2$. However, at high k_m^+—high monomer coverage—$J_n \propto c$, because every adsorbing monomer has a high probability of finding a monomer that has already adsorbed. Thus, although the need to dock a monomer to the side of a row leads to a quadratic dependence on c for nucleation of rows $n \geq 2$, a high coverage of adsorbed monomers produces a linear dependence on c for the first row of any island.

Finally, to determine the impact of sequence and surface on the pathway, we investigated assembly on MoS_2 (0001) by three other sequences—the reversed sequence MoSBP1-R (Tyr-Thr-Phe-Thr-Ala-Ser-Tyr; YTFTASY), the scrambled sequence MoSBP1-S (Ser-Ala-Tyr-Phe-Tyr-Thr-Thr; SAYFYTT), and a weak-binding sequence, MoSBP20 (Thr-Ser-His-Met-Ser-Asn-Thr; TSHMSNT)—as well as assembly of the original sequence on highly ordered pyrolytic graphite (HOPG). The reversed sequence MoSBP1-R assembled on MoS_2 into a structure similar to that of MoSBP1 (fig. S13, A to C), although a larger concentration (5 μM) was required to initiate nucleation and growth. For both the scrambled version MoSBP1-S, which still contained the phenyl rings, and the weak-binding sequence MoSBP20, which contained no phenyl rings, no assembly occurred (fig. S13, D and E) even at c = 5 μM.

Substitution of HOPG for MoS_2 revealed yet another assembly pathway made possible through the row-by-row nucleation process. MoSBP1 still assembled into 2D films similar to those seen on MoS_2 (Fig. 4), but most of the rows constituting these films began as isolated independent nuclei (Fig. 4, A to D). Over time, the MoSBP1 rows, which were immobile on MoS_2, were able to diffuse across the HOPG surface and aggregate to form the final compact, highly ordered 2D domains (Fig. 4, E and F). Individual rows aligned along metastable orientations were more mobile, aiding in the aggregation process (fig. S14). These results highlight the key role of epitaxial match in tuning the assembly pathway. Although MoSBP1 exhibits commensurate epitaxial growth on MoS_2, the mismatch with the HOPG lattice leads to strained epitaxy (fig. S14). The effect of this strain is revealed through the smaller row spacing of 3.4 nm on HOPG versus 4.1 nm on MoS_2 and weaker binding, which leads to the observed mobility of the rows.

The use of peptides identified through phage display (*13*–*15*) has enabled control over the formation of a wide range of materials (*13*–*15*, *21*–*24*), and surface-directed assembly of such peptides has been shown to modulate the electronic properties of 2D materials (*25*). In cases where structure has been investigated, patterns like those observed here are commonly reported. Our findings provide a mechanistic description of their formation and define the key controlling parameters.

The peptides investigated here exhibit structural features common to many polymeric and chain-like organic molecules that self-assemble on surfaces (*2*–*5*, *8*, *21*, *25*, *26*): They possess a mix of hydrophobic and hydrophilic groups; they form many contacts between side chains and with both neighboring molecules and the underlying substrate; and, relative to side-to-side binding, they exhibit weak end-to-end binding. Indeed, a wide variety of systems form ordered 2D films exhibiting a row-by-row structure (*21*, *25*–*28*). In addition, many peptides and other polymers form 1D fibers in bulk solution that then interact to form 2D and 3D structures (*29*–*32*). The above findings place these systems in the context of well-developed theories for the emergence of order and post-nucleation growth and provide a guide for interpreting and controlling their assembly.

REFERENCES AND NOTES

1. J. V. Barth, G. Costantini, K. Kern, *Nature* **437**, 671–679 (2005).
2. J. A. Elemans, S. Lei, S. De Feyter, *Angew. Chem. Int. Ed.* **48**, 7298–7332 (2009).
3. J. C. Love, L. A. Estroff, J. K. Kriebel, R. G. Nuzzo, G. M. Whitesides, *Chem. Rev.* **105**, 1103–1169 (2005).
4. F. Rosei *et al.*, *Science* **296**, 328–331 (2002).
5. J. A. Theobald, N. S. Oxtoby, M. A. Phillips, N. R. Champness, P. H. Beton, *Nature* **424**, 1029–1031 (2003).
6. X. Y. Wang, A. Narita, K. Müllen, *Nat. Rev. Chem.* **2**, 0100 (2017).
7. S. Whitelam, I. Tamblyn, J. P. Garrahan, P. H. Beton, *Phys. Rev. Lett.* **114**, 115702 (2015).
8. M. Lingenfelder *et al.*, *Angew. Chem. Int. Ed.* **46**, 4492–4495 (2007).
9. A. K. Geim, I. V. Grigorieva, *Nature* **499**, 419–425 (2013).
10. Y. Suzuki *et al.*, *Nature* **533**, 369–373 (2016).
11. D. Kashchiev, *Nucleation: Basic Theory with Applications* (Butterworth-Heinemann, 2000).
12. J. J. De Yoreo *et al.*, *Science* **349**, aaa6760 (2015).
13. M. Sarikaya, C. Tamerler, A. K. Y. Jen, K. Schulten, F. Baneyx, *Nat. Mater.* **2**, 577–585 (2003).
14. S. R. Whaley, D. S. English, E. L. Hu, P. F. Barbara, A. M. Belcher, *Nature* **405**, 665–668 (2000).
15. C. Y. Chiu *et al.*, *Nat. Chem.* **3**, 393–399 (2011).
16. L. Gross *et al.*, *Nat. Chem.* **2**, 821–825 (2010).
17. H. Heinz, T. J. Lin, R. K. Mishra, F. S. Emami, *Langmuir* **29**, 1754–1765 (2013).
18. F. S. Emami *et al.*, *Chem. Mater.* **26**, 5725–5734 (2014).
19. J. J. De Yoreo, P. G. Vekilov, *Rev. Mineral. Geochem.* **54**, 57–93 (2003).
20. S. Auer, C. M. Dobson, M. Vendruscolo, *HFSP J.* **1**, 137–146 (2007).
21. C. R. So *et al.*, *ACS Nano* **6**, 1648–1656 (2012).
22. M. Umetsu *et al.*, *Adv. Mater.* **17**, 2571–2575 (2005).
23. W. J. Chung, K. Y. Kwon, J. Song, S. W. Lee, *Langmuir* **27**, 7620–7628 (2011).
24. R. R. Naik, L. L. Brott, S. J. Clarson, M. O. Stone, *J. Nanosci. Nanotechnol.* **2**, 95–100 (2002).
25. Y. Hayamizu *et al.*, *Sci. Rep.* **6**, 33778 (2016).
26. M. Nalbach *et al.*, *J. Phys. Chem. C* **121**, 24144–24151 (2017).
27. C. Fu *et al.*, *Chem. Mater.* **28**, 951–961 (2016).
28. L. Liu *et al.*, *Adv. Sci.* **3**, 1500369 (2016).
29. A. T. Haedler *et al.*, *J. Am. Chem. Soc.* **138**, 10539–10545 (2016).
30. J. D. Hartgerink, E. Beniash, S. I. Stupp, *Science* **294**, 1684–1688 (2001).
31. H. K. Murnen, A. M. Rosales, J. N. Jaworski, R. A. Segalman, R. N. Zuckermann, *J. Am. Chem. Soc.* **132**, 16112–16119 (2010).
32. L. E. O'Leary, J. A. Fallas, E. L. Bakota, M. K. Kang, J. D. Hartgerink, *Nat. Chem.* **3**, 821–828 (2011).

ACKNOWLEDGMENTS

In situ AFM and analysis were performed at the Pacific Northwest National Laboratory, operated by Battelle for the U.S. Department of Energy (DOE) under contract DE-AC05-76RL01830. **Funding:** Supported by the NSF EFRI 2DARE Program (NSF EFRI-1433541), the NSF CBET program (NSF 1530790), and the NSF DMREF program (NSF 1623947). Simulations were performed using the Argonne Leadership Computing Facility, which is a DOE Office of Science User Facility supported under contract DE-AC02-06CH11357, and the Janus supercomputer at the University of Colorado–Boulder, which is supported by NSF through award CNS-0821794. **Author contributions:** J.C. performed the in situ AFM and high-speed AFM experiments and data analysis, developed the kinetic model, and wrote the manuscript; E.Z. designed and synthesized the peptides; J.L. performed MD simulations and wrote the manuscript; S.Z. performed the high-speed AFM experiments; Z.L. and X.D. provided MoS_2 substrates for peptide selection; H.H. designed the simulations and wrote the manuscript; Y.H. designed the study and the peptides and wrote the manuscript; and J.J.D.Y. designed the study, developed the kinetic model, performed data analysis, and wrote the manuscript. **Competing interests:** The authors declare no competing financial interests. **Data and materials availability:** All data are available in the main text or the supplementary materials.

SUPPLEMENTARY MATERIALS

www.sciencemag.org/content/362/6419/1135/suppl/DC1
Materials and Methods
Supplementary Text
Figs. S1 to S14
Tables S1 and S2
Movie S1
References (*33*–*41*)

8 June 2018; accepted 15 October 2018
10.1126/science.aau4146

COMPUTER SCIENCE

A general reinforcement learning algorithm that masters chess, shogi, and Go through self-play

David Silver[1,2]*†, Thomas Hubert[1]*, Julian Schrittwieser[1]*, Ioannis Antonoglou[1], Matthew Lai[1], Arthur Guez[1], Marc Lanctot[1], Laurent Sifre[1], Dharshan Kumaran[1], Thore Graepel[1], Timothy Lillicrap[1], Karen Simonyan[1], Demis Hassabis[1]†

The game of chess is the longest-studied domain in the history of artificial intelligence. The strongest programs are based on a combination of sophisticated search techniques, domain-specific adaptations, and handcrafted evaluation functions that have been refined by human experts over several decades. By contrast, the AlphaGo Zero program recently achieved superhuman performance in the game of Go by reinforcement learning from self-play. In this paper, we generalize this approach into a single AlphaZero algorithm that can achieve superhuman performance in many challenging games. Starting from random play and given no domain knowledge except the game rules, AlphaZero convincingly defeated a world champion program in the games of chess and shogi (Japanese chess), as well as Go.

The study of computer chess is as old as computer science itself. Charles Babbage, Alan Turing, Claude Shannon, and John von Neumann devised hardware, algorithms, and theory to analyze and play the game of chess. Chess subsequently became a grand challenge task for a generation of artificial intelligence researchers, culminating in high-performance computer chess programs that play at a superhuman level (*1*, *2*). However, these systems are highly tuned to their domain and cannot be generalized to other games without substantial human effort, whereas general game-playing systems (*3*, *4*) remain comparatively weak.

A long-standing ambition of artificial intelligence has been to create programs that can instead learn for themselves from first principles (*5*, *6*). Recently, the AlphaGo Zero algorithm achieved superhuman performance in the game of Go by representing Go knowledge with the use of deep convolutional neural networks (*7*, *8*), trained solely by reinforcement learning from games of self-play (*9*). In this paper, we introduce AlphaZero, a more generic version of the AlphaGo Zero algorithm that accommodates, without special casing, a broader class of game rules. We apply AlphaZero to the games of chess and shogi, as well as Go, by using the same algorithm and network architecture for all three games. Our results demonstrate that a general-purpose reinforcement learning algorithm can learn, tabula rasa—without domain-specific human knowledge or data, as evidenced by the same algorithm succeeding in multiple domains—superhuman performance across multiple challenging games.

A landmark for artificial intelligence was achieved in 1997 when Deep Blue defeated the human world chess champion (*1*). Computer chess programs continued to progress steadily beyond human level in the following two decades. These programs evaluate positions by using handcrafted features and carefully tuned weights, constructed by strong human players and programmers, combined with a high-performance alpha-beta search that expands a vast search tree by using a large number of clever heuristics and domain-specific adaptations. In (*10*) we describe these augmentations, focusing on the 2016 Top Chess Engine Championship (TCEC) season 9 world champion Stockfish (*11*); other strong chess programs, including Deep Blue, use very similar architectures (*1*, *12*).

In terms of game tree complexity, shogi is a substantially harder game than chess (*13*, *14*): It is played on a larger board with a wider variety of pieces; any captured opponent piece switches sides and may subsequently be dropped anywhere on the board. The strongest shogi programs, such as the 2017 Computer Shogi Association (CSA) world champion Elmo, have only recently defeated human champions (*15*). These programs use an algorithm similar to those used by computer chess programs, again based on a highly optimized alpha-beta search engine with many domain-specific adaptations.

AlphaZero replaces the handcrafted knowledge and domain-specific augmentations used in traditional game-playing programs with deep neural networks, a general-purpose reinforcement learning algorithm, and a general-purpose tree search algorithm.

Instead of a handcrafted evaluation function and move-ordering heuristics, AlphaZero uses a deep neural network $(\mathbf{p}, v) = f_\theta(s)$ with parameters θ. This neural network $f_\theta(s)$ takes the board position s as an input and outputs a vector of move probabilities $\mathbf{p}$ with components $p_a = \Pr(a|s)$ for each action a and a scalar value v estimating the expected outcome z of the game from position s, $v \approx \mathbb{E}[z|s]$. AlphaZero learns these move probabilities and value estimates entirely from self-play; these are then used to guide its search in future games.

Instead of an alpha-beta search with domain-specific enhancements, AlphaZero uses a general-purpose Monte Carlo tree search (MCTS) algorithm. Each search consists of a series of simulated games of self-play that traverse a tree from root state s_{root} until a leaf state is reached. Each simulation proceeds by selecting in each state s a move a with low visit count (not previously frequently explored), high move probability, and high value (averaged over the leaf states of

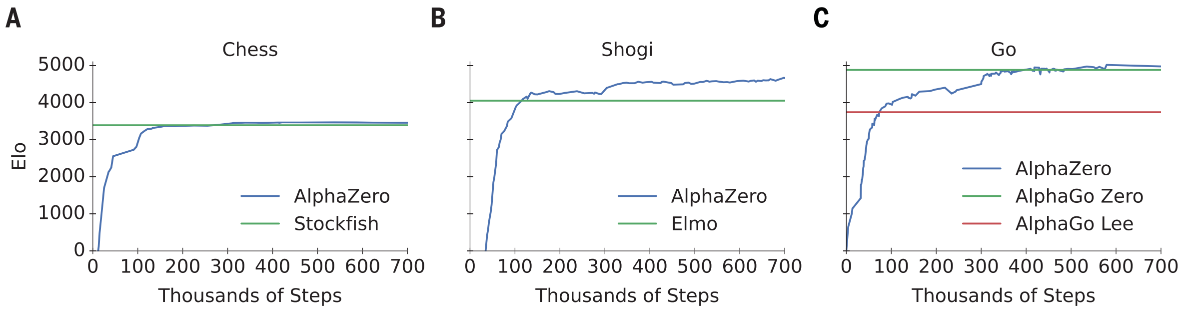

Fig. 1. Training AlphaZero for 700,000 steps. Elo ratings were computed from games between different players where each player was given 1 s per move. (**A**) Performance of AlphaZero in chess compared with the 2016 TCEC world champion program Stockfish. (**B**) Performance of AlphaZero in shogi compared with the 2017 CSA world champion program Elmo. (**C**) Performance of AlphaZero in Go compared with AlphaGo Lee and AlphaGo Zero (20 blocks over 3 days).

---

[1]DeepMind, 6 Pancras Square, London N1C 4AG, UK. [2]University College London, Gower Street, London WC1E 6BT, UK.
*These authors contributed equally to this work.
†Corresponding author. Email: davidsilver@google.com (D.S.); dhcontact@google.com (D.H.)

Downloaded from http://science.sciencemag.org/ on December 10, 2018

simulations that selected a from s) according to the current neural network f_θ. The search returns a vector π representing a probability distribution over moves, $\pi_a = \Pr(a|s_{\text{root}})$.

The parameters θ of the deep neural network in AlphaZero are trained by reinforcement learning from self-play games, starting from randomly initialized parameters θ. Each game is played by running an MCTS from the current position $s_{\text{root}} = s_t$ at turn t and then selecting a move, $a_t \sim \pi_t$, either proportionally (for exploration) or greedily (for exploitation) with respect to the visit counts at the root state. At the end of the game, the terminal position s_T is scored according to the rules of the game to compute the game outcome z: −1 for a loss, 0 for a draw, and +1 for a win. The neural network parameters θ are updated to minimize the error between the predicted outcome v_t and the game outcome z and to maximize the similarity of the policy vector $\mathbf{p}_t$ to the search probabilities π_t. Specifically, the parameters θ are adjusted by gradient descent on a loss function l that sums over mean-squared error and cross-entropy losses

$$(\mathbf{p}, v) = f_\theta(s), l = (z - v)^2 - \pi^{\mathrm{T}} \log \mathbf{p} + c\|\theta\|^2, \quad (1)$$

where c is a parameter controlling the level of L_2 weight regularization. The updated parameters are used in subsequent games of self-play.

The AlphaZero algorithm described in this paper [see (*10*) for the pseudocode] differs from the original AlphaGo Zero algorithm in several respects.

AlphaGo Zero estimated and optimized the probability of winning, exploiting the fact that Go games have a binary win or loss outcome. However, both chess and shogi may end in drawn outcomes; it is believed that the optimal solution to chess is a draw (*16*–*18*). AlphaZero instead estimates and optimizes the expected outcome.

The rules of Go are invariant to rotation and reflection. This fact was exploited in AlphaGo and AlphaGo Zero in two ways. First, training data were augmented by generating eight symmetries for each position. Second, during MCTS, board positions were transformed by using a randomly selected rotation or reflection before being evaluated by the neural network, so that the Monte Carlo evaluation was averaged over different biases. To accommodate a broader class of games, AlphaZero does not assume symmetry; the rules of chess and shogi are asymmetric (e.g., pawns only move forward, and castling is different on kingside and queenside). AlphaZero does not augment the training data and does not transform the board position during MCTS.

In AlphaGo Zero, self-play games were generated by the best player from all previous iterations. After each iteration of training, the performance of the new player was measured against the best player; if the new player won by a margin of 55%, then it replaced the best player. By contrast, AlphaZero simply maintains a single neural network that is updated continually rather than waiting for an iteration to complete. Self-play games are always generated by using the latest parameters for this neural network.

As in AlphaGo Zero, the board state is encoded by spatial planes based only on the basic rules for each game. The actions are encoded by either spatial planes or a flat vector, again based only on the basic rules for each game (*10*).

AlphaGo Zero used a convolutional neural network architecture that is particularly well-suited to Go: The rules of the game are translationally invariant (matching the weight-sharing structure of convolutional networks) and are defined in terms of liberties corresponding to the adjacencies between points on the board (matching the local structure of convolutional networks). By contrast, the rules of chess and shogi are position dependent (e.g., pawns may move two steps forward from the second rank and promote on the eighth rank) and include long-range interactions (e.g., the queen may traverse the board in one move). Despite these differences, AlphaZero uses the same convolutional network architecture as AlphaGo Zero for chess, shogi, and Go.

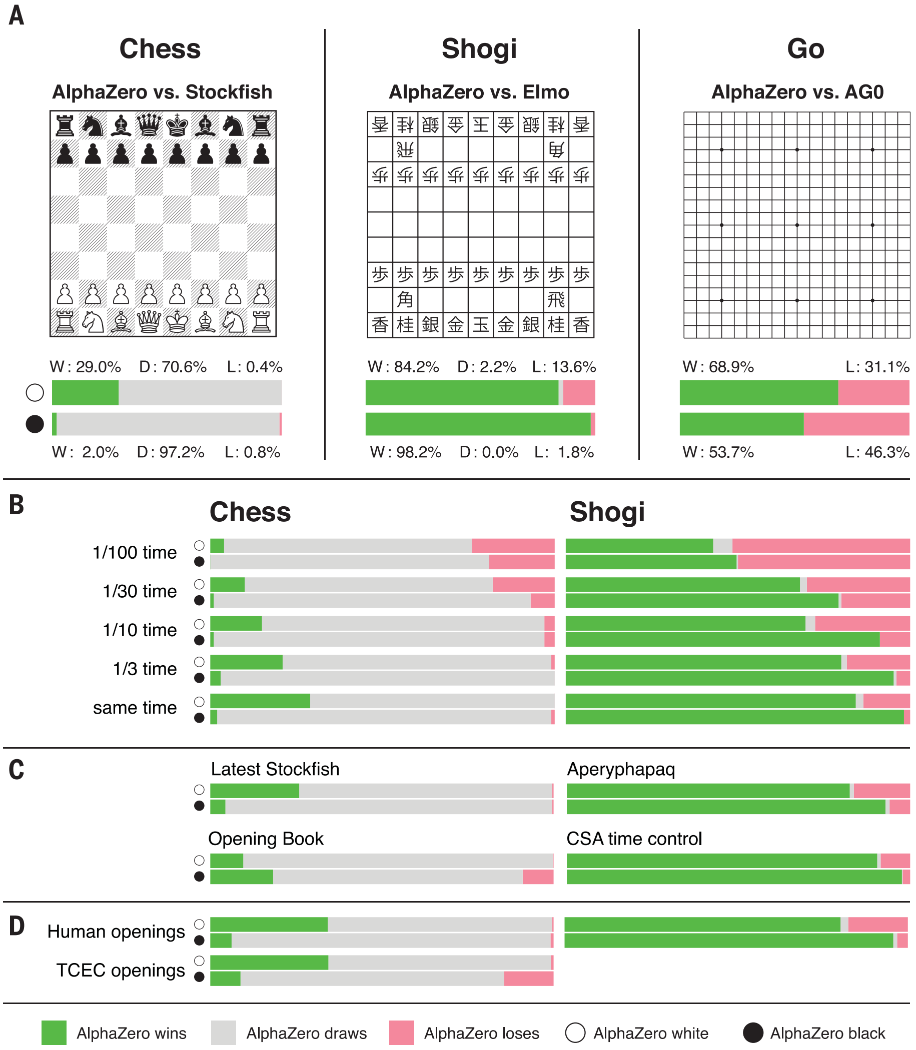

Fig. 2. Comparison with specialized programs. (**A**) Tournament evaluation of AlphaZero in chess, shogi, and Go in matches against, respectively, Stockfish, Elmo, and the previously published version of AlphaGo Zero (AG0) that was trained for 3 days. In the top bar, AlphaZero plays white; in the bottom bar, AlphaZero plays black. Each bar shows the results from AlphaZero's perspective: win (W; green), draw (D; gray), or loss (L; red). (**B**) Scalability of AlphaZero with thinking time compared with Stockfish and Elmo. Stockfish and Elmo always receive full time (3 hours per game plus 15 s per move); time for AlphaZero is scaled down as indicated. (**C**) Extra evaluations of AlphaZero in chess against the most recent version of Stockfish at the time of writing (*27*) and against Stockfish with a strong opening book (*28*). Extra evaluations of AlphaZero in shogi were carried out against another strong shogi program, Aperyqhapaq (*29*), at full time controls and against Elmo under 2017 CSA world championship time controls (10 min per game and 10 s per move). (**D**) Average result of chess matches starting from different opening positions, either common human positions (see also Fig. 3) or the 2016 TCEC world championship opening positions (see also fig. S4), and average result of shogi matches starting from common human positions (see also Fig. 3). CSA world championship games start from the initial board position. Match conditions are summarized in tables S8 and S9.

Downloaded from http://science.sciencemag.org/ on December 10, 2018

The hyperparameters of AlphaGo Zero were tuned by Bayesian optimization. In AlphaZero, we reuse the same hyperparameters, algorithm settings, and network architecture for all games without game-specific tuning. The only exceptions are the exploration noise and the learning rate schedule [see (*10*) for further details].

We trained separate instances of AlphaZero for chess, shogi, and Go. Training proceeded for 700,000 steps (in mini-batches of 4096 training positions) starting from randomly initialized parameters. During training only, 5000 first-generation tensor processing units (TPUs) (*19*) were used to generate self-play games, and 16 second-generation TPUs were used to train the neural networks. Training lasted for approximately 9 hours in chess, 12 hours in shogi, and 13 days in Go (see table S3) (*20*). Further details of the training procedure are provided in (*10*).

Figure 1 shows the performance of AlphaZero during self-play reinforcement learning, as a

Fig. 3. Matches starting from the most popular human openings. AlphaZero plays against (**A**) Stockfish in chess and (**B**) Elmo in shogi. In the left bar, AlphaZero plays white, starting from the given position; in the right bar, AlphaZero plays black. Each bar shows the results from AlphaZero's perspective: win (green), draw (gray), or loss (red). The percentage frequency of self-play training games in which this opening was selected by AlphaZero is plotted against the duration of training, in hours.

Downloaded from http://science.sciencemag.org/ on December 10, 2018

function of training steps, on an Elo (*21*) scale (*22*). In chess, AlphaZero first outperformed Stockfish after just 4 hours (300,000 steps); in shogi, AlphaZero first outperformed Elmo after 2 hours (110,000 steps); and in Go, AlphaZero first outperformed AlphaGo Lee (*9*) after 30 hours (74,000 steps). The training algorithm achieved similar performance in all independent runs (see fig. S3), suggesting that the high performance of AlphaZero's training algorithm is repeatable.

We evaluated the fully trained instances of AlphaZero against Stockfish, Elmo, and the previous version of AlphaGo Zero in chess, shogi, and Go, respectively. Each program was run on the hardware for which it was designed (*23*): Stockfish and Elmo used 44 central processing unit (CPU) cores (as in the TCEC world championship), whereas AlphaZero and AlphaGo Zero used a single machine with four first-generation TPUs and 44 CPU cores (*24*). The chess match was played against the 2016 TCEC (season 9) world champion Stockfish [see (*10*) for details]. The shogi match was played against the 2017 CSA world champion version of Elmo (*10*). The Go match was played against the previously published version of AlphaGo Zero [also trained for 700,000 steps (*25*)]. All matches were played by using time controls of 3 hours per game, plus an additional 15 s for each move.

In Go, AlphaZero defeated AlphaGo Zero (*9*), winning 61% of games. This demonstrates that a general approach can recover the performance of an algorithm that exploited board symmetries to generate eight times as much data (see fig. S1).

In chess, AlphaZero defeated Stockfish, winning 155 games and losing 6 games out of 1000 (Fig. 2). To verify the robustness of AlphaZero, we played additional matches that started from common human openings (Fig. 3). AlphaZero defeated Stockfish in each opening, suggesting that AlphaZero has mastered a wide spectrum of chess play. The frequency plots in Fig. 3 and the time line in fig. S2 show that common human openings were independently discovered and played frequently by AlphaZero during self-play training. We also played a match that started from the set of opening positions used in the 2016 TCEC world championship; AlphaZero won convincingly in this match, too (*26*) (fig. S4). We played additional matches against the most recent development version of Stockfish (*27*) and a variant of Stockfish that uses a strong opening book (*28*). AlphaZero won all matches by a large margin (Fig. 2).

Table S6 shows 20 chess games played by AlphaZero in its matches against Stockfish. In several games, AlphaZero sacrificed pieces for long-term strategic advantage, suggesting that it has a more fluid, context-dependent positional evaluation than the rule-based evaluations used by previous chess programs.

In shogi, AlphaZero defeated Elmo, winning 98.2% of games when playing black and 91.2% overall. We also played a match under the faster time controls used in the 2017 CSA world championship and against another state-of-the-art shogi program (*29*); AlphaZero again won both matches by a wide margin (Fig. 2).

Table S7 shows 10 shogi games played by AlphaZero in its matches against Elmo. The frequency plots in Fig. 3 and the time line in fig. S2 show that AlphaZero frequently plays one of the two most common human openings but rarely plays the second, deviating on the very first move.

AlphaZero searches just 60,000 positions per second in chess and shogi, compared with 60 million for Stockfish and 25 million for Elmo (table S4). AlphaZero may compensate for the lower number of evaluations by using its deep neural network to focus much more selectively on the most promising variations (Fig. 4 provides an example from the match against Stockfish)—arguably a more humanlike approach to searching, as originally proposed by Shannon (*30*). AlphaZero also defeated Stockfish when given $^1/_{10}$ as much thinking time as its opponent (i.e., searching ~$^1/_{10,000}$ as many positions) and won 46% of games against Elmo when given $^1/_{100}$ as much time (i.e., searching ~$^1/_{40,000}$ as many positions) (Fig. 2). The high performance

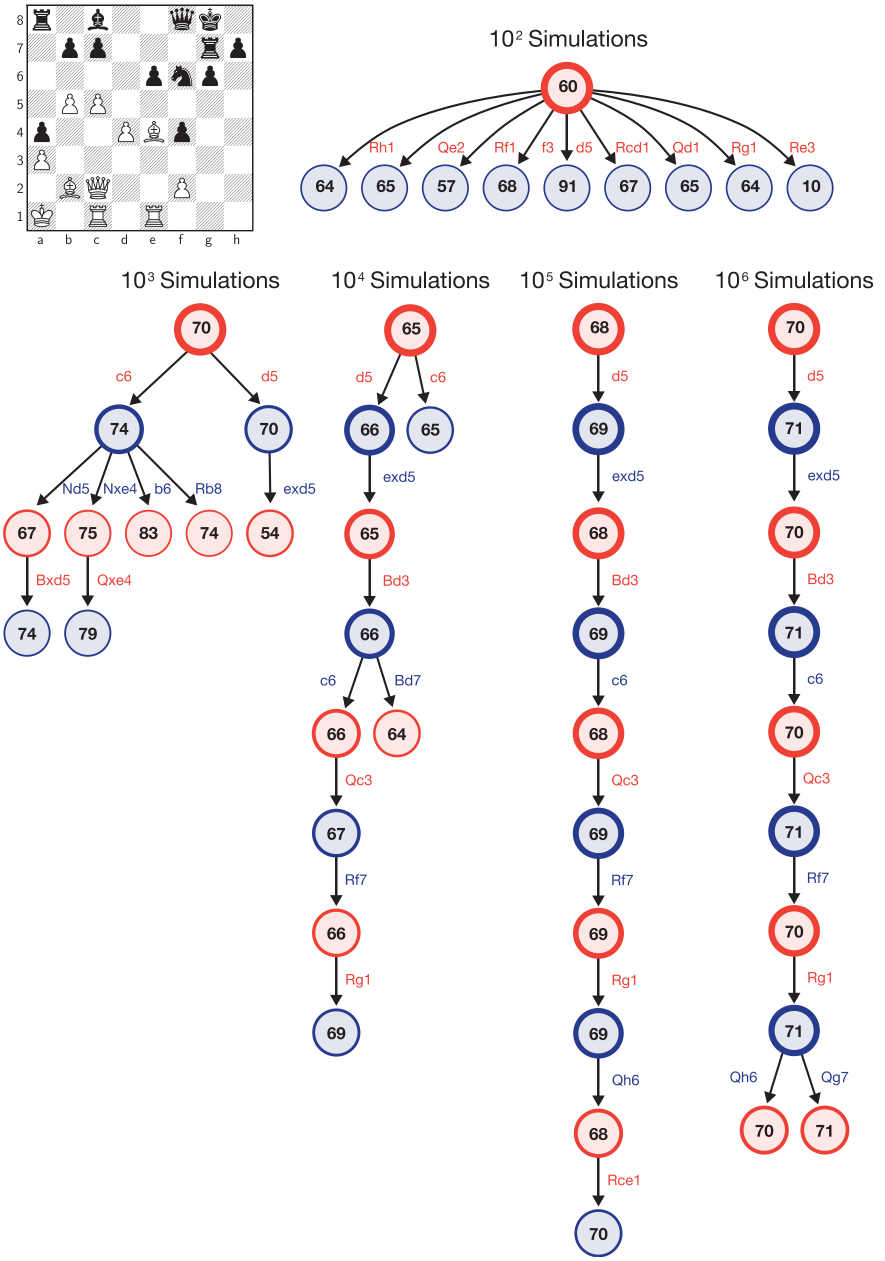

Fig. 4. AlphaZero's search procedure. The search is illustrated for a position (**inset**) from game 1 (table S6) between AlphaZero (white) and Stockfish (black) after 29. ... Qf8. The internal state of AlphaZero's MCTS is summarized after 10^2, ..., 10^6 simulations. Each summary shows the 10 most visited states. The estimated value is shown in each state, from white's perspective, scaled to the range [0, 100]. The visit count of each state, relative to the root state of that tree, is proportional to the thickness of the border circle. AlphaZero considers 30. c6 but eventually plays 30. d5.

Downloaded from http://science.sciencemag.org/ on December 10, 2018

of AlphaZero with the use of MCTS calls into question the widely held belief (*31*, *32*) that alpha-beta search is inherently superior in these domains.

The game of chess represented the pinnacle of artificial intelligence research over several decades. State-of-the-art programs are based on powerful engines that search many millions of positions, leveraging handcrafted domain expertise and sophisticated domain adaptations. AlphaZero is a generic reinforcement learning and search algorithm—originally devised for the game of Go—that achieved superior results within a few hours, searching $^1/_{1000}$ as many positions, given no domain knowledge except the rules of chess. Furthermore, the same algorithm was applied without modification to the more challenging game of shogi, again outperforming state-of-the-art programs within a few hours. These results bring us a step closer to fulfilling a longstanding ambition of artificial intelligence (*3*): a general game-playing system that can learn to master any game.

REFERENCES AND NOTES

1. M. Campbell, A. J. Hoane Jr., F. Hsu, *Artif. Intell.* **134**, 57–83 (2002).
2. F.-H. Hsu, *Behind Deep Blue: Building the Computer That Defeated the World Chess Champion* (Princeton Univ., 2002).
3. B. Pell, *Comput. Intell.* **12**, 177–198 (1996).
4. M. R. Genesereth, N. Love, B. Pell, *AI Mag.* **26**, 62–72 (2005).
5. A. L. Samuel, *IBM J. Res. Dev.* **11**, 601–617 (1967).
6. G. Tesauro, *Neural Comput.* **6**, 215–219 (1994).
7. C. J. Maddison, A. Huang, I. Sutskever, D. Silver, paper presented at the International Conference on Learning Representations 2015, San Diego, CA, 7 to 9 May 2015.
8. D. Silver *et al*., *Nature* **529**, 484–489 (2016).
9. D. Silver *et al*., *Nature* **550**, 354–359 (2017).
10. See the supplementary materials for additional information.
11. Stockfish: Strong open source chess engine; https://stockfishchess.org/ [accessed 29 November 2017].
12. D. N. L. Levy, M. Newborn, *How Computers Play Chess* (Ishi Press, 2009).
13. V. Allis, "Searching for solutions in games and artificial intelligence," Ph.D. thesis, Transnational University Limburg, Maastricht, Netherlands (1994).
14. H. Iida, M. Sakuta, J. Rollason, *Artif. Intell.* **134**, 121–144 (2002).
15. Computer Shogi Association, Results of the 27th world computer shogi championship; www2.computer-shogi.org/wcsc27/index_e.html [accessed 29 November 2017].
16. W. Steinitz, *The Modern Chess Instructor* (Edition Olms, 1990).
17. E. Lasker, *Common Sense in Chess* (Dover Publications, 1965).
18. J. Knudsen, *Essential Chess Quotations* (iUniverse, 2000).
19. N. P. Jouppi *et al.*, in *Proceedings of the 44th Annual International Symposium on Computer Architecture*, Toronto, Canada, 24 to 28 June 2017 (Association for Computing Machinery, 2017), pp. 1–12.
20. Note that the original AlphaGo Zero study used graphics processing units (GPUs) to train the neural networks.
21. R. Coulom, in *Proceedings of the Sixth International Conference on Computers and Games*, Beijing, China, 29 September to 1 October 2008 (Springer, 2008), pp. 113–124.
22. The prevalence of draws in high-level chess tends to compress the Elo scale, compared with that for shogi or Go.
23. Stockfish is designed to exploit CPU hardware and cannot make use of GPUs or TPUs, whereas AlphaZero is designed to exploit GPU-TPU hardware rather than CPU hardware.
24. A first generation TPU is roughly similar in inference speed to a Titan V GPU, although the architectures are not directly comparable.
25. AlphaGo Zero was ultimately trained for 3.1 million steps over 40 days.
26. Many TCEC opening positions are unbalanced according to both AlphaZero and Stockfish, resulting in more losses for both players.
27. Newest available version of Stockfish as of 13 January 2018 (resolved_base b508f9561cc2302c129efe8d60f201ff03ee72c8), from https://github.com/official-stockfish/Stockfish/commit/.
28. The Stockfish variant used the Cerebellum opening book downloaded from https://zipproth.de/#Brainfish. AlphaZero did not use an opening book. To ensure diversity against a deterministic opening book, AlphaZero used a small amount of randomization in its opening moves (*10*); this avoided duplicate games but also resulted in more losses.
29. Aperyqhapaq's evaluation files are available at https://github.com/qhapaq-49/qhapaq-bin/releases/tag/eloqhappa.
30. C. E. Shannon, *London Edinburgh Dublin Philos. Mag. J. Sci.* **41**, 256–275 (1950).
31. O. Arenz, "Monte Carlo chess," master's thesis, Technische Universität Darmstadt (2012).
32. O. E. David, N. S. Netanyahu, L. Wolf, in *Artificial Neural Networks and Machine Learning—ICANN 2016*, *Part II*, Barcelona, Spain, 6 to 9 September 2016 (Springer, 2016), pp. 88–96.

ACKNOWLEDGMENTS

We thank M. Sadler for analyzing chess games; Y. Habu for analyzing shogi games; L. Bennett for organizational assistance; B. Konrad, E. Lockhart, and G. Ostrovski for reviewing the paper; and the rest of the DeepMind team for their support. **Funding:** All research described in this report was funded by DeepMind and Alphabet. **Author contributions:** D.S., J.S., T.H., and I.A. designed the AlphaZero algorithm with advice from T.G., A.G., T.L., K.S., M.Lai, L.S., and M.Lan.; J.S., I.A., T.H., and M.Lai implemented the AlphaZero program; T.H., J.S., D.S., M.Lai, I.A., T.G., K.S., D.K., and D.H. ran experiments and/or analyzed data; D.S., T.H., J.S., and D.H. managed the project; D.S., J.S., T.H., M.Lai, I.A., and D.H. wrote the paper. **Competing interests:** DeepMind has filed the following patent applications related to this work: PCT/EP2018/063869, US15/280,711, and US15/280,784. **Data and materials availability:** A full description of the algorithm in pseudocode as well as details of additional games between AlphaZero and other programs is available in the supplementary materials.

SUPPLEMENTARY MATERIALS

www.sciencemag.org/content/362/6419/1140/suppl/DC1
Materials and Methods
Figs. S1 to S4
Tables S1 to S9
References (*33–50*)
Data S1

2 March 2018; accepted 7 November 2018
10.1126/science.aar6404

Downloaded from http://science.sciencemag.org/ on December 10, 2018

BATTERIES

Room-temperature cycling of metal fluoride electrodes: Liquid electrolytes for high-energy fluoride ion cells

Victoria K. Davis[1]*, Christopher M. Bates[2]†, Kaoru Omichi[3]‡, Brett M. Savoie[2]§, Nebojša Momčilović[2]¶, Qingmin Xu[3], William J. Wolf[2], Michael A. Webb[2], Keith J. Billings[1], Nam Hawn Chou[3], Selim Alayoglu[4], Ryan K. McKenney[3], Isabelle M. Darolles[2]#, Nanditha G. Nair[2], Adrian Hightower[2], Daniel Rosenberg[4], Musahid Ahmed[4], Christopher J. Brooks[3], Thomas F. Miller III[2], Robert H. Grubbs[2], Simon C. Jones[1]**

Fluoride ion batteries are potential "next-generation" electrochemical storage devices that offer high energy density. At present, such batteries are limited to operation at high temperatures because suitable fluoride ion–conducting electrolytes are known only in the solid state. We report a liquid fluoride ion–conducting electrolyte with high ionic conductivity, wide operating voltage, and robust chemical stability based on dry tetraalkylammonium fluoride salts in ether solvents. Pairing this liquid electrolyte with a copper–lanthanum trifluoride (Cu@LaF_3) core-shell cathode, we demonstrate reversible fluorination and defluorination reactions in a fluoride ion electrochemical cell cycled at room temperature. Fluoride ion–mediated electrochemistry offers a pathway toward developing capacities beyond that of lithium ion technology.

The search for batteries that offer the high energy density necessary to meet emerging energy storage needs is increasingly focused on alternatives to lithium ion electrochemistry (*1*). Energy density is dictated by the number of electrons transferred in the reaction (n), the cell voltage or potential difference between cathode and anode ($E^{o}_{cell} = E^{o}_{c} - E^{o}_{a}$), Faraday's constant ($F$), and the cell volume ($\Sigma M_i$):

$$\text{Energy density} = \frac{nFE^{o}_{cell}}{\Sigma M_i} \tag{1}$$

Exploitation of multi-electron redox processes ($n > 1$) is an attractive route to achieve improved energy density. Next-generation lithium electrochemical systems, such as lithium-air and lithium-sulfur (Li/S), offer high theoretical energies due to multi-electron reactions at the cathode, but they use lithium metal anodes that have poor cycle life and raise safety concerns (*2*, *3*). Magnesium anode cells can afford two-electron transfer per Mg^{2+} ion, but they are limited at their cathodes by the poor mobility and the large structural reorganization imposed by this cation with high charge density in a solid lattice (*4*).

Alternatively, multi-electron electrochemistries can use anionic species as the charge carrier. With mono-anionic charge carriers, reversible multi-electron reactions may be facilitated by moving several singly charged anions per reaction step, rather than one highly polarizing, multiply charged cation. In general, anions have a lower charge density and a lesser degree of solvation than cations of the same absolute charge, and therefore display greater mobilities. High-power devices that use anion-mediated multi-electron redox reactions in aqueous alkaline solution are well established—for example, nickel-cadmium and nickel-zinc batteries, although their energy density is limited (<300 Wh/liter) (*5*). For higher-energy devices, nonaqueous electrolytes are required to operate reversibly at potentials beyond that of the thermodynamic voltage window of water (1.23 V at 298 K).

In this context, fluoride ion batteries (FIBs) are of considerable interest (*6*). In contrast to the intercalation/deintercalation mechanisms that operate for most lithium ion batteries, FIBs function by conversion processes. FIB conversion reactions occur, for example (upon discharge), when a high-valent metal fluoride cathode (MF_n, Eq. 2) becomes reduced to the metal concomitant with the oxidation of a low-potential metal anode (M', Eq. 3) to a metal fluoride:

Cathode:

$$MF_n + ne^- \rightarrow M + nF^- \text{ at potential } E^{o}_{c} \tag{2}$$

Anode:

$$M' + nF^- \rightarrow M'F_n + ne^- \text{ at potential } E^{o}_{a} \tag{3}$$

Multivalent fluoride conversion reactions have high thermodynamic reaction potentials (>3 V) and volumetric capacities (>1000 Ah/liter). Hence, batteries based on these materials offer theoretical energy densities up to 5000 Wh/liter (*7*), ≥8 times the theoretical values for current lithium ion technologies. Rechargeable FIB devices were reported in 2011 (*8*), following principles established for primary galvanic cells in the 1970s (*6*). FIBs can only operate at high temperatures (≥150°C) because they use solid-state fluoride electrolytes with very limited ionic conductivity at room temperature (10^{-6} S/cm) (*6*, *8*). A few electrochemical cells have been reported that exhibit fluoride-mediated conversion reactions in a liquid electrolyte (*9*–*12*); however, these cells either contain bifluoride ions (HF_2^-) with a very small electrolyte voltage window (~0.7 V) (*11*) or operate through irreversible F^- complexation to the metal charge carrier (*12*). Hence, electrolyte limitations present a serious challenge for designing FIBs at room temperature.

Metal fluoride electrolyte salts are universally insoluble in organics at concentrations exceeding 0.05 M (*13*). Organic fluoride electrolyte salts, like those with tetraalkylammonium (R_4N^+) cations (*14*), could have improved solubility; however, these are nontrivial to synthesize in truly anhydrous form because decomposition of F^- to HF_2^- occurs readily through elimination processes at elevated temperatures (*15*–*17*). Commercial anhydrous tetramethylammonium fluoride (TMAF) is of limited solubility in organics. We therefore selected neopentyl-substituted (Np, or 2,2-dimethylpropyl-) alkylammonium salts, as the Np chain is both branched (to improve solubility) and lacks β-hydrogens (to inhibit decomposition upon drying). Both dry *N*,*N*,*N*-trimethyl-*N*-neopentylammonium fluoride (Np_1F) and *N*,*N*-dimethyl-*N*,*N*-dineopentylammonium fluoride (Np_2F) were synthesized in batches as large as 100 g using an HF-titration procedure (*18*–*20*) and demonstrated greatly improved solubility relative to TMAF (Fig. 1A).

Initial screening of these NpF salts revealed three broad classes of organic solvents: (i) NpF insoluble; (ii) NpF soluble (at appreciable electrolyte concentrations, >0.5 M) but F^- reactive; or (iii) NpF soluble, F^- stable (but at very limited concentrations). Certain ionic liquids, such as 1-methyl-1-propylpyrrolidinium bis(trifluorosulfonyl)imide (MPPy-TFSI), were found in the third class (fig. S1); however, the associated expense and high viscosity of ionic liquids, and additional complications for battery operation that might arise from the presence of other anions (e.g., TFSI) in the mixture, kept our focus on simple organic solvents. Inspired by studies of Li/S battery systems, we turned to partially fluorinated ethers (*21*). Bis(2,2,2-trifluoroethyl) ether (BTFE) is the only organic solvent we found to dissolve NpF at substantially high concentrations (>2.2 M) while not reacting with F^- (Fig. 1B and fig. S2). Long-term ^{19}F nuclear magnetic resonance (NMR) monitoring confirmed that the

---

[1]Electrochemical Technologies Group, Jet Propulsion Laboratory, California Institute of Technology, Pasadena, CA 91109, USA. [2]Division of Chemistry and Chemical Engineering, California Institute of Technology, Pasadena, CA 91125, USA. [3]Honda Research Institute Inc., 1381 Kinnear Road, Suite 116, Columbus, OH 43212, USA. [4]Chemical Sciences Division, Lawrence Berkeley National Laboratory, Berkeley, CA 94720, USA.
*Present address: Department of Chemistry, University of North Carolina, Chapel Hill, NC 27599, USA. †Present address: Materials Department and Department of Chemical Engineering, University of California, Santa Barbara, CA 93106, USA. ‡Present address: Honda R&D Co., Ltd. Automobile R&D Center, Haga-machi, Haga-gun, Tochigi 321-3393, Japan. §Present address: Department of Chemical Engineering, Purdue University, West Lafayette, IN 47907, USA. ¶Deceased. #Present address: Sienza Energy Inc., 133 North Altadena Street, Suite 307, Pasadena, CA 91107, USA.
****Corresponding author: Email: simon.c.jones@jpl.nasa.gov**

Downloaded from http://science.sciencemag.org/ on December 6, 2018

solution is stable at room temperature for more than 3000 hours (fig. S3) (*20*). This contrasts with, for example, the stability of F⁻ in dichloromethane, which shows complete decomposition to HF_2^- within 12 hours (*22*).

Molecular dynamics (MD) simulations (*20*) were used to characterize the solvation free energies of F⁻, TMA⁺, Np_1^+, and Np_2^+ in BTFE, bis(perfluoroethyl) ether (BPFE), and bis(2-methoxyethyl) ether (diglyme) solvents (Fig. 1C). The F⁻ solvation free energy was much less favorable in BPFE ($\Delta G_{S,F}$ = −8 kcal/mol) than in diglyme ($\Delta G_{S,F}$ = −59 kcal/mol) and BTFE ($\Delta G_{S,F}$ = −63 kcal/mol), which suggests that the α-CH_2 feature plays an important role in dissolving F⁻. The solvation free energies for each R_4N^+ are similar, indicating that the introduction of bulkier alkyl substituents onto the cation should favorably reduce the salt lattice energy with little effect on the cation solubility.

Analysis of the radial distribution function for solvated F⁻ (for which the largest probability of F⁻ interaction occurs about 2 Å from the H atom of the α-CH_2 moiety in BTFE) (Fig. 1D), in concert with quantum chemical calculations to characterize the partial charge distribution in BTFE and diglyme (fig. S4), presents a consistent physical picture of F⁻ solvation. MD simulations reveal the innermost coordination shell of F⁻ in liquid BTFE (Fig. 1E); on average, at least one

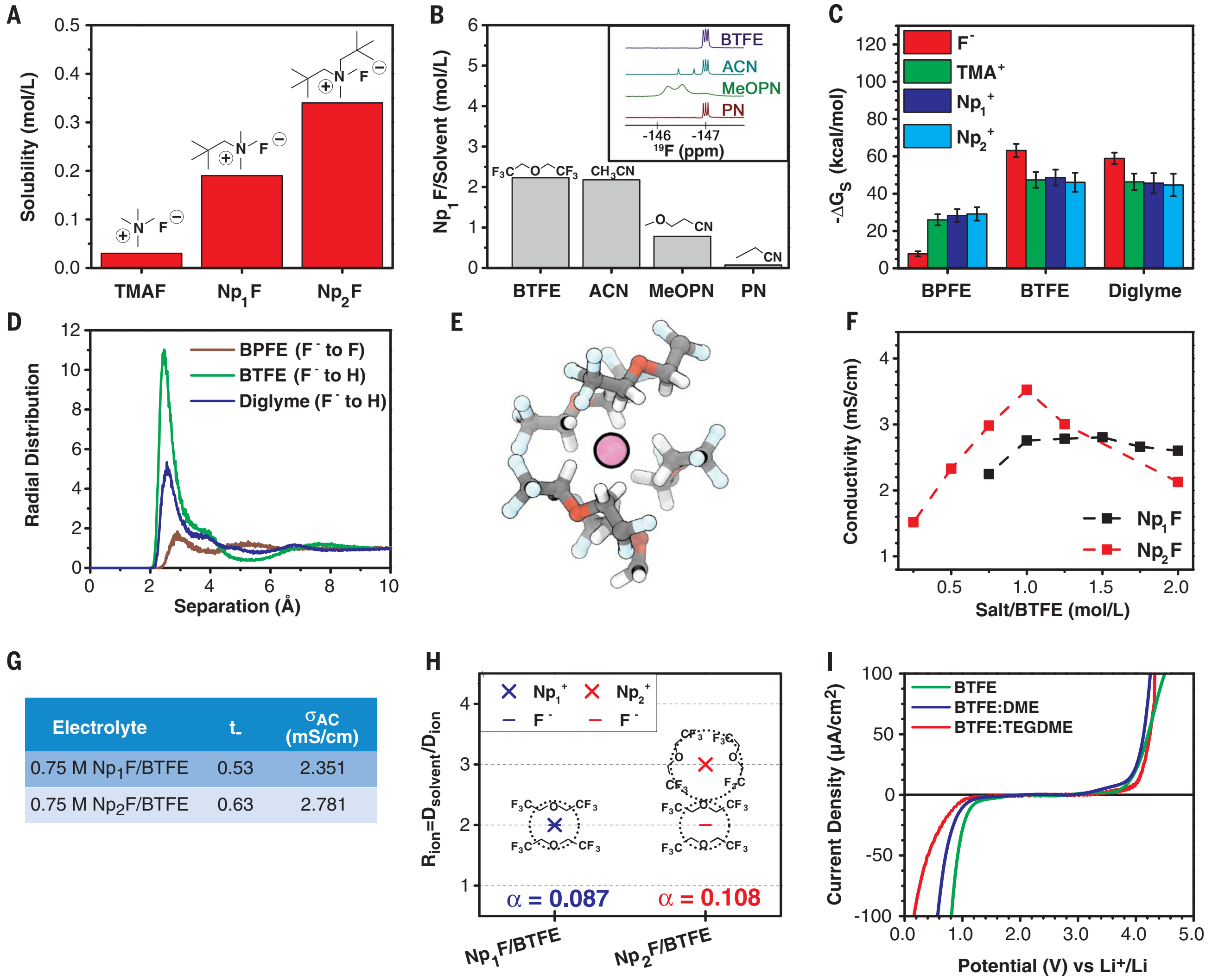

Electrolyte	t₋	σ_{AC} (mS/cm)
0.75 M Np_1F/BTFE	0.53	2.351
0.75 M Np_2F/BTFE	0.63	2.781

Fig. 1. Physical and electrochemical properties of nonaqueous, fluoride ion–conducting liquid electrolytes (25°C). (**A**) Influence of tetraalkylammonium cation structure on fluoride salt solubility in 3-fluorobenzonitrile. Solubility (mol/liter) represents the approximate salt saturation concentration. (**B**) Np_1F solubility in BTFE, acetonitrile (ACN), 3-methoxypropionitrile (MeOPN), and propionitrile (PN). Inset shows ^{19}F NMR spectra in the bifluoride region for Np_1F dissolved in each solvent. Reactivity of F⁻ with solvent protons results in HF_2^- formation (doublet, −146.6 ppm); F⁻ reacts with CD_3CN NMR solvent to produce DF_2^- in all cases (triplet, −147.0 ppm). (**C** to **E**) Molecular dynamics simulations for ions in BPFE, BTFE, and diglyme. (C) Comparison of ion solvation free energies. Data are means ± SD. (D) Comparison of F⁻ radial distribution functions calculated with respect to the H (or F) atoms bonded to the α-CX_2 moiety of the solvent. (E) Simulated solvation shell of BTFE molecules surrounding F⁻ (pink sphere). (**F**) Ionic conductivity of Np_1F (black) or Np_2F (red) in liquid BTFE electrolyte solutions as a function of concentration. (**G**) F⁻ transport numbers (t_-) from PFG-SE ^1H and ^{19}F NMR experiments, and ionic conductivity values (σ_{AC}) from AC impedance measurements, for 0.75 M Np_1F in BTFE and 0.75 M Np_2F in BTFE. (**H**) Stokes radii (R_{ion}) for electrolyte ions in 0.75 M Np_1F/BTFE (blue) or 0.75 M Np_2F/BTFE (red). The degree of ion dissociation (α) is also shown (SD = ±0.003) (*20*). (**I**) Linear sweep voltammograms for 0.75 M Np_1F in BTFE, BTFE:DME (3:2 v/v), and BTFE:TEGDME (3:2 v/v) collected using a scan rate of 1 mV/s. DME, 1,2-dimethoxyethane; TEGDME, bis[2-(2-methoxyethoxy)ethyl] ether.

Downloaded from http://science.sciencemag.org/ on December 6, 2018

BTFE molecule has both α-CH_2 groups oriented toward the anion. Overall, F^- solvation is facilitated by interactions of F^- with partial positive charges on the α-CH_2 moiety that are enhanced by adjacent electron-withdrawing groups (as such, these are greatest for BTFE). Thus, ethereal media possessing these structural features, such as BTFE and to a lesser extent diglyme, may be considered as useful solvents for room-temperature fluoride ion electrolytes.

Baseline measurements of NpF/BTFE electrolytes indicate ionic conductivities (Fig. 1F) that are comparable to those of lithium ion battery electrolytes (10^{-3} to 10^{-2} S/cm) (*23*). To fully characterize the electrolyte solution properties, we carried out pulsed-field gradient spin-echo (PFG-SE) ^1H and ^{19}F NMR and AC impedance measurements for these electrolyte formulations (tables S1 and S2). High F^- transport numbers ($t_- > 0.5$) support the assignment of F^- as the major contributor to the ionic conductivity and charge mobility in BTFE solutions (Fig. 1G). The degree of ion dissociation (α) for the Np_1F/BTFE and Np_2F/BTFE electrolytes was estimated from NMR and impedance data to be α = 0.087 and 0.108, respectively, suggesting a considerable degree of ion pairing in solution (*20*). Stokes radii of the ions (R_{ion}) at room temperature reveal that three BTFE molecules diffuse together with Np_2^+, whereas only two BTFE molecules diffuse together with Np_1^+ (Fig. 1H). The increased degree of ion separation and the greater solvation of the Np_2^+ cation are likely contributing factors for improved conductivity in Np_2F/BTFE electrolytes.

Linear sweep voltammetry (LSV) of 0.75 M Np_1F/BTFE reveals a cathodic voltage limit of +0.7 V versus Li^+/Li and an anodic voltage limit of +4.8 V versus Li^+/Li, for an overall electrolyte voltage window of 4.1 V (Fig. 1I and fig. S5). Cathodic stability can be extended up to 400 mV by blending BTFE with a range of straight-chain glycol ethers, motivated by the MD simulations. These wide voltage windows offer the potential to support interfacial redox chemistry for a variety of metal cathode materials in FIB cells. For example, metals such as bismuth [$E^o_c(Bi^{3+}/Bi)$ = +3.4 V versus Li^+/Li], lead [$E^o_c(Pb^{2+}/Pb)$ = +2.9 V versus Li^+/Li], and copper [$E^o_c(Cu^{2+}/Cu)$ = +3.4 V versus Li^+/Li] should be fully compatible as cathode materials with this liquid electrolyte. These metals have previously demonstrated fluoride conversion reactions with limited cycling in high-temperature FIBs (*6*, *8*, *24*). We achieved electrochemical cycling of Bi, Pb, and Cu electrodes in a three-electrode cell at room temperature using our liquid electrolytes (Fig. 2A), whereby up to 10 cycles were carried out (Fig. 2, B to E, and fig. S6). In all cases, however, considerable metal dissolution into the electrolyte was found (*20*). Similar studies of cerium anodes [$E^o_a(Ce^{3+}/Ce)$ = +0.7 V versus Li^+/Li] and calcium anodes [$E^o_a(Ca^{2+}/Ca)$ = +0.2 V versus Li^+/Li] indicated that electrolyte breakdown was considerable (fig. S7), consistent with their potentials at the edge of the electrolyte cathodic window. However, performance was improved by modification of the metal with a fluorinated solid-electrolyte interphase (SEI) layer (*25*). Pretreatment of Ca or Ce electrodes with 1*H*,1*H*,2*H*,2*H*–perfluorooctyltriethoxysilane (FOTS) additive (fig. S8) (*20*) allowed for the desired formation of a CF_n-containing SEI layer on the metal surface, whereby reversibility of the Ce-to-CeF_3 conversion reaction was improved (Fig. 2, F and G).

To mitigate challenges associated with cathode metal dissolution, we designed composite cathode materials featuring a core-shell nanostructure with an inert thin shell around the active material (essentially an artificial SEI) (*26*). This would serve to (i) protect this active core from dissolution, (ii) protect the electrolyte from decomposition, (iii) restrict volume expansion and maintain structural integrity of the core, and (iv) selectively percolate electrolyte ions into the core. We selected Cu and LaF_3 for the core and shell, respectively, because of the high theoretical specific capacity of CuF_2 [528 mAh/g (*27*)] and the inert nature and highly selective F^- conductivity of LaF_3 (*6*), which we assumed would lead to facile F^- diffusion between the liquid electrolyte and the Cu core. Figure 3A shows transmission electron microscopy (TEM) images of pristine Cu@LaF_3 core-shell nanoparticles isolated after synthesis. These spherical nanoparticles are composed of a core 50 nm in diameter and a shell 5 nm thick (Fig. 3A, inset). Energy-dispersive x-ray spectroscopy (EDS) confirmed the elemental composition and stoichiometry of the core and shell regions of the material (Fig. 3B and fig. S9).

Electrodes fabricated with these Cu@LaF_3 nanoparticles were cycled reversibly at room temperature in a three-electrode cell for seven

Downloaded from http://science.sciencemag.org/ on December 6, 2018

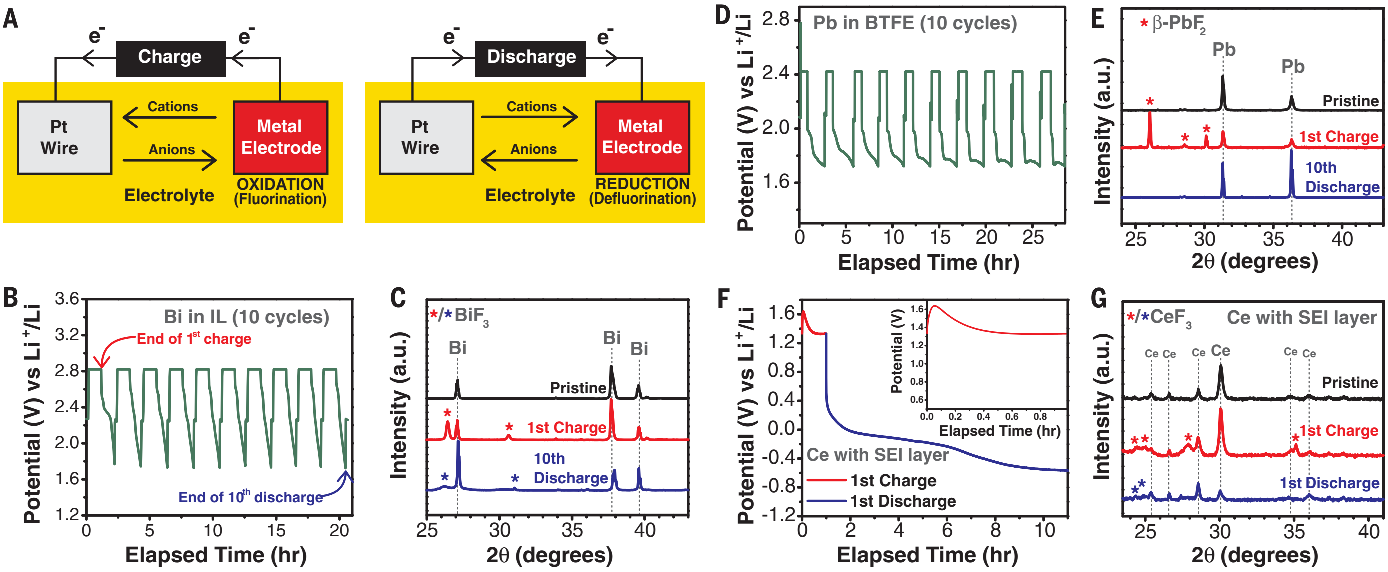

Fig. 2. Room-temperature performance of metal electrode materials reversibly cycled in nonaqueous, fluoride ion–conducting liquid electrolytes. (**A**) Schematic of external electron flow, electrolyte ion shuttling, and redox reactions occurring at FIB electrodes during charge or discharge cycles. (**B** and **C**) Data collected for Bi. (**D** and **E**) Data collected for Pb. (**F** and **G**) Data collected for Ce with an SEI layer formed from FOTS additive. Voltage profiles of Bi (B), Pb (D), and Ce (F) electrodes were collected during electrochemical cycling in a three-electrode cell (*20*). Ionic liquid (IL) = 0.1 M TMAF in MPPy-TFSI; BTFE = 0.1 M Np_1F in BTFE. Inset in (F) shows expanded view of charge cycle. Ce was cycled in 0.75 M Np_1F/BTFE. pXRD patterns were obtained for Bi (C), Pb (E), and Ce (G) electrodes in pristine condition (black), after first charge or fluorination (red), and after final discharge shown or defluorination (blue). Asterisks indicate new peaks corresponding to BiF_3, β-PbF_2, or CeF_3 due to metal fluorination after charge.

cycles (Fig. 3C). Reversible conversion of Cu to CuF_2 is evidenced by powder x-ray diffraction (pXRD) (Fig. 3D), which suggests that the LaF_3 shell permits passage of F^- to enable CuF_2 formation as intended. The desired protective nature of this shell is also clear, as inductively coupled plasma mass spectrometry of the electrolyte solution after cycling found no evidence for Cu or La dissolution within the limits of instrument detection (<10 μg), unlike for the uncoated Cu electrodes discussed above. A control experiment using these Cu@LaF_3 particles in electrolyte containing no F^- confirmed that the LaF_3 shell does not act as the F^- source for the formation of CuF_2; rather, the conversion of Cu to CuF_2 does indeed occur via F^- diffusion from the liquid electrolyte to the nanoparticle core and vice versa (fig. S10).

Detailed analysis of the fluorinated Cu@LaF_3 nanoparticles (i.e., after charging) was carried out using electron energy-loss spectroscopy (EELS) by scanning TEM (Fig. 3, E to G) (*20*). In contrast to the pristine Cu@LaF_3 nanoparticles, the nanoparticle structure after the first charge resembles a yolk-shell structure, where distinct void spaces (or interface) can be seen between the shell and the core (Fig. 3E and fig. S11). Representative EELS spectra show discrete F K, La $M_{5,4}$, and Cu $L_{3,2}$ edges for three regions at different depths within the fluorinated nanoparticle (Fig. 3F). Averaged elemental compositions show Cu-only cores, Cu- and F-containing interfaces, and La- and F-containing shells (Fig. 3G). In a limited number (2/13) of spectra taken from the interface region, quantitative analysis revealed a >2:1 ratio of F to Cu, indicating that more F^- is available in the interface region than Cu is available to react with it. These results suggest that F^- diffusion into the core (rather than through the shell) is a limiting factor, and if so, the limited total electrode capacity observed may be due to this bottleneck.

This hypothesis was confirmed through studies of thin-film structures of similar core-shell composition (*20*). Cyclic voltammetry of the thin film (Fig. 3H) reveals behavior similar to that of the nanoparticle material, with distinct peaks for the Cu-to-CuF_2 conversion process evident (oxidation at ~3.2 V, reduction at ~2.3 V); the relative asymmetry of the anodic peak indicates that the CuF_2 formation process is the most difficult electrochemical process, consistent with limited F^- diffusion into the Cu core film. X-ray photoelectron spectroscopy (XPS) depth-profile studies of thin-film structures confirm this assessment (Fig. 3I), indicating that F^- penetrates through the entire shell but through only ~4.9 nm of the Cu core, for a total F^- diffusion length of ~8.4 nm. On the basis of this observed diffusion length, Cu@LaF_3 nanoparticles with a shell thickness of 2 nm and a core diameter of 12 nm might allow for complete conversion of the Cu core to CuF_2 upon first charge, and much higher practical use of the material upon cycling.

Using a simple yet robust liquid electrolyte with high fluoride ion conductivity and wide voltage window, we have demonstrated reversible electrochemical cycling of metal fluoride electrodes at room temperature whereby F^-, not the metal cation, is the active ion shuttle. These results point toward FIBs that operate at room temperature. In particular, optimization of a Cu@LaF_3 core-shell

Downloaded from http://science.sciencemag.org/ on December 6, 2018

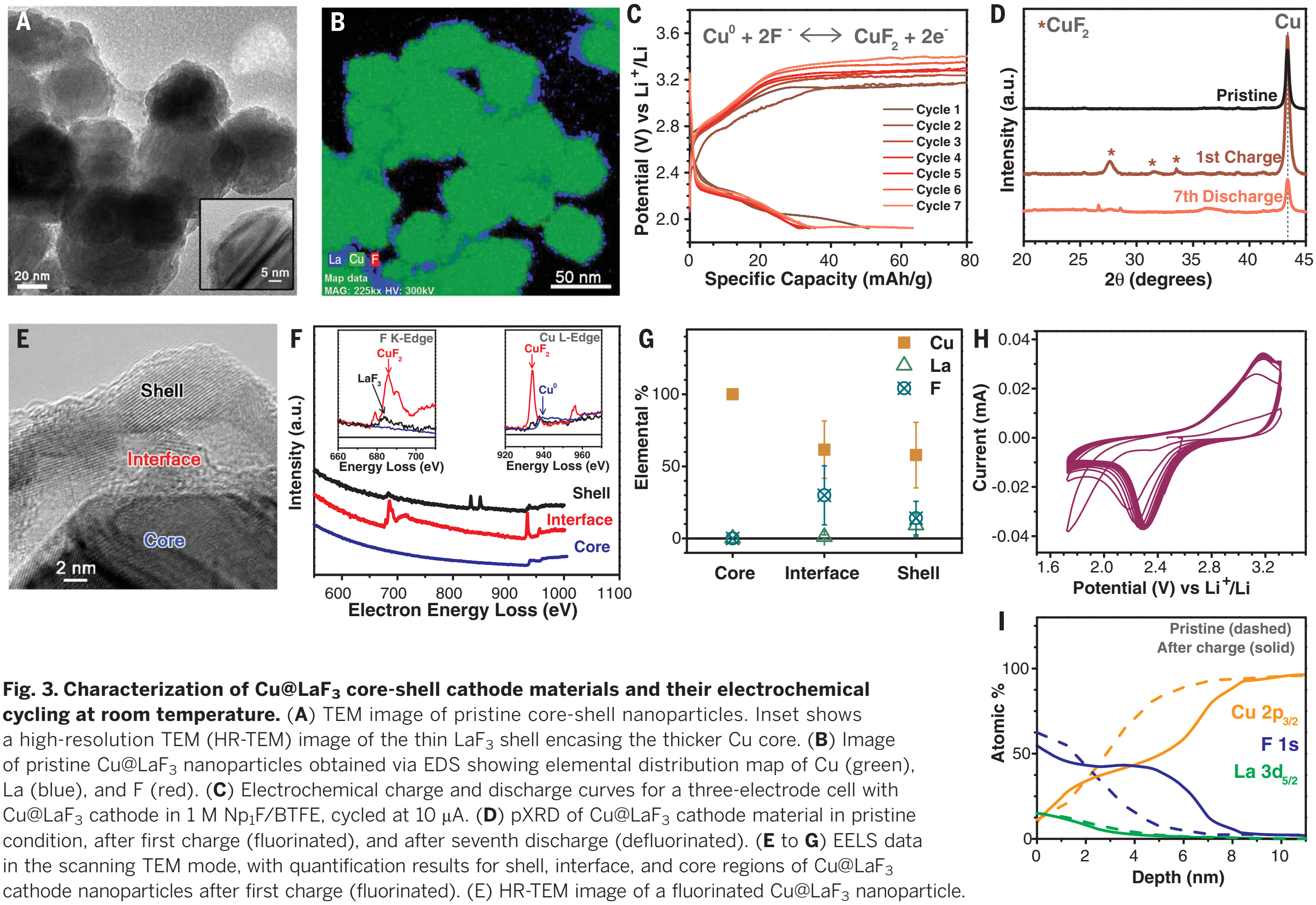

Fig. 3. Characterization of Cu@LaF_3 core-shell cathode materials and their electrochemical cycling at room temperature. (**A**) TEM image of pristine core-shell nanoparticles. Inset shows a high-resolution TEM (HR-TEM) image of the thin LaF_3 shell encasing the thicker Cu core. (**B**) Image of pristine Cu@LaF_3 nanoparticles obtained via EDS showing elemental distribution map of Cu (green), La (blue), and F (red). (**C**) Electrochemical charge and discharge curves for a three-electrode cell with Cu@LaF_3 cathode in 1 M Np_1F/BTFE, cycled at 10 μA. (**D**) pXRD of Cu@LaF_3 cathode material in pristine condition, after first charge (fluorinated), and after seventh discharge (defluorinated). (**E** to **G**) EELS data in the scanning TEM mode, with quantification results for shell, interface, and core regions of Cu@LaF_3 cathode nanoparticles after first charge (fluorinated). (E) HR-TEM image of a fluorinated Cu@LaF_3 nanoparticle. (F) Representative EELS spectra showing F K, La $M_{5,4}$, and Cu $L_{3,2}$ edges obtained for the fluorinated sample in the shell, interface, and core regions. Insets show the F K-edge and Cu $L_{3,2}$-edge from the graph below. (G) Plot of averaged elemental percent of Cu, La, and F obtained from 36 different EELS spectra, 12 each from shell, interface, and core regions of multiple fluorinated particles. (**H**) Cyclic voltammogram of Cu-LaF_3 thin-film electrode in 0.1 M TMAF/MPPy-TFSI for 10 cycles. (**I**) X-ray photoelectron spectroscopy (XPS) depth profiles for Cu-LaF_3 thin-film electrodes in pristine condition (dashed curves) and after charge (solid curves).

cathode and its pairing with an electropositive metal anode, such as Ce, offers a path toward developing a high-energy device.

REFERENCES AND NOTES

1. D. Larcher, J. M. Tarascon, *Nat. Chem.* **7**, 19–29 (2015).
2. A. Manthiram, Y. Fu, S. H. Chung, C. Zu, Y. S. Su, *Chem. Rev.* **114**, 11751–11787 (2014).
3. A. C. Luntz, B. D. McCloskey, *Chem. Rev.* **114**, 11721–11750 (2014).
4. R. Mohtadi, F. Mizuno, *Beilstein J. Nanotechnol.* **5**, 1291–1311 (2014).
5. F. Beck, P. Ruetschi, *Electrochim. Acta* **45**, 2467–2482 (2000).
6. N. I. Sorokin, B. P. Sobolev, *Crystallogr. Rep.* **52**, 842–863 (2007).
7. A. A. Potanin, U.S. Patent 7,722,993 B2 (2010).
8. M. Anji Reddy, M. Fichtner, *J. Mater. Chem.* **21**, 17059 (2011).
9. F. Gschwind, Z. Zhao-Karger, M. Fichtner, *J. Mater. Chem. A Mater. Energy Sustain.* **2**, 1214–1218 (2014).
10. F. Gschwind, J. Bastien, *J. Mater. Chem. A* **3**, 5628–5634 (2015).
11. K. Okazaki, Y. Uchimoto, T. Abe, Z. Ogumi, *ACS Energy Lett.* **2**, 1460–1464 (2017).
12. H. Konishi, T. Minato, T. Abe, Z. Ogumi, *J. Electrochem. Soc.* **164**, A3702–A3708 (2017).
13. D. A. Wynn, M. M. Roth, B. D. Pollard, *Talanta* **31**, 1036–1040 (1984).
14. H. O. House, E. Feng, N. P. Peet, *J. Org. Chem.* **36**, 2371–2375 (1971).
15. R. A. Bartsch, *J. Org. Chem.* **35**, 1023–1025 (1970).
16. J. S. Martin, F. Y. Fujiwara, *Can. J. Chem.* **49**, 3071–3073 (1971).
17. H. Sun, S. G. DiMagno, *J. Am. Chem. Soc.* **127**, 2050–2051 (2005).
18. K. O. Christe, W. W. Wilson, R. D. Wilson, R. Bau, J. A. Feng, *J. Am. Chem. Soc.* **112**, 7619–7625 (1990).
19. A. R. Mahjoub, X. Zhang, K. Seppelt, . *Chem. Eur. J.* **1**, 261–265 (1995).
20. See supplementary materials.
21. M. L. Gordin *et al*., *ACS Appl. Mater. Interfaces* **6**, 8006–8010 (2014).
22. R. K. Sharma, J. L. Fry, *J. Org. Chem.* **48**, 2112–2114 (1983).
23. J.-H. Shin, W. A. Henderson, S. Passerini, *Electrochem. Commun.* **5**, 1016–1020 (2003).
24. D. T. Thieu *et al*., *Adv. Funct. Mater.* **27**, 1701051 (2017).
25. P. Verma, P. Maire, P. Novák, *Electrochim. Acta* **55**, 6332–6341 (2010).
26. R. Ghosh Chaudhuri, S. Paria, *Chem. Rev.* **112**, 2373–2433 (2012).
27. G. G. Amatucci, N. Pereira, *J. Fluor. Chem.* **128**, 243–262 (2007).

ACKNOWLEDGMENTS

This work is dedicated to the memory of Nebojša Momčilović. **Funding:** The research was carried out at the Jet Propulsion Laboratory, California Institute of Technology, under a contract with NASA. V.K.D. thanks the NSF Graduate Research Fellowship Program for support under grant NSF-DGE-1650116. T.F.M. acknowledges NSF under DMREF award NSF-CHE-1335486. M.A.W. acknowledges the Resnick Sustainability Institute. This research used computational resources from the Oak Ridge Leadership Computing Facility at the Oak Ridge National Laboratory, which is supported by the Office of Science of the U.S. Department of Energy (DOE) under contract DE-AC05-00OR22725. This research also used resources of the National Energy Research Scientific Computing Center (NERSC), a DOE Office of Science User Facility supported by the DOE Office of Science under contract DE-AC02-05CH11231. STEM/EELS work at the Molecular Foundry was supported by the DOE Office of Science, Office of Basic Energy Sciences, under contract DE-AC02-05CH11231. We acknowledge support from the Beckman Institute of the California Institute of Technology to the Molecular Materials Research Center. **Author contributions:** The project was conceptualized by S.C.J. and supervised by K.O., C.J.B., R.H.G., and S.C.J.; fluoride salt synthesis procedures were developed and performed by V.K.D., C.M.B., N.M., I.M.D., and N.G.N.; salt characterization, analysis and solvent screening was performed by V.K.D., C.M.B., and N.M.; ionic conductivity and voltage window studies were performed by V.K.D. and K.J.B.; PFG-SE NMR experiments and analysis was carried out by W.J.W. and V.K.D.; computational studies were performed by B.M.S. and M.A.W. under the supervision of T.F.M.; electrochemical cells were built and tested by Q.X., N.H.C., and K.O.; cathode materials were synthesized by R.K.M.; TEM, EDS, and pXRD was performed by Q.X.; EELS was performed by S.A., D.R., and M.A.; V.K.D. and A.H. performed XPS measurements; V.K.D. made all figures in the main paper and in the supplement; and the manuscript was written by V.K.D. with input from S.C.J. and all authors. Two patent applications have been filed by Caltech and Honda Motor Co. Ltd.: US 15/228,876 (inventors: S.C.J., V.K.D., C.M.B., N.M., B.M.S., M.A.W., T.F.M., R.H.G., C.J.B., and K.O.) and US 15/844,079 (inventors: N.H.C., K.O., R.K.M., Q.X., C.J.B., S.C.J., I.M.D., and Hongjin Tan). **Competing interests:** All authors declare that they have no competing interests. **Data and materials availability:** Force-field parameters and example inputs for the MD simulations performed are available for download (data S1). All other data are available in the manuscript or the supplementary materials.

SUPPLEMENTARY MATERIALS

www.sciencemag.org/content/362/6419/1144/suppl/DC1
Materials and Methods
Supplementary Text
Figs. S1 to S20
Tables S1 to S4
References (*28*–*53*)
Data S1

28 March 2018; resubmitted 6 August 2018
Accepted 31 October 2018
10.1126/science.aat7070

Downloaded from http://science.sciencemag.org/ on December 6, 2018

VALLEYTRONICS

A valley valve and electron beam splitter

Jing Li[1]*, Rui-Xing Zhang[1], Zhenxi Yin[1], Jianxiao Zhang[1], Kenji Watanabe[2], Takashi Taniguchi[2], Chaoxing Liu[1], Jun Zhu[1,3]†

Developing alternative paradigms of electronics beyond silicon technology requires the exploration of fundamentally new physical mechanisms, such as the valley-specific phenomena in hexagonal two-dimensional materials. We realize ballistic valley Hall kink states in bilayer graphene and demonstrate gate-controlled current transmission in a four-kink router device. The operations of a waveguide, a valve, and a tunable electron beam splitter are demonstrated. The valley valve exploits the valley-momentum locking of the kink states and reaches an on/off ratio of 8 at zero magnetic field. A magnetic field enables a full-range tunable coherent beam splitter. These results pave a path to building a scalable, coherent quantum transportation network based on the kink states.

The advent of two-dimensional layered materials such as graphene and transition metal dichalcogenides has inspired the concept of devices that exploit the valley degrees of freedom in materials with hexagonal symmetry (*1*–*4*). Experiments have shown that a valley polarization can be created by current (*5*–*7*) or optical excitation (*8*). However, the realization of valleytronic devices remains challenging. In bilayer graphene, a perpendicular electric field applied through a pair of top and bottom gates breaks the symmetry of the two constituent layers and opens a gap Δ in its band structure (*9*, *10*). This gap can be inverted by switching the direction of the applied electric field; if two electric fields of opposite sign are applied on two neighboring regions in the sample, metallic, helical, quantum valley Hall kink states (hereafter kink states) emerge along the zero gap line (*11*). Topological in origin, the kink states are chiral in each valley and have opposite chiralities, that is, group velocities, in the two valleys K and K′ (−K) (Fig. 1A). They are expected to be immune from backscattering in the absence of valley-mixing scattering events and thus capable of carrying current ballistically over long distances without dissipation (*11*–*18*).

The intrinsic properties of the kink states enable several in situ transmission control mechanisms. Figure 1A illustrates the generation of kink states in bilayer graphene through asymmetric gapping (*11*, *12*). The shown chiralities correspond to the (− +) gating configuration. A (+ −) configuration simultaneously flips the chirality of the kink states in both valleys. Symmetric gapping configurations (+ +) or (− −) do not produce kink states and serve as controls in our experiment (fig. S3). The existence of two helicities produced by the (− +) and (+ −) gating is a unique attribute of the kink states and leads to the proposal of an all-electric valley valve (*12*, *14*), the operation of which relies on the valley-momentum locking of the kink states. Different from a classical spin valve (*19*), a valley polarization is not a requirement for the proposed valley valve. Here we show the realization of the valley valve with a transmission on/off ratio of 8 at zero magnetic field and greater than 100 at several teslas.

Figure 1, B to E, shows schematics and optical and scanning electron micrographs of the four-terminal valley router device, which consists of four pairs of split top and bottom gates and a global Si backgate (see fig. S1 for device fabrication). The aligned edges of the eight gates define the four kink channels shown in magenta in Fig. 1C. The dual-gated region (yellow areas in Fig. 1C) in each quadrant is gapped and placed at the charge neutrality point (CNP) (See fig. S2 for device characterization.) We first measure the resistance of each kink channel R_{kink} separately. As an example, Fig. 1G plots the resistance of the east channel R_{E} as a function of the Si backgate voltage V_{Si}, which controls the Fermi level E_{F} in the channel, at fixed magnetic fields $B = 0$ to 8 T. R_{E} exhibits a broad peak at $B = 0$, which evolves into a wide plateau as B increases and saturates at about 7.3 kilohm. This plateaued region corresponds to the gapped regime of the channel, where the kink states reside. We call this the kink regime. Its resistance value of 7.3 kilohm is a sum of the ballistic resistance of the kink states, that is, $h/4e^2$ = 6.5 kilohm, where h is the Planck constant, and a contact resistance R_c ~ 800 ohm. Additional plateaus outside the kink regime correspond to the sequential addition of fourfold degenerate quantum Hall edge states in the channel (Fig. 1F). The application of a perpendicular magnet field has little effect on the energy spectrum of the kink states (*11*, *20*) and does not generate additional edge states inside the bandgap [fig. S3; (*21*, *22*)]. It, however, turns the conduction and valence bands of the junction into Landau levels (Fig. 1F), as evidenced by the appearance of additional resistance plateaus. The devices studied here are of higher quality than those reported in our previous work (*11*), owing to the adoption of the van der Waals transfer method (*23*). A side effect of this approach, however, is a large width/length ratio of the dual-gated regions (Fig. 1D), which enhances parallel hopping conduction. At small magnetic fields, the associated resistance R_{para} causes R_{E} to be less than $h/4e^2$ (see curves for B = 0 and 2 T in Fig. 1G). We measure R_{para} independently using the symmetric gapping configurations (figs. S3 and S5) and extract R_{E} using a two-resistor model $R_{\mathrm{E}} = \frac{(R_{24}-R_{\mathrm{c}})R_{\mathrm{para}}}{R_{\mathrm{para}}-(R_{24}-R_{\mathrm{c}})}$, where R_{24} is the resistance from terminal 2 to terminal 4. As B increases, hopping conduction becomes increasingly suppressed, and R_{para} grows to hundreds of megohms. R_{para} becomes inconsequential at 4 T, which leads to the observed saturation of $R_{24} = h/4e^2 + R_{\mathrm{c}}$ in Fig. 1G. We determine R_{c} by fitting a series of quantized resistance plateaus and have observed robust resistance quantization of the kink states at $h/4e^2$ in different devices (fig. S4).

Similar measurements and analyses were performed on other channels in the same device and in a second device; the results are shown in Fig. 1H. At B = 0, R_{kink} is about 7000 ohm for our 300-nm-long channels, which corresponds to a transmission coefficient $\tau_{\mathrm{kink}} = h/4e^2/R_{\mathrm{kink}} = 0.92$ and an estimated mean free path of 3.5 μm (*11*). This is on par with the mean free path of the quantum spin Hall edge states (*24*, *25*) and affirms the topological protection provided by the valley-momentum locking of the kink states. Because this protection vanishes in the armchair cryostallographic orientation, we ensure that neither of the two perpendicular directions of the channels is aligned with either zigzag or armchair orentations in our devices. Indeed, the similar performances of channels perpendicular to one another in our devices (Fig. 1H) support the existence of topological protection for both channels. The presence of a magnetic field improves the ballisticity of the kink states, which exhibit a quantized resistance plateau at B ~ 4 T. As discussed in our previous work (*11*), we suspect that the backscattering of the kink states is caused by one-dimensional nonchiral states bound in the junction, as well as by charge puddles inside the gap. The application of a magnetic field moves both types of states to higher energy, thus reducing their interactions with the kink states. Additionally, in the 0th Landau level of bilayer graphene, states in K and K′ occupy different graphene layers (*22*). If kink states behave similarly, this could contribute to reduced backscattering as well. A quantitative study can shed more light on this issue.

We now demonstrate the operation of the valley router as a reconfigurable waveguide for the kink states. Figure 2, A to C, shows three configurations of the waveguide, which we

---

[1]Department of Physics, The Pennsylvania State University, University Park, PA 16802, USA. [2]National Institute for Material Science, 1-1 Namiki, Tsukuba 305-0044, Japan. [3]Center for 2-Dimensional and Layered Materials, The Pennsylvania State University, University Park, PA 16802, USA.
*Present address: National High Magnetic Field Laboratory, Los Alamos, NM 87545, USA.
†Corresponding author. Email: jzhu@phys.psu.edu

Downloaded from http://science.sciencemag.org/ on December 6, 2018

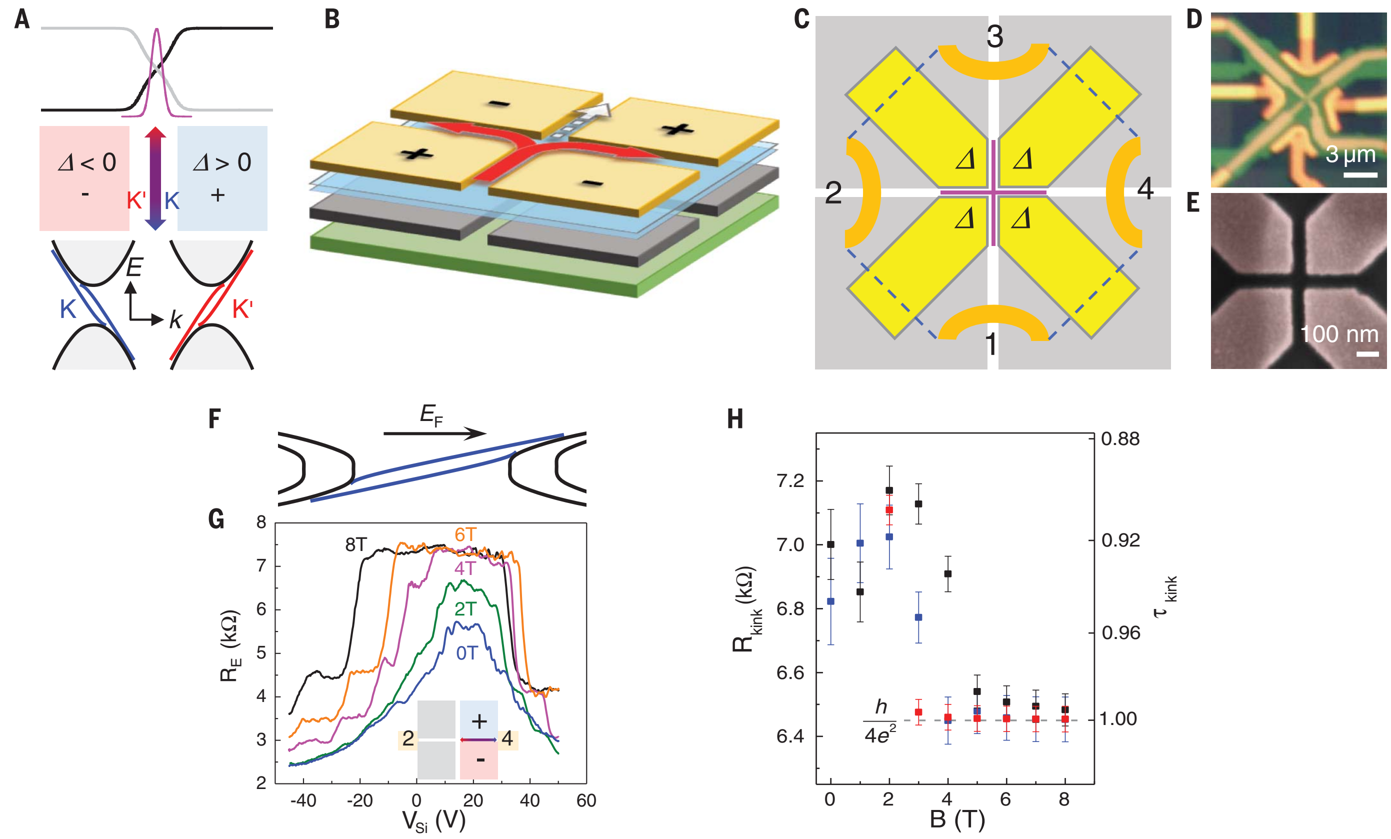

Fig. 1. A valley router device and ballistic conduction of the kink states. (**A**) The potential profile and wave function distribution (magenta curve) of the valley-momentum locked kink states in a 70-nm-wide junction (*11*). Including spin and layer isospin, there are four chiral modes in each valley. (**B** and **C**) Schematics of our quad-split-gated valley router device. The four graphite bottom gates are shown in gray. The four top gates are yellow. The bottom gates are set to ±3 V, with the polarity given in diagrams, unless otherwise specified. The top gates are set to place the dual-gated regions at the CNP. Three volts applied to the gates correspond to a bulk gap of $\Delta \sim 86$ meV [see section 2 of (*27*)]. The blue sheet in (B) and dashed lines in (C) represent the bilayer graphene sheet. The global Si backgate is light green. The four gold arcs are Cr/Au side contacts. The magenta cross in (C) represents the four kink channels. Each is 70 nm wide and 300 nm long. The red arrows and white dashed arrow in (B) represent the valley valve and beam splitting actions discussed in Fig. 3. (**D**) An optical image of device 1. (**E**) A false-colored scanning electron micrograph of the central region taken on another device. (**F**) A band diagram of the junction in magnetic field (*11*). (**G**) R_E (V_{Si}) at different magnetic fields, as labeled in the graph. R_E is obtained by measuring R_{24}, that is, the resistance from terminal 2 to terminal 4, while doping the left quadrants heavily, as illustrated in the inset. (**H**) Resistance of the kink state R_{kink} as a function of the magnetic field in the east (black) and south (blue) channels of device 1 and south (red) channel of device 2. The right axis labels the corresponding transmission coefficient τ_{kink}. $T = 1.6$ K in all our measurements. Error bars indicate the uncertainties of R_{kink}.

label as “through,” “right turn,” and “left turn,” respectively. In all three, the kink states only exist in two of the four channels, and the chirality in each valley is preserved along the paths. Figure 2D plots the measured through resistance R_{13}, together with the resistance of each individual kink channel R_N (north) and R_S (south) at 6 T. All three curves overlap in the kink regime, suggesting that the transmission through the intersection region is ballistic. Similar ballistic transmission is also observed in the two 90° bends (Fig. 2E), consistent with the results of numerical simulations (*14*, *26*). This four-terminal device thus serves as an in situ reconfigurable electronic waveguide of the kink states. The ability to go around a corner is a direct consequence of the topological nature of the kink states.

Deviation from perfect transmission starts to occur as the magnetic field B is lowered to $B < 6$ T. Figure 2F plots the transmission coefficient of the intersection region τ_i (B) determined using the two-resistor model shown as the inset (see fig. S5 for details). τ_i increases from 0.63 at $B = 0$ to unity at $B \sim 6$ T. τ_i is smaller than τ_{kink} of individual channels shown in Fig. 1H. This is not surprising because the confining bulk gaps in the intersection region are smaller and, consequently, nonchiral states may be present at lower energies to cause backscattering of the kink states (*11*). Increasing Δ—our device does not allow this owing to gate leakage—should enable further increase of τ_i toward unity. We discuss the current devices and improvements that can enable fully ballistic guiding of the kink states at $B = 0$ in section 2 of (*27*).

A more powerful operation of the valley router enables it to function as a valley valve and a coherent electron beam splitter simultaneously. In this operation, the polarity of the electric field changes sign between adjacent quadrants. Kink states in opposing channels have opposite helicities, that is, states with the same chirality carry opposite valley indices K and K′ and vice versa. This situation is depicted in the middle panel of Fig. 3A and leads to the suppression of straight current transmission in the absence of intervalley scattering. This valley-valve effect occurs regardless of the presence of a magnetic field and directly confirms the valley-momentum locking of the kink states. The application of a magnetic field, however, offers additional control of the wave function of the kink states. Calculations have shown that although the wave functions of the K and K′ valley kink states overlap at the CNP, where $E_F = 0$, they gradually shift in opposite directions as E_F moves into the electron or hole regime (*11*, *20*, *28*). The shifts are illustrated in the five panels of Fig. 3A. As the kink states shift away from the midlines of the channels, the wave function of a state coming from a particular channel has unequal overlap with states of adjacent channels, thus leading

Downloaded from http://science.sciencemag.org/ on December 6, 2018

Fig. 2. Transmission of the kink states in the waveguide mode of the router. (**A** to **C**) Illustrations of the through (A), right turn (B), and left turn (C) configurations of the waveguide, respectively. (**D**) Two-terminal resistance R_{13} (V_{Si}) corresponding to the resistance of the north channel R_N (blue), the south channel R_S (red), and the through configuration (black). The overlap of all three indicates ballistic transmission through the intersection region in (A), that is, $\tau_i = 1$. $B = 6$ T. (**E**) R_{34} (orange) and R_{14} (green) as a function of V_{Si} in the configurations shown in (B) and (C), respectively. $B = 5$ T. (**F**) The transmission coefficient τ_i of the intersection region in (A) as a function of the magnetic field, with the schematic of the two-resistor model shown in the inset. Error bars indicate the uncertainties of τ_i.

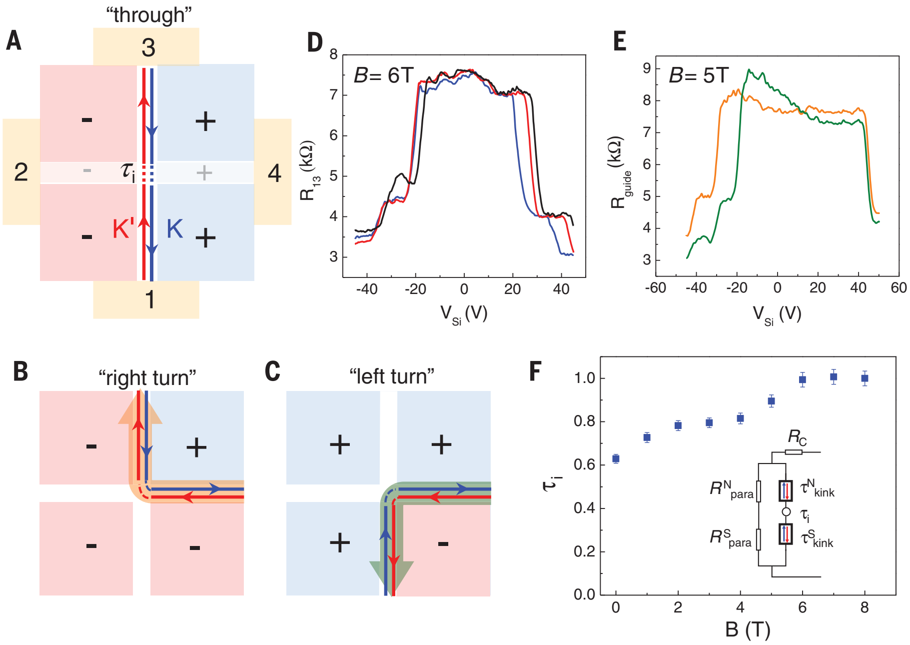

Fig. 3. A valley valve and electron beam splitter. (**A**) Evolution of the K and K′ kink state wave function center as a function of E_F in a moderate magnetic field. The arrows mark the chirality of the kink states, from the perspective of an electron. The middle panel represents the CNP, where the K and K′ states overlap. It also represents the $B = 0$ situation for all E_F. The dashed arrow illustrates the valley-valve blocking effect. (**B**) Measurements of the normalized percentage current I_i = [(current to drain i)/(total current)] ×100% received at terminals 2 to 4 as labeled in the graph while using terminal S1 as the current source. $B = 8$ T. The current flow is opposite of the arrows in (A). (**C**) I_3 (V_{Si}) at selected B fields from 0 to 11 T, demonstrating the robustness of the valley-valve effect. (**D**) The six independent current transmission coefficients used in our model (*27*), which reflects an empirical C_2 rotational symmetry of our device. (**E**) Measured (magenta) and calculated (black) two-terminal resistance R_{13}. A contact resistance R_c = 1 kilohm is added to the calculated curve. $B = 8$ T. The discrepancy between theory and experiment may be caused by local microscopic imperfections of the device beyond the S-matrix model.

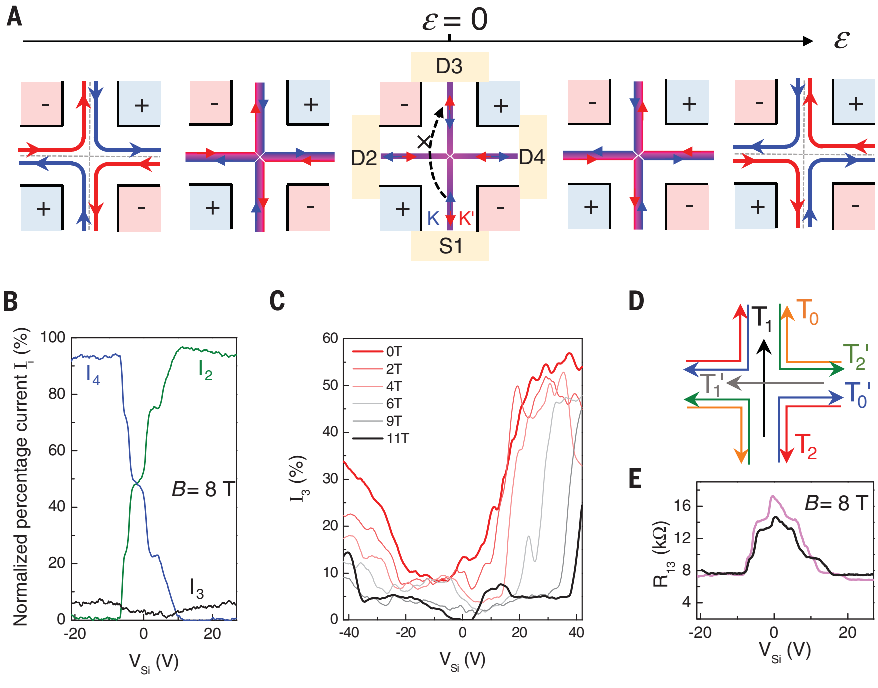

to unequal current partition. Simulations show that the wave function separation is tunable as a function of E_F and B and can become comparable to or greater than the width of the wave functions themselves at several teslas (*11*, *28*). Consequently, a current partition from 0 to 1 is possible.

To test these predictions experimentally, we source a constant current from one terminal and measure the normalized percentage current I_i = [(current to drain i)/(total current)] × 100% received at the other three terminals simultaneously. Figure 3B plots I_2, I_3, and I_4 at $B = 8$ T using S1 labeled in Fig. 3A as the current source. Notably, I_3 remains low in the entire range of V_{Si} when all four channels are in the kink regime. Similar behavior is observed in measurements using other source terminals (fig. S7) and in device 2 (fig. S8). The suppression of current flow between opposing terminals provides compelling evidence of the valley-valve effect, which also confirms the valley-momentum locking of the kink states. As Fig. 3C shows, the valley-valve effect is already very strong at $B = 0$, with a small I_3 of 8% near the CNP. I_3 further decreases to less than 1% at $B = 11$ T, as the magnetic field works to suppress residual intervalley scattering in the intersection region. The transmission on/off ratio of I_3 between the through configuration (Fig. 2A) and the blocking configuration

Downloaded from http://science.sciencemag.org/ on December 6, 2018

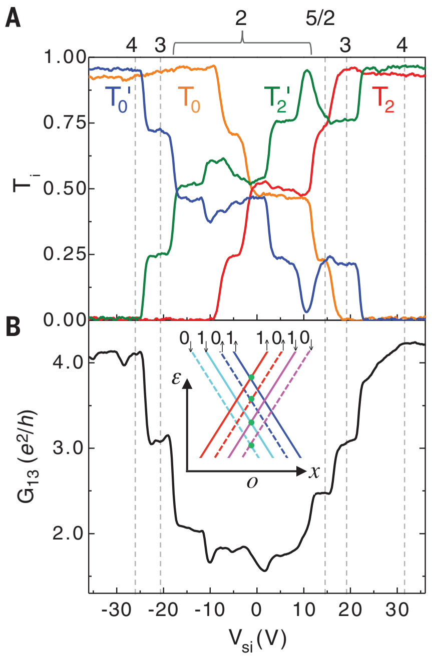

Fig. 4. Quantized transmission coefficients in a strong magnetic field. (**A** and **B**) Measured transmission coefficients T_0, T_2, T_0', and T_2' (A) and G_{13} (B) as a function of V_{Si} at B = 16 T. The locations of the quantized G_{13} are marked in the plot; their conductance values are labeled at the top axis in units of e^2/h. Spikes in the middle of a plateau are likely caused by microscopic potential irregularities. A contact resistance of R_c = 1174 ohm is subtracted. The inset of (B) shows a guiding center description of the energy spectrum of the valley kink states in strong magnetic and electric fields.

(Fig. 3A) is about 8 at B = 0 and greater than 100 in a magnetic field. The performance of the valley valve is similar to a recently reported state-of-the-art all-electric spin valve (*29*). Unlike a spin valve, however, here the source current is nearly valley-unpolarized. The omission of the valley injection step is an advantage of the underlying topological valleytronic concept.

Instead of propagating forward, the kink state wave functions from S1 split at the intersection and propagate toward terminals D2 and D4. Both I_2 and I_4 vary colinearly with V_{Si}, forming a prominent X-like feature at 8 T (Fig. 3B). The tunable range of I_2 (I_4) increases with B until it saturates close to the full range of 0 to 1 at ~5 T (fig. S7, A and B). This current partition behavior is reproducible using different source terminals (fig. S7C) and in different devices (fig. S8). It is in excellent agreement with the wave function separation scenarios depicted in Fig. 3A and represents an electron analog of an optical beam splitter and a quantum point contact for the kink states. Furthermore, in fig. S7D, we show the large impact of unequal gap size on the current partition. By adjusting the size of the gap on the four quadrants at a fixed E_F, I_2 (I_4) can change by 50%. These results are promising steps toward the implementation of a zero-magnetic field beam splitter (*28*).

We developed an S-matrix model [section 8 of (*27*)] to describe the transmissions of the kink states between different channels with six independent coefficients schematically shown in Fig. 3D. These coefficients are obtained directly from measurements shown in Fig. 3B and in other source-drain setups (fig. S7). Using the experimental input and the Landauer-Büttiker formula, we have calculated the resistance for various two-terminal and nonlocal measurement geometries and compared them to measurements. The agreement between theory and experiment is excellent and affirms the one-dimensional transport nature of the kink states. As an example, Fig. 3E shows the calculated and measured two-terminal resistance R_{13}; other scenarios are discussed in fig. S10. More fundamental understandings and predictions of the transmission process would require details of the electrostatics (*28*) and also possibly band-structure effects such as trigonal wrapping (*30*, *31*).

When the magnetic field increases to above 6 T, plateaus at ¼, ½, and ¾ start to appear in the transmission coefficient T_i. Correspondingly, conductance plateaus in integer and half-integer units of e^2/h appear in the measured conductance between terminals 1 and 3 G_{13}. The quantization becomes increasingly prominent and precise as B increases, with the data of T_i and G_{13} at B = 16 T given in Fig. 4, A and B. (See fig. S11 for data up to 18 T.) Their appearance is caused by the energy splitting of the four kink-state modes in a strong magnetic field (inset of Fig. 4B) (*32*) and, consequently, the spatial separation of the modes in a guiding center description. The large spatial separation between the modes leads to values of T_i taking either 0 or 1 for each mode, with the choice given by the position of E_F with respect to the crossing point of that mode. The average of all four modes then produces quantized coefficients at multiples of ¼. This leads to conductance plateaus quantized in integer and half integer units of e^2/h, as Fig. 4B shows. In section 9 of (*27*), we provide a detailed understanding of the fractional quantization of T_i and its manifestation in transport, which reflect the coexisting helical and chiral nature of the kink states in a magnetic field.

REFERENCES AND NOTES

1. A. Rycerz, J. Tworzydlo, C. W. J. Beenakker, *Nat. Phys.* **3**, 172–175 (2007).
2. W. Yao, D. Xiao, Q. Niu, *Phys. Rev. B* **77**, 235406 (2008).
3. D. Xiao, M.-C. Chang, Q. Niu, *Rev. Mod. Phys.* **82**, 1959–2007 (2010).
4. X. Xu, W. Yao, D. Xiao, T. F. Heinz, *Nat. Phys.* **10**, 343–350 (2014).
5. R. V. Gorbachev *et al.*, *Science* **346**, 448–451 (2014).
6. Y. Shimazaki *et al.*, *Nat. Phys.* **11**, 1032–1036 (2015).
7. M. Sui *et al.*, *Nat. Phys.* **11**, 1027–1031 (2015).
8. K. F. Mak, K. L. McGill, J. Park, P. L. McEuen, *Science* **344**, 1489–1492 (2014).
9. Y. Zhang *et al.*, *Nature* **459**, 820–823 (2009).
10. E. McCann, M. Koshino, *Rep. Prog. Phys.* **76**, 056503 (2013).
11. J. Li *et al.*, *Nat. Nanotechnol.* **11**, 1060–1065 (2016).
12. I. Martin, Y. M. Blanter, A. F. Morpurgo, *Phys. Rev. Lett.* **100**, 036804 (2008).
13. J. Li, A. F. Morpurgo, M. Büttiker, I. Martin, *Phys. Rev. B* **82**, 245404 (2010).
14. Z. Qiao, J. Jung, Q. Niu, A. H. Macdonald, *Nano Lett.* **11**, 3453–3459 (2011).
15. J. Jung, F. Zhang, Z. Qiao, A. H. MacDonald, *Phys. Rev. B* **84**, 075418 (2011).
16. F. Zhang, A. H. MacDonald, E. J. Mele, *Proc. Natl. Acad. Sci. U.S.A.* **110**, 10546–10551 (2013).
17. L. Ju *et al.*, *Nature* **520**, 650–655 (2015).
18. J. Lee, K. Watanabe, T. Taniguchi, H. J. Lee, *Sci. Rep.* **7**, 6466 (2017).
19. S. Datta, B. Das, *Appl. Phys. Lett.* **56**, 665–667 (1990).
20. M. Zarenia, J. M. Pereira Jr., G. A. Farias, F. M. Peeters, *Phys. Rev. B* **84**, 125451 (2011).
21. E. McCann, V. I. Fal'ko, *Phys. Rev. Lett.* **96**, 086805 (2006).
22. J. Li, Y. Tupikov, K. Watanabe, T. Taniguchi, J. Zhu, *Phys. Rev. Lett.* **120**, 047701 (2018).
23. L. Wang *et al.*, *Science* **342**, 614–617 (2013).
24. M. König *et al.*, *Science* **318**, 766–770 (2007).
25. L. Du, I. Knez, G. Sullivan, R.-R. Du, *Phys. Rev. Lett.* **114**, 096802 (2015).
26. Z. Qiao *et al.*, *Phys. Rev. Lett.* **112**, 206601 (2014).
27. See supplementary materials.
28. K. Wang *et al.*, *Phys. Rev. B* **95**, 245420 (2017).
29. P. Chuang *et al.*, *Nat. Nanotechnol.* **10**, 35–39 (2015).
30. D. A. Cosma, V. I. Fal'ko, *Phys. Rev. B* **92**, 165412 (2015).
31. A. Varlet *et al.*, *Phys. Rev. Lett.* **113**, 116602 (2014).
32. M. Victoria, S. Efrat, H. Chia-Wei, T. C. Sam, H. A. Fertig, *Phys. Scr. T* **165**, 014019 (2015).
33. J. Li, Data for "A valley valve and electron beam splitter," Version 1, Harvard Dataverse (2018); https://doi.org/10.7910/DVN/UIFTE6.

ACKNOWLEDGMENTS

We are grateful for helpful discussions with J. Teo. We thank J. Jaroszynski of the NHMFL for experimental assistance. **Funding:** J.L., Z.Y., and J.Zhu are supported by the NSF (grant no. DMR-1506212 and DMR-1708972). C.L., J.Zha., and R.-X.Z. acknowledge support from the Office of Naval Research (grant nos. N00014-15-1-2675). K.W. and T.T. acknowledge support from the Elemental Strategy Initiative conducted by the MEXT, Japan, and the CREST (JPMJCR15F3), JST. Part of this work was performed at the NHMFL, which was supported by the NSF through NSF-DMR-1157490 and the state of Florida. Part of this work was carried out in the Nanofabrication Laboratory at Penn State's Materials Research Institute. **Author contributions:** J.Zhu and J.L. conceived the experiment. J.L. designed and fabricated the devices and made the measurements. Z.Y. assisted in device fabrications. J.L. and J.Zhu analyzed the data. R.-X.Z. and J.Zha. performed the theoretical calculations. R.-X.Z. and C.L. analyzed theoretical results. K.W. and T.T. synthesized the hexagonal boron nitride crystals. J.Zhu, J.L., R.-X.Z., and C.L. wrote the manuscript with input from all authors. **Competing financial interests:** The authors declare no competing financial interests. **Data and materials availability:** Data shown in this paper are available at (*33*).

SUPPLEMENTARY MATERIALS

www.sciencemag.org/content/362/6419/1149/suppl/DC1
Supplementary Text
Figs. S1 to S14
Table S1
References (*34*–*36*)

7 August 2017; resubmitted 28 March 2018
Accepted 30 October 2018
10.1126/science.aao5989

Downloaded from http://science.sciencemag.org/ on December 6, 2018

QUANTUM MATERIALS

Photonic crystals for nano-light in moiré graphene superlattices

S. S. Sunku[1,2], G. X. Ni[1], B. Y. Jiang[3], H. Yoo[4], A. Sternbach[1], A. S. McLeod[1], T. Stauber[5], L. Xiong[1], T. Taniguchi[6], K. Watanabe[6], P. Kim[4], M. M. Fogler[3], D. N. Basov[1]*

Graphene is an atomically thin plasmonic medium that supports highly confined plasmon polaritons, or nano-light, with very low loss. Electronic properties of graphene can be drastically altered when it is laid upon another graphene layer, resulting in a moiré superlattice. The relative twist angle between the two layers is a key tuning parameter of the interlayer coupling in thus-obtained twisted bilayer graphene (TBG). We studied the propagation of plasmon polaritons in TBG by infrared nano-imaging. We discovered that the atomic reconstruction occurring at small twist angles transforms the TBG into a natural plasmon photonic crystal for propagating nano-light. This discovery points to a pathway for controlling nano-light by exploiting quantum properties of graphene and other atomically layered van der Waals materials, eliminating the need for arduous top-down nanofabrication.

When light of wavelength λ_0 travels through media with periodic variations of the refractive index, one witnesses an assortment of optical phenomena categorized under the notion of a photonic crystal (*1*). The additional periodicity imposed on light can trigger the formation of a full photonic bandgap (*2*) and may also produce chiral one-dimensional (1D) edge states (*3*) or exotic photonic dispersions emulating those of Dirac and Weyl quasiparticles (*4*). In principle, the photonic crystal concept is also applicable for controlling the propagation of "nano-light": coupled oscillations of photons and electrons confined to the surface of the conducting medium and referred to as surface plasmon polaritons (SPPs) (*5*–*7*). The wavelength of SPPs, λ_p, is reduced compared with λ_0 by up to three orders of magnitude (*8*). However, this virtuous confinement poses challenges for the implementation of the nano-light photonic crystals by standard top-down techniques (*9*, *10*). In this study, we demonstrate a lithography-free photonic crystal for plasmons in twisted bilayer graphene (TBG). Periodic variations in the optical response of these van der Waals heterostructures arise naturally because of modification of the electronic structures at moiré domain walls (solitons) formed in rotationally misaligned graphene layers (Fig. 1B). The most important feature of the modified electron dispersion is the appearance of chiral 1D states (one pair per valley) (Fig. 1C), which are known to be topologically protected (*11*). The optical transitions involving these 1D states (arrow in Fig. 1C) produce an enhancement of the local optical conductivity across the solitons (*11*). A characteristic profile of the attendant near-field signal is displayed in Fig. 1D and will be discussed below. By using infrared (IR) nano-imaging experiments (Fig. 1A), we visualize the interference between SPPs propagating in solitonic networks and predict the formation of a full plasmonic bandgap.

Graphene has emerged as an extremely capable plasmonic medium in view of ultrastrong confinement, quantified by $\lambda_0/\lambda_p \geq 1000$ (*8*), attained in the regime of weak loss (*12*, *13*). The plasmonic properties of graphene can be readily controlled by the carrier density (*6*, *7*), the dielectric environment (*12*, *14*), and ultrafast optical pulses (*15*). In this study, we have explored and exploited yet another control route based on the twist angle θ between neighboring graphene layers (*14*, *16*–*20*). In TBG, the local stacking order changes smoothly across the narrow solitons separating AB from BA domains (*21*), as revealed (Fig. 1B) by dark-field transmission electron microscopy (TEM). Previous nano-IR experiments on isolated solitons in Bernal-stacked bilayer graphene (BLG) have shown that SPPs in BLG are scattered by the solitons (*11*, *22*), analogous to the scattering of SPPs by grain boundaries in monolayer graphene (*23*). Therefore, a regular pattern of such solitons (Fig. 1B) is expected to act as a periodic array of scatterers, thus fulfilling the key precondition for a nano-light photonic crystal. Unlike all previous implementations of photonic crystals (*24*, *25*), our approach exploits local changes in the electronic band structure of the plasmonic medium, a quantum effect, to control optical phenomena. We explored this novel and fundamentally quantum approach for manipulating plasmons via direct nano-imaging experiments, modeling, and theory.

IR nano-imaging (Fig. 1A) is central to unveiling the physics of a quantum photonic crystal for plasmons. In our experiments, IR light at frequency $\omega = 1/\lambda_0$ is focused on the apex of a metallic tip. The amplitude of the backscattered signal $s(\omega)$ and its phase $\phi(\omega)$ are recorded by using an interferometric detection method (*26*). When ω is close to the optical phonon of the SiO_2 substrate, as in Fig. 1B, IR nano-imaging effectively reveals local variations of the optical conductivity (*26*, *27*). In Fig. 1B, we observed a sixfold pattern of bright line-like features with even stronger contrast at the intersections. A dark-field TEM image of a similar TBG sample also reveals the same sixfold symmetry with features matching the nano-IR data. The periods of both patterns are consistent with the moiré length scales anticipated for a nominal twist angle of ~ 0.1°. An accurate estimate of the periodicity a for our device can be directly read off the near-field image: Given the observed a = 230 nm, we obtain a twist angle of $\theta = 0.06°$ (*26*). We therefore conclude that the near-field image constitutes a direct visualization of the solitonic lattice.

The nano-IR contrast at the solitons is the result of topological changes to the electronic structure. When inversion symmetry is broken by an application of a perpendicular displacement field using the back gate, the Bernal-stacked AB and BA domains open a bandgap (*28*) and the valley Chern number at *K* and *K*′ valleys is ±1 (*29*). As the stacking order reverses across the soliton, the Chern numbers also change sign. The difference in Chern number leads to topologically protected 1D states along the soliton (*30*, *31*). The key implication of this band structure effect (*11*) is that optical transitions from the topologically protected states to empty states above the Fermi level prompt an enhanced conductivity at the soliton (Fig. 1C). Consistent with this view, resistivity experiments signal ballistic electron transport along the solitonic channels (*17*, *32*).

Our qualitative understanding of the near-field contrast is corroborated by modeling. The near-field amplitude and phase profiles $s_{sol}(x)$ and $\phi_{sol}(x)$, where x is the coordinate normal to the soliton, depend on the Fermi energy μ, the interlayer bias V_i, and the plasmonic damping rate η [section S4 of (*26*)]. These latter profiles obtained for isolated solitons (*11*, *22*) were fully elucidated by combining electronic structure calculations, scattering theory, and numerical modeling of the tip-sample coupling (*11*, *33*). Figure 1D shows $s_{sol}(x)$ calculated by using parameters that most closely correspond to the experiment in Fig. 1B.

We now discuss the effect of periodic soliton networks in TBG on propagating plasmon polaritons. In our experiments, SPPs of wavelength λ_p of the order of the soliton periodicity a are introduced by the metallic tip (Fig. 1A) (*12*, *15*). To launch propagating polaritons, we choose ω to be away from phonon resonances. In this regime, the scattering of SPPs by the solitons

---

[1]Department of Physics, Columbia University, New York, NY 10027, USA. [2]Department of Applied Physics and Applied Mathematics, Columbia University, New York, NY 10027, USA. [3]Department of Physics, University of California–San Diego, La Jolla, CA 92093, USA. [4]Department of Physics, Harvard University, Cambridge, MA 02138, USA. [5]Departamento de Teoría y Simulación de Materiales, Instituto de Ciencia de Materiales de Madrid, CSIC, E-28049 Madrid, Spain. [6]National Institute for Materials Science, Namiki 1-1, Tsukuba, Ibaraki 305-0044, Japan.
***Corresponding author. Email: db3056@columbia.edu**

Downloaded from http://science.sciencemag.org/ on December 6, 2018

produces fringes in both $s(\omega)$ (*6*, *7*) and $\phi(\omega)$ (*34*) corresponding to standing waves. 2D maps of both observables are displayed in Fig. 2. We obtained these images in different regimes of λ_p/a by tuning the gate voltage V_G and/or λ_0. All images are dominated by maxima and minima in the nano-IR contrast, indicating the presence of constructive and destructive interference of SPPs triggered by the solitonic lattice.

The Fourier analysis of the $s(\omega)$ images shown in Fig. 3, A and B, supports our conjecture of a photonic crystal. We denote the magnitude of the 2D spatial Fourier transform of the $s(\omega)$ image as $\tilde{s}(q)$. Figure 3A shows $\tilde{s}(q)$ extracted from the spatially varying conductivity image displayed in Fig. 1B and is seen to have sixfold rotational symmetry. This symmetry is preserved in the $\tilde{s}(q)$ images obtained by transforming data in

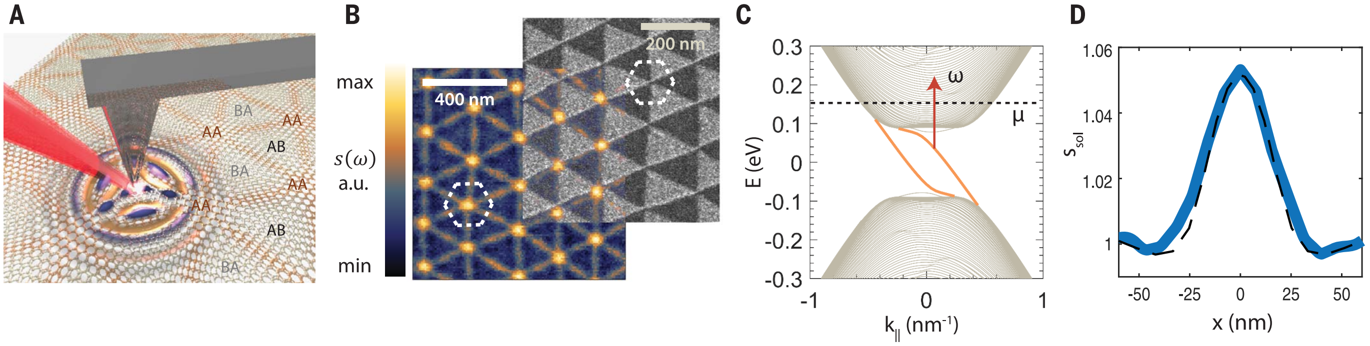

Fig. 1. Nano-light photonic crystal formed by a network of solitons in TBG. (**A**) Schematic of the IR nano-imaging experimental setup. AB, BA, and AA label periodically occurring stacking types of graphene layers. (**B**) (Left) Visualizing the nano-light photonic crystal formed by the soliton lattice. The contrast is due to enhanced local optical conductivity at solitons. (Right) Dark-field TEM image of a TBG sample showing contrast between AB and BA triangular domains. The dashed hexagons represent unit cells of the crystals. a.u., arbitrary units. (**C**) Electronic band structure of a single infinitely long soliton (only the *K* valley is shown). Chiral 1D states are depicted in orange. Optical transitions such as those indicated by the arrow are responsible for the enhanced local conductivity at the location of solitons. E, energy; $k_\parallel$, momentum along the soliton. (**D**) Experimental (solid) and calculated (dashed) near-field signal $s_{sol}(x)$ across a single soliton line. Calculation parameters are frequency $\omega = 1180\ \mathrm{cm}^{-1}$, Fermi energy $\mu = 0.3$ eV, interlayer bias $V_i = 0.2$ V, and dimensionless damping $\eta = 0.2$.

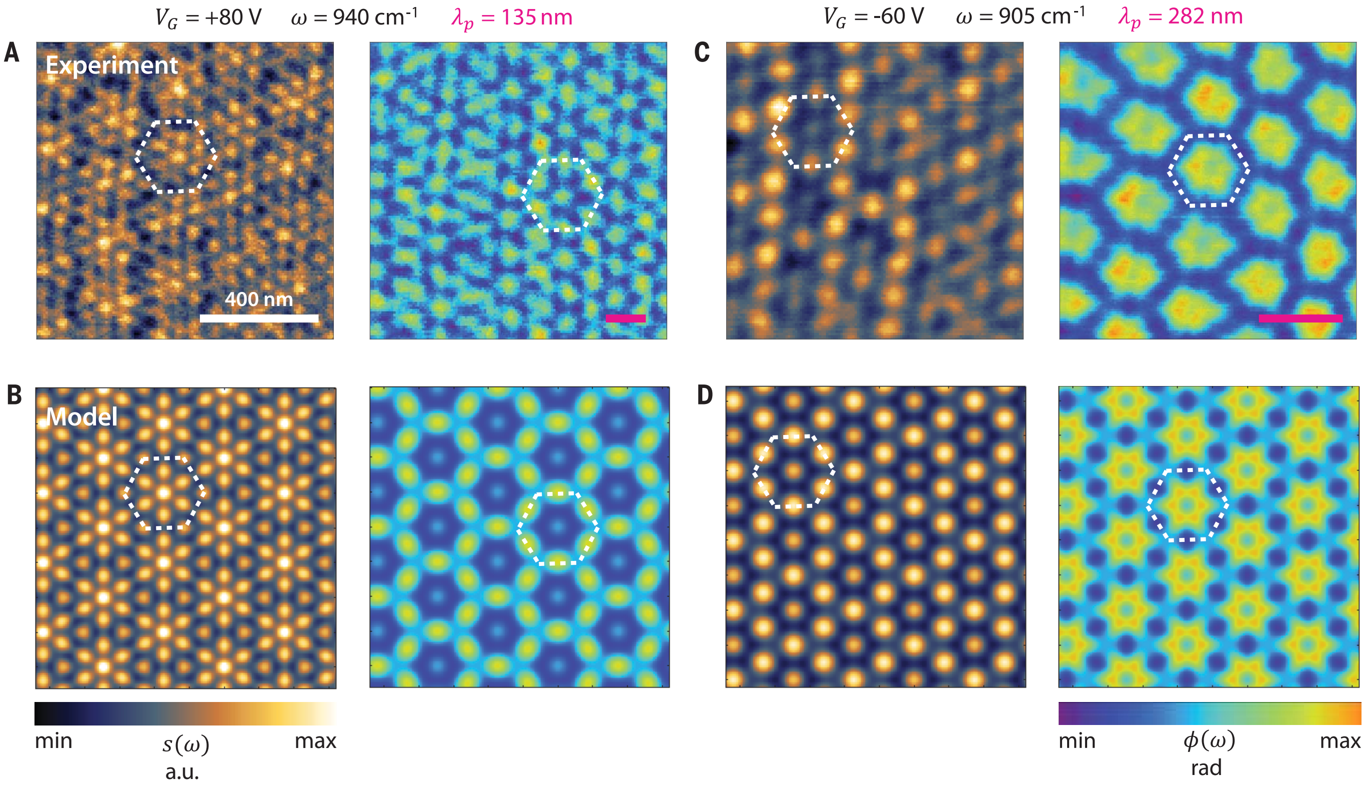

Fig. 2. Plasmon interference patterns and superposition model analysis. (**A** and **C**) Nano-IR images obtained for λ_p = 135 nm and 282 nm. (**B** and **D**) Near-field amplitude and phase images calculated using the superposition model (introduced in the text). The model parameters used to obtain the images are (B) $\mu = 0.23$ eV, $V_i = 0.3$ V, and $\eta = 0.2$ and (D) $\mu = 0.35$ eV, $V_i = 0.1$ V, and $\eta = 0.2$. The dashed hexagons represent the boundaries of a single unit cell, and the magenta bars represent the SPP wavelengths.

Downloaded from http://science.sciencemag.org/ on December 6, 2018

Fig. 2 in the regime where our structures support propagating SPPs. Figure 3B shows the line profiles taken along one of the high-symmetry directions for all $\tilde{s}(q)$ images. The peaks in all the line profiles are anchored at the same momenta in Fourier space, indicating that the periodicity of the polaritonic nano-IR patterns matches that of the moiré lattice. Our nano-IR imaging and its Fourier-transformed patterns thus give further evidence of plasmonic interference in the soliton crystal formed in TBG.

For a quantitative analysis of the SPP interference, we introduce a superposition model. In this simplified model, we neglect multiple scattering of plasmons by these domain walls and disregard any interaction of the domain walls at their intersections. In other words, we treat the domain walls as interpenetrating and decoupled objects. We compute the near-field signal produced by a single (infinitely long) soliton via microscopic calculations of the electron band structure, optical conductivity, and tip-sample coupling (*11*, *33*). The superposition model takes as a basic input the profiles of the near-field amplitude $s_{\text{sol}}(x)$ and phase $\phi_{\text{sol}}(x)$ [Fig. 1D and section S4 of (*26*)] for a single soliton. It is easy to see that the 2D soliton lattice consists of three 1D periodic arrays rotated in-plane by 120° with respect to one another. Consider one such array with solitons located at equidistant positions x_k. Within the superposition model, this array produces the complex near-field signal equal to the sum $\sum_k s_{\text{sol}}(x-x_k)e^{i\phi_{\text{sol}}(x-x_k)}$. Since $s_{\text{sol}}(x)$ is rapidly decreasing away from the solitons, it is sufficient to keep only a few nearest-neighbor terms in this summation. The signal from the remaining 1D arrays is calculated in a similar way. The superposition of all these signals yields the images displayed in Fig. 2, B and D. This procedure yields a close correspondence between the experimental data and the model in both amplitude and phase.

A key feature of moiré photonic crystal is its tunability. The periodicity a of the crystal can be continuously varied by changing the twist angle (*17*), and the SPP-soliton scattering strength can be modulated by the carrier density and the interlayer bias (*11*). To illustrate the tunability, we introduce the dimensionless scattering strength

$$t = \frac{1}{a}\int_{-\infty}^{\infty} dx\,\frac{\sigma_s(x)-\sigma_0}{\sigma_0} \qquad (1)$$

that governs the interaction between the SPPs and the solitons. Here, $\sigma_s(x)$ is the local IR conductivity along the direction perpendicular to the soliton, and σ_0 is the asymptotic value of this conductivity far away from the soliton (*11*, *33*). Parameter t governs the long-range behavior of the SPP waves scattered by a soliton. The details of the short-range behavior (an example of which is shown in Figs. 1D and 2, B and D) depend, in general, on the exact profile $\sigma_s(x)$. However, the plasmon band structure is predominantly sensitive to the long-range processes, so a single parameter t suffices. We now evaluate the plasmonic band structure in momentum space for selected t values by using a reciprocal-space method (*26*, *35*). Figure 3C shows the band structure for parameters that correspond most closely to our current experiment (a = 230 nm, t = 0.02); we notice that the plasmonic gap is insignificant. However, a larger scattering strength that is likely to be attained in future experiments does yield a full bandgap, arresting plasmonic propagation (Fig. 3E). We also note that a point-like source in plain graphene launches an isotropic cylindrical wave (Fig. 3D, left) whose amplitude decays asymptotically as the square root of the distance. Although the decay is expected to be the same for a plasmonic crystal at frequencies within the plasmonic bands, the rotational

Downloaded from http://science.sciencemag.org/ on December 6, 2018

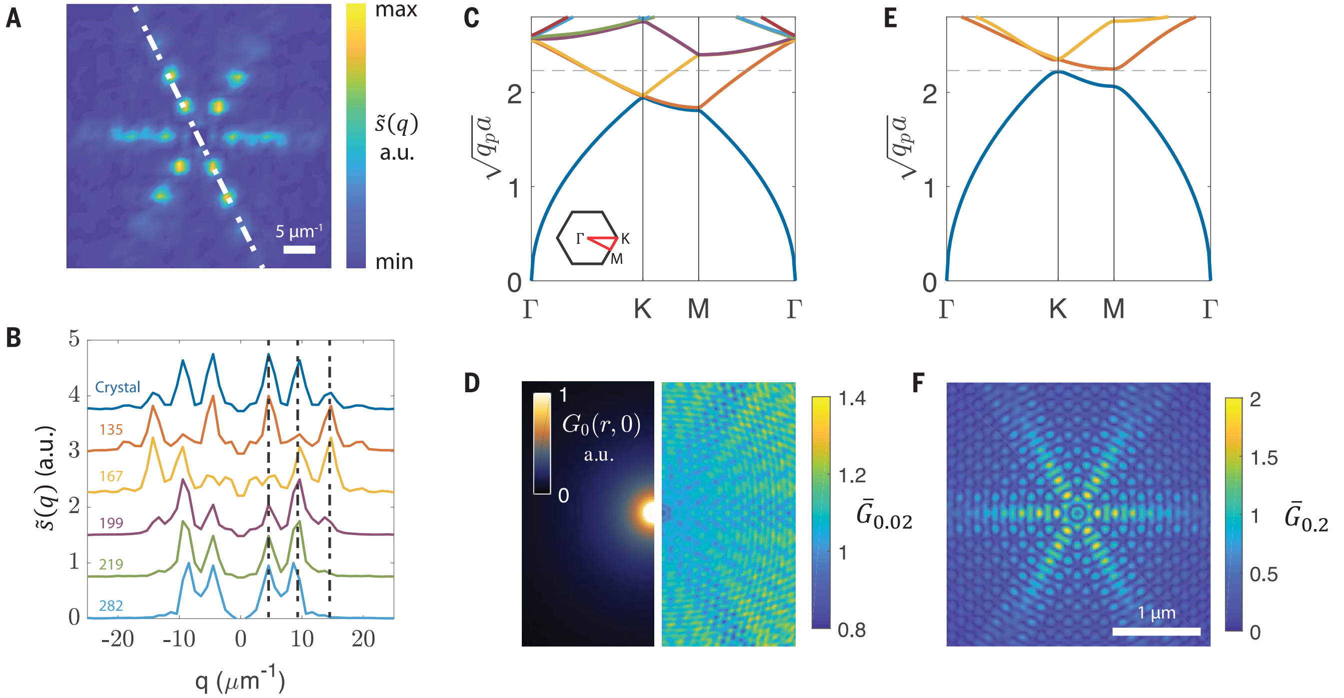

Fig. 3. Properties of the graphene-based quantum photonic crystal. (**A**) Fourier transform $\tilde{s}(q)$ of the photonic crystal image with no propagating SPPs (as in Fig. 1B). (**B**) Line profiles of $\tilde{s}(q)$ taken along the dashed line in (A) for the crystal devoid of propagating SPPs and for the same crystal with propagating SPPs of various wavelengths λ_p. The curves are vertically offset for clarity. (**C**) Plasmonic band structure for dimensionless scattering strength t = 0.02, defined in the text; t = 0.02 most closely corresponds to the experimentally studied crystal. Γ, K, and M are high-symmetry points in the Brillouin zone, as indicated in the inset. (**D**) Near-field signal calculated for a point source at an AA vertex. (Left) G_0, the near-field signal computed for the empty lattice (t = 0). r, spatial coordinate. (Right) The ratio $\bar{G}_{0.02} = G_{0.02}/G_0$, where $G_{0.02}$ is the signal for t = 0.02. (**E**) Plasmonic band structure for t = 0.2 showing the formation of a full plasmonic gap. (**F**) Near-field signal ratio $\bar{G}_{0.2} = G_{0.2}/G_0$, where $G_{0.2}$ is the signal for t = 0.2. The frequency in both (D) and (F) corresponds to the plasmon momentum q_p that satisfies $\sqrt{q_p a} = 2.23$, shown by the dashed lines in (C) and (E). When this frequency is outside (inside) the bandgap, the plasmonic patterns are delocalized (localized) and weakly (strongly) anisotropic; compare (D) [(F)]. See section 7 of (*26*) for details of these calculations.

symmetry of the waves must reduce to comply with the symmetry of the crystal. The reduction to sixfold symmetry for our crystal can be revealed by dividing the signals with and without the crystal pointwise (Fig. 3D, right). By contrast, excitations at frequencies inside the bandgap must be localized, showing exponential decay of the amplitude away from the source. We also predict that the localized states are strongly anisotropic, yielding signal distributions resembling snowflakes (Fig. 3F) or three-pointed stars [Fig. 1A and (*26*)]. To generate patterns of this kind, one can add pointlike plasmonic emitters, such as small gold disks (*36*), to the system.

The nano-light photonic crystal devised, implemented, and investigated in this work is distinct in a number of ways. First, the local variation of the response is rooted in topological electronic phenomena occurring at the solitons, at variance with commonplace classical photonic crystals based on locally perforated media. Second, its key parameters (periodicity and band structure) can be continuously tuned electrostatically and/or nanomechanically (*37*) and do not require challenging top-down fabrication. It would be of interest to explore the regime close to the charge neutrality, where the solitons are predicted to host 1D plasmon modes (*11*, *38*). In this regime, our structure would act as a 2D network or possibly as a controllable circuit capable of routing such 1D plasmons.

REFERENCES AND NOTES

1. J. D. Joannopoulos, S. G. Johnson, J. N. Winn, R. Meade, *Photonic Crystals: Molding the Flow of Light* (Princeton Univ., 2008).
2. L. Lu, J. D. Joannopoulos, M. Soljačić, *Nat. Photonics* **8**, 821–829 (2014).
3. Z. Wang, Y. Chong, J. D. Joannopoulos, M. Soljacić, *Nature* **461**, 772–775 (2009).
4. L. Lu *et al.*, *Science* **349**, 622–624 (2015).
5. D. N. Basov, M. M. Fogler, F. J. García de Abajo, *Science* **354**, aag1992 (2016).
6. Z. Fei *et al.*, *Nature* **487**, 82–85 (2012).
7. J. Chen *et al.*, *Nature* **487**, 77–81 (2012).
8. D. Alcaraz Iranzo *et al.*, *Science* **360**, 291–295 (2018).
9. D. Jin *et al.*, *Phys. Rev. Lett.* **118**, 245301 (2017).
10. M. Jung, Z. Fan, G. Shvets, *Phys. Rev. Lett.* **121**, 086807 (2018).
11. B. Y. Jiang *et al.*, *Nano Lett.* **17**, 7080–7085 (2017).
12. A. Woessner *et al.*, *Nat. Mater.* **14**, 421–425 (2015).
13. G. X. Ni *et al.*, *Nature* **557**, 530–533 (2018).
14. G. X. Ni *et al.*, *Nat. Mater.* **14**, 1217–1222 (2015).
15. G. X. Ni *et al.*, *Nat. Photonics* **10**, 244–247 (2016).
16. C. R. Woods *et al.*, *Nat. Phys.* **10**, 451–456 (2014).
17. H. Yoo *et al.*, arXiv:1804.03806 [cond-mat.mtrl.-sci] (2 October 2018).
18. Z. Fei *et al.*, *Nano Lett.* **15**, 4973–4978 (2015).
19. F. Hu *et al.*, *Phys. Rev. Lett.* **119**, 247402 (2017).
20. S. Huang *et al.*, *Phys. Rev. Lett.* **121**, 037702 (2018).
21. J. S. Alden *et al.*, *Proc. Natl. Acad. Sci. U.S.A.* **110**, 11256–11260 (2013).
22. L. Jiang *et al.*, *Nat. Mater.* **15**, 840–844 (2016).
23. Z. Fei *et al.*, *Nat. Nanotechnol.* **8**, 821–825 (2013).
24. A. Drezet *et al.*, *Nano Lett.* **7**, 1697–1700 (2007).
25. A. M. Lakhani, M. K. Kim, E. K. Lau, M. C. Wu, *Opt. Express* **19**, 18237–18245 (2011).
26. Materials and methods are available as supplementary materials.
27. Z. Fei *et al.*, *Nano Lett.* **11**, 4701–4705 (2011).
28. Y. Zhang *et al.*, *Nature* **459**, 820–823 (2009).
29. F. Zhang, A. H. MacDonald, E. J. Mele, *Proc. Natl. Acad. Sci. U.S.A.* **110**, 10546–10551 (2013).
30. I. Martin, Y. M. Blanter, A. F. Morpurgo, *Phys. Rev. Lett.* **100**, 036804 (2008).
31. Z. Qiao, J. Jung, Q. Niu, A. H. Macdonald, *Nano Lett.* **11**, 3453–3459 (2011).
32. L. Ju *et al.*, *Nature* **520**, 650–655 (2015).
33. B. Y. Jiang *et al.*, *Phys. Rev. Lett.* **117**, 086801 (2016).
34. J. A. Gerber, S. Berweger, B. T. O'Callahan, M. B. Raschke, *Phys. Rev. Lett.* **113**, 055502 (2014).
35. I. Silveiro, A. Manjavacas, S. Thongrattanasiri, F. J. García De Abajo, *New J. Phys.* **15**, 033042 (2013).
36. S. Dai *et al.*, *Nano Lett.* **17**, 5285–5290 (2017).
37. R. Ribeiro-Palau *et al.*, *Science* **361**, 690–693 (2018).
38. E. H. Hasdeo, J. C. W. Song, *Nano Lett.* **17**, 7252–7257 (2017).

ACKNOWLEDGMENTS

Funding: Research on topological properties of moiré superlattices is supported as part of Programmable Quantum Materials, an Energy Frontier Research Center funded by the U.S. Department of Energy (DOE), Office of Science, Basic Energy Sciences (BES), under award DE-SC0019443. Research in topological phenomena in graphene is supported by DOE, BES, under award DE-SC0018426. Work on photonic crystals is supported by ONR-N000014-18-1-2722. Work on self-assembled photonic structures is funded by DARPA EXTREME program award HR001110720034. Development of nano-optics instrumentation is supported by AFOSR: FA9550-15-1-0478 and DOE-BES DE-SC0018218. D.N.B. and P.K. are Gordon and Betty Moore Foundation investigators in the Quantum Materials EPIQS program under GBMF4533 and GBMF4543. P.K. acknowledges support from ARO (W911NF-17-1-0574) and ONR MURI (N00014-15-1-2761). T.S. acknowledges additional funding from the Ministerio de Economia y Competitividad, Spain (FIS2017-82260-P). K.W. and T.T. acknowledge support from the Elemental Strategy Initiative conducted by the MEXT, Japan, and the CREST (JPMJCR15F3), JST. **Author contributions:** All authors were involved in designing the research, performing the research, and writing the paper. **Competing interests:** The authors declare no competing financial interests. **Data and materials availability:** All data are available in the main text or the supplementary materials.

SUPPLEMENTARY MATERIALS

www.sciencemag.org/content/362/6419/1153/suppl/DC1
Materials and Methods
Supplementary Text
Figs. S1 to S9
References (*39*–*46*)

29 July 2018; accepted 29 October 2018
10.1126/science.aau5144

Downloaded from http://science.sciencemag.org/ on December 6, 2018

MICROBIOLOGY

Salmonella persisters undermine host immune defenses during antibiotic treatment

Daphne A. C. Stapels[1]*†, Peter W. S. Hill[1]*, Alexander J. Westermann[2,3], Robert A. Fisher[1], Teresa L. Thurston[1], Antoine-Emmanuel Saliba[3], Isabelle Blommestein[1], Jörg Vogel[2,3], Sophie Helaine[1]‡

Many bacterial infections are hard to treat and tend to relapse, possibly due to the presence of antibiotic-tolerant persisters. In vitro, persister cells appear to be dormant. After uptake of *Salmonella* species by macrophages, nongrowing persisters also occur, but their physiological state is poorly understood. In this work, we show that *Salmonella* persisters arising during macrophage infection maintain a metabolically active state. Persisters reprogram macrophages by means of effectors secreted by the *Salmonella* pathogenicity island 2 type 3 secretion system. These effectors dampened proinflammatory innate immune responses and induced anti-inflammatory macrophage polarization. Such reprogramming allowed nongrowing *Salmonella* cells to survive for extended periods in their host. Persisters undermining host immune defenses might confer an advantage to the pathogen during relapse once antibiotic pressure is relieved.

During growth, genetically clonal bacterial populations contain a small fraction of nongrowing, nondividing cells that arise from transient, reversible, phenotype switching. These growth-arrested cells are usually tolerant to antibiotics and are called antibiotic persisters (*1*). Previously, we showed that a large proportion of the intracellular pathogen *Salmonella enterica* serovar Typhimurium (*Salmonella* Typhimurium) adopts a nongrowing, antibiotic-tolerant state within macrophages (*2*). We also showed that the first *Salmonella* persister cells that regrow upon release from their host cells are those that maintain metabolic activity during infection (*2*). Similar nongrowing but metabolically active bacteria have also been observed in macrophages infected with *Mycobacterium tuberculosis* (*3*). By contrast, when *Salmonella* and other bacterial species are grown in laboratory culture media, persisters are often observed to be inactive (i.e., dormant) (*4*–*6*).

To assess whether retention of transcriptional and translational activity might confer an additional physiological benefit to nongrowing bacteria within a host cell, we infected mouse bone marrow–derived macrophages with wild-type *Salmonella* Typhimurium cells carrying a reporter plasmid that allowed for tracking of bacterial proliferation and activity (*7*) (figs. S1 and S2). Spontaneous regrowth of nongrowing *Salmonella* cells following infection and antibiotic treatment arose exclusively from active rather than inactive bacteria; the latter failed to regrow even after days of incubation (Fig. 1A). In addition, we artificially generated a population of nongrowing and translation-incompetent *Salmonella* cells through exposure to bacteriostatic concentrations of chloramphenicol (fig. S3) and subsequently monitored survival of these dormant bacteria after exposure to the bactericidal antibiotic cefotaxime. Although the inactive *Salmonella* cells withstood exposure to cefotaxime in laboratory medium, they did not survive within macrophages cultured with antibiotics (Fig. 1A).

After entry into macrophages, *Salmonella* Typhimurium induces expression of the *Salmonella* pathogenicity island 2 (SPI-2) type 3 secretion system (T3SS), through which it translocates ~30 effectors that inhibit host cell processes that are detrimental to the pathogen (*8*, *9*). We hypothesized that as well as maintaining transcriptional and translational activity, persisters also translocate SPI-2 effectors. We used the SPI-2 *ssaG* promoter fused to unstable enhanced green fluorescent protein (eGFP) (*10*) to test for SPI-2 gene expression in single cells. *ssaG* promoter expression was observed in nongrowing bacteria that retained transcriptional and translational activity (Fig. 1B). Furthermore, *Salmonella* effector proteins were detected in the host cell cytosol via Western blotting of macrophages containing pure populations of growing or persister cells (Fig. 1C and fig. S4).

To understand how persisters shape their host environment, we used dual RNA sequencing (RNA-seq) (*11*) on infected macrophage subpopulations to analyze host and pathogen transcriptomes simultaneously (*12*) (fig. S5). The majority of dual RNA-seq reads from infected macrophages aligned to the host genome, with relative amounts of bacterial reads being proportional to the average number of bacteria present per cell (fig. S5D and table S1).

Principal component analysis (fig. S6A) and clustering analysis (Fig. 2A and table S2) on the transcriptome profiles of all macrophage populations confirmed the expected general differences between challenged and naïve macrophages (Fig. 2A, clusters I and II, and fig. S6A). Among challenged macrophages, the greatest differences occurred between macrophages containing viable bacteria (growing or nongrowing) and macrophages that had killed the bacteria they had engulfed [host killed (HK)] or bystander macrophages. Clustering analysis pinpointed two large groups of genes (Fig. 2A, clusters III and IV) responsible for this separation (Fig. 2B). Of these, members of cluster III were enriched with genes involved in classical, proinflammatory macrophage activation (i.e., M1), and cluster IV was enriched with genes associated with alternative, anti-inflammatory (i.e., M2) macrophage activation. Inspection of the dual RNA-seq data for five representative M1 activation markers (*Nfkb2*, *Cd40*, *Il1b*, *Nlrp3*, and *Tnf*) (fig. S6B, left panel) confirmed that their up-regulation during infection was dampened in macrophages containing viable bacteria. In contrast, five M2 activation markers (*Il4ra*, *Arg1*, *Odc1*, *Ppard*, and *Timp1*) (fig. S6B, right panel) were up-regulated in macrophages containing viable bacteria. There was a significant overlap of these gene clusters with our previously defined M1 gene set ($P = 5.2 \times 10^{-19}$, hypergeometric test) and M2 gene set ($P = 1.2 \times 10^{-38}$, hypergeometric test) (Fig. 2C), deduced from single-cell RNA-seq data (*13*). As clusters III and IV contain considerably more genes, we consider them more complete M1 and M2 polarization gene sets.

Principal component analysis (fig. S6A) and clustering analysis of bacterial genes in the dual RNA-seq dataset (fig. S6C and table S3) showed expected differences, such as expression of flagellar genes in the inoculum. By comparison, intracellular bacteria showed elevated expression of infection-associated genes (*14*). Notably, the transcriptomes of intracellularly growing and nongrowing bacteria were similar (fig. S6, A and C), and both expressed genes encoding the SPI-2 T3SS apparatus and its translocated effectors (fig. S6D).

We performed interspecies expression correlation analysis on the dual RNA-seq data to reveal the host consequences of bacterial SPI-2 T3SS expression. Of the 4817 defined murine gene sets tested, SPI-2 T3SS gene expression showed the strongest positive correlation with M2 anti-inflammatory cluster IV genes and the strongest negative correlation with M1 proinflammatory cluster III genes (Fig. 2, D and E, and table S4). Of the *Salmonella* regulons, only PhoP/Q and SPI-2 T3SS showed this (anti-)correlation pattern with the M1 and M2 host gene sets (table S5 and fig. S6, F and G). Because PhoP/Q is required for SPI-2 T3SS activation (*15*), the data suggest

---

[1]MRC Centre for Molecular Bacteriology and Infection, Imperial College London, London, UK. [2]Institute of Molecular Infection Biology, University of Würzburg, Würzburg, Germany. [3]Helmholtz Institute for RNA-based Infection Research, Würzburg, Germany.
*These authors contributed equally to this work. †Present address: Department of Medical Microbiology, University Medical Center Utrecht, Utrecht, Netherlands.
‡Corresponding author. Email: s.helaine@imperial.ac.uk

Downloaded from http://science.sciencemag.org/ on December 6, 2018

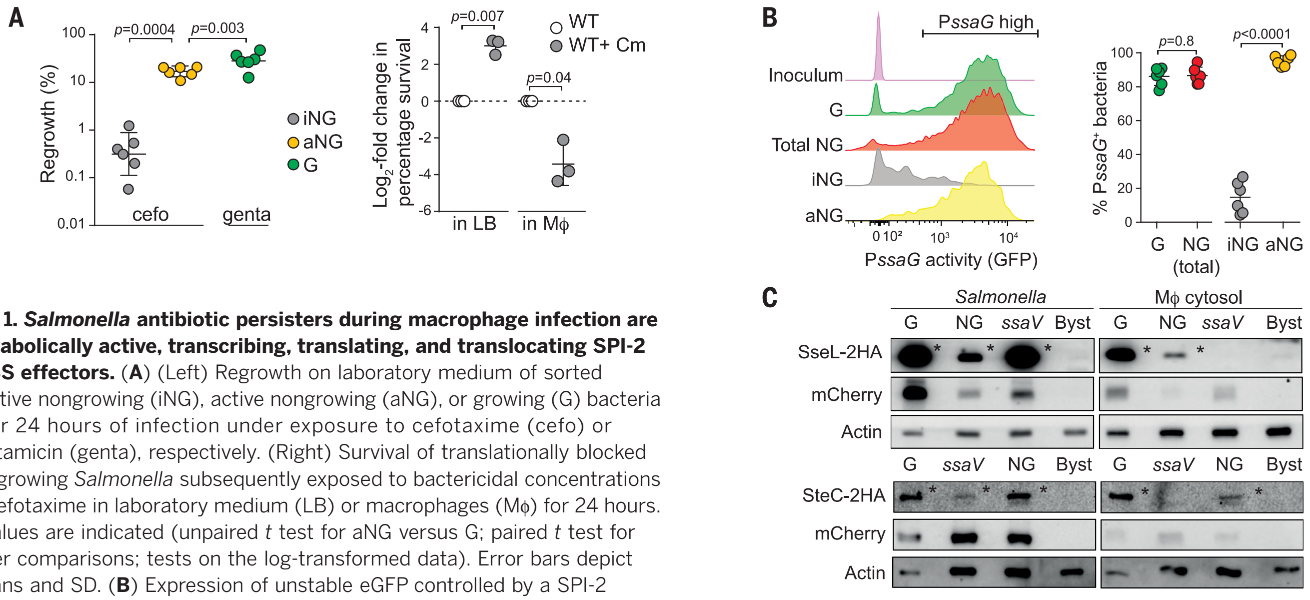

Fig. 1. *Salmonella* antibiotic persisters during macrophage infection are metabolically active, transcribing, translating, and translocating SPI-2 T3SS effectors. (**A**) (Left) Regrowth on laboratory medium of sorted inactive nongrowing (iNG), active nongrowing (aNG), or growing (G) bacteria after 24 hours of infection under exposure to cefotaxime (cefo) or gentamicin (genta), respectively. (Right) Survival of translationally blocked nongrowing *Salmonella* subsequently exposed to bactericidal concentrations of cefotaxime in laboratory medium (LB) or macrophages (Mϕ) for 24 hours. *P* values are indicated (unpaired *t* test for aNG versus G; paired *t* test for other comparisons; tests on the log-transformed data). Error bars depict means and SD. (**B**) Expression of unstable eGFP controlled by a SPI-2 promoter (*PssaG*) in intracellular bacteria at 24 hours postuptake depends on the growth and activity status. A representative histogram is shown on the left, and quantification of results from six independent repeats is shown on the right. *P* values are indicated (paired *t* test); error bars depict means and SD. (**C**) Translocation of hemagglutinin (HA)–tagged SPI-2 T3SS effectors detected in the bacterial pellet or host cell cytosol after lysis of bystander (Byst) Mϕ or Mϕ containing growing (G) or nongrowing (NG) *Salmonella* Typhimurium or a secretion-deficient (*ssaV*) mutant 20 hours after uptake. *, detected effector.

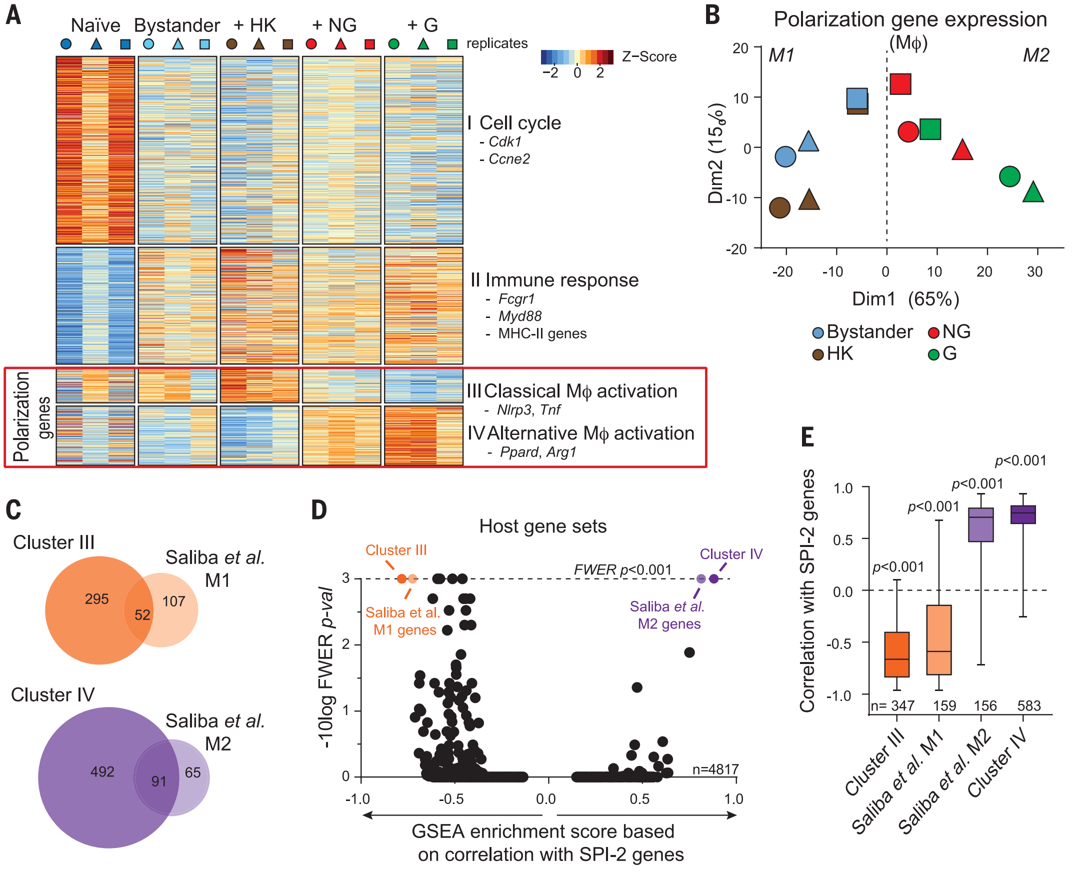

Fig. 2. Dual RNA-seq implicates SPI-2 in dampening M1 and promoting M2 macrophage polarization. (**A**) Clustering analysis of host genes differentially expressed between any two subpopulations, with selected enriched terms. Analyzed subpopulations of Mϕ were naïve, bystander, or contained host-killed (HK), nongrowing (NG), or growing (G) bacteria. (**B**) Principal components analysis of Mϕ transcriptomes based on M1 (cluster III in panel A) and M2 (cluster IV in panel A) polarization genes. The subsets of Mϕ are color coded, and the three biological repeats are indicated with different symbols. (**C**) Venn diagram showing the overlap between M1 (top) and M2 (bottom) polarization genes identified in (*13*) and extended M1 and M2 genes identified here (clusters III and IV). Numbers of genes within each gene set are indicated. (**D**) Interspecies correlation analysis between SPI-2 apparatus and effector gene expression patterns in *Salmonella* and gene expression patterns of defined host gene sets in infected dual RNA-seq samples. Plot of the gene set enrichment analysis (GSEA) score (x axis) and $-\log_{10}$ family-wise error rate (FWER)–adjusted P value (y axis), based on correlations between z-score–normalized host gene expression and average z-score–normalized SPI-2 apparatus and effector expression for all 4817 tested murine gene sets. (**E**) Boxplots with boxes (the median upper and lower quartiles) and whiskers (the lowest and highest values) depicting the distribution of correlations of interesting gene sets with SPI-2 genes (FWER-adjusted P values are indicated).

Downloaded from http://science.sciencemag.org/ on December 6, 2018

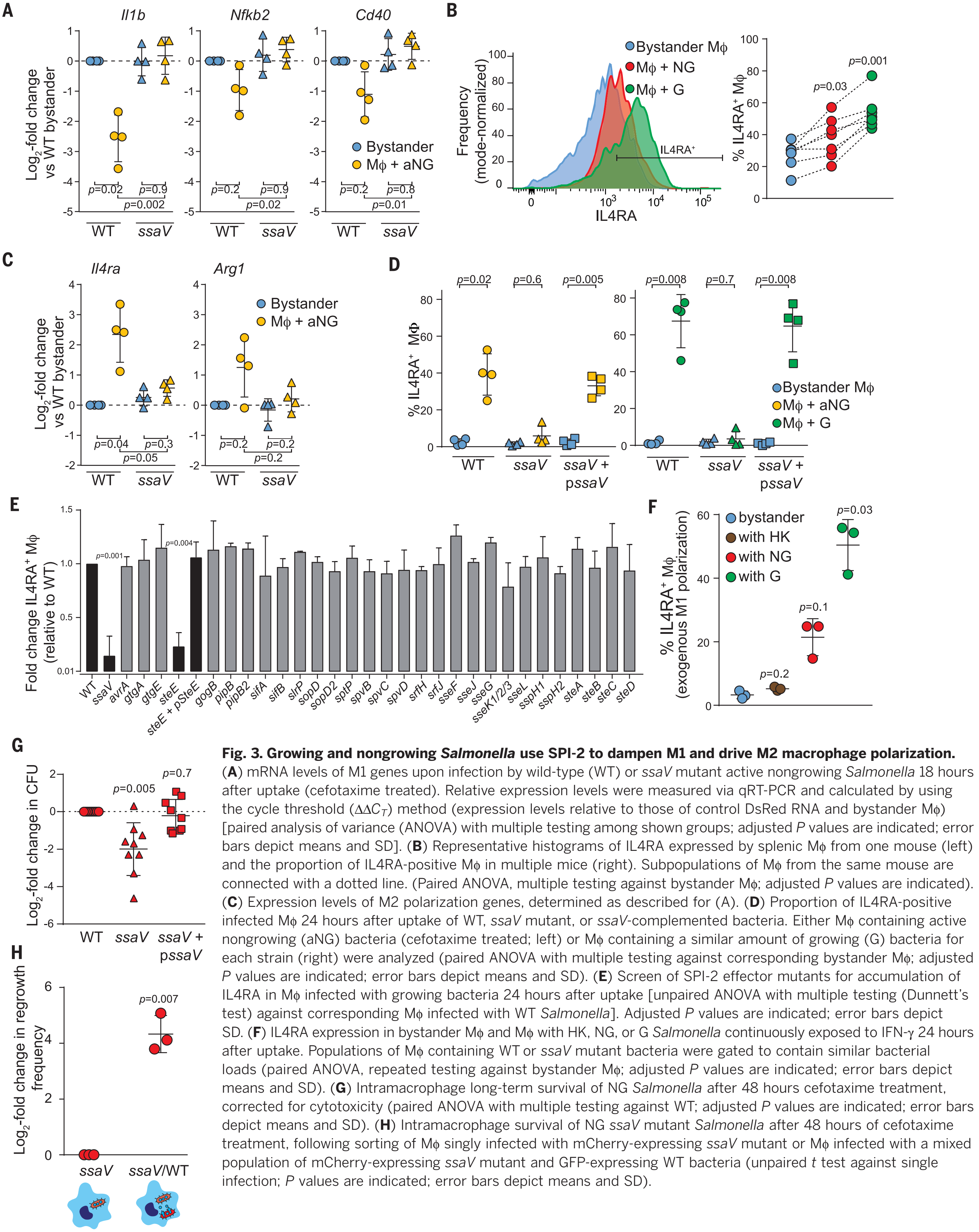

Fig. 3. Growing and nongrowing *Salmonella* use SPI-2 to dampen M1 and drive M2 macrophage polarization. (**A**) mRNA levels of M1 genes upon infection by wild-type (WT) or *ssaV* mutant active nongrowing *Salmonella* 18 hours after uptake (cefotaxime treated). Relative expression levels were measured via qRT-PCR and calculated by using the cycle threshold ($\Delta\Delta C_T$) method (expression levels relative to those of control DsRed RNA and bystander Mϕ) [paired analysis of variance (ANOVA) with multiple testing among shown groups; adjusted *P* values are indicated; error bars depict means and SD]. (**B**) Representative histograms of IL4RA expressed by splenic Mϕ from one mouse (left) and the proportion of IL4RA-positive Mϕ in multiple mice (right). Subpopulations of Mϕ from the same mouse are connected with a dotted line. (Paired ANOVA, multiple testing against bystander Mϕ; adjusted *P* values are indicated). (**C**) Expression levels of M2 polarization genes, determined as described for (A). (**D**) Proportion of IL4RA-positive infected Mϕ 24 hours after uptake of WT, *ssaV* mutant, or *ssaV*-complemented bacteria. Either Mϕ containing active nongrowing (aNG) bacteria (cefotaxime treated; left) or Mϕ containing a similar amount of growing (G) bacteria for each strain (right) were analyzed (paired ANOVA with multiple testing against corresponding bystander Mϕ; adjusted *P* values are indicated; error bars depict means and SD). (**E**) Screen of SPI-2 effector mutants for accumulation of IL4RA in Mϕ infected with growing bacteria 24 hours after uptake [unpaired ANOVA with multiple testing (Dunnett's test) against corresponding Mϕ infected with WT *Salmonella*]. Adjusted *P* values are indicated; error bars depict SD. (**F**) IL4RA expression in bystander Mϕ and Mϕ with HK, NG, or G *Salmonella* continuously exposed to IFN-γ 24 hours after uptake. Populations of Mϕ containing WT or *ssaV* mutant bacteria were gated to contain similar bacterial loads (paired ANOVA, repeated testing against bystander Mϕ; adjusted *P* values are indicated; error bars depict means and SD). (**G**) Intramacrophage long-term survival of NG *Salmonella* after 48 hours cefotaxime treatment, corrected for cytotoxicity (paired ANOVA with multiple testing against WT; adjusted *P* values are indicated; error bars depict means and SD). (**H**) Intramacrophage survival of NG *ssaV* mutant *Salmonella* after 48 hours of cefotaxime treatment, following sorting of Mϕ singly infected with mCherry-expressing *ssaV* mutant or Mϕ infected with a mixed population of mCherry-expressing *ssaV* mutant and GFP-expressing WT bacteria (unpaired *t* test against single infection; *P* values are indicated; error bars depict means and SD).

Downloaded from http://science.sciencemag.org/ on December 6, 2018

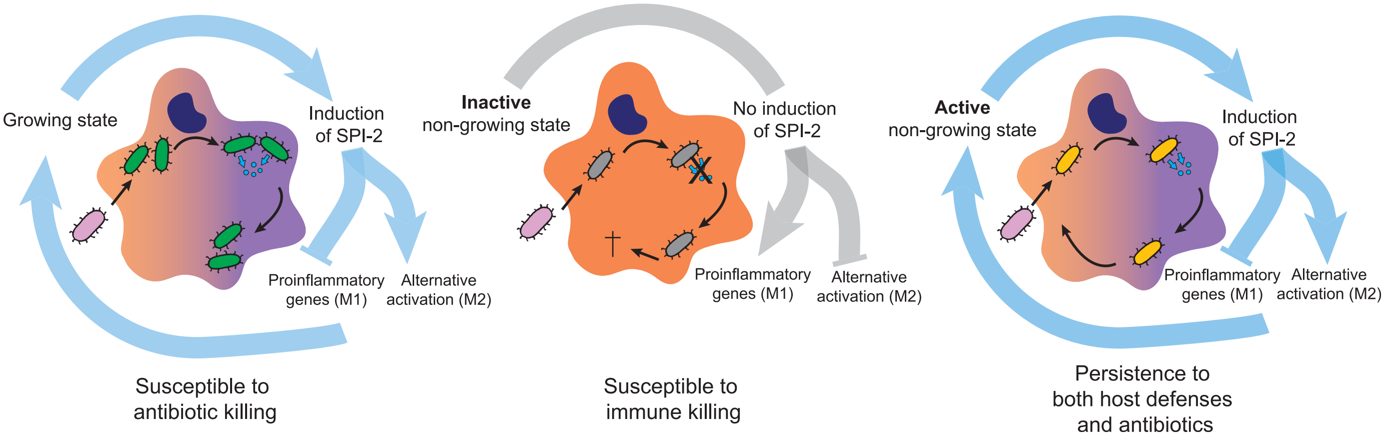

Fig. 4. Persisters undermine the host innate immune response and enable long-term survival. Model of macrophage manipulation by *Salmonella* persisters. Growing *Salmonella* bacteria translocate SPI-2 effectors that manipulate host cell polarization and create a less hostile environment. Proliferation makes the bacteria susceptible to antibiotic killing (left). Inactive nongrowing *Salmonella* cannot translocate SPI-2 effectors and are killed in the strongly antimicrobial environment (middle). Active persisters manipulate host cell polarization through translocation of SPI-2 effectors, and in turn they retain their activity and maintain the ability to survive in the host while being antibiotic tolerant (right).

that SPI-2 T3SS effectors modulate M1 and M2 polarization.

Macrophages containing active nongrowing *Salmonella* displayed an intermediate expression profile between the M1 and M2 phenotypes (Fig. 2B). Previous single-cell RNA-seq data led us to conclude that nongrowing bacteria inhabit M1-like cells whereas growing *Salmonella* associate with M2-like macrophages (*13*). Reanalysis of our previous single-cell RNA-seq data (*13*) with the extended M1 and M2 gene sets showed there was a bimodality of M1 and M2 gene expression in macrophages containing nongrowing bacteria (fig. S7A). By contrast, bystander macrophages had an M1 bias, and those containing growing bacteria had a clear M2 bias (fig. S7a). The levels of the macrophage surface M2 marker IL4RA (the alpha-subunit of the interleukin-4 receptor) were significantly increased in macrophages containing nongrowing active *Salmonella* compared with macrophages containing nongrowing inactive or host-killed bacteria (fig. S7B). Therefore, the intermediate population-level M1 and M2 expression profile of the host cell probably reflects an underlying heterogeneity of transcriptional and translational activity and also SPI-2 expression in nongrowing intramacrophage *Salmonella* (Fig. 1) (*2*).

The correlation between SPI-2 effector expression and macrophage polarization could be explained by the presence of subsets of macrophages prior to infection with depressed inflammatory responses and/or increased permissiveness. Alternatively, this could be a direct result of activity of SPI-2 effectors, some of which are known to downregulate proinflammatory responses, such as NF-κB activation (*9*). Consistent with the latter, when we compared the levels of three mRNAs for established M1 markers (*Cd40*, *Il1b*, and *Nfkb2)* between macrophages containing active nongrowing wild-type or SPI-2–null (*ssaV* mutant) bacteria via reverse transcription quantitative polymerase chain reaction (RT-qPCR), wild-type *Salmonella* was associated with down-regulated expression of the three markers during exposure to antibiotics, whereas cells infected with the SPI-2–null mutant bacteria were not (Fig. 3A). Therefore, active nongrowing bacteria use SPI-2 T3SS effectors to counteract macrophage M1 activation (*9*) and are able to do so despite sustained exposure to the proinflammatory interferon gamma (IFN-γ) cytokine (fig. S8, A and B).

In addition, analysis of the dual RNA-seq data and our previous single-cell RNA-seq data (*13*) suggested that *Salmonella* Typhimurium actively promotes macrophage M2 polarization. In a murine model of long-term infection, *Salmonella* Typhimurium resided in M2 macrophages (*16*) rather than in proinflammatory M1 macrophages (*17–19*), suggesting that the conditions within M2 macrophages enable prolonged bacterial survival. Consistent with this conclusion, in a mouse model of acute systemic infection (fig. S8C) the M2 marker IL4RA was highly expressed by splenic macrophages isolated 3 days after intraperitoneal *Salmonella* Typhimurium injection, with the majority of the growing bacteria inside the macrophages showing high IL4RA expression (Fig. 3B). There was greater heterogeneity in IL4RA expression within the macrophage population containing nongrowing bacteria (Fig. 3B). Despite exposure to antibiotics, active nongrowing wild-type *Salmonella* cells, but not SPI-2–null mutant cells, showed up-regulated expression of the two M2 markers tested in macrophages (Fig. 3C).

Further investigation revealed that during infection with a SPI-2–null strain, accumulation of IL4RA was abrogated in all macrophages infected with viable bacteria regardless of the bacterial growth state (Fig. 3D and fig. S8D) (*20*). The M2-like polarization profile induced by *Salmonella* was recapitulated best by exposure to both IL-4 and IL-10 (fig. S9). Screening a collection of all SPI-2 effector mutants revealed that M2-like polarization is driven solely by the SteE (also known as SarA) effector (Fig. 3F and fig. S8F); a recent report showed that SteE promotes secretion of IL-10 from infected B cells (*21*). Although an *steE* mutant no longer triggered M2-like polarization of host cells, the mutant still dampened the M1 response (figs. S8, E and F, and S10), suggesting that M1 suppression and M2 polarization are independent of each other. Nongrowing intracellular *Salmonella* can thus express and translocate sufficient quantities of effectors to cause major changes in the immune status of the infected host cell, even during exposure to antibiotics and IFN-γ.

Finally, after 48 hours of antibiotic exposure within macrophages, nongrowing mutant bacteria lacking a functional SPI-2 apparatus showed significantly reduced survival compared with their wild-type counterparts (Fig. 3G). However, in mixed strain infections we found that wild-type persisters rescued survival of SPI-2–null persisters in coinfected cells (Fig. 3H), illustrating that the decreased survival of SPI-2–null persisters was exclusively a consequence of a failure to manipulate the intracellular host environment in which they resided.

Collectively, our data show that after infection of macrophages, maintenance of transcriptional and translational activity enables nongrowing *Salmonella* Typhimurium to translocate SPI-2 T3SS effectors into the host cell. Thus, unlike bacterial persisters in laboratory medium, which apparently become dormant (*2*, *4–6*), intracellular *Salmonella* cells maintain effector delivery but cease to grow. This strategy enables a subpopulation of intracellular bacteria to survive antibiotic exposure and reprogram their macrophage host cell to promote long-term bacterial survival (Fig. 4). Reprogramming of the host cell by *Salmonella* not only suppresses M1 bactericidal responses (*9*) but also increases permissiveness of the now–M2-biased cells for the pathogen, potentially by modulating host cell metabolism (*17*, *22*). We showed that the capacity of *Salmonella* to direct macrophage M2 polarization is driven by the SPI-2 T3SS effector SteE.

Downloaded from http://science.sciencemag.org/ on December 6, 2018

Similarly, *M. tuberculosis* infections have been accompanied by an expansion of a population of permissive macrophages (*23*–*27*), raising the possibility that mycobacteria and other intracellular pathogens employ similar mechanisms for modulating host cell polarization. Pathogen manipulation of host cells is accompanied by changes in the repertoire of secreted cytokines (*21*). Rather than being dormant, nongrowing persister cells of an intracellular bacterial pathogen are able to subvert host immune defenses, even under antibiotic treatment, potentially making the host environment more permissive for recrudescent infection.

REFERENCES AND NOTES

1. R. A. Fisher, B. Gollan, S. Helaine, *Nat. Rev. Microbiol.* **15**, 453–464 (2017).
2. S. Helaine *et al.*, *Science* **343**, 204–208 (2014).
3. G. Manina, N. Dhar, J. D. McKinney, *Cell Host Microbe* **17**, 32–46 (2015).
4. E. Maisonneuve, K. Gerdes, *Cell* **157**, 539–548 (2014).
5. Y. Shan *et al.*, *mBio* **8**, e02267-16 (2017).
6. B. P. Conlon *et al.*, *Nat. Microbiol.* **1**, 16051 (2016).
7. S. Helaine *et al.*, *Proc. Natl. Acad. Sci. U.S.A.* **107**, 3746–3751 (2010).
8. K. McGourty *et al.*, *Science* **338**, 963–967 (2012).
9. E. Jennings, T. L. M. Thurston, D. W. Holden, *Cell Host Microbe* **22**, 217–231 (2017).
10. J. A. Ibarra *et al.*, *Microbiology* **156**, 1120–1133 (2010).
11. A. J. Westermann *et al.*, *Nature* **529**, 496–501 (2016).
12. A. J. Westermann, L. Barquist, J. Vogel, *PLOS Pathog.* **13**, e1006033 (2017).
13. A.-E. Saliba *et al.*, *Nat. Microbiol.* **2**, 16206 (2016).
14. S. Eriksson, S. Lucchini, A. Thompson, M. Rhen, J. C. D. Hinton, *Mol. Microbiol.* **47**, 103–118 (2003).
15. E. Fass, E. A. Groisman, *Curr. Opin. Microbiol.* **12**, 199–204 (2009).
16. P. J. Murray *et al.*, *Immunity* **41**, 14–20 (2014).
17. N. A. Eisele *et al.*, *Cell Host Microbe* **14**, 171–182 (2013).
18. M. W. McCoy, S. M. Moreland, C. S. Detweiler, *Infect. Immun.* **80**, 3642–3649 (2012).
19. R. N. Nix, S. E. Altschuler, P. M. Henson, C. S. Detweiler, *PLOS Pathog.* **3**, e193 (2007).
20. R. Figueira, K. G. Watson, D. W. Holden, S. Helaine, *mBio* **4**, e00065-13 (2013).
21. S. L. Jaslow *et al.*, *Cell Reports* **23**, 3525–3536 (2018).
22. J. Van den Bossche, L. A. O'Neill, D. Menon, *Trends Immunol.* **38**, 395–406 (2017).
23. D. M. Hardbower *et al.*, *Proc. Natl. Acad. Sci. U.S.A.* **114**, E751–E760 (2017).
24. F. O'Rourke *et al.*, *Cell. Microbiol.* **17**, 1447–1463 (2015).
25. K. A. Shirey, L. E. Cole, A. D. Keegan, S. N. Vogel, *J. Immunol.* **181**, 4159–4167 (2008).
26. M. Benoit, B. Barbarat, A. Bernard, D. Olive, J. L. Mege, *Eur. J. Immunol.* **38**, 1065–1070 (2008).
27. L. Huang, E. V. Nazarova, S. Tan, Y. Liu, D. G. Russell, *J. Exp. Med.* **215**, 1135–1152 (2018).

ACKNOWLEDGMENTS

We thank members from the Holden and Helaine labs for sharing constructs and protocols and scientific discussions; I. Glegola-Madejska for help with the animal experiments; and D. Holden for careful reading of the manuscript. **Funding:** This research was supported by an MRC Career Development Award (MR/M009629/1) from the Medical Research Council (UK) and Lister Institute Research Prize 2017 to S.H., an EMBO long-term fellowship (ALTF 441-2015) to D.A.C.S., and an Elite Advancement Ph.D. stipend from the Universität Bayern e.V., Germany, to A.J.W. **Author contributions:** S.H. and J.V. outlined the study; D.A.C.S., P.W.S.H., A.J.W., R.F., I.B., and S.H. performed experiments; P.W.S.H. conducted the bioinformatic analysis; D.A.C.S., P.W.S.H., A.J.W., R.F., I.B., A.-E.S., and T.L.T. analyzed the data; D.A.C.S., P.W.S.H., A.J.W., and S.H. interpreted data; and D.A.C.S., P.W.S.H., and S.H. wrote the manuscript with contributions of other authors. **Competing interests:** We declare no competing interests. **Data and materials availability:** The dual RNA-seq data are summarized in table S1; results of analyses are in tables S2 to S5, S8, and S9; and the data are archived on GEO (accession: GSE104785).

SUPPLEMENTARY MATERIALS

www.sciencemag.org/content/362/6419/1156/suppl/DC1
Materials and Methods
Figs. S1 to S10
Tables S1 to S9
References (*28*–*32*)

28 March 2018; resubmitted 25 July 2018
Accepted 31 October 2018
10.1126/science.aat7148

Downloaded from http://science.sciencemag.org/ on December 6, 2018

HUMAN GENETICS

Quantifying the contribution of recessive coding variation to developmental disorders

Hilary C. Martin[1]*, Wendy D. Jones[1,2], Rebecca McIntyre[1], Gabriela Sanchez-Andrade[1], Mark Sanderson[1], James D. Stephenson[1,3], Carla P. Jones[1], Juliet Handsaker[1], Giuseppe Gallone[1], Michaela Bruntraeger[1], Jeremy F. McRae[1], Elena Prigmore[1], Patrick Short[1], Mari Niemi[1], Joanna Kaplanis[1], Elizabeth J. Radford[1,4], Nadia Akawi[5], Meena Balasubramanian[6], John Dean[7], Rachel Horton[8], Alice Hulbert[9], Diana S. Johnson[6], Katie Johnson[10], Dhavendra Kumar[11], Sally Ann Lynch[12], Sarju G. Mehta[13], Jenny Morton[14], Michael J. Parker[15], Miranda Splitt[16], Peter D. Turnpenny[17], Pradeep C. Vasudevan[18], Michael Wright[16], Andrew Bassett[1], Sebastian S. Gerety[1], Caroline F. Wright[19], David R. FitzPatrick[20], Helen V. Firth[1,13], Matthew E. Hurles[1], Jeffrey C. Barrett[1]*, on behalf of the Deciphering Developmental Disorders Study

We estimated the genome-wide contribution of recessive coding variation in 6040 families from the Deciphering Developmental Disorders study. The proportion of cases attributable to recessive coding variants was 3.6% in patients of European ancestry, compared with 50% explained by de novo coding mutations. It was higher (31%) in patients with Pakistani ancestry, owing to elevated autozygosity. Half of this recessive burden is attributable to known genes. We identified two genes not previously associated with recessive developmental disorders, *KDM5B* and *EIF3F*, and functionally validated them with mouse and cellular models. Our results suggest that recessive coding variants account for a small fraction of currently undiagnosed nonconsanguineous individuals, and that the role of noncoding variants, incomplete penetrance, and polygenic mechanisms need further exploration.

Large-scale sequencing studies of phenotypically heterogeneous rare-disease patients can discover new disease genes (*1*–*3*) and characterize the genetic architecture of such disorders. In the Deciphering Developmental Disorders (DDD) study, we previously estimated the fraction of patients with a causal de novo coding mutation in both known and as-yet-undiscovered disease genes to be 40 to 45% (*4*), and in this work we extended this approach to recessive variants. It has been posited that there are thousands of as-yet-undiscovered recessive intellectual disability (ID) genes (*5*, *6*), which could imply that recessive variants explain a large fraction of undiagnosed rare disease cases. However, attempts to estimate the prevalence of recessive disorders have been restricted to known disorders (*7*) or known pathogenic alleles (*8*). We quantified the total autosomal recessive coding burden using a robust and unbiased statistical framework in 6040 exome-sequenced DDD trios from the British Isles. Our approach provides a better-calibrated estimate of the exome-wide burden of recessive disease than those of previously published methods (*3*, *9*).

We analyzed 5684 European and 356 Pakistani probands (EABI, European ancestry from the British Isles; PABI, Pakistani ancestry from the British Isles) (figs. S1 and S2) with developmental disorders (DDs). The clinical features are heterogeneous and representative of genetically undiagnosed DD patients from British and Irish clinical genetics services: 88% have an abnormality of the nervous system, and 88% have multiple affected organ systems (Fig. 1, fig. S3, and table S1). Clinical features are largely similar between EABI and PABI (Fig. 1 and table S1).

To assess the genome-wide recessive burden, we compared the number of rare [minor allele frequency (MAF) <1%] biallelic genotypes observed in our cohort to the number expected by chance (*10*). We used the phased haplotypes from unaffected DDD parents to estimate the expected number of biallelic genotypes. Reassuringly, the number of observed biallelic synonymous genotypes matched the expectation (fig. S4). We observed no significant burden of biallelic genotypes of any consequence class in 1389 probands with a likely diagnostic de novo, inherited dominant, or X-linked variant. We therefore evaluated the recessive coding burden in the remaining 4318 EABI and 333 PABI probands. This "undiagnosed" cohort were more likely to have a recessive cause because they did not have a likely dominant or X-linked diagnosis (*11*), had at least one affected sibling, or >2% autozygosity (Fig. 2A).

As expected because of their higher autozygosity (fig. S5), PABI individuals had more rare biallelic genotypes than those of EABI individuals (Fig. 2A); 92% of these were homozygous (rather than compound heterozygous), versus only 28% for the EABI samples. We observed a significant enrichment of biallelic loss-of-function (LOF) genotypes in both undiagnosed ancestry groups (Poisson $P = 3.5 \times 10^{-5}$ in EABI, $P = 9.7 \times 10^{-7}$ in PABI) and, in the EABI group, a nominally significant enrichment of biallelic damaging missense genotypes ($P = 0.025$) and a significant enrichment of compound heterozygous LOF/damaging missense genotypes ($P = 6 \times 10^{-7}$) (Fig. 2A).

Among the 4651 EABI+PABI undiagnosed probands, a set of 903 clinically curated DD-associated recessive genes showed a higher recessive burden (1.7-fold; Poisson $P = 6 \times 10^{-18}$) (fig. S6) than average (1.1-fold for all genes). Indeed, 48% of the observed excess of biallelic genotypes lay in these known genes. By contrast, we did not observe any recessive burden in 243 DD-associated genes with a dominant LOF mechanism, nor in any gene sets tested in the 1389 diagnosed probands (Poisson $P > 0.05$).

We developed a method to estimate the proportion of probands with a causal variant in a particular genotype class (*10*) in either known and as-yet-undiscovered genes. Unlike our previously published approach (*4*), this method accounts for the fact that some fraction of the variants expected by chance are actually causal

Downloaded from http://science.sciencemag.org/ on December 10, 2018

---

[1]Wellcome Trust Sanger Institute, Wellcome Trust Genome Campus, Hinxton, UK. [2]Great Ormond Street Hospital for Children, National Health Service (NHS) Foundation Trust, Great Ormond Street Hospital, Great Ormond Street, London WC1N 3JH, UK. [3]European Molecular Biology Laboratory–European Bioinformatics Institute, Wellcome Trust Genome Campus, Hinxton, Cambridgeshire CB10 1SD, UK. [4]Department of Paediatrics, Cambridge University Hospitals NHS Foundation Trust, Cambridge, UK. [5]Division of Cardiovascular Medicine, Radcliffe Department of Medicine, University of Oxford, Oxford, UK. [6]Sheffield Clinical Genetics Service, Sheffield Children's NHS Foundation Trust, OPD2, Northern General Hospital, Herries Rd., Sheffield, S5 7AU, UK. [7]Department of Genetics, Aberdeen Royal Infirmary, Aberdeen, UK. [8]Wessex Clinical Genetics Service, G Level, Princess Anne Hospital, Coxford Road, Southampton SO16 5YA, UK. [9]Cheshire and Merseyside Clinical Genetic Service, Liverpool Women's NHS Foundation Trust, Crown Street, Liverpool L8 7SS, UK. [10]Department of Clinical Genetics, City Hospital Campus, Hucknall Road, Nottingham NG5 1PB, UK. [11]Institute of Cancer and Genetics, University Hospital of Wales, Cardiff, UK. [12]Temple Street Children's Hospital, Dublin, Ireland. [13]Department of Clinical Genetics, Cambridge University Hospitals NHS Foundation Trust, Cambridge, UK. [14]Clinical Genetics Unit, Birmingham Women's Hospital, Edgbaston, Birmingham B15 2TG, UK. [15]Sheffield Clinical Genetics Service, Sheffield Children's Hospital, Western Bank, Sheffield S10 2TH, UK. [16]Northern Genetics Service, Newcastle upon Tyne Hospitals, NHS Foundation Trust, Newcastle upon Tyne, UK. [17]Clinical Genetics, Royal Devon and Exeter NHS Foundation Trust, Exeter, UK. [18]Department of Clinical Genetics, University Hospitals of Leicester NHS Trust, Leicester Royal Infirmary, Leicester LE1 5WW, UK. [19]University of Exeter Medical School, Institute of Biomedical and Clinical Science, Research, Innovation, Learning and Development (RILD), Royal Devon and Exeter Hospital, Barrack Road, Exeter, EX2 5DW, UK. [20]Medical Research Council (MRC) Human Genetics Unit, MRC Institute of Genetics and Molecular Medicine (IGMM), University of Edinburgh, Western General Hospital, Edinburgh EH4 2XU, UK.
***Corresponding author. Email: hcm@sanger.ac.uk (H.C.M.); jeff.barrett@genomicsplc.com (J.C.B.)**

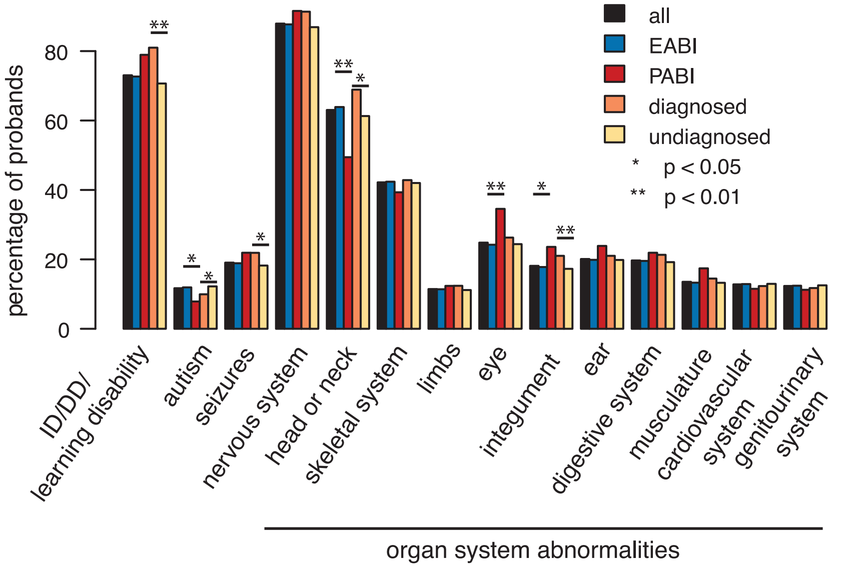

Fig. 1. Clinical features of DDD probands analyzed here. Proportion of probands in different groups with clinical features indicated, extracted from Human Phenotype Ontology terms. Asterisks indicate nominally significant differences between indicated groups (Fisher's exact test).

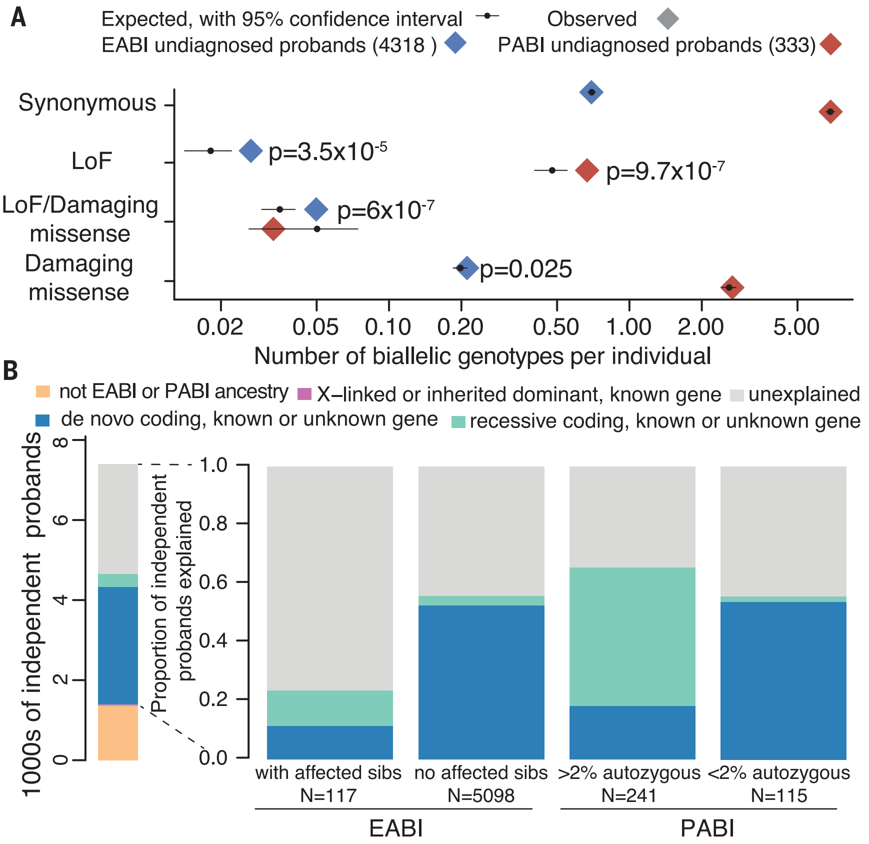

Fig. 2. Contribution of recessive coding variants to genetic architecture in this study. (**A**) Number of observed and expected biallelic genotypes per individual across all genes. Nominally significant *P* values from a Poisson test of enrichment are shown. (**B**) (Left) Number of probands grouped by diagnostic category. The inherited dominant and X-linked diagnoses (narrow pink bar) include only those in known genes, whereas the proportion of probands with de novo and recessive coding diagnoses was inferred as described in (*10*), including those in as-yet-undiscovered genes. (Right) The proportion of probands in various patient subsets inferred to have diagnostic variants in the indicated classes.

(fig. S7). We estimated that 3.6% (~205) of the 5684 EABI probands have a recessive coding diagnosis, compared with 49.9% (~2836) with a de novo coding diagnosis. Recessive coding genotypes explain 30.9% (~110) of the 356 PABI individuals, compared with 29.8% (~106) for de novos. The contribution from recessive variants was higher in EABI probands with affected siblings than those without (12.0% of 117 versus 3.2% of 5,098) and highest in PABI probands with high autozygosity (47.1% of 241) (Fig. 2B and table S2). By contrast, it did not differ between 115 PABI probands with low autozygosity and all 5684 EABI probands.

We caution that the PABI results may be less reliable because of modest sample size (wide confidence intervals are shown in table S2), exacerbated by consistent overestimation of rare variant frequencies in our limited sample of parents. Reassuringly, our estimated recessive contribution in PABI is close to the 31.5% reported in Kuwait (*12*), which has a similar level of consanguinity (*13*). Our results are consistent with previous reports of a low fraction of recessive diagnoses in European cohorts (*3*, *11*, *14*), but unlike those studies, our estimates further show that the recessive contribution in as-yet-undiscovered genes is also small. Although it has been hypothesized that there are thousands of undiscovered recessive DD-associated genes

Downloaded from http://science.sciencemag.org/ on December 10, 2018

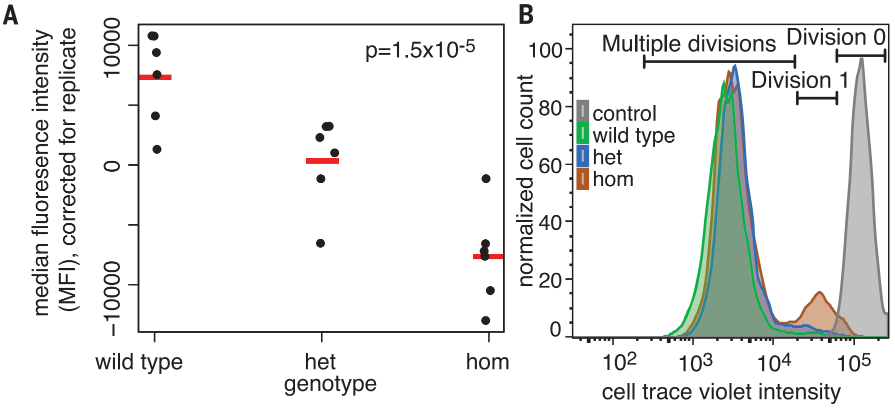

Fig. 3. Functional consequences of the pathogenic *EIF3F* recessive missense variant. (**A**) The Phe^{232}→Val variant impairs translation. Plot shows median fluorescence intensity (MFI) in iPSC lines heterozygous or homozygous for or without the Phe^{232}→Val variant (correcting for replicate effects), measured using a Click-iT protein synthesis assay (*10*). MFI correlates with methionine analog incorporation in nascent proteins. The *P* value indicates a nonzero effect of genotype from a linear regression of MFI on genotype and replicate. Red lines indicate means. (**B**) The Phe^{232}→Val variant impairs iPSC proliferation in the homozygous but not heterozygous form. Results from a cell trace violet (CTV) proliferation assay, in which CTV concentration reduces on each division. The population of cells that have been through zero, one, or multiple divisions is labeled.

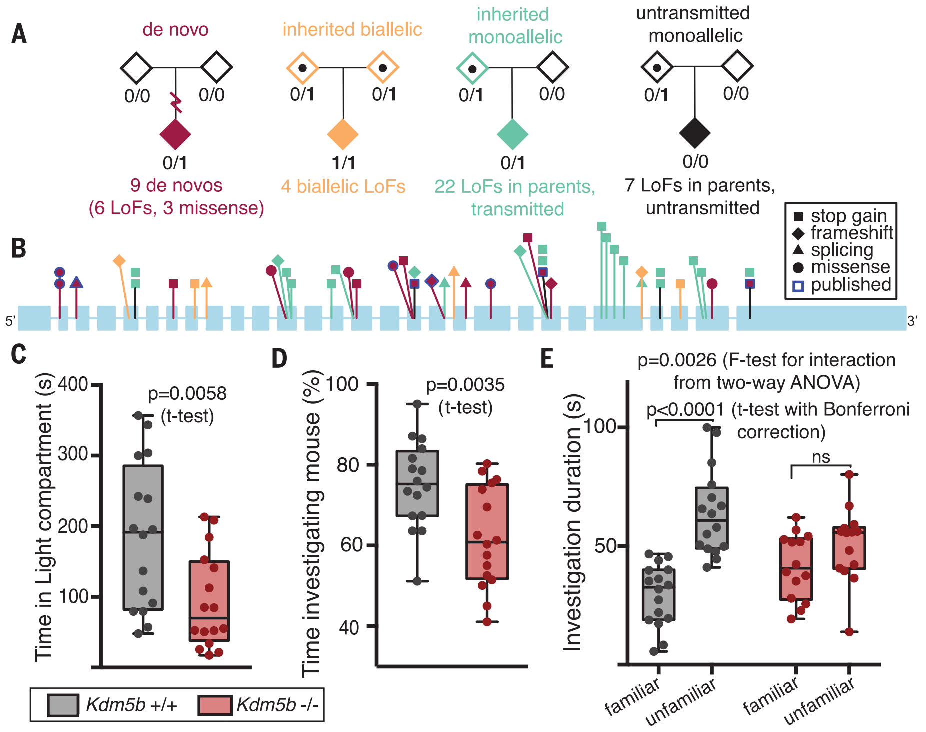

Fig. 4. *KDM5B* is a recessive DD gene in which heterozygous LOFs are incompletely penetrant. (**A**) Summary of damaging variants found in *KDM5B*. (**B**) Positions of likely damaging variants found in this and previous studies in *KDM5B* (ENST00000367264.2; introns not to scale), omitting two large deletions. Colors correspond to those shown in (A). There are no differences in the spatial distribution of LOFs by inheritance mode, nor in their likelihood of escaping nonsense-mediated decay by alternative splicing in GTex (*28*). (**C** to **E**) Behavioral defects of homozygous *Kdm5b*-null versus wild-type mice (n = 14 to 16 mice). (C) Knockout mice displayed increased anxiety, spending significantly less time in the light compartment of the light-dark box. (D) Reduced sociability, in the three-chamber sociability test. Knockout mice spent less time investigating a new mouse. (E) Twenty-four hour memory impairment. Whereas wild-type mice preferentially investigated an unfamiliar mouse over a familiar one, homozygous knockout mice showed no discrimination.

Downloaded from http://science.sciencemag.org/ on December 10, 2018

(*5*, *6*), our analyses suggest that the cumulative impact of these discoveries on diagnostic yield will be modest in nonconsanguineous populations.

We next tested each gene for an excess of biallelic genotypes in the undiagnosed probands (table S3) (*10*). Three genes passed stringent Bonferroni correction ($P < 3.4 \times 10^{-7}$) (*10*): *THOC6* [previously reported in (*15*)], *EIF3F*, and *KDM5B*. Thirteen additional genes had $P < 10^{-4}$ (table S4), of which 11 are known recessive DD-associated genes, and known genes were enriched for lower *P* values (fig. S8).

We observed five probands with an identical homozygous missense variant in *EIF3F* (binomial $P = 1.2 \times 10^{-10}$) (ENSP00000310040.4:p.Phe232Val), plus four additional homozygous probands who had been excluded from our discovery analysis for various reasons (table S5). The variant (rs141976414) has a frequency of 0.12% in non-Finnish Europeans (one of the most common protein-altering variants in the gene), and no homozygotes were observed in gnomAD (*16*).

All nine individuals homozygous for Phe^{232}→Val had ID, and a subset also had seizures (6 of 9), behavioral difficulties (3 of 9), and sensorineural hearing loss (3 of 9) (table S5). There was no obvious distinctive facial appearance (fig. S9). *EIF3F* encodes a subunit of the mammalian eIF3 (eukaryotic initiation factor) complex, which negatively regulates translation. The genes encoding eIF2B subunits have been implicated in severe autosomal recessive neurodegenerative disorders (*17*). We edited induced pluripotent stem cell (iPSC) lines with CRISPR-Cas9 to be heterozygous or homozygous for the Phe^{232}→Val variant, and Western blots showed that EIF3F protein levels were ~27% lower in homozygous cells relative to heterozygous and wild-type cells (fig. S10), which may be due to reduced protein stability (fig. S11). The Phe^{232}→Val variant significantly reduced translation rate (Fig. 3A and fig. S12). Proliferation rates were also reduced in the homozygous but not heterozygous cells (Fig. 3B and fig. S13), although the viability of the cells was unchanged (fig. S14).

Another recessive gene we identified was *KDM5B* (binomial $P = 1.1 \times 10^{-7}$) (Fig. 4), encoding a histone H3K4 demethylase. Three probands had biallelic LOFs passing our filters, and a fourth was compound heterozygous for a splice-site variant and a large gene-disrupting deletion.

Several of these patients were recently reported with less compelling statistical evidence (*18*). *KDM5B* is also enriched for de novo mutations in our cohort (binomial $P = 5.1 \times 10^{-7}$) (*4*). We saw nominally significant over-transmission of LOFs from the mostly unaffected parents ($P = 0.002$, transmission-disequilibrium test) (table S6), but no parent-of-origin bias. Theoretically, all the *KDM5B* LOFs observed in probands might be acting recessively, and heterozygous probands may have a second (missed) coding or regulatory hit or modifying epimutation. However, we found no evidence supporting this (figs. S15 and S16) (*10*), nor of potentially modifying coding variants in likely interactor genes, nor that some LOFs avoid nonsense-mediated decay (Fig. 4B). Genome-wide levels of DNA methylation in whole blood did not differ between probands with different types of *KDM5B* mutations or between these and controls (fig. S17).

These lines of evidence, along with previous observations of *KDM5B* de novos in both autism patients and unaffected siblings (*19*), suggest that heterozygous LOFs in *KDM5B* are pathogenic with incomplete penetrance, whereas homozygous LOFs are likely fully penetrant. Several microdeletions (*20*) and LOFs in other dominant ID genes are incompletely penetrant (*20*). Other H3K4 methylases and demethylases also cause neurodevelopmental disorders (*21*). *KDM5B* is atypical; the others are mostly dominant (*22*), typically with pLI scores >0.99 and very low pRec scores, whereas *KDM5B* has pLI = 5×10^{-5} and pRec > 0.999 (*23*).

KDM5B is the only gene that showed significant enrichment for both biallelic variants and de novo mutations in our study. We saw significant enrichment of de novo missense (373 observed versus 305 expected; ratio = 1.25, upper-tailed Poisson $P = 1 \times 10^{-4}$) but not de novo LOF mutations across all known recessive DD genes (excluding those known to also show dominant inheritance). One hypothesis is that the de novo missense mutations are acting as a "second hit" on the opposite haplotype from an inherited variant in the same gene. However, we saw only two instances of this in the cohort, and if it were driving the signal, we would expect to see a burden of de novo LOFs in recessive genes too, which we do not. A better explanation is that recessive DD genes are also enriched for dominant activating mutations. There are known examples of this; for example, in *NALCN* (*24*, *25*) and *MAB21L2* (*26*), heterozygous missense variants are activating or dominant-negative, whereas the biallelic mechanism is loss of function. By contrast, the six de novo LOFs in *KDM5B* suggest that it follows a different pattern. Of the 21 recessive genes with nominally significant de novo missense enrichment in our data, only one showed evidence of mutation clustering by using our previously published method (*CTC1*; $P = 0.03$) (*1*), which could suggest an activating/dominant-negative mechanism. Larger sample sizes will be needed to establish which of these genes also act dominantly, and by which mechanism.

All four individuals with biallelic *KDM5B* variants have ID, variable congenital abnormalities (table S7), and a distinctive facial appearance (fig. S18). Other than ID, there were no consistent phenotypes or distinctive features shared between the biallelic and monoallelic individuals or within the monoallelic group (table S7).

We created a mouse LOF model for *Kdm5b*. Heterozygous knockout mice appear normal and fertile, whereas homozygous *Kdm5b*-null mice are subviable (44% of expected, from heterozygous in-crosses). This partially penetrant lethality, in addition to a fully penetrant vertebral patterning defect (fig. S19), is consistent with previously published work (*27*). We additionally identified numerous behavioral abnormalities in homozygous *Kdm5b*-null mice: increased anxiety, less sociability, and reduced long-term memory compared with that of wild-types (Fig. 4).

We have quantified the contribution of recessive coding variants in both known and as-yet-undiscovered genes to a large UK cohort of DD patients and found that overall, they explain a small fraction. Our methodology allowed us to carry out an unbiased burden analysis that was not possible with previous methods (fig. S4). We identified two new recessive DD genes that are less likely to be found by typical studies because they result in heterogeneous and nonspecific phenotypes, and we present strong functional evidence supporting their pathogenicity.

Our results can be used to improve recurrence risk estimates for undiagnosed families with a particular ancestry and pattern of inheritance. Extrapolating our results more widely requires some care; our study is slightly depleted of recessive diagnoses because some recessive DDs (such as metabolic disorders) are relatively easily diagnosed through current clinical practice in the United Kingdom and less likely to have been recruited. Furthermore, country-specific diagnostic practices and levels of consanguinity may make the exact estimates less applicable outside the United Kingdom.

Overall, we estimated that identifying all recessive DD genes would allow us to diagnose 5.2% of the EABI+PABI subset of DDD, whereas identifying all dominant DD genes would yield diagnoses for 48.6%. The high proportion of unexplained patients, even among those with affected siblings or high consanguinity, suggests that future studies should investigate a wide range of modes of inheritance, including oligogenic and polygenic inheritance as well as noncoding recessive variants.

REFERENCES AND NOTES

1. The Deciphering Developmental Disorders Study, *Nature* **519**, 223–228 (2015).
2. R. K. C Yuen *et al*., *Nat. Neurosci.* **20**, 602–611 (2017).
3. S. C. Jin *et al*., *Nat. Genet.* **49**, 1593–1601 (2017).
4. Deciphering Developmental Disorders Study, *Nature* **542**, 433–438 (2017).
5. H. H. Ropers, *Annu. Rev. Genomics Hum. Genet.* **11**, 161–187 (2010).
6. L. E. L. M. Vissers, C. Gilissen, J. A. Veltman, *Nat. Rev. Genet.* **17**, 9–18 (2016).
7. P. A. Baird, T. W. Anderson, H. B. Newcombe, R. B. Lowry, *Am. J. Hum. Genet.* **42**, 677–693 (1988).
8. S. J. Schrodi *et al*., *Hum. Genet.* **134**, 659–669 (2015).
9. N. Akawi *et al*., *Nat. Genet.* **47**, 1363–1369 (2015).
10. Materials and methods are available as supplementary materials.
11. C. F. Wright *et al*., *Lancet* **385**, 1305–1314 (2015).
12. A. S. Teebi, *J. Med. Genet.* **31**, 224–233 (1994).
13. G. O. Tadmouri *et al*., *Reprod. Health* **6**, 17 (2009).
14. C. Gilissen *et al*., *Nature* **511**, 344–347 (2014).
15. C. L. Beaulieu *et al*., *Orphanet J. Rare Dis.* **8**, 62 (2013).
16. http://gnomad.broadinstitute.org
17. A. Fogli, O. Boespflug-Tanguy, *Biochem. Soc. Trans.* **34**, 22–29 (2006).
18. V. Faundes *et al*., *Am. J. Hum. Genet.* **102**, 175–187 (2018).
19. I. Iossifov *et al*., *Nature* **515**, 216–221 (2014).
20. G. L. Carvill, H. C. Mefford, *Curr. Opin. Genet. Dev.* **23**, 232–239 (2013).
21. H. H. Ropers, T. Wienker, *Eur. J. Med. Genet.* **58**, 715–718 (2015).
22. C. N. Vallianatos, S. Iwase, *Epigenomics* **7**, 503–519 (2015).
23. M. Lek *et al*., *Nature* **536**, 285–291 (2016).
24. J. X. Chong *et al*., *Am. J. Hum. Genet.* **96**, 462–473 (2015).
25. M. D. Al-Sayed *et al*., *Am. J. Hum. Genet.* **93**, 721–726 (2013).
26. J. Rainger *et al*., *Am. J. Hum. Genet.* **94**, 915–923 (2014).
27. M. Albert *et al*., *PLOS Genet.* **9**, e1003461 (2013).
28. https://gtexportal.org/home

ACKNOWLEDGMENTS

We thank the DDD families, the Sanger Human Genome Informatics team, P. Danacek for help with bcftools/roh, K. de Lange for help with figures, K. Samocha for mutability estimates, J. Matte and G. Turner for help with experiments, and A. Sakar for patient review. Families gave informed consent to participate, and the study was approved by the UK Research Ethics Committee (10/H0305/83, granted by the Cambridge South Research Ethics Committee and GEN/284/12, granted by the Republic of Ireland Research Ethics Committee). **Funding:** The DDD study presents independent research commissioned by the Health Innovation Challenge Fund (grant HICF-1009-003). Details are available in the supplementary materials. H.C.M. acknowledges support from a Research Fellowship at St John's College, Cambridge, and E.J.R. is funded by a National Institute for Health Research Academic Clinical Fellowship. **Author contributions:** Data analysis: H.C.M., J.F.M., J.H., P.S., and N.A.; Clinical interpretation: W.D.J.; *EIF3F* experiments: R.M., C.P.J.., and M.Br.; Mouse phenotyping: G.S.-A. and M.Sa.; Protein structure modelling: J.D.S.; Data processing: G.G., M.N., J.K., C.F.W., and E.J.R.; Experimental validation: E.P.; Patient recruitment: M.Ba., J.D., R.H., A.H., D.S.J., K.J., D.K, S.A.L., S.G.M., J.M., M.J.P., M.Sp., P.D.T., P.C.V., and M.W.; Experimental and analytical supervision: A.B., S.S.G., C.F.W., D.R.F., H.V.F., M.E.H., and J.C.B.; Writing: H.C.M., W.D.J., R.M., G.S.-A., J.D.S., M.B., A.B., J.H., M.E.H., and J.C.B. **Competing interests:** M.E.H. is a cofounder of, consultant to, and holds shares in, Congenica, a genetics diagnostic company. **Data and materials availability:** Exome sequencing and phenotype data are accessible via the European Genome-phenome Archive (EGA) (Datafreeze 2016-10-03) (www.ebi.ac.uk/ega/studies/EGAS00001000775).

SUPPLEMENTARY MATERIALS

www.sciencemag.org/content/362/6419/1161/suppl/DC1
Materials and Methods
Figs. S1 to S20
Tables S1 to S7
References (*29–56*)

6 December 2017; resubmitted 10 August 2018
Accepted 29 October 2018
Published online 8 November 2018
10.1126/science.aar6731

Downloaded from http://science.sciencemag.org/ on December 10, 2018

CANCER

A mechanistic classification of clinical phenotypes in neuroblastoma

Sandra Ackermann[1,2]*, Maria Cartolano[2,3]*, Barbara Hero[4], Anne Welte[1,2], Yvonne Kahlert[1,2], Andrea Roderwieser[1,2], Christoph Bartenhagen[1,2], Esther Walter[1,2], Judith Gecht[4], Laura Kerschke[5], Ruth Volland[4], Roopika Menon[6], Johannes M. Heuckmann[6], Moritz Gartlgruber[7], Sabine Hartlieb[7], Kai-Oliver Henrich[7], Konstantin Okonechnikov[8], Janine Altmüller[2,9], Peter Nürnberg[2,9,10], Steve Lefever[11], Bram de Wilde[11], Frederik Sand[1,2], Fakhera Ikram[1,2,12], Carolina Rosswog[1,2], Janina Fischer[1,2], Jessica Theissen[1,4], Falk Hertwig[1,2,13,14,15], Aatur D. Singhi[16], Thorsten Simon[4], Wenzel Vogel[17,18], Sven Perner[17,18], Barbara Krug[19], Matthias Schmidt[20], Sven Rahmann[21,22], Viktor Achter[23], Ulrich Lang[23,24], Christian Vokuhl[25], Monika Ortmann[26], Reinhard Büttner[26], Angelika Eggert[13,14,15], Frank Speleman[11], Roderick J. O'Sullivan[27], Roman K. Thomas[3,14,26,28], Frank Berthold[4]*, Jo Vandesompele[11]*, Alexander Schramm[29]*, Frank Westermann[7]*, Johannes H. Schulte[13,14,15,28]*, Martin Peifer[2,3]*, Matthias Fischer[1,2]*†

Neuroblastoma is a pediatric tumor of the sympathetic nervous system. Its clinical course ranges from spontaneous tumor regression to fatal progression. To investigate the molecular features of the divergent tumor subtypes, we performed genome sequencing on 416 pretreatment neuroblastomas and assessed telomere maintenance mechanisms in 208 of these tumors. We found that patients whose tumors lacked telomere maintenance mechanisms had an excellent prognosis, whereas the prognosis of patients whose tumors harbored telomere maintenance mechanisms was substantially worse. Survival rates were lowest for neuroblastoma patients whose tumors harbored telomere maintenance mechanisms in combination with RAS and/or p53 pathway mutations. Spontaneous tumor regression occurred both in the presence and absence of these mutations in patients with telomere maintenance–negative tumors. On the basis of these data, we propose a mechanistic classification of neuroblastoma that may benefit the clinical management of patients.

Neuroblastoma is a pediatric tumor of the sympathetic nervous system with substantially varying clinical courses (*1*). Roughly half of neuroblastoma patients have a dismal outcome despite intensive multimodal treatment, whereas other patients have an excellent outcome because their tumors either spontaneously regress or differentiate into benign ganglioneuromas. Patients are considered to be at high risk of death if they are diagnosed with metastatic disease when they are older than 18 months or when their tumor exhibits genomic amplification of the proto-oncogene *MYCN* (*2*). All other patients are classified as intermediate or low risk (referred to as non–high-risk patients in this study) and receive limited or no cytotoxic treatment. In addition to *MYCN* amplification, rearrangements of the *TERT* locus (encoding the catalytic subunit of telomerase) or inactivating mutations in *ATRX* (encoding a chromatin remodeling protein) have been found predominantly in high-risk tumors (*3*–*7*). Whereas both *MYCN* and *TERT* alterations lead to telomere maintenance by induction of telomerase, *ATRX* loss-of-function mutations have been associated with activation of the alternative lengthening of telomeres (ALT) pathway (*5*, *8*). Neuroblastomas also harbor recurrent mutations in *ALK* (encoding a receptor tyrosine kinase) (*9*, *10*). To date, these genomic data have not produced a coherent model of pathogenesis that can explain the extremely divergent clinical phenotypes of neuroblastoma.

In the study, we aimed to evaluate whether the divergent clinical phenotypes in neuroblastoma are defined by specific genetic alterations. To this end, we examined 218 pretreatment tumors and matched normal control tissue (i.e., blood) by whole-exome or whole-genome sequencing (WES and WGS, respectively) from patients covering the entire spectrum of the disease (fig. S1 and tables S1 to S3). In line with previous studies, we found 14.9 somatic single-nucleotide variations (SNVs) per tumor exome on average (median, 12 SNVs per tumor exome; fig. S2) (*4*, *6*). Because mutations in genes of the RAS and p53 pathways have been detected in relapsed neuroblastoma (*11*–*13*), we hypothesized that such alterations may not only be relevant at the time of relapse but may also determine the clinical course of neuroblastoma at diagnosis. We thus defined a panel of 17 genes related to the RAS pathway (11 genes including *ALK*) or the p53 pathway (6 genes) based on our own and published data (fig. S3 and tables S4 to S7) and examined their mutation frequency in pretreatment tumors (Fig. 1A). Focal amplifications, homozygous deletions, and variants of amino acids recorded in the Catalogue of Somatic Mutations in Cancer (*14*) were considered. We found alterations of these genes in 46 of 218 cases of the combined WES and WGS cohort. In an independent cohort of 198 pretreatment tumors examined by targeted sequencing (fig. S1 and tables S1 and S2), we detected alterations of these genes in 28 of 198 cases, resulting in an overall mutation frequency of 17.8% in the combined cohorts (74 of 416 cases; fig. S4 and tables S8 and S9). RAS and p53 pathway mutations were enriched in overall clonal cancer cell populations (95% versus 71% clonal events, $P = 0.021$; fig. S5), indicating their evolutionary selection during tumor development.

Mutations in RAS and p53 pathway genes occurred in both high- and non–high-risk tumors, although at lower frequencies in the latter group

Downloaded from http://science.sciencemag.org/ on December 6, 2018

---

[1]Department of Experimental Pediatric Oncology, University Children's Hospital of Cologne, Medical Faculty, Cologne, Germany. [2]Center for Molecular Medicine Cologne (CMMC), University of Cologne, Cologne, Germany. [3]Department of Translational Genomics, Center of Integrated Oncology Cologne–Bonn, Medical Faculty, University of Cologne, Cologne, Germany. [4]Department of Pediatric Oncology and Hematology, University Children's Hospital of Cologne, Medical Faculty, Cologne, Germany. [5]Institute of Biostatistics and Clinical Research, University of Münster, Münster, Germany. [6]NEO New Oncology GmbH, Cologne, Germany. [7]Division of Neuroblastoma Genomics (B087), German Cancer Research Center, and Hopp Children´s Cancer Center at NCT Heidelberg (KiTZ), Heidelberg, Germany. [8]Division of Pediatric Neurooncology, German Cancer Research Center, and Hopp Children's Cancer Center at NCT Heidelberg (KiTZ), Heidelberg, Germany. [9]Cologne Center for Genomics, University of Cologne, Cologne, Germany. [10]Cologne Excellence Cluster on Cellular Stress Responses in Aging-Associated Diseases (CECAD), University of Cologne, Cologne, Germany. [11]Center for Medical Genetics, Ghent University, Ghent, Belgium. [12]Interdisciplinary Research Centre in Biomedical Materials (IRCBM), COMSATS University Islamabad, Lahore Campus, Lahore, Pakistan. [13]Department of Pediatric Oncology and Hematology, Charité – Universitätsmedizin Berlin, Berlin, Germany. [14]German Cancer Consortium (DKTK), Heidelberg, Germany. [15]Berlin Institute of Health, Berlin, Germany. [16]Department of Pathology, University of Pittsburgh Medical Center, Pittsburgh, PA, USA. [17]Pathology of the University Medical Center Schleswig-Holstein, Campus Luebeck, Luebeck, Germany. [18]Research Center Borstel, Leibniz Center for Medicine and Biosciences, Borstel, Germany. [19]Department of Diagnostic and Interventional Radiology, University Hospital of Cologne, Cologne, Germany. [20]Department of Nuclear Medicine, University of Cologne, Cologne, Germany. [21]Genome Informatics, Institute of Human Genetics, University Hospital Essen, University of Duisburg-Essen, Essen, Germany. [22]Computer Science, TU Dortmund, Dortmund, Germany. [23]Computing Center, University of Cologne, Cologne, Germany. [24]Department of Informatics, University of Cologne, Cologne, Germany. [25]Kiel Pediatric Tumor Registry, Department of Pediatric Pathology, University of Kiel, Kiel, Germany. [26]Department of Pathology, University of Cologne, Cologne, Germany. [27]Department of Pharmacology and Chemical Biology, University of Pittsburgh Cancer Institute (UPCI), Hillman Cancer Center, Pittsburgh, PA, USA. [28]German Cancer Research Center (DKFZ), Heidelberg, Germany. [29]Department of Medical Oncology, West German Cancer Center Essen, University of Duisburg-Essen, Essen, Germany.
*These authors contributed equally to this work.
†Corresponding author. Email: matthias.fischer@uk-koeln.de

(21.3% versus 13.3%, P = 0.048, fig. S6). Overall, the presence of such alterations was strongly associated with poor patient outcome (Fig. 1B and fig. S7). We did not observe significant differences between the prognostic effects of RAS and p53 pathway alterations; however, patients whose tumors had *ALK* mutations had better event-free survival than those whose tumors harbored other RAS pathway mutations (fig. S8). In high-risk patients, alterations of RAS or p53 pathway genes were also associated with poor outcome (Fig. 1C and fig. S9, A and B), both in *MYCN*-amplified and non–*MYCN*-amplified cases (fig. S9C). Such alterations also identified patients with unfavorable clinical courses in the non–high-risk cohort (Fig. 1D and fig. S9D). The presence of these mutations predicted dismal outcome in multivariable analyses independently of prognostic markers currently used for neuroblastoma risk stratification (*15*) in the entire cohort and in both high-risk and non–high-risk patients (fig. S10). Together, our findings point to a crucial role of RAS and p53 pathway genes in the development of unfavorable neuroblastoma, which is in line with increased frequencies of such mutations at clinical relapse (*11–13*) and with data from genetically engineered mouse models showing that RAS pathway activation augments neuroblastoma aggressiveness (*16–18*).

Despite the overall association of RAS and p53 pathway mutations with poor outcome, however, we noticed that the clinical courses of non–high-risk patients bearing such mutations varied greatly, ranging from spontaneous regression to fatal tumor progression (fig. S11). On the basis of previous work (*5*, *19–21*), we hypothesized that these differences may be related to the presence or absence of telomere maintenance mechanisms. We therefore examined the genomic status of the *MYCN* and *TERT* loci, as well as ALT-associated promyelocytic leukemia nuclear bodies (APBs) and *TERT* expression in a cohort of 208 of 416 tumors (fig. S1). We observed *MYCN* amplification in 52 cases, *TERT* rearrangements in 21 cases, and APBs in 31 cases (Fig. 2A and table S10). In line with previous observations (*5*, *22*), *TERT* expression was elevated in tumors bearing *TERT* rearrangements or *MYCN* amplification, indicating telomerase activation (fig. S12, A and B). In APB-positive tumors, *TERT* expression was low and telomere length ratios high, thus supporting an ALT phenotype (fig. S12, A, C, and D). We also assessed the genomic status of *ATRX* in 83 evaluable tumors and found mutations that were likely to be inactivating in eight of these, all of which were ALT positive (Fig. 2A and table S10); by contrast, mutations of *DAXX*, which encodes another protein participating in chromatin remodeling at telomeres, were not detected. We observed neither significant alterations in *ATRX* or *DAXX* gene methylation status or gene expression patterns in ALT-positive tumors (fig. S13) nor significant associations between ALT and p53 pathway mutations (3 of 31 ALT-positive cases mutated, 7 of 177 ALT-negative cases mutated; P = 0.173) (*23*). Immunohistochemical staining revealed loss of nuclear ATRX expression in one tumor bearing an *ATRX* nonsense mutation, whereas expression was retained in tumors with *ATRX* in-frame deletions (fig. S14) (*23*). Furthermore, we noticed that a small fraction of neuroblastomas lacking *MYCN* or *TERT* alterations had elevated *TERT* mRNA levels (fig. S12A). We therefore determined and validated a *TERT* expression threshold to identify wild-type *MYCN* and *TERT* ($MYCN^{WT}$ and $TERT^{WT}$) tumors whose *TERT* mRNA levels are comparable to those of tumors bearing genomic *MYCN* or *TERT* alterations, pointing toward telomerase activation (fig. S15). In fact, high *TERT* mRNA levels corresponded to elevated enzymatic telomerase activity in these tumors, as well as in tumors harboring *MYCN* amplification or *TERT*

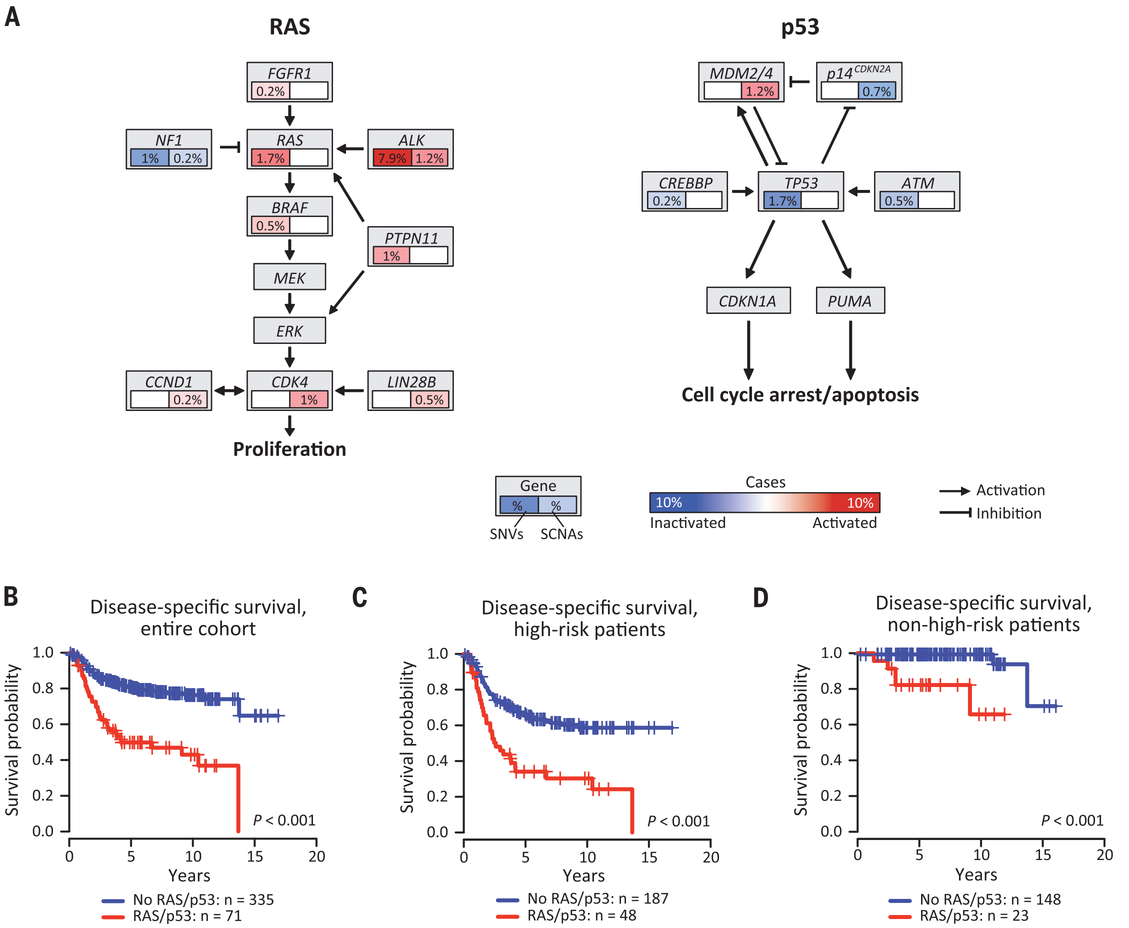

Fig. 1. Mutations of RAS and p53 pathway genes in pretreatment neuroblastomas are associated with poor survival of patients. (**A**) Schematic representation of the RAS and p53 pathways highlighting genes mutated in pretreatment neuroblastoma of the combined WES and WGS and targeted sequencing cohort (n = 416). The fraction of tumors affected by SNVs or by somatic copy number alterations (SCNAs) is indicated in the gene boxes as percentages and by color code. RAS represents the genes *NRAS*, *HRAS*, and *KRAS*. (**B** to **D**) Disease-specific survival of all patients (B), high-risk patients (C), and non–high-risk patients (D) of the same cohort (n = 416) according to the absence (blue) or presence (red) of RAS or p53 pathway gene mutations (5-year disease-specific survival ± SE: 0.807 ± 0.023 versus 0.498 ± 0.061, 0.657 ± 0.037 versus 0.341 ± 0.071, and 0.993 ± 0.007 versus 0.822 ± 0.081, respectively).

Downloaded from http://science.sciencemag.org/ on December 6, 2018

rearrangements (Fig. 2B). On the basis of these and our previous observations (*5*), we considered tumors telomere maintenance positive if they harbored *TERT* rearrangements or *MYCN* amplification, elevated *TERT* expression in the absence of these alterations, or were positive for APBs as a marker of ALT (Fig. 2A).

In the set of non–high-risk tumors bearing RAS or p53 pathway mutations (23 of 208 cases), we found evidence for telomerase or ALT activation in nine cases (fig. S16A). The outcome of these patients was poor, whereas all patients whose tumors lacked telomere maintenance mechanisms have survived to date, with no or limited cytotoxic therapy (fig. S16B). Importantly, this finding was validated in an additional series of 20 pretreatment non–high-risk neuroblastomas with RAS pathway gene mutations that had not been part of the initial WES and WGS or targeted sequencing cohorts (figs. S1 and S16, C and D, and table S11). Together, telomere maintenance mechanisms thus clearly discriminated the divergent clinical phenotypes occurring in non–high-risk tumors bearing RAS or p53 pathway mutations (Fig. 3, A and B).

The prognostic dependence of RAS pathway mutations on telomere maintenance in non–high-risk disease was highlighted in a patient subgroup that was genetically defined by the presence of *ALK*$^{\mathrm{R1275Q}}$ (R1275Q, Arg^{1275}→Gln) mutations (n = 11 patients): Outcome was excellent only if telomere maintenance mechanisms were absent, and spontaneous regression had been documented in four of these children (Fig. 3C and fig. S16E). Similarly, complete regression of osteomedullary metastases without any chemotherapy had been noticed in a stage 4 patient whose tumor carried the particularly aggressive *ALK*$^{\mathrm{F1174L}}$ (F1174L, Phe^{1174}→Leu) mutation (Fig. 3D) (*16*). In two other patients with *ALK*-mutant tumors (NBL8 and NBL-V16), spontaneous differentiation into ganglioneuroblastoma had been found after partial regression in patient NBL8 (Fig. 3E and fig. S16F). Finally, long-term event-free survival without chemotherapy was also recorded in patient NBL59, whose tumor harbored both *HRAS* and *TP53* mutations in the absence of telomere maintenance, whereas patients whose tumors harbored *HRAS*, *NRAS*, or *TP53* mutations had fatal outcome when telomerase or ALT was activated (Fig. 3A).

We hypothesized that a general pathogenetic hierarchy of telomere maintenance and RAS or p53 pathway mutations might mechanistically define the different clinical subgroups of neuroblastoma. Indeed, we observed that the outcome of patients whose tumors lacked telomere

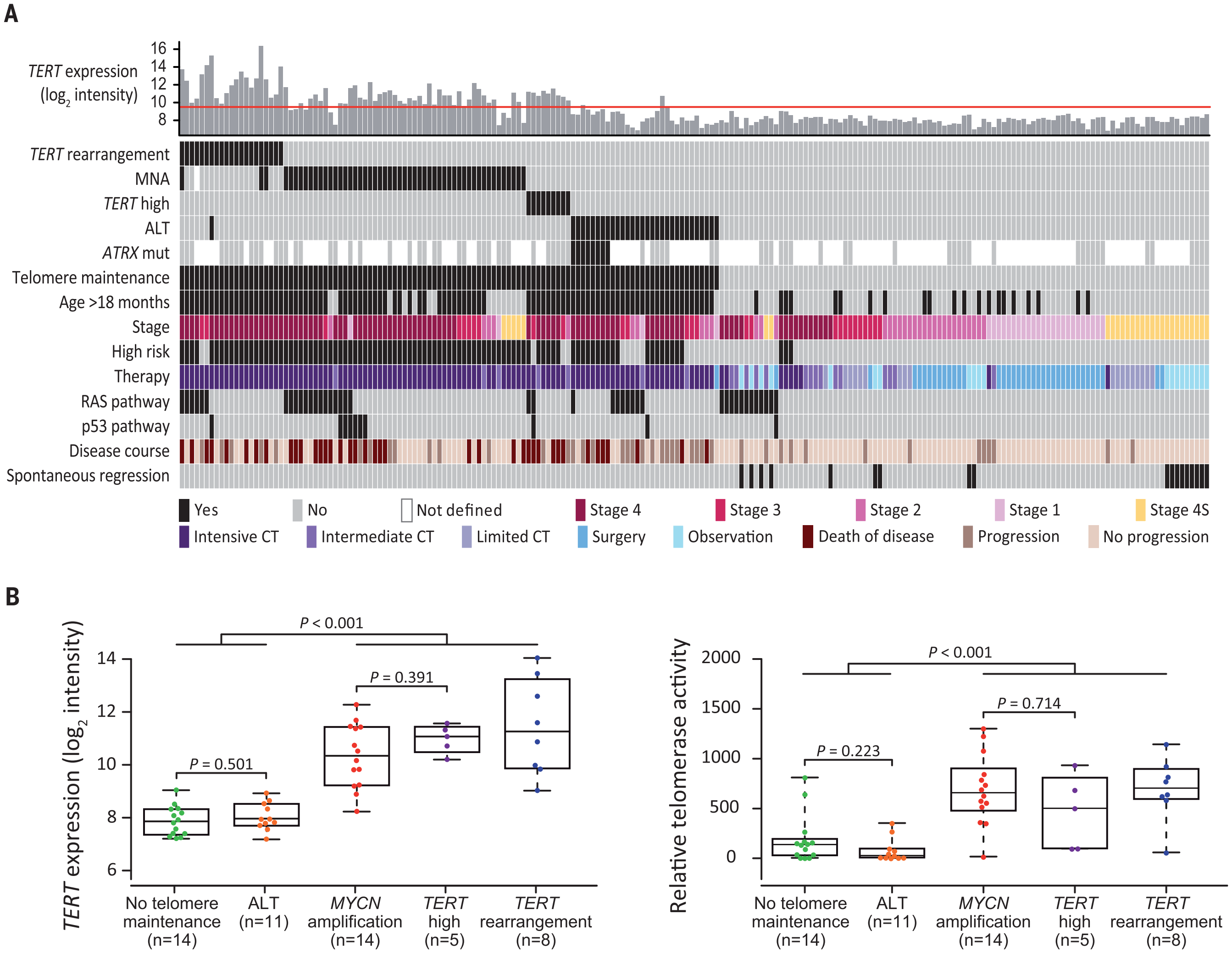

Fig. 2. Telomere maintenance mechanisms in pretreatment neuroblastomas. (**A**) Distribution of telomere maintenance mechanisms, RAS and p53 pathway gene mutations, and clinical covariates in 208 pretreatment neuroblastomas (ordered from left to right). The red line in the top panel indicates the *TERT* expression threshold as described in fig. S15. CT, chemotherapy; MNA, *MYCN* amplification. (**B**) *TERT* mRNA expression (left) and corresponding enzymatic telomerase activity (right) in 52 neuroblastoma samples. Boxes represent the first and third quartiles; whiskers represent minimum and maximum values; *TERT* high represents tumors lacking genomic *MYCN* or *TERT* alterations with *TERT* expression above threshold.

Downloaded from http://science.sciencemag.org/ on December 6, 2018

maintenance (n = 99) was excellent, irrespective of the presence of RAS or p53 pathway mutations (Fig. 4A). Fifty-seven of these patients had never received cytotoxic treatment, including 18 cases with documented spontaneous regression (Fig. 2A and table S10). Our data indicate that RAS or p53 pathway mutations are not sufficient for full malignant transformation and continuous growth of human neuroblastoma in the absence of telomere maintenance. Consistent with this observation, telomerase has been shown to be essential for full malignant transformation of human cells bearing oncogenic *HRAS* in experimental systems (*24*), whereas cellular senescence occurs in response to oncogenic *HRAS* in the absence of telomerase (*25*). Neuroblastomas lacking telomere maintenance were mainly derived from young patients (mean age at diagnosis, 378 days; fig. S17A) classified as clinical low or intermediate risk (96 of 99 cases; P < 0.001); the remaining three tumors had been obtained from young

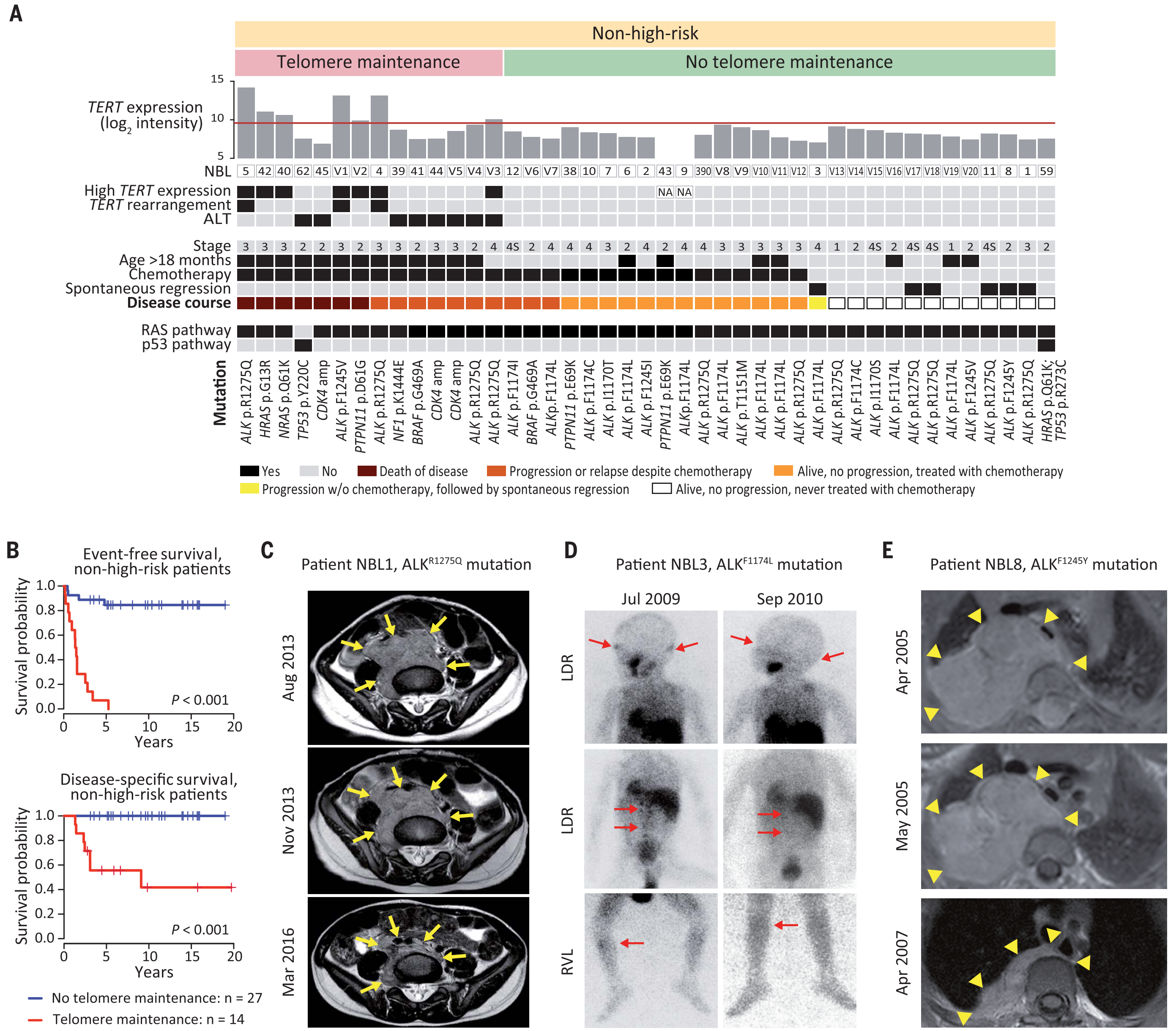

Fig. 3. Telomere maintenance mechanisms discriminate favorable and adverse clinical course in non–high-risk neuroblastoma bearing RAS or p53 pathway mutations. (**A**) Telomere maintenance status and clinical covariates in the combined discovery and validation cohort of non–high-risk patients whose tumors harbored RAS or p53 pathway mutations (n = 43). Patients are ordered from left to the right. The red line in the top panel indicates the *TERT* expression threshold. NBL, neuroblastoma ID; w/o, without. (**B**) Event-free (top) and disease-specific (bottom) survival of the same patients according to the absence (blue) or presence (red) of telomere maintenance mechanisms (n = 41; 5-year event-free survival ± SE, 0.847 ± 0.071 versus 0.071 ± 0.069; 5-year disease-specific survival ± SE, 1.0 versus 0.556 ± 0.136). (**C**) Magnetic resonance imaging (MRI) scans of a patient whose tumor harbored an *ALK*^{R1275Q} mutation in the absence of telomere maintenance activity at diagnosis and upon partial tumor regression. (**D**) Iodine-123 metaiodobenzylguanidine scintigraphy scans of a stage 4 patient with an *ALK*^{F1174L} mutated, telomere maintenance–negative neuroblastoma at diagnosis and upon complete regression of osteomedullary metastases. LDR, posterior projection (left–dorsal–right); RVL, anterior projection (right–ventral–left). (**E**) MRI scans of a patient with *ALK*^{F1245Y} (F1245Y, Phe^{1245}→Tyr) mutated, telomere maintenance–negative thoracic neuroblastoma at diagnosis and after partial regression. Tumor lesions are highlighted by arrows or arrowheads.

Downloaded from http://science.sciencemag.org/ on December 6, 2018

stage 4 patients (age at diagnosis, 732 to 1035 days) who all have survived event-free to date. By contrast, children whose tumors harbored telomerase or ALT activation were mainly clinical high-risk patients (92 of 109 cases; $P < 0.001$). Seventeen patients had been clinically classified as low or intermediate risk; however, their clinical course was as unfavorable as that of high-risk patients (fig. S17B), thus supporting the notion that telomere maintenance is a major determinant of neuroblastoma outcome. We also found no significant difference in the outcome of patients whose tumors displayed *MYCN* amplification compared with those whose tumors had other telomere maintenance mechanisms (fig. S18A). In addition, we observed that the outcome of patients whose tumors exhibited telomere maintenance was devastating when additional RAS or

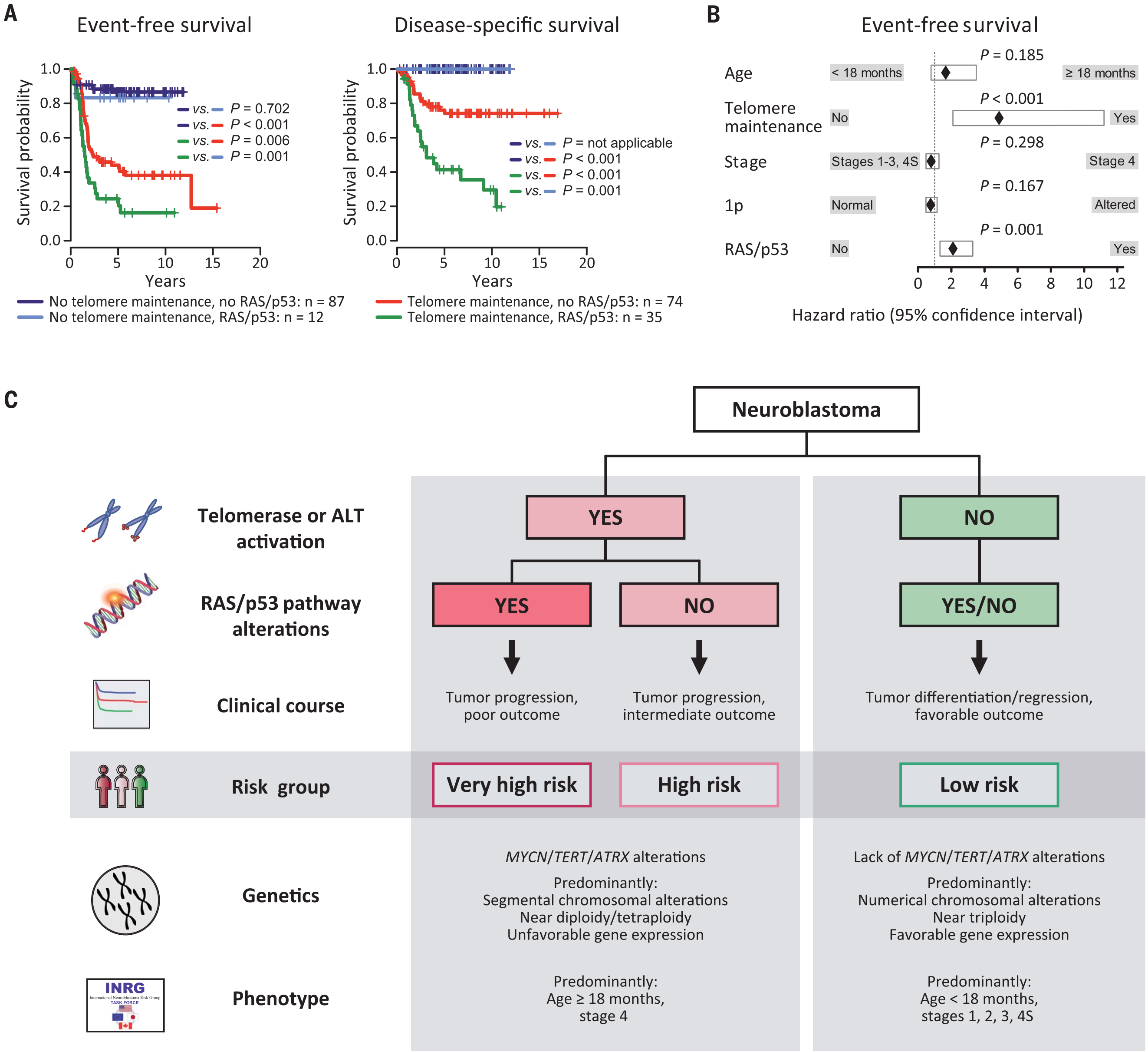

Fig. 4. Clinical neuroblastoma subgroups are defined by telomere maintenance and RAS and p53 pathways alterations. (**A**) Event-free (left) and disease-specific (right) survival of patients according to the absence or presence of RAS or p53 pathway gene mutations and telomere maintenance activity ($n = 208$; 5-year event-free survival ± SE, 0.867 ± 0.038 versus 0.833 ± 0.108 versus 0.440 ± 0.061 versus 0.245 ± 0.075; 5-year disease-specific survival ± SE, 1.0 versus 1.0 versus 0.742 ± 0.055 versus 0.414 ± 0.088). Statistical results of pairwise group comparisons are indicated. (**B**) Multivariable Cox regression analysis for event-free survival ($n = 201$), considering the prognostic variables age at diagnosis, stage, chromosome 1p status, RAS or p53 pathway mutation, and telomere maintenance activation. *MYCN* status was not considered separately, as telomere maintenance–positive cases comprised all *MYCN*-amplified cases by definition. Multivariable analysis for disease-specific survival could not be calculated, because no deadly event occurred in patients whose tumors lacked telomere maintenance, and thus, no hazard ratio can be calculated for this variable. (**C**) Schematic representation of the proposed mechanistic definition of clinical neuroblastoma subgroups. The classification is built on the presence or absence of telomere maintenance mechanisms and RAS or p53 pathway mutations. In addition, associations with other genetic features [*MYCN*, *TERT*, and *ATRX* alterations; segmental copy number alterations (*35*); tumor cell ploidy (*1*, *2*); gene expression–based classification (*36*)] and clinical characteristics (age at diagnosis, stage of disease) are indicated.

Downloaded from http://science.sciencemag.org/ on December 6, 2018

p53 pathway mutations were present, whereas survival was considerably better in their absence (Fig. 4A). Among the former patients, those whose tumors harbored *ALK* mutations tended to have a more favorable outcome than those whose tumors carried other RAS pathway mutations (fig. S18B). We also observed that the telomere maintenance status did not change over the disease course in 19 of 20 paired neuroblastoma samples biopsied at diagnosis and relapse or progression; in one case, de novo *MYCN* amplification accompanied by *TERT* up-regulation occurred at the time of relapse (table S12). This finding suggests that the telomere maintenance status is mostly fixed at diagnosis, which is in line with the notion that low-risk neuroblastoma rarely develops into high-risk disease (*26*, *27*). The clinical relevance of telomere maintenance and RAS or p53 pathway alterations was substantiated by multivariable analysis, in which both alterations independently predicted unfavorable outcome (Fig. 4B). Additional backward selection of variables in this model identified only telomere maintenance and RAS or p53 pathway mutations as independent prognostic markers (telomere maintenance: hazard ratio, 5.184, confidence interval, 2.723 to 9.871, $P < 0.001$; RAS and/or p53 pathway mutation: hazard ratio, 2.056, confidence interval, 1.325 to 3.190, $P = 0.001$), whereas the established markers (stage, age, and chromosome 1p status) were not considered in the final model.

Together, our findings demonstrate that the divergent clinical phenotypes of human neuroblastoma are driven by molecular alterations affecting telomere maintenance and RAS or p53 pathways, suggesting a mechanistic classification of this malignancy (Fig. 4C): High-risk neuroblastoma is defined by telomere maintenance caused by induction of telomerase or the ALT pathway. Additional mutations in genes of the RAS or p53 pathway increase tumor aggressiveness, resulting in a high likelihood of death from disease. By contrast, low-risk tumors invariably lack telomere maintenance mechanisms. Because telomere maintenance is essential for cancer cells to achieve immortal proliferation capacity (*8*, *28*), its absence is likely a prerequisite for spontaneous regression and differentiation in neuroblastoma. Our data also indicate that mutations of RAS or p53 pathway genes in tumors without telomere maintenance do not affect patient outcome.

Our findings may have important implications for the diagnosis and treatment of neuroblastoma patients, which should be validated in future prospective clinical trials. Assessment of telomere maintenance mechanisms and a limited set of RAS and p53 pathway genes may be sufficient to accurately estimate patient risk at diagnosis and to guide treatment stratification. In a clinical setting, telomerase activation may be readily determined by examining the genomic status of *MYCN* and *TERT* in the majority of cases and supplemented by analysis of *TERT* expression levels in *MYCN*$^{\mathrm{WT}}$ and *TERT*$^{\mathrm{WT}}$ tumors. It is important to note, though, that classification of patients based on a *TERT* expression threshold may bear a certain risk of misclassification because of potential confounding factors, such as tumor cell content or RNA integrity of the sample. In addition to analysis of telomerase activation, ALT can be assessed by detection of APBs or, potentially, by polymerase chain reaction (PCR) amplification of extrachromosomal circles of telomeric DNA (*29*). We propose that patients whose tumors lack telomere maintenance may require limited or no cytotoxic treatment, as suggested by the high prevalence of spontaneous regression in these cases, whereas patients whose tumors harbor such mechanisms need intensive therapy. Patients whose tumors carry both telomere maintenance and RAS or p53 pathway alterations, however, are at high risk of treatment failure and death (Fig. 4A). Nonetheless, the fact that these alterations can act in concert provides a rationale for developing novel combination therapies. Compounds interfering with aberrant RAS pathway signaling have shown promising antitumor effects in preclinical models of neuroblastoma (*12*, *16*, *30*, *31*), and ALK inhibitors have entered clinical trials (*32*). In addition, therapeutic strategies directed against telomerase or the ALT pathway are the subject of current investigations (*28*, *33*, *34*). A combination of therapies targeting these two critical oncogenic pathways in neuroblastoma may thus merit investigation.

REFERENCES AND NOTES

1. J. M. Maris, M. D. Hogarty, R. Bagatell, S. L. Cohn, *Lancet* **369**, 2106–2120 (2007).
2. S. L. Cohn *et al.*, *J. Clin. Oncol.* **27**, 289–297 (2009).
3. N. K. Cheung *et al.*, *JAMA* **307**, 1062–1071 (2012).
4. J. J. Molenaar *et al.*, *Nature* **483**, 589–593 (2012).
5. M. Peifer *et al.*, *Nature* **526**, 700–704 (2015).
6. T. J. Pugh *et al.*, *Nat. Genet.* **45**, 279–284 (2013).
7. L. J. Valentijn *et al.*, *Nat. Genet.* **47**, 1411–1414 (2015).
8. D. Hanahan, R. A. Weinberg, *Cell* **144**, 646–674 (2011).
9. S. C. Bresler *et al.*, *Cancer Cell* **26**, 682–694 (2014).
10. Y. P. Mossé *et al.*, *Nature* **455**, 930–935 (2008).
11. J. Carr-Wilkinson *et al.*, *Clin. Cancer Res.* **16**, 1108–1118 (2010).
12. T. F. Eleveld *et al.*, *Nat. Genet.* **47**, 864–871 (2015).
13. A. Schramm *et al.*, *Nat. Genet.* **47**, 872–877 (2015).
14. S. A. Forbes *et al.*, *Nucleic Acids Res.* **43**, D805–D811 (2015).
15. T. Simon, R. Spitz, A. Faldum, B. Hero, F. Berthold, *J. Pediatr. Hematol. Oncol.* **26**, 791–796 (2004).
16. L. C. Heukamp *et al.*, *Sci. Transl. Med.* **4**, 141ra91 (2012).
17. W. A. Weiss, K. Aldape, G. Mohapatra, B. G. Feuerstein, J. M. Bishop, *EMBO J.* **16**, 2985–2995 (1997).
18. T. Berry *et al.*, *Cancer Cell* **22**, 117–130 (2012).
19. L. M. Choi *et al.*, *Med. Pediatr. Oncol.* **35**, 647–650 (2000).
20. E. Hiyama *et al.*, *Nat. Med.* **1**, 249–255 (1995).
21. C. Poremba *et al.*, *J. Clin. Oncol.* **18**, 2582–2592 (2000).
22. S. M. Mac, C. A. D'Cunha, P. J. Farnham, *Mol. Carcinog.* **29**, 76–86 (2000).
23. X. Y. Liu *et al.*, *Acta Neuropathol.* **124**, 615–625 (2012).
24. W. C. Hahn *et al.*, *Nature* **400**, 464–468 (1999).
25. P. L. Patel, A. Suram, N. Mirani, O. Bischof, U. Herbig, *Proc. Natl. Acad. Sci. U.S.A.* **113**, E5024–E5033 (2016).
26. F. H. Schilling *et al.*, *N. Engl. J. Med.* **346**, 1047–1053 (2002).
27. W. G. Woods *et al.*, *N. Engl. J. Med.* **346**, 1041–1046 (2002).
28. C. B. Harley, *Nat. Rev. Cancer* **8**, 167–179 (2008).
29. J. D. Henson *et al.*, *Nat. Biotechnol.* **27**, 1181–1185 (2009).
30. L. S. Hart *et al.*, *Clin. Cancer Res.* **23**, 1785–1796 (2017).
31. N. R. Infarinato *et al.*, *Cancer Discov.* **6**, 96–107 (2016).
32. Y. P. Mossé *et al.*, *Lancet Oncol.* **14**, 472–480 (2013).
33. R. L. Flynn *et al.*, *Science* **347**, 273–277 (2015).
34. I. Mender, S. Gryaznov, Z. G. Dikmen, W. E. Wright, J. W. Shay, *Cancer Discov.* **5**, 82–95 (2015).
35. I. Janoueix-Lerosey *et al.*, *J. Clin. Oncol.* **27**, 1026–1033 (2009).
36. A. Oberthuer *et al.*, *Clin. Cancer Res.* **21**, 1904–1915 (2015).

ACKNOWLEDGMENTS

We thank the patients and their parents for making available the tumor specimens that were analyzed in this study, and we thank the German neuroblastoma biobank for providing these samples. The Institutional Review Board (IRB) approved collection and use of all specimens in this study. We thank our colleagues N. Hemstedt, H. Düren, and E. Hess for technical assistance and C. Reinhardt for critical reading of the manuscript. We also thank the CMMC light microscope facility for helping us obtain high-quality images of fluorescence in situ hybridization analyses. **Funding:** This work was supported by the German Cancer Aid (grant no. 110122 to M.F., F.W., A.S., and J.H.S.; grant no. 70-443, 70-2290-BE I, T12/97/Be1 and 70107712 to F.B.; the Mildred-Scheel professorship to M.P.), the German Ministry of Science and Education (BMBF) as part of the e:Med initiative (grant no. 01ZX1303 and 01ZX1603 to M.P., U.L., R.B., R.K.T., J.H.S., and M.F.; grant no. 01ZX1406 to M.P.; grant no. 01ZX1307 and 01ZX1607 to A.E., F.W., A.S., J.H.S., and M.F.), and the MYC-NET (grant no. 0316076A to F.W.), the Deutsche Forschungsgemeinschaft (DFG) as part of the SFB 876 (subproject C1, S.R. and A.S.) and as part of the KFO 286 (M.P.), the Berlin Institute of Health (Terminate-NB, A.E. and J.H.S.), the European Union (grant no. 259348 to F.W.), and as part of the OPTIMIZE-NB and ONTHETRRAC consortia (A.E.), the Fördergesellschaft Kinderkrebs-Neuroblastom-Forschung e.V. (M.F.), the German Cancer Research Center (DKFZ) intramural program for interaction projects and the DKFZ–Heidelberg Center for Personalized Oncology (HIPO) and National Center for Tumor Diseases (NCT) Precision Oncology Program (F.W.), the St. Baldricks Foundation (R.J.O.), the German Cancer Consortium (DKTK) Joint Funding program, and the Center for Molecular Medicine Cologne (CMMC). **Author contributions:** Conception and design: S.A., M.P., and M.F. Administrative support and provision of study materials and patients: B.H., T.S., W.V., S.P., B.K., M.S., S.R., V.A., U.L., C.V., R.B., A.E., F.Sp., R.J.O., R.K.T., F.B., J.V., A.S., F.W., J.H.S., M.P., and M.F. Conduct of the experiments, data analysis, and interpretation: S.A., M.C., B.H., A.W., Y.K., A.R., C.B., E.W., J.G., L.K., R.V., R.M., J.M.H., M.G., S.H., K.O.H., K.O., J.A., P.N., S.L., B.D.W., F.Sa., F.I., C.R., J.F., J.T., F.H., A.D.S., M.O., F.Sp., R.J.O., R.K.T., F.B., J.V., A.S., F.W., J.H.S., M.P., and M.F. Manuscript writing: S.A., M.C., M.P., and M.F. All authors read and approved the final manuscript. **Competing interests:** J.V. is a cofounder of Biogazelle, a company developing RNA-based assays to assess health and treat disease. J.V. is also a cofounder of pxlence, a company providing PCR assays for targeted amplification and sequencing of the human exome. R.K.T. has received consulting fees from NEO New Oncology, a company developing technologies for molecular pathology and clinical research. The other authors declare no competing interests. **Data and materials availability:** All high-throughput sequencing data have been deposited at the European Genome-phenome Archive (www.ebi.ac.uk/ega/) under accession number EGAS00001003244. Microarray data can be accessed from the GEO database (www.ncbi.nlm.nih.gov/geo/) with accession numbers GSE120572 and GSE120650.

SUPPLEMENTARY MATERIALS

www.sciencemag.org/content/362/6419/1165/suppl/DC1
Materials and Methods
Figs. S1 to S18
Tables S1 to S13
References (*37*–*47*)

23 March 2018; resubmitted 26 July 2018
Accepted 31 October 2018
10.1126/science.aat6768

Downloaded from http://science.sciencemag.org/ on December 6, 2018

SIGNAL TRANSDUCTION

LZTR1 is a regulator of RAS ubiquitination and signaling

Johannes W. Bigenzahn[1], Giovanna M. Collu[2], Felix Kartnig[1], Melanie Pieraks[1], Gregory I. Vladimer[1], Leonhard X. Heinz[1], Vitaly Sedlyarov[1], Fiorella Schischlik[1], Astrid Fauster[1,3], Manuele Rebsamen[1], Katja Parapatics[1], Vincent A. Blomen[3], André C. Müller[1], Georg E. Winter[1], Robert Kralovics[1,4], Thijn R. Brummelkamp[1,3,5,6], Marek Mlodzik[2], Giulio Superti-Furga[1,7]*

In genetic screens aimed at understanding drug resistance mechanisms in chronic myeloid leukemia cells, inactivation of the cullin 3 adapter protein-encoding leucine zipper-like transcription regulator 1 (*LZTR1*) gene led to enhanced mitogen-activated protein kinase (MAPK) pathway activity and reduced sensitivity to tyrosine kinase inhibitors. Knockdown of the *Drosophila LZTR1* ortholog *CG3711* resulted in a Ras-dependent gain-of-function phenotype. Endogenous human LZTR1 associates with the main RAS isoforms. Inactivation of *LZTR1* led to decreased ubiquitination and enhanced plasma membrane localization of endogenous KRAS (V-Ki-ras2 Kirsten rat sarcoma viral oncogene homolog). We propose that LZTR1 acts as a conserved regulator of RAS ubiquitination and MAPK pathway activation. Because *LZTR1* disease mutations failed to revert loss-of-function phenotypes, our findings provide a molecular rationale for *LZTR1* involvement in a variety of inherited and acquired human disorders.

Chronic myeloid leukemia (CML) is characterized by the expression of the constitutively active oncogenic tyrosine kinase fusion BCR-ABL (*1*). The proliferation and survival of BCR-ABL^{+} CML cells depends on the activation state of key cellular signaling networks, including the mitogen-activated protein kinase (MAPK) pathway (*1*). The development of the tyrosine kinase inhibitor (TKI) imatinib has provided a successful targeted therapeutic, however limited by the development of resistance (*2*).

Genetic screens in the near-haploid human CML cell line KBM-7 allow unbiased identification of candidate genes that affect inhibitor resistance (*3*). We performed comprehensive haploid genetic screening with six TKIs in clinical use or under evaluation (fig. S1A). Retroviral gene-trap mutagenized cells were exposed to the TKIs at concentrations corresponding to half maximal inhibitory concentration (IC^{50}) to IC^{70} dosage (fig. S1B), resistant cell populations were collected after selection, and genomic gene-trap insertions were identified by means of deep sequencing. Each screen resulted in enrichment of disruptive insertions in 5 to 18 different genes (Fig. 1A; figs. S1, C to G, and S2A; and table S1). We identified a recurrent set (≥4 screens) of six genes (*NF1*, *WT1*, *PTPN1*, *PTPN12*, *LZTR1*, and *BAP1*; "TOP6" set) (Fig. 1B) with overrepresentation of disruptive genomic gene-trap integrations, strongly indicating a selective advantage upon drug treatment (fig. S2B).

We used a lentiviral CRISPR/Cas9 multicolor competition assay (MCA)–based coculture system to evaluate gene-mediated drug-resistance effects. *SpCas9*-expressing KBM-7 (KBM-7^{Cas9}) cells were infected with lentiviral single-guide RNA (sgRNA) vectors that coexpress reporter fluorophores, which enabled the tracing of knockout and control cell populations by means of flow cytometry in the same well (fig. S3A). Mixed sg*Ren* (targeting *Renilla luciferase*) control cell populations that express fluorescent proteins (GFP^{+} or mCherry^{+}) did not show any preferential outgrowth of resistant cells upon 14 days of TKI treatment (Fig. 1C and fig. S3H). By contrast, KBM-7^{Cas9} GFP^{+} cells harboring sgRNAs that target the TOP6 genes showed a decreased amount of cognate protein (fig. S3, B to G) and demonstrated enhanced cell survival and outgrowth in the presence of imatinib (Fig. 1C) and rebastinib (fig. S3H). Thus, we functionally validated the TOP6 genes as important for drug action in *BCR-ABL*$^{+}$ CML cells.

Although *NF1*, *PTPN1*, and *PTPN12* share the ability to modulate MAPK pathway activation, and *WT1* as well as *BAP1* function through transcriptional regulation (fig. S2C), we could not deduce any mechanistic explanation for the role of leucine zipper–like transcription regulator 1 (*LZTR1*) in enhanced CML cell survival from the existing literature (*4*, *5*). To exclude cell line–specific effects, we confirmed that loss of *LZTR1* expression induced resistance to imatinib and rebastinib in other CML cell lines (fig. S4, A to C). Although we identified significant *LZTR1* enrichment only in four of the genetic screens, KBM-7^{Cas9} sg*LZTR1* cells exhibited various degrees of resistance against all tested BCR-ABL TKIs (fig. S3I). We used a CRISPR/Cas9–based domain scanning strategy to test whether both N-terminal Kelch domains and C-terminal Broad-Complex, Tramtrack, and Bric a brac (BTB) and partial BACK domains are essential for the drug-resistance phenotype (*6*–*8*). All protein domain-targeting sgRNAs showed efficient indel formation (fig. S3J) and induced resistant outgrowth of targeted cell populations exposed to rebastinib, indicating that the entire protein is functionally required (fig. S3K). To determine whether LZTR1 exerts its function only in a CML-specific context, we infected FLT3-ITD^{+} acute myeloid leukemia (AML) MV4-11^{Cas9} cells with *LZTR1*, targeting sgRNAs (fig. S4D). FLT3 inhibitor treatment led to an outgrowth of resistant cells, underlining a more general role for *LZTR1* in the drug response of hematopoietic cancers driven by different tyrosine kinases (fig. S4, E to G).

KBM-7^{Cas9} CML cells infected with distinct sgRNAs targeting *LZTR1* displayed enhanced phosphorylation of MAPK kinase 1 (MEK1) and -2 and extracellular signal–regulated kinase 1 (ERK1) and -2, which is indicative of augmented MAPK pathway activation (Fig. 2A). By contrast, global tyrosine phosphorylation as well as phosphorylation of AKT (at S473 and T308), the protein kinase S6K1, ribosomal protein S6, and the direct BCR-ABL substrate signal transducer and activator of transcription 5 (STAT5) remained unchanged (fig. S4, J and K). Additional CML (K-562 and LAMA-84) and AML (MV4-11) cell lines had similarly enhanced MAPK pathway activation under normal growth conditions as well as, in the case of CML cells, upon increasing concentration of imatinib treatment (Fig. 2A and figs. S4, H and I, and S5, A to C). *LZTR1* full-length cDNA complementation in K-562^{Cas9} sg*LZTR1* cells reverted both enhanced MEK and ERK phosphorylation as well as TKI resistance (Fig. 2, B and C). Treatment of K-562^{Cas9} sg*LZTR1* cells with the clinically approved inhibitor of MEK1 and -2 trametinib reverted enhanced activation of ERK1 and -2 and pharmacologically counteracted the drug-resistance phenotype (Fig. 2, D and E). Furthermore, cDNA expression of constitutively active *Mek1*$^{D218, D222}$ (Mek1 DD) in K-562^{rtTA3} cells led to enhanced phosphorylation of ERK1 and -2 and reduced imatinib sensitivity (fig. S6A, and B). Activation of the MAPK pathway could also be inferred by the gene expression and transcription factor enrichment signature obtained with RNA sequencing experiments in KBM-7^{Cas9} sg*LZTR1* compared with sg*Ren* cells (fig. S5, D and E, and table S2). Altogether, the data established a causal role for enhanced MAPK pathway activation in the resistance of CML cells toward TKI therapy as elicited by loss of LZTR1 function.

Because BTB domain-containing proteins serve as adaptor proteins for the cullin 3 (CUL3) E3

---

[1] CeMM Research Center for Molecular Medicine of the Austrian Academy of Sciences, 1090 Vienna, Austria. [2] Department of Cell, Developmental, and Regenerative Biology and Graduate School of Biomedical Sciences, Icahn School of Medicine at Mount Sinai, 1 Gustave L. Levy Place, New York, NY 10029, USA. [3] Netherlands Cancer Institute, Plesmanlaan 121, 1066 CX, Amsterdam, Netherlands. [4] Department of Laboratory Medicine, Medical University of Vienna, 1090 Vienna, Austria. [5] Oncode Institute, Division of Biochemistry, Netherlands Cancer Institute, Plesmanlaan 121, 1066 CX, Amsterdam, Netherlands. [6] Cancer Genomics Center (CGC.nl), Plesmanlaan 121, 1066 CX, Amsterdam, Netherlands. [7] Center for Physiology and Pharmacology, Medical University of Vienna, 1090 Vienna, Austria.
***Corresponding author. Email: gsuperti@cemm.oeaw.ac.at**

Downloaded from http://science.sciencemag.org/ on December 11, 2018

ubiquitin ligase complex, enabling specific substrate recognition and ubiquitination (*9*), we tested whether loss of CUL3 expression could mimic the observed LZTR1 loss-of-function phenotype. K-562^{Cas9} sg*CUL3* cells demonstrated enhanced MAPK pathway activation and, in contrast to sg*LZTR1* cells, increased phosphorylation of AKT (fig. S4K). However, sgRNAs that target *CUL3* had a pronounced antiproliferative effect both in KBM-7^{Cas9} and K-562^{Cas9} cells (fig. S6, C and D), providing a potential explanation why *CUL3* was not detected in our genetic screens (fig. S2A).

In contrast to the CML cell lines, depletion of LZTR1 with CRISPR sgRNAs in HeLa, human embryonic kidney (HEK)–293T, or HAP1 cells did not increase MAPK pathway activation under comparable culture conditions (fig. S7, A and C). However, after serum stimulation of cells cultured without serum, HEK293T^{Cas9} sg*LZTR1* cells showed a more pronounced activation of MEK and ERK than in control cells (fig. S7B). Similarly, in HAP1 cells, a non-hematopoietic derivative of the KBM-7 cell line (*10*), phorbol-12-myristat-13-acetat (PMA) treatment led to enhanced MAPK pathway activation in the absence of *LZTR1* compared with that in wild-type (WT) cells (fig. S7C). Whereas HAP1^{Cas9} sg*CUL3* cells exhibited increased phosphorylation of ERK1, ERK2, and AKT (fig. S7F), loss of *LZTR1* expression in HAP1^{Cas9} altered only the MAPK pathway as identified by means of pathway array-based assessment of kinase activation (fig. S7, D and E, and table S3).

Genetic studies have identified *LZTR1* mutations in glioblastoma (GBM) (*11*), schwannomatosis (SWNMT) (*8*), and Noonan syndrome (NS) (*5*), a developmental syndrome that is part of the larger group of RASopathies characterized by mutations in components of the RAS-MAPK pathway (*12*). Identification of *NF1* and *LZTR1* loss-of-function–induced MAPK pathway activation in our haploid resistance screens combined with human *LZTR1* mutations in NS indicated that LZTR1 might directly regulate guanosine triphosphatases (GTPases) of the RAS family.

Drosophila wing vein formation and eye development serve as excellent in vivo readouts for RAS signaling (*13*–*15*). *CG3711* encodes the *Drosophila* ortholog of mammalian *LZTR1*, which contains a specific N-terminal domain (amino

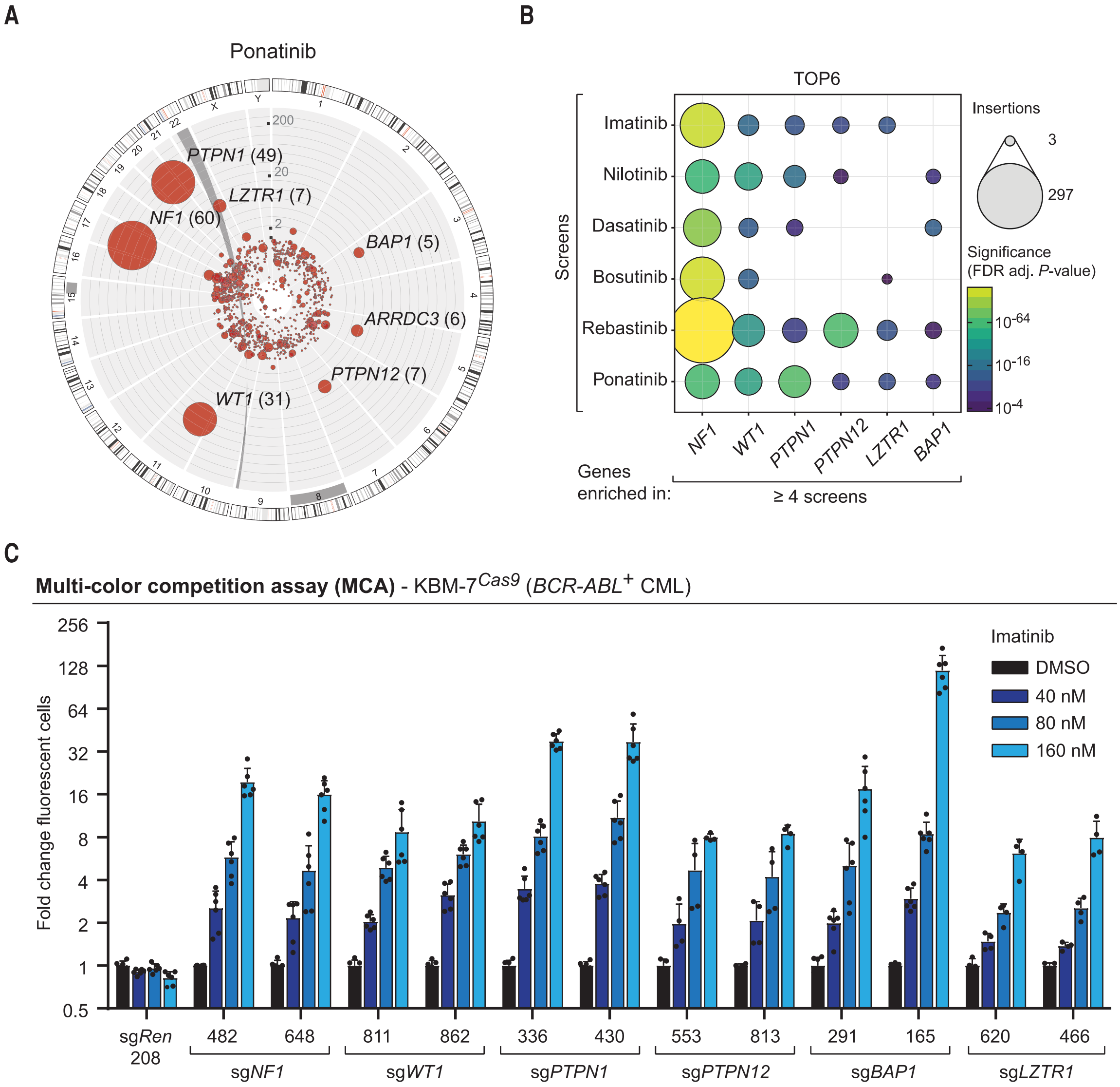

Fig. 1. Haploid genetic screens identify gene knockouts that promote BCR-ABL inhibitor resistance. (**A**) Circos plot of the haploid genetic screen in the CML cell line KBM-7 upon treatment with ponatinib. Each dot represents a mutagenized gene identified in the resistant cell population, the dot size corresponds to the number of independent insertions identified per gene, and the distance from the circos plot center indicates the significance of enrichment compared with an unselected control data set. Hits with a false discovery rate (FDR)–adjusted *P* value lower than 10^{-4} are labeled by gene name. (**B**) Bubble plot depicting the "TOP6" set of genes identified in four or more of the six haploid screens upon treatment with first-, second- and third-generation BCR-ABL inhibitors. The size of each bubble corresponds to the number of independent insertions per gene, and the color gradient depicts the FDR-adjusted *P* value of enrichment significance. (**C**) MCA-derived fold change of cell populations after imatinib treatment of KBM-7^{Cas9} CML cells transduced with sgRNAs targeting the "TOP6" genes or sg*Ren*.208 (targeting *Renilla luciferase*) as negative control. sgRNA-infected cell populations were mixed in a 1:1 ratio, treated with increasing drug concentrations, and analyzed by means of flow cytometry after 14 days. Data are shown as mean value ± SD of at least two independent experiments ($n \geq 2$) performed in duplicates. sgRNAs are labeled by gene name followed by the genomic targeting sequence position numbered according to the sequence position on the corresponding mRNA.

Downloaded from http://science.sciencemag.org/ on December 11, 2018

acids 1 to 184) that is only found in *Drosophila*. This is followed by the highly conserved remaining part of the protein (54% sequence identity) (fig. S8, A to C). Systemic depletion of *CG3711* with RNA interference (RNAi) by using *act5C-Gal4* yielded viable flies; however, the majority of wings of these flies displayed wing vein defects characterized by extra veins and vein tissue (Fig. 3, A and B, and fig. S8D). This phenotype closely resembles a gain-of-function increase of RAS-MAPK signaling (*15*) and could be rescued by a decrease in abundance of RAS via *dRas* (*Drosophila* Ras) heterozygosity (Fig. 3C). *Drosophila* R7 photoreceptor induction requires RAS function (*13*, *14*). We used a mild dominant negative version, Ras^{V12C40}, which although locked in the active guanosine 5′-triphosphate (GTP)–bound state does not activate MAPK signaling (*16*). Ras^{V12C40} expression in the developing eyes (via the *sevenless*/*sev-Gal4* expression system) led to a frequent loss of the R7 photoreceptor (~30% of ommatidia display R7 loss, and some also lost other R-cells) (fig. S8, E and H). Because Ras^{V12C40} is constitutively active, it also causes defects in ommatidial rotation (*16*, *17*), serving as internal control. When both *sev-Gal4*–driven *CG3711* RNAi and Ras^{V12C40} were expressed, the loss of R7 phenotype was almost completely suppressed (fig. S8, F and H). The ommatidial rotation defects were enhanced

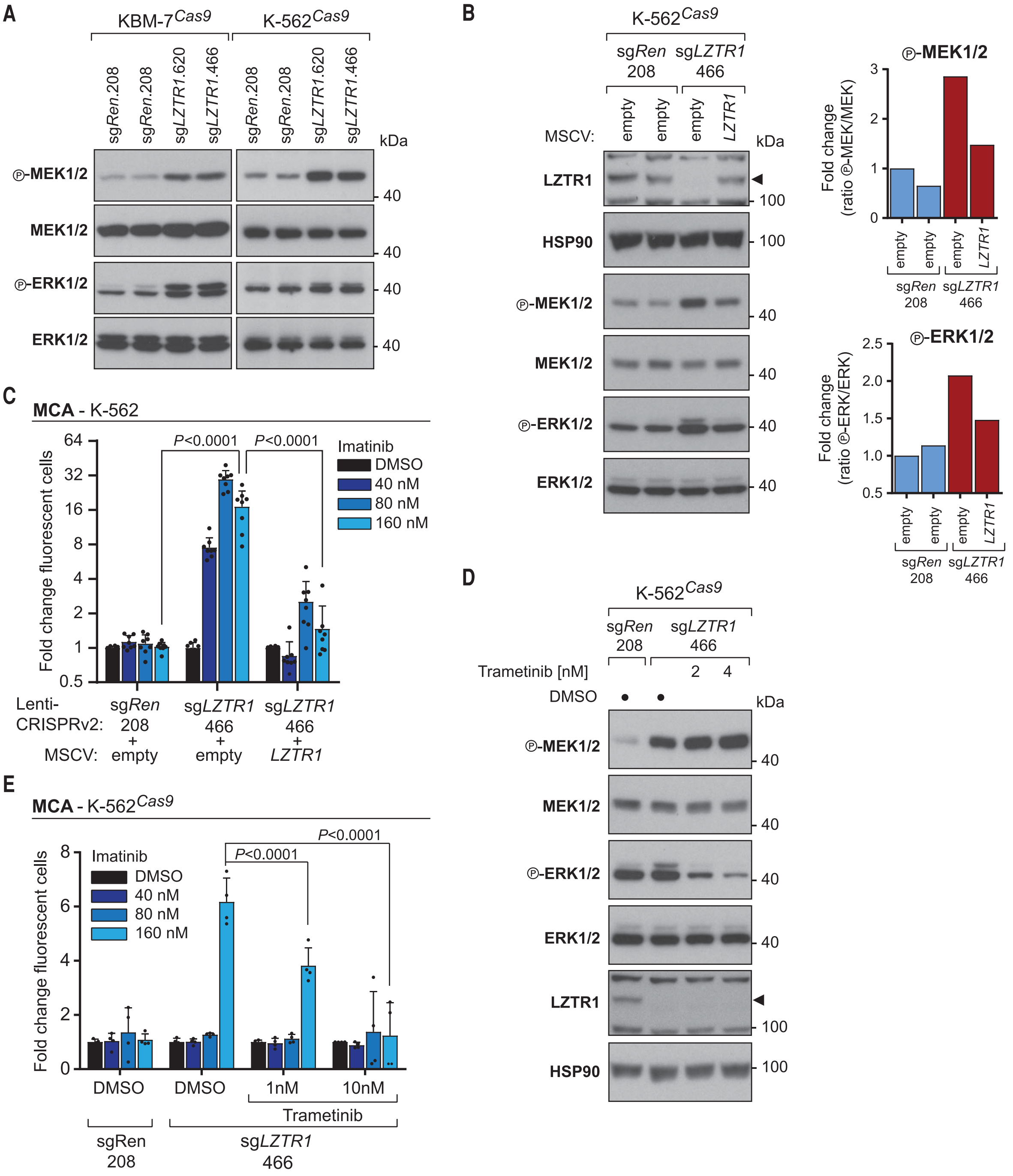

Fig. 2. Loss of *LZTR1* enhances MAPK pathway activation. (**A**) Phosphorylation of MEK and ERK in KBM-7^{Cas9} and K-562^{Cas9} CML cells transduced with the indicated sgRNAs. (**B**) Immunoblot analysis of MEK and ERK phosphorylation as well as LZTR1 expression in sg*Ren*.208–expressing K-562^{Cas9} CML cells transduced with empty vector, and sg*LZTR1*.466–expressing cells transduced with empty vector or *LZTR1*-cDNA–containing murine stem cell virus (MSCV) retrovirus. Quantification of MEK and ERK phosphorylation is shown next to the corresponding immunoblots. (**C**) Competitive proliferation assay (MCA) of K-562^{Cas9} sg*Ren*.208 cells transduced with empty vector and sg*LZTR1*.466 cells transduced with empty vector or *LZTR1* cDNA after treatment with increasing concentrations of imatinib for 14 days. (**D**) Phosphorylation of MEK and ERK in K-562^{Cas9} cells expressing sg*LZTR1*.466 and treated with increasing concentrations of trametinib for 3 hours. (**E**) Changes in cell populations measured with MCA of K-562^{Cas9} CML cells expressing sg*Ren*.208 or sg*LZTR1*.466 after 14 days of treatment with increasing concentrations of imatinib alone or in combination with trametinib. Immunoblot results in (A), (B), and (D) are representative of at least two independent biological experiments ($n \geq 2$). MCA data in (C) and (E) are shown as mean value ± SD of at least two independent experiments ($n \geq 2$). Dimethyl sulfoxide (DMSO) treatment served as negative control.

Downloaded from http://science.sciencemag.org/ on December 11, 2018

rather than suppressed because these involve MAPK-independent RAS signaling (fig. S8F) (*16*). Expression of *CG3711* RNAi in the eye alone did not induce phenotypic changes (fig. S8, G and H). Thus, RAS is crucial for the phenotypes induced by depletion of *CG3711*.

To explore possible interactions of LZTR1 with RAS, we used a BirA* fusion protein–based proximity biotinylation-dependent (BioID) proteomic approach, which allows identification of weak interaction partners. We expressed KRAS4A, KRAS4B, NRAS, and HRAS as N-terminal FLAG-BirA* fusion proteins in K-562^{rtTA3} CML cells. This led to enhanced MEK and ERK activation, demonstrating that the BirA* tag does not generally interfere with RAS signaling (fig. S9A). We identified between 153 and 258 proteins in proximity of or interacting with human RAS proteins, among them several known interactors and pathway components (fig. S9, B to F, and table S4). A common set of 123 proteins repeatedly purified with all four RAS proteins, with gene ontology analysis showing a significant enrichment in components associated with plasma membrane and Golgi apparatus as well as the MAPK pathway (fig. S9, G and H). We identified LZTR1 among the most significant interactors of all four RAS proteins (fig. S9, B to F). Intersection of the 123 common interactors identified with BioID, with a fluorescence-activated cell sorting (FACS)–based haploid genetic pathway screen for the identification of gene knockout alleles that influence phosphorylation of ERK1 and -2 (*18*), revealed LZTR1 as the only common RAS interactor in our proteomic data with a negative regulatory function within the RAS-MAPK pathway (fig. S10A).

BioID proximity biotinylation-based and FLAG tag–based coimmunoprecipitation experiments confirmed the interaction of all four RAS proteins with endogenous LZTR1 (fig. S10, B and C). Only the four main RAS isoforms interacted specifically with LZTR1, whereas six related RAS family GTPases showed no interaction (fig. S11A). Nine other canonical positive RAS-MAPK pathway regulators also failed to interact with endogenous LZTR1 (fig. S11B). Immunoprecipitations with extracts derived from *LZTR1* knockout cells confirmed the specificity of the interaction (fig. S11C). The C-terminal posttranslational acylations of KRAS proteins appeared to be required for the interaction with LZTR1 (Fig. 3D and fig. S11D). Thus, proper membrane-associated localization mediated by this region may be required for specific interaction with LZTR1.

Stably expressed full-length hemagglutinin (HA)–tagged LZTR1 protein showed a speckled and vesicular staining pattern in HeLa, HEK293T, and HAP1 cells, whereas all domain mutants had a homogenous cytoplasmic distribution (fig. S12, A to D). Full-length LZTR1 displayed an overlapping localization within speckled and vesicular compartments with transiently transfected V5-tagged CUL3 in HeLa cells (fig. S13A). The LZTR1-stained speckles further overlapped with the autophagosome marker LC3B fused to mCherry (fig. S13B), but we failed to detect LZTR1 localization with marker proteins of the Golgi, lysosome, peroxisome, or early and late endosome compartments (fig. S13C). Isoform-specific antibodies that recognize endogenous human RAS isoforms are not available (*19*). We therefore endogenously tagged KRAS (fig. S14A) and confirmed specificity of detection in immunofluorescence and immunoblotting by means of genetic inactivation of the tagged genomic allele (fig. S14, B to D). KRAS localized to a large number of small-punctate structures, likely membrane-containing small vesicles (Fig. 3E and fig. S14D). Inactivation of endogenous *LZTR1* led to an increased RAS signal, particularly at the periphery of cells, at regions of cell-to-cell contacts (Fig. 3E and fig. S14D). This phenotype appeared to be dependent on the CUL3 E3 ligase complex because genetic inactivation of *CUL3* led to similar phenotypic changes (Fig. 3E and fig. S14E).

We also assessed interaction of endogenously tagged KRAS with exogenous LZTR1 in HAP1 cells (fig. S15A). Exogenous LZTR1 localized to fewer, larger, and more oblong structures than did endogenous KRAS (fig. S15B). A fraction of the LZTR1-stained structures also contained KRAS. Treatment with the cullin neddylation inhibitor MLN4924 caused clustering of LZTR1-containing structures that appeared to surround particles strongly stained with KRAS (fig. S15B, MLN4924 panel). Caution is required for the interpretation of these patterns because LZTR1 was overexpressed, and KRAS was at endogenous concentration. However, the images could represent a trapped proteostatic process that involves the two proteins.

We tested whether LZTR1 affected ubiquitination of RAS proteins by acting as a substrate adaptor for the CUL3 E3 ligase complex (*11*, *20*). Ubiquitination of RAS proteins is known, but little is known of its consequences (*21*–*25*). Coexpression of HA-ubiquitin with either one of the four RAS isoforms alone only resulted in a basal state of ubiquitination, but addition of MYC-tagged CUL3 and V5-tagged LZTR1 led to increased ubiquitination of RAS proteins (fig. S16, A to D). LZTR1-deletion mutants that lack either one or both C-terminal BTB domains or the N-terminal Kelch domain failed to induce an equivalent degree of ubiquitination of KRAS4A (fig. S16A). KRAS4A required the presence of its C-terminal hypervariable region (HVR) and the farnesylated cysteine 186 for LZTR1-mediated ubiquitination (fig. S16E). LZTR1-induced ubiquitination was unchanged in cells treated with a proteasome inhibitor but could be blocked by cullin neddylation inhibition, which is consistent with the observed subcellular localization changes (fig. S16F). Specificity for LZTR1 in the process was further underscored by the failure of two prominent CUL3 adaptors, Kelch-like ECH-associated protein 1 (KEAP1) and Speckle-type POZ protein (SPOP), to cause a comparable ubiquitination (fig. S16G). We used HAP1 cells that bear endogenously tagged KRAS and tandem ubiquitin binding domain (TUBE) reagents to capture endogenously ubiquitinated proteins and evaluate the contribution of endogenous LZTR1 (*26*). In the absence of any stimulation, immunoprecipitation with TUBE purified several proteins that reacted with pan-ubiquitin antibodies (Fig. 3F, third from top, and fig. S16H). The same precipitates contained proteins that react with pan-RAS antibodies (Fig. 3F, second from top). Last, FLAG antibodies detected a protein not visible in the whole-cell extract (Fig. 3F, top, and fig. S16H). TUBE-mediated immunoprecipitation from corresponding cells in which LZTR1 had been genetically inactivated did not contain amounts of RAS detectable with these antibodies (Fig. 3F, top and second from top, and fig. S16H). The signal obtained with pan-ubiquitin antibodies was unchanged (Fig. 3F, third from top, and fig. S16H). Thus, human LZTR1 appears to mediate ubiquitination of endogenous human KRAS and possibly other RAS proteins.

If a main function of LZTR1 is to regulate RAS, then loss of RAS function should compensate for loss of LZTR1 activity, as suggested in the fruitfly epistatic analysis, representing an ideal experimental setup to assess the disease-associated *LZTR1* mutations by their dependency on RAS activity. We confirmed that loss of LZTR1 function enhanced RAS activity in K-562 cells (fig. S17A). We then performed CRISPR/Cas9–based double-knockout MCA experiments (fig. S17, B to D). Single sg*LZTR1* and sg*LZTR1*-sg*Ren* double-infected cells were resistant to imatinib compared with control sg*Ren* cells (fig. S17, E and F). sgRNAs that target *KRAS* abolished cellular outgrowth, whereas sgRNAs that target *NRAS*, *HRAS*, and *RIT1* failed to do so (fig. S17, E and F). sg*LZTR1*-sg*KRAS* cells had reduced MEK phosphorylation comparable with that of sg*Ren* cells, whereas sg*NRAS* and sg*HRAS* cells maintained enhanced MAPK pathway activation (fig. S17G). *KRAS* inactivation led to a strong antiproliferative phenotype in KBM-7^{Cas9} cells and, to a lesser extent, K-562^{Cas9} cells (fig. S18, A and B), indicating that the selective requirement of *KRAS* in mediating *LZTR1*-induced enhanced MAPK pathway activation might represent a prerequisite of *KRAS* for BCR-ABL signaling in CML cells. We additionally used a fibronectin-fold–based monobody, NS1, which bears low nanomolar affinity for the dimerization interface of both KRAS and HRAS and is able to interfere with their signaling activities (*27*). Cells that stably express the NS1 monobody did not show increased activation of the MAPK pathway or drug resistance associated with loss of LZTR1 function (fig. S18, C and D).

More than 50 different mutations have been mapped to the human *LZTR1* gene in various diseases (fig. S19, A and B, and table S5) (*5*, *8*, *11*, *28*–*30*). To establish a mechanistic link between mutations that affect human diseases and the biochemical processes described here, we focused on *LZTR1* missense mutations identified in GBM (*11*), NS (*5*), and SWNMT (*8*) (fig. S20B). Mutation-bearing *LZTR1* cDNAs were tested for their ability to complement K-562 CML cells deficient in endogenous *LZTR1* (fig. S20A). In contrast to WT LZTR1, the disease-associated mutations

Downloaded from http://science.sciencemag.org/ on December 11, 2018

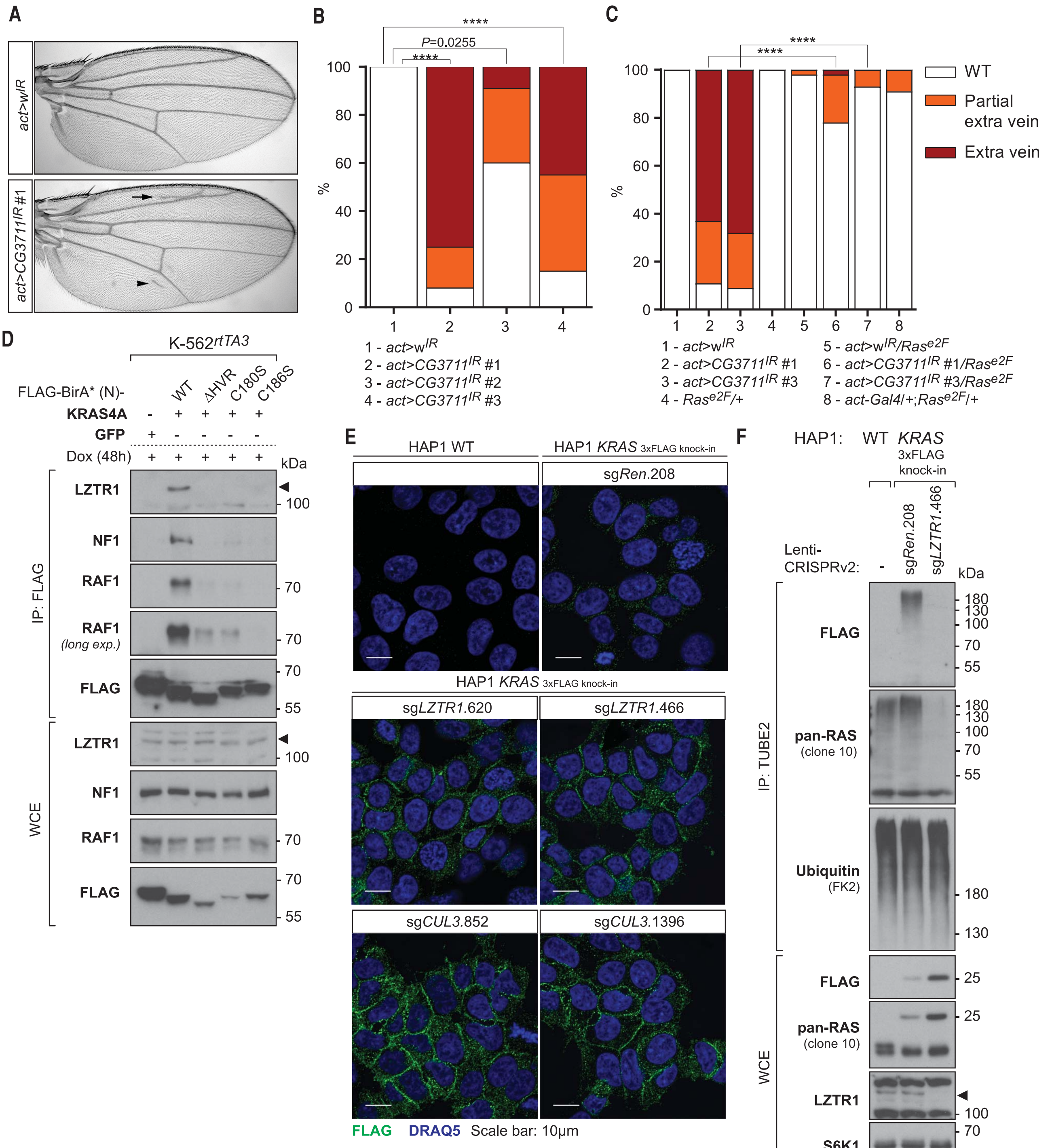

Fig. 3. LZTR1 modulates MAPK pathway activation through RAS regulation. (**A**) Morphology of adult wings from *act5C-Gal4*, *UAS-w^IR* (*act>w^IR* for short), and *act>CG3711^IR* #1 RNAi fly lines. Arrow, extra vein; arrowhead, partial extra vein. (**B**) Quantification of *act>w^IR* and *act>CG3711^IR* RNAi lines as percentage of wings with ectopic wing vein formation. *P* value for RNAi #1 and #3 in the wing is <0.0001 (****) and for #2 is 0.0255. (**C**) Quantification of *act>w^IR* and *act>CG3711^IR* RNAi lines alone or in a *Ras^e2F*/+ background as percentage of wings with ectopic wing vein formation. For statistical assessment, partial extra vein and extra vein formation have been combined. *P* value for both RNAi line comparisons in the wing is <0.0001 (****). (**D**) FLAG immunoprecipitates (IP) and whole-cell extracts (WCE) from K-562^{rtTA3} cells expressing FLAG-BirA*–tagged GFP or KRAS4A WT, ΔHVR, C180S, or C186S after 48 hours of doxycycline treatment were immunoblotted for the indicated proteins. (**E**) Confocal microscopy of HAP1 WT cells and HAP1 cells with endogenously FLAG-tagged KRAS transduced with sg*Ren*.208, sg*LZTR1*.620, sg*LZTR1*.466, sg*CUL3*.852, or sg*CUL3*.1396 and stained with antibody to FLAG. Scale bars, 10 µm. (**F**) TUBE-based purifications of ubiquitinated proteins and WCE from HAP1 WT and endogenously FLAG-tagged KRAS cells transduced with sg*Ren*.208 or sg*LZTR1*.466 were analyzed by means of immunoblotting with the indicated antibodies.

Downloaded from http://science.sciencemag.org/ on December 11, 2018

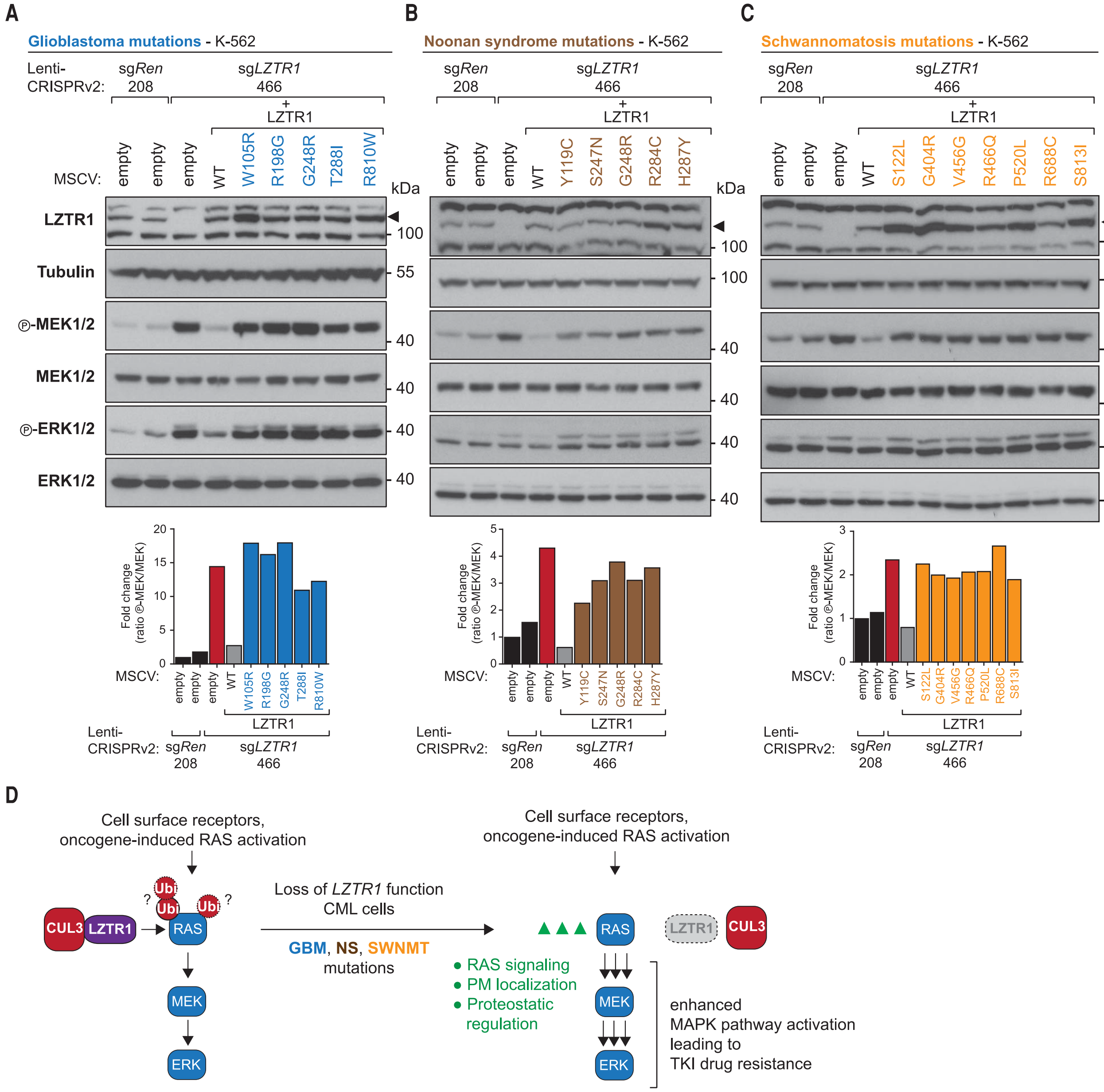

Fig. 4. *LZTR1* disease missense mutations fail to rescue the loss-of-function phenotype. (**A** to **C**) Immunoblotting for MEK and ERK phosphorylation as well as LZTR1 expression of K-562^{Cas9} *sgRen*.208–expressing cells retrovirally transduced with empty vector, and sg*LZTR1*.466-expressing cells transduced with either empty vector, LZTR1 WT, or LZTR1 mutations identified in (A) GBM (blue), (B) NS (brown), or (C) SWNMT (orange). The LZTR1 G248R mutation has been identified in both GBM and NS. Immunoblot results are representative of at least two independent biological experiments ($n \geq 2$), and quantification of MEK phosphorylation in the displayed blots is shown. (**D**) Mechanistic model of CUL3-LZTR1–mediated RAS ubiquitination and enhanced MAPK pathway activation and BCR-ABL inhibitor drug resistance induced by loss of *LZTR1* function.

failed to reduce MAPK pathway activation, despite being expressed at a comparable or higher amount (Fig. 4, A to C). Similarly, all missense mutations apart from the GBM-associated T288I and R810W failed to restore sensitivity to imatinib treatment (fig. S20, C to E). LZTR1 mutations within the Kelch domain partially retained their localization pattern in comparison with the WT protein, whereas mutations in the BTB/BACK domains mislocalized to the cytoplasm (fig. S21, A and B). In agreement, expression of LZTR1 Kelch domain mutations identified in GBM, NS, and SWNMT in K-562 WT cells had a resistance-mediating effect in MCA assays in cells treated with imatinib, whereas BTB/BACK domain mutations did not (fig. S22, A to C). Furthermore, in contrast to the LZTR1 WT protein, the two mutants R198G and G248R identified in GBM and NS failed to induce a similar increase in ubiquitination on KRAS4A (fig. S22D). These findings provide functional evidence that human LZTR1 missense mutations identified in GBM, NS, and SWNMT represent loss-of-function toward ubiquitination and inhibition of RAS activity.

Together with the accompanying manuscript on the role of LZTR1 in diseases driven by the dysregulation of RAS ubiquitination and signaling (*31*), our work illustrates the importance of an additional, underappreciated layer of RAS regulation (Fig. 4D).

REFERENCES AND NOTES

1. R. Ren, *Nat. Rev. Cancer* **5**, 172–183 (2005).
2. T. O'Hare, M. S. Zabriskie, A. M. Eiring, M. W. Deininger, *Nat. Rev. Cancer* **12**, 513–526 (2012).
3. J. E. Carette *et al.*, *Nat. Biotechnol.* **29**, 542–546 (2011).
4. D. K. Simanshu, D. V. Nissley, F. McCormick, *Cell* **170**, 17–33 (2017).
5. G. L. Yamamoto *et al.*, *J. Med. Genet.* **52**, 413–421 (2015).
6. P. Canning *et al.*, *J. Biol. Chem.* **288**, 7803–7814 (2013).

Downloaded from http://science.sciencemag.org/ on December 11, 2018

7. T. G. Nacak, K. Leptien, D. Fellner, H. G. Augustin, J. Kroll, *J. Biol. Chem.* **281**, 5065–5071 (2006).
8. A. Piotrowski *et al.*, *Nat. Genet.* **46**, 182–187 (2014).
9. L. Xu *et al.*, *Nature* **425**, 316–321 (2003).
10. J. E. Carette *et al.*, *Nature* **477**, 340–343 (2011).
11. V. Frattini *et al.*, *Nat. Genet.* **45**, 1141–1149 (2013).
12. W. E. Tidyman, K. A. Rauen, *Curr. Opin. Genet. Dev.* **19**, 230–236 (2009).
13. M. Therrien *et al.*, *Cell* **83**, 879–888 (1995).
14. F. D. Karim *et al.*, *Genetics* **143**, 315–329 (1996).
15. K. Oishi *et al.*, *Hum. Mol. Genet.* **18**, 193–201 (2009).
16. K. Gaengel, M. Mlodzik, *Development* **130**, 5413–5423 (2003).
17. K. E. Brown, M. Freeman, *Development* **130**, 5401–5412 (2003).
18. M. Brockmann *et al.*, *Nature* **546**, 307–311 (2017).
19. A. M. Waters *et al.*, *Sci. Signal.* **10**, eaao3332 (2017).
20. E. J. Bennett, J. Rush, S. P. Gygi, J. W. Harper, *Cell* **143**, 951–965 (2010).
21. N. Jura, E. Scotto-Lavino, A. Sobczyk, D. Bar-Sagi, *Mol. Cell* **21**, 679–687 (2006).
22. H. Yan, M. Jahanshahi, E. A. Horvath, H.-Y. Liu, C. M. Pfleger, *Curr. Biol.* **20**, 1378–1382 (2010).
23. A. T. Sasaki *et al.*, *Sci. Signal.* **4**, ra13 (2011).
24. R. Baker *et al.*, *J. Biol. Chem.* **288**, 36856–36862 (2013).
25. C. M. Rose *et al.*, *Cell Syst.* **3**, 395–403.e4 (2016).
26. R. Hjerpe *et al.*, *EMBO Rep.* **10**, 1250–1258 (2009).
27. R. Spencer-Smith *et al.*, *Nat. Chem. Biol.* **13**, 62–68 (2017).
28. J. J. Johnston *et al.*, *Genet. Med.* **20**, 1175–1185 (2018).
29. S. N. Gröbner *et al.*, *Nature* **555**, 321–327 (2018).
30. Cancer Genome Atlas Research Network, *Cell* **169**, 1327–1341.e23 (2017).
31. M. Steklov *et al.*, *Science* **362**, 1177–1182 (2018).

ACKNOWLEDGMENTS

We are grateful to all members of the Superti-Furga laboratory for help, discussions, and advice; E. Girardi and E. Salzer for critically reading the manuscript; and P. Májek for feedback on the bioinformatic analysis of BioID proteomic experiments. We thank the Biomedical Sequencing Facility for advice on Illumina sequencing and the Core Facility Imaging of the Medical University of Vienna for technical support. **Funding:** This work was supported by the Austrian Academy of Sciences, European Research Council (ERC) grants (i-FIVE 250179 and Game of Gates 695214), and Austrian Science Fund grant (FWF SFB F4711) to G.S.-F; European Molecular Biology Organization long-term fellowships to M.R. (ALTF 1346-2011) and G.I.V. (ALTF 1543-2012); an Austrian Science Fund grant (FWF SFB F4702) to R.K.; NIH grants R01 EY013256 and GM102811 to M.M.; and funding from the CGC.nl, KWF grant NKI 2015-7609, and ERC Starting Grant (ERC-2012-StG 309634) to T.R.B. **Author contributions:** J.W.B. and G.S.-F. conceived the study based on discussions with T.R.B.; J.W.B., F.K., and M.P. performed research; and G.M.C. and M.M. designed and performed *Drosophila* experiments. L.X.H., G.I.V., A.F., M.R., and G.E.W. generated reagents and provided scientific insight. F.S. analyzed haploid genetic screening data and created circos plots and the graphical display of insertion sites. V.S. performed RNA sequencing and enrichment analysis and compiled cBioPortal mutation data. K.P. and A.C.M. performed proteomic sample analysis. V.A.B. and T.R.B. provided reagents and gave experimental advice. R.K. supervised sequencing data analysis and gave experimental advice. J.W.B., G.M.C., F.K., G.I.V., L.X.H., F.S., M.M., and G.S.-F. analyzed and interpreted the data. J.W.B., M.M., and G.S.-F. wrote the paper. **Competing interests:** The authors declare no competing financial interest. T.R.B. is cofounder and SAB member of Haplogen GmbH and cofounder and managing director of Scenic Biotech. G.I.V. is cofounder and employee of Allcyte GmbH. G.S.-F. is cofounder and shareholder of Allcyte GmbH and Haplogen GmbH. **Data and materials availability:** Deep sequencing datasets have been deposited in the National Center for Biotechnology Information Sequence Read Archive under the accession no. SRP157890, and BioID mass spectrometry proteomics data have been deposited to the ProteomeXchange Consortium via the PRIDE partner repository under the accession no. PXD011280. The KBM-7 cell line is available from T.R.B. under a materials transfer agreement with the Netherlands Cancer Institute.

SUPPLEMENTARY MATERIALS

www.sciencemag.org/content/362/6419/1171/suppl/DC1
Materials and Methods
Figs. S1 to S22
Tables S1 to S5
References (*32–59*)

30 August 2017; resubmitted 26 June 2018
Accepted 30 October 2018
Published online 15 November 2018
10.1126/science.aap8210

Downloaded from http://science.sciencemag.org/ on December 11, 2018

SIGNAL TRANSDUCTION

Mutations in LZTR1 drive human disease by dysregulating RAS ubiquitination

M. Steklov[1,2]*, S. Pandolfi[1,2]*, M. F. Baietti[1,2]*, A. Batiuk[1,2], P. Carai[3], P. Najm[1,2], M. Zhang[4], H. Jang[4], F. Renzi[1,2], Y. Cai[1,2], L. Abbasi Asbagh[1,2], T. Pastor[1,2], M. De Troyer[1,2], M. Simicek[1,2], E. Radaelli[5], H. Brems[5], E. Legius[5], J. Tavernier[6,7], K. Gevaert[6,7], F. Impens[8], L. Messiaen[5,9], R. Nussinov[4,10], S. Heymans[3,11,12], S. Eyckerman[6,7], A. A. Sablina[1,2]†

The leucine zipper–like transcriptional regulator 1 (LZTR1) protein, an adaptor for cullin 3 (CUL3) ubiquitin ligase complex, is implicated in human disease, yet its mechanism of action remains unknown. We found that Lztr1 haploinsufficiency in mice recapitulates Noonan syndrome phenotypes, whereas LZTR1 loss in Schwann cells drives dedifferentiation and proliferation. By trapping LZTR1 complexes from intact mammalian cells, we identified the guanosine triphosphatase RAS as a substrate for the LZTR1-CUL3 complex. Ubiquitome analysis showed that loss of Lztr1 abrogated Ras ubiquitination at lysine-170. LZTR1-mediated ubiquitination inhibited RAS signaling by attenuating its association with the membrane. Disease-associated *LZTR1* mutations disrupted either LZTR1-CUL3 complex formation or its interaction with RAS proteins. RAS regulation by LZTR1-mediated ubiquitination provides an explanation for the role of LZTR1 in human disease.

Mutations concurrent with loss of heterozygosity at leucine zipper–like transcriptional regulator 1 (*LZTR1*) are associated with glioblastoma and schwannomatosis (*1*–*3*). LZTR1 mutations predispose for pediatric neoplasms and are increased over background in liver and testicular cancers (*4*, *5*). The most recurrent LZTR1 mutation in cancer is an inactivating splice-site mutation at codon 217 (fig. S1) (*4*, *6*). LZTR1 constitutes to Noonan syndrome caused by dysregulation of the guanosine triphosphatase RAS (*7*–*9*). However, how LZTR1 contributes to human disease is not known.

To uncover Lztr1 disease mechanisms, we used an Lztr1 deletion mouse model. We found that loss of Lztr1 is lethal between embryonic day 17.5 (E17.5) and birth (fig. S2A). *Lztr1*$^{+/-}$ male mice exhibited decreased weight (fig. S2, B to D) and facial dysmorphia (Fig. 1A). *Lztr1*$^{+/-}$ mice, both male and female, displayed heart malformations, including decreased left ventricular systolic function, increased diastolic dimensions, eccentric hypertrophy, increased cardiomyocyte area, and reduced longevity (Fig. 1, B and C, and fig. S2, E and F). Collectively, our results show that *Lztr1*$^{+/-}$ mice recapitulate some phenotypes of human Noonan syndrome patients, indicating that LZTR1 function is evolutionary conserved.

We engineered several cellular models of LZTR1 loss: mouse embryo fibroblasts (MEFs) derived from *Lztr1*$^{+/+}$ and *Lztr1*$^{-/-}$ mouse embryos, primary human Schwann cells expressing short hairpin green fluorescent protein (shGFP) or shLZTR1, and immortalized human Schwann cells and HeLa cells with CRISPR-Cas9–mediated LZTR1-indels (fig. S3). In all tested models, LZTR1 loss increased growth rate (Fig. 1D and fig. S4, A to C). Overexpression of wild-type LZTR1 (wt-LZTR1), but not of LZTR1 mutants, reduced the enhanced growth rate (Fig. 1E and fig. S4, D and E). Loss of LZTR1 in Schwann cells enhanced two-dimensional colony and anchorage-independent (AI) growth (Fig. 1F and fig. S4, F to H), and overexpression of wt-LZTR1, but not of disease-associated

Downloaded from http://science.sciencemag.org/ on December 11, 2018

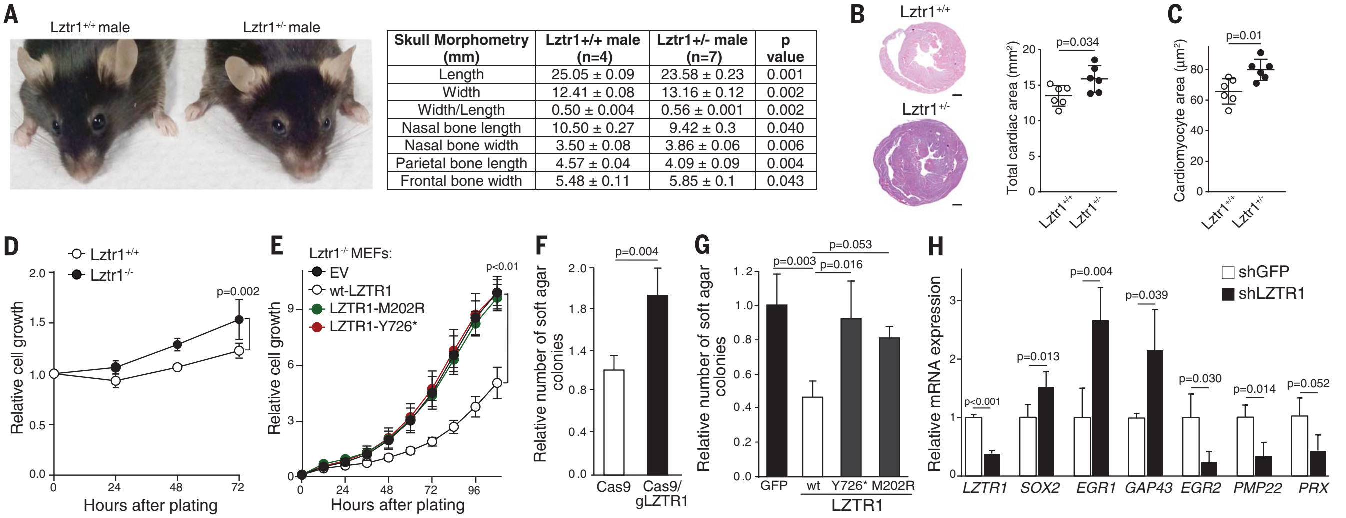

Skull Morphometry (mm)	Lztr1+/+ male (n=4)	Lztr1+/- male (n=7)	p value
Length	25.05 ± 0.09	23.58 ± 0.23	0.001
Width	12.41 ± 0.08	13.16 ± 0.12	0.002
Width/Length	0.50 ± 0.004	0.56 ± 0.001	0.002
Nasal bone length	10.50 ± 0.27	9.42 ± 0.3	0.040
Nasal bone width	3.50 ± 0.08	3.86 ± 0.06	0.006
Parietal bone length	4.57 ± 0.04	4.09 ± 0.09	0.004
Frontal bone width	5.48 ± 0.11	5.85 ± 0.1	0.043

Fig. 1. LZTR1 loss recapitulates disease phenotypes. (**A**) Morphometric characteristics of the skulls of 12-month-old *Lztr1*$^{+/+}$ and *Lztr1*$^{+/-}$ male mice. (**B**) Haematoxylin and eosin–stained heart ventricular sections. Scale bar, 0.5 mm. The total cardiac area was quantified by Fiji. In the graph, horizontal lines represent means ± SD. (**C**) A mean area of 200 cardiomyocytes measured in laminin-stained heart sections of *Lztr1*$^{+/+}$ and *Lztr1*$^{+/-}$ mice. Horizontal lines represent means ± SD. (**D**) Growth rate of early-passage MEFs isolated from three *Lztr1*$^{+/+}$ and three *Lztr1*$^{-/-}$ embryos. (**E**) Growth rate of *Lztr1*$^{-/-}$ MEFs expressing an empty vector (EV), wt-LZTR1, or LZTR1 mutants. $n = 3$. (**F**) AI growth of Schwann cells expressing Cas9 or Cas9/gLZTR1 (gLZTR1, guide RNA targeting LZTR1). $n = 3$. (**G**) AI growth of LZTR1-indel Schwann cells expressing the indicated constructs. $n = 3$. M202R, Met^{202}→Arg. (**H**) Quantitative real time polymerase chain reaction (qRT-PCR) analysis of mRNA expression in primary human Schwann cells expressing shGFP or pooled shLZTR1. $n = 3$. For (D) to (H), values are means ± SEM. For (A) to (C) and (F) to (H), P values are from a two-sided Student's t test. For (D) and (E), P values were detected by two-way analysis of variance (ANOVA).

LZTR1 mutants, suppressed AI growth in LZTR1-indel cells (Fig. 1G). Furthermore, depletion of LZTR1 in Schwann cells showed a gene expression signature (Fig. 1H) resembling that of proliferating Schwann cells during nerve regeneration (*10*). These data suggest that LZTR1 loss drives Schwann cells from quiescent, myelinating cells into proliferating cells.

LZTR1 acts a substrate adaptor for cullin 3 (CUL3) ubiquitin ligase complexes (*11*). To identify candidate LZTR1 substrates, we used a mass spectrometry (MS) Virotrap method, which allowed the trapping of protein complexes from intact mammalian cells (fig. S5A) (*12*). The screen with LZTR1 as bait detected CUL3, Harvey rat sarcoma viral oncogene homolog (HRAS), and neuroblastoma RAS viral oncogene homolog (NRAS) among the top hits (Fig. 2A). The reciprocal Virotrap screen with the HRAS-deltaCAAX mutant, which lacks the last four amino acids, confirmed the complex formation with LZTR1 and identified CUL3 (Fig. 2B). Furthermore, a panRAS antibody that recognizes all RAS isoforms coimmunoprecipitated with hemagglutinin (HA)–tagged LZTR1. Similarly, Flag-tagged LZTR1 coimmunoprecipitated with endogenous RAS proteins, but not RAC1 (fig. S5B). Moreover, we introduced a Halo-tag HiBiT (*13*) to the *LZTR1* locus in HeLa cells and MEFs (Fig. 2C and fig. S5, C and D). panRAS antibody coimmunoprecipitated with endogenous RAS and endogenous HiBiT-LZTR1 (Fig. 2C and fig. S5E). Reciprocal coimmunoprecipitations (co-IPs) demonstrated that LZTR1 interacted with each of the three Flag-RAS isoforms (fig. S5F). Together, these results indicate that LZTR1, CUL3, and RAS form a complex.

To test whether the LZTR1-CUL3 complex might control RAS ubiquitination, we performed an in vitro ubiquitination reaction. We observed ubiquitination of wt-HRAS specifically in the presence of the LZTR1-CUL3 complex (fig. S6A). Coexpression of LZTR1 and CUL3 in human embryonic kidney (HEK) 293T cells increased amounts of ubiquitinated RAS (Fig. 2D and fig. S6B). By contrast, treatment with the cullin

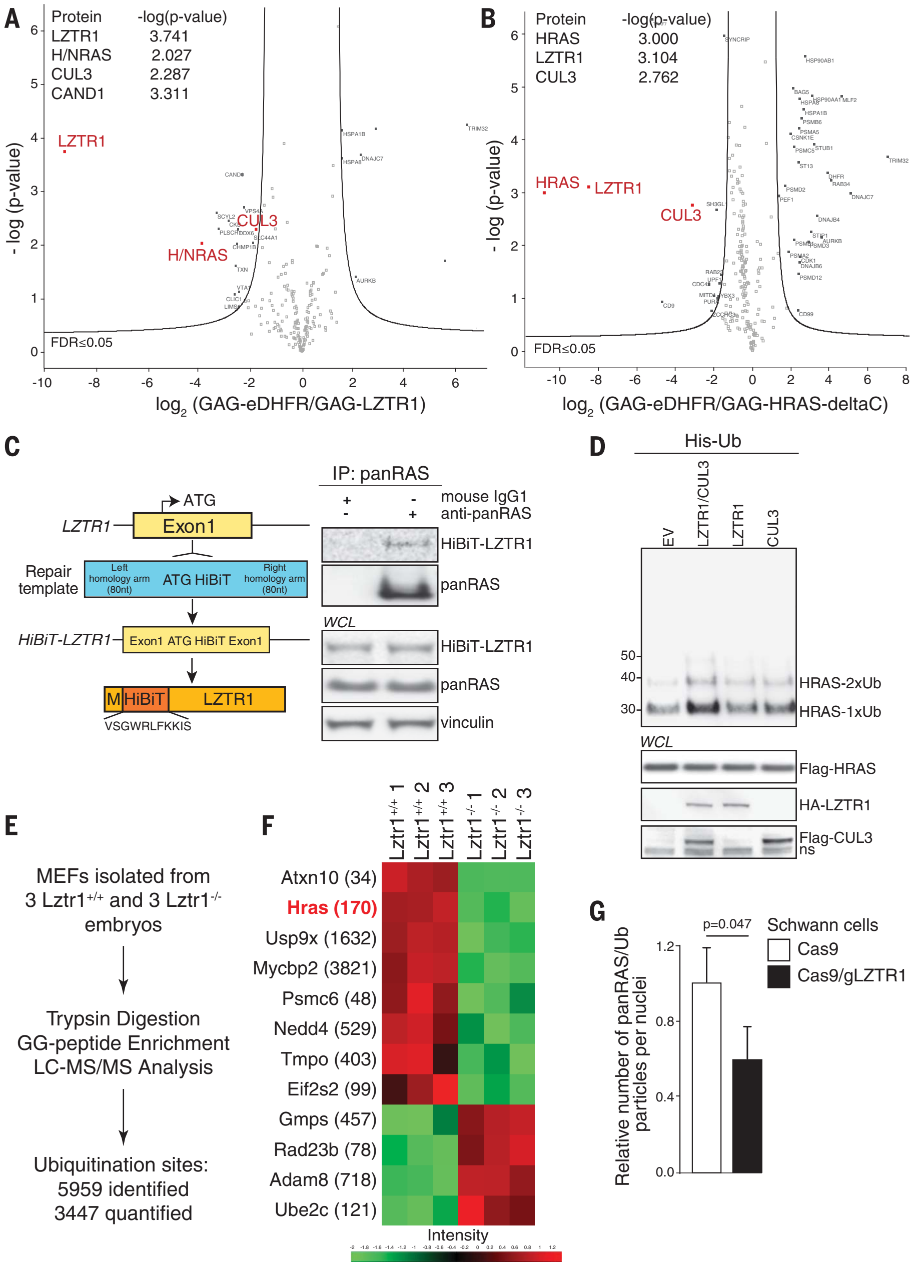

Fig. 2. The LZTR1-CUL3 complex ubiquitinates RAS proteins. (**A** and **B**) Virotrap screens performed in HEK293T cells using group-specific antigen (GAG)–LZTR1 (A) or GAG-HRAS–deltaCAAX (deltaC) (B) as baits. *Escherichia coli* dihydrofolate reductase (eDHFR) fused to GAG was used as a negative control. (**C**) A scheme for the generation of cells expressing in-frame HiBiT-LZTR1 protein. RAS was immunoprecipitated from the HiBiT-LZTR1 edited HeLa cell lysates with panRAS antibody. Luminescent signal was generated by HiBiT incubated with LgBiT. nt, nucleotide. (**D**) Ubiquitinated RAS was purified from HEK293T cells expressing the indicated constructs by Co^{2+} metal affinity chromatography and detected by immunoblotting. Numbers on the left are molecular masses in kDa. 2xUb, two Ub; 1xUb, one Ub; EV, empty vector, WCL, whole-cell lysate; ns, nonspecific. (**E**) A workflow for the ubiquitome analysis. LC-MS/MS, liquid chromatography–tandem mass spectrometry. (**F**) A heatmap showing differentially ubiquitinated peptides in *Lztr1*$^{+/+}$ and *Lztr1*$^{-/-}$ MEFs. The scale shows *Z*-scored site intensity values. (**G**) The quantification of the PLA analysis of Schwann cells expressing Cas9 or Cas9/gLZTR1 using antibodies against panRAS and Ub. Values are means ± SEM; *n* = 3. *P* values are from a two-sided Student's *t* test. Single-letter abbreviations for the amino acid residues are as follows: A, Ala; C, Cys; D, Asp; E, Glu; F, Phe; G, Gly; H, His; I, Ile; K, Lys; L, Leu; M, Met; N, Asn; P, Pro; Q, Gln; R, Arg; S, Ser; T, Thr; V, Val; W, Trp; and Y, Tyr.

---

[1]VIB-KU Leuven Center for Cancer Biology, VIB, 3000 Leuven, Belgium. [2]Department of Oncology, KU Leuven, Herestraat 49, 3000 Leuven, Belgium. [3]Department of Cardiovascular Sciences, Centre for Molecular and Vascular Biology, KU Leuven, Herestraat 49, 3000 Leuven, Belgium. [4]Cancer and Inflammation Program, Leidos Biomedical Research, Inc., Frederick National Laboratory for Cancer Research, National Cancer Institute at Frederick, Frederick, MD 21702, USA. [5]Department of Human Genetics, KU Leuven, Herestraat 49, 3000 Leuven, Belgium. [6]VIB Medical Biotechnology Center, Albert Baertsoenkaai 3, 9000 Ghent, Belgium. [7]Department of Biochemistry, Ghent University, Albert Baertsoenkaai 3, 9000 Ghent, Belgium. [8]VIB Proteomics Core, Albert Baertsoenkaai 3, 9000 Ghent, Belgium. [9]Department of Genetics, University of Alabama, Birmingham, AL 35294, USA. [10]Department of Human Molecular Genetics and Biochemistry, Sackler School of Medicine, Tel Aviv University, Tel Aviv 69978, Israel. [11]Department of Cardiology, CARIM School for Cardiovascular Diseases Faculty of Health, Medicine and Life Sciences, Maastricht University, Netherlands. [12]The Netherlands Heart Institute, Nl-HI, Utrecht, Netherlands.
*These authors equally contributed to this work.
†Corresponding author. Email: anna.sablina@kuleuven.vib.be

Downloaded from http://science.sciencemag.org/ on December 11, 2018

neddylation inhibitor MLN4924 or loss of LZTR1 led to decreased ubiquitination of all Flag-tagged RAS protein isoforms (fig. S6, C to F). Thus, the LZTR1-CUL3 complex can promote ubiquitination of RAS.

To investigate the role of LZTR1 in ubiquitination of endogenous RAS, we characterized ubiquitination profiles of *Lztr1*$^{+/+}$ and *Lztr1*$^{-/-}$ MEFs by MS (Fig. 2E). Ubiquitome analysis revealed that ubiquitination of Hras at Lys^{170} (K170) was abrogated in MEFs lacking Lztr1 (Fig. 2F and fig. S6G), indicating that endogenous Ras may serve as a substrate for the LZTR1-CUL3 complex. We also optimized a proximity ligation assay (PLA) with paired antibodies to ubiquitin (Ub) and panRAS. Consistent with the MS results, Hras-K170R (Lys^{170}→Arg) knock-in or depletion of LZTR1 led to a decrease in panRAS-Ub proximity signals (Fig. 2G and fig. S7). MS analyses failed to detect any C-terminal peptides of Nras or Kras, perhaps because these isoforms are not highly expressed in MEFs and their C termini are lysine-rich (fig. S8A). However, LZTR1 interacted with (fig. S5F) and ubiquitinated all three RAS isoforms (fig. S6F), consistent with evolutionary conservation of K170 (fig. S8D). Thus, the LZTR1-CUL3 complex appears to mediate ubiquitination of all RAS isoforms.

Although multiple truncating and missense mutations of *LZTR1* have been reported in Noonan syndrome and schwannomatosis (*1*–*3*, *14*), no recurrent germline *LZTR1* mutations have been identified to date. Additional sequencing analysis of blood samples from schwannomatosis patients revealed several recurrent germline mutations of *LZTR1* within the BTB (broad-complex, tramtrack, and bric-a-brac)–BACK domains predicted to mediate dimerization and CUL3 binding (*11*, *15*) (Fig. 3A). Concordantly, the BTB-BACK LZTR1 mutants, except L812P (Leu^{812}→Pro), exhibited reduced binding to CUL3 (Fig. 3B and fig. S9A). Although LZTR1-L812P retained interaction with CUL3, it failed to form dimers (Fig. 3C). Oligomerization of BTB domains determines the subcellular distribution of CUL3 adaptors (*15*, *16*). Indeed, both endogenous and ectopically expressed HA-tagged LZTR1 showed punctate endomembrane immunostaining (fig. S9B), whereas the BTB-BACK domain LZTR1 mutants, including LTZR1-L812P, showed diffuse cytoplasmic staining (Fig. 3D and fig. S9C).

Missense mutations within the LZTR1 Kelch domain predicted to mediate substrate binding are also found in human disease. In co-IP assays, Kelch domain LZTR1 mutants showed decreased binding to RAS (Fig. 3E). The Kelch domain mutants, like wt-LZTR1, displayed punctate immunostaining, but only wt-LZTR1 led to relocalization of RAS to the LZTR1-CUL3–containing puncta, which represent loci of LZTR1-CUL3–mediated ubiquitination (Fig. 3F and fig. S9, D and E). Consistently, the LZTR1-L812P mutant, which does not form puncta, only weakly ubiquitinated RAS, as did the LZTR1-Y726* (Tyr^{726}→Stop) mutant (Fig. 3G). Thus, disease-associated LZTR1 mutations appear to abrogate RAS ubiquitination by disrupting the formation of the RAS-LZTR1-CUL3 complex.

RAS ubiquitination affects RAS–mitogen-activated protein kinase (MAPK) signaling (*17*). Loss of LZTR1 led to increased RAS activity and phosphorylation of MEK1/MEK2 and ERK1/ERK2 in all tested model systems, whereas enhanced phosphorylation of V-Akt murine thymoma viral oncogene homolog (AKT) was cell dependent (Fig. 4A and fig. S10). After serum stimulation, *Lztr1*$^{-/-}$ MEFs showed higher MEK1/MEK2 activity at all time points, whereas *Lztr1*$^{+/-}$ MEFs had higher MEK1/MEK2 phosphorylation only at later time points (fig. S11A). Thus, Lztr1 abundance may fine-tune the activation of Ras signaling. Restoration of wt-LZTR1 expression in LZTR1-indel cells decreased MEK1/MEK2 activity (fig. S11B). Finally, LZTR1-mutated schwannomas showed strong

Downloaded from http://science.sciencemag.org/ on December 11, 2018

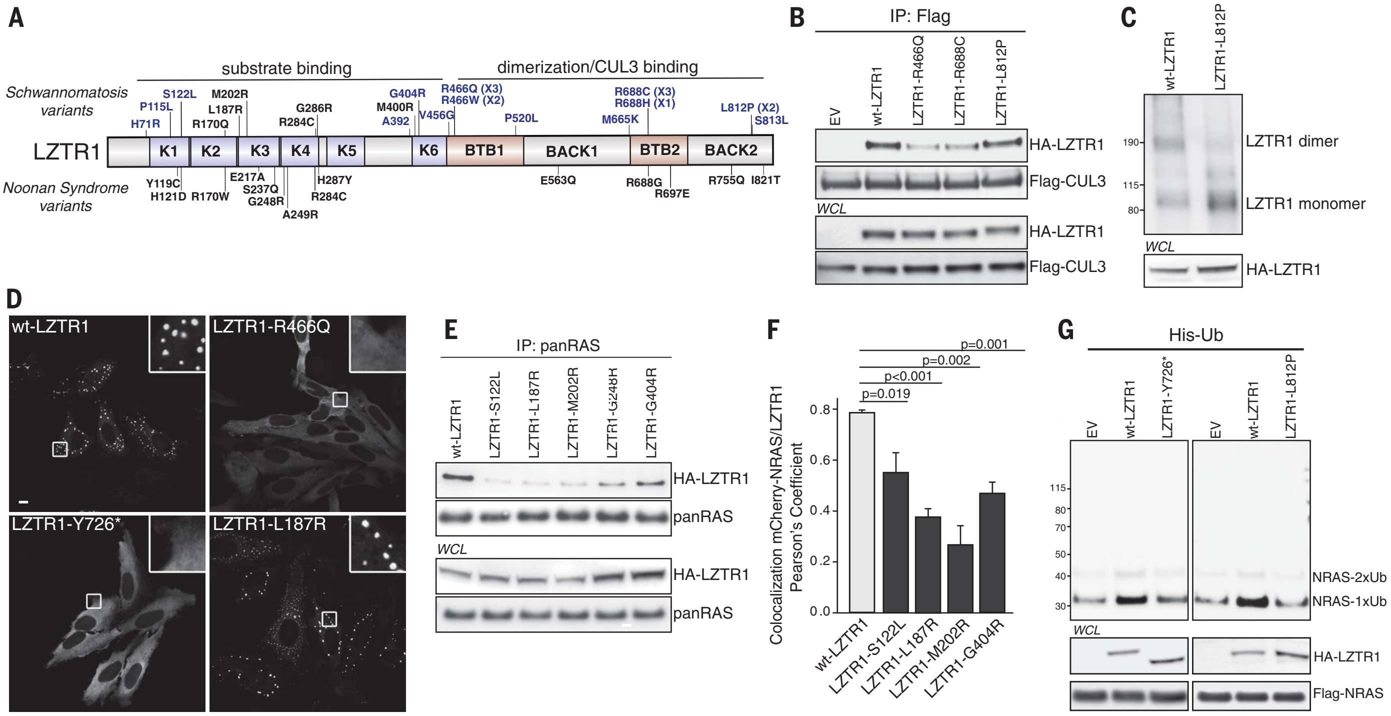

Fig. 3. Disease-associated LZTR1 mutations are loss of function. (**A**) LZTR1 mutations in schwannomatosis and Noonan syndrome individuals. Missense LZTR1 mutations identified in our cohort of schwannomatosis patients are shown in blue. In the schematic, K indicates Kelch domain. See Fig. 2 legend for amino acid abbreviations. (**B**) Flag-tagged CUL3 purified from HEK293T cells was incubated with HA-tagged LZTR1-overexpressing cell lysates and then immunoprecipitated using anti-Flag resin. LZTR1 was detected by immunoblotting with anti-HA antibody. (**C**) Cross-linking reactions were performed using HA-tagged LZTR1 purified from HEK293T cells. LZTR1 was detected by immunoblotting using anti-HA antibody. (**D**) Immunostaining of HeLa cells expressing HA-tagged wt-LZTR1 or LZTR1 mutants with anti-HA antibody. Scale bar, 10 μm. (**E**) RAS proteins were immunoprecipitated with antibody against panRAS. LZTR1 was detected by immunoblotting with anti-HA antibody. (**F**) Colocalization of mCherry-NRAS and HA-tagged LZTR1 expressed in HeLa-Cas9/gLZTR1 cells. Values are means ± SEM. *P* values were detected by two-sided Student's *t* test. (**G**) Ubiquitinated NRAS was purified from HEK293T cells expressing the indicated constructs by Co^{2+} metal affinity chromatography and detected by anti-Flag antibody.

staining of phosphorylated ERK1/ERK2 compared to wt-LZTR1 nerve trunk (fig. S11, C and D). The MEK1 inhibitor pimasertib abolished the colony growth difference between wt-LZTR1 and LZTR1-mutant cells (fig. S11E). Pimasertib treatment also rescued the embryonic lethality of *Lztr1*$^{-/-}$ mice (Fig. 4B). Thus, LZTR1-mediated phenotypes arise, at least in part, from increased RAS signaling.

Although our MS analysis detected Ras ubiquitination at several lysines, loss of Lztr1 abrogated ubiquitination of Ras only at K170 (Fig. 4C). Thus, ubiquitination of Hras at K170 may specifically require Lzrt1. Indeed, though LZTR1 depletion hindered ubiquitination of wt-HRAS, it did not affect ubiquitination of the HRAS-K170R mutant (Fig. 4D). Loss of LZTR1 also abolished the difference in Ras ubiquitination between wt-Hras and Hras-K170R MEFs (Fig. 4E and fig. S12A). Nonetheless, the LZTR1-CUL3 complex did ubiquitinate mutant HRAS-K170R in vitro (fig. S6A). The site specificity in vivo could be directed by anchoring of RAS to the membrane. Moreover, overexpression of the HRAS-K170R mutant led to higher activation of ERK1/ERK2 than did overexpression of wt-HRAS, and LZTR1 depletion did not affect ERK1/ERK2 activity in cells overexpressing HRAS-K170R (Fig. 4F and fig. S12B). K170R knock-in MEFs also showed increased MAPK signaling and growth rates (fig. S12, C and D). Collectively, these data indicate that LZTR1-mediated ubiquitination of RAS at K170 suppresses RAS-MAPK signaling.

Ubiquitination of RAS can inhibit its activity by triggering its degradation (*18*). However, quantitative MS analysis did not reveal an increase in RAS protein abundance in *Lztr1*$^{-/-}$ MEFs (fig. S6G). wt-LZTR1 and LZTR1-indel Schwann cells treated with the protein synthesis inhibitor cycloheximide also showed similar RAS stability (fig. S12E), Thus, LZTR1 regulates RAS by a

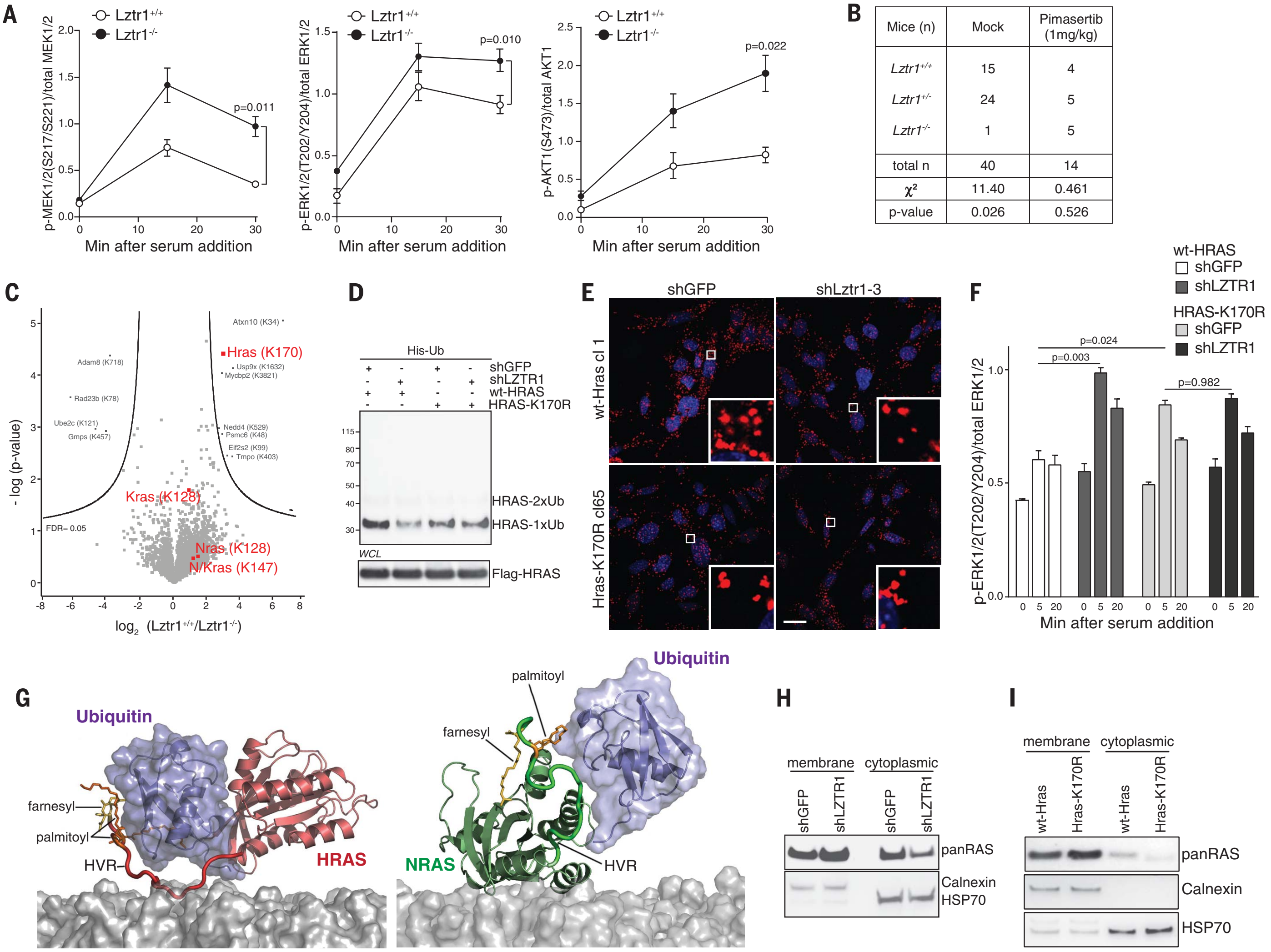

Mice (n)	Mock	Pimasertib (1mg/kg)
Lztr1$^{+/+}$	15	4
Lztr1$^{+/-}$	24	5
Lztr1$^{-/-}$	1	5
total n	40	14
χ^2	11.40	0.461
p-value	0.026	0.526

Fig. 4. Ubiquitination at K170 inhibits RAS by impairing its association to the membrane. (**A**) MEFs isolated from three *Lztr1*$^{+/+}$ and three *Lztr1*$^{-/-}$ embryos were serum-starved, stimulated with 10% serum, and analyzed by immunoblotting. Values are means of phosphorylated (p) relative to nonphosphorylated protein levels ± SEM. *P* values are from a two-way ANOVA. (**B**) Progeny from the indicated *Lztr1*$^{+/-}$ matings. Pregnant mice were treated with pimasertib starting from E7.5. (**C**) Quantitative ubiquitome analysis of *Lztr1*$^{+/+}$ and *Lztr1*$^{-/-}$ MEFs. FDR, false discovery rate. (**D**) Ubiquitinated RAS was purified from HEK293T cells expressing the indicated constructs by Co^{2+} metal affinity chromatography and detected by immunoblotting. (**E**) The PLA analysis of wt-Hras and Hras-K170R MEFs expressing shGFP or shLztr1 using antibodies against panRAS and Ub. Red, PLA signal; blue, 4′,6-diamidino-2-phenylindole; scale bar, 10 μm. (**F**) HEK293T cells expressing the indicated constructs were serum-starved overnight, stimulated with 10% serum, and analyzed by immunoblotting. Values are means of phosphorylated relative to nonphosphorylated protein levels ± SEM; *n* = 3. *P* values are from a two-way ANOVA. (**G**) Snapshots of Ub-conjugated RAS at the lipid bilayer composed of 1,2-dioleoyl-*sn*-glycero-3-phosphocholine (DOPC) and 1,2-dioleoyl-*sn*-glycero-3-phosphoethanolamine (DOPE) lipids (3:1 molar ratio). (**H** and **I**) Immunoblotting of the membrane and cytoplasmic fractions isolated from HeLa cells expressing shGFP and shLZTR1 (H) or wt-Hras and Hras-K170R MEFs (I). HSP70, heat shock protein 70.

Downloaded from http://science.sciencemag.org/ on December 11, 2018

nondegradative mechanism. Ubiquitination of RAS also induces its relocalization to endomembranes (*19*, *20*). However, LZTR1 overexpression increased the endomembrane fraction of both wt-RAS and the HRAS-K170R mutant (fig. S12F). LZTR1 alone also only slightly increased RAS ubiquitination (Fig. 2D) and did not affect the MAPK pathway (fig. S12G), suggesting that LZTR1 overexpression promotes endomembrane localization of RAS independently of its ability to mediate ubiquitination at K170.

To assess how ubiquitination of RAS at K170 controls its activity, we elucidated modes of the interaction between RAS and conjugated Ub. LZTR1 colocalized with NRAS at RAB11–Transferrin receptor–positive recycling endosomes (fig. S13), suggesting that LZTR1 regulates ubiquitination of farnesylated and palmitoylated RAS. Therefore, we performed molecular simulations on lipidated RAS. In the initial structures of Ub conjugated to K170 of RAS, the hypervariable regions (HVRs) of RAS exposed their anchor portions to the solution. The long-lasting simulations showed that Ub secured the anchor portion of the HVR by sequestering the farnesyl and palmitoyl groups (fig. S14). Concordantly to a rapid kinetics of spontaneous insertion of lipidated RAS into the membrane (*21*–*24*), the HVRs of nonubiquitinated RAS straightforwardly associated with membranes. However, Ub conjugation to K170 of RAS prevented the HVRs from binding to and inserting into membranes (Fig. 4G). Thus, ubiquitination at K170 may disrupt the association of RAS to the membrane. Indeed, loss of LZTR1 or Hras-K170R knock-in increased the fraction of membrane-bound RAS (Fig. 4, H and I, and fig. S15). These results are all consistent with RAS ubiquitination at K170 inhibiting RAS activity by impairing its association with the membrane.

Our results indicate that LZTR1-mediated ubiquitination of RAS on K170 modulates RAS activity, dysregulation of which leads to human disease. An accompanying study shows that LZTR1 dysregulation also confers drug resistance (*25*). Understanding this unconventional mechanism of RAS activation may help to identify patients who might benefit from RAS pathway inhibitors and inform new therapeutic approaches for these patients.

REFERENCES AND NOTES

1. I. Paganini *et al.*, *Eur. J. Hum. Genet.* **23**, 963–968 (2015).
2. A. Piotrowski *et al.*, *Nat. Genet.* **46**, 182–187 (2014).
3. M. J. Smith *et al.*, *Neurology* **84**, 141–147 (2015).
4. Cancer Genome Atlas Research Network, *Cell* **169**, 1327–1341.e23 (2017).
5. Z. Ge *et al.*, *Cell Rep.* **23**, 213–226.e3 (2018).
6. A. K. Witkiewicz *et al.*, *Nat. Commun.* **6**, 6744 (2015).
7. P. C. Chen *et al.*, *Proc. Natl. Acad. Sci. U.S.A.* **111**, 11473–11478 (2014).
8. J. J. Johnston *et al.*, *Genet. Med.* **20**, 1175–1185 (2018).
9. G. L. Yamamoto *et al.*, *J. Med. Genet.* **52**, 413–421 (2015).
10. K. R. Jessen, R. Mirsky, *J. Anat.* **200**, 367–376 (2002).
11. P. J. Stogios, G. S. Downs, J. J. S. Jauhal, S. K. Nandra, G. G. Privé, *Genome Biol.* **6**, R82 (2005).
12. S. Eyckerman *et al.*, *Nat. Commun.* **7**, 11416 (2016).
13. M. K. Schwinn *et al.*, *ACS Chem. Biol.* **13**, 467–474 (2018).
14. S. Hutter *et al.*, *Acta Neuropathol.* **128**, 449–452 (2014).
15. P. Genschik, I. Sumara, E. Lechner, *EMBO J.* **32**, 2307–2320 (2013).
16. M. R. Marzahn *et al.*, *EMBO J.* **35**, 1254–1275 (2016).
17. L. K. Nguyen, W. Kolch, B. N. Kholodenko, *Cell Commun. Signal.* **11**, 52 (2013).
18. T. Zeng *et al.*, *Cell Rep.* **7**, 871–882 (2014).
19. L. Xu, V. Lubkov, L. J. Taylor, D. Bar-Sagi, *Curr. Biol.* **20**, 1372–1377 (2010).
20. H. Yan, M. Jahanshahi, E. A. Horvath, H. Y. Liu, C. M. Pfleger, *Curr. Biol.* **20**, 1378–1382 (2010).
21. H. Jang *et al.*, *J. Biol. Chem.* **290**, 9465–9477 (2015).
22. H. Jang, A. Banerjee, T. Chavan, V. Gaponenko, R. Nussinov, *J. Biol. Chem.* **292**, 12544–12559 (2017).
23. H. Jang *et al.*, *FASEB J.* **30**, 1643–1655 (2016).
24. H. Jang, S. Muratcioglu, A. Gursoy, O. Keskin, R. Nussinov, *Biochem. J.* **473**, 1719–1732 (2016).
25. J. W. Bigenzahn *et al.*, **362**, 1171–1177 (2018).

ACKNOWLEDGMENTS

We thank R. Sciot for providing us with nerve trunk samples and N. Samyn for technical support in performing Virotrap experiments. **Funding:** H2020 European Research Council (ub-RASDisease) (A.A.S.), Research Foundation Flanders (FWO) fellowships (M.F.B.), FWO Research project G068715N (A.A.S.), and Stichting Tegen Kanker F/2014/257 (A.A.S.); European Research Council FP7 305507 (HOMAGE) (S.H.); FP7-Health-2013-Innovations-1 602156 (HECATOS) (S.H.); the Netherlands Cardiovascular Research Initiative, the Dutch Heart Foundation, CVON2011-ARENA (S.H.), CVON2016-Early HFPEF (S.H.), CVON 2017 (S.H.), ShePREDICTS (S.H.), and CVON2017-ARENA PRIME (S.H.); and federal funds from the Frederick National Laboratory for Cancer Research, NIH, under contract HHSN261200800001E (R.N.), and the Intramural Research Program of the NIH Frederick National Laboratory, Center for Cancer Research (R.N.). The content of this publication does not necessarily reflect the views or policies of the U.S. Department of Health and Human Services nor does mention of trade names, commercial products, or organizations imply endorsement by the U.S. government. All simulations were performed using the high-performance computational facilities of the Biowulf PC/Linux cluster at the National Institutes of Health, Bethesda, MD (https://hpc.nih.gov/). **Author contributions**: M.St., F.R., S.P., and M.Si. performed biochemical experiments; M.St., M.F.B., and S.P. performed cellular experiments; M.F.B. and T.P. performed qRT-PCR analysis; M.F.B. performed PLA analyses; M.F.B. and P.N. performed immunofluorescence experiments; S.P. and M.D.T. performed mice experiments; A.B. and Y.C. generated CRISPR clones; L.A.A. performed experiments on nonimmortalized Schwann cells; E.R. and P.C. performed the immunohistochemistry staining and analysis; S.E., K.G., and J.T. designed and performed the Virotrap screen; F.I. performed the MS analysis; L.M., E.L., and N.R. performed mutation analysis of schwannomatosis patients; R.N., M.Z., and H.J. performed protein simulations; P.C. and S.H. performed the echocardiography analysis; M.St., M.F.B., S.P., and A.A.S. analyzed the data; and A.A.S. wrote the manuscript. All authors discussed the results and commented on the manuscript. **Competing interests:** No potential conflict of interest was reported by the authors. **Data and materials availability:** We thank the EUCOMM Consortium for providing us $Lztr1^{tm1a(EUCOMM)Wtsi}$ embryonic stem cells. $Lztr1^{tm1a(EUCOMM)Wtsi}$ embryonic stem cells are available from EUCOMM under a material transfer agreement with the EUCOMM Consortium.

SUPPLEMENTARY MATERIALS

www.sciencemag.org/content/362/6419/1177/suppl/DC1
Materials and Methods
Figs. S1 to S15
References (*26*–*41*)

30 August 2017; resubmitted 31 May 2018
Accepted 30 October 2018
Published online 15 November 2018
10.1126/science.aap7607

Downloaded from http://science.sciencemag.org/ on December 11, 2018

MOLECULAR BIOLOGY

A DNA methylation reader complex that enhances gene transcription

C. Jake Harris[1]*, Marion Scheibe[2]*, Somsakul Pop Wongpalee[1]†, Wanlu Liu[1], Evan M. Cornett[3], Robert M. Vaughan[3], Xueqin Li[4], Wei Chen[4], Yan Xue[1], Zhenhui Zhong[1,5], Linda Yen[1], William D. Barshop[6], Shima Rayatpisheh[6]‡, Javier Gallego-Bartolome[1], Martin Groth[1]§, Zonghua Wang[5,7], James A. Wohlschlegel[6], Jiamu Du[4], Scott B. Rothbart[3], Falk Butter[2]||, Steven E. Jacobsen[1,8]||

DNA methylation generally functions as a repressive transcriptional signal, but it is also known to activate gene expression. In either case, the downstream factors remain largely unknown. By using comparative interactomics, we isolated proteins in *Arabidopsis thaliana* that associate with methylated DNA. Two SU(VAR)3-9 homologs, the transcriptional antisilencing factor SUVH1, and SUVH3, were among the methyl reader candidates. SUVH1 and SUVH3 bound methylated DNA in vitro, were associated with euchromatic methylation in vivo, and formed a complex with two DNAJ domain-containing homologs, DNAJ1 and DNAJ2. Ectopic recruitment of DNAJ1 enhanced gene transcription in plants, yeast, and mammals. Thus, the SUVH proteins bind to methylated DNA and recruit the DNAJ proteins to enhance proximal gene expression, thereby counteracting the repressive effects of transposon insertion near genes.

DNA methylation frequently marks transposable elements (TEs) in eukaryotic genomes (*1*–*3*). In plants, the RNA-directed DNA methylation (RdDM) pathway is responsible for the initial establishment of methylation in CG, CHG, and CHH contexts (*4*). TE insertions can exert a transcriptional effect on neighboring genes (*5*–*8*), and promoter methylation is typically associated with gene repression (*9*). However, exceptions exist where promoter methylation is required for gene expression (*10*–*14*). The downstream factors that perceive methylation to mediate these divergent transcriptional effects are still poorly characterized, and little is known of how methylation can stimulate gene transcription.

To identify proteins in *Arabidopsis thaliana* that recognize methylated DNA, we incubated nuclear extract from floral bud tissue with either methylated or unmethylated biotinylated double-stranded DNA oligonucleotides, affinity purified the DNA, and subjected the associated proteins to high-resolution mass spectrometry followed by label-free comparative analysis (*15*) (fig. S1). We used DNA sequences that are naturally methylated in vivo and two distinct DNA sequences for each of the CG, CHG, and CHH methylation contexts (fig. S2). A total of 41 proteins were significantly methyl enriched in at least one pull-down assay, including many candidates with known or predicted methyl-binding activity involved in gene silencing and methylation control (fig. S3). By requiring that candidates be significantly enriched in both DNA sequences for each of CG, CHG, and CHH, we obtained a stringent list of 10 candidates (Fig. 1A). Of these, relatively little is known about the role of the highly related SUVH1 and SUVH3 proteins (*16*) or the DNAJ proteins.

Recently, SUVH1 was isolated from an antisilencing screen and was shown to promote the expression of promoter methylated genes (*17*). As SUVH1 and SUVH3 contain a SET- and RING-associated (SRA) domain (*18*), they are predicted to bind methylated DNA directly. Using fluorescence polarization (FP) and microscale thermophoresis (MST), we confirmed an SRA-dependent methyl-binding preference for recombinant SUVH1 and SUVH3 proteins, respectively, in CG, CHG, and CHH contexts (Fig. 1B and fig. S4). Chromatin immunoprecipitation sequencing (ChIP-seq) of transgenic lines expressing FLAG-tagged SUVH1 or SUVH3 showed that their localization was essentially identical (fig. S5A) and that they colocalized with CHH methylation deposited by the RdDM pathway (Fig. 2A and fig. S5B). SUVH1 and SUVH3 displayed enrichment directly over NRPE1 sites (*19*) [the largest subunit of the RdDM component RNA polymerase V (Pol V)] (Fig. 2B and fig. S5C) and showed preferential localization over short TEs and at the edges of long TEs (Fig. 2C and fig. S5D), which are hallmarks of RdDM localization (*20*, *21*). There was a positive correlation between SUVH1 and SUVH3 enrichment and RdDM-deposited CHH methylation (mCHH) at both local and genome-wide scales (fig. S5, E to H). Using random forest regression, we observed that mCHH was the strongest predictor for SUVH1 binding in vivo (Fig. 2, D and E).

The nearly perfect colocalization of SUVH1 with RdDM sites predicts that RdDM pathway mutants might reduce SUVH1 occupancy. ChIP-seq of SUVH1 in *nrpd1*, *nrpe1*, or *drm1/2* RdDM mutant backgrounds (*4*) showed that SUVH1 enrichment was essentially eliminated (Fig. 2F and fig. S6). To exclude the possibility that interaction with RdDM proteins, rather than DNA methylation itself, was responsible for SUVH1 recruitment, we compared ChIP-seq results for an SRA domain amino acid change mutant [with tyrosine-277 mutated to alanine (Y277A)] that abrogated methyl binding, SUVH1^{Y277A} (Fig. 1B). Indeed, SUVH1^{Y277A} showed highly reduced recruitment and association with CHH methylation (Fig. 2G and fig. S7).

Whole-genome bisulfite sequencing (WGBS) revealed that SUVH1 ChIP-seq peaks were characterized by local CHH methylation maxima and that in *suvh1*, *suvh3*, and double mutant *suvh1 suvh3* plants, methylation levels were unperturbed (*17*) (fig. S8A). This indicated that SUVH1 and SUVH3 are not required for methylation maintenance and act strictly as methyl readers. RNA sequencing (RNA-seq) of *suvh1*, *suvh3*, and *suvh1 suvh3* confirmed many of the previously identified (*17*) promoter methylated genes that require SUVH1 for expression (fig. S8B) and showed reduced expression at genes proximal to RdDM sites (*22*) (fig. S8C).

SUVH1 and SUVH3 might enhance transcription by directly impacting chromatin (*18*), as both encode SET domains of the SU(VAR)3-9 family that typically methylate histone H3's lysine-9 (*23*). However, we were unable to detect histone methyltransferase (HMT) activity in vitro (fig. S9) or changes in dimethylation of histone 3 lysine-9 (H3K9me2) levels in *suvh1 suvh3* mutants in vivo (*17*) (fig. S10). Furthermore, SUVH1^{Y524F} and SUVH1^{Y638F} predicted HMT catalytic mutants (*18*), but not the SUVH1^{Y277A} methyl-binding mutant, were able to complement *suvh1*, indicating that HMT activity is nonessential for function in vivo (fig. S11). Chromatin accessibility, as profiled by ATAC-seq (a sequencing technique based on an assay for transposase-accessible chromatin), was also unchanged in *suvh1 suvh3* mutants (fig. S12).

Next, we assessed whether SUVH1 and SUVH3 might enhance transcription by acting as a recruitment platform (*24*). Immunoprecipitation followed by mass spectrometry (IP-MS) of SUVH1 and SUVH3 identified that each pulled down the other and also DNAJ1 and DNAJ2 (Figs. 1A and 3A and fig. S13). IP-MS of DNAJ1 and DNAJ2

---

[1]Department of Molecular, Cell and Developmental Biology, University of California at Los Angeles, Los Angeles, CA 90095, USA. [2]Quantitative Proteomics, Institute of Molecular Biology, 55128 Mainz, Germany. [3]Center for Epigenetics, Van Andel Research Institute, Grand Rapids, MI 49503, USA. [4]National Key Laboratory of Plant Molecular Genetics, CAS Center for Excellence in Molecular Plant Sciences, Shanghai Center for Plant Stress Biology, Shanghai Institutes for Biological Sciences, Chinese Academy of Sciences, Shanghai 201602, China. [5]State Key Laboratory of Ecological Pest Control for Fujian and Taiwan Crops, Fujian Agriculture and Forestry University, 350002 Fuzhou, China. [6]Department of Biological Chemistry, David Geffen School of Medicine, University of California, Los Angeles, Los Angeles, CA 90095, USA. [7]Institute of Oceanography, Minjiang University, 350108 Fuzhou, China. [8]Howard Hughes Medical Institute, University of California at Los Angeles, Los Angeles, CA, USA.
*These authors contributed equally to this work. †Present address: Department of Microbiology, Faculty of Medicine, Chiang Mai University, Chiang Mai, Thailand 50200. ‡Present address: Genomic Institute of the Novartis Research Foundation, 10675 John Jay Hopkins Dr., San Diego, CA 92121, USA. §Present address: Helmholtz Zentrum München, Institute of Biochemical Plant Pathology, 85764 Neuherberg, Germany. **||Corresponding author. Email: f.butter@imb-mainz.de (F.B.); jacobsen@ucla.edu (S.E.J.)**

Downloaded from http://science.sciencemag.org/ on December 6, 2018

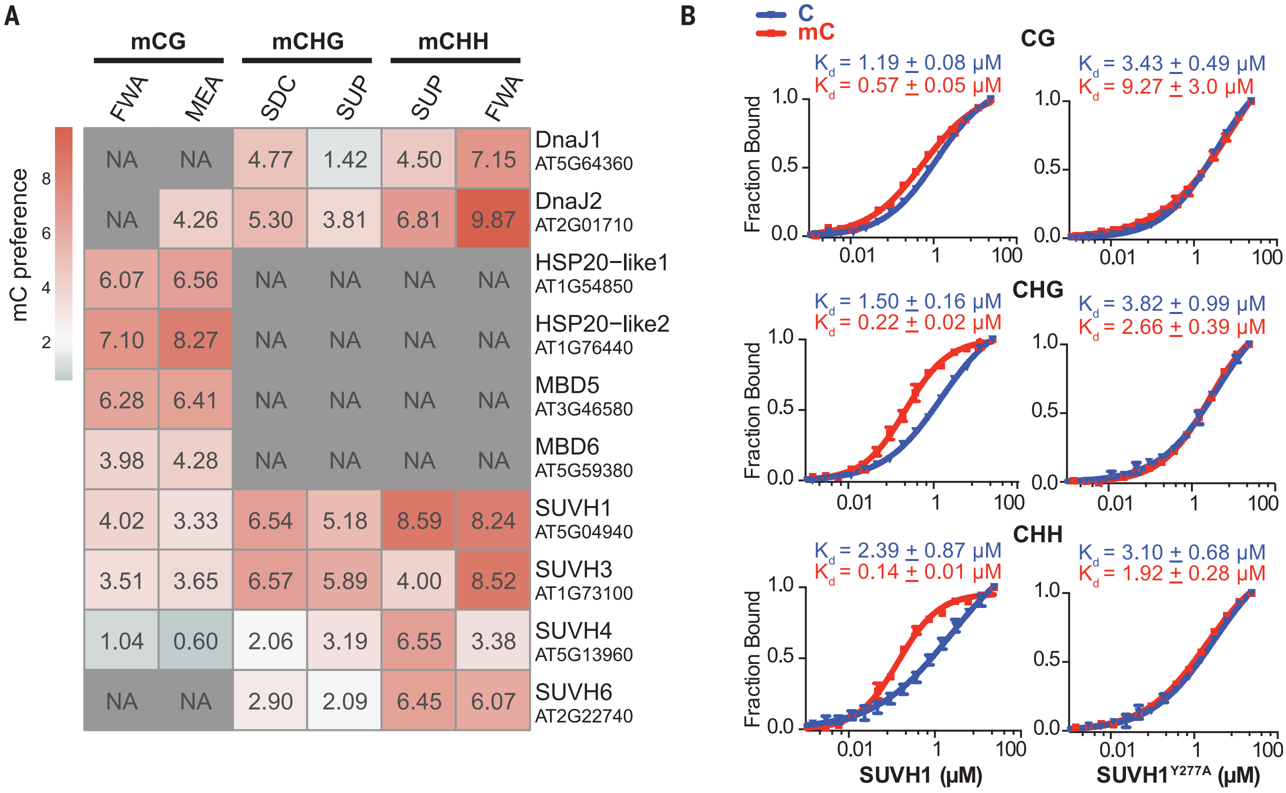

	mCG		mCHG		mCHH	
	FWA	MEA	SDC	SUP	SUP	FWA
DnaJ1 AT5G64360	NA	NA	4.77	1.42	4.50	7.15
DnaJ2 AT2G01710	NA	4.26	5.30	3.81	6.81	9.87
HSP20−like1 AT1G54850	6.07	6.56	NA	NA	NA	NA
HSP20−like2 AT1G76440	7.10	8.27	NA	NA	NA	NA
MBD5 AT3G46580	6.28	6.41	NA	NA	NA	NA
MBD6 AT5G59380	3.98	4.28	NA	NA	NA	NA
SUVH1 AT5G04940	4.02	3.33	6.54	5.18	8.59	8.24
SUVH3 AT1G73100	3.51	3.65	6.57	5.89	4.00	8.52
SUVH4 AT5G13960	1.04	0.60	2.06	3.19	6.55	3.38
SUVH6 AT2G22740	NA	NA	2.90	2.09	6.45	6.07

Fig. 1. Comparative interactomics identifies methyl reader proteins. (**A**) Heatmap of methyl-binding preferences for proteins identified as significantly enriched in two different underlying DNA sequences per methyl-cytosine (mC) context (mCG, mCHG, mCHH). NA, the protein was not detected. *FWA*, *MEA*, *SDC*, and *SUP* represent four in vivo-methylated loci. Probes are listed in fig. S2. (**B**) FP binding assays to quantify the interaction of SUVH1 with methylated or unmethylated probes in CG, CHG, and CHH contexts (left) or an amino acid change version, SUVH1^{Y277A}, predicted to abrogate methyl binding (*18*) (right). Binding affinities are indicated by dissociation constants (K_d) values. Error bars represent SEM of technical replicates. The data are representative of two independent experiments.

showed that each of these pulled down the other and also SUVH1 and SUVH3 (Fig. 3A and fig. S13), indicating that SUVH1, SUVH3, DNAJ1, and DNAJ2 interact in vivo. We confirmed the interactions between SUVH1 and SUVH3 with DNAJ and DNAJ2 by coimmunoprecipitation in *Nicotiana benthamiana* and in yeast two-hybrid assays (figs. S14 and S15). To assess the strength of the interaction, we expressed all four proteins in the same bacterial cell and performed affinity purification of either SUVH1 or SUVH3, finding that both DNAJ1 and DNAJ2 remained associated even under 500mM NaCl conditions (fig. S16).

DNAJ1 and DNAJ2 lack any discernible methyl-binding domain, but they are robustly associated with SUVH1 and SUVH3, suggesting that SUVH1 and SUVH3 may be responsible for recruiting DNAJ1 and DNAJ2 to methylated DNA (Fig. 1A). We repeated a CHH context pulldown experiment with *suvh1 suvh3* and *dnaj1 dnaj2* double mutant plants. DNAJ1 and DNAJ2 were no longer associated with methyl-DNA in *suvh1 suvh3*, while SUVH1 and SUVH3 methyl-DNA binding was unaffected in *dnaj1 dnaj2* (fig. S17). Thus, SUVH1 and SUVH3 are required to recruit DNAJ1 and DNAJ2 to methylated DNA. We performed ChIP-seq of DNAJ1 and DNAJ2 and found a tight genome-wide correlation with SUVH1 and SUVH3 (Fig. 3, B and C, and fig. S18, A and B). As with *suvh1 suvh3*, there was no effect on DNA methylation levels in *dnaj1 dnaj2* mutants, consistent with a downstream reader function (fig. S18C). To assess whether DNAJ1 and DNAJ2 are required for the transcriptional enhancement activity of SUVH1 and SUVH3, we performed RNA-seq on *dnaj1*, *dnaj2*, and double mutant *dnaj1 dnaj2* plants. The *dnaj1 dnaj2* transcriptome was strongly positively correlated with that of *suvh1 suvh3* (Fig. 3D and fig. S19), and RdDM proximal genes showed reduced expression in both *suvh1 suvh3* and *dnaj1 dnaj2* double mutants (fig. S20). *ROS1* is one of the few loci known to require methylation for expression (*11*, *12*), and indeed we observed reduced expression of *ROS1* in both the *suvh1 suvh3* and *dnaj1 dnaj2* backgrounds, despite methylation levels being maintained (fig. S21). Furthermore, genes with promoters proximal to SUVH1 peaks generally showed reduced expression in both the *suvh1 suvh3* and *dnaj1 dnaj2* double mutants (Fig. 3E). Together, these data indicate that DNAJ1 and DNAJ2 interact with SUVH1 and SUVH3, are recruited to sites of RdDM, and promote the expression of proximal genes.

The yeast two-hybrid experiments revealed that binding domain (BD)-fused DNAJ1 induced expression of the reporter even when cotransformed with an unfused activation domain construct (fig. S15). This suggested that DNAJ1 alone may be sufficient to stimulate expression of the reporter, which we confirmed in a yeast one-hybrid assay (fig. S22A). We fused DNAJ1 to a zinc finger protein (ZF108) (*24*) behind the *UBQ10* promoter and cotransformed it into *N. benthamiana* with a reporter construct containing either the ZF108 target site or a scrambled target site in the promoter region. Expression of the ZF108 target reporter was increased by approximately threefold above that of the scrambled promoter (fig. S22B). To assess whether DNAJ1 can function in a mammalian context (*25*), we transfected N2a cells and found that Gal4 DNA-binding domain (Gal4BD)–fused DNAJ1 was able to stimulate transcription of the reporter by 5- to 10-fold (fig. S22C).

Next, we generated stable transgenic *A. thaliana* lines using the *UBQ10*::ZF108-DNAJ1 construct. The first-generation independent transgenic lines displayed severe morphological defects (fig. S23). RNA-seq and ChIP-seq (Fig. 4A) on these *UBQ10*::ZF108-DNAJ1 lines showed that up- but not down-regulated genes were significantly enriched for overlap with ZF108-DNAJ1 ChIP-seq peaks (observed over expected = 2.26, hypergeometric test $P = 7.7e^{-71}$) (fig. S24). As controls, we generated *UBQ10*::ZF108-YPET and *UBQ10*::DNAJ1 (without ZF108) transgenic plants and found no

Downloaded from http://science.sciencemag.org/ on December 6, 2018

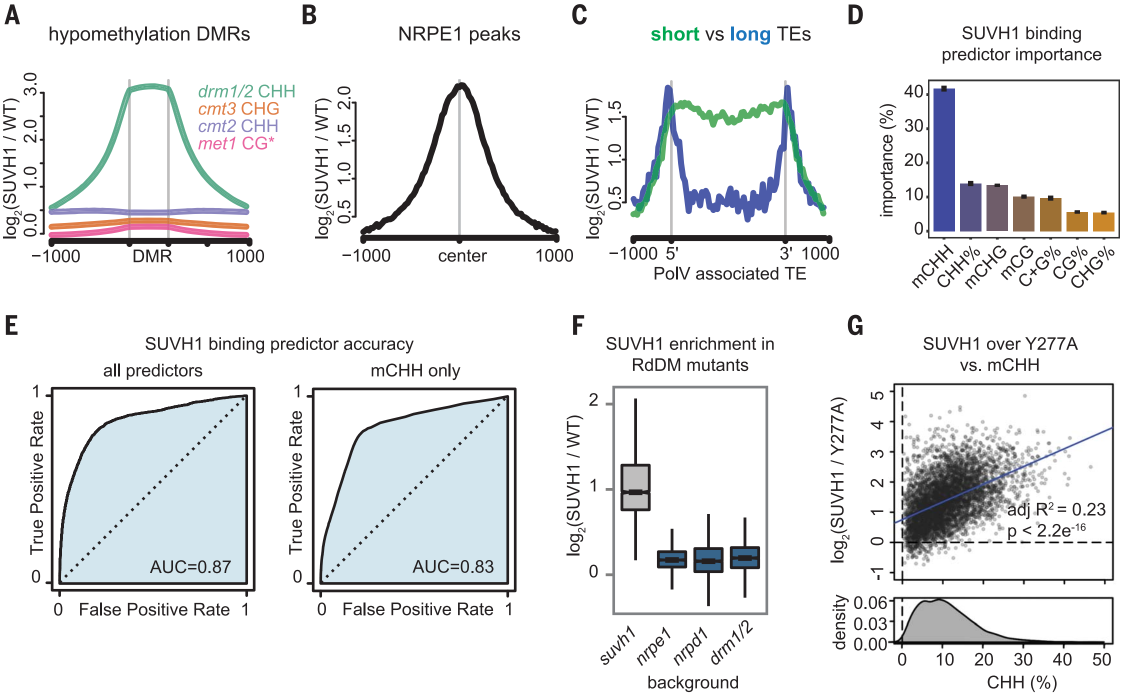

Fig. 2. SUVH1 is recruited by RdDM-associated mCHH. (**A**) SUVH1 enrichment at loci defined by loss of methylation (hypomethylation). Differentially methylated regions (DMRs) in mutant genotypes are indicated. The DRM1 and DRM2 methyltransferases are responsible for mCHH at RdDM target sites, while mCG, mCHG, and heterochromatic mCHH are maintained by MET1, CMT3, and CMT2, respectively (*1*). *, *met1* hypo CG DMRs that overlap with *drm1/2* hypo CHH DMRs were removed. (**B**) SUVH1 enrichment at NRPE1 peaks. (**C**) SUVH1 enrichment at NRPE1-associated short (<500-bp) vs. long (>5-kb) TEs. (**D**) Relative importance of genomic features in predicting SUVH1 binding, based on the random forest regressor algorithm. Error bars represent SEM from five random permutations of the training set. (**E**) Area under receiver–operating characteristic curves (AUC) model accuracy using all features (left) vs. accuracy using mCHH alone (right). (**F**) Boxplot of SUVH1 enrichment in *suvh1*, *nrpe1*, *nrpd1*, and *drm1 drm2* mutant backgrounds at SUVH1 peaks. (**G**) Scatterplot of SUVH1 over SUVH1^{Y277A} enrichment vs. mCHH methylation percentage at SUVH1 peaks. Line of best fit is shown in blue, with adjusted R^2 and P values indicated. Data in the lower panel indicate kernel density for mCHH. Average methylation levels and enrichment are calculated from the 200-bp regions surrounding the peak summits.

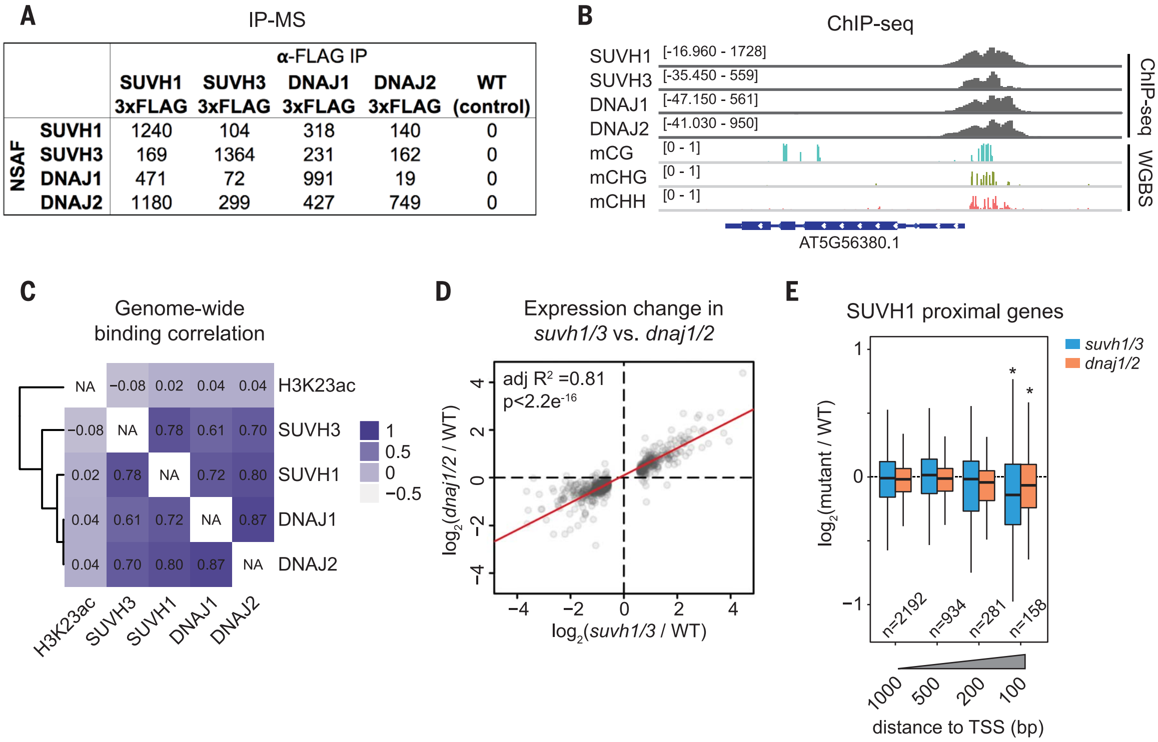
A IP-MS

		α-FLAG IP				
		SUVH1 3xFLAG	SUVH3 3xFLAG	DNAJ1 3xFLAG	DNAJ2 3xFLAG	WT (control)
NSAF	SUVH1	1240	104	318	140	0
	SUVH3	169	1364	231	162	0
	DNAJ1	471	72	991	19	0
	DNAJ2	1180	299	427	749	0

Fig. 3. SUVH1, SUVH3, DNAJ1, and DNAJ2 interact, colocalize, and are required for the expression of proximal genes. (**A**) IP-MS results for tagged lines. Only proteins present in each of the four transgenic [but not wild-type (WT)] pull-downs are presented. NSAF, normalized spectral abundance factor, averaged from two biological replicates. (**B**) Representative browser track showing ChIP-seq of SUVH1, SUVH3, DNAJ1, and DNAJ2 (normalized reads, FLAG-tagged versions minus WT) (top four lines) and methylation fraction (bottom three lines) at a methylated locus. (**C**) Pearson's correlation of genome-wide ChIP-seq profiles at 1-kb resolution. H3K23ac from (*20*) was used as an outgroup control. (**D**) Scatterplot of FPKM fold change over WT of *dnaj1 dnaj2* double vs. *suvh1 suvh3* double at genes that were differentially expressed in *suvh1 suvh3*. Line of best fit is shown in red, with adjusted R^2 and P values indicated. (**E**) Boxplot of expression change for genes proximal to SUVH1 binding sites. *n*, number of genes. *$P < 0.05$ (Mann-Whitney test).

Downloaded from http://science.sciencemag.org/ on December 6, 2018

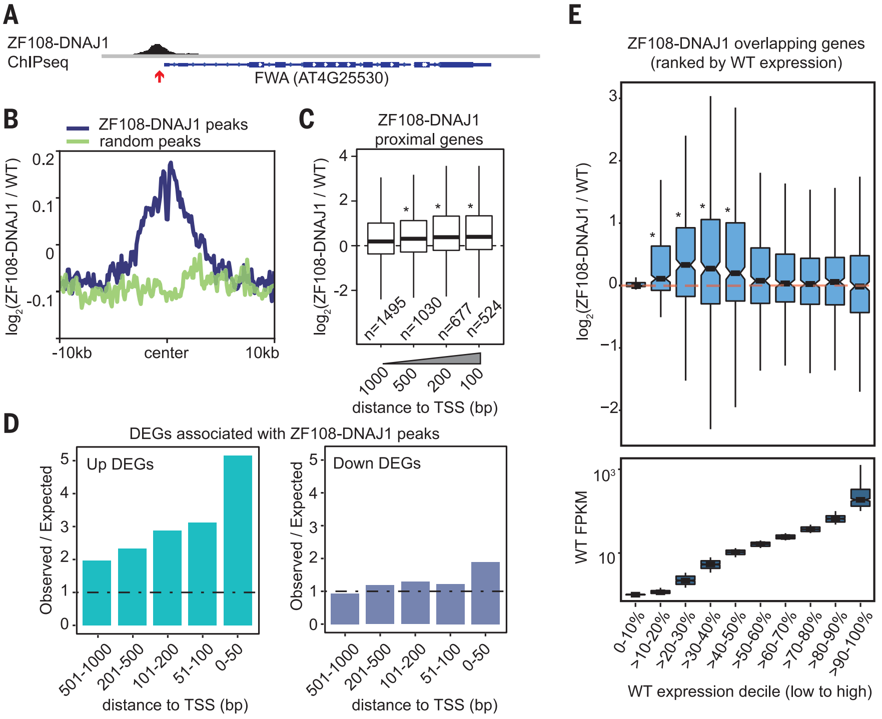

Fig. 4. ZF108-DNAJ1 transcriptionally activates mildly expressed proximal loci. (**A**) Browser track showing the ZF108-DNAJ1 ChIP-seq profile at *FWA*. The red arrow indicates the genomic location of the designed ZF108 target binding site. (**B**) Metaplot of expression change, centered on ZF108-DNAJ1 vs. random peaks. (**C**) Boxplot of expression changes for genes with promoters proximal to ZF108-DNAJ1 binding sites. *n*, number of genes. $*P < 0.05$ (Mann-Whitney test). (**D**) Observed over expected ratio for overlap of ZF108-DNAJ1 sites with up- or down-regulated ZF108-DNAJ1 gene promoters. (**E**) Boxplot of expression change for genes that overlap with ZF108-DNAJ1 peaks (upper panel), arranged by ascending WT expression decile (lower panel). Genes that lacked expression in both genotypes were removed. $*P < 0.05$ (Mann-Whitney test).

morphological defects or transcriptional changes associated with ZF108 peaks, indicating that neither ZF108 binding nor DNAJ1 overexpression was sufficient to cause the transcriptional defects observed (fig. S24). In addition, bulk levels of RNA were increased over ZF108-DNAJ1 peaks ($n = 4951$), and there was a clear promoter proximal effect on transcription (Fig. 4, B to D). In contrast, neither up- nor down-regulated gene sets showed an association with TEs or RdDM sites, indicating that ZF108-DNAJ1 acts primarily at ectopic locations driven by ZF108 binding (fig. S25). Together, these data showed that recruitment of DNAJ1 increases the expression of proximal neighboring genes.

Given that SUVH1, SUVH3, DNAJ1, and DNAJ2 are localized at RdDM sites, including many TE sequences, an interesting paradox is what prevents TEs themselves from being reactivated. *FWA*, the gene that ZF108 was designed to target (*24*), is stably silent in wild-type plants and experienced no transcriptional up-regulation in transgenic plants, despite clear localization of ZF108-DNAJ1 to *FWA* (Fig. 4A and fig. S26). We reasoned that the transcriptional enhancement effect of DNAJ1 may be limited to genes that are already expressed, as opposed to traditional transcriptional activator proteins, such as VP16, that can activate transcription of stably silent genes (*26*). Parsing the ZF108-DNAJ1 overlapping genes into expression deciles revealed that only genes with moderate expression in the wild type, but not those in the lowest or higher expression deciles, experienced transcriptional assistance (Fig. 4E). This provides a simple explanation for the paradox, as only proximal expressed genes would be affected, leaving TEs silent.

We propose that SUVH1 and SUVH3 in complex with DNAJ1 and DNAJ2 evolved to counteract the repressive effect of TE insertion near genes (*8*, *27*, *28*), thereby facilitating access to the gene regulatory diversity provided by TE proliferation (*29*–*31*). This is consistent with SUVH1, SUVH3, DNAJ1, and DNAJ2 being recruited downstream of the RdDM pathway, which is known to target evolutionarily young TEs and to cause mild repression of genes near TEs (*22*). The complex of SUVH1, SUVH3, DNAJ1, and DNAJ2 also reveals a potential mechanism to explain examples of methylation-dependent gene expression (*11*–*13*). Overall, these findings shed light on how methylation can act to fine-tune gene expression by balancing both repressive and activating transcriptional effects.

REFERENCES AND NOTES

1. J. Du, L. M. Johnson, S. E. Jacobsen, D. J. Patel, *Nat. Rev. Mol. Cell Biol.* **16**, 519–532 (2015).
2. S. Feng *et al.*, *Proc. Natl. Acad. Sci. U.S.A.* **107**, 8689–8694 (2010).
3. A. Zemach, I. E. McDaniel, P. Silva, D. Zilberman, *Science* **328**, 916–919 (2010).
4. M. A. Matzke, R. A. Mosher, *Nat. Rev. Genet.* **15**, 394–408 (2014).
5. A. E. Van't Hof *et al.*, *Nature* **534**, 102–105 (2016).
6. T. Stuart *et al.*, *eLife* **5**, e20777 (2016).
7. L. Quadrana *et al.*, *eLife* **5**, e15716 (2016).
8. J. D. Hollister, B. S. Gaut, *Genome Res.* **19**, 1419–1428 (2009).
9. J. A. Law, S. E. Jacobsen, *Nat. Rev. Genet.* **11**, 204–220 (2010).
10. K. Bahar Halpern, T. Vana, M. D. Walker, *J. Biol. Chem.* **289**, 23882–23892 (2014).
11. B. P. Williams, D. Pignatta, S. Henikoff, M. Gehring, *PLOS Genet.* **11**, e1005142 (2015).
12. M. Lei *et al.*, *Proc. Natl. Acad. Sci. U.S.A.* **112**, 3553–3557 (2015).
13. K. Shibuya, S. Fukushima, H. Takatsuji, *Proc. Natl. Acad. Sci. U.S.A.* **106**, 1660–1665 (2009).
14. J. Moreno-Romero, H. Jiang, J. Santos-González, C. Köhler, *EMBO J.* **35**, 1298–1311 (2016).
15. D. Kappei *et al.*, *Nat. Commun.* **8**, 14334 (2017).
16. L. O. Baumbusch *et al.*, *Nucleic Acids Res.* **29**, 4319–4333 (2001).
17. S. Li *et al.*, *Nucleic Acids Res.* **44**, 608–620 (2016).
18. J. Du *et al.*, *Mol. Cell* **55**, 495–504 (2014).
19. W. Liu *et al.*, *Nat. Plants* **4**, 181–188 (2018).
20. H. Stroud *et al.*, *Nat. Struct. Mol. Biol.* **21**, 64–72 (2014).
21. A. Zemach *et al.*, *Cell* **153**, 193–205 (2013).
22. X. Zhong *et al.*, *Nat. Struct. Mol. Biol.* **19**, 870–875 (2012).
23. J. P. Jackson, A. M. Lindroth, X. Cao, S. E. Jacobsen, *Nature* **416**, 556–560 (2002).
24. L. M. Johnson *et al.*, *Nature* **507**, 124–128 (2014).
25. T. Y. Erkina, A. M. Erkine, *Epigenetics Chromatin* **9**, 40 (2016).
26. L. G. Lowder *et al.*, *Plant Physiol.* **169**, 971–985 (2015).
27. X. Wang, D. Weigel, L. M. Smith, *PLOS Genet.* **9**, e1003255 (2013).
28. D. Meng *et al.*, *PLOS Genet.* **12**, e1006141 (2016).
29. K. Naito *et al.*, *Nature* **461**, 1130–1134 (2009).
30. V. Sundaram, T. Wang, *BioEssays* **40**, 170155 (2018).
31. H. Ito *et al.*, *Nature* **472**, 115–119 (2011).

ACKNOWLEDGMENTS

We thank S. Feng and M. Akhavan for the high-throughput sequencing performed at the UCLA Broad Stem Cell Research Center BioSequencing Core Facility. We thank J. A. Long for advice on nuclear isolation, M. F. Carey for providing plasmids for N2a transfections, and Y. Ma, J. Appell, J. Zhao, A. Thai, J. Nail, G. Anigol, R. Sahu, and A. Desouza for technical assistance. **Funding:** This work was supported by grants NIH R01 GM60398 (to S.E.J.), NIH R01 GM089778 (to J.A.W.), and NIH R35 GM124736 (to S.B.R), by an EMBO Long-Term Fellowship (ALTF 1138-2014) (to C.J.H), and by a Ruth L. Kirschstein National Research Service Award (GM007185) (to L.Y.). S.E.J. is an investigator of the Howard Hughes Medical Institute. **Author contributions:** F.B. and S.E.J. conceived the study; C.J.H., M.S., J.A.W., J.D., S.B.R., F.B., and S.E.J. designed the research; C.J.H., S.P.W., Y.X., L.Y., J.G.B., and M.G. performed the experiments; M.S. performed the comparative interactomics; W.L. performed the random forest regression analysis; E.M.C. and R.M.V. performed the FP assays; X.L. and W.C. performed MST assays; W.D.B. and S.R. performed the mass spectrometry from immunoprecipitated samples; C.J.H., W.L., and Z.Z. performed bioinformatic analysis; C.J.H and S.E.J. wrote the paper. **Competing interests:** The authors declare no competing interests. **Data and materials availability:** The high-throughput sequencing data generated in this paper have been deposited in the Gene Expression Omnibus (GEO) database (GSE108414).

SUPPLEMENTARY MATERIALS

www.sciencemag.org/content/362/6419/1182/suppl/DC1
Materials and Methods
Figs. S1 to S26
References (*32*–*60*)

17 December 2017; resubmitted 7 September 2018
Accepted 31 October 2018
10.1126/science.aar7854

Downloaded from http://science.sciencemag.org/ on December 6, 2018

BIOPHYSICS

Viscous control of cellular respiration by membrane lipid composition

Itay Budin[1,2]*, Tristan de Rond[1,3]†, Yan Chen[1,4], Leanne Jade G. Chan[1]‡, Christopher J. Petzold[1,4], Jay D. Keasling[1,2,5,6,7,8]*

Lipid composition determines the physical properties of biological membranes and can vary substantially between and within organisms. We describe a specific role for the viscosity of energy-transducing membranes in cellular respiration. Engineering of fatty acid biosynthesis in *Escherichia coli* allowed us to titrate inner membrane viscosity across a 10-fold range by controlling the abundance of unsaturated or branched lipids. These fluidizing lipids tightly controlled respiratory metabolism, an effect that can be explained with a quantitative model of the electron transport chain (ETC) that features diffusion-coupled reactions between enzymes and electron carriers (quinones). Lipid unsaturation also modulated mitochondrial respiration in engineered budding yeast strains. Thus, diffusion in the ETC may serve as an evolutionary constraint for lipid composition in respiratory membranes.

Cell membranes contain a multitude of distinct lipid components, but understanding how specific lipids influence biological function is challenged by limited tools for their manipulation in vivo (*1*). Lipids can determine the physical characteristics of membranes (*2*), such as their viscosity, and these properties are homeostatically maintained by cells (*3*). In a classic example (fig. S1), the bacterium *Escherichia coli* increases the proportion of phospholipid acyl chains with double bonds (unsaturation) with decreasing growth temperatures, thereby maintaining a constant membrane viscosity (*4*). Similar lipid adaptations have been widely observed across organisms (*5*), suggesting that universal processes are mediated by membrane viscosity.

To investigate functions for membrane viscosity in vivo, we used metabolic engineering strategies to genetically modulate lipid composition in *E. coli* (fig. S2). FabB [β-ketoacyl-(acyl carrier protein) synthase I] carries out the rate-limiting step (*6*) for production of unsaturated fatty acids (UFAs) during fatty acid (FA) biosynthesis (Fig. 1A). We replaced the chromosomal copy of *fabB* with one under control of an L-arabinose–induced promoter (P_{BAD}) in a strain background that allows for titratable and homogeneous expression (*7*, *8*). After further tuning FabB levels with Shine-Dalgarno sequence variants (fig. S2C), we generated strains with controllable UFA amounts ranging from ~15% [the minimum amount for survival (*9*)] to ~80% of all FAs at 37°C (Fig. 1B). This modulation resulted primarily from the substitution of palmitate (C16:0) with vaccenate (C18:1) acyl chains (fig. S3A), which was observed in all phospholipid species (fig. S3B) and maintained throughout exponential growth (fig. S3D). Membrane ordering, as measured by steady-state anisotropy of diphenylhexatriene (DPH), steadily decreased with increasing lipid unsaturation in both inner membrane vesicles and protein-free liposomes (Fig. 1C). To estimate the effect of lipid unsaturation on membrane microviscosity, we measured diffusion coefficients of a nitrobenzoxadiazole (NBD)–conjugated phosphoethanolamine (PE) in giant *E. coli* inner membrane vesicles (GEVs) using fluorescence recovery after photobleaching (FRAP) (Fig. 1D). From these data, viscosities were derived by using the Saffman-Delbrück approximation (*10*) and showed a 10-fold range (~2 to 20 poise) as UFA content was modulated.

To identify physiological functions for UFAs, we correlated exponential growth rates with sampled lipid compositions in cells producing various amounts of FabB (Fig. 2A). Growth rates generally featured a biphasic dependence on lipid unsaturation: a sharp fitness cliff leading to a cessation of cell growth at low UFA levels (15 to 20% at 37°C, regime I), followed by increasing growth rates with higher UFA content (regime II). Regime I corresponded to the minimum amount of UFAs required (e.g., in fig. S1) and was observed under all conditions. By contrast, regime II was dependent on media with nonfermentable carbon sources, where growth is tightly coupled to adenosine 5′-triphosphate production through the electron transport chain (ETC) (*11*). Under fermentation conditions, when cells depend on glycolysis and are resistant to respiratory uncouplers (fig. S4D), growth rates were unaffected by UFAs in regime II (Fig. 2A). An analysis of stress response factors (Fig. 2B) showed that that low UFA levels caused both an oxidative stress response (OSR), which can result from ETC inhibition (*12*), and a heat shock response (HSR), which is activated by misfolded proteins (*13*). However, HSR activation occurred only as membranes approached a gel phase transition at the growth temperature (fig. S5B), and coincided with the mislocalization of membrane proteins (fig. S5C) and defects in cell division (fig. S5D). We therefore concluded that increasing proportions of saturated lipids trigger envelope stress as membranes become highly ordered (regime I), but also have a second, respiratory role over a broader range of stoichiometry (regime II).

When titrating FA synthesis, cellular respiration rates were tightly coupled to changes in unsaturated lipid content (Fig. 2C). This effect was independent of electron donor (for example, succinate or glycerol), electron acceptor (oxygen or nitrate), proton motive force (PMF) uncoupling, oxygen concentration (fig. S6A), and growth stage (fig. S6B). Wild-type cells overproducing UFAs through *fabB* overexpression or deletion of the regulator *fabR* similarly showed increased respiratory rates (fig. S6C). Under glucose fermentation, low lipid unsaturation led to the accumulation of pyruvate and lactate as secreted organic acids and a depletion of succinate. Such a mixed acid fermentation profile is consistent with ETC inhibition (fig. S6D).

To test if respiratory regulation occurs through a physical effect, we engineered a heterologous system for controlling membrane viscosity based on branched-chain fatty acid (BCFA) synthesis (Fig. 2D). Introduction of the *bkd* operon (for biosynthesis of β-ketoacids) and *fabH* (for initiation of BCFA synthesis) from *Bacillus subtilis* led to the accumulation of BCFAs in membrane lipids (fig. S7A), especially when amounts of UFA were low (fig. S7B). BCFA biosynthesis fluidized membranes (fig. S7C) and rescued growth defects from low lipid unsaturation (fig. S7D), even at amounts of UFAs that were otherwise lethal (fig. S7E). Uncoupled respiration rates were increased by BCFAs in addition to UFAs, and the effects of both FA species were preserved in isolated membrane vesicles (Fig. 2E).

We considered three mechanisms by which membrane viscosity could control ETC function. First, substrate uptake could be dependent on membrane properties, especially the passive permeation of oxygen. However, lipids act on respiration independently of substrate and oxygen concentrations (fig. S6A). Alternatively, viscosity could affect individual ETC enzymes, but their partial activities with soluble substrates were not inhibited by saturated lipids (fig. S6E). Lastly, we considered whether viscosity mediates collisions between electron carriers (ubiquinone) and enzyme complexes in the ETC, because a rate dependence on solvent viscosity is a hallmark of diffusion-limited reactions (*14*). On the basis of

---

[1] Joint BioEnergy Institute, 5885 Hollis Street, Emeryville, CA 94608, USA. [2] Department of Chemical and Biomolecular Engineering, University of California, Berkeley, Berkeley, CA 94720, USA. [3] Department of Chemistry, University of California, Berkeley, Berkeley, CA 94720, USA. [4] Biological Systems and Engineering, Lawrence Berkeley National Laboratory, Berkeley, CA 94720, USA. [5] Department of Bioengineering, University of California, Berkeley, Berkeley, CA 94720, USA. [6] QB3 Institute, University of California, Berkeley, Berkeley, CA 94270, USA. [7] The Novo Nordisk Foundation Center for Sustainability, Technical University of Denmark, Denmark. [8] Center for Synthetic Biochemistry, Institute for Synthetic Biology, Shenzhen Institutes for Advanced Technologies, Shenzhen, China.

***Corresponding author. Email: keasling@berkeley.edu (J.D.K.); budin@berkeley.edu (I.B.)** †Present address: Scripps Institution of Oceanography, University of California, San Diego, CA, USA. ‡Present address: Calico Life Sciences, South San Francisco, CA, USA.

Downloaded from http://science.sciencemag.org/ on December 11, 2018

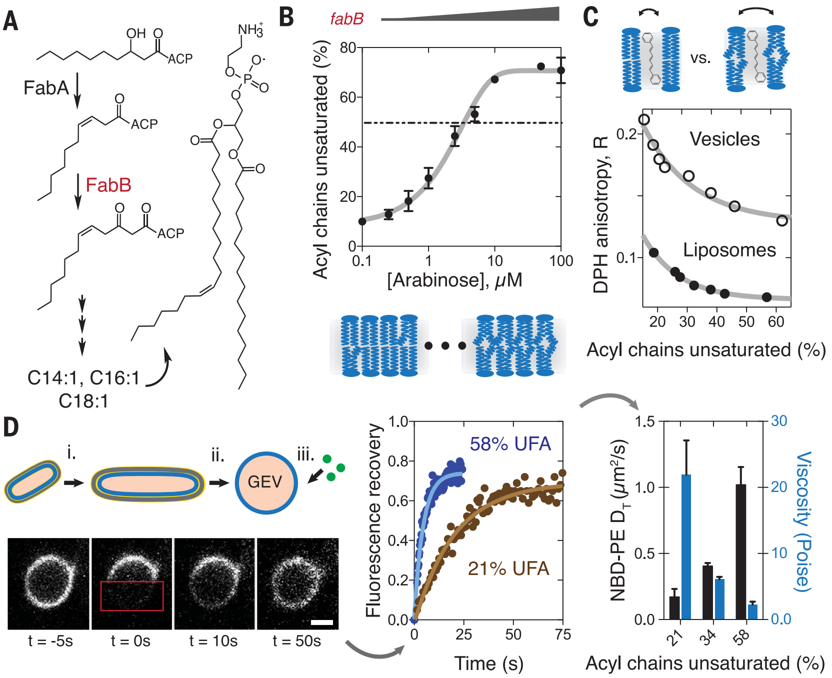

Fig. 1. Genetic titration of inner membrane viscosity in *E. coli*. (**A**) The pathway for bacterial UFA synthesis. The activity of FabB is rate-limiting for UFA synthesis and incorporation into phospholipids. (**B**) Titration of *fabB* expression with the P_{BAD} promoter modulates UFA stoichiometry as a function of inducer (arabinose) concentration. This leads to membranes with increasing amounts of *cis* double bonds, as shown in the model. Data are mean ± SD (*N* = 3 independent experiments). (**C**) Characterization of membrane ordering using DPH anisotropy. Higher anisotropy values indicate restricted motion of the probe and therefore a more ordered membrane. (**D**) A FRAP-based assay for measuring inner membrane diffusivities and its application in estimating membrane microviscosity. GEVs were generated by elongating cells with cephalexin (i). Cell walls were then digested (ii), thereby generating large, inner membrane vesicles to which lipid fluorophores can be added externally (iii). Shown is an experiment for a model substrate, NBD-PE, with recovery curves for two lipid compositions. Translational diffusion coefficients (D_T) were generated from the exponential constant of the recovery curve, and viscosity values were then estimated from these. Black bars show the calculated diffusion coefficients for NBD-PE (left *y* axis), and blue bars show the extrapolated estimated membrane viscosity (right *y* axis). Data are mean ± SEM (*N* = 5 independent experiments).

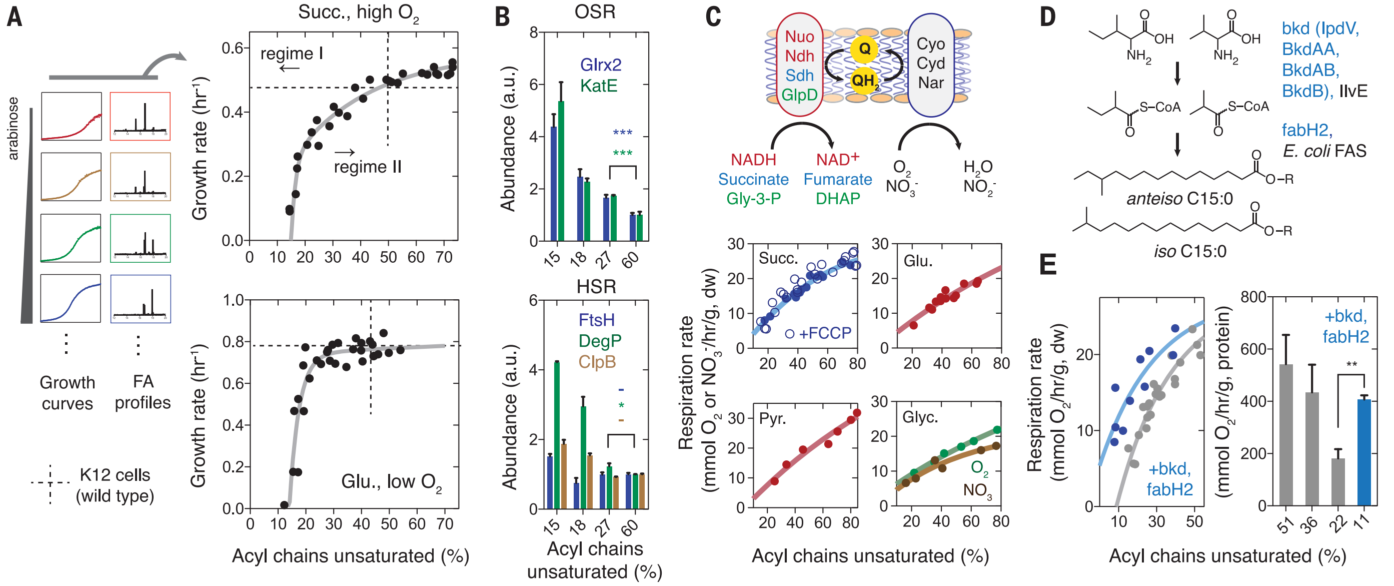

Fig. 2. Effects of FA composition on physiology and respiratory metabolism. (**A**) Growth rates and FA compositions were characterized for a series of batch cultures with various arabinose concentrations. The growth rate dependence on UFA levels occurs in two phases: a fitness cliff at low levels (regime I) and a gradual increase in growth rates at intermediate levels (regime II); these can be described by two exponential constants: k_1 ~ 0.6%$^{-1}$, k_2 ~ 0.03%$^{-1}$ at 37°C. The top plot shows the growth rate dependence under respiratory conditions and the bottom shows it for fermentative conditions, when regime II is absent. Succ., succinate; Glu., glucose. (**B**) Abundance of stress response factors in response to different proportions of unsaturated acyl chains. Data are mean ± SEM (*N* = 3), and overlaid are the results of *t* tests for significance between abundances in high (60%) and intermediate (27%) lipid unsaturation. ****p* < 0.001, **p* < 0.05; -, no significance. (**C**) The modular *E. coli* ETC consists of dehydrogenase (red) and terminal oxidase (blue) enzymes that react via an intermediate quinone pool. The different enzyme complexes used are color coded according to substrate. The corresponding respiration rates, as measured by oxygen or nitrate consumption, show a similar dependence (*k* ~ 0.01 to 0.03%$^{-1}$) on lipid unsaturation regardless of the electron donor or acceptor and whether the ETC is uncoupled by carbonyl cyanide-4-(trifluoromethoxy)phenylhydrazone (FCCP). Q, ubiquinone; NADH and NAD+, reduced and oxidized nicotinamide adenine dinucleotide; Gly-3-P, glycero-3-phosphate; DHAP, dihydroxyacetone phosphate; Pyr., pyruvate; Glyc., glycerol. (**D**) Heterologous biosynthesis of *anteiso* and *iso* BCFAs from amino acid precursors in *E. coli* using genes (highlighted in blue) from *B. subtilis*. (**E**) Effects of BCFA biosynthesis on uncoupled succinate respiration rates with various levels of lipid unsaturation (left). In purified membrane vesicles (right), the abundance of UFAs also mediates succinate respiration and a UFA deficiency can be rescued by BCFA biosynthesis, which increases respiration rates in UFA-depleted membranes (*t* test for significance, ***p* = 0.002). Data are mean ± SEM (*N* = 3 independent experiments).

Downloaded from http://science.sciencemag.org/ on December 11, 2018

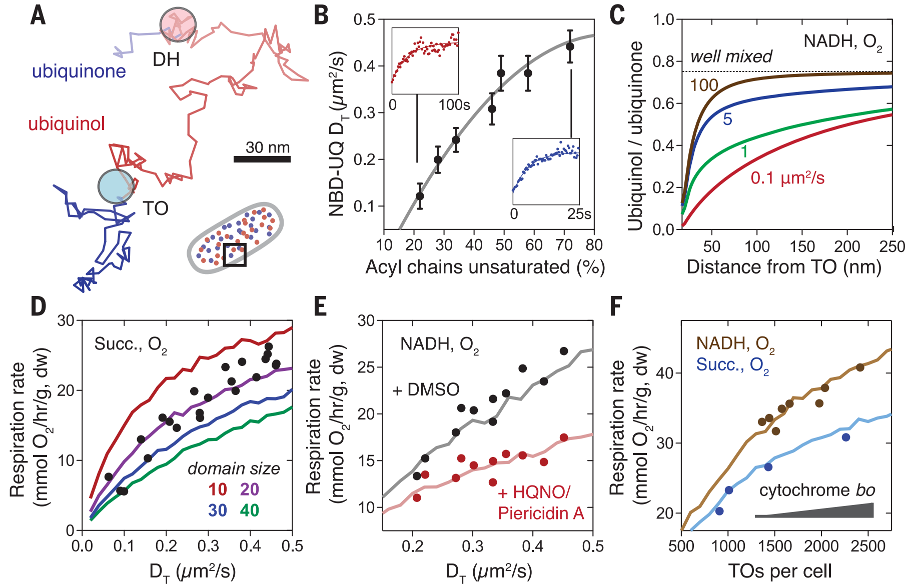

Fig. 3. Testing a diffusion-coupled reaction model for bacterial respiration. (**A**) A simulated random walk by a ubiquinone, which becomes reduced to ubiquinol (red) upon interaction with a DH domain and then reoxidized (blue) upon subsequent collisions with a TO, an oxygen-consuming reaction. The opacity of the path indicates progression during the time course (100 ms). (**B**) Experimental measurements of ubiquinone diffusivity in GEVs. Values are shown as averages from eight GEVs for each preparation. Solid line shows a quadratic function fit to the data and is used as a standard curve to convert lipid composition to diffusivity in subsequent experiments. Insets show example FRAP exponential recovery curves. Data are mean ± SEM ($N = 5$ independent experiments). (**C**) The distribution of the ubiquinone pool as a function of its diffusivity in whole-cell simulations, expressed as the steady-state average ubiquinol:ubiquinone ratio within a given radius of a TO. (**D**) Comparison of the simulated dependence of ubiquinone diffusivity (D_T) on respiration rates (solid lines) with measurements of uncoupled respiration in succinate medium (dots). Values in the legend are the domain size of the modeled ETC enzyme pair. (**E**) Modeling the effect of reducing enzymatic activity using the inhibitors *N*-oxo-2-heptyl-4-hydroxyquinoline (HQNO) and piericidin A, which act on TOs and NADH DH, respectively. Simulated rates of NADH-linked respiration (solid lines), modeled using 20-mer homotypic domains, are shown alongside uncoupled respiration rates in pyruvate medium (dots) under various UFA levels with HQNO (20 μM) and piericidin A (100 nM), or with no inhibitors (DMSO, dimethyl sulfoxide). (**F**) The effect of changes in TO concentration—achieved by titrating expression of *cyoABCD*—on respiratory rates. Simulation results (solid lines) are superimposed with experimental measurements of NADH respiration with pyruvate (brown) and succinate respiration (blue); measured TO abundance includes both aerobic cytochrome oxidases (*bo* and *bd*-I).

the pool behavior of quinones (*15*, *16*), their diffusion between complexes has been proposed to be rate-limiting in mitochondrial respiration (*17*, *18*), but this concept was disputed (*19*, *20*).

To investigate the role of diffusion in cellular respiration, we developed a model of the *E. coli* ETC based on the Brownian motion of membrane components and their collision-mediated reactions (Fig. 3A and fig. S8). As inputs, we combined activities of purified ETC enzymes—dehydrogenases (DHs) and terminal oxidases (TOs)—with measurements of their absolute abundances using quantitative mass spectrometry (supplementary materials) and their organization into homotypic domains as previously described (*21*, *22*). Whole-cell simulations were then carried out to quantify the rate of electron transfer as a function of ubiquinone diffusivity. To measure this parameter, we used FRAP experiments with an NBD-conjugated ubiquinone (NBD-UQ, fig. S9), thereby defining lipid-dependent diffusion coefficients (Fig. 3B).

Our model predicted that ubiquinone diffusivity controls respiratory flux in membranes spanning the tested range of lipid compositions. Diffusion control was measured by quinone anisotropy, with reduced electron carriers becoming depleted in the vicinity of TOs (Fig. 3C and movie S1). As diffusion increased, the quinone pool became well-mixed and rates were increasingly determined by enzyme activities (fig. S8B). Simulations matched measured respiratory rates when enzymes were modeled as domains of 10 to 30 proteins (Fig. 3D), consistent with their reported organization in cells (*21*). Simulations also predicted changes to respiratory rates upon inhibition of ETC enzymes (Fig. 3E), which reduces the rate dependence on diffusion, and during genetic titration of TO abundance (Fig. 3F), which modulates the average diffusion distance for a reactive collision.

As in bacteria, respiration in eukaryotic mitochondria is also dependent on quinone-mediated electron transfer. In animal models, correlations between mitochondrial FA composition and metabolic rate have been observed between species (*23*), and membrane-fluidizing steroids have been shown to promote respiration (*24*). To test whether lipid composition controls mitochondrial respiration, we used a set of constitutive promoters to manipulate Ole1 (acyl–coenzyme A desaturase) levels in *Saccharomyces cerevisiae* (Fig. 4A). In strains that showed regular mitochondrial morphology (fig. S10A), greater lipid unsaturation led to increased respiratory activity but, as in *E. coli*, did not inhibit fermentative metabolism or growth (fig. S10, B and C). In isolated mitochondria, UFA content controlled the rate of respiration coupled to adenosine 5´-diphosphate (ADP) phosphorylation (state 3) and uncoupled (state 3u) from the PMF (Fig. 4B).

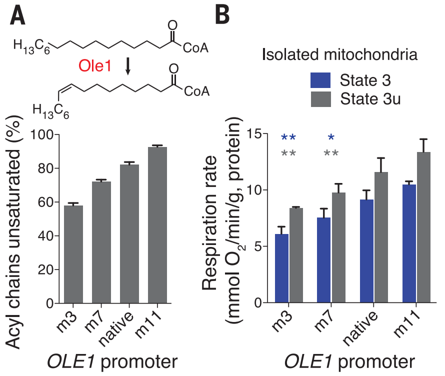

Fig. 4. Lipid-mediated respiration in mitochondria. (**A**) The desaturase Ole1 generates all UFAs in yeast. Unsaturated lipid composition is controlled by the promoter driving expression of *OLE1*—either the native one, or one of three variants (m3, m7, m11) in engineered strains. (**B**) Mitochondrial respiration rates in coupled (state 3, 0.5 mM ADP) and uncoupled (state 3u, 4 μM FCCP) conditions corresponded with unsaturated lipid content. Mitochondria were incubated with 5 mM succinate as a substrate. Data are mean ± SEM ($N = 3$ independent experiments), and overlaid are the results of *t* tests for significance against m11. $^{**}p < 0.01$, $^{*}p < 0.05$.

The role for diffusion in respiration provides a functional rationale for variations in lipids within and between cells. In eukaryotes, lipid species that increase membrane viscosity—sterols and sphingolipids—are depleted from energy-transducing membranes (*25*). In prokaryotes, analogous rigidifying lipids, such as hopanoids and archaeal ether lipids, are associated with niches where the robustness of the membrane as a permeability barrier is paramount over rapid metabolic activity (*26*). Such a trade-off is evident in *E. coli*, which eliminates lipid unsaturation through cyclopropanation during stationary phase to survive in acidic conditions (*27*). Localizing ETCs to fluid internal membranes while maintaining rigid outer membranes could thus have served as an advantage during the evolution of dedicated metabolic organelles. In some mitochondria, ETCs are additionally organized into supercomplexes of respiratory enzymes (*28*, *29*).

Downloaded from http://science.sciencemag.org/ on December 11, 2018

In our simulations, tethering of DH and TO enzymes increased respiration rates and reduced anisotropy in the quinone pool (fig. S11, movie S2, supplementary text). A diffusion-coupled reaction model could therefore be important for understanding how the interplay between lipid composition, enzymatic activity, and membrane organization dictates respiratory function in a wide range of systems.

REFERENCES AND NOTES

1. E. Muro, G. E. Atilla-Gokcumen, U. S. Eggert, *Mol. Biol. Cell* **25**, 1819–1823 (2014).
2. T. Harayama, H. Riezman, *Nat. Rev. Mol. Cell Biol.* **19**, 281–296 (2018).
3. R. Covino *et al.*, *Mol. Cell* **63**, 49–59 (2016).
4. M. Sinensky, *Proc. Natl. Acad. Sci. U.S.A.* **71**, 522–525 (1974).
5. J. R. Hazel, *Annu. Rev. Physiol.* **57**, 19–42 (1995).
6. Y. Feng, J. E. Cronan, *J. Biol. Chem.* **284**, 29526–29535 (2009).
7. A. Khlebnikov, K. A. Datsenko, T. Skaug, B. L. Wanner, J. D. Keasling, *Microbiology* **147**, 3241–3247 (2001).
8. M. A. Kay, C. Y. He, Z. Y. Chen, *Nat. Biotechnol.* **28**, 1287–1289 (2010).
9. J. E. Cronan Jr., E. P. Gelmann, *J. Biol. Chem.* **248**, 1188–1195 (1973).
10. P. G. Saffman, M. Delbrück, *Proc. Natl. Acad. Sci. U.S.A.* **72**, 3111–3113 (1975).
11. K. B. Andersen, K. von Meyenburg, *J. Bacteriol.* **144**, 114–123 (1980).
12. A. N. Woodmansee, J. A. Imlay, *J. Biol. Chem.* **277**, 34055–34066 (2002).
13. T. Yura, K. Nakahigashi, *Curr. Opin. Microbiol.* **2**, 153–158 (1999).
14. A. C. Brouwer, J. F. Kirsch, *Biochemistry* **21**, 1302–1307 (1982).
15. A. Kröger, M. Klingenberg, *Eur. J. Biochem.* **34**, 358–368 (1973).
16. P. R. Rich, *FEBS Lett.* **130**, 173–178 (1981).
17. B. Chazotte, C. R. Hackenbrock, *J. Biol. Chem.* **264**, 4978–4985 (1989).
18. S. Gupte *et al.*, *Proc. Natl. Acad. Sci. U.S.A.* **81**, 2606–2610 (1984).
19. C. Bianchi, M. L. Genova, G. Parenti Castelli, G. Lenaz, *J. Biol. Chem.* **279**, 36562–36569 (2004).
20. R. Fato, M. Battino, M. Degli Esposti, G. Parenti Castelli, G. Lenaz, *Biochemistry* **25**, 3378–3390 (1986).
21. I. Llorente-Garcia *et al.*, *Biochim. Biophys. Acta* **1837**, 811–824 (2014).
22. T. Lenn, M. C. Leake, C. W. Mullineaux, *Mol. Microbiol.* **70**, 1397–1407 (2008).
23. M. D. Brand, P. Couture, P. L. Else, K. W. Withers, A. J. Hulbert, *Biochem. J.* **275**, 81–86 (1991).
24. M. J. Torres *et al.*, *Cell Metab.* **27**, 167–179.e7 (2018).
25. G. van Meer, D. R. Voelker, G. W. Feigenson, *Nat. Rev. Mol. Cell Biol.* **9**, 112–124 (2008).
26. D. L. Valentine, *Nat. Rev. Microbiol.* **5**, 316–323 (2007).
27. Y.-Y. Chang, J. E. Cronan Jr., *Mol. Microbiol.* **33**, 249–259 (1999).
28. D. Milenkovic, J. N. Blaza, N. G. Larsson, J. Hirst, *Cell Metab.* **25**, 765–776 (2017).
29. J. A. Letts, K. Fiedorczuk, L. A. Sazanov, *Nature* **537**, 644–648 (2016).

ACKNOWLEDGMENTS

N. Oppenheimer, H. Stone, and D. Arlow contributed helpful discussions, and the Coates (University of California, Berkley) and Lippincott-Schwartz (Janelia Research Campus) labs contributed experimental assistance. **Funding:** This work was part of the DOE Joint BioEnergy Institute supported by the U.S. Department of Energy, Office of Science, Office of Biological and Environmental Research, through contract DE-AC02-05CH11231 between Lawrence Berkeley National Laboratory and the U.S. Department of Energy. This work was also supported by National Science Foundation grants MCB-1442724 and MCB-1715681 to J.D.K, and a Junior Fellowship to I.B. from the Miller Institute for Basic Research. **Author contributions:** I.B. designed the study and performed the experiments. T.d.R. developed the model with I.B. and performed chemical synthesis. Y.C., L.J.G.C., and C.J.P. performed protein mass spectrometry analysis. All authors wrote the paper and discussed the results. **Competing interests:** J.D.K. has a financial interest in Amyris, Lygos, Demetrix, Constructive Biology, Maple Bio, and Napigen. The research described in this publication is not related to the work of these companies. **Data and material availability:** All strains are available from the Joint BioEnergy Institute public registry (https://public-registry.jbei.org). Protein mass spectrometry SRM data and methods are available at Panamoramaweb (http://goo.gl/JJySak). The ETC simulation script, written in Python, as well as examples of commands to invoke it, are available at GitHub (http://github.com/tderond/Budin2018).

SUPPLEMENTARY MATERIALS

www.sciencemag.org/content/362/6419/1186/suppl/DC1
Materials and Methods
Supplementary Text
Figs. S1 to S11
Tables S1 to S3
References (*30*–*68*)
Movies S1 and S2

5 April 2018; accepted 11 October 2018
Published online 25 October 2018
10.1126/science.aat7925

Downloaded from http://science.sciencemag.org/ on December 11, 2018

NEW ENGLAND BioLabs® Inc.

be INSPIRED
drive DISCOVERY
stay GENUINE

Flexible Precision.

NEBNext Direct® Custom Ready Panels for NGS target enrichment

Employing the unique NEBNext Direct hybridization-based enrichment method, NEBNext Direct Custom Ready Panels allow rapid customization of targeted gene panels for Illumina® sequencing. Select from a list of genes for which baits have been carefully designed and optimized to give complete coverage of the full coding regions. High quality panels can be designed by you and rapidly delivered, from any combination of genes. NEBNext Direct Custom Ready Panels provide the content you want with the performance you need.

- Choose from a single gene to hundreds of genes
- Experience unmatched specificity and coverage uniformity
- Eliminate synthesis and optimization steps for faster turnaround
- Improve sensitivity with our Unique Molecule Index (UMI)
- Generate results in one day with our automation-friendly workflow

For more information visit

NEBNextDirect.com

NEBNext Direct Custom Ready Panels demonstrate optimum performance across a wide range of panel sizes

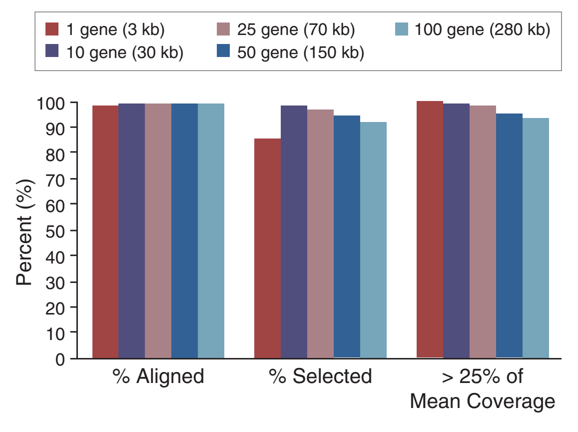

Key target enrichment metrics demonstrate consistent performance across a range of panel sizes. 100 ng of DNA was tested against panels of 1, 10, 25, 50 and 100 genes, and sequenced using Illumina® paired-end 150 bp sequencing. Larger panels included all genes present in smaller panels.

For research use only; not intended for diagnostic use.
One or more of these products are covered by patents, trademarks and/or copyrights owned or controlled by New England Biolabs, Inc.
For more information, please email us at gbd@neb.com.
The use of these products may require you to obtain additional third party intellectual property rights for certain applications.
ILLUMINA® is a registered trademark of Illumina, Inc.
© Copyright 2018, New England Biolabs, Inc.; all rights reserved.

FUJITSU Human Centric AI

Zinrai

Fujitsu's Artificial Intelligence Framework

FUJITSU

"Zinrai" is Fujitsu's approach to human-centric Artificial Intelligence (AI). Based on many years of research and development, Zinrai incorporates the latest AI technologies across both products and services to transform business and create new value for all.

Fujitsu's Zinrai has many applications, including:

City Surveillance

Real time observation using image recognition systems

Retail

Analysis of shopper preferences by gaze tracking

Healthcare

Helping doctors make faster medical diagnosis

Digital Business Platform – MetaArc

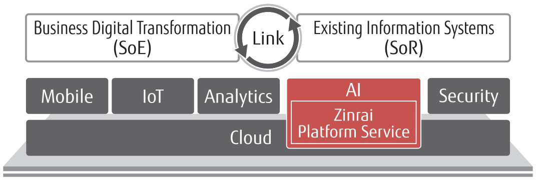

Services developed on Zinrai technology are available through MetaArc, accelerating innovation to creat new value.

*SoE: Systems of Engagement, SoR: Systems of Record

shaping tomorrow with you

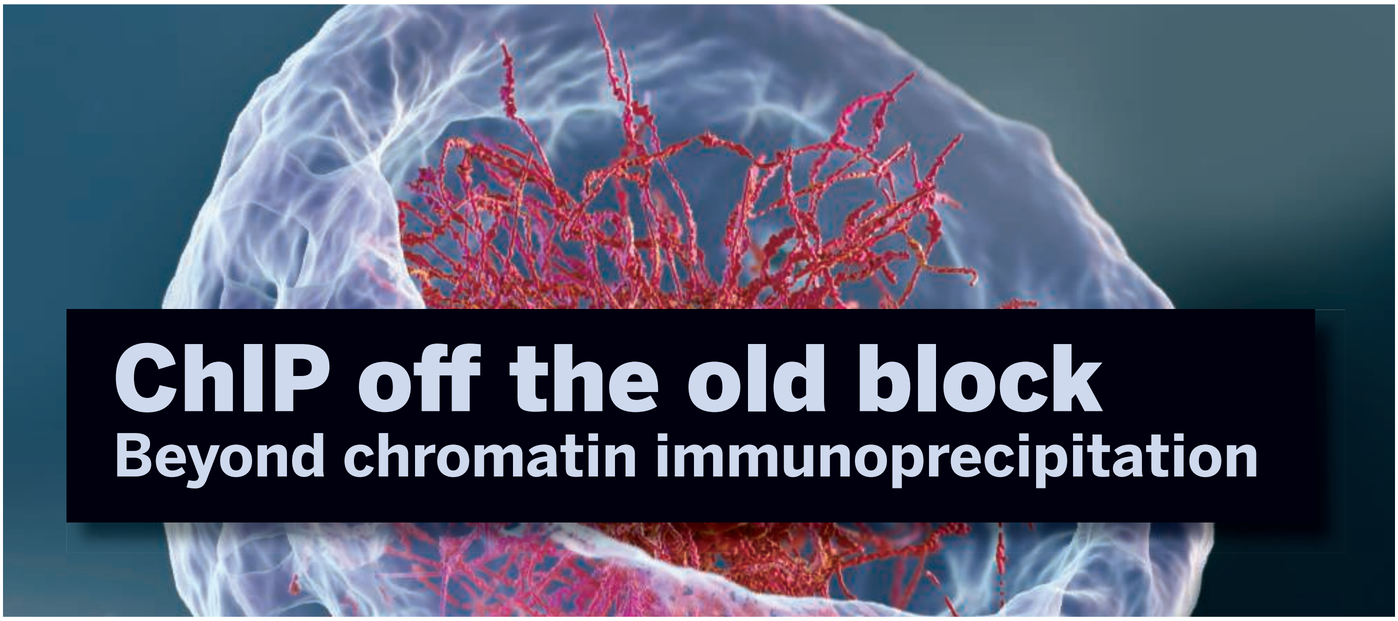

ChIP off the old block

Beyond chromatin immunoprecipitation

A host of techniques are building from a classic method—chromatin immunoprecipitation (ChIP)—to assess what binds to DNA and where. Emerging techniques whittle down the size of samples, interrogate DNA-bound protein complexes, or more closely assess the nucleotides involved. All of these approaches aim to overcome long-standing limitations of ChIP, and broaden the questions scientists can ask about gene regulation, development, and disease. **By Charlotte Schubert**

Chromatin immunoprecipitation, one of the most widely used techniques in molecular biology, was invented over 30 years ago—and some things about it have changed, while others have stayed the same.

The basic protocol is still similar to one developed in the 1980s, involving crosslinking proteins to DNA with formaldehyde and then fragmenting the DNA. A DNA-interacting protein is immunoprecipitated using an antibody, the crosslinks reversed with heat, and the associated DNA analyzed. Researchers later linked the technique to deep sequencing, developing the ChIP-seq technique to probe protein–DNA interactions at the genomic scale.

ChIP has been harnessed to address how transcription factors operate, how histones modulate gene expression, and other basic questions with implications for biological development and disease. In September, C. David Allis and Michael Grunstein won the prestigious Lasker award for their work on histones—research that relied on ChIP. And ChIP-seq is now a cornerstone of the ENCODE (ENCyclopedia Of DNA Elements) project, an effort to map regulatory regions of the genome in various cell types.

Chromatin biologists are also developing an array of spin-off or parallel technologies to go beyond what ChIP and ChIP-seq offer—to examine complexes of proteins, to more accurately assess the exact nucleotides a factor binds to, to look at small pools of cells, and to begin, tentatively, to assess protein–DNA interactions at the single-cell level.

All of these techniques aim to do things that ChIP-seq alone cannot, or does only sluggishly. And all of them have the same basic goal: to find out what molecules are associated with DNA and where.

"We really don't understand the fundamental principles by which regulatory functional sequences in our genome determine where and when genes come on," says Bradley Bernstein, director of the **Broad Institute's Epigenomics Program** in Cambridge, Massachusetts. He adds that ChIP is "limited in many ways. And so there are these efforts to try and innovate new approaches or adapt the technology in new ways."

Making it work

"Calling [ChIP-seq] a dark art is too much," says Nir Friedman, a professor of computer science and biology at **The Hebrew University of Jerusalem,** Israel. But despite it being a commonly used technique, "very few people are patient enough to calibrate their experiments," he says.

ChIP-seq experiments generate a lot of noise, notes Friedman. Formaldehyde can crosslink uninvolved molecules, antibodies can pull down nontarget proteins, and sonication—the most common way to break up DNA—tends to break up DNA that is in an open conformation. Says Friedman, "It can be that more than half of what you end up sequencing or looking at is nonspecific binding."

ENCODE publishes guidelines for assessing the quality of antibodies and screening out meaningless data, Friedman notes. The project also provides access to recent computational tools that are used, for instance, to normalize data to controls and to identify "peaks" or regions of possible DNA binding.

Choosing the right antibody, in particular, can be challenging, notes Michael-Christopher Keogh, chief scientific officer at **EpiCypher,** an epigenomics company in Research Triangle Park, Durham, North Carolina. Keogh was involved in a recent study showing that many antibodies popular for histone research perform poorly in ChIP, for instance, binding to off-target epitopes. The study also proposes validation steps beyond the ENCODE guidelines.

Some researchers bypass the antibody problem by engineering an epitope tag onto their target, as with CETCh-seq (CRISPR epitope tagging ChIP-seq). A long-standing technique, DamID (DNA adenine methyltransferase identification), involves engineering factors to tag neighboring DNA with molecular marks.

IMAGE: © YURIIHRB/SHUTTERSTOCK.COM

Upcoming features

Next-Gen Sequencing: RNA Seq—February 22 ■ Microscopy: Multiphoton Microscopy—March 22 ■ Molecular Biology: Epitranscriptomics—May 17

Other researchers are still improving on the basic ChIP technique, such as Alon Goren's group at the University of California San Diego's Department of Medicine, which has fully automated ChIP-seq. Goren says that the optimal antibody concentration can vary substantially among antibodies and cell types, and that some steps, such as reverse crosslinking, are unnecessary. The **Goren Lab** has also shown that monoclonal antibodies have the edge over polyclonal antibodies.

But even when fully optimized, ChIP-seq is still fundamentally limited. For instance, it generally requires 100,000 or more cells to assess transcription factors and 10,000 or more to assess histone proteins, says Goren. And in most cases, the method is geared to look at one protein, one antibody at a time.

Says Goren, "Once we are able to shift the view from thinking about proteins to thinking about complexes, we will get a much better understanding of how biology works and what happens in disease."

Getting a handle on protein complexes

One approach to examine complexes is to combine ChIP-seq with mass spectrometry (MS), using methods such as RIME (Rapid Immunoprecipitation Mass spectrometry of Endogenous proteins) and ChIP-MS.

One drawback of these methods, however, is that proteins not associated with DNA can also be pulled down by immunoprecipitation, says David Steger, a molecular biologist at the **University of Pennsylvania,** in Philadelphia. Instead, says Steger, "What everybody is trying to develop is locus-specific proteomics at a particular enhancer."

One emerging technique to assess chromatin-bound complexes is ChIP-SICAP (selective isolation of chromatin-associated proteins), developed by Jeroen Krijgsveld's team at the **German Cancer Research Center** in Heidelberg, Germany, and his colleagues. The technique involves tagging antibody-bound DNA with biotin, which is then pulled down with biotin-binding streptavidin beads before mass spec.

Steger is applying ChIP-SICAP to examine proteins bound to enhancers that drive the transition of mesenchymal stem cells to adipocytes. Says Steger, "What we are trying to do is identify an enhancer proteome."

Other approaches harness the gene-editing system involving Cas9, which recognizes guide RNAs targeted to specific DNA sequences. Researchers have tagged Cas9 with biotin or an enzyme that promotes the biotin labeling of nearby proteins, which are analyzed by MS. This approach has also been deployed to reveal interactions between distant genomic elements. Such methods could potentially extend the repertoire of ChIP-seq–related methods that can assess the 3D architecture of the genome, such as Hi-C, ChIA-PET (Chromatin Interaction Analysis by Paired-End Tag sequencing), and HiChIP, and more recent methods such SPRITE (Split-Pool Recognition of Interactions by Tag Extension).

These emerging methods to assess DNA-bound complexes promise to sharpen biologists' view of gene regulation. But when harnessed to MS, they face the limitation that MS does not readily detect low-abundance proteins, notes Steger. Moreover, not all newer techniques are accessible to the nonexpert.

Several companies offer services for outsourcing of more-established techniques such as RIME or ChIP-seq. Companies that offer ChiP-seq and related services include **Active Motif,** in Carlsbad, California; **Diagenode** in Liege, Belgium and Denville, New Jersey; and Beijing-based **Novogene.** These and other companies also offer ChIP-seq kits and components, though many labs generate their own reagents. Keogh also notes that in-house research can mean greater control of optimization steps.

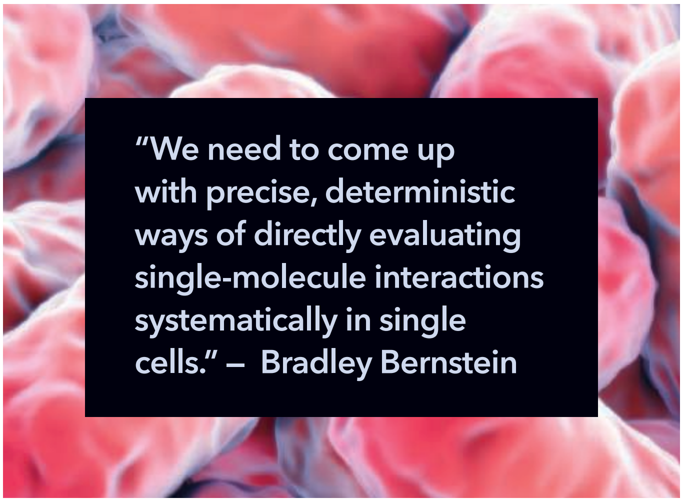

> "We need to come up with precise, deterministic ways of directly evaluating single-molecule interactions systematically in single cells." — Bradley Bernstein

IMAGE: © IMAGENTLE/SHUTTERSTOCK.COM

Care with experimental parameters during ChIP experiments can itself boost the quality of data, says Cigall Kadoch, whose group studies several large macromolecular protein complexes at **Dana-Farber Cancer Institute** and **Harvard Medical School** in Boston, Massachusetts.

Kadoch is careful to optimize the concentration of formaldehyde used to crosslink proteins together with each other and DNA, for each antibody and cell type. When choosing antibodies, she notes whether the epitope is predicted to be accessible on the surface and therefore amenable to immunoprecipitation. And to see the DNA footprint of a fully assembled complex, she advises choosing an antibody to a protein that is added on late in the assembly process. "These are the things that make or break a project," Kadoch says.

Zeroing in on factor binding

Another technique Steger uses is ChIP-exo (ChIP exonuclease). He deploys it to identify—at base-pair resolution—where various factors bind the genome.

This technique starts with DNA fragmentation by sonication. An exonuclease chews up the DNA (in the 5'–3' direction) to the edge of where the DNA is linked by formaldehyde to its bound protein. This approach results in a sharp DNA "footprint" for bound factors, which can be more exact than the inferred motifs generated computationally using ChIP-seq.

"We always start with ChIP-seq, and as our questions evolve, we move to ChIP-exo," says Steger, who has used the technique to assess the binding of the glucocorticoid receptor to DNA. The receptor binds as a dimer to two abutting, short DNA sequences. Steger was able to resolve binding of one monomer, which he was unable to do with ChIP-seq.

The team of Frank Pugh, a professor of biochemistry and molecular biology at Penn State University in University Park, Pennsylvania, recently simplified its ChIP-exo method and adapted it to the commonly used **Illumina** sequencing platform. Similarly, Julia Zeitlinger, associate investigator at Stowers Institute for Medical Research in Kansas City, Missouri, and her colleagues, have published a related technique, ChIP-nexus. Both developments are "promising," says Michael Snyder, chair of genetics and director of the **Stanford Center for Genomics and Personalized Medicine** at Stanford University, in California.

cont.>

Featured participants

Active Motif www.activemotif.com	**Goren Lab, University of California, San Diego** goren-lab.github.io/index.html
Altius Institute for Biomedical Sciences www.altius.org	**Harvard Medical School** hms.harvard.edu
Benner Lab, University of California, San Diego homer.ucsd.edu/BennerLab	**Illumina** www.illumina.com
Broad Institute Epigenetics Program www.broadinstitute.org/epigenomics	**Novogene** en.novogene.com
Dana-Farber Cancer Institute www.dana-farber.org	**Stanford Center for Genomics and Personalized Medicine** med.stanford.edu/scgpm.html
Diagenode www.diagenode.com/en	**The Hebrew University of Jerusalem** new.huji.ac.il/en
EpiCypher www.epicypher.com	**University of Pennsylvania** www.upenn.edu
Fred Hutchinson Cancer Research Center www.fredhutch.org/en.html	
German Cancer Research Center www.dkfz.de/en/index.html	

Additional resources

ENCODE
www.encodeproject.org/pipelines

Going smaller and deeper

Researchers have been able to shave off the number of cells required for ChIP-seq by adjusting experimental parameters, such as using a high-quality antibody, says Friedman.

Some techniques, including one developed by Friedman, use barcoded sequencing adaptors, enabling decreased sample size. And a new technique called "ChIPmentation" reduces the steps involved in making sequencing libraries.

One method making its way to new labs is CUT&RUN (Cleavage Under Targets and Release Using Nuclease), developed by Steve Henikoff and his colleagues at **Fred Hutchinson Cancer Research Center** in Seattle, Washington. This method dispenses with crosslinking by formaldehyde as well as DNA shearing with sonication. Instead, an antibody against the target is tethered to micrococcal nuclease (MNase), which is activated by calcium to cleave the DNA on either side of the target. The resulting DNA fragments are sequenced.

"You get a large signal-to-noise reduction" as compared to ChIP-seq, says John Stamatoyannopoulos, director of the **Altius Institute for Biomedical Sciences** in Seattle. That's in part because of the clean cutting of DNA by the nuclease, with low levels of off-site cutting. As a result, CUT&RUN typically requires fewer DNA sequencing reads than ChIPseq—reducing costs—and can be applied to much lower cell numbers. Henikoff's team recently applied the technique to 1,000 cells for a transcription factor and 100 cells for a histone modification. Stamatoyannopoulos says the method has largely supplanted ChIP-seq in his labs.

CUT&RUN also has advantages beyond low cell numbers. Stuart Orkin, a molecular biologist and professor at Harvard University, touts the technique for its "essentially nucleotide-level" resolution. With minor tweaks to computational tools, his group was able to differentiate the closely spaced binding sites of a transcription factor involved in controlling the expression of fetal hemoglobin. Prior to obtaining this result, he was unable to immunoprecipitate the transcription factor with conventional ChIP, possibly because formaldehyde crosslinking hid the epitopes. CUT&RUN "worked right off the bat," he says.

Henikoff's lab has adapted the technique to assess long-range, 3D DNA interactions, and to perform immunoprecipitation on the cleaved-out fragments using a second antibody. The group interrogated two molecular features on the same protein complex—an approach that could help resolve questions such as which combinations of histone marks are associated with various gene states.

Working at the single-cell level

For many molecular biologists, including chromatin researchers, the single cell is the final frontier.

"We need to come up with precise, deterministic ways of directly evaluating single-molecule interactions systematically in single cells," says Bernstein. "It is a long-term goal." Single-cell data could potentially track DNA-binding factors as cells exit the stem-cell state during development, or in tumors with high levels of cellular heterogeneity.

Several approaches are edging closer to this goal. However, "A lot of the single-cell methods have limited sensitivity," says Christopher Benner, a genome biologist at the **University of California, San Diego.** Bernstein and his colleagues for instance, generated single-cell ChIPseq data using a microfluidic system and barcoding. From each cell, the technique captured between 500–10,000 unique "reads," representing a DNA-binding event, in contrast to the millions of reads captured with populations of cells.

Several methods can also yield data on the active regions of the genome. ATAC-seq (Assay for Transposase-Accessible Chromatin using sequencing) deploys a hyperactive transposase that integrates into the genome in open chromatin regions and introduces sequencing adaptors. ATAC-seq can be adapted to single cells and the resulting sequence data interrogated with a variety of computational approaches. These approaches can, for instance, identify promoter sequences—or identify patterns in experiments simultaneously knocking out DNA control elements or assessing RNA expression.

ATAC-seq suffers from drawbacks, such as incomplete integration into accessible regions, notes Snyder. But the technique can be powerful: It can be deployed to insert and image fluorophores, resulting in imaging data on 3D genomic organization prior to sequencing, notes Snyder.

Snyder points to imaging work in labs such as that of Alistair Boettiger at Stanford, who is developing ways to simultaneously image genetic elements and nascent RNA transcripts with super-resolution imaging, to assess which elements promote or quell gene expression. "Imaging is the future," adds Stamatoyannopoulos. Other researchers note that as "third-generation" nanopore sequencing improves, ChIP-like methods will be developed to plug into it.

"We may need entirely orthogonal ways of doing this," says Bernstein of single-cell chromatin analysis. That goal will likely will be accomplished successfully in the end, he says, with "technologies that are a radical departure from what we are using now."

Charlotte Schubert is a freelance journalist based in Seattle. From 2015–2016 she also worked at the bench in Steve Henikoff's lab, on a project unrelated to the work highlighted here.

ChIP-Seq Library Preparation

The UniqSeq ChIP library preparation kit is highly sensitive, especially for low-abundance transcription factors, and can be used for both quantitative PCR and sequencing. This kit is compatible with both high and low chromatin loadings with an increased slurry volume of 1 mL, offering greater flexibility with more difficult samples. UniqSeq requires a cleanup step, but due to the increased binding of the column, enough DNA is obtained from one column to eliminate the need to pool samples for library preparation. The kit offers a simple, cost-effective solution for generating ChIP-Seq libraries from chromatin immunoprecipitation (ChIP)-derived DNA. Leveraging NGS, ChIP-Seq can quickly and efficiently determine the distribution and abundance of DNA-bound protein targets of interest across the genome. ChIP-Seq is one of the most widely used NGS applications, enabling researchers to simultaneously and reliably identify binding sites from a broad range of targets across the entire genome, with high resolution and without constraints.

Chromatrap
For info: +44-(0)-1978-666222
www.chromatrap.com/uniqseq

PBS-Only Antibodies

Abcam's new phosphate buffered saline (PBS)-only recombinant antibodies are free from preservatives and stabilizing agents, offering improved flexibility for researchers conducting more complex experiments. Typically, antibodies are stored in a buffer composed of bovine serum albumin (BSA), glycerol, and sodium azide to ensure stability. However, these components can inhibit effective conjugation to certain dyes and enzymes, or they can be toxic to live cells. In a concentrated solution, without BSA, glycerol, or azide, PBS-only antibodies are ideally suited to antibody-labeling, functional, and cell-based assays as well as live-cell imaging applications. Developed using Abcam's rabbit monoclonal recombinant technology, these antibodies are highly reproducible, ensuring batch-to-batch consistency. They are extensively validated across a wide range of applications, including flow cytometry, Western blot, chromatin immunoprecipitation, immunocytochemistry, immunohistochemistry, and knockout validation. Abcam is now making over 2,300 PBS-only antibodies available via its catalog for global researchers.

Abcam
For info: 888-772-2226
www.abcam.com/pbs-only

Single-Cell Analyzer

The Celsee Genesis system provides a robust, scalable, and flexible way to analyze and interpret cellular behavior, and to collect critical cell-based information that was previously undetectable. The system uses a gentle, gravity-based method to capture and isolate individual cells while maintaining viability and structural integrity. The workflow achieves capture efficiencies of >70% and improved sensitivity versus other techniques for single-cell analysis. This open, flexible platform can be used directly with blood and tissue samples, offering a practical solution for understanding and monitoring cell-based diseases, whether users are interested in studying an individual cell or millions of cells from one sample.

Celsee
For info: 734-233-3089
www.celsee.com

Rabbit Monoclonal Antibodies

Abwiz Bio has a unique phospho antibody development platform for the creation of antibodies recognizing site-specific phosphorylation of target proteins. Our rabbit monoclonal antibodies (mAbs) are made using our phage-based RabWiz technology, which is ideally suited for phosphospecific applications; they are rigorously validated and optimized for use in Western blotting and flow cytometry (fluorescence-activated cell sorting) for the detection of protein phosphorylations. All our phospho antibody reagents are recombinant rabbit mAbs. Recombinant antibodies are more reliable than their polyclonal or hybridoma-produced counterparts; they exhibit little lot-to-lot variability due to complete immunoglobulin sequence characterization. Our RabWiz platform enables high-throughput capture, sequencing, and validation of dozens of possible phosphospecific antibodies, ensuring that only the best phospho antibody product is developed for each target. Contact us today and tell us to add your favorite phosphosite target to our constantly expanding product portfolio.

Abwiz Bio
For info: 858-352-6911
www.abwizbio.com/products/phospho-antibodies

Sonicator

The Covaris M220 Focused-ultrasonicator is designed for NGS applications that require high-quality DNA fragmentation for library preparation. It efficiently focuses the minimum amount of energy required directly into a sample, enabling precise control of the hydrodynamic shearing forces that fragment nucleic acids to the selected size. The process is isothermal, so fragmentation is unbiased, the sample is undamaged, and yields are high. Covaris focused-ultrasonic technology is considered a DNA-shearing standard in many labs worldwide.

Thermo Fisher Scientific
For info: 800-955-6288
www.thermofisher.com

ChIP Kit

The EpiQuik Chromatin Immunoprecipitation (ChIP) Kit is a complete set of optimized reagents to perform chromatin immunoprecipitation (ChIP) via a convenient, microplate-based format. It is ready-to-use and provides all the essential components needed to carry out a successful ChIP experiment. EpiQuik ChIP kits are suitable for combining the specificity of immunoprecipitation with qualitative and quantitative PCR, ChIP-Seq, and ChIP-on-chip. The kit enables the procedure to be completed within 5 h. The Strip microwell format allows the assay to be either manual or high throughput. EpiQuik is also compatible with all DNA-amplification-based approaches.

Epigentek
For info: 877-374-4368
www.epigentek.com

Electronically submit your new product description or product literature information! Go to www.sciencemag.org/about/new-products-section for more information.

Newly offered instrumentation, apparatus, and laboratory materials of interest to researchers in all disciplines in academic, industrial, and governmental organizations are featured in this space. Emphasis is given to purpose, chief characteristics, and availability of products and materials. Endorsement by *Science* or AAAS of any products or materials mentioned is not implied. Additional information may be obtained from the manufacturer or supplier.

Opportunities to shine at ShanghaiTech University

ShanghaiTech University is a young and dynamic higher education institution aiming for high-quality research and global influence. To address challenges faced by China and the world, it seeks innovative solutions in energy, materials, environment, human health, data science, artificial intelligence (AI), and electrical engineering. An integral part of the Zhangjiang Comprehensive National Science Center, the university is now leading several frontier research projects at large-scale facilities. For more information, please visit: www.shanghaitech.edu.cn.

We are now seeking talented researchers for multiple faculty positions at all ranks in the following fields:
School of Physical Science and Technology: energy, system materials, photon and condensed state, material biology, environmental science and engineering
School of Life Science and Technology: molecular and cell biology, structural biology, neuroscience, immunology, stem cells and regenerative medicine, system biology and biological data, molecular imaging, biomedical engineering
School of Information Science and Technology: computer science, electrical engineering, information engineering, artificial intelligence, network and communication, virtual reality, statistics, big data and data mining
School of Entrepreneurship and Management: economics, finance, accounting, management, marketing, strategy and entrepreneurship
School of Creativity and Art: film production, life drawing, photography, VR and game coding, illustration & visualization, performing arts
Shanghai Institute for Advanced Immunochemical Studies: antibody therapy, Immunotherapy, cell therapy, regeneration medicine
iHuman Institute: bio-imaging, biology, chemistry, computational biology, AI/ML
Institute of Mathematical Sciences: pure mathematics, theory of computing, applied mathematics

Successful applicants will have a doctoral degree, and are expected to establish a record for independent, internationally recognized research, supervise students and teach high-quality courses.

ShanghaiTech University will offer attractive compensation packages, **including: Initial research support package:** reasonable start-up funds, research associates and post-doctoral fellows, laboratory space to meet research needs

Compensation and benefits: highly competitive salary commensurate with experience and academic accomplishments, a comprehensive benefit package
Subsidized housing: on-campus, 80/100/120 m2 faculty apartments available at low rent for tenure and tenure-track faculty
Relocation & travel allowance: reimbursement of expenses for household relocation and family’s one-way travel
Family assistance: support with children’s education; affiliated kindergarten, primary and middle schools are under construction

To apply: using this format, please submit a cover letter (Firstname_Lastname_Cover_Letter.pdf), a research plan (Firstname_Lastname_Research_Plan.pdf), and a CV (Firstname_Lastname_CV.pdf) to shanghaitechuniversity@gmail.com.

PCR

applied biosystems invitrogen

One run—and done

Get to your PCR destination faster with Invitrogen™ Platinum™ II *Taq* Hot-Start DNA Polymerase, enabling 4x faster DNA synthesis and universal primer annealing, so you can co-cycle your assays together. One run and done. It's that simple.

Find out more at **thermofisher.com/platinumiitaq**

ThermoFisher
SCIENTIFIC

For Research Use Only. Not for use in diagnostic procedures. © 2018 Thermo Fisher Scientific Inc. All rights reserved.
All trademarks are the property of Thermo Fisher Scientific and its subsidiaries unless otherwise specified. **COL23024 1018**

Science Careers

SCIENCE CAREERS ADVERTISING

For full advertising details, go to ScienceCareers.org and click For Employers, or call one of our representatives.

AMERICAS

+1 202 326-6577
+1 202 326-6578
advertise@sciencecareers.org

EUROPE, INDIA, AUSTRALIA, NEW ZEALAND, REST OF WORLD

+44 (0) 1223 326527
advertise@sciencecareers.org

CHINA, KOREA, SINGAPORE, TAIWAN, THAILAND

+86 131 4114 0012
advertise@sciencecareers.org

JAPAN

+81 3-6459-4174
advertise@sciencecareers.org

CUSTOMER SERVICE

AMERICAS

+1 202 326-6577

REST OF WORLD

+44 (0) 1223 326528

advertise@sciencecareers.org

All ads submitted for publication must comply with applicable U.S. and non-U.S. laws. *Science* reserves the right to refuse any advertisement at its sole discretion for any reason, including without limitation for offensive language or inappropriate content, and all advertising is subject to publisher approval. *Science* encourages our readers to alert us to any ads that they feel may be discriminatory or offensive.

ScienceCareers
FROM THE JOURNAL SCIENCE AAAS

ScienceCareers.org

UT Health
San Antonio

Faculty Position – Department of Biochemistry and Structural Biology
University of Texas Health at San Antonio
Joe R. and Teresa Lozano Long School of Medicine

We are seeking outstanding candidates at all tenure-track or tenure levels for a faculty position in Biochemistry. All areas will be considered, but we are particularly interested in structural biology (X-ray crystallography, cryo-EM, NMR, or other biophysical approaches) and research that fits with our strategic focus on cancer, aging, infectious disease and diabetes. The Department houses University-supported core facilities in Macromolecular Structure and Interactions [NMR Spectroscopy, X-ray Crystallography, Surface Plasmon Resonance, Calorimetry (ITC, DSC)], Mass Spectrometry (proteomics and metabolomics), and the Center for Innovative Drug Discovery (High Throughput Screening and Medicinal Chemistry). (http://biochem.uthscsa.edu/core_facilities.php).

UT Health San Antonio, comprised of Medical, Graduate, Dental, Nursing and Health Profession schools, is home to the Nathan Shock Center for Aging, an NCI-designated cancer center and NIH Clinical Translational Science Award and the Center for Neuroscience. San Antonio is the 7th largest city in the U.S., with a historical downtown, diverse entertainment and restaurants on the Riverwalk, a vibrant economy, affordable housing and easy access to the scenic Texas Hill Country, with its many recreational opportunities.

Applicants must have high quality peer-reviewed publications and demonstrated ability to secure extramural funding. The position offers a generous start-up package, significant scientific resources and the potential for unique additional recruitment funds from the UT System and the State of Texas. Successful applicants will join a multidisciplinary team of 20 faculty in Biochemistry and Structural Biology (http://www.biochem.uthscsa.edu/), and will be expected to develop collaborative research programs, serve as mentors for students and research fellows and contribute to teaching in our graduate and professional programs. We are committed to a culturally and gender diverse faculty and all qualified applicants will receive consideration. The UT Health Science Center is designated as a Hispanic Serving Institution.

Interested candidates should visit http://uthscsa.edu/hr/employment.asp and apply online. Select the Faculty tab and enter job number **18000547** on the Keyword box. Please upload a *curriculum vitae*, a description of research interests, a list of three-four referees and a cover letter addressed to **Dr. Dmitri Ivanov, Chair of the Structural Biology Search Committee**. Please also have three reference letters sent directly to Esther James at jamese@uthscsa.edu. Review of applications will begin on January 1, 2019 and continue until the position is filled.

All faculty appointments are designated as security sensitive positions. The University of Texas Health at San Antonio is an Equal Employment Opportunity/Affirmative Action Employer including protected veterans and persons with disabilities.

FORCEFORSCIENCE.ORG

GET THE FACTS
FOLLOW AAAS ADVOCACY
TAKE ACTION

STAND TOGETHER

Be a Force for Science

AAAS

AMERICAN ASSOCIATION FOR THE ADVANCEMENT OF SCIENCE

National University of Defense and Technology

Welcome to join National University of Defense Technology and be a proud Nudter.

NUDT offers an extensive career platform, high-end working conditions, and a pleasant working environment. We provide anything you may want, and even things you may not have thought of.

Don’t be timid, feel free to contact us, we will always be looking forward to your message.

Contacts: Mr. Ke

Tel:+86-731-87000636

Mobile: +86-18707498661(Wechat available)

Email: rcb@nudt.edu.cn

Stress-Free Primary Education and Stricter Higher Education: Toward the Systematic Evolution of
Chinese Education

“We shouldn’t encourage high school students to study overly hard, nor should we encourage undergraduates to indulge themselves.” This remark was made by a leader of the Chinese Ministry of Education (MOE) at the International Forum on Higher Education Annual Conference, held in Ningbo, China, in early November of this year. Observers believe that his words summarize the systematic evolution of Chinese education that is intended in the government’s new policies for reforming both primary and undergraduate education, and in the Double First-Class University Project.

Bridging the divide between elementary and secondary education

For a long time, taking the college entrance exam—a “wooden bridge” that is extremely narrow relative to China’s huge population—has marked a dividing line for Chinese students between their lives before and after. Under the pressure of great competition and the traditional idea that “learning is the noblest of human pursuits,” many Chinese children receive education even before birth (prenatal education), and attend various training courses at a young age, including painting and foreign languages, to cultivate their tastes and learning abilities. For most students, such courses will run throughout their primary education years. At the same time, from kindergarten on, they are required to do a great deal of studying. Thick glasses and a heavy school bag can be seen on many children. For such reasons, Chinese students have been praised by overseas universities for their strong knowledge base, yet criticized for their lack of creativity and imagination.

However, this “Purgatory-like” schooling ends immediately after a student’s admission to university. For those who do not have enough self-discipline, the university is their paradise. Their lives will become a series of games, romantic relationships, and sleep. Learning will become secondary. Four years of shiftless pursuits results in a great waste of students’ academic ability and educational resources.

In summary, in the eyes of Chinese policy mak-

Shixin Wang
Deputy Chief Editor of China Education Online,
Chief Executive Editor of AcaBridge

ers, the problem lies, on the one hand, in the "cramming" method of primary education. Students are physically and mentally exhausted, and thus emptied of creativity. On the other hand, higher education is too lenient, and encourages students to waste their last golden years of learning before entering the real world.

The basic logic of treating diseases is to suit the remedy to the cause. For example, since the burden on students is heavy at the primary education stage, alleviating that burden is a natural cure, particularly for kindergarteners and very young pupils. Courses in kindergarten should be given in the form of games, and typical primary school curricula should be forbidden. Meanwhile, in-school time as well as homework should be reduced. Training institutions should be regulated to minimize burdens on K–12 students. The MOE has also formulated an implementation plan to clarify the responsibilities of all parties as well as prevent and control myopia among children and adolescents. The purpose of the plan is to reduce the heavy academic burden both in and out of the classroom.

As for higher education, we believe it is necessary to increase the burden on students and, more precisely, to become stricter with them, which is also in line with China's ongoing Double First-Class University Project.

Recently, Huazhong University of Science and Technology caused a great sensation by transferring 18 students whose credits are not up to standard from undergraduate to junior-college status—the incident can be regard as a landmark. China's MOE has also issued relevant policies to speed up the construction of high-level undergraduate education, known as the reformational "40 Polices on Higher Education for the New Era." The overall goal of these changes is to build several benchmark schools and first-class undergraduate programs within five years, and to form a world-class, high-level undergraduate education system with Chinese characteristics. This is also the first clear timetable and roadmap given by China for undergraduate education reform.

One of the new policies requires that for college students, examinations should "increase the proportion of process assessment results in the total results of a course" and should "improve the monitoring, evaluation, and feedback mechanism for the students' learning process." In terms of the form that examinations should take, it is emphasized that faculty should "integrate written examinations, oral examinations, nonstandard answer examinations, and other types of examinations." Another policy addresses the problem of students simply "going through the motions" in writing their graduate theses, and stipulates that the overall management of designing thesis topics and proposals should be strengthened, and that the form, content, and complexity of thesis defenses should be strictly supervised.

Focusing on faculty and students alike

It is worth noting that the new policies are not only strict with students, but also with university faculty. Many adjustments have been made to the evaluation system for faculty, including strengthening the evaluation of teaching performance and implementing a "one-vote veto" in the promotion of teachers. The policies state that the reward for outstanding teachers should be increased, and that teaching quality and scientific research ability should be regarded as equally important in professional evaluations, performance appraisals, and allowance allocations. For staff mainly engaged in teaching, basic salaries should be raised to a reasonable level.

The reforms also require monitoring teachers' personal credit histories, improving disciplinary mechanisms for teachers, constructing teacher development centers in colleges and universities, and providing training courses to improve faculty skills, so as to comprehensively enhance teachers' sense of responsibility and confidence.

In addition, the director of the MOE's Department of Higher Education mentioned in his recent speech that "unconscientious programs should be closed down." This remark is worth pondering. We should expect that as China's colleges and universities have been expanding rapidly for many years, some substandard programs would inevitably result. But if we want to build high-quality programs, we should eliminate those of poor quality. Therefore, the effective exercise of authority and standard-setting will have a great impact on the development of colleges and universities.

Evaluating policies: a work in progress

To build first-class undergraduate education is actually an important aspect of the Double First-Class University Project, and will certainly impact the standards of that project. After all, there are only two years left before the final evaluation of the project in 2020, and it has been reported that there will be a midterm evaluation, of which the most pressing concern is still the standards.

AcaBridge invites outstanding scholars from home and abroad to reach out to us. We'll help you contact colleges and universities, provide one-on-one, personal consultation, and help you learn about and apply for talent-recruitment programs. If you need any help, please contact our recruitment consultant at consultant@acabridge.edu.cn. For more details, visit our website at www.edu.cn/jjzg.

Introduction of Harbin Institute of Technology, Shenzhen

About Us

Founded in 1920, Harbin Institute of Technology (HIT), which is under the Ministry of Industry and Information Technology, is a national key university offers specializations in science, engineering, management and many other fields. It is a member of the C9 League and also the first universities to be part of Project 985 and one in list of "Double First-Class" University project.

HIT was ranked as the world's sixth best university for engineering, and the second in China, according to the 2018 US NEWS Global Universities ranking. In the Academic Ranking of World Universities (ARWU) 2017 ranking, it was eighth in China and among the global top 200. In the same year, HIT had a subject area ranked among the global top 0.01%, according to Essential Science Indicators (ESI) data.

Together with the Shenzhen Municipal Government, HIT founded Harbin Institute of Technology, Shenzhen (HITSZ), which was established in 2002 as HIT Shenzhen Graduate School and currently serves as a key campus of HIT. It is the first university in Shenzhen which belong to C9 League member, also in the list of Project 985 and "Double First-Class" University project which starts to enroll undergraduate students.

Shenzhen is a city born to innovate, Shenzhen has become a frontrunner in promoting innovation-driven development when China's economy steps into the new normal. Shenzhen is now widely known as a 'City of Makers' and a 'City of Innovation.' With a brand-new look, HITSZ will follow the HIT tradition, keep on the philosophy of high starting point, high standard to attract more international excellent talents and carries forward the Shenzhen spirit to serve as a contributor to national and regional economic and social development.

Teaching and Research

Among the 330+ full-time teachers in HITSZ, 80% of them have studied or worked overseas, and 90% have been recognized as high-level talents by the city and nation. HITSZ owns more than 40 key laboratories, engineering laboratories, and public platforms above municipal level. In terms of funds, HITSZ has years of accumulated scientific study funds amounting to over 1200 million RMB. What is more, HITSZ has undertaken more than 3000 scientific study programs and established cooperation with over 800 enterprises in Shenzhen, and has solved more than 1400 major technological issues. HITSZ has realized annual increase of 30% in the number of SCI paper for the last 5 years. Additionally, 10.3% ESI high cited papers of Shenzhen were from HITSZ.

Schools and Research Centers

HITSZ promotes interdisciplinary studies within 10 schools covering 22 disciplines. 34 research centers in different schools serve as the basic teaching and research units, which focus on developing avant-garde research to promote regional economic development.

For more details, please refer to www.hitsz.edu.cn.

ADVERTISEMENT

Northeast Forestry University

Invites Excellent Talents at Home and Abroad

Established in 1952 and located in Harbin – the beautiful “Ice City”, Northeast Forestry University is in national “211 Project” directly under the Ministry of Education of the People’s Republic of China and key construction projects of “Advantage Discipline Innovation Platform”. It is a multidisciplinary university integrating agriculture, science, industry, economics, management, culture, law, medicine and art with forestry science as its advantage and forestry engineering as its feature.

I. Recruitment of high-level talents

Relevant support policies for talents

NFEU vigorously implements the “5211” talent introduction plan, and provides a guarantee of talent for realizing the grand goal of building NEFU into a world-class forestry university and comprehensively promoting the construction of the “Double First class” university.

The level and treatment of imported talents (house purchase subsidy and personal emolument are both pre-tax) are as follows:

1. Leading Talents or Teams

Academicians of the Chinese Academy of Sciences, academicians of the Chinese Academy of Engineering, and foreign academicians of famous overseas academic institutions; Or someone who has obtained important scientific research results recognized by domestic and foreign counterparts, and has quite strong competitiveness and wide academic influence in the industry.

Remuneration: it depends on the talents’ condition

2. Distinguished Young Scholars

Scholars with a PhD who have published high-level academic papers in the top academic journals in the field; Outstanding young scholars at home and abroad who have the potential to get awards of talent programs such as Recruitment Program of Global Experts, National Science Fund for Distinguished Young Scholars, Changjiang Scholars Program, Young overseas high-level talents introduction plan, and National special support program for high-level talents, etc.; Scholars with a title at or above the level of associate professor from well-known overseas universities, or researchers with the same title as those from overseas well-known research academy (institute); The age is generally under 40 years old, especially distinguished ones can be relaxed to 45 years old.

Remuneration: Appointment as professor; Annual salary system, starting from RMB 300, 000 a year, Subsidies for house purchase starting from RMB500, 000,Start-up funds for scientific research in natural science and acquisition expenses of equipment starting from RMB 2, 000, 000, Start-up funds for scientific research in humanities and social science starting from RMB 300, 000 .

3. Excellent Young Scholars

Scholars with a PhD who have published high-level academic papers in the influential academic journals in the field; Outstanding young scholars at home and abroad who have the potential to get awards of projects such as Provincial Science Fund for Distinguished Young Scholars, Longjiang Scholars and Provincial Outstanding Young and Middle-aged experts, etc.; Generally under 35 years old, especially outstanding ones can be relaxed.

Remuneration: Appointment as professor or associate professor; House purchase subsidies are from RMB 150, 000 to RMB 300, 000; Start-up funds for scientific research in natural science and acquisition expenses of equipment range from RMB 300, 000 to RMB 1, 000, 000; Start-up funds for scientific research in humanities and social science range from RMB 100, 000 to RMB 300, 000 Implementation of the national wage and school allowance standard and additional post subsidy RMB 1000 per month in the first 2 years during the first employment period.

4. Young Backbone

A doctorate holder who is from a well-known university at home or abroad or who has been engaged in teaching or scientific research in a well-known academic institution at home or abroad for more than 3 years. Young backbone who has published high-level academic papers in the outstanding academic journals in the field, who has the ability to obtain the National Natural Science Foundation or the National Foundation for Philosophy and Social Sciences, and who has great development potential in academic and scientific research, etc. The age is generally under 35 years old, especially outstanding ones can be relaxed.

Remuneration: Appointment as associate professor or lecturer; House purchase subsidies are from RMB 80, 000 to RMB 150, 000; Start-up funds for scientific research in natural science and acquisition expenses of equipment range from RMB 150, 000 to RMB 300, 000; Start-up funds for scientific research in humanities and social science range from RMB 50, 000 to RMB 100, 000; Implementation of the national wage and school allowance standard and additional post subsidy RMB 1000 per month in the first 2 years during the first employment period.

5. Excellent Young Teachers

The excellent young teacher whose moral quality is high, with outstanding achievements and good academic development potential. The first degree should be a full-time undergraduate degree from a well-known university, and applicants should possess a doctoral candidate education background and a degree at a non-equivalent education level; A non-foreign language teacher should be proficient in a foreign language, and a foreign language teacher should reach level 8 of a professional foreign language. In principle, doctoral education background and degree are required and the age is generally under 35 years old.

Remuneration: The position of appointment shall be executed in accordance with the relevant documents; Implementation of the national wage and school allowance standards; House purchase subsidies are RMB 50, 000; Start-up funds for scientific research in natural science range from RMB 50, 000 to RMB 150, 000; Start-up funds for scientific research in humanities and social science range from RMB 30, 000 to RMB 50, 000.

NEFU recruits the flexible talents, and the treatment of flexible talents depends on the circumstances.

Contact Information

Ni Songyuan (**Tel:** +86-0451-82191327),
Zhang Chunlei (**Tel:** +86-0451-82190165)
Please submit your resume to nefumoe@vip.163.com

II. Recruitment of Full-time postdoctoral

Someone who has high moral quality, outstanding achievements and good academic development potential, and could do full-time post-doctoral research in our university. Received a doctorate from a well-known university or research institution at home and abroad, and the doctoral time is generally no more than 3 years, generally under 35 years old.

Contact information

Zhang Ran (**Tel:**+86-0451-82192070)
Please submit your resume to nefubgb@nefu.edu.cn

The Second Laoshan Young Scholars Forum of Qingdao University in 2018

Time: December 19, 2018

Introduction to the Forum

As the poem goes, "Though the Mountain Tai is very high, it is not as gorgeous as Laoshan Mountain."Laoshan Mountain is the first peak of China's coastline, and has the name of "first mountain" at sea. It stands on the shore of the Yellow Sea, tall and majestic, with a long history and a strong culture. With its name coming from Laoshan Mountain, "Laoshan Forum" is one of the main platforms hosted by Qingdao University for talents introduction, aiming at building a high-level academic exchange platform for outstanding young scholars at home and abroad in various disciplines to discuss the hot researches of different subjects around the academic development frontier, promote academic exchanges and cooperation, and enhance mutual understanding and friendship.

Qingdao University is a key comprehensive university in Shandong Province. Located in the famous historical and cultural city of Qingdao, it nestles below Fushan Mountain and faces the Yellow sea. The university now has a number of national science and technology innovation platforms: State Key Laboratory, National Joint Engineering Research Center, National-level International Research Collaboration Base, Programme of Introducing Talents of Discipline to Universities, National-level International Joint Research Center etc. The university has more than 40 provincial science and technology innovation platforms: Provincial Collaborative Innovation Center, Provincial Key Laboratory, Provincial Engineering Laboratory, Provincial Engineering Technical Research Center, Provincial Research Institute of Humanities and Social Sciences etc. There are 9 post-doctoral stations in the university and 13 first-level doctoral disciplines, 2 professional doctoral degree program, 37 first-level master degree programs, 6 second-level master degree programs, 23 professional master programs.

Qingdao University has fine disciplines, i.e., clinical medicine, engineering, chemistry, neuroscience and behavioral science, and materials science, listed as top 1% ESI disciplines, and ranks 50th in terms of top 1% disciplines among Chinese universities in the ESI global ranking in 2018. According to Shanghai Ranking's academic ranking of the world universities, Qingdao University ranks 701-800 in the world and 80th in Chinese mainland in 2018, and is considered as "the world's top 500 potential universities". It ranks 82nd among Chinese universities and 959th among world universities in US News 2019 world university rankings.

Adhering to the motto of "Morality Promotion, Extensive Learning, Truth Adherence and Innovative Practice", we insist on the school philosophy of "student-oriented education, teacher-oriented school running, service-oriented management and innovation-oriented development". With the idea of emancipating minds and deepening reform, we persist in connotation promotion, characteristic development, and striving for best, in order to build the school into an internationally renowned high-level university.

Subject Fields and Application Conditions

The subject fields of the Forum mainly focus on the characteristic and preponderant disciplines of our school, such as systematic science, medicine, textile science, chemistry, material science, engineering, biology, mathematics, physics, economics, management, etc.

1. Young talents, being eligible for applying for "Thousand Youth Talents Plan" of the Organization Department of the Central Committee of CPC, under 40 years old, with a doctor's degree from overseas well-known university or a doctor's degree from a domestic first-class university, continuously working abroad for more than 3 years or working at home within one year, and having achieved outstanding achievements or having great potential for development in the relevant areas.

2. Overseas outstanding young talents, being in line with the relevant requirements of our university's distinguished professor, under 40 years old, with a doctor's degree in domestic first-class university, and engaging in post-doctoral research or working for more than 2 years overseas.

3. Outstanding young talents, listed in "China's Four Important Young Academic Titles".

Contact Information

Contact: Jiang Junkai and Ji Chaobin
Email: qdutalents@qdu.edu.cn / qddxrsc@163.com
Tel: +86-0532-85955849 / +86-0532-85951142
Fax: +86-0532-85953161
Web: http://www.qdu.edu.cn
Address: Human Resources Department of Qingdao University, 308 Ningxia Road, Qingdao, Shandong, China

Talents At Home And Abroad Are Invited By Harbin Engineering University For "Recruitment Program of Global Young Experts"

Harbin Engineering University (HEU) lies on the bank of the Songhua River in the "Ice City"--Harbin of northern China. The predecessor of HEU, the PLA Military Engineering Institute was established in 1953 (HaJungong). Now it is China's "three ocean disciplines and one nuclear discipline" (shipbuilding industry, naval equipment, marine engineering, nuclear energy applications) important personnel training fields and scientific research base. The university has typical feature of "three ocean disciplines and one nuclear discipline" as the advantage, it has entered into the list of "Double First-Class" construction.

I. Outstanding Leading Talents:

Annual Salary:

¥ 500,000 - ¥ 1,200,000/year.

Platform:

We will provide no less than ¥3,000,000 to the scientific researchers and no less than ¥ 1.000,000 to the social researchers to set up and start your study.

We will provide research offices and labs which are 20-150m^2.

We will provide important and necessary equipment and ensure the prior right of using the present experimental equipment.

We will provide supportive policies and opportunities to go abroad for visiting, communicating, and researching.

Team:

Your entire team of the research is welcome.

We can offer you academic secretary.

You have the right of hiring, promoting, distributing and commenting on your own team.

Environment:

You will enjoy the "Safe Family"---the policy of your settling green channel.

Smooth Transition--our Personnel Office will serve you at all aspects.

Relocation Expenses--we will offer ¥ 300,000-500,000 at your disposal.

Housing--we will offer you a house which is 110m^2or purchase subsidies ¥ 1,500,000 - ¥ 2,000,000.

Settlements of Relatives--we can help with the admission of your children and the employment of your spouse.

II. Young Leading Talents:

Annual Salary:

¥ 300,000 - ¥ 500,000/ year

Platform:

We will provide ¥500,000 - ¥1,500,000 to set up and start your study if necessary.

We will provide research offices and labs which are 20-120m^2.

We will provide important and necessary equipment and ensure your right of using the present experimental equipment.

We will provide you good policies and opportunities to go abroad for visiting, communicating, and researching.

Team:

We are looking forward to your own staffs or team of your research.

We can offer you academic secretary.

You will have the right of hiring, promoting, distributing and commenting on your own team.

Environment:

You will enjoy the "Safe Family"--the policy of your settling green channel.

Smooth Transition--our Personnel Office will serve you at all the aspects.

Relocation Expenses--we will offer ¥ 300,000 at your disposal.

Housing--we will offer you a house which is no less than 80m^2or purchase subsidies ¥ 1,000,000 - ¥ 1,500,000.

Settlements of Relatives - we can help with the admission of your children and employment of your spouse.

III. Young Top Talents:

Annual Salary:

¥ 200,000 - ¥ 300,000/ year

Platform:

We will provide ¥ 300,000 for you to set up and start your research if necessary.

We will provide research offices and labs which are 20-100m^2.

We will hire you as senior (vice-senior) professional.

We will let you enjoy the supportive policy of treatment for the HEU's young leading talents.

Team:

We are supporting the young leading talents of your own team cooperating with the HEU's team.

You are supporting to set up the youth academic team.

Environment:

We will offer settling in allowance: ¥100,000 - ¥200,000 at your disposal.

We will offer you relocating house or purchase subsidies according to HEU's regulations.

Contact person:
You Dandan, Ming Ming
Tel: +86-0451-82518061
mail: rencai@hrbeu.edu.cn

Chinese Universities Global Online Job Fair

For promoting the idea of connecting the world and servicing global talent, AcaBridge will convene a global online job fair in January, 2019, cordially inviting talent of various levels to sign up.

January, 10th, 2019.

(Beijing Time: 7:00 – 23: 00)

Online Interviews Portal:
www.edu.cn/cv, both computers and mobile devices work.

Sign up:
Scan the QR code to schedule a direct meeting with universities

Job Search please scan the QR code

2019

Email: zhaojia@eol.cn
Contact: Zhao Jia
Phone (WeChat) :
(+86) 13426240515

北京大学定量生物学中心
CENTER FOR QUANTITATIVE BIOLOGY

Faculty Positions in Biological Physics and Systems Biology

The Center for Quantitative Biology (CQB) at **Peking University (PKU)** invites applications for faculty positions at all ranks. We seek for creative individuals in all areas of biological physics and quantitative systems biology, broadly defined.

CQB (http://cqb.pku.edu.cn/) is dedicated to research and education at the interface between the physical and biological sciences. Current research areas include physical biology, mathematical biology, systems biology, synthetic biology and computational biology.

Applications are welcome all year round. For qualified applicants, PKU can sponsor their applications to the national (Young) Thousand Talents Program. Application materials (cover letter, CV, summary of research achievements and future research plan, all in a single PDF file) and three letters of reference should be sent to **Ms. Wei Xiao (gsmkyb@pku.edu.cn)**.

10 ways that *Science* Careers can help advance your career

1. Register for a free online account on **ScienceCareers.org**.
2. Search thousands of job postings and find your perfect job.
3. Sign up to receive e-mail alerts about job postings that match your criteria.
4. Upload your resume into our database and connect with employers.
5. Watch one of our many webinars on different career topics such as job searching, networking, and more.
6. Download our career booklets, including Career Basics, Careers Beyond the Bench, and Developing Your Skills.
7. Complete an interactive, personalized career plan at “my IDP.”
8. Visit our Career Forum and get advice from career experts and your peers.
9. Research graduate program information and find a program right for you.
10. Read relevant career advice articles from our library of thousands.

Visit **ScienceCareers.org** today — all resources are free

Science Careers

FROM THE JOURNAL SCIENCE AAAS

SCIENCECAREERS.ORG

DISCOVER THE FUTURE

TWO LEADING POSITIONS AT SCILIFELAB

To further strengthen our research environment and complement research areas already present at SciLifeLab, we are now looking to recruit two outstanding young group leaders to new Fellows positions. As part of the SciLifeLab Fellows program, you become an associate at our research center, as well as contract a position at one of our host universities.

Read more at: www.scilifelab.se/fellows. Application deadline: January 15, 2018.

Stockholm University

Assistant Professor in Computational Biology

Studies of algorithms, modelling and methodology, with applications in life sciences

Stockholm University

Assistant Professor in Environmental Genomics

Genomic studies of all kinds of non-human biota and their relationships to the environment, focusing on structure and function of ancient or recent systems

About SciLifeLab

As a national hub for molecular biosciences in Sweden, SciLifeLab (Science for Life Laboratory) facilitates cutting-edge, multi-disciplinary life science research and promotes its translation to the benefit of society. The center focuses on both health and environmental research and is jointly operated by its four founder universities: KTH Royal Institute of Technology, Karolinska Institutet, Stockholm University, and Uppsala University. About 200 research groups, 1500 researchers and 40 national infrastructure facilities are associated with SciLifeLab.

SciLifeLab

Science Careers online @sciencecareers.org

Advance your career with expert advice from *Science* Careers.

Download Free Career Advice Booklets!
ScienceCareers.org/booklets

Featured Topics:

- Networking
- Industry or Academia
- Job Searching
- Non-Bench Careers
- And More

Science Careers
FROM THE JOURNAL SCIENCE AAAS

myIDP: A career plan customized for you, by you.

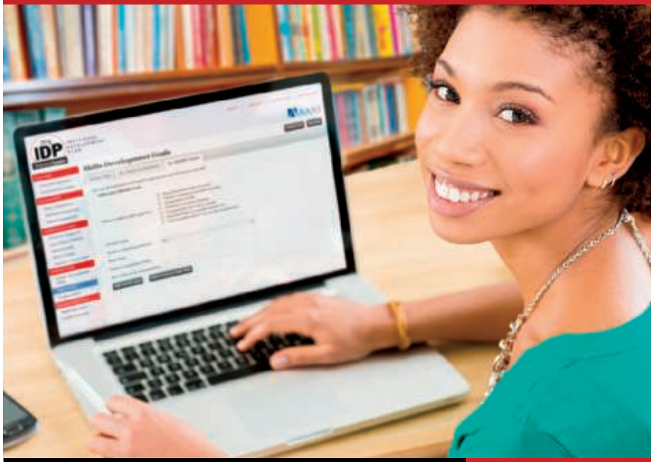

For your career in science, there's only one **Science**

my IDP ScienceCareers

Recommended by leading professional societies and the NIH

Features in myIDP include:

- Exercises to help you examine your skills, interests, and values.
- A list of 20 scientific career paths with a prediction of which ones best fit your skills and interests.
- A tool for setting strategic goals for the coming year, with optional reminders to keep you on track.
- Articles and resources to guide you through the process.
- Options to save materials online and print them for further review and discussion.
- Ability to select which portion of your IDP you wish to share with advisors, mentors, or others.
- A certificate of completion for users that finish myIDP.

Visit the website and start planning today!
myIDP.sciencecareers.org

ScienceCareers AAAS In partnership with:

advancing the life sciences 1912-2012 FASEB Federation of American Societies for Experimental Biology

Medical College of Wisconsin

UCSF University of California San Francisco

BURROUGHS WELLCOME FUND

AUS | الجامعة الأمريكية في الشارقة
American University of Sharjah

American University of Sharjah, one of the Middle East's leading universities, has set itself an ambitious research agenda, pushing the limits of science and engineering and providing exciting opportunities for those seeking to realize the university's research goals.

AUS is a preeminent and top-ranked university in the region, currently embarking on a massive new era in research, founding seven new research entities:

- Biosciences and Bioengineering Research Institute (BBRI)
- Materials Science and Engineering Research Institute (MSERI)
- Gulf Environments Research Institute (GERI)
- Smart Cities Research Institute (SCRI)
- High-Performance Computing Center (HPCC)
- Geospatial Analysis Center (GAC)
- Genomics Research Laboratory (GRL)

To learn more about the AUS research agenda, and the opportunities available, visit: **www.aus.edu/research**

WORKING LIFE

By **Paul N. Frater** *and* **Lauren L. Sullivan**

A short guide to working remotely

We were ecstatic when our supervisors allowed us to work remotely. Friends in graduate school, we hadn't worked in the same place in years. But our lives had taken a similar turn. Paul—a scientist at a state agency at the time—was living apart from his wife on weekdays. Every Friday he'd leave his office and drive 3 hours to spend the weekend at home, but with his wife pregnant with their first child, that situation would soon become untenable. Lauren, a newly married postdoc, lived in a different state than her husband and was growing weary of long-distance romance. Our work lives revolved around computer analyses and writing, so remote work was feasible. It seemed like an ideal solution.

Paul, an introvert, harbored fantasies of burying himself in computer tasks, free of the noise and distractions of offices. But when he started to work from home, he struggled to maintain focus and avoid getting sucked into house chores. As Wisconsin's bitter winter took hold, snow buried his office window, and he felt closed in. Three months into his new arrangement, he learned that Lauren, an extrovert, was also working from home. He found some relief in learning that she, too, was struggling with isolation.

ILLUSTRATION: ROBERT NEUBECKER

> ***"We weren't about to give up on remote work, but we needed better ways to cope."***

We weren't about to give up on remote work, but we needed better ways to cope. The two of us began to email back and forth, sharing challenges we faced and methods we'd found helpful for staying productive. After we got into the swing of things, we surveyed 16 other remote scientists to generate some tips for success.

SET REALISTIC GOALS. When you don't have a boss looking over your shoulder, you become your own taskmaster. Setting small, manageable daily tasks that contribute to your longer-term goals can help keep you on track. Make sure to hold yourself accountable, for instance by scheduling regular check-ins with a supervisor or colleague.

BE CONSISTENT. Wake up each morning, change out of your pajamas, and maintain a regular schedule. Act as if you have a job to go to—because, after all, you do.

REDUCE DISTRACTIONS. Do not let laundry, dishwashing, cleaning, and other chores consume your workday. You may also have to guard against social disruptions, as some people seem to think that if you work remotely, you can do whatever you want at any time of day.

CREATE A DISCRETE WORKSPACE. When you're working, be at work—both mentally and physically. It helps to have a separate office. If that's not possible, try to arrange your furniture in a way that distinguishes your work and nonwork space.

REWARD PRODUCTIVITY. If you are productive for an hour or two and accomplish a task, then treat yourself to a 15-minute break. Get a cup of coffee, take a walk, browse the internet, play with your dog, or do something else that you enjoy.

SEEK OUT HUMAN INTERACTION. Scientific discovery is collaborative, and it can be difficult to interact with colleagues while working from home. Get out and attend meetings and conferences. Schedule Skype calls with other scientists or communicate via Slack. Consider spending a few hours working in a social setting such as a coffee shop.

When we first started to work remotely, we suffered from feelings of entrapment and isolation. But now—3.5 years in for Paul and 2 years in for Lauren—we've learned how to manage our new arrangement so that we can be productive scientists and live in the same city as our loved ones. We're not planning on a lifetime of full-time remote work—in fact, Lauren's remote journey will be over when she starts a faculty position next month—but we have to say that remote working has its perks. For one thing, it's hard to complain about a 10-second commute. ■

Paul N. Frater is a Ph.D. candidate at the University of Iceland, working in Stevens Point, Wisconsin. Lauren L. Sullivan is a postdoctoral researcher at the University of Minnesota, working in St. Louis, Missouri. Send your career story to SciCareerEditor@aaas.org.

Downloaded from http://science.sciencemag.org/ on December 10, 2018

Published by AAAS